Metal nanostructures supported on carbon nanomaterials as a novel catalyst for heterogeneous reactions

A thesis submitted in partial fulfilment of the requirements for the Degree of

Doctor of Philosophy in Chemical and Process Engineering

by

Luqmanulhakim Baharudin

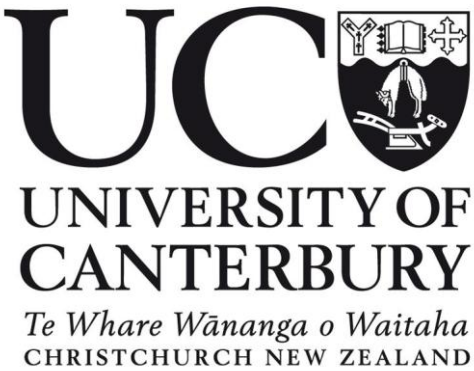

May 2019

Abstract

Carbon nanomaterials offer a sufficient surface area for hosting highly-dispersed catalytically active metal nanostructures, for an effective diffusion of reactant/product molecules in gas-phase heterogeneous reactions. This thesis has a main general objective to develop a novel copper (Cu)-based catalyst supported on multi-walled carbon nanotubes (MWCNT) for reactions that involve carbon monoxide (CO) conversion. A family of novel catalysts was generated using chemically synthesised, atomically precise hexameric Cu nanoclusters (Cu_6) deposited on carboxyl (–COOH)-pre-functionalised MWCNT ($MWCNT_{COOH}$); $Cu_6/MWCNT_{COOH}$. The fabrication, characterisation, and activity study of the synthesised catalysts were developed in three stages: Catalyst Development; Catalyst Fabrication and Hypothesis Development; and Catalytic Assessment and Feasibility Studies, with a specific objective to produce a finalised novel catalyst that: (1) is optimal in terms of its synthesis parameters, Cu loading content, Cu nanostructure precursor, and catalyst support; (2) possesses structural characteristics of reasonably high dispersion of Cu nanostructures of sufficiently small crystallite size and high surface area; and (3) exhibits satisfactory level of catalytic activity in the CO conversion reaction.

The Cu_6 cluster complex has a crystal structure of $[(PPh_3)CuH]_6.0.75THF$ as determined by single-crystal X-ray diffraction (SCXRD). When deposited on the MWCNT support, the hexameric copper hydride, $(CuH)_6$ changed its phase to Cu_2O by oxidation with air at ambient as determined by powder X-ray diffraction (PXRD). The active site characterisation analysis based on interpretation of the CO temperature-programmed desorption (CO-TPD) profiles elucidated by Langmuir–Hinshelwood (L–H) mechanism for low-temperature water–gas shift (LTWGS) reaction predicted that the optimal catalyst, $1\%Cu_6/MWCNT_{COOH}$ was active for LTWGS reaction from 120 °C (governed by dew point of water) up to well below 190 °C (constrained by temperature rise due to the exothermic reaction that leads to Cu sintering).

To experimentally validate the hypothetical prediction, actual activity tests were conducted in CO oxidation, a reaction of which the elementary steps in its mechanism involve the same

surface-reaction elementary step as in the LTWGS reaction mechanism where the CO molecules scavenge the surface-adsorbed oxygen molecules and react to produce carbon dioxide (CO_2). It was demonstrated that the bare pristine MWCNT by itself was catalytically active for CO oxidation from approximately 150 °C, and a CO conversion of greater than 98% was reached at approximately 230 °C. However, in these temperatures, the bare MWCNT modified with the –COOH groups adsorbed significant quantities of CO molecules without further catalytic converting. The –COOH groups degraded thermally progressively from approximately 250 °C. The Cu_2O species from the Cu_6 cluster species precursor was demonstrated to have formed $CuCO_3$ under the CO oxidation reaction conditions of below 330 °C. The $CuCO_3$ decomposed effectively from 400 °C to release CO_2 product. A minimum working temperature of 400 °C was required to allow an effective conversion of CO into CO_2 on the $Cu_6/MWCNT_{COOH}$ catalysts. On the other hand, a reference $MWCNT_{COOH}$-supported catalyst prepared using copper nanoparticles (Cu_{NP}) precursor that was not covered by any surfactants or capping agents was demonstrated to be active from 190 °C and approached a full CO conversion at slightly below 330 °C.

Keywords: active site characterisation; adsorption limited; carbon nanomaterials; carboxyl groups; catalyst synthesis; catalytic activity; copper nanoclusters; copper nanoparticles; CO chemisorption; CO conversion; CO temperature-programmed desorption; CO oxidation; CO oxidation inhibition; heterogeneous reactions; kinetic study; Langmuir–Hinshelwood; multi-walled carbon nanotubes; rate-determining step; reaction mechanism; reaction rate expression; steam methane reforming; water–gas shift.

Graphical abstract

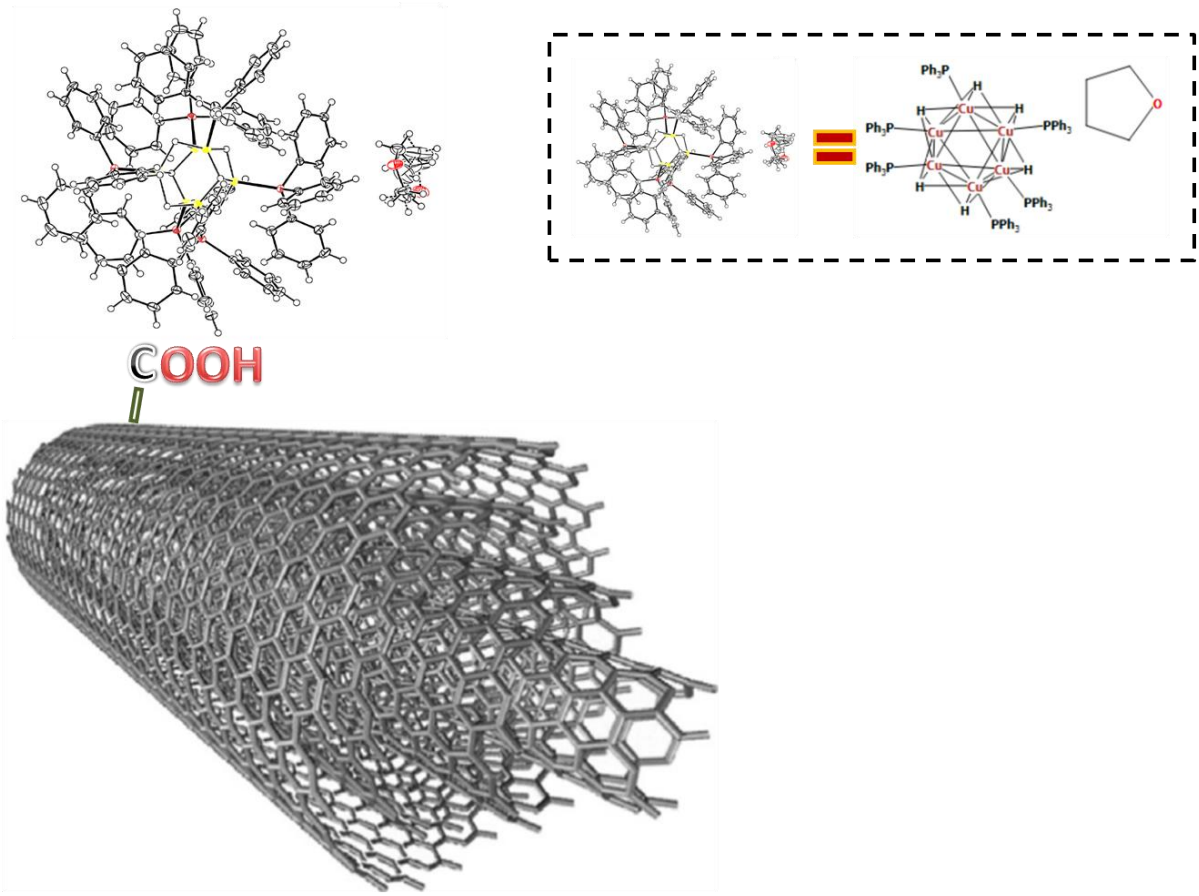

Deputy Vice-Chancellor's Office
Postgraduate Research Office

UNIVERSITY OF CANTERBURY
Te Whare Wānanga o Waitaha
CHRISTCHURCH NEW ZEALAND

Co-Authorship Form

This form is to accompany the submission of any thesis that contains research reported in co-authored work that has been published, accepted for publication, or submitted for publication. A copy of this form should be included for each co-authored work that is included in the thesis. Completed forms should be included at the front (after the thesis abstract) of each copy of the thesis submitted for examination and library deposit.

Please indicate the chapter/section/pages of this thesis that are extracted from co-authored work and provide details of the publication or submission from the extract comes:

Parts of Sections 1.1 and 1.2 of Chapter 1 contain excerpts of published article:

1) **Baharudin, L. & Watson, M.J. (2017). Hydrogen applications and research activities in its production routes through catalytic hydrocarbon conversion. *Reviews in Chemical Engineering*, 34(1), 43-72.**

Please detail the nature and extent (%) of contribution by the candidate:

The candidate contributed 100% to the authorship of the article as the lead author who wrote the text (which includes revisions and addressing the comments). The co-authorship line is made up of the candidate's supervisory team who played role as the candidate's supervisors; providing feedback, critical review/insights, comments and questions for clarifications, arguments and suggestions for improvements of the article.

Certification by Co-authors:
If there is more than one co-author then a single co-author can sign on behalf of all
The undersigned certifies that:

- The above statement correctly reflects the nature and extent of the PhD candidate's contribution to this co-authored work
- In cases where the candidate was the lead author of the co-authored work he or she wrote the text

Name: *Associate Professor Matthew Watson* Signature: Matthew Watson Date: *31 May 2019*

Deputy Vice-Chancellor's Office
Postgraduate Research Office

UNIVERSITY OF CANTERBURY
Te Whare Wānanga o Waitaha
CHRISTCHURCH NEW ZEALAND

Co-Authorship Form

This form is to accompany the submission of any thesis that contains research reported in co-authored work that has been published, accepted for publication, or submitted for publication. A copy of this form should be included for each co-authored work that is included in the thesis. Completed forms should be included at the front (after the thesis abstract) of each copy of the thesis submitted for examination and library deposit.

Please indicate the chapter/section/pages of this thesis that are extracted from co-authored work and provide details of the publication or submission from the extract comes:

Parts of Sections 1.1, 1.2.1, 1.2.2, 1.2.3 and 1.3.1 of Chapter 1 contain excerpts of published article:

2) **Baharudin, L. & Watson, M.J. (2017). Monolithic substrate support catalyst design considerations for steam methane reforming operation. *Reviews in Chemical Engineering*, 34(4), 481-501.**

Please detail the nature and extent (%) of contribution by the candidate:

The candidate contributed 100% to the authorship of the article as the lead author who wrote the text (which includes revisions and addressing the comments). The co-authorship line is made up of the candidate's supervisory team who played role as the candidate's supervisors; providing feedback, critical review/insights, comments and questions for clarifications, arguments and suggestions for improvements of the article.

Certification by Co-authors:
If there is more than one co-author then a single co-author can sign on behalf of all
The undersigned certifies that:

- The above statement correctly reflects the nature and extent of the PhD candidate's contribution to this co-authored work
- In cases where the candidate was the lead author of the co-authored work he or she wrote the text

Name: *Associate Professor Matthew Watson* Signature: Matthew Watson Date: *31 May 2019*

Deputy Vice-Chancellor's Office
Postgraduate Research Office

UNIVERSITY OF CANTERBURY
Te Whare Wānanga o Waitaha
CHRISTCHURCH NEW ZEALAND

Co-Authorship Form

This form is to accompany the submission of any thesis that contains research reported in co-authored work that has been published, accepted for publication, or submitted for publication. A copy of this form should be included for each co-authored work that is included in the thesis. Completed forms should be included at the front (after the thesis abstract) of each copy of the thesis submitted for examination and library deposit.

Please indicate the chapter/section/pages of this thesis that are extracted from co-authored work and provide details of the publication or submission from the extract comes:

Chapter 2 is a complete reproduction of a published article:

3) **Baharudin, L., Yip, A.C.K., Golovko, V. & Watson, M. (2018). Potential of metal monoliths with grown carbon nanomaterials as catalyst support in intensified steam reformer: a perspective. *Reviews in Chemical Engineering*, 0(0), pp.**

Please detail the nature and extent (%) of contribution by the candidate:

The candidate contributed 100% to the authorship of the article as the lead author who wrote the text (which includes revisions and addressing the comments). The co-authorship line is made up of the candidate's supervisory team who played role as the candidate's supervisors; providing feedback, critical review/insights, comments and questions for clarifications, arguments and suggestions for improvements of the articles.

Certification by Co-authors:
If there is more than one co-author then a single co-author can sign on behalf of all
The undersigned certifies that:

- The above statement correctly reflects the nature and extent of the PhD candidate's contribution to this co-authored work
- In cases where the candidate was the lead author of the co-authored work he or she wrote the text

Name: *Associate Professor Matthew Watson*	Signature: Matthew Watson	Date: *31 May 2019*

Deputy Vice-Chancellor's Office
Postgraduate Research Office

UNIVERSITY OF CANTERBURY
Te Whare Wānanga o Waitaha
CHRISTCHURCH NEW ZEALAND

Co-Authorship Form

This form is to accompany the submission of any thesis that contains research reported in co-authored work that has been published, accepted for publication, or submitted for publication. A copy of this form should be included for each co-authored work that is included in the thesis. Completed forms should be included at the front (after the thesis abstract) of each copy of the thesis submitted for examination and library deposit.

Please indicate the chapter/section/pages of this thesis that are extracted from co-authored work and provide details of the publication or submission from the extract comes:

Chapter 4 is a complete reproduction of a published article:

4) **Baharudin, L., Yip, A.C.K., Golovko, V.B., Polson, M.I.J. & Watson, M.J (2018). CO temperature-programmed desorption of a hexameric copper hydride nanocluster catalyst supported on functionalised MWCNTs for active site characterisation in a low-temperature water–gas shift reaction.** ***Chemical Engineering Journal*****, 0(0), pp.**

Please detail the nature and extent (%) of contribution by the candidate:

The candidate contributed 100% to the research work carried out in the preparation of the published article. The candidate contributed 100% to the authorship of the article as the lead author who wrote the text (which includes revisions and addressing the comments). The co-authorship line is made up of the candidate's supervisory team who played role as the candidate's supervisors; providing feedback, critical review/insights, comments and questions for clarifications, arguments and suggestions for improvements of the articles.

Certification by Co-authors:
If there is more than one co-author then a single co-author can sign on behalf of all
The undersigned certifies that:

- The above statement correctly reflects the nature and extent of the PhD candidate's contribution to this co-authored work
- In cases where the candidate was the lead author of the co-authored work he or she wrote the text

Name: *Associate Professor Matthew Watson* Signature: Date: *31 May 2019*

Deputy Vice-Chancellor's Office
Postgraduate Research Office

UNIVERSITY OF CANTERBURY
Te Whare Wānanga o Waitaha
CHRISTCHURCH NEW ZEALAND

Co-Authorship Form

This form is to accompany the submission of any thesis that contains research reported in co-authored work that has been published, accepted for publication, or submitted for publication. A copy of this form should be included for each co-authored work that is included in the thesis. Completed forms should be included at the front (after the thesis abstract) of each copy of the thesis submitted for examination and library deposit.

Please indicate the chapter/section/pages of this thesis that are extracted from co-authored work and provide details of the publication or submission from the extract comes:

Chapter 5 is a complete reproduction of a manuscript submitted for publication:

5) **Baharudin, L., Yip, A.C.K., Golovko, V.B., Polson, M.I.J. & Watson, M.J (2019). CO oxidation and the inhibition effects of carboxyl groups and copper-clusters on multi-walled carbon nanotubes. *Applied Catalysis B: Environmental*, submitted.**

Please detail the nature and extent (%) of contribution by the candidate:

The candidate contributed 100% to the research work carried out in the preparation of the manuscript. The candidate contributed 100% to the authorship of the manuscript as the lead author who wrote the text (which includes revisions and addressing the comments). The co-authorship line is made up of the candidate's supervisory team who played role as the candidate's supervisors; providing feedback, critical review/insights, comments and questions for clarifications, arguments and suggestions for improvements of the manuscript.

Certification by Co-authors:
If there is more than one co-author then a single co-author can sign on behalf of all
The undersigned certifies that:

- The above statement correctly reflects the nature and extent of the PhD candidate's contribution to this co-authored work
- In cases where the candidate was the lead author of the co-authored work he or she wrote the text

Name: *Associate Professor Matthew Watson* Signature: Matthew Watson Date: *31 May 2019*

Deputy Vice-Chancellor's Office
Postgraduate Research Office

UNIVERSITY OF CANTERBURY
Te Whare Wānanga o Waitaha
CHRISTCHURCH NEW ZEALAND

Co-Authorship Form

This form is to accompany the submission of any thesis that contains research reported in co-authored work that has been published, accepted for publication, or submitted for publication. A copy of this form should be included for each co-authored work that is included in the thesis. Completed forms should be included at the front (after the thesis abstract) of each copy of the thesis submitted for examination and library deposit.

Please indicate the chapter/section/pages of this thesis that are extracted from co-authored work and provide details of the publication or submission from the extract comes:

Chapter 6 is a complete reproduction of a manuscript prepared for a publication submission:

6) **Baharudin, L., Severinsen, I., Yip, A.C.K., Golovko, V.B. & Watson, M.J (2019). Kinetics and constraints of CO oxidation over hexameric copper nanocluster catalyst supported on carboxyl-functionalised MWCNT at high temperatures. *Applied Catalysis A: General*, ready for submission.**

Please detail the nature and extent (%) of contribution by the candidate:

The candidate contributed 100% to the experimental research work carried out in the preparation of the manuscript, prepared for publication submission. The candidate contributed 95% (based on word count) to the authorship of the manuscript as the lead author who wrote the text (which includes revisions and addressing the comments), whereas the remaining 5% was contributed by Isaac Severinsen, a Master's degree candidate who provided numerical analysis to complement the experimental analysis to determine the reaction kinetic data (identified and highlighted accordingly in Chapter 6 of the thesis). The remaining co-authorship line is made up of the candidate's supervisory team who played role as the candidate's supervisors; providing feedback, critical review/insights, comments and questions for clarifications, arguments and suggestions for improvements of the manuscript.

Certification by Co-authors:
If there is more than one co-author then a single co-author can sign on behalf of all
The undersigned certifies that:

- The above statement correctly reflects the nature and extent of the PhD candidate's contribution to this co-authored work
- In cases where the candidate was the lead author of the co-authored work he or she wrote the text

Name: *Associate Professor Matthew Watson* Signature: Date: *31 May 2019*

Publications / conferences

Published journal articles

Baharudin, L. & Watson, M.J. (2017). Hydrogen applications and research activities in its production routes through catalytic hydrocarbon conversion. *Reviews in Chemical Engineering*, 34(1), 43-72.

Baharudin, L. & Watson, M.J. (2017). Monolithic substrate support catalyst design considerations for steam methane reforming operation. *Reviews in Chemical Engineering*, 34(4), 481-501.

Published (in press) journal articles

Baharudin, L., Yip, A.C.K., Golovko, V. & Watson, M. (2018). Potential of metal monoliths with grown carbon nanomaterials as catalyst support in intensified steam reformer: a perspective. *Reviews in Chemical Engineering*, 0(0), pp.

Baharudin, L., Yip, A.C.K., Golovko, V.B., Polson, M.I.J. & Watson, M.J (2018). CO temperature-programmed desorption of a hexameric copper hydride nanocluster catalyst supported on functionalised MWCNTs for active site characterisation in a low-temperature water–gas shift reaction. *Chemical Engineering Journal*, 0(0), pp.

Submitted manuscript

Baharudin, L., Yip, A.C.K., Golovko, V.B., Polson, M.I.J. & Watson, M.J (2019). CO oxidation and the inhibition effects of carboxyl-modification and copper-clusters on multi-walled carbon nanotubes. *Applied Catalysis B: Environmental*, correction stage post peer-review as at thesis submission date.

Manuscript ready for submission

Baharudin, L., Severinsen, I., Yip, A.C.K., Golovko, V.B. & Watson, M.J (2019). Kinetics and constraints of CO oxidation over hexameric copper nanocluster catalyst supported on carboxyl-functionalised MWCNT at high temperatures. *Applied Catalysis A: General*, ready for submission.

Conferences (oral presentation)

Baharudin, L., Yip, A.C.K., Golovko, V. & Watson, M. (2018). CO temperature-programmed desorption of hexameric copper hydride nanocluster catalyst supported on functionalised MWCNTs for active site characterisation in low-temperature water–gas shift. *25th International Conference on Chemical Reaction Engineering (ISCRE25)*, Florence, Italy, 20 – 23 May 2018.

Baharudin, L., Yip, A.C.K., Golovko, V. & Watson, M. (2018). Structural and active site characterisations of Cu_6 nanoclusters/multi-walled carbon nanotubes for low-temperature water–gas shift reaction. *3rd Australasian Particle Technology Society (APTS) Students Conference*, Lake Hayes, Queenstown, New Zealand, 29 Sep 2018.

Baharudin, L., Yip, A.C.K., Golovko, V. & Watson, M. (2018). Structural and active site characterisations of Cu_6 nanoclusters/multi-walled carbon nanotubes for low-temperature water–gas shift reaction. *47th Chemeca Conference*, Queenstown, New Zealand, 30 Sep – 3 Oct 2018.

Conferences (poster presentation)

Baharudin, L., Yip, A.C.K., Abrahamson, J. & Watson, M. (2017). Potential of carbon nanomaterials as metal monolith's surface textural promoter for well dispersed catalyst. *25th International Conference on Processing and Fabrication of Advanced Materials (PFAM-XXV)*, University of Auckland, New Zealand, 22 – 25 January 2017.

Baharudin, L., Yip, A.C.K., Golovko, V. & Watson, M. (2018). On validating the hypothetically predicted activity of supported hexameric copper hydride nanocluster catalysts in a CO conversion reaction (CO oxidation). *Materials Cluster Conference*, University of Canterbury, Christchurch, New Zealand, 3 – 4 December 2018.

Acknowledgements

I am forever indebted to my beloved Mak, Puan Azizah Kasim, who has been pouring countless unconditional love throughout this wonderful journey of my life and to my arwah (late) Pak, Allahyarham Tuan Haji Baharudin Abd. Manaf who had loved me till his last breath. My PhD adventure could have never been as smooth without their blessings and prayers.

It was before the crack of dawn of May 1, 2016 while the people of Christchurch were still sleeping that I first set foot on this Kiwi land when I first met my main supervisor, Associate Professor Matthew Watson. He waited for me at the arrival hall of Christchurch Airport, drove and dropped me at the Graduate House at 23, Creyke Road with a bag filled with a full-week supply of groceries. I felt so warmly welcomed, and this foreign land had since become my home. I hit many bumps on this incredible quest but Matt was nothing short of motivational words. His continued support was beyond amazing. Matt empowered me to walk my own research path, believed in my capability every time I doubted my own self, and always ensured I was in my best state. Not only had he rendered moral supports to continuously drive and boost my motivation, Matt was also very generous in lending financial supports in approving my requests to purchase equipment parts and chemicals to fulfil my research needs, approving my requests for attending conferences, and supporting my proposal to collaborate with an external institution outside of New Zealand (even though the collaboration did not work out well). I hope I did not fail him for putting his trust on me every time he approved my extramural study applications to conduct work from outside New Zealand, and my leave applications to visit my family whenever I missed home and needed a break to keep my sanity intact. All these supports were rendered to ensure I reach my PhD goal successfully and for that, I can never thank Matt enough.

The appointment of my second supervisor, Dr. Alex Yip happened by chance. It started with me walking into his office to borrow some commercial catalyst samples from his research group to use in my reaction tests. What was meant to be a brief two-minute visit became an exciting long-hours discussion. After I finished explaining about my research plan, Alex

straight away got off his chair and walked towards the whiteboard hanging on the wall. He picked up a marker, listed down the steps in catalyst synthesis, and sketched a proposed experimental rig with some imaginary reactant conversion trends, which had shed light on important fundamentals in catalysis research I was lacking at that time. At that very moment I knew I would never agree to a second supervisor other than Alex. That decision was never wrong. Alex had offered tremendous support throughout my PhD journey.

My third supervisor, Associate Professor Vladimir Golovko appeared not so friendly and difficult the first time I met him when being introduced by Matt at Café 101. We went to seek for his help to illuminate some wet chemistry fundamentals in synthesising carbon nanotubes. Vlad offered a totally different approach than my other two supervisors. I must admit I would always feel uncomfortable and unready whenever I wanted to see him for advice and guidance that I would think more than twice every single time it happened. Indeed, Vlad had been tough (with a good intention) until the very last day of my PhD, but I truly appreciated his uneasy-to-please personality. I was very certain that his only intention was nothing more than to get the best out of me. His commitment, level of details and thoroughness in reviewing my thesis made me realise that he really cared and appreciated my work. This thesis could have not got any better without going through his honest critics and constructive feedback, even though it could be painful at times. It also made me realise that no matter how big the effort I had put in my work was, it would never be good enough as there would always be rooms for improvement. Hopefully, this will set as a reminder for me to always strive for betterment and to never be complacent. It was a truly humbling experience to have worked with Vlad.

I was blessed with wonderful friends, colleagues, administrative staff and technicians at both the Department of Chemical and Process Engineering (CAPE) and the School of Physical and Chemical Sciences to help me around whenever I needed support. This PhD course would have not sailed smoothly without these people whom had crossed-path my journey to be my angels. I would like to record my expression of gratitude to:

- Associate Professor Aaron Marshall and Associate Professor Ken Morison for their constructive feedback during my PhD proposal defense;

- Members of Alex's research group in general, especially: Dr. Matthew Macdonald and Dr. Dahong Jiang for showing the way around the Special Purpose Lab and for opening the path to my first catalyst synthesis attempt (I do not know where they are right now but I wish them success in their endeavours); Wasim Ullah Khan for showing the way on how to use BELCAT unit and the reactor setup, for the troubleshooting of the equipment and for all the useful discussions on the experimental results; Dr. Iman Hashemizadeh for his guidance on TEM's sample preparation and acid reflux setup; and Xuemin Li for showing how to use the TGA;
- Members of Vlad's research group: Felicitas Jansen and Mai Siriluck Tesana for their guidance around wet chemistry lab at West and Ernest Rutherford buildings especially in showing the way on how to use the Schlenk technique to synthesis the copper clusters;
- Friendly and efficient people of CAPE: Ranee Hearst and Joanne Pollard for handling my scholarship and other administrative matters; Glenn Wilson for easing all the procurement processes; Leigh Richardson, Graham Mitchell, Frank Weerts for fabricating the reactor tube; Stephen Beuzenberg and Graham Furniss for solving my electrical/electronics and computer issues; Rayleen Fredericks for showing how to use the zeta potentiostat; and Tim Moore and Michael Sandridge for all the general issues pertaining to the lab safety that I even lost count on how many times I turned to them for assistance;
- Wonderful people of the School of Physical and Chemical Sciences: Dr. Matthew Polson for his guidance in using the X-ray diffractometer and the analysis of the XRD patterns and the crystal data; Associate Professor Sally Gaw and Robert Stainthorpe for their guidance and help on ICP-MS; Dr. Paula Brooksby and Dr. Anna Farquhar for their guidance and help on FTIR; and Nick Oliver and Geoffrey Graham for getting the 5-channels reactor ready even though I did not get the chance to use the experimental rig;
- Mike Flaws (retired) of the Department of Mechanical Engineering for his guidance and help on TEM;
- Martin Ryan of Callaghan Innovation for XRD patterns and Dugra Devi of NANOCAT Research Centre for paving the way to my early analysis of XRD patterns;
- Professor Susan Krumdieck of the Department of Mechanical Engineering and Professor John Abrahamson (retired) for their knowledge sharing on the synthesis of carbon nanotubes in general;
- Gary Bennington of Johnson Matthey (JM) PLC for his generous supply of the JM's commercial catalyst samples;

- Isaac Severinsen for his numerical contribution in complementing my experimental analysis in the determination of the reaction kinetic data; AND
- Amazing postgraduates of CAPE!

Being away from home, my journey on this foreign land would have not been jovial without the presence of the fellow Malaysians by my side. Thank you my Malaysian brothers, sisters, nephews and nieces for being there and making me feel at home.

Last but not the least, my utmost appreciation goes to John Sutherland's Fund, Department of Chemical and Process Engineering, University of Canterbury for the financial support, without which this doctoral work would have not been possible. Thank you for the opportunity to let me taste the sweetness of this beautiful and breathtaking country, New Zealand!

Luqmanulhakim Baharudin

Abbreviations

Carbon nanomaterials' growth techniques

CVD	chemical vapour deposition
CCVD	catalytic chemical vapour deposition
PECVD	plasma enhanced chemical vapour deposition
PPCVD	pulsed pressure chemical vapour deposition

Carbon materials

CNF	carbon nanofibers
CNM	carbon nanomaterials
CNT	carbon nanotubes
MWCNT	multi-walled carbon nanotubes
$MWCNT_{acid}$	functionalised multi-walled carbon nanotubes by reflux of H_2SO_4 (98%): HNO_3 (62%) as the oxidising agent
$MWCNT_{acid,air}$	air-treated acid-functionalised multi-walled carbon nanotubes
$MWCNT_{COOH}$	carboxyl-functionalised multi-walled carbon nanotubes
$MWCNT_{hp}$	H_2O_2-treated multi-walled carbon nanotubes
$MWCNT_{hp,air}$	air-oxidised H_2O_2-treated multi-walled carbon nanotubes
$MWCNT_{p}$	pristine multi-walled carbon nanotubes
$MWCNT_{p,air}$	air-oxidised pristine multi-walled carbon nanotubes
SWCNT	single-walled carbon nanotubes

Chemicals / solvents for carbon functionalisation

DCM	dichloromethane
DI	deionised (water)
PDDA	poly(diallyldimethyl) ammonium chloride
PSS	polystyrene sulfonate
THF	tetrahydrofuran

Oxygen groups

–C=O	carbonyl groups
–COOH	carboxyl groups
–OH	hydroxyl groups

Fabricated materials / catalysts

Cu_n	copper clusters of atomic number (core size) *n*
Cu_{NP}	copper nanoparticles
Cu_6	hexameric copper nanoclusters
$[(PPh_3)CuH]_6.0.75THF$	empirical formula for the crystal structure of hexameric copper hydride ligated by triphenylphosphine and solvated with 0.75 mole of tetrahydrofuran molecule
Cu/MWCNT	copper catalyst supported on multi-walled carbon nanotubes
$Cu/MWCNT_{acid}$	copper nanoparticles deposited on acid-reflux-treated multi-walled carbon nanotubes by wet impregnation
$Cu/MWCNT_{COOH}$	copper nanoparticles deposited on carboxyl-functionalised multi-walled carbon nanotubes by wet impregnation

$Cu/MWCNT_{hp}$	copper nanoparticles from copper (II) chloride dihydrate precursor deposited on H_2O_2-treated multi-walled carbon nanotubes by wet impregnation
$Cu/MWCNT_{hp,CuAc}$	copper nanoparticles from copper (II) acetate monohydrate precursor deposited on H_2O_2-treated multi-walled carbon nanotubes by wet impregnation
$Cu/MWCNT_{hp,incipient}$	copper nanoparticles deposited on H_2O_2-treated multi-walled carbon nanotubes by incipient wetness impregnation
$Cu/MWCNT_{p}$	copper nanoparticles deposited on pristine multi-walled carbon nanotubes by wet impregnation
$Cu_{NC}/MWCNT_{COOH}$	copper nanoclusters deposited on carboxyl-functionalised multi-walled carbon nanotubes (= $Cu_6/MWCNT_{COOH}$)
$Cu_{NP}/MWCNT_{COOH}$	copper nanoparticle catalyst (methanol as the solvent in the copper solution) supported on carboxyl-functionalised multi-walled carbon nanotubes
$Cu_{NP,H2O}/MWCNT_{COOH}$	copper nanoparticles (deionised water as the solvent in the copper solution) deposited on carboxyl-functionalised multi-walled carbon nanotubes
Cu_6/Al_2O_3	hexameric copper nanocluster catalyst supported on alumina
$Cu_6/MWCNT_{COOH}$	hexameric copper nanocluster catalyst supported on carboxyl-functionalised multi-walled carbon nanotubes
$Cu_6/MWCNT_{p}$	hexameric copper nanocluster catalyst supported on pristine multi-walled carbon nanotubes
$(Cu_6/MWCNT_{COOH})_{calcined}$	calcined hexameric copper nanoclusters deposited on carboxyl-functionalised multi-walled carbon nanotubes

51%CuO/31%ZnO-Al_2O_3	51 wt.% copper oxide catalyst supported on alumina containing 31 wt.% zinc oxide promoter (reference commercial catalyst supplied by Johnson Matthey PLC)

Characterisations

ATR	attenuated total reflectance
ATR-FTIR	attenuated total reflectance Fourier-transform infrared
COA	Certificate of Analysis
CO-TPD	carbon monoxide temperature-programmed desorption
FTIR	Fourier-transform infrared
HRTEM	high resolution transmission electron microscopy
H_2-TPR	hydrogen temperature-programmed reduction/reaction
ICP-MS	inductively coupled plasma mass spectrometry
PXRD	powder X-ray diffraction
SEM	scanning electron microscopy
SCXRD	single-crystal X-ray diffraction
TEM	transmission electron microscopy
TGA	thermogravimetric analysis
TG-DTA	thermogravimetry and differential thermal analysis
TG-EGA	thermogravimetry and evolved gas analysis
TPD	temperature-programmed desorption
TPR	temperature-programmed reduction/reaction
XPS	X-ray photoelectron spectroscopy
XRD	X-ray diffraction

X-ray diffraction standard patterns/registrations

CCDC	Cambridge Crystallographic Data Centre
COD	Crystallography Open Database
ICDD	International Centre for Diffraction Data
PDF	powder diffraction file

Material properties

BET	Brunauer–Emmett–Teller
CTE	coefficient of thermal expansion
$CTE_{substrate}$	coefficient of thermal expansion of catalyst support substrate material
CTE_{tube}	coefficient of thermal expansion of reformer tube material
d	dispersion percentage of metal nanostructures on its support material
MW	molecular weight
SPV	specific pore volume
SSA	specific surface area

Reactions and mechanisms

E–R	Eley–Rideal
HTWGS	high-temperature water–gas shift
LTWGS	low-temperature water–gas shift
L–H	Langmuir–Hinshelwood
SMR	steam methane reforming

SR	steam reforming
WGS	water–gas shift
WGSR	water–gas shift reaction

Reaction conditions

GHSV	gas hourly space velocity
STP	standard temperature and pressure (T = 25 °C, P = 1 atm)
S:C	steam to carbon ratio

Hydrocarbons and chemical compounds

HHC	higher hydrocarbons
PAH	polycyclic aromatic hydrocarbons
VOC	volatile organic compounds

Instruments / detectors

FID	flame ionisation detector
GC	gas chromatography
MFC	mass flow controller
TCD	thermal conductivity detector

Table of contents

List of figures

In chapters

In appendices

List of tables

In chapters

In appendices

CHAPTER 1

Introduction

Research background

1.1 Motivation: Towards process intensification and heat transfer improvement by monolithic catalytic support system

In the big picture, the **motivation** that sets the stage of this doctoral work is **derived** based on challenges faced in the operations of an energy-intensive process; steam methane reforming (SMR), and opportunities towards achieving process intensification by monolithic catalytic support system.

The following section (*Italicised*) is an excerpt from a published review article [1]: "Baharudin, L. & Watson, M.J. (2017a). Hydrogen applications and research activities in its production routes through catalytic hydrocarbon conversion. *Reviews in Chemical Engineering*, 34(1), 43-72."

Steam reforming is a principal process for hydrogen and synthesis gas production in the industry, where more than 80% of global ammonia production is based on the hydrogen produced by steam reforming [2] prior to synthesis with nitrogen. The cost effectiveness of steam reforming of natural gas (methane) makes it the most common pathway for producing hydrogen and synthesis gas (syngas, i.e. hydrogen + carbon monoxide). The first step of the SMR process involves reaction of methane with steam at 697 – 827 °C to produce syngas (eq. (1.1)) [3].

SMR [4-5]:

$CH_4 + H_2O \leftrightarrow CO + 3\ H_2$ $\Delta H^0_{298} = +206\ kJ/mol$ *(1.1)*

Water–gas shift reaction (WGSR) or CO shift conversion (eq. (1.2)) is an important reaction step following SMR in a typical hydrogen or chemical plant or refinery where the remaining CO content in the reformer outlet (eq. (1.1)) is further converted for additional hydrogen generation alongside with carbon dioxide [3].

WGSR:

$CO + H_2O \leftrightarrow CO_2 + H_2$ $\Delta H^0_{298} = -41.09\ kJ/mol$ *(1.2)*

The overall SMR reaction is represented by the combined reaction (eq. (1.3)) [3].

Combined SMR and WGSR:

$CH_4 + 2\ H_2O \leftrightarrow CO_2 + 4\ H_2$ *(1.3)*

Excerpt from Baharudin & Watson (2017a) [1] ends here.

1.2 Research problem: Opportunities and challenges faced in the operations of energy-intensive processes – deriving the problem based on SMR operation

The following section (*Italicised*) is an excerpt from a published review article [1]:

"Baharudin, L. & Watson, M.J. (2017a). Hydrogen applications and research activities in its production routes through catalytic hydrocarbon conversion. *Reviews in Chemical Engineering*, 34(1), 43-72."

SMR is highly endothermic and takes place at very high temperatures (typical inlet temperature of 450 – 650 °C and outlet temperature of 700 – 950 °C). As commonly practiced, the SMR reaction takes place in metal tubes typically made of nickel chromium alloy steel such as HK40: Cr 25%, Ni 20%, Co 4% and IN519: Cr 24%, Ni 24%, Nb 1.5%, Co 3%, containing a packed bed of typically Ni/Al_2O_3 pellets. The slow and highly endothermic reaction requires large amounts of heat supplied via external combustion surrounding the reformer tubes, in which conventionally the heat transfer inside each tube is ineffective due to poor convection from the reactant species to the active catalyst sites and poor pellet-to-pellet heat conduction.

One significant research area in SMR of late is the modification of the catalyst support substrate to a monolith. Monolithic support substrates have been introduced where the catalysts are deposited on it and heat transfer efficiency is hence improved via the enhanced thermal conductivity of the monoliths, transferring the heat from the tube wall to the catalyst sites. This enhanced heat transfer leads to the realisation of the concept of a compact reformer process intensification, where a higher reaction rate is achieved in a smaller reactor at a significantly lower pressure drop. In the current industrial scale reformers, this novel reactor packing offers the benefits of overcoming the heat conduction limitation, decreasing the overall pressure drop in each reformer tube, and process intensification for an overall plant optimisation.

Excerpt from Baharudin & Watson (2017a) [1] ends here.

The following section (*Italicised*) is an excerpt from a published review article [6]:

"Baharudin, L. & Watson, M.J. (2017b). Monolithic substrate support catalyst design considerations for steam methane reforming operation. *Reviews in Chemical Engineering*, 34(4), 481-501."

In general, ceramics or metals are the most commonly used materials for the manufacturing of monolith support structures. Material selection criteria when considering specific

applications include cost and weight [7]. A monolithic structure such as honeycomb can be made of ceramics like cordierite ($2MgO\ 2Al_2O_3\ 5SiO_2$), or metals such as an iron/chromium alloy, FeCr alloy (Fe 72.8/Cr 22/Al 5/Y 0.1/Zr 0.1). These substrate materials exhibit excellent resistance to oxidation at elevated temperatures [8]. Cordierite, an extruded multi-cell ceramic of low thermal expansion was the substrate of choice of the monoliths used in the US's first large-scale catalytic converter installed in new vehicles, taking advantage of the material's property of high resistance to thermal shock fracture [7]. Other substrates of metal monolith are typically aluminium, stainless steel, and other comparable alloys. Aluminium is only good for application in mild temperatures well below its melting point of 660 °C. Between metal and ceramic monoliths, the possibility of fabricating thinner walls is greater for metal, where the open frontal area can approach 90% [6]. This would allow bigger channel diameter and hence offer even lower pressure drop at an equal or greater geometric surface area.

Listed in Table 1.1 are thermal and mechanical properties of possible monolithic support substrate materials; alumina, cordierite and carbon steel, for the purpose of making a judgement on which substrate material class is suitable for the selection in an application in a steam reformer. The reformer tube material IN519 is used as a basis for relative comparison with the monolithic substrate materials in terms of the thermal conductivity and the coefficient of thermal expansion (CTE). The three substrate materials are used in this comparison for the following reasons; alumina is a typical support material in the pelletised catalysts, cordierite is a typical ceramic material used as a monolithic support structure, and carbon steel is a typical metal substrate that could potentially be fabricated as a monolithic support structure. The products from Special Metals Corporation, INCOLOY ® 800H/800HT and INCONEL ® 625 are included as potential superalloy candidates for fabricating the metal monoliths, while HAYNES ® 230 is added as one of the candidates from Haynes International's portfolio of high-temperature alloys, for the purpose of making the comparison among some of the metal alloys commercially available in the market.

Table 1.1: *Thermal and mechanical properties of typical ceramic and metal materials used as supports in catalytic systems in comparison to the properties of a typical reformer tube material, IN519.*

	Thermal conductivity (W/m.K)	***Coefficient of thermal expansion (CTE) (µm/m.K)***	***$CTE_{substrate}$/ CTE_{tube}***	***Tensile strength (MPa)***	***Young's modulus (GPa)***	***Weibull modulus***
IN519	*12.7*[a]	*17.1*[a]				
Alumina	*35*[b]	*5.5*[b]	*0.32*	*280*[c]	*395*[b]	*10*[b]
Cordierite	*3*[c]	*1.7*[c]	*0.1*	*25.5*[c]	*70*[c]	*4.2*[d]
Carbon steel	*50*[e]	*13*[e]	*0.76*	*1095*[f]	*208*[f]	*Very large*[g]
INCOLOY ® 800H/800HT	*11.5*[h]	*14.4*[h]	*0.84*	*536*[h]	*196.5*[h]	*NA*
INCONEL ® 625	*9.8*[h]	*12.8*[h]	*0.75*	*965.3*[h]	*206.2*[h]	*NA*
HAYNES ® 230	*8.9*[i]	*16.1*[i]	*0.94*	*839*[i]	*211*[i]	*NA*

Each property value presented is an average of typical values at room temperature. NA indicates unavailable information.

[a] *INCO Europe Limited (1976) [9].*

[b] *Auerkari (1996) [10].*

[c] *Material Properties Charts (2013) [11].*

[d] *Martinez et al. (2008) [12].*

[e] *HyperPhysics Online Database [13].*

[f] *Materials Data Book, Cambridge University Engineering Department (2003) [14].*

[g] *Donald et al. (2010) [15].*

[h] *Special Metals Corporation [16].*

[i] *Haynes International [17].*

Based on the properties listed in Table 1.1, for the purpose of selecting the material that has good mechanical properties for sustainability in the harsh reaction condition of steam methane reforming, metal substrate appears to be the better candidate for the monolithic support, when compared with ceramics. In addition, metal (i.e. carbon steel in this comparison) as the monoliths also has higher thermal conductivity for more effective radial conduction of heat from the reformer tube to the catalytic active sites. Most importantly, metals generally have a CTE closer to the coefficient of the tube material, which is vital for the reformer operation that is subject to heating and cooling from time to time.

Excerpt from Baharudin & Watson (2017b) [6] ends here.

1.3 Research gap and hypothesis

1.3.1 Research gap

The following section (*Italicised*) is an excerpt from a published review article [6]:

"Baharudin, L. & Watson, M.J. (2017b). Monolithic substrate support catalyst design considerations for steam methane reforming operation. *Reviews in Chemical Engineering*, 34(4), 481-501."

The metal substrates however have a disadvantage in comparison to the ceramics when it comes to the compatibility between the monolith materials and the catalyst washcoat materials. Catalyst washcoat, which is the layer deposited on the walls of the geometric surface of the monolithic structure, comprises of a high surface area carrier of typically an inorganic oxide such as alumina, stabilisers, and a dispersion of active metal or metal oxide catalyst particles [7-8].

The material selection for the monolithic substrate affects the adhesion of the catalyst layer washcoating to the walls and channels of the structure. Decent anchoring between the washcoat and the monolith's support materials is ensured by the porosity of the substrate material [8]. A brief comparison between the scanning electron microscopy (SEM) images (Figure 1.1) of a bare cordierite [18] and a bare FeCr alloy [19] reveals a highly distinctive surface morphology between the two substrate materials. The cordierite possesses a highly porous surface which promotes a stronger adhesion bonding with the washcoat layer [18], in comparison to the FeCr alloy.

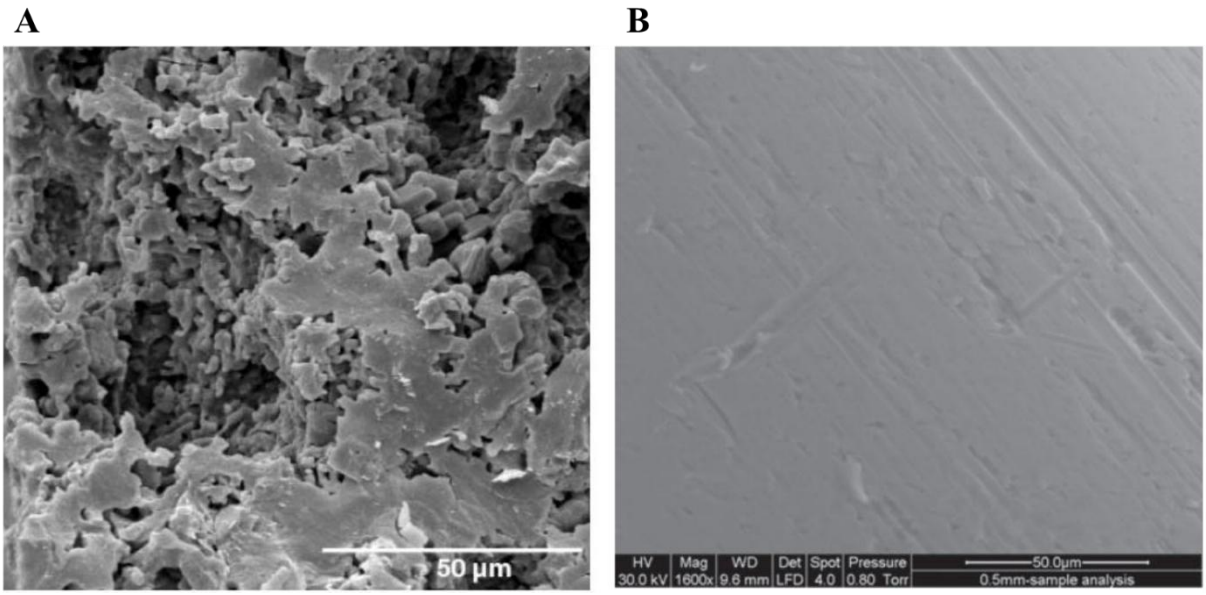

Figure 1.1: *SEM image of bare substrate's surface.*

(A) Cordierite [18]. Reproduced with permission from Taylor & Francis; and (B) FeCr alloy [19]. Reproduced with permission from Elsevier.

For the ceramic monolithic support such as cordierite, the precious catalytic metal in the washcoat does not usually migrate into the support, and vice versa. This stays true even in the harsh conditions where steam content is high and sulphur is present, and in a reducing environment. For the monoliths made of a metal, their compatibility with the catalyst washcoat in terms of the CTE must be considered. A poor adhesion is highly possible during thermal cycles if the compatibility of the CTE of the two materials is not satisfactory. In addition to the washcoat adhesion issue, metals or alloys may have components that are not

stable in quick and extreme temperature changes during transitioning from shutdown and startup to normal operation, where they could potentially migrate into the catalytic washcoat and hence poison the catalyst shortly after the operation commences [8].

Excerpt from Baharudin & Watson (2017b) [6] ends here.

The surface of the metal has low porosity in comparison to the surface of ceramics substrate, which results in poor adhesion with the conventional catalytic washcoating layer [7-8]. The insufficient external surface area of the metal and the poor adhesion of the catalytic washcoating material with its surface have been identified as the **gaps** that need closure and hence, the need for this doctoral work to be undertaken.

1.3.2 Hypothesis

A more in-depth literature review has been conducted to analyse a potential solution to the research gaps identified above, which will be presented in Chapter 2 [20]. Based on the properties of carbon nanomaterials (CNM), a filamentous carbon layer was investigated to find a suitable substitute to the washcoating layer in overcoming the adhesion issue. The CNM grown on a metal structure also acts as a surface textural promoter to increase the structure's external surface area. A comprehensive introduction to carbon material nanostructures is presented in APPENDIX A for reference. The basis for the selection of the CNM is briefly presented here and will be elaborated in detailed in Chapter 2: Literature Review and Theoretical Framework [20].

The selection of the monolithic structure's substrate material is recommended to exhibit a comparable CTE with the reformer tube material so that the expansion and contraction of both the monolith and the reformer tube would take place at similar rates during operation, to avoid catalyst crushing. Similarly, the CTE compatibility of the metal monolith and its surface textural promoter is crucial to prevent the textural promoter layer from peeling off the

monolith's surface. The CTE values of single-walled carbon nanotubes (SWCNT) and multi-walled carbon nanotubes (MWCNT) were reported to be negligible [21]. In spite of the CTE difference between the monolith substrate material and the carbon nanotubes (CNT), the length scale at the adhesion point is so small that it is hypothesised that the stress generation due to the CTE mismatch is small, and hence, it is predicted that the filamentous textural promoter layer would continue to strongly adhere on the monolith's structure regardless of the thermal cycles.

A highlighted summary of the relevant properties of the CNM below, which are drawn from Section 2.3 of Chapter 2 [20], makes the hypothesis that this novel material could potentially serve as a solution to the identified research gaps, and hence, its investigation becomes the subject of interest in this doctoral research work. Thin layers of CNM as a surface textural promoter of the metal monolithic structure have the potential as an alternative to the oxide layers where they can offer not only a sufficient surface area for hosting the active metal particles [22], but they also possess the additional characteristics of high porosity and low tortuosity [22-25] that subsequently enhance the internal mass transfer of the reactant molecules at the interface of the graphitic wall and the active particles. More importantly, the metallic catalyst particles can be distributed well and homogeneously dispersed on the surface of the CNM [26-29], for an effective diffusion of the reactant and product process gas to and from the active catalyst site. It is hypothesised that the use of CNM as a catalyst support will enhance the catalytic activity of the fabricated carbon nanomaterials-supported catalysts in many heterogeneous reactions.

The analysis based on findings reported in the literature, which is concluded in Chapter 2 [20], found that clean MWCNT that is of high crystallinity with well aligned vertical and parallel walls, made of graphitic sheets of hexagonally arranged carbon is expected to not only improve the mass transfer of the reacting systems due to a well-dispersed metal catalyst, but is also predicted to possess a high thermal conductivity. Therefore, the work in this doctoral thesis explored the use of MWCNT as the selected structure of the CNM textural promoter.

Based on the evidence from the work [30] reported on the purification of the as-synthesised carbon nanotubes by steam treatment at 900 °C (comparable to steam reforming operation conditions), which removed the carbonaceous impurities but left behind stable and purified MWCNT, it is highly convincing that the highly purified MWCNT will be stable and survive in the steam reforming conditions without simultaneously being gasified. This makes a **Theoretical Framework** of this thesis.

In this doctoral work, the low-temperature water–gas shift (LTWGS) reaction was selected as the reaction model of interest in forming the basis of developing a novel catalyst to study the kinetics of an energy-intensive reaction. LTWGS is a reaction that produces hydrogen and carbon dioxide in a moderately exothermic reversible reaction between steam and carbon monoxide at operating temperatures of 190 – 250 °C, which converts CO from a concentration of 1% – 5%, down to sub-1% at the reaction outlet [31].

In this thesis, the work on the development of a **novel copper-based catalyst supported on CNM** is presented. Copper was used as the active metal in the novel catalyst due to its known and established activity in LTWGS reaction [31] and other reactions that involve CO conversion at low temperatures such as alcohol synthesis and CO oxidation [32]. MWCNT support was selected as the type of CNM used in this work.

The gasification of the MWCNT-support material of the catalyst will not be favourable under the LTWGS operating conditions. This is also supported by the study reported by Baker & Sherwood (1981) [33] summarised in Section 2.4.2 of Chapter 2, where it was demonstrated that the gasification of graphite deposited on nickel particles in the presence of pure steam, pure hydrogen, and wet hydrogen (H_2/H_2O = 40:1) flow took place at above 900 °C, 845 °C and 780 °C respectively.

Under the steam reforming operating conditions where coke formation can occur (Section 2.4.1.2 of Chapter 2 [20]), the coke deposition is removable by gasification of the coke in a

controlled presence of the reactive gases such as steam, hydrogen and carbon dioxide, but this may introduce a risk (if any) of parallel gasification of the MWCNT used as the support. Since a monolithic structure is not present in this doctoral work, a reaction under which the operating conditions do not favour the coke formation should be selected as the reaction model of interest and hence, the LTWGS was a well justified choice.

Additionally, in order to ensure a better chance of successful demonstration of the objective intended in this study (*i.e.* kinetic study of the reaction model of interest), it is still best to avoid the coke formation so that the interference from the coke deposition and gasification is avoided in the first place, to not complicate the investigation. Nielsen (1972) [27] in their study observed a formation of carbon (coke) when subjecting an undisclosed catalyst to a flow of pure CO at 280 °C [31, 34]. In addition, at this temperature, a self-pyrolysis (non-catalytic, thermal decomposition) of the CO is also thermodynamically not possible to form pyrolytic coke, which will be discussed further in Section 2.4.1.1 of Chapter 2. Therefore, under the conditions of the LTWGS reaction operations of below 250 °C, not only coke formation by eq. (1.4) is not possible, but the steam used in the LTWGS (eq. (1.2)) as well as the carbon dioxide and hydrogen produced by the reaction will not cause gasification of the MWCNT support by the reverse of eq. (1.4) – (1.6) [4-5, 27, 35-38].

$$2\ CO \leftrightarrow C + CO_2 \qquad \Delta H^0_{298} = -172.5\ \text{kJ/mol} \qquad (1.4)$$

$$CH_4 \leftrightarrow C + 2\ H_2 \qquad \Delta H^0_{298} = +75\ \text{kJ/mol} \qquad (1.5)$$

$$CO + H_2 \leftrightarrow C + H_2O \qquad \Delta H^0_{298} = -524.8\ \text{kJ/mol} \qquad (1.6)$$

The avoidance of coke formation further supported the justification to use the LTWGS reaction as the basis in developing the novel catalyst in this doctoral work.

Equilibrium conversion is the maximum conversion that can be reached, limited by thermodynamics, and is not catalyst activity-dependent. Due to equilibrium-limited CO conversions, research has been focused on the higher-activity catalysts [34, 39-41] that are capable of improving the reaction rates at the thermodynamically favourable low-temperature

operation regime of the exothermic LTWGS reaction. Whilst the Cu-ZnO catalysts are active in the temperature range of 190 – 250 °C, their low catalytic activity calls for the use of low gas hourly space velocity (GHSV) of 3,000 – 5,000 hr^{-1} [31, 34]. An increased catalytic activity in the LTWGS reaction could lead to an increase in GHSV, reducing the catalyst volume in the adiabatic bed and thus saving operational and capital costs. This further motivated the development of the novel catalyst for the LTWGS reaction in this doctoral work.

The research activities undertaken in this doctoral work were divided into three stages: **1) Catalyst Development**, **2) Catalyst Fabrication and Hypothesis Development**, and **3) Catalytic Assessment and Feasibility Studies**. Whilst the activities in the first two stages (presented in Chapter 3 [42]) were based on an aim to demonstrate the catalyst's potential performance in the LTWGS reaction, however, its actual activity tests in the third stage were performed in CO oxidation (eq. (1.7)) reaction (presented in Chapter 4 (Stage 3a)) followed by its kinetic study (Chapter 5 (Stage 3b)).

CO oxidation [43]:

$$CO + ½\ O_2 \rightarrow CO_2 \qquad \Delta H^0_{298} = -283\ kJ/mol \qquad (1.7)$$

The surface redox mechanism for LTWGS involves the elementary steps whereby water is adsorbed and dissociated on the active site by [31, 34, 41, 44]:

$$H_2O\ (g) + * \leftrightarrow H_2O* \qquad (1.8)$$

$$H_2O* + * \rightarrow H* + OH* \qquad (1.9)$$

$$2\ OH* \leftrightarrow O* + H_2O* \qquad (1.10)$$

$$OH* + * \rightarrow O* + H* \qquad (1.11)$$

$$2\ H* \leftrightarrow H_2\ (g) + 2\ * \qquad (1.12)$$

Overall: $H_2O\ (g) + * \leftrightarrow O* + H_2\ (g)$ (1.13)

In the CO oxidation reaction, the molecular oxygen is dissociated into surface-adsorbed oxygen atoms by [45-46]:

$$O_2\,(g) + * \leftrightarrow O_2* \quad (1.14)$$

$$O_2* + * \rightarrow 2\,O* \quad (1.15)$$

In LTWGS reaction, CO molecules scavenge the surface-adsorbed hydroxyl or oxygen produced by water dissociation on the active site in the same manner they react with the surface-adsorbed oxygen atoms that are produced from the dissociation of O_2 gas molecules in CO oxidation [46-47]. Therefore, the study of oxidation of CO over the copper-based catalysts is imperative in understanding the LTWGS reaction over the same catalysts.

1.4 Research scope, approach, methodology and objective

The main thrust of this research work has a near-term aim (*i.e.* outside the scope of this thesis) of demonstrating an alternative to the identified research gap of poor anchorage between the catalytic washcoating material and the metal monolith's surface for an application in SMR as the overall scope in the research theme. However, within the **scope** of this doctoral work, a closer look towards reaching the big goal above has the **objectives** of optimising various factors in synthesising powdered catalysts supported on MWCNTs that were purchased off-the-shelf, characterise, and demonstrate their application in a heterogeneous gas-phase reaction of interest for activity study and kinetic investigation, in order to demonstrate a relationship between the metal active sites dispersion and the catalytic activity performance.

A bird's-eye view of the research approach in each of the three stages of activities undertaken in this doctoral work (mentioned earlier in Section 1.3) is briefly described here. Elaborated

descriptions of the experimental techniques used in each activity will be presented in the relevant Chapters in this thesis.

In this work, a catalyst system made of copper nanostructures supported on powdered MWCNT purchased off-the-shelf is synthesised with an objective to demonstrate well dispersed active metal nanostructures (nanoparticles and nanoclusters) of sufficiently small crystallite size and high surface area for effective reactant diffusion, using selected metal deposition techniques.

In the **Catalyst Development stage (Stage 1)**, the details on the catalyst synthesis and optimisation procedures will be reported in the relevant chapter (Part I, Chapter 3). They include:

i) MWCNT supports preparation by functionalisation using different oxidative agents and techniques;
ii) copper solution preparation using different copper precursors, solvents, concentrations (*i.e.* copper loading contents) and methods;
iii) copper deposition on the supports by selected techniques such as wet impregnation and incipient wetness impregnation;
iv) characterisation analysis of the support samples and synthesised catalyst samples that includes zeta potential, Fourier-transform infrared spectrometry (FTIR), thermogravimetric analysis (TGA) and transmission electron microscopy (TEM).

In the **Catalyst Fabrication and Hypothesis Development stage (Stage 2)**, the finalised synthesis procedure that improves the earlier work in the **Catalyst Development stage** will be established for the fabrication of a family of novel copper-based catalysts supported on MWCNTs. The catalyst surface characterisation by CO chemisorption (Cu dispersion, crystallite size and surface area) and characterisation of the active phase composition and oxidation state by X-ray diffraction (XRD) will be employed to examine the physical characteristics and surface chemical properties of the finalised fabricated catalysts.

The study of the interaction between active sites in these materials with CO at low temperatures using CO temperature-programmed desorption (CO-TPD) in conjunction with the elementary steps in the Langmuir–Hinshelwood (L–H) mechanism of LTWGS reaction will allow a prediction of the potential catalytic performance of the synthesised catalysts in the LTWGS. Optimal copper loading will be identified based on the highest Cu surface area per sample weight and dispersion, and the amount of CO adsorbed per sample weight. The predicted catalytic performance will also be analysed as a function of support type: functionalised MWCNT *cf.* non-functionalised MWCNT and alumina with fixed optimal Cu loading content. The change in the predicted activity behaviours of the catalysts synthesised from different copper nanostructure precursors (nanoclusters *vs.* nanoparticles) will also be hypothesised. All the synthesised catalysts will be benchmarked with a reference commercial catalyst, 51%CuO/31%ZnO-Al_2O_3. This will be presented in Part II, Chapter 3 [42].

In the mechanism of LTWGS reaction, the surface hydroxyls or oxygen produced by water dissociation is removed by CO in the feed gas [47]. In the **Catalytic Assessment and Feasibility Studies stage (Stage 3)**, the catalytic activity of the novel catalysts will be experimentally tested in CO oxidation reaction (Chapters 4 and 5). In Chapter 4 (Stage 3a), the outcome of the experimentally measured cataytic activity will be attempted to match with the hypothesis developed in the **Catalyst Fabrication and Hypothesis Development stage**, at which the operating conditions where the catalyst activity is at its highest potential and the conditions where the catalyst deactivation would likely occur are predicted. In Chapter 5 (Stage 3b), the kinetics of CO oxidation over the most optimal copper-based/MWCNT catalyst will be studied with an aim to experimentally determine the reaction mechanism for the CO oxidation and its rate-limiting step over the novel catalyst, and propose a reaction rate expression.

In summary, this thesis has the main objective of introducing a novel copper-based catalyst supported on MWCNT for reactions that involve CO conversion, by meeting the following sub-objectives:

i) to demonstrate effective preparative wet chemistry techniques in copper nanostructures syntheses and catalyst fabrication supported on MWCNT by

optimising the syntheses parameters and other factors such as copper loading content, copper nanostructure precursor, and different supports;

ii) to perform relevant characterisation analyses on the synthesised catalysts, of which the structure should exhibit reasonably high dispersion of copper nanostructures of sufficiently small crystallite size and high surface area, which should also demonstrate satisfactory thermal and chemical stability in the environment of the reaction under study and its operating conditions;

iii) to predict the catalytic activity of the synthesised catalysts in LTWGS reaction based on hypothesis drawn from characterisation analysis of CO interaction with the active sites of the fabricated materials, using a commercial LTWGS catalyst as a reference; AND

iv) to experimentally validate the hypothetically predicted activity in a series of actual activity tests in a temperature range from low to high, which is then extended to a kinetic investigation to establish the reaction mechanism and the rate-limiting step of the mechanism, and finally propose reaction rate expression of CO oxidation over the finalised synthesised catalyst.

1.5 Research contribution and novelty

1.5.1 Near-term: Process intensification of steam methane reforming operation

The demonstration of an application of the powdered novel catalyst developed in this doctoral work in reactions that involve CO conversion will provide a useful insight on the feasibility and potential of the carbon nanomaterials grown on metal monolithic structures as a textural promoter. The filament layer promotes a well-dispersed active metal nanoparticle deposition and allows effective diffusion of the reactants and products to and from the active sites. It is worth mentioning that the first structure of CNT was found by the University of Canterbury's very own distinguished researcher, retired Associate Professor John Abrahamson, whose discovery was reported in the 1970s [48-49]. The proposed concept of the CNT growth on the monolithic support for catalysis application was presented (poster) at the *25th International Conference on Processing and Fabrication of Advanced Materials*

(PFAM-XXV), University of Auckland, New Zealand, 22 – 25 January 2017. A perspective article on this subject has also been published [20] and part of its content relevant to this thesis is presented as Chapter 2 in this thesis.

1.5.2 Present: Novel catalyst for CO conversion reactions

Within the specific scope and objectives of this doctoral thesis, the **novelty** of the work lies within the success in introducing **a newly developed material** in which an application is experimentally proven in the oxidation of CO to produce CO_2 in the **Catalytic Assessment and Feasibility Studies stage** (Chapters 4 and 5). The overall findings will be concluded in Chapter 6. A family of novel catalysts was generated using chemically synthesised, atomically precise hexameric copper hydride nanoclusters (Cu_6) deposited on carboxyl-pre-functionalised multi-walled carbon nanotubes ($MWCNT_{COOH}$) for an application in reactions that involve CO conversion such as alcohol synthesis, LTWGS and CO oxidation.

In most cases, copper is alloyed or made to form a composite oxide with a second metal to improve the overall stability of the catalyst (*e.g.* Cu-ZnO) for LTWGS reaction [50]. Having said that, understanding the physicochemical and catalytic properties of the nanostructure of copper is critical to help establish structure–catalytic activity relationship and provide missing fundamental knowledge for this type of catalyst structures.

1.5.3 Contributions to existing literature

Initially, in the **Catalyst Development stage** (Part I, Chapter 3), lessons from the failures in the preliminary attempts to synthesise the catalyst were learned and rectified prior to the success of the fabrication of the novel $Cu_6/MWCNT_{COOH}$ catalyst. The intensive wet chemistry laboratory work, which included the support preparation through functionalisation of the MWCNT's surface and the techniques of copper nanostructure deposition on the MWCNT, demonstrated unsatisfactory outcomes of the desired copper dispersion on the

surface of the MWCNT and the loss of samples post catalyst calcination step as revealed in the characterisation analysis.

The implemented corrective actions resulted in a successful fabrication of the novel $Cu_6/MWCNT_{COOH}$ catalyst in the **Catalyst Fabrication and Hypothesis Development stage** (Part II, Chapter 3 [42]), which **marks the rise of the potential of metal nanoclusters as the next generation metal nanostructure precursor in catalyst synthesis research**. The copper nanoclusters precursor was shown to provide an improved active copper dispersion and results in crystallite sizes of as small as below 4 nm when deposited on the supports, in comparison to its conventional nanoparticles precursor counterpart. The inorganic material synthesis of the crystallised hexameric copper nanoclusters, Cu_6 has also recorded a **success** for solving **hexameric copper hydride ligated by triphenylphosphine and solvated with tetrahydrofuran molecules, a new crystal structure of empirical formula $[(PPh_3)CuH]_6.0.75THF$** by single-crystal X-ray diffraction (SCXRD), which has been registered with the **Cambridge Crystallographic Data Centre (CCDC)** and assigned a CCDC number; # 1864974.

By **experimental measurements** on the catalytic activity performance of the **supported** copper clusters in an **actual gas-phase heterogeneous reaction**, this doctoral study provides a novel insight into the claim made in the literature on the promise of the catalytic activity of **unsupported** copper nanoclusters that was based on studies on **single-crystal clusters probed by the chemisorption of single reactant-molecule gas** [51-57].

Additionally, in the **Catalyst Fabrication and Hypothesis Development stage**, the study of the interaction between active sites in these materials with CO at low temperatures using CO-TPD in conjunction with the elementary steps in the L–H mechanism of LTWGS reaction allowed the prediction of the potential catalytic performance of the synthesised catalysts in the LTWGS. This in itself presents a **novelty** in the **technique to predict the catalytic activity of the catalysts**, which eliminates the computationally-intensive microkinetic simulation using the kinetics of the elementary steps involved in the reaction. The technique, which combines active site characterisation by CO-TPD and its elucidation by L–H

mechanism of the reaction, estimates the surface coverage and activation energy of the reaction for determination of the reaction performance. This technique, which is presented in this thesis, used in predicting the catalytic activity behaviours of the synthesised catalysts based on the interaction between CO reactant molecules and the active site attributed to the copper species in a set of operating temperatures, was reported for the first time in the literature [42]. This part of the work was presented (oral) at the:

- *47th Chemeca Conference*, Queenstown, New Zealand, 30 September – 3 October 2018;
- *3rd Australasian Particle Technology Society (APTS) Students Conference*, Lake Hayes, Queenstown, New Zealand, 29 September 2018;
- *25th International Conference on Chemical Reaction Engineering (ISCRE25)*, Florence, Italy, 20 – 23 May 2018.

Experimental validation of the hypothesis of the catalytic activity of the catalysts in the **Catalytic Assessment and Feasibility Studies stage** by the measurements in actual activity tests in CO oxidation reaction revealed interesting results that will be presented in Chapter 4 (Stage 3a), and the Chapter had been made a manuscript that has been submitted to *Applied Catalysis B: Environmental* (under review at the point of submission of this thesis). This part of the work was presented (poster) at the *Materials Cluster Conference*, University of Canterbury, Christchurch, New Zealand, 3 – 4 December 2018. The kinetic study of the CO oxidation reaction over the hexameric copper nanocluster catalyst supported on carboxyl-functionalised MWCNT is presented in Chapter 5 (Stage 3b) and makes a manuscript that will be submitted to *Applied Catalysis A: General*.

1.6 Organisation of thesis

Chapter 1 presents the underlying motivation that drives the research idea behind this doctoral work that is based on the objective of achieving process intensification by an application of the monolithic catalytic support structures in energy-intensive reaction operations. This Chapter also gives an overview of the literature in the area of monolithic

structure where the focus of the research boundaries is further defined based on the selection of the monolith's substrate material, which is a metal substrate. The selection of the metal monolith further leads to the identification of the current research gap for the purpose of underlining the specific research objectives in this thesis, which are to develop a novel MWCNT-supported catalyst and demonstrate its activity in a kinetic study of a gas-phase heterogeneous reaction of interest. The research approach is then presented to set a clear picture of the activities that need to be undertaken and to define a clear goal of the potential findings and achievements that would be demonstrated as the outcome of the research investigation. The detailed review of the literature that drives the motivation for undertaking this doctoral study, which makes the backbone of this Chapter has been published in Baharudin & Watson (2017a) [1] and Baharudin & Watson (2017b) [6].

Chapter 2 addresses the research gap in the issue of poor anchorage of the conventional inorganic oxide catalytic washcoat material on the metal monolithic support based on literature. The research objectives were developed by drawing the hypothesis from the findings in the literature on the properties of the carbon nanomaterials that were expected to be able to address the identified gap as an alternative to the inorganic oxide washcoat. A perspective on the potential of carbon nanomaterials as a structural surface textural promoter makes the theoretical framework of the research. This Chapter is a complete reproduction of Baharudin *et al.* (2018a) [20].

Chapter 3 presents: (i) Part I – the preliminary attempts in the **Catalyst Development stage** (Stage 1) to synthesise the catalyst, which includes the support pre-treatment through functionalisation of the MWCNT's surface, the techniques of copper nanoparticles deposition on the MWCNT, and the characterisation analysis of the samples; and (ii) Part II – the final work on the fabrication of the novel catalyst in the **Catalyst Fabrication and Hypothesis Development stage** (Stage 2).

In Part I (Stage 1), an analysis on the unsatisfactory outcome in the desired copper nanoparticles dispersion on the surface of the MWCNT and the loss of samples post catalyst calcination step is discussed to reflect on what could have possibly gone wrong for lessons to

be learned. Corrective actions in the catalyst preparation techniques to rectify the issue are identified and proposed accordingly. This Chapter then presents the materials preparation, the techniques employed, and the optimisation of the catalyst synthesis parameters based on the proposed rectification steps identified in the previous lessons learned. An additional investigation parameter is introduced where instead of using only copper salt as the copper precursor for preparing the copper nanoparticles; the effect of the copper nanostructure is also studied by using copper nanoclusters of the form of Cu_6 crystals as the copper precursor. The preparation and the procedures for the synthesis of the Cu_6 nanoclusters are described, in addition to the description of the improved techniques in MWCNT functionalisation and the copper deposition on the support. The results and analysis of the achieved outcome are presented.

In Part II (Stage 2), the series of synthesised catalysts deemed successful for the catalytic activity investigation based on their characterisation in surface properties, surface chemistry and phase composition are presented. The Chapter discusses in detail the analysis of the interaction between active sites in these materials with CO molecules at low temperatures using CO-TPD, which is interpreted based on the elementary steps in L–H mechanism of LTWGS reaction to predict the potential (hypothetical) catalytic performance of the synthesised catalysts in LTWGS as the reaction model under study. Part II of this Chapter is a complete reproduction of Baharudin *et al.* (2018b) [42].

Chapter 4 describes the **Catalytic Assessment and Feasibility Studies stage** that has the objective to experimentally validate the novelty of the new developed catalysts in a reaction that involves CO conversion in this thesis (Stage 3a). The Chapter reports the outcome of the actual experimental activity tests in CO oxidation as the reaction model under study. The comparison between catalytic activity behaviour measured experimentally and predicted hypothetically based on active site characterisation using CO-TPD is discussed. This Chapter has been submitted for a publication (correction stage post peer-review at the point of submission of this thesis).

Chapter 5 presents the kinetics of the CO oxidation reaction over the finalised $Cu_6/MWCNT_{COOH}$ catalyst (Stage 3b) where the reaction mechanism and its rate-limiting step are established, and the rate of reaction expression is proposed. This Chapter is intended to be submitted for a publication.

Chapter 6 concludes the research proposal and objectives described in Chapter 1: Introduction – Research Background by giving a summary of the preliminary, rectified and final works accomplishment in the three stages of research work conducted in this thesis; 1) Catalyst Development, 2) Catalyst Fabrication and Hypothesis Development, and 3) Catalytic Assessment and Feasibility Studies.

Chapter 7 gives a closure to the **Catalytic Assessment and Feasibility Studies stage** of the $Cu_6/MWCNT_{COOH}$ catalyst by briefly presenting recommended extended research that can be undertaken to complete its feasibility study and kinetic study. Additionally, this Chapter mainly attempts to complement the overall big-picture scope of the research project by presenting recommendations for future work in fabricating the prototype of nickel nanostructure-MWCNT-metal monolith structured catalyst; attesting its physical, chemical, structural and thermodynamic properties as hypothesised in the theoretical framework (Chapter 2 [20]); and investigating its catalytic activity in SMR.

References of Chapter 1

1. Baharudin, L. and M.J. Watson, *Hydrogen applications and research activities in its production routes through catalytic hydrocarbon conversion.* Reviews in Chemical Engineering, 2017a. **34**(1): p. 43-72.
2. Mondal, K.C. and S.R. Chandran, *Evaluation of the economic impact of hydrogen production by methane decomposition with steam reforming of methane process.* International Journal of Hydrogen Energy, 2014. **39**(18): p. 9670-9674.

3. LeValley, T.L., A.R. Richard, and M. Fan, *Development of catalysts for hydrogen production through the integration of steam reforming of methane and high temperature water gas shift.* Energy, 2015. **90**: p. 748-758.
4. Trimm, D.L., *Coke formation and minimisation during steam reforming reactions.* Catalysis Today, 1997. **37**(3): p. 233-238.
5. Bartholomew, C.H. and R.J. Farrauto, *Hydrogen production and synthesis gas reactions*, in *Fundamentals of Industrial Catalytic Processes, Second Edition*. 2006, John Wiley & Sons, Inc. p. 339-486.
6. Baharudin, L. and M.J. Watson, *Monolithic substrate support catalyst design considerations for steam methane reforming operation.* Reviews in Chemical Engineering, 2017b. **34**(4): p. 481-501.
7. Heck, R.M., S. Gulati, and R.J. Farrauto, *The application of monoliths for gas phase catalytic reactions.* Chemical Engineering Journal, 2001. **82**(1): p. 149-156.
8. Giroux, T., et al., *Monolithic structures as alternatives to particulate catalysts for the reforming of hydrocarbons for hydrogen generation.* Applied Catalysis B: Environmental, 2005. **56**(1): p. 95-110.
9. *INCO Databooks. IN-519 Cast Chromium-Nickel-Niobium Heat-Resisting Steel* 1976: INCO Europe Limited. Available from: https://www.nickelinstitute.org/~/media/Files/TechnicalLiterature/IN_519CastChromium_Nickel_NiobiumHeat_ResistingSteel_EngineeringProperties_4383_.ashx (accessed on 07.02.18).
10. Auerkari, P., *Mechanical and physical properties of engineering alumina ceramics*. 1996: Technical Research Centre of Finland Finland.
11. *Material Properties Charts*, in *Ceramic Industry Magazine. Available from: https://www.ceramicindustry.com/ext/resources/pdfs/2013-CCD-Material-Charts.pdf (accessed on 30.01.17)*. 2013.
12. Martinez, A.T., M. Camerucci, and A. Cavalieri, *Thermal stress analysis of cordierite materials subjected to thermal shock.* Journal of materials science, 2008. **43**(8): p. 2731-2738.
13. *HyperPhysics*, Georgia State University, Atlanta, Georgia 30302-5060. Department of Physics and Astronomy. Available from: http://hyperphysics.phy-astr.gsu.edu/hbase/hph.html (accessed on 30.01.17).
14. *Materials Data Book*. 2003, Cambridge University Engineering Department. : Available from: http://www-

mdp.eng.cam.ac.uk/web/library/enginfo/cueddatabooks/materials.pdf (accessed on 30.01.17).

15. Donald R. Askeland, P.P.F., Wendelin J. Wright, *Mechanical Properties: Part Two*, in *The Science and Engineering of Materials*. 2010, Global Engineering: Stamford, USA.
16. *Special Metals Corporation* Available from: Available from: http://www.specialmetals.com/products (accessed on 30.01.17).
17. *Haynes International*. Available from: https://www.haynesintl.com/alloys/alloy-portfolio (accessed on 30.01.17).
18. Nijhuis, T.A., et al., *Preparation of monolithic catalysts.* Catalysis Reviews, 2001. **43**(4): p. 345-380.
19. Rallan, C. and A. Garforth, *Growth of hierarchically structured high-surface area alumina on FeCralloy® rods.* Chinese Journal of Chemical Engineering, 2014. **22**(8): p. 861-868.
20. Baharudin, L., et al., *Potential of metal monoliths with grown carbon nanomaterials as catalyst support in intensified steam reformer: a perspective.* Reviews in Chemical Engineering, 2018a. **ahead of print**.
21. Ma, P.-C., et al., *Dispersion and functionalization of carbon nanotubes for polymer-based nanocomposites: a review.* Composites Part A: Applied Science and Manufacturing, 2010. **41**(10): p. 1345-1367.
22. Jarrah, N.A., et al., *Immobilization of a layer of carbon nanofibres (CNFs) on Ni foam: A new structured catalyst support.* Journal of Materials Chemistry, 2005. **15**(19): p. 1946-1953.
23. Morales-Torres, S., et al., *Palladium and platinum catalysts supported on carbon nanofiber coated monoliths for low-temperature combustion of BTX.* Applied Catalysis B: Environmental, 2009. **89**(3–4): p. 411-419.
24. Chinthaginjala, J.K. and L. Lefferts, *Influence of hydrogen on the formation of a thin layer of carbon nanofibers on Ni foam.* Carbon, 2009. **47**(14): p. 3175-3183.
25. Chinthaginjala, J.K., et al., *How Carbon-Nano-Fibers attach to Ni foam.* Carbon, 2008. **46**(13): p. 1638-1647.
26. Li, P., et al., *Synthesis of carbon nanofiber/graphite-felt composite as a catalyst.* Microporous and Mesoporous Materials, 2006. **95**(1–3): p. 1-7.
27. Rostrup-Nielsen, J.R., *Equilibria of decomposition reactions of carbon monoxide and methane over nickel catalysts.* Journal of Catalysis, 1972. **27**(3): p. 343-356.

28. Li, Y., et al., *Novel Ni catalysts for methane decomposition to hydrogen and carbon nanofibers.* Journal of Catalysis, 2006. **238**(2): p. 412-424.
29. Teo, K.B., et al., *Catalytic synthesis of carbon nanotubes and nanofibers*, in *Encyclopedia of nanoscience and nanotechnology (Vol. 10)*, H.S. Nalwa, Editor. 2003, American Scientific Publishers: USA. p. 1-22.
30. Tobias, G., et al., *Purification and opening of carbon nanotubes using steam.* The Journal of Physical Chemistry B, 2006. **110**(45): p. 22318-22322.
31. Mendes, D., et al., *Determination of the Low-Temperature Water− Gas Shift Reaction Kinetics Using a Cu-Based Catalyst.* Industrial & Engineering Chemistry Research, 2010. **49**(22): p. 11269-11279.
32. Yang, F., et al., *Autocatalytic reduction of a Cu2O/Cu (111) surface by CO: sTM, XPS, and DFT studies.* The Journal of Physical Chemistry C, 2010. **114**(40): p. 17042-17050.
33. Baker, R. and R. Sherwood, *Catalytic gasification of graphite by nickel in various gaseous environments.* Journal of Catalysis, 1981. **70**(1): p. 198-214.
34. Ratnasamy, C. and J.P. Wagner, *Water gas shift catalysis.* Catalysis Reviews, 2009. **51**(3): p. 325-440.
35. Trimm, D.L., *Catalysts for the control of coking during steam reforming.* Catalysis Today, 1999. **49**(1): p. 3-10.
36. Wu, H., et al., *Ni-based catalysts for low temperature methane steam reforming: recent results on Ni-Au and comparison with other bi-metallic systems.* Catalysts, 2013. **3**(2): p. 563-583.
37. Helveg, S., J. Sehested, and J. Rostrup-Nielsen, *Whisker carbon in perspective.* Catalysis today, 2011. **178**(1): p. 42-46.
38. Moisala, A., A.G. Nasibulin, and E.I. Kauppinen, *The role of metal nanoparticles in the catalytic production of single-walled carbon nanotubes—a review.* Journal of Physics: condensed matter, 2003. **15**(42): p. S3011.
39. Luengnaruemitchai, A., S. Osuwan, and E. Gulari, *Comparative studies of low-temperature water–gas shift reaction over Pt/CeO2, Au/CeO2, and Au/Fe2O3 catalysts.* Catalysis Communications, 2003. **4**(5): p. 215-221.
40. Oliveira, N.M., G.P. Valençaa, and R. Vieirab, *Water Gas Shift Reaction On Copper Catalysts Supported On Alumina And Carbon Nanofibers.* Chemical Engineering, 2015. **43**.

41. Schumacher, N., et al., *Trends in low-temperature water–gas shift reactivity on transition metals.* Journal of Catalysis, 2005. **229**(2): p. 265-275.
42. Baharudin, L., et al., *CO temperature-programmed desorption of a hexameric copper hydride nanocluster catalyst supported on functionalized MWCNTs for active site characterization in a low-temperature water–gas shift reaction.* Chemical Engineering Journal, 2018b. **In Press, Corrected Proof**.
43. Wagman, D.D., et al., *Heats, free energies, and equilibrium constants of some reactions involving O2, H2, H2O, C, CO, CO2, and CH4.* J. Res. Natl. Bur. Stand, 1945. **34**(2): p. 143-201.
44. Smith, R., M. Loganathan, and M.S. Shantha, *A review of the water gas shift reaction kinetics.* International Journal of Chemical Reactor Engineering, 2010. **8**(1).
45. Matsushima, T. and J. White, *On the mechanism and kinetics of the CO-oxidation reaction on polycrystalline palladium: I. The reaction paths.* Journal of Catalysis, 1975. **39**(2): p. 265-276.
46. Domagala, M.E. and C.T. Campbell, *The mechanism of CO oxidation over Cu (110): effect of CO gas energy.* Catalysis Letters, 1991. **9**(1-2): p. 65-70.
47. Jernigan, G. and G.A. Somorjai, *Carbon monoxide oxidation over three different oxidation states of copper: metallic copper, copper (I) oxide, and copper (II) oxide-a surface science and kinetic study.* Journal of Catalysis, 1994. **147**(2): p. 567-577.
48. Wiles, P. and J. Abrahamson, *Carbon fibre layers on arc electrodes—I: their properties and cool-down behaviour.* Carbon, 1978. **16**(5): p. 341-349.
49. Abrahamson, J., *Saturated platelets are new intermediates in hydrocarbon pyrolysis and carbon formation.* Nature, 1977. **266**(5600): p. 323.
50. Spencer, M., *The role of zinc oxide in Cu/ZnO catalysts for methanol synthesis and the water–gas shift reaction.* Topics in Catalysis, 1999. **8**(3-4): p. 259.
51. Padilla-Campos, L., *Theoretical study of the adsorption of carbon monoxide on small copper clusters.* Journal of Molecular Structure: THEOCHEM, 2008. **851**(1-3): p. 15-21.
52. Grönbeck, H. and A. Rosén, *CHEMISORPTION OF O 2 AND CO ON COPPER CLUSTERS.* Surface Review and Letters, 1996. **3**(01): p. 687-693.
53. Cox, D., et al., *CO chemisorption on free gas phase metal clusters.* The Journal of chemical physics, 1988. **88**(1): p. 111-119.

54. Nygren, M.A. and P.E. Siegbahn, *Theoretical study of chemisorption of carbon monoxide on copper clusters.* The Journal of Physical Chemistry, 1992. **96**(19): p. 7579-7584.
55. Padilla-Campos, L., *Theoretical investigation of the adsorption of oxygen on small copper clusters.* Journal of Molecular Structure: THEOCHEM, 2007. **815**(1-3): p. 63-69.
56. Ribarsky, M., W. Luedtke, and U. Landman, *Molecular-orbital-self-consistent-field cluster model of H 2 O adsorption on copper.* Physical Review B, 1985. **32**(2): p. 1430.
57. Chen, L., et al., *A first principles study of water dissociation on small copper clusters.* Physical Chemistry Chemical Physics, 2010. **12**(33): p. 9845-9851.

CHAPTER 2

Literature Review and Theoretical Framework

Potential of metal monoliths with grown carbon nanomaterials as catalyst support in intensified steam reformer: a perspective

This Chapter is a partial reproduction of a published review article:

"Baharudin, L., Yip, A.C.K., Golovko, V. & Watson, M. (2018). Potential of metal monoliths with grown carbon nanomaterials as catalyst support in intensified steam reformer: a perspective. *Reviews in Chemical Engineering*, 0(0), pp."

Abstract

A monolithic catalytic support is potentially a thermally effective system for application in an intensified steam reforming (SR) process. In contrast to ceramic analogues, metal monoliths exhibit better mechanical strength, thermal conductivity and a thermal expansion coefficient equivalent to that of the reformer tube. A layer of carbon nanomaterials grown on the metal monolith's surface can act as textural promoter offering sufficient surface area for hosting homogeneously dispersed catalytically active metal particles. Carbon nanomaterials possess good thermal conductivities and mechanical properties. The future potential of this system in SR is envisaged based on hypothetical speculation supported by fundamental carbon studies from as early as the 1970s and sufficient literature evidence from relatively recent research on the use of monolith and carbon in catalysis.

Thermodynamics and active interaction between metal particle surface and carbon-containing gas result in coke deposition on the nickel-based catalysts in SR. The coke is removable *via* gasification by increasing steam to carbon ratio to above stoichiometric but risks a parallel

gasification of the carbon nanomaterials textural promoter, leading to nickel particles sintering. Here, a perspective is presented based on literature that under the same coke gasification conditions, the highly crystallised carbon nanomaterials maintains high chemical and thermal stability.

Keywords: carbon nanomaterials; metal monolith; process intensification; steam reforming; textural promoter.

Graphical abstract

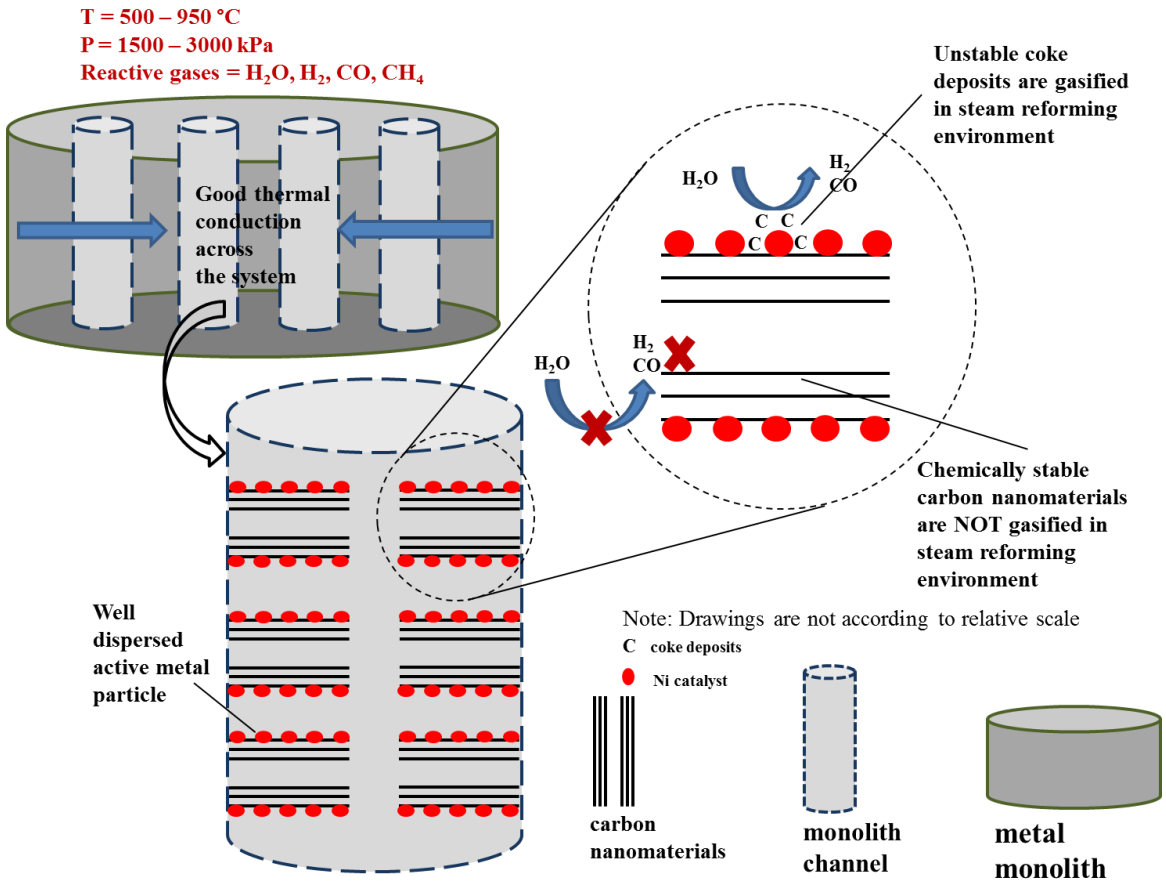

Graphical abstract: Excellent mechanical and thermal properties and chemical stability of carbon nanomaterials textural promoter on metal monolith allow the carbon nanomaterials to withstand steam reforming conditions and enhance catalytic activity for improved reaction performance.

2.1 Introduction

A material of a monolithic structure does not only rely on its good thermal properties for a great heat transfer performance. It also depends on its available contact surface area. The monolith needs to contain sufficient active catalytic sites for the desired conversion efficiencies [1]. However, metals in general do not possess sufficient external surface area for the purpose of making it a good substrate for a catalyst support. One way to overcome this issue is by using high surface area structures such as fins, corrugated foils, foams and felts, which are also capable of inducing turbulence within the process gas flow. For an application in the context of our discussion, a metallic foam is an attractive porous material as it possesses pores of diameter of around 0.5 mm that leads to low viscous losses, a high porosity (~95%) that creates a relatively large specific surface area of around 1 m^2/g, and definitely, a good thermal conductivity [2].

Another way of introducing high surface area on the metal structures is by adding a porous layer [3] onto the metal surface as a textural promoter. A synergistic effect on the increased specific surface area of the metal monolithic structure is introduced when both means are combined, whereby not only can the mass and heat transfer rates in the catalytic reactions be maximised, but a higher catalyst loading can also be achieved. To make the most effective monolithic catalytic structure, the above factors are combined where a more active catalytic component is deposited in the coating layer, at a higher loading amount [4]. To achieve this, the added porous layer coating the high-surface-area metal structure should also produce well dispersed metal catalyst nanoparticles on its surface for an efficient reaction, and be mechanically stable to withstand the high temperature gradient [3] in the steam methane reforming (SMR) reaction. For more works concerning washcoating of complex geometry supports, a couple of references [5-6] can be useful.

Poor adhesion of inorganic oxide washcoating layer typically used to host the catalytically active metal particles on metal monoliths has been identified as a gap that raises the need to

research an alternative textural promoter [7]. Works demonstrating growth of carbon nanomaterials for an application as a textural promoter on the surface of metals [3, 8-15], ceramics [16-17], and graphite [18] structured supports have inspired us to envision an application of this state-of-the-art knowledge in the field of chemical engineering by presenting critical insights to its potential in a new development of a monolithic catalytic support technology for an employment in an intensified steam reforming process.

In this Chapter, a perspective on the potential of growing carbon nanomaterials on metal monoliths as the alternative textural promoter is presented. An analysis of the properties of the carbon nanomaterials that suit the steam reforming operation is presented. It is also note that the nickel-based catalyst in steam reforming operation is susceptible to coke deposition due to thermodynamics and active interaction between the metal particle surface and the carbon-containing gas. The challenge in the industrial reforming operation of preventing the deposition of undesired carbon coke on the internal reformer tube is real, as it threatens the lifetime of the tube due to formation of hot spots.

To justify the perspective on the potential of the carbon nanomaterials in this particular application, coke formation as a common problem in steam reforming is analysed, regardless of the substrate materials used as the catalyst supports; be it inorganic oxides or carbon nanomaterials. Steam reforming *operando* conditions under which coke formation can be avoided and the conditions under which the coke deposits, if formed, are removed by gasification, is also discussed. Efforts to remove the laydown *via* coke gasification by increasing the steam to carbon ratio to above stoichiometric however introduces a risk of parallel gasification of the carbon nanomaterials used as the textural promoter. A perspective based on literature is presented that under the same conditions needed for coke gasification, the textural promoter in the form of high purity, highly crystallised carbon nanomaterials still maintains high stability and is not simultaneously gasified with the disordered, more reactive coke. In summary, based on the hypothetical speculation made here, supported by fundamental carbon studies dated back from as early as the 1970s and sufficient literature evidence from relatively recent research on the use of carbon in catalysis, the future potential of metal monoliths with grown carbon nanomaterials as catalyst support in steam reformer is envisioned.

2.2 Carbon nanomaterials growth

In overcoming the issue regarding the poor adhesion of the washcoat layer on monolithic structures made of metal substrates, the potential of growing carbon nanomaterials on the metal monoliths as an alternative to the inorganic oxide layer washcoating is analysed. Various works [3, 8-18] reported in the demonstration of the growth of carbon nanomaterials directly on various types of monolithic structures, serve as evidence that not only can this novel material be a good potential alternative to the oxide washcoated layers; it can also be grown directly on the metal structure. Indeed, the formation of carbon filament layers on a structured material such as foam, monolith, or felt helps shorten the diffusion path length of the process gas [19].

The closest hypothesis on the carbon nanomaterials' stability on a metal surface that can be made is based on a reported work by Abad *et al.* (2008) [20]. In their work, the tribological behaviour of carbon nanotubes (CNT) grown by plasma enhanced chemical vapour deposition (PECVD) on a stainless steel coated with a layer of metallic cobalt nanoparticles was investigated under humid ambient air of 25 – 40% relative humidity at room temperature using reciprocating ball-on-flat sliding. It was revealed that the friction coefficients over 200 cycles of growing loads (0.25 to 5 N) decreased to steady state values of around 0.1 – 0.2. The wear scars on the steel balls and the CNT samples of the test at 0.25 N (200 cycles) were examined by optical microscopy. Only a thin layer of CNT debris was seen on the ball after friction test, in comparison to another sample of CNT grown directly on a stainless steel without the presence of a layer of metallic cobalt nanoparticles that showed a distinctive clear worn out of CNT from the stainless steel structure surface.

The growth of carbon nanomaterials on the macroscopic monolith is a great challenge, especially in creating uniform growth conditions to cover the large monolith surface. The standard thermal chemical vapour deposition (CVD) would be quite good for carbon nanomaterials growth on the metal monolith as the monolith itself will conduct heat from

external furnace into its inner parts. A demonstration of such a work was presented by Sano *et al.* (2012) [21]. A synthesis of multi-walled carbon nanotubes (MWCNT) of high purity and uniformity at all locations in a stainless steel porous block was successfully achieved by activating the inner surface of the block by heat treatment at 800 °C in O_2–Ar environment, followed by reduction at 700 °C in H_2–Ar. A mixture of ethylene and Ar was then diffused into the pores for the ethylene decomposition to form the uniform MWCNT.

Parthangal *et al.* (2007) [22] presented a simple catalytic CVD (CCVD) technique to directly grow well-aligned arrays of CNT at growth temperature of 625 °C using iron/alumina composite catalyst on a series of metal and metal alloy substrates. Of all the metallic substrates, NiCr is the most interesting structure for a discussion, especially in relation with its application as the monolith's substrate material in the steam reformer. The tubes in a commercial reformer are made of nickel chromium alloy steel for example, HK40 (Cr 25%, Ni 20%, and Co 4%) and IN519 (Cr 24%, Ni 24%, Nb 1.5%, and Co 3%) [23]. The outcome of the study by Parthangal *et al.* (2007) [22] provides a meaningful analysis of the CNT growth on the NiCr, as this metal alloy substrate possesses compatible CTE with the reformer tubes material where both expand and contract to the similar extent during heating and cooling in the reformer operation.

In Parthangal *et al.* (2007) [22], the procedure employed involved micropipetting an aqueous solution of equal concentration of iron nitrate and aluminium nitrate onto the substrate structure to disperse the Fe/Al_2O_3 composite catalyst nanoparticles. The catalysed structure was then dried at room temperature, followed by a treatment in a mixture of Ar-H_2 flow in a tubular furnace at 625°C, prior to submission to a flow of acetylene at the same temperature for the nucleation and growth of the CNT. The scanning electron microscopic (SEM) images revealed the growth of uniform and vertically well-aligned CNT arrays at positions wherever the catalyst particles were dispersed. In comparison to the array of CNT grown on a steel substrate, the adhesion of the filamentous carbon layer was so weak that the filament was readily peeled off the steel surface, but not on the NiCr surface. No CNT adhesion strength test was reported in their work for us to provide an insight on the CNT's stability on the NiCr structure's surface grown by the demonstrated technique, if employed in the steam reforming.

The PECVD technique is also capable of synthesising uniform CNT growth. The technique allows for good control of a surface-bound growth of CNT with the desired quality and uniformity on a substrate surface [24-25]. Berenguer *et al.* (2009) [24] demonstrated the growth of CNT on a structured substrate using colloidal catalysts by employing this technique. Catalyst precursors in the form of colloidal nanoparticles are useful in catalysis applications to grow the CNT on the surfaces of three dimensional (3D) complex monolithic structures, even with uneven geometries. Using PECVD method, a dc discharge current of 20 – 40 mA was generated by employing a voltage of 800 V between the sample heater and the gas inlet, with acetylene as the carbon precursor. The result was an abundant production of vertically aligned MWCNT that covered almost the entire surface of the substrate, with generally well crystallised tubes, although there were also some defects observed in the graphitic structure.

In their work, Berenguer *et al.* (2009) [24] presented the preparation of colloidal catalyst precursors with a narrow size distribution for achieving good control of the structural type of carbon nanomaterials formed. They reported the synthesis of a stable bimetallic Co/Pd colloidal catalyst for growing the carbon nanomaterials, with a demonstration of a successful formation of vertically aligned non-bundled forests of CNT grown from the Co/Pd colloids.

Earlier to the work by Berenguer *et al.* (2009) [24], several disadvantages of using the metal colloidal nanoparticles were identified by Geng *et al.* (2004) [25]. Their manipulations in an attempt to control the size distribution of the particles are often difficult, and hence may limit the production of uniform carbon nanotubes on a large monolith, as the metal colloidal particles are normally sensitive to air. The work presented Geng *et al.* (2004) [25] would be a potential alternative method to overcome the problem of instability in air of the metal colloid by demonstrating the use of nickel formate as the catalyst precursor, taking advantage of not only its stability in the air but also its commercial availability at low cost. Nickel formate was demonstrated to be suitable for a surface-bound growth of MWCNT on a SiO_2/Si structure, where the formation of the Ni nanoparticles was done *in situ via* thermal decomposition of the nickel formate precursor during the growth process of the carbon nanotubes. The self-

redox reaction of the nickel formate resulted in decomposition of the formate directly to metallic Ni particles without the formation of nickel oxide, and hence, the requirement for the activation of the catalyst particles *via* reduction in the presence of hydrogen, was eliminated.

The substrate material of the monolith also plays a role in determining the uniformity of the CNT grown on it. Duy *et al.* (2009) [26] studied the growth of CNT on Ni-coated stainless steel substrates (NiFe, NiCr) and Ni-coated silicon substrates ($NiSi_2$) by dc PECVD and found that the diameter of the CNT grown on the former was more uniform, which was due to the uniformity in the size of the Ni particles on the stainless steel substrates. The deposition of the Ni layer and a TiN buffer layer of thickness of 50 and 1000 Å respectively was performed using a radio-frequency magnetron sputtering system on both the substrate types. The Ni activation was done by an introduction of NH_3 gas for 6 min to create uniform Ni particles, followed by annealing procedures at 600 °C in H_2, forming Ni grains. The growth of the CNT took place at 600 °C for 15 min by decomposition of acetylene in ammonia carrier.

Other than PECVD, another modified CVD technique that has the potential to be adopted for synthesising the uniform carbon nanomaterials on the 3D structures is pulsed pressure chemical vapour deposition (PPCVD). This technique has been extensively employed in the manufacturing of thin films deposition and coatings on large surface areas for various applications. Examples include the growth of titania (TiO_2) film layers on nickel substrates [27-29] and on patterned Si and silicon nitride (SiN) substrates [30]; and zirconia films deposited on metal, alumina and porous nickel cement substrates [31] and on various solid and porous substrates [32].

Even though there has not been any work published in the literature regarding the synthesis of carbon nanomaterials using this method, the PPCVD technique is promising for an adoption in growing the carbon nanomaterials on the 3D substrates. Carbon nanofibers' (CNF's) growth on a structured surface by this technique has been demonstrated in the laboratory of the Department of Mechanical Engineering, University of Canterbury. Principally, PPCVD is a non-catalytic CVD process. The carbon precursor gas is supplied

from a high pressure source, which flows through a supersonic choked orifice, to the evacuated CVD reactor where the 3D substrate is placed, during a short 0.4-second injection. Rapid diffusion of the carbon precursor to the substrate takes place, followed by the thermal decomposition of the precursor, where the carbon nanomaterials are formed on the substrate. The pressure in the reactor reaches 800 Pa at the termination of the injection, and reduces to 30 Pa during a 20-second pump-down phase by a vacuum pump. The resulting carbon nanomaterial length can be controlled by repeating the pulse cycles until the desired length is reached.

2.3 Properties of carbon nanomaterials as a textural promoter candidate for steam reforming

An analysis of the properties of the carbon nanomaterials that suit the steam reforming operation is presented here. In general, the fundamental role of the support in a catalytic system is to keep the active catalytic particles in a well dispersed state. A good catalyst must have high surface area and it has to be stable and sufficiently strong mechanically. An advantage offered by a highly porous support material is the ability to spread and disperse well the active metal catalyst phase throughout the pore system. Hence obtaining a large surface area per unit weight of active catalyst particles is possible.

A good catalyst support facilitates the external mass transfer of the process gas in the reactor to the surface of the catalyst support, and more importantly, it eases the internal mass transfer of the reacting system, where reactants and products counter-diffuse into and out of the pores of the catalyst support, to and from the catalytically active phase. This carries the benefits of improving the reaction heat dissipation, retarding the sintering of the active metal catalyst, and increasing the catalyst's resistance to poison.

The selection of the support is therefore important and must be based on desirable characteristics such as good stability under reaction conditions; satisfactory mechanical properties; and high surface area and porosity per unit volume [33]. In this section, the

properties of a filamentous carbon layer are reviewed to analyse its potential as a substitute to the washcoating layer in overcoming the lack of available surface area and poor adhesion on the metal structures. Based on the review of the properties as presented below, the structural form of the carbon nanomaterials should be an important specification if one wishes to take advantage of the properties of this novel material in the application of energy intensive heterogeneous reactions of gas-phase reactants and products.

2.3.1 Surface textural properties

Carbon nanomaterials have porous properties that are principally governed by their texture, defined by the anisotropic hexagonal layers' degree of orientation [34]. In general, aggregates of entangled carbon nanomaterials (at times referred to as interwoven nanomaterial layer [16]) provide reasonably high surface areas of 100 – 200 m^2/g. This makes the carbon nanomaterial layer a potential candidate as a surface textural promoter on a metal monolith to enhance the structure's external surface area. In addition, the nanomaterials possess low tortuosity, high meso- and macro-porosity in the absence of micropores [9, 12-13, 16], which is the kind of porosity that is being sought after in many reactions for effective internal diffusion of reactant and product molecules to the active metal sites. They also possess high specific pore volume in the range of 0.5 – 2 cm^3/g [9].

These textural properties are desirable in a catalyst support material as they provide sufficient surface area to maximise the effective diffusion coefficient [9] and minimise the internal mass transfer limitations within the thin filamentous layers [12]. Due to the presence of mesoporous texture and large external surface area in the filamentous carbon, the resistance to inner pore diffusion of the reactants or the products could be considerably reduced during catalytic reactions. This has the possibility to dampen the effects of catalyst deactivation by the formation of coke molecules in the pores [18], which is a vital feature in energy intensive reactions.

2.3.2 Thermal and chemical stability

The filamentous carbon layers also serve as an excellent candidate for catalyst supports due to their properties such as good resistance to oxidation [16]; exceptional structural strength even under acidic environments [12] despite their surface chemistry properties may be altered due to modification, addition or elimination of certain functional groups; and stability towards sintering avoidance for an application in high-temperature gas reactions [19]. Thermogravimetric analysis (TGA) reveals that different structural forms of carbon exhibit different levels of stability [35-36].

In an inert environment such as in helium, argon or nitrogen flow, the thermal stability of the carbonaceous materials depends solely on their morphology and graphitic structure or crystallinity. In a reactive environment such as in the presence of hydrogen, steam and oxygen, the stability of the carbon depends on the thermal condition (operating temperature) and the chemical reactivity of the process gas on top of the different degree of carbon crystallinity. In the reactive gases, carbon has the tendency to be reactive at above certain temperatures that they become gasified and yield methane or carbon monoxide. In an oxygen flow, the disordered (amorphous) carbon has the tendency to get oxidised under mild conditions of approximately 500 °C due to its high density of defects, whereas temperatures of 600 °C or higher are required to combust the well graphitised carbon structure due to a higher activation energy requirement [35-36]. In an inert, non-reacting gas flow, the thermal stability of the carbonaceous materials is expected to be better as compared to one in the presence of oxygen, in that a much higher temperature is required to gasify the carbon, and the gasification temperature increases with the level of carbon crystallinity.

One of the typical steps in a catalyst synthesis procedure is the calcination process, where a thermal treatment is conducted by subjecting the prepared catalyst to a gas flow at a certain temperature in order to improve the interaction between the metal active particles and the support, for an enhanced metal dispersion. In the previous works on the synthesis of the catalysts made of the metal nanoparticles deposited on the carbon nanomaterials support, the calcination was reported to have taken place in a nitrogen flow at 350 – 400 °C for 2 – 3

hours [37-39], or in an air flow at 350 °C for 1 – 4 hours [40-42], a condition where the carbon nanomaterial supports remain stable without a thermal degradation or gasification.

For utilisation in a steam reforming operation, the results from an experimental study by Tobias *et al.* (2006) [43] with the objective to purify post-synthesised carbon nanotubes using steam at 1 atm water pressure can be used as an indication of the stability of the filamentous carbon in the presence of steam. The findings revealed that the purification by steam treatment at temperatures of up to 900 °C for 4 hours removed amorphous carbon and some of the graphitic particles (following reactions $C + H_2O \rightarrow CO + H_2$ and $CO + H_2O \rightarrow CO_2 + H_2$) entangling the single-walled carbon nanotubes (SWCNT), leaving behind only cleaner and steam-stable SWCNT. The metal particles used to catalyse the SWCNT growth were exposed due to the gasification of the nanotubes' end cap by the steam. The exposed metal particles were then removed by concentrated HCl. This demonstrates a potential of stable SWCNT as the textural promoter for utilisation in the steam reforming operation. Similar results were observed in the case of MWCNT in a pure steam treatment at 900 °C but the purification took place in a shorter period, leaving behind cleaner, steam-stable MWCNT for potential utilisation in steam reforming.

Several studies employing carbon nanomaterials-based catalysts in gas phase reactions involving steam have been reported in the literature but the stability of the carbon nanomaterials was not reported at the end of each of the experiments; Ni/MWCNT, Co/MWCNT, Pt/MWCNT and Rh/MWCNT catalysts for steam ethanol reforming [44], Cu-ZnO/MWCNT for steam methanol reforming [41], NiO/MWCNT catalyst for steam propane reforming [37], Cu/MWCNT catalyst for oxy-steam methanol reforming [40], and Cu/CNF catalyst for water–gas shift [42]. As far as we are concerned, there have not been any articles published in the literature that reported a demonstration of SWCNT-based catalyst in a reaction involving steam as one of the reactants in the gas phase. The highest operating temperature demonstrated thus far is the experimental study on steam reforming of propane over MWCNT-supported nickel catalyst [37], in which the reactions were run up to a maximum temperature of 800 °C.

However, the stability of the MWCNT/CNF in terms of chemical stability and/or thermal degradation was not made part of the above studies. Therefore, it is not possible to analyse at which temperature point the carbon nanomaterials supports of the spent catalysts used in their respective work would have started to thermally deteriorate or been gasified. With the industrial SMR operation typically taking place between 500 and 950 °C [23, 45], it is expected that the carbon nanomaterials would maintain good stability in the presence of steam in the SMR operation, but a thorough analysis of the condition of the catalysts in the reactions over reaction time must be performed to validate this. In addition, the duration of the reaction was not reported in any of the works above. All of the studies were performed at laboratory scale with the reactions over the same catalysts typically lasting only a few hours, and the catalysts were not operated in a continuous mode. Therefore, the stability of the carbon nanomaterials in the presence of steam at high temperatures for energy intensive reactions such as SMR may have not been satisfied by the existing studies reported in the literature.

2.3.3 Mechanical properties

The synthesis techniques to produce carbon nanomaterials have the capability to control the amount, thickness, and homogeneity of the coating on a monolith structure as a novel catalyst support material [13, 16]. Growth of thin carbon nanomaterials (~12 nm) is faster and relatively straight, preventing their entanglement. On the other hand, the growth of thicker carbon nanomaterials (~35 nm) occurs at a lower rate, and in random and changing directions, which results in highly interweaving structures. This interweaving or entanglement has been found to be responsible for the formation of stronger aggregates. In addition, an increase in the growth time would increase the density of the carbon nanomaterial agglomerates, and subsequently contributes to further increase their mechanical strength [19]. The application of a layer of carbon nanomaterials as a catalyst support relies on its mechanical properties.

Based on various experimental works reported in the literature, Qian *et al.* (2002) [46] summarised the tensile strength of CNT in the range of 50 – 200 GPa. It was also reported

that the entangled carbon nanomaterial clusters have a bulk crushing strength of 1 MPa [47], making them attractive in fixed bed reactor applications. Satrio *et al.* (2005) [48] developed a steam reforming methane catalyst for a laboratory-scale system in the form of small spherical pellets made of alumina and loaded with nickel particles. The average radial crushing strength in their work varies between 0.6 MPa (4.5 N/mm based on pellet diameter (pellet overall diameter = 4.5 mm)) and 1.3 MPa (9.9 N/mm based on pellet diameter (pellet overall diameter = 4.7 mm)). Redwan *et al.* (1990) [49] developed the mechanical test methods using a Lorentzen & Werte (Stockholm, Sweden) Model 506 crush tester to determine the crushing strength of three different commercial SMR catalysts used in an industrial-scale operation. At least 25 catalyst pellets (to get a fair average of the crushing strength of one catalyst pellet) were crushed between a moving top plate and a stationary bottom plate, and the force at rupture was recorded automatically for each pellet. The measurements were performed according to ASTM D4179-82. The average radial crushing strength values were reported to be 1.0, 1.6 and 3.3 MPa each.

Based on the information above, it is believed that the entangled carbon nanomaterial clusters would mechanically survive in the SMR operation conditions. Nevertheless, there is another critical property that requires special attention. As discussed in Baharudin & Watson (2017b) [7] (Chapter 1), one crucial criterion when selecting the monolithic substrate material for an application in the highly endothermic SMR operation is the CTE. It is recommended that the structure's substrate material of choice exhibits a comparable CTE with the reformer tube material so that the expansion and contraction of both the monolith and the reformer tube would take place at similar rates during operation, to avoid catalyst crushing. While a typical reformer tube made of IN519 exhibits a CTE of 17.1 x 10^{-6} K^{-1} [50], the CTE of both SWCNT and MWCNT was reported to be negligible [51].

D. Wu & Zhang (2013) [52] discussed the applications of monolithic catalysts in the industry and concluded that more often than not the shutdowns for catalyst replacements were due to the mechanical failure, not the loss of catalytic activity. This makes the mechanical test a very crucial step in qualifying the employability of the monolithic catalysts. The mechanical test method has been mainly by ultrasonic means due to the convenience of the laboratory setup and quick measurement of weight loss of the catalytic washcoat layer from the

ultrasonic vibration. The ultrasonic vibration and thermal shock tests to investigate the stability of the adhesion of washcoat layer made of γ-alumina on cordierite monoliths demonstrated by D. Wu & Zhang (2013) [52] can be adopted to test the adhesion of carbon nanomaterials on the metal monoliths. Other methods that can be adopted in the adhesion examination include exposing the monoliths in a hot air stream in a laboratory-scale tubular reactor with weight loss being measured as a function of time [53-55].

2.3.4 Thermal conductivity

Carbon nanostructures have a highly anisotropic thermal conductivity. For instance, at room temperature, the thermal conductivity of carbon nanotubes was found to be greater than 3000 W/(mK) [56-57] along the filament axis, which is the a-axis (in-plane) of the graphene layer but only 1.52 W/(mK) [58] along the c-axis (out of plane), which is along radial direction of a nanotube [59]. This suggests that the structural arrangement of graphene layers influences significantly the thermal properties of the substrate material [2, 59].

There are three main structural arrangements of the graphene layer; the graphene sheets of perfect cylindrical arrangement (*i.e.* CNT), conical arrangement (fishbone CNF) and flat arrangement (stacked CNF). The parallel walls of the carbon nanotubes exhibit a greater thermal conductivity in the axial direction of the filament. This is attributed to the continuous straight graphene planes in the axial direction. The graphene sheets of the fishbone structures on the other hand are short and placed cross-wise to the axial direction, one on top of the other. The axial heat transfer is less efficient due to weak interlayer interactions between those short sheets. The fishbone structured arrays have thermal conductivity of 12 – 40 W/(mK) [2].

Based on theoretical calculations and experimental measurements, it has been demonstrated by Han (2005) [57] that carbon nanotubes have excellent thermal properties at room and elevated temperatures. An extremely high thermal conductivity due to the strong carbon-carbon bond of the graphene layers makes carbon nanotubes a novel material in the research

of heat transfer improvement [59]. Separate studies have been undertaken to measure the thermal conductivities of the SWCNT and the MWCNT at different temperatures and the results have been compiled in a number of review papers. Based on the compilation of the thermal properties between the single-walled and the multi-walled carbon nanotubes [60] at room temperature, single-walled carbon nanotubes were demonstrated to possess a wide range of thermal conductivity values from 1750 to 5800 W/(mK), while all multi-walled carbon nanotubes exhibited a thermal conductivity of above 3000 W/(mK). Based on the information obtained from these findings, it is suggested that the multi-walled carbon nanotubes' structure should be the structure of choice for the application in highly energy intensive heterogeneous reactions in the context of our discussion, as their average thermal conductivity values are always greater than 3000 W/(mK).

However, the thermal properties of the carbon nanotubes also strongly depend on their quality, which is measured in the form of degree of crystallinity, shape and size of the crystallite, and presence of any impurities [2, 59]. The thermal conductivity of a layer of carbon nanotubes can go down as low as 80 W/(mK) as a result of material imperfections such as structural defects, the presence of amorphous carbon, or the presence of impurities [2].

In summary, CNT is favoured in applications where effective heat transfer is desired, and MWCNT, which has a high degree of crystallinity and an absence of impurities have been identified to exhibit a very good thermal conductivity. However, this is not an ultimate conclusion as there has never been any comparison made in a single study on understanding the heat transfer characteristics in carbon nanofibers, single-walled carbon nanotubes, multi-walled carbon nanotubes and other carbonaceous materials such as graphene, graphene oxides and activated carbon, for a concrete finding to be established.

2.3.5 Surface chemistry properties

The graphene layered structure in carbon nanomaterials (Figure 2.1) has surfaces that can be divided into two kinds, namely basal plane and prismatic plane surfaces. The basal plane surfaces consist of only carbon atoms. These surfaces are homogeneous and "smooth", and therefore are ideal, and free of contaminants and defects. On the other hand, the prismatic surfaces have oxygen-containing groups other than carbon and are heterogeneous and "rough" [61-62].

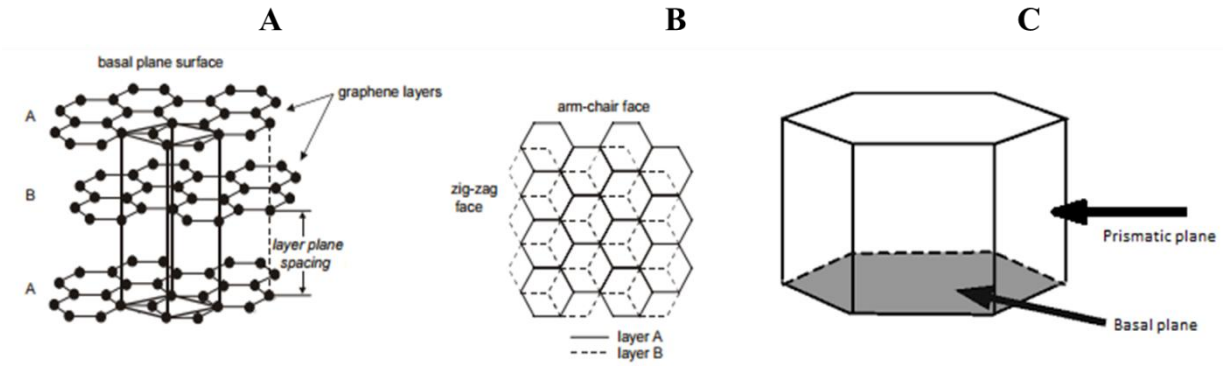

Figure 2.1: Two typical carbon nanomaterials arrangements that can be formed, which depend on the arrangements of the hexagonal cylindrical graphite sheet around the circumference, known as zig-zag and armchair.

(A) Schematic of AB hexagonal graphene layer stacking sequence and the unit cell [61]. Reproduced with permission from the author. Paper presented at the Proceedings of the ABA-2, International Conference on Advanced Batteries and Accumulators, Brno (Czech Republic); (B) upright view of the basal plane of hexagonal graphite, where prismatic surfaces can be further subdivided into arm-chair and zig-zag faces [61]. Reproduced with permission from the author. Paper presented at the Proceedings of the ABA-2, International Conference on Advanced Batteries and Accumulators, Brno (Czech Republic); and (C) 3-dimensional view of a unit of hexagonal graphene layers stack.

A good metal dispersion and stability is induced when the active metal particles are deposited on the prismatic graphene edges. The metal–carbon interaction is peculiar and varies with

various carbon growth factors that determine the crystallinity of the grown carbon structure. Similarly, a controlled ratio between the prismatic edge and the basal plane is possible but it requires synthesis investigations and an in-depth analysis through selection of the various combined factors in the carbon nanomaterials' growth synthesis, which include the catalyst type and precursor, the carbon source, and the growth conditions [18, 60, 63-64].

Typically, the as-synthesised (pristine) carbon nanomaterials contain carbonaceous impurities in the form of amorphous carbon sitting on the outer surface of the graphitic carbon. Metal impurities may also be present in the carbon nanomaterials synthesised by the catalytic techniques [65]. The use of an etchant gas such as alcohol, ammonia or steam [43, 66] to remove the carbonaceous impurities *via* gasification has been a common practice as these disordered carbon are less stable than the highly crystallised graphitic carbon nanostructures. This is normally followed by removing the metal impurities (used to catalyse the growth of the carbon nanomaterials) by concentrated acid treatment [65]. Such less stable carbon species can also be removed under steam-rich SMR conditions. However, an idea of removing them by the etchant gases treatment prior to their employment in the SMR reaction will leave behind only highly purified and highly ordered carbon nanomaterials that will survive under the SMR conditions without being gasified by the reactive gases.

The filamentous carbon offers the ability to modify the surface chemistry to suit as a catalyst support [3, 13], for an improved interaction between the carbon and the active metal particles that enhances the catalytic performance [17]. In addition, the large surface area of carbon nanotubes, both inside and outside, can be usefully exploited to support the reactant particles in catalytic conversion reactions [60]. For this purpose, an interesting property of the carbon nanomaterials surface is its electrical property [19, 60]. The sidewall surfaces of the carbon nanomaterials exhibit negative surface charge [67] and these surfaces can further be functionalised using various oxidative agents *via* techniques such as acid or basic treatment [35-37, 41, 67-72], polymer wrapping [73-77] and Hummers' method [71, 78-80], to introduce various oxygen functional groups (*e.g.* carboxyl, hydroxyl, carbonyl, *etc.*).

In general, carbon surface is hydrophobic in nature [33]. The oxygen groups are able to alter the surface to a more negative charge that decreases the hydrophobicity of the sidewall, in order to effectively adsorb the positive-charged cationic metal particles in aqueous solution for the catalyst synthesis. Therefore, the metal particles will be anchored and dispersed well on the surface of carbon nanomaterials. Although the oxygen-based functional groups may hypothetically not survive under the SMR conditions, in an oxygen-rich surface however, such oxygen groups will not be completely removed. Therefore, it is hypothesised that the nickel catalyst for the SMR reaction would continue to have a strong interaction with the carbon nanomaterials support. However, experimental evidence is still needed to demonstrate if CNT would be advantageous to not allow the oxygenated groups to "creep" over the nickel nanoparticle's surface, blocking it at high temperatures.

Other than finding the importance of decreasing the hydrophobicity of the carbon nanomaterials surface for an effective catalyst synthesis, the functionalised surface also contributes to an enhanced catalytic reaction performance. A comparative study on the effect of hydrophobic (untreated) and hydrophilic (HNO_3-treated) surfaces of CNT-supported catalysts on the catalytic performance of the hydrogenation of phenol by Xiang *et al.* (2014) [81] revealed that the selectivity of producing cyclohexanone (more desirable product) over cyclohexanol (less desirable) was increased in the treated catalyst due to the surface hydrophilicity that preferentially adsorbed H_2O. This observation is of particular importance when designing the industrial catalysts used in the reactions that involve polar media such as H_2O, which should also be able to be extended to reactions such as steam reforming and water–gas shift.

The effective removal of metal and carbonaceous impurities, as well as enhanced hydrophilicity or wettability of the graphitic carbon nanomaterials by measuring the concentration of the functional groups present in the treated carbon nanomaterials, as well as the zeta potential of their surfaces can be measured by various characterisation tools. The characterisation and analysis techniques include X-ray diffraction (XRD) or inductively coupled plasma mass spectrometry to measure the content of the metal impurities; Raman spectroscopy to measure the content of disordered and graphitic carbons in the samples; X-ray photoelectron spectroscopy and Fourier transform infrared (FTIR) spectroscopy to

measure and identify the presence of the various functional groups on the surface; and zeta potential to measure the negativity of the surface charge of the samples. The completion of the analyses is aided by morphology characterisation using SEM and transmission electron microscopy to analyse the effect of functionalisation on the crystallinity of the graphitic structure of the carbon nanomaterials, and TGA on the thermal stability. These characterisation analyses and measurements on carbon nanomaterials pre- and post-functionalisation using acid or basic treatment, polymer wrapping and Hummers' method mentioned earlier have been demonstrated in their respective work for further reference.

In the works investigating steam reforming reactions of various hydrocarbons and alcohols over various active metals supported on MWCNT listed in Section 2.3.2, some of the authors reported the oxygen functional groups that were grafted on the surface of the acid-functionalised MWCNT by presenting their FTIR analysis, but some did not mention the specific oxygen groups obtained from their acid-functionalisation work. Seelam *et al.* (2010) [44] treated their MWCNT with HNO_3 (70%) reflux for 13 hours and obtained carboxyl group (–COOH). Yang & Liao (2007) [41] treated using HNO_3:H_2SO_4 (3:1) followed by dropping ethanol slowly into the solution and obtained carbonyl (–C=O) and hydroxyl (–OH) groups. López *et al.* (2012) [37] treated using 3:1 ratio of H_2SO_4:HNO_3 at 80 °C for half an hour and obtained –COOH group. Mierczynski *et al.* (2016) [40] did not report any MWCNT pre-treatment technique and the oxygen groups in their work, while Oliveira *et al.* (2015) [42] used HNO_3 (65%) but did not report the oxygen group obtained (although it is believed to be –COOH as the functionalisation work is similar to the one performed by Seelam *et al.* (2010) [44]). On this basis, it is not possible to make a judgement on the best oxygen groups for SMR, especially when the individual studies above were conducted on different steam reforming reactions under different conditions, using different active metals.

When the sidewall surface is grafted with the oxygen-moiety groups, the acidity level of the carbon nanomaterials increases and this introduces a potential coke deposition problem as the acidic surface promotes their capability to form coke. However, a lot of research initiatives in the catalyst synthesis stage that demonstrate a suppression of coke formation by controlling the nickel crystallite size [64, 82-83] and doping the nickel with a second metal to create a

basic (alkalised) surface [84-85] can be considered for an adoption when synthesising the catalyst in order to prevent the coke formation issue under the SMR conditions.

2.4 Challenges in employing carbon nanomaterials textural promoter in steam reforming

Coke formation is a common problem in steam reforming. It is however removable *via* coke gasification by increasing the steam to carbon ratio to above stoichiometric, but this option introduces a risk of parallel gasification of the carbon nanomaterials textural promoter on the metal monolith. This section presents the perspective based on sufficient literature evidence that under the same coke gasification conditions, the textural promoter in the form of high purity, highly crystallised carbon nanomaterials still maintains high stability and is not simultaneously gasified with the disordered, more reactive coke.

Balancing the coke formation and gasification at equilibria is also possible and an idea of making the carbon nanomaterials as a template for growing a conventional oxide support on the monolith structure would allow any risk of crystallised carbon support gasification to be completely eliminated. Other initiatives include research activities in optimisation of the catalyst formulation during synthesis stage that creates unfavorable surface chemistry of the active metal-carbon interaction with respect to the formation of coke from the intermediates, and hence alleviating the coke formation in the first place.

2.4.1 Formation of carbonaceous materials in steam reforming operation

There are three mechanisms hot spots can occur as a result of coke deposition. Firstly, the pyrolytic carbon when deposited on the reformer tube's internal wall in a significant amount hinders the process gas flow and hence, creates hot spots due to uneven distribution of heat. Secondly, the hot spots occur due to encapsulation of the metal active sites by the coke deposits, leading to diminished catalytic performance, which in turn leads to the development of the hot-spot area as the externally supplied heat is no longer efficiently utilised by the

reaction/process. This occurs when the metal active phase is surface-poisoned due to prevalence of metal carbide accumulation over gasification (see discussion of mechanism in Section 2.4.1.1.2). The carbides encapsulating the active surface are however removable and the catalyst activity can be regenerated by their gasification. If left untreated, such surface-only carbon atoms will form bulk coke deposits (amorphous or whisker coke). Thirdly, due to relatively higher mechanical strength of the whisker coke, fragmentation of the catalyst pellets would result when the growing whisker is forced into the catalyst supports' pore wall. Drift of the microscopic fragments of the catalyst pellets downstream can create plugs that will lead to pressure build-up in the reactor [86-87]. Similar outcome could be envisaged in the case of formation of truly bulk amounts of coke that block the large pores of the extruded oxide support pellets eventually mechanically breaking the catalyst pellets into fragments. Either way, such inorganic oxide will form plugs which can NOT be gasified, irreversibly shutting down the reactor tube. This mechanism starves the zones below the coke-blocked pellets zone from the feedstock gas supply and in this way creates hot-spot zone there due to excessive externally supplied heat not being consumed by the reaction. At this stage the catalyst must be changed.

There are two ways the undesired coke deposition can occur in the steam reforming operation. Firstly, coke in the form of pyrolytic amorphous carbon is formed by non-catalytic decomposition of carbon-containing gas (thermal cracking/spontaneous-pyrolysis) at high temperatures (*ca.* 600 °C, depending on the types of carbon precursor); and secondly, coke in the form of whisker carbon is formed *via* catalytic cracking of the carbon-containing gas. The coke deposits in a reformer tube are present in the form of pyrolytic coke, whisker coke, and carbon nano-onion-like structures containing metal particles inside [84].

It is therefore very crucial to understand the steam reforming conditions favouring the two ways of coke formation. Thermodynamically, coke formation under steam reforming reaction conditions is unfortunately unavoidable [84]. The pyrolytic coke deposition by both hydrocarbons cracking and CO disproportionation through spontaneous self-pyrolysis can take place at the high operating temperatures of steam reforming. In addition, nickel catalysts are vulnerable to deactivation by the catalytic formation of whisker carbon, even at a normal steam reforming operation conditions at which the high steam-hydrocarbon ratios ensure no

thermodynamic affinity to form amorphous carbon deposits [85]. The detailed mechanisms of catalytic whisker carbon formation over the nickel metal particles will be discussed later in order to understand it from the catalyst surface science point of view.

The catalyst deactivation by carbon poisoning is the subject of interest in the discussion in this section. Other mechanisms of catalyst activity loss include sulphur poisoning and catalyst sintering [84, 86, 88] especially in the presence of steam in the process gas. For example, the sintering phenomenon is well-known in the γ-alumina-supported nickel catalyst as the reaction proceeds over long period at high temperature, causing the loss of catalytically active phase surface area and hence activity loss [89]. At a high operating temperature, the latter two causes of catalyst deactivation are equally crucial as the coke deposition, but they are not part of the discussion in this Chapter.

In general, the reactions involved in a hydrocarbon steam reforming operation are [86]:

Overall reaction:

$$C_nH_{2n+2} + \frac{1}{2}(n-1)\,H_2O \rightarrow \frac{1}{4}(3n+1)\,CH_4 + \frac{1}{4}(n-1)\,CO_2 \qquad (2.1)$$

For paraffin:

$$C_nH_{2n+2} + n\,H_2O \rightarrow n\,CO + (2n+1)\,H_2 \qquad (2.2)$$

For methane [86, 90]:

$$CH_4 + H_2O \leftrightarrow CO + 3\,H_2 \qquad -\Delta H^0_{298} = -206\ \text{kJ/mol} \qquad (2.3)$$

For olefins [90-91]:

$$C_nH_m + n\,H_2O \leftrightarrow n\,CO + \left(n + \frac{m}{2}\right)H_2 \qquad -\Delta H^0_{298} = -1175\ \text{kJ/mol (for } n\text{-}C_7H_{16}) \qquad (2.4)$$

$CO + 3\ H_2 \leftrightarrow CH_4 + H_2O$ (2.5)

The water–gas shift (WGS) reaction also takes place in the reforming operation.

WGS [86, 90-91]:

$CO + H_2O \leftrightarrow CO_2 + H_2$ $-\Delta H^0_{298}$ = +41 kJ/mol (2.6)

In the presence of steam, carbon monoxide, hydrogen, methane and/or other higher hydrocarbons (paraffins, olefins or aromatics), the reactions involved in the coke formation are possible through endothermic hydrocarbon dissociation and/or exothermic carbon monoxide dissociation (the Boudouard reaction) [63, 84-87, 90]:

$2\ CO \leftrightarrow C + CO_2$ (Boudouard Reaction) $-\Delta H^0_{298}$ = +172.5 kJ/mol (2.7)

$CH_4 \leftrightarrow C + 2\ H_2$ $-\Delta H^0_{298}$ = –75 kJ/mol (2.8)

$CO + H_2 \leftrightarrow C + H_2O$ $-\Delta H^0_{298}$ = +524.8 kJ/mol (2.9)

$C_nH_{2n+2} \rightarrow n\ C + (n + 1)\ H_2$ $-\Delta H^0_{298}$ = –188 kJ/mol (for n-C_7H_{16}) (2.10)

2.4.1.1 Underlying mechanisms

2.4.1.1.1 Pyrolytic coke

In the absence of a catalyst, hydrocarbons and carbon monoxide decompose at elevated temperatures to form amorphous pyrolytic carbon. Moisala *et al.* (2003) [92] presented the thermodynamics of the decomposition of carbon precursors in the form of Gibb's free energy change as a function of temperature (Figure 2.2).

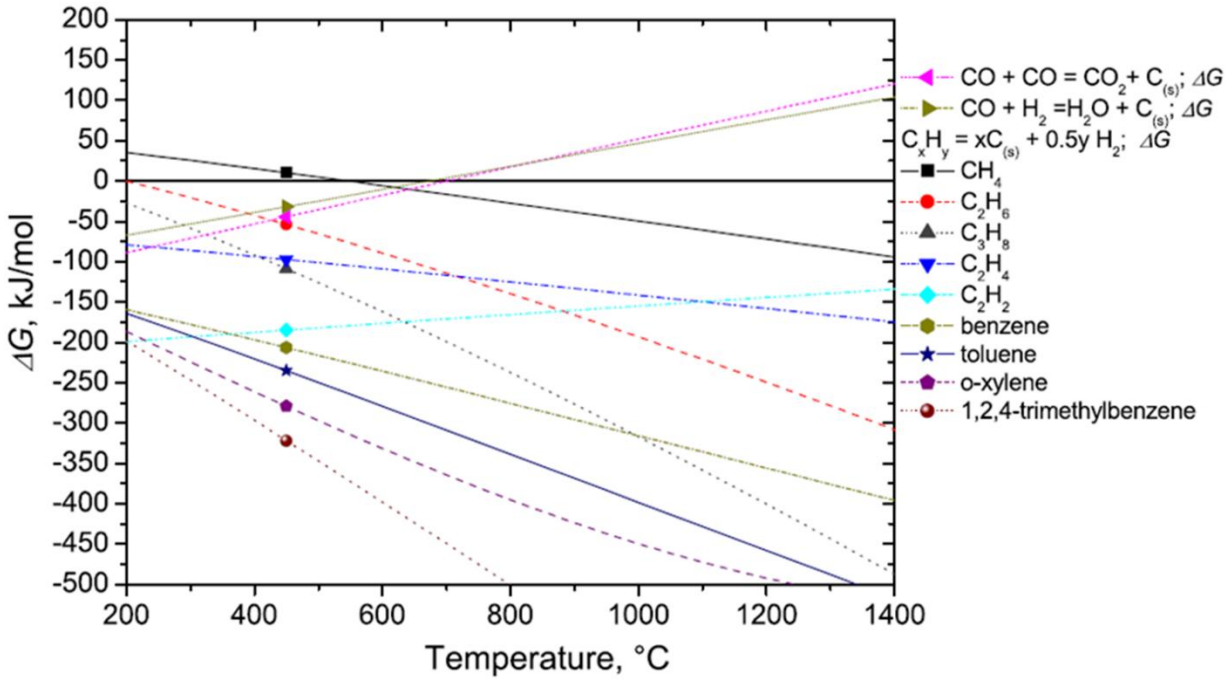

Figure 2.2: Thermodynamic data for self-pyrolysis of hydrocarbons and carbon monoxide [92]. Reproduced with permission from IOP Publishing.

In general, an increase in carbon atom numbers per molecule in paraffinic hydrocarbons decreases the molecules' stability and hence, the thermal decomposition takes place at a lower temperature. The most stable hydrocarbon is methane and its thermal cracking begins at *ca.* 900 °C. For unsaturated hydrocarbons, the π-bonds in their structure are more easily activated making them more reactive with onset of their decomposition being as low as 200 °C based on thermodynamics calculation. However, at low temperature, the decomposition of the unsaturated hydrocarbons does not self-sustain without further energy input, and halts. At higher temperatures, however, their decomposition proceeds readily [92]. The complexity of the self-pyrolysis of the hydrocarbons emphasises the importance of screening the gas composition and the concentration of the feed gas in the steam reformer to prevent an uncontrolled accumulation of amorphous coke deposits.

2.4.1.1.2 Whisker coke

Unlike pyrolytic coke that consists of only amorphous carbon at high temperatures, the whisker coke produced in the presence of a catalytic metal can have different degrees of graphitisation from fully amorphous structures to highly ordered ones [57, 60, 93-96]. The coke deposit's morphology has been identified and compiled, including but not limited to whisker coke deposits of disoriented or amorphous nature and well-graphitised structures closely related to the carbon nanomaterials, as well as various carbides [88] and coke deposits adapted to the metal particle shape such as a pear-like shape with small metal fragments encapsulated inside [87].

The ability of the metal catalysts to form the whisker is peculiar in that it varies with the chemical nature of the active metal catalyst and its precursor; the metal crystallite size; the carbon feedstock gas; and the conditions (chemical composition of the reactive gas atmosphere, temperature and pressure) of the whisker formation [18-19, 60, 63-64], which in turn affects the morphology and the degree of graphitisation of the formed carbon structure can vary [19, 84, 87-88].

The peculiarity is believed to be associated with their catalytic activity in each step involved in the mechanism of the whisker carbon growth model. There are many carbon growth models postulated by researchers, with the one developed by R. Baker *et al.* (1972) [97] being the most commonly agreed upon. The sequence starts when the carbon precursor gas dissociates on the exposed-side surface of the active metal particle; then the dissociated carbon dissolves in the metal particle; followed by the dissolved carbon diffuses through the particle; and finally the diffusing carbon precipitates at the other side of the metal particle's surface resulting in the growth of the carbon. The carbon precipitation eventually encapsulates the metal particles until they are no longer active (*i.e.* there is no clean metal surface available to continue decomposition of the feedstock gas) which stops further growth of the carbon. Similarly to the growth of carbon nanomaterials by CCVD on a monolithic structured substrate, the deposition of the coke can yield a tip- or a base-growth filament on the metal nanoparticles anchored onto porous support depending on the strength of the

interaction between the catalytic active metal and the catalyst support [25]. There are various other debatable versions of the growth model suggesting different mechanisms proposed by the research community and they have been reviewed by Teo *et al.* (2003) [60], Chinthaginjala *et al.* (2007) [19], and Kock *et al.* (1985) [98] for further reference.

The deactivated metal (when completely encapsulated) will become active again and the growth of the carbon may resume after regeneration of active metal particle surface by removal of encapsulating carbon *via* gasification by reactive gases such as oxygen, steam and/or hydrogen [63, 84, 86, 99-100], which can be achieved under conditions of the steam reforming. The coking and decoking cycle continues but the phenomena could vary with changes in the composition of the reactive gases and the temperature. This will be discussed in further detail in Section 2.4.2.

As discussed by Moisala *et al.* (2003) [92] in their review article, specifically for carbon monoxide disproportionation (eq. (2.7)) on the surface of a highly porous nickel at a normal pressure, the effective decomposition temperature is limited by kinetics and thermodynamics to a range of 520 – 800 °C, where the carbon dissolution through and precipitation from the metal particle may not be optimal. An increase in the CO pressure shifts the effective decomposition temperature to a higher range, as specified in Figure 2.3. This means that the higher the concentration of CO in the process gas, the less effective its decomposition becomes at a constant operating temperature. We are of the opinion that this phenomenon may be attributed to the decomposition of formed nickel carbide at the catalyst surface in this temperature range, which relates to prior studies back in the 1970s [63] and 1980s [98, 101] described hereafter.

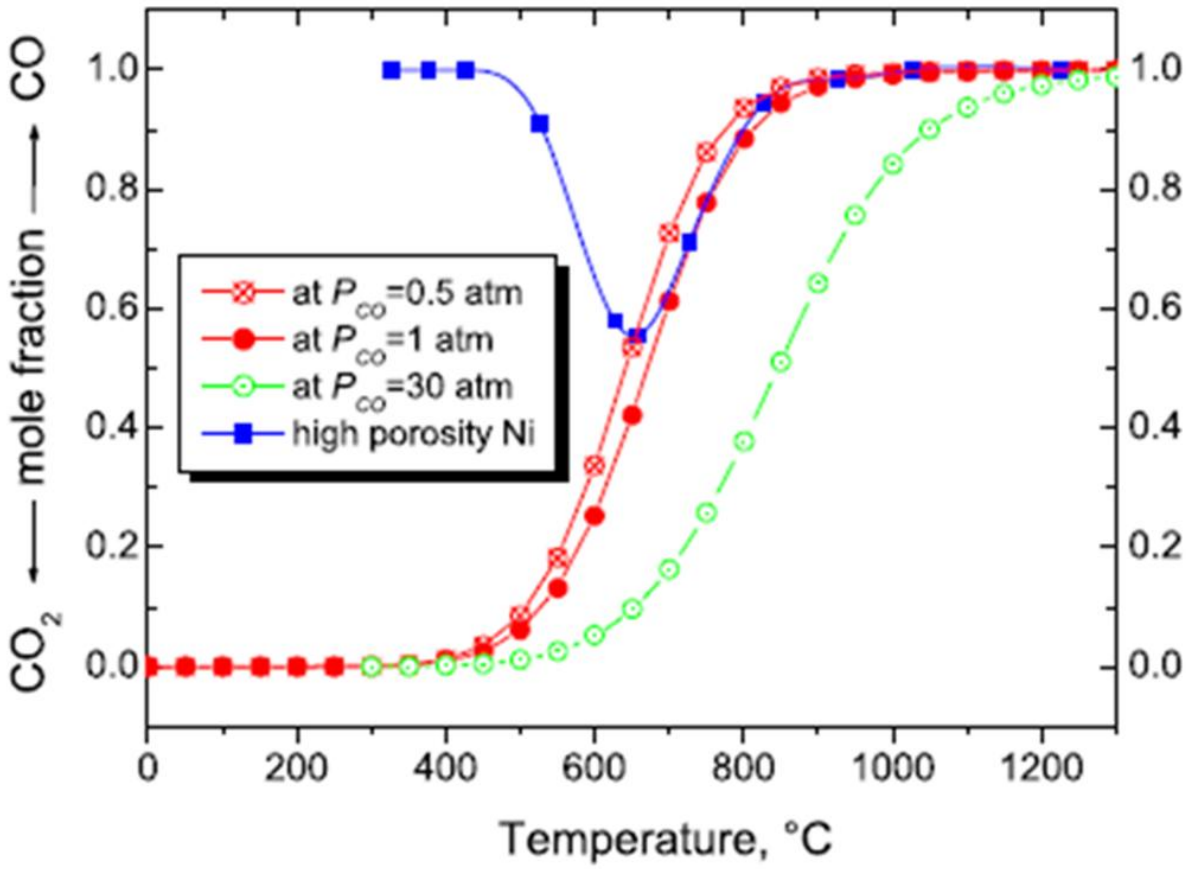

Figure 2.3: CO equilibrium concentration as a function of temperature at different pressures, and kinetic data for CO dissociation on a highly porous nickel [92]. Reproduced with permission from IOP Publishing.

De Bokx *et al.* (1985) [101] and Kock *et al.* (1985) [98] proved that the carbon dissolution into the nickel particle in the carbon growth mechanism model is preceded by a formation of sub-stoichiometric nickel carbide intermediate at the Ni catalyst surface following the proposed reaction equations of:

CO disproportionation (eq. (2.7)) on a Ni particle:

$$2\ CO + 3\ Ni \rightarrow Ni_3C + CO_2 \qquad (2.11)$$

CH_4 decomposition (eq. (2.8)) on a Ni particle:

$$CH_4 + 3\ Ni \rightarrow Ni_3C + 2\ H_2 \qquad (2.12)$$

The nickel carbide decomposes to carbon upon heating in the temperature range it becomes unstable; 400 to 1600 °C, followed by carbon dissolution into the nickel particle [63]:

$$Ni_3C \rightarrow 3\ Ni + C \qquad (2.13)$$

Based on Figure 2.3, the CO disproportionation on the nickel is not effective between 520 and 800 °C due to the kinetics and thermodynamics limitation. The ineffectiveness could be explained by the decomposition of the nickel carbide that is taking place in this temperature range. Nonetheless, the carbide does not change the equilibrium constant of the CO decomposition reaction [63].

There have also been studies involving characterising the metastable carbide intermediates formed on other metals, such as iron, reported in the literature [63, 98, 101]. Indeed, in some cases, the mechanism of carbon nucleation over the metal particles did not even involve a metal carbide formation. These studies are not discussed in detail here as we are only interested in analysing the carbon formation specifically on nickel since it is used as a catalyst for the steam reforming reaction.

In principle, the surface of the various coke species formed in steam reforming could show some activity in further decomposition of methane, perpetuating the growth of such structures. This is evident by research initiatives [100, 102-103] that investigated the catalytic decomposition of methane using carbonaceous materials of different structural and surface chemistry properties due to different morphologies and degrees of crystallinity that determine their structural and surface chemistry properties (*e.g.* activated carbon, carbon black, graphite, fullerenes, carbon nanotubes, diamond, *etc.*) as an active catalyst, without a presence of any active metals. The relevance of these investigations to our current context is the issue arising with the use of carbon materials as a textural promoter in the steam

reforming reaction, which apparently could also be active for coke formation in the reforming environment.

The analysis based on the outcomes of these studies [100, 102-103] that were conducted at 850 – 900 °C indicates that the activity of the carbonaceous materials in methane decomposition follows a general trend of carbon-based materials' activity which decreases in the direction from the disordered form to well-graphitised, crystalline structures. This is evident by the kinetics curves of methane decomposition as a function of time over a range of carbonaceous materials tested by N1 Muradov (2001) [102] and Nazim Muradov *et al.* (2005) [100] as shown in Figure 2.4. Noteworthy, the MWCNT (Figure 2.4C) exhibited one of the lowest catalytic activities amongst the tested materials, with no increased activity during the initial period typical for other materials. Thus, pure MWCNT is the form of carbon nanomaterials that are suitable to act as a textural promoter on a metal monolith for steam reforming as they have low catalytic activity in decomposition of methane.

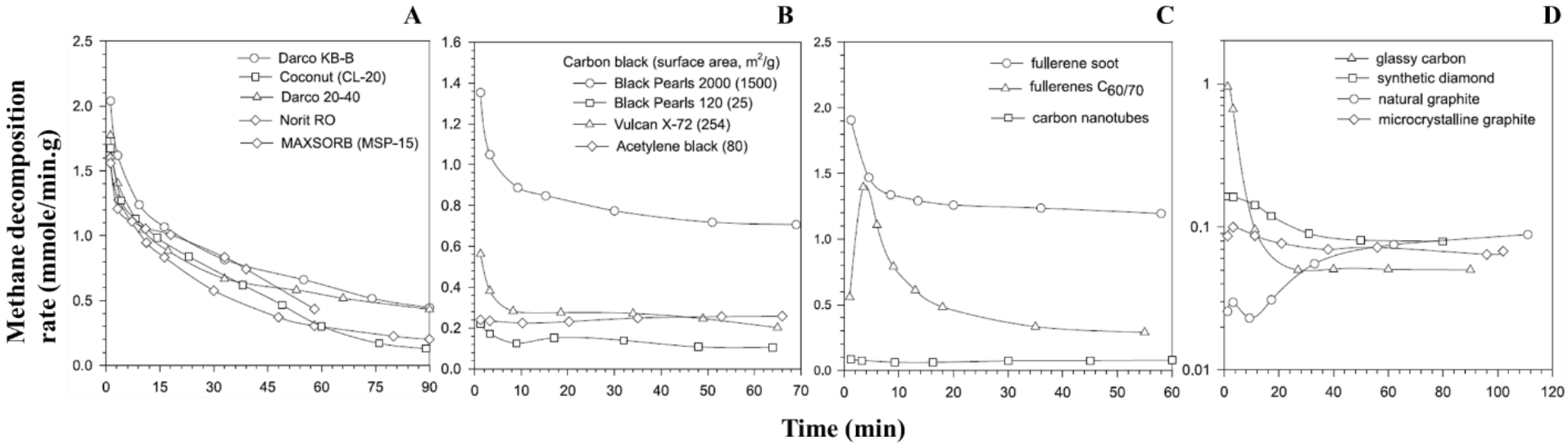

Figure 2.4: Methane decomposition over various carbonaceous materials.

(A) Activated carbon; (B) carbon black; (C) nanostructured carbon; and (D) glassy carbon, synthetic diamond and graphite [102]. Reproduced with permission from Elsevier.

For a more detailed discussion on the activity behaviour of the carbonaceous materials in relation to their textural properties (*e.g.* surface area) and surface chemistry (*i.e.* the kinetics of the carbon-catalysed methane decomposition rate that varies with the apparent activation energy), reference can be made to the articles cited in this discussion [100, 102-103]. A half-order reaction kinetic equation has been proposed for the carbon-catalysed methane decomposition investigated over a range of carbon-based catalysts, giving the rate equation of [100]:

$$-r_{CH_4} = kP_{CH_4}^{0.5} \quad (2.14)$$

However, the studies that have been conducted so far have not managed to gather sufficient information on the intrinsic catalytic properties of the carbonaceous materials, for a well understood decomposition mechanism over the different carbon forms and the nature of the active sites accountable for the catalytic activity to be established [102].

Nazim Muradov *et al.* (2005) [100] also extended their investigation to elucidate the effect of the surface oxygen group presence or absence on two samples of activated carbon; naturally oxygenated (*i.e.* containing some oxygen-based functional groups generated during fabrication of material) and deoxygenated (where such functional groups were chemically removed by treatment with pure hydrogen at 850 °C) respectively, and found that the carbons' catalytic activity could not be solely attributed to the oxygen-moiety groups, although these groups could have played a role in enhancing reactivity during the initial stage of the methane dissociation.

2.4.1.2 Reaction conditions

CCVD is a catalytic decomposition of a carbon-containing gas, a method that offers flexibility to produce the carbon nanomaterials in the range of morphologies, from CNF to CNT in the forms of either MWCNT or SWCNT, by manipulating the chemical interaction

between carbon and the catalyst metals. Hydrocarbon decomposition is also an upcoming popular reaction pathway in the production of the high purity hydrogen [104]. The reaction conditions in the "controlled" synthesis of carbon nanomaterials through CCVD by the carbon precursor's cracking in the presence of metal nanoparticle catalysts, typically cobalt, iron and nickel [19, 60, 92] needs to be understood first. They follow the same pathways and take place under somewhat similar conditions where the "uncontrolled" undesired coke is formed in the steam reforming operation through eq. (2.7), (2.8) and/or (2.10). The only critical difference between the "controlled" carbon nanomaterials' synthesis and the "uncontrolled" coke formation is that in the former, the hydrocarbons cracking and/or CO disproportion take place in the absence of steam, which is active for carbon gasification. However, there are exceptions to this critical difference when the "controlled" synthesis methods of the carbon nanomaterials use an etchant gas such as alcohol, ammonia or steam as a treatment to remove the disordered carbon. This is somewhat similar to the "uncontrolled" formation of coke under the reforming conditions where steam is present. This will be detailed further in Section 2.4.2 when the chemical stability of the different degrees of graphitisation of the carbon nanostructures is discussed.

In a well-understood and "controlled" environment for carbon filament growth by a proper optimisation of the growth factors discussed earlier, the formed carbon eventually deactivates the metal particles by encapsulation regardless of the morphology and crystallinity of the carbon nanostructure being formed. Therefore, it will be worthwhile to analyse under what conditions coke formation can occur when nickel is used as the active material supported on various inorganic oxides. The objective is to understand the conditions under which undesired coke deposition is not favourable in the presence of nickel-based catalysts in the steam reforming operating environment, which is more critical especially when nickel/multi-walled carbon nanotubes (Ni/MWCNT) is used as the catalyst.

A temperature range of between 500 and 550 °C has been established as the range where the reaction (eq. (2.8)) is stable, but 550 °C is the most optimal as the reaction at any temperatures below this takes a longer time due to a slower decomposition of methane even though the carbon yield is the same, whereas an elevated temperature leads to an uncontrollable carbon growth leading to rapid catalyst deactivation.

Interestingly, the gasification of carbon on nickel catalysts (reverse of eq. (2.8)) also approaches its maximum at close to the same temperature; 552 °C reproducing the methane [101]. The rate of the methane re-formation falls significantly with an increase in temperature and at 627 °C, the rate drops down to zero. The temperature of 550 °C is regarded as the optimal temperature based on the principles of atomic carbon accumulated on the active faces of the nickel surface responsible for the catalyst deactivation, which are then gasified to make these faces active again. At this temperature, based on the commonly accepted carbon growth mechanism model described earlier, the carbon formed by methane cracking at the nickel surface has not been dissolved into the nickel particle and is gasified at a maximum rate [105]. Zhang & Amiridis (1998) [99] concluded that the catalyst eventually becomes deactivated due to coke deposition through blocking of the active sites or coke accumulation at the entrance of the particle pores that plug the access of the reactants to the particle's interior.

A small number of studies have been selected to be reviewed in this Chapter based on their common findings. They were conducted with the objective of studying the production of hydrogen over various oxides-supported nickel catalysts at 550 °C by methane decomposition. Their findings can be useful in understanding the carbon (coke) yield in the context of our discussion.

Zhang & Amiridis (1998) [99] observed slow deactivation of their silica-supported nickel-containing catalyst in the first 2 hours. This was followed by an accelerated loss of activity in the next hour, and the catalyst was deactivated completely in less than half an hour after that. An analysis of the spent and deactivated catalyst showed a carbon yield of 18 g/g Ni, which corresponds to a carbon accumulation of approximately 2700 carbon atoms per nickel atom, based on the carbon amount calculated by methane conversion integration. It was said that only 10 carbon atoms are needed to block one active surface of a nickel atom. Ermakova *et al.* (1999) [106] and (2000) [105] conducted the study over nickel-containing catalysts supported on individual and mixes of two or three different oxides; Al_2O_3, ZrO_2, SiO_2 and MgO to study the contribution of different oxide supports. The reaction was stopped at the point where the hydrogen production reached 5% in the outlet gas concentration, but the

duration taken to reach that point was not reported. The highest carbon yield of 375 g/g Ni for samples with an average NiO particle size of 22 – 36 nm was reported on SiO_2-supported catalyst, followed by Al_2O_3, ZrO_2 and MgO in the order of decreasing carbon yield. Mixes of support materials at different NiO particle diameters were also tested but not listed here.

Shaikhutdinov *et al.* (1997) [39] in their work conducted two years earlier kept the same temperature of 550 °C in a methane decomposition reaction over nickel catalyst supported on CNF, which showed a similar global catalytic performance as that over the alumina-supported catalyst, implying a common mechanism of carbon growth on the nickel surface regardless of the support. In addition to this, they also demonstrated the different outcomes of carbon yield and catalyst "life-time" based on different nickel precursors; chloride and nitrate. It was demonstrated that the chloride precursor gave a higher carbon yield of 245 g/g Ni but longer catalyst "life-time" of 17 hours before a complete deactivation, in comparison to 40 g/g Ni and 5 hours in the nitrate precursor. This also provides us with a piece of information that the "life-time" of the catalyst is longer before it gets to a complete deactivation when using CNF as the support, compared to only slightly above 2 hours of the catalyst's "survival" in the study reported by Zhang & Amiridis (1998) [99] using SiO_2 support.

2.4.2 Gasification of carbonaceous materials

In the environment where reactive gaseous components exist, the deactivated nickel particles encapsulated with the coke will become active again after its regeneration by carbon removal *via* gasification. In the steam reforming environment, the coke gasification follows the reverse of eq. (2.7) – (2.10) [63, 84, 86, 99] in the presence of steam, hydrogen or carbon dioxide.

In addition, the removal of the undesired coke at the conditions where the reaction mechanisms are favouring gasification of the coke (*i.e.* decoking) is highly desirable by industrial operators in resolving the coke deposition issue. A couple of experimental works

[99, 107] conducted to study the conditions for the gasification of the carbon on nickel surface in the presence of hydrogen and steam, are reviewed here. The catalyst regeneration can also be done by air oxidation following carbon combustion ($C + O_2 \leftrightarrow CO_2$) [99], but this is not part of the discussion as we are analysing only the decoking pathways in a typical steam reforming environment, where free diatomic oxygen is not present.

R. Baker & Sherwood (1981) [107] reported the gasification of graphite deposited on nickel particles in the presence of steam, hydrogen, and steam–hydrogen flow. In brief, the gasification took place at above 900 °C in the presence of pure steam, 845 °C in dry hydrogen and 780 °C in wet hydrogen with a ratio of H_2/H_2O = 40:1. Zhang & Amiridis (1998) [99] on the other hand investigated the gasification of carbon by steam to regenerate a completely deactivated nickel catalyst at a fixed temperature of 550 °C and observed a full restoration of the catalyst activity as evident by the formation of carbon monoxide and methane.

Typically, a ratio higher than the stoichiometric of the steam to carbon (in the hydrocarbon feed) ratio, S:C in the feed gas can also be applied in an attempt to halt the coke formation through the reverse of eq. (2.7) – (2.10), but this comes with a price of significant energy waste to generate more steam [83]. On the other hand, the decoking of the formed coke *via* gasification would risk the gasification of the carbon nanomaterials support under the same conditions, when using this material as the textural promoter in the steam reforming reaction. The removal of the support causes activity loss of the catalyst due to sintering of the nickel particles.

There is also a rhetorical question of whether the active metal particles used to grow the carbon nanomaterials textural promoter in the CCVD process that get encapsulated in the grown carbon structure could be active in growing coke. Based on the discussion earlier, these metal particles are completely deactivated when encapsulated by the grown filamentous carbon. However, when being used in steam reforming where the reactive gases are present, the carbon filament end-caps (and perhaps the graphitic wall of the carbon nanomaterials too)

have a tendency to get removed *via* gasification. If this happened, two possibilities are foreseen here:

i) The loss of carbon nanomaterials support would cause the nickel particles meant for the steam reforming to sinter with each other, and with the previously encapsulated metal particles (used to grow the carbon nanomaterials), and hence, poison the steam reforming catalyst. The examination by Y. Li *et al.* (2006) [64] who tracked the evolution of nickel particles during methane decomposition might be useful to support the speculation of this possibility. Based on their findings, the formed carbon changed the crystalline size and the morphology of the nickel particles. The nickel particles evolved from a fibrous structure to bigger-size particles due to sintering, which were then dispersed on the *in situ* formed carbon, resulting in pear-like shaped nickel particles.

ii) The now exposed metal particles would be active to re-grow (undesired) carbon of random morphologies and crystallinities and completely deactivate the catalyst.

As far as existing literature is concerned, the closest work to address the change in surface properties of the nickel catalyst before and after the reaction is the study by López *et al.* (2012) [37] in steam propane reforming using Ni/MWCNT. Unfortunately, they only reported the characterisation analysis of their as-synthesised catalysts of varied Ni loading content but did not do that on the spent catalysts post reaction tests.

As we are well informed, the as-synthesised CNT by CCVD typically contain impurities in the form of: (1) the metal particles used to catalyse their growth are encapsulated by the carbon layers and capped at the end of the nanotubes; and (2) carbonaceous materials that include amorphous carbon, fullerenes, and carbon nanoparticles. The carbonaceous impurities are generally less stable in comparison to the highly crystallised graphitic carbon nanostructures in the conditions where reactive gas(es) is/are present, while the metal impurities are normally removed by concentrated acid treatment after the more reactive (less stable) carbonaceous impurities are removed (by gasification) from the as-synthesised CNT [65].

Presented below is the work reported in the literature that demonstrated the purification of the as-synthesised CNT by using steam to remove the impurities at temperatures comparable to the operating conditions of the steam reforming, that serve as evidences that high purity CNT left behind post the steam treatment are highly stable. Therefore, it is convinced that they can survive in the steam reforming conditions when being used as the textural promoter without being gasified in parallel with the gasification of the disordered carbon coke deposit. With these evidences, both the possibilities of (i) and (ii) described above do not arise after the as-synthesised CNT is purified with steam treatment and concentrated acid since the less stable carbonaceous impurities and metal impurities are removed respectively, prior to depositing the active nickel nanoparticles for the purpose of catalysing the steam reforming reaction.

The work by Tobias *et al.* (2006) [43] revealed that there was no evolution of gas (formation of CO and H_2 from the gasification of carbon by steam based on eq. (2.9)) when their as-synthesised SWCNT was treated with pure steam at 750 °C for 2 hours. Only when the treatment temperature was raised to 900 °C, the reactivity of the amorphous carbon with the steam was observed, where there was no amorphous carbon after 2 hours of treatment seen on the high resolution transmission electron microscopic (HRTEM) image. At the end of 4 hours of steam treatment, cleaner SWCNT was clearly observed on the HRTEM image, with no presence of the amorphous carbon and graphitic carbon particles entangling the as-synthesised SWCNT that was seen prior to the treatment. In addition, the ends of the SWCNT were also removed, revealing clearly the metal particles that were encapsulated earlier on, which was then removed by concentrated HCl. As-synthesised MWCNT on the other hand showed an even shorter time to remove the impurities by steaming at 900 °C. This work provides a strong support and basis for the employment of CNTs as a textural promoter in steam reforming operation, where they are sufficiently stable (low reactivity) in the reaction conditions. A relatively recent study by F. Yang *et al.* (2016) [66] introduced steps to synthesise highly purified SWCNT that included steam treatment at 550 °C during the synthesis process, resulting in a final SWCNT purity of 99.8% that presented an advantage of uniform band structure for high-end applications, which can be adopted when growing the CNT on the monolithic structure as the textural promoter for the catalytic application discussed in this Chapter.

Other than purification, steam is also used as an etchant to create higher specific surface area (SSA) and specific pore volume (SPV) of CNT for various applications. The work by Xiao *et al.* (2014) [108] demonstrated that steam etching of SWCNT at 750 – 950 °C showed increasing values of both SSA and SPV of the SWCNT as the treatment temperature increased, which introduced a novelty in the technique of synthesising porous carbon nanotubes for making high rate, large capacity lithium-sulphur batteries demonstrated in their work. This knowledge is also useful when synthesising the CNT for an application as a textural promoter in the catalysis application, since the above mentioned textural properties are useful for an effective diffusion of the reactant and product to and from the catalytic active sites. More importantly, based on XRD data, the steam etching in the work by Xiao *et al.* (2014) [108] showed a large reservation of the intrinsic structure of the SWCNT with only a small amount of damage, which could be deterioration of the amorphous carbon and the less stable carbonaceous impurities as in the case of the work by Tobias *et al.* (2006) [43].

Another work on the etching of CNT by steam was demonstrated at a lower temperature; Xia *et al.* (2007) [109] conducted it at 600 °C, a slightly lower temperature than Xiao *et al.* (2014) [108] but in the presence of iron nanoparticles that were impregnated on the surface of the originally non-etched MWCNT. After the removal of the iron particles by acid treatment, the final result was MWCNT of stable etched-tubular structure. The schematic of the steam etching of the MWCNT by Xia *et al.* (2007) [109] is shown in Figure 2.5. A successful steam etching work for synthesising a porous graphene oxide network for a chemical sensing application performed by T. H. Han *et al.* (2011) [110] at a very low temperature of 200 °C serves as an indication that graphene oxide is a lot less stable than CNT (which require temperatures of as high as 750 – 900 °C to etch), supporting the perspective that CNT can be the carbon nanomaterials that will survive steam reforming conditions without the risk of gasification when being employed as a textural promoter.

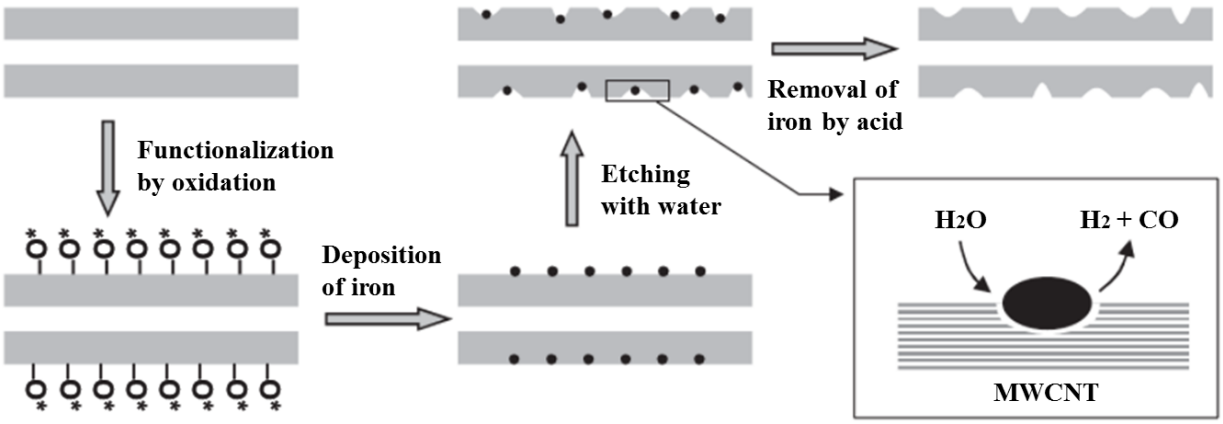

Figure 2.5: Schematic of steam etching of MWCNT in the presence of iron particles [109]. Copyright Wiley-VCH Verlag GmbH&Co. KGaA. Reproduced with permission.

2.5 Conclusions

It is hypothesised that the carbon nanomaterials have the desired mechanical properties and chemical/thermal stability to sustain in a properly controlled steam reforming condition. Their thermal properties make the conductive heat transport effective for the highly endothermic reaction. Their surface textural and surface modifiable properties for a good metal dispersion make them a good support for the reactant/product internal mass transfer in the diffusion-limited reaction. Although the oxygen-based functional groups grafted on the sidewall surface of the carbon nanomaterials by acid treatment may hypothetically not survive under the SMR conditions, in an oxygen-rich surface however, such oxygen groups will not be completely removed. Therefore, the nickel catalyst for the SMR reaction would hypothetically continue to have a strong interaction with the carbon nanomaterials support, but experimental evidence will still be needed to investigate this.

Clean multi-walled carbon nanotubes that are of high crystallinity with well aligned vertical and parallel walls, made of graphitic sheets of hexagonally arranged carbon are expected to not only improve the mass transfer of the reacting systems due to a well-dispersed metal catalyst, but also predicted to possess a high thermal conductivity. Nanotubes growing in multiple directions produce highly interweaving structures, which introduces a greater mechanical strength of the overall composite, vital for sustainability in the harsh physical and

chemical conditions of energy intensive heterogeneous reactions. Therefore, finding a balance between having high thermal conductivity (by having vertically aligned and parallel walls) and good mechanical strength (by growing nanotubes in changing directions that produce interweaving structures), is crucial. However, this is not an ultimate conclusion as there have never been any comparisons made in a single study to demonstrate the homogeneity of the metal catalyst dispersion on carbon nanofibers, single-walled carbon nanotubes and multi-walled carbon nanotubes. In addition, for a concrete finding to be established, the characterisations of the thermal and the mechanical properties of the various carbon nanomaterial structures and their varying morphology and crystallinity qualities (defected/non-defected) need to be performed.

The deactivation of the nickel-based catalysts in steam reforming operation by coke formation is undeniable due to thermodynamics and active interaction between the metal particle surface and the carbon-containing gas, but coke deposition is avoidable and it could be removed if formed, by altering operating conditions. Alleviating the formation of the undesired coke deposition from a surface chemistry standpoint has been one of the research focuses, indicating that an optimisation of the catalysts' formulation performed at the synthesis stage plays a key role. This includes optimising the nickel crystallite size, use of other metals to replace nickel or as dopants for a bi-metallic catalyst system, and investigation of alkali doping of various oxide supports to neutralise the acidic sites on support that promote formation of coke.

Accelerating the coke gasification by increasing the steam to carbon ratio to above its stoichiometric in an attempt to decoke has been the practice in the industrial operating guideline. However, this raises question regarding the suitability for an adoption of the carbon nanomaterials as the textural promoter on metal monoliths, since the coke gasification conditions are risking a parallel gasification of the carbon support, which could lead to nickel particles sintering and hence, deactivate the catalyst due to loss of active surface area.

Based on sufficient evidence from the literature, the indications in these articles leave an open door to the possibility of the carbon nanomaterials' survival in high temperature

applications, in catalytic environment and in presence of steam. It is believed that highly ordered and graphitised, purified carbon nanomaterials could maintain their stability under steam-rich reforming operating conditions without being gasified (*cf.* gasification of the amorphous coke (disordered carbon)), but an experimental validation needs to be undertaken.

However, it is still best to avoid the coke formation in the first place. Achieving a balance between formation of the carbide species at the active surface of metal and their gasification at equilibrium is possible. Yet, an alternative approach could involve use of the carbon nanomaterials grown directly on the monolithic structure as sacrificial templates for growth of the highly porous oxide support firmly attached to the monolithic, eliminating any risk of the catalyst structure collapse due to gasification of the nanostructured carbon materials.

The proposed concept of the direct growth of carbon nanomaterials on a metal monolith as a complete package of a textured catalytic support system for steam reforming could suppress the coke formation as the monolithic system has the potential to enhance the heat transfer in the reformer. Proposed nano-carbon textured monolithic system enhances the heat conduction within the reformer, making it plausible to achieve an optimal operating temperature under which the formation of both pyrolytic amorphous carbon and the growth of new highly anisotropic carbonaceous deposits (whisker coke, could have different degrees of graphitisation/order depending on conditions) is not favored. A reactor design and process parameter optimisation study is still necessary to pinpoint operating conditions such as the feedstock gas flow rate, reaction duration, operating temperature and pressure, as well as S:C ratio required to prevent formation of both pyrolytic and whisker coke.

Acknowledgement

The authors acknowledge the financial support of the Department of Chemical and Process Engineering, University of Canterbury (UC), Christchurch, New Zealand. We would also like to express our gratitude to Professor Susan Krumdieck of the Department of Mechanical

Engineering, UC for her sharing on the employment of pulsed pressure chemical vapour deposition technique in synthesising carbon nanomaterials.

References of Chapter 2

1. Heck, R.M., S. Gulati, and R.J. Farrauto, *The application of monoliths for gas phase catalytic reactions.* Chemical Engineering Journal, 2001. **82**(1–3): p. 149-156.
2. Tuzovskaya, I., et al., *Heat exchange performance of stainless steel and carbon foams modified with carbon nano fibers.* International Journal of Heat and Mass Transfer, 2012. **55**(21–22): p. 5769-5776.
3. Chinthaginjala, J.K., J.H. Bitter, and L. Lefferts, *Thin layer of carbon-nano-fibers (CNFs) as catalyst support for fast mass transfer in hydrogenation of nitrite.* Applied Catalysis A: General, 2010. **383**(1–2): p. 24-32.
4. Giroux, T., et al., *Monolithic structures as alternatives to particulate catalysts for the reforming of hydrocarbons for hydrogen generation.* Applied Catalysis B: Environmental, 2005. **56**(1–2): p. 95-110.
5. Nijhuis, T.A., et al., *Preparation of monolithic catalysts.* Catalysis Reviews, 2001. **43**(4): p. 345-380.
6. Almeida, L., et al., *Washcoating of metallic monoliths and microchannel reactors*, in *Studies in Surface Science and Catalysis*. 2010, Elsevier. p. 25-33.
7. Baharudin, L. and M.J. Watson, *Monolithic substrate support catalyst design considerations for steam methane reforming operation.* Reviews in Chemical Engineering, 2017b. **34**(4): p. 481-501.
8. Baird, T., J.R. Fryer, and B. Grant, *Carbon formation on iron and nickel foils by hydrocarbon pyrolysis—reactions at 700°C.* Carbon, 1974. **12**(5): p. 591-602.
9. Jarrah, N.A., et al., *Immobilization of a layer of carbon nanofibres (CNFs) on Ni foam: A new structured catalyst support.* Journal of Materials Chemistry, 2005. **15**(19): p. 1946-1953.
10. Pacheco Benito, S. and L. Lefferts, *The production of a homogeneous and well-attached layer of carbon nanofibers on metal foils.* Carbon, 2010. **48**(10): p. 2862-2872.

11. Pacheco Benito, S. and L. Lefferts, *Influence of reaction parameters on the attachment of a carbon nanofiber layer on Ni foils.* Surface and Coatings Technology, 2012. **206**(15): p. 3366-3373.
12. Chinthaginjala, J.K., et al., *How Carbon-Nano-Fibers attach to Ni foam.* Carbon, 2008. **46**(13): p. 1638-1647.
13. Chinthaginjala, J.K. and L. Lefferts, *Influence of hydrogen on the formation of a thin layer of carbon nanofibers on Ni foam.* Carbon, 2009. **47**(14): p. 3175-3183.
14. Chinthaginjala, J.K., et al., *Carbon nanofiber growth on thin rhodium layers.* Carbon, 2012. **50**(3): p. 1434-1437.
15. Tribolet, P. and L. Kiwi-Minsker, *Palladium on carbon nanofibers grown on metallic filters as novel structured catalyst.* Catalysis Today, 2005. **105**(3–4): p. 337-343.
16. Morales-Torres, S., et al., *Palladium and platinum catalysts supported on carbon nanofiber coated monoliths for low-temperature combustion of BTX.* Applied Catalysis B: Environmental, 2009. **89**(3–4): p. 411-419.
17. Zhu, J., et al., *Carbon Nanofibers Grown on Anatase Washcoated Cordierite Monolith and Its Supported Palladium Catalyst for Cinnamaldehyde Hydrogenation.* Industrial & Engineering Chemistry Research, 2013. **52**(3): p. 1224-1233.
18. Li, P., et al., *Synthesis of carbon nanofiber/graphite-felt composite as a catalyst.* Microporous and Mesoporous Materials, 2006. **95**(1–3): p. 1-7.
19. Chinthaginjala, J.K., K. Seshan, and L. Lefferts, *Preparation and Application of Carbon-Nanofiber Based Microstructured Materials as Catalyst Supports.* Industrial & Engineering Chemistry Research, 2007. **46**(12): p. 3968-3978.
20. Abad, M., et al., *Catalytic growth of carbon nanotubes on stainless steel: characterization and frictional properties.* Diamond and Related Materials, 2008. **17**(11): p. 1853-1857.
21. Sano, N., S. Yamamoto, and H. Tamon, *Uniform synthesis of multi-walled carbon nanotubes in a stainless steel porous block.* Carbon, 2012. **50**(15): p. 5628-5630.
22. Parthangal, P.M., R.E. Cavicchi, and M.R. Zachariah, *A generic process of growing aligned carbon nanotube arrays on metals and metal alloys.* Nanotechnology, 2007. **18**(18): p. 185605.
23. Mohammadzadeh, J.S. and A. Zamaniyan, *Catalyst shape as a design parameter—optimum shape for methane-steam reforming catalyst.* Chemical Engineering Research and Design, 2002. **80**(4): p. 383-391.

24. Berenguer, A., et al., *Stable colloidal Co–Pd nanocatalysts for carbon nanotube growth.* physica status solidi (b), 2009. **246**(11-12): p. 2436-2439.
25. Geng, J., et al., *Nickel formate route to the growth of carbon nanotubes.* The Journal of Physical Chemistry B, 2004. **108**(48): p. 18446-18450.
26. Duy, D.Q., et al., *Growth of carbon nanotubes on stainless steel substrates by DC-PECVD.* Applied Surface Science, 2009. **256**(4): p. 1065-1068.
27. Krumdieck, S. and R. Raj, *Conversion Efficiency of Alkoxide Precursor to Oxide Films Grown by an Ultrasonic-Assisted, Pulsed Liquid Injection, Metalorganic Chemical Vapor Deposition (Pulsed-CVD) Process.* Journal of the American Ceramic Society, 1999. **82**(6): p. 1605-1607.
28. Krumdieck, S. and R. Raj, *Growth rate and morphology for ceramic films by pulsed-MOCVD.* Surface and Coatings Technology, 2001. **141**(1): p. 7-14.
29. Krumdieck, S.P. and R. Raj, *Experimental characterization and modeling of pulsed MOCVD with ultrasonic atomization of liquid precursor.* Chemical Vapor Deposition, 2001. **7**(2): p. 85-90.
30. Siriwongrungson, V., M.M. Alkaisi, and S.P. Krumdieck, *Step coverage of thin titania films on patterned silicon substrate by pulsed-pressure MOCVD.* Surface and Coatings Technology, 2007. **201**(22): p. 8944-8949.
31. Krumdieck, S.P., et al., *Solid Yttria-Stabilized Zirconia Films by Pulsed Chemical Vapor Deposition from Metal-organic Precursors.* Journal of the American Ceramic Society, 2002. **85**(11): p. 2873-2875.
32. Krumdieck, S., et al., *Growth rate, microstructure and conformality as a function of vapor exposure for zirconia thin films by pulsed-pressure MOCVD.* Surface and Coatings Technology, 2007. **201**(22): p. 8908-8913.
33. Rodríguez-reinoso, F., *The role of carbon materials in heterogeneous catalysis.* Carbon, 1998. **36**(3): p. 159-175.
34. Beguin, F.F., E.; Linares-Solano, A.; Pinson, J., *Surface Properties, Porosity, Chemical and Electrochemical Applications*, in *Understanding Carbon Nanotubes: From Basics to Applications*, A.L. Loiseau, P.; Petit, P.; Roche, S.; Salvetat, J.P., Editor. 2006, Springer, Berlin Heidelberg: The Netherlands. p. 495.
35. Datsyuk, V., et al., *Chemical oxidation of multiwalled carbon nanotubes.* Carbon, 2008. **46**(6): p. 833-840.

36. Moraes, R.A., et al., *The effect of different chemical treatments on the structure and stability of aqueous dispersion of iron-and iron oxide-filled multi-walled carbon nanotubes.* Journal of the Brazilian Chemical Society, 2011. **22**(11): p. 2191-2201.
37. López, E., et al., *Multiwalled carbon nanotubes-supported Nickel catalysts for the steam reforming of propane.* Journal of Materials Science, 2012. **47**(6): p. 2985-2994.
38. Abbaslou, R.M.M., et al., *Iron catalysts supported on carbon nanotubes for Fischer–Tropsch synthesis: Effect of catalytic site position.* Applied Catalysis A: General, 2009. **367**(1): p. 47-52.
39. Shaikhutdinov, S.K., et al., *Nickel catalysts supported on carbon nanofibers: structure and activity in methane decomposition.* Catalysis letters, 1997. **47**(1): p. 35-42.
40. Mierczynski, P., et al., *Monometallic copper catalysts supported on multi-walled carbon nanotubes for the oxy-steam reforming of methanol.* Reaction Kinetics, Mechanisms and Catalysis, 2016. **117**(2): p. 675-691.
41. Yang, H.-M. and P.-H. Liao, *Preparation and activity of Cu/ZnO-CNTs nano-catalyst on steam reforming of methanol.* Applied Catalysis A: General, 2007. **317**(2): p. 226-233.
42. Oliveira, N.M., G.P. Valençaa, and R. Vieirab, *Water Gas Shift Reaction On Copper Catalysts Supported On Alumina And Carbon Nanofibers.* Chemical Engineering, 2015. **43**.
43. Tobias, G., et al., *Purification and opening of carbon nanotubes using steam.* The Journal of Physical Chemistry B, 2006. **110**(45): p. 22318-22322.
44. Seelam, P., et al., *CNT-based catalysts for H 2 production by ethanol reforming.* international journal of hydrogen energy, 2010. **35**(22): p. 12588-12595.
45. Zamaniyan, A., et al., *Comparative model analysis of the performance of tube fitted bulk monolithic catalyst with conventional pellet shapes for natural gas reforming.* Journal of Industrial and Engineering Chemistry, 2011. **17**(4): p. 767-776.
46. Qian, D., et al., *Mechanics of carbon nanotubes.* Applied mechanics reviews, 2002. **55**(6): p. 495-533.
47. De Jong, K.P. and J.W. Geus, *Carbon nanofibers: catalytic synthesis and applications.* Catalysis Reviews, 2000. **42**(4): p. 481-510.
48. Satrio, J.A., B.H. Shanks, and T.D. Wheelock, *Development of a novel combined catalyst and sorbent for hydrocarbon reforming.* Industrial and Engineering Chemistry Research, 2005. **44**(11): p. 3901-3911.

49. Redwan, D., A. Lee, and A. Aitani, *Changes in crushing strength of hydrocarbon steam-reforming catalyst along the reactor tube under operating conditions.* Journal of Chemical Technology and Biotechnology, 1990. **47**(4): p. 307-317.
50. *INCO Databooks. IN-519 Cast Chromium-Nickel-Niobium Heat-Resisting Steel* 1976: INCO Europe Limited. Available from: https://www.nickelinstitute.org/~/media/Files/TechnicalLiterature/IN_519CastChromium_Nickel_NiobiumHeat_ResistingSteel_EngineeringProperties_4383_.ashx (accessed on 07.02.18).
51. Ma, P.-C., et al., *Dispersion and functionalization of carbon nanotubes for polymer-based nanocomposites: a review.* Composites Part A: Applied Science and Manufacturing, 2010. **41**(10): p. 1345-1367.
52. Wu, D. and H. Zhang, *Mechanical Stability of Monolithic Catalysts: Scattering of Washcoat Adhesion and Failure Mechanism of Active Material.* Industrial & Engineering Chemistry Research, 2013. **52**(41): p. 14713-14721.
53. Agrafiotis, C., A. Tsetsekou, and A. Ekonomakou, *The effect of particle size on the adhesion properties of oxide washcoats on cordierite honeycombs.* Journal of materials science letters, 1999. **18**(17): p. 1421-1424.
54. Agrafiotis, C. and A. Tsetsekou, *The effect of powder characteristics on washcoat quality. Part I: Alumina washcoats.* Journal of the European Ceramic Society, 2000. **20**(7): p. 815-824.
55. Agrafiotis, C. and A. Tsetsekou, *The effect of powder characteristics on washcoat quality. Part II: Zirconia, titania washcoats—multilayered structures.* Journal of the European Ceramic Society, 2000. **20**(7): p. 825-834.
56. Kim, P., et al., *Thermal transport measurements of individual multiwalled nanotubes.* Physical review letters, 2001. **87**(21): p. 215502.
57. Han, J., *Structures and Properties of Carbon Nanotubes*, in *Carbon Nanotubes Science and Applications*, M. Meyyappan, Editor. 2005, CRC Press: United States of America. p. 1.
58. Sinha, S., et al., *Off-axis thermal properties of carbon nanotube films.* Journal of Nanoparticle Research, 2005. **7**(6): p. 651-657.
59. Taha, T.J., et al., *Effect of carbon nanofiber surface morphology on convective heat transfer from cylindrical surface: Synthesis, characterization and heat transfer measurement.* International Journal of Thermal Sciences, 2016. **105**: p. 13-21.

60. Teo, K.B., et al., *Catalytic synthesis of carbon nanotubes and nanofibers*, in *Encyclopedia of nanoscience and nanotechnology (Vol. 10)*, H.S. Nalwa, Editor. 2003, American Scientific Publishers: USA. p. 1-22.
61. Olivier, J., et al., *The relevance of graphite surface properties for anode performance in lithium ion cells-III. Surface area and surface heterogeneieties.* Proceedings of the ABA-2, International Conference on Advanced Batteries and Accumulators, Brno (Czech Republic), 2001.
62. Olivier, J. and M. Winter, *Determination of the absolute and relative extents of basal plane surface area and "non-basal plane surface" area of graphitesand their impact on anode performance in lithium ion batteries.* Journal of Power Sources, 2001. **4155**: p. 1-5.
63. Rostrup-Nielsen, J.R., *Equilibria of decomposition reactions of carbon monoxide and methane over nickel catalysts.* Journal of Catalysis, 1972. **27**(3): p. 343-356.
64. Li, Y., et al., *Novel Ni catalysts for methane decomposition to hydrogen and carbon nanofibers.* Journal of Catalysis, 2006. **238**(2): p. 412-424.
65. Hou, P.-X., C. Liu, and H.-M. Cheng, *Purification of carbon nanotubes.* Carbon, 2008. **46**(15): p. 2003-2025.
66. Yang, F., et al., *Water-assisted preparation of high-purity semiconducting (14, 4) carbon nanotubes.* ACS nano, 2016. **11**(1): p. 186-193.
67. Hamilton Jr, R.F., et al., *Purification and sidewall functionalization of multiwalled carbon nanotubes and resulting bioactivity in two macrophage models.* Inhalation toxicology, 2013. **25**(4): p. 199-210.
68. Špitalský, Z., et al., *Effect of oxidation treatment of multiwalled carbon nanotubes on the mechanical and electrical properties of their epoxy composites.* Composites Part A: Applied Science and Manufacturing, 2009. **40**(6): p. 778-783.
69. Basahel, S.N., et al., *Chemical modification of multi-walled carbon nanotubes using different oxidising agents: optimisation and characterisation.* International Journal of Nanoparticles, 2009. **2**(1-6): p. 200-208.
70. Salmoria, G., et al. *Oxidative treatment of carbon nanotubes by hydrogen peroxide and O2 plasma for rapid manufacturing applications*. in *High Value Manufacturing: Advanced Research in Virtual and Rapid Prototyping: Proceedings of the 6th International Conference on Advanced Research in Virtual and Rapid Prototyping, Leiria, Portugal, 1-5 October, 2013*. 2013: CRC Press.

71. Dreyer, D.R., et al., *The chemistry of graphene oxide.* Chemical Society Reviews, 2010. **39**(1): p. 228-240.
72. Stancu, M., et al., *Purification of multiwall carbon nanotubes obtained by AC arc discharge method.* Optoelectronics and Advanced Materials, 2011. **5**(8): p. 846-850.
73. Correa-Duarte, M.A. and L.M. Liz-Marzán, *Carbon nanotubes as templates for one-dimensional nanoparticle assemblies.* Journal of Materials Chemistry, 2006. **16**(1): p. 22-25.
74. Correa-Duarte, M.A., et al., *Aligning Au nanorods by using carbon nanotubes as templates.* Angewandte Chemie International Edition, 2005. **44**(28): p. 4375-4378.
75. Correa-Duarte, M.A., et al., *Linear Assemblies of Silica-Coated Gold Nanoparticles Using Carbon Nanotubes as Templates.* Advanced Materials, 2004. **16**(23-24): p. 2179-2184.
76. Nam, I., H. Souri, and H. Lee, *Percolation threshold and piezoresistive response of multi-wall carbon nanotube/cement composites.* Smart Structures and Systems, 2016. **18**(2): p. 217-231.
77. Nam, I., et al., *Electromagnetic characteristics of cement matrix materials with carbon nanotubes.* ACI Materials Journal-American Concrete Institute, 2012. **109**(3): p. 363.
78. Chen, J., et al., *An improved Hummers method for eco-friendly synthesis of graphene oxide.* Carbon, 2013. **64**: p. 225-229.
79. Dimiev, A.M. and J.M. Tour, *Mechanism of graphene oxide formation.* ACS nano, 2014. **8**(3): p. 3060-3068.
80. Marcano, D.C., et al., *Improved synthesis of graphene oxide.* ACS nano, 2010. **4**(8): p. 4806-4814.
81. Xiang, Y., et al., *Carbon Nanotubes and Activated Carbons Supported Catalysts for Phenol in Situ Hydrogenation: Hydrophobic/Hydrophilic Effect.* Industrial & Engineering Chemistry Research, 2014. **53**(6): p. 2197-2203.
82. Chen, D., et al., *Synthesis of carbon nanofibers: effects of Ni crystal size during methane decomposition.* Journal of Catalysis, 2005. **229**(1): p. 82-96.
83. Guo, X., et al., *Carbon formation and steam reforming of methane on silica supported nickel catalysts.* Catalysis Communications, 2012. **19**: p. 61-65.
84. Trimm, D.L., *Catalysts for the control of coking during steam reforming.* Catalysis Today, 1999. **49**(1): p. 3-10.

85. Wu, H., et al., *Ni-based catalysts for low temperature methane steam reforming: recent results on Ni-Au and comparison with other bi-metallic systems.* Catalysts, 2013. **3**(2): p. 563-583.
86. Trimm, D.L., *Coke formation and minimisation during steam reforming reactions.* Catalysis Today, 1997. **37**(3): p. 233-238.
87. Helveg, S., J. Sehested, and J. Rostrup-Nielsen, *Whisker carbon in perspective.* Catalysis today, 2011. **178**(1): p. 42-46.
88. Rostrup-Nielsen, J. and D.L. Trimm, *Mechanisms of carbon formation on nickel-containing catalysts.* Journal of Catalysis, 1977. **48**(1-3): p. 155-165.
89. Moseley, F., et al., *The poisoning of a steam hydrocarbon gasification catalyst.* Journal of Catalysis, 1972. **24**(1): p. 18-39.
90. Bartholomew, C.H. and R.J. Farrauto, *Hydrogen production and synthesis gas reactions*, in *Fundamentals of Industrial Catalytic Processes, Second Edition*. 2006, John Wiley & Sons, Inc. p. 339-486.
91. Rostrup-Nielsen, J.R., *Coking on nickel catalysts for steam reforming of hydrocarbons.* Journal of Catalysis, 1974. **33**(2): p. 184-201.
92. Moisala, A., A.G. Nasibulin, and E.I. Kauppinen, *The role of metal nanoparticles in the catalytic production of single-walled carbon nanotubes—a review.* Journal of Physics: condensed matter, 2003. **15**(42): p. S3011.
93. Harris, P.J.F., *Synthesis: Preparation methods, growth mechanisms and processing techniques*, in *Carbon Nanotubes and Related Structures (New Materials for the Twenty-first Century)*, P.J.F. Harris, Editor. 1999, Cambridge University Press: Cambridge, United Kingdon. p. 16.
94. Harris, P.J.F., *Carbon nanotube science: synthesis, properties and applications*. 2009: Cambridge university press.
95. Wunderlich, W.T., M., *Plasma-CVD Growth of Carbon nano-Tubes on Metal Substrates*, in *Trends in Nanotubes Research*, D.A. Martin, Editor. 2006, Nova Science Publishers: New York.
96. Baker, R.T.K., *Catalytic growth of carbon filaments.* Carbon, 1989. **27**(3): p. 315-323.
97. Baker, R., et al., *Nucleation and growth of carbon deposits from the nickel catalyzed decomposition of acetylene.* Journal of catalysis, 1972. **26**(1): p. 51-62.
98. Kock, A., et al., *The formation of filamentous carbon on iron and nickel catalysts: II. Mechanism.* Journal of catalysis, 1985. **96**(2): p. 468-480.

99. Zhang, T. and M.D. Amiridis, *Hydrogen production via the direct cracking of methane over silica-supported nickel catalysts.* Applied Catalysis A: General, 1998. **167**(2): p. 161-172.
100. Muradov, N., F. Smith, and T. Ali, *Catalytic activity of carbons for methane decomposition reaction.* Catalysis Today, 2005. **102**: p. 225-233.
101. De Bokx, P., et al., *The formation of filamentous carbon on iron and nickel catalysts: I. Thermodynamics.* Journal of catalysis, 1985. **96**(2): p. 454-467.
102. Muradov, N., *Catalysis of methane decomposition over elemental carbon.* Catalysis communications, 2001. **2**(3): p. 89-94.
103. Suelves, I., et al., *Carbonaceous materials as catalysts for decomposition of methane.* Chemical Engineering Journal, 2008. **140**(1): p. 432-438.
104. Baharudin, L. and M.J. Watson, *Hydrogen applications and research activities in its production routes through catalytic hydrocarbon conversion.* Reviews in Chemical Engineering, 2017a. **34**(1): p. 43-72.
105. Ermakova, M., D.Y. Ermakov, and G. Kuvshinov, *Effective catalysts for direct cracking of methane to produce hydrogen and filamentous carbon: Part I. Nickel catalysts.* Applied Catalysis A: General, 2000. **201**(1): p. 61-70.
106. Ermakova, M., et al., *New nickel catalysts for the formation of filamentous carbon in the reaction of methane decomposition.* Journal of catalysis, 1999. **187**(1): p. 77-84.
107. Baker, R. and R. Sherwood, *Catalytic gasification of graphite by nickel in various gaseous environments.* Journal of Catalysis, 1981. **70**(1): p. 198-214.
108. Xiao, Z., et al., *Porous carbon nanotubes etched by water steam for high-rate large-capacity lithium–sulfur batteries.* Journal of Materials Chemistry A, 2014. **2**(23): p. 8683-8689.
109. Xia, W., et al., *Controlled Etching of Carbon Nanotubes by Iron-Catalyzed Steam Gasification.* Advanced Materials, 2007. **19**(21): p. 3648-3652.
110. Han, T.H., et al., *Steam etched porous graphene oxide network for chemical sensing.* Journal of the American Chemical Society, 2011. **133**(39): p. 15264-15267.

CHAPTER 3

Experimental Work, Results and Discussion: Catalyst Development (Stage 1) and Catalyst Fabrication and Hypothesis Development (Stage 2)

Part I (Stage 1): Development of copper nanostructure/multi-walled carbon nanotubes (Cu/MWCNT) catalyst

3.1 Preliminary investigations

This part of the Chapter reports the preliminary work on the attempts to synthesise the catalyst, which includes the support preparation through functionalisation of the multi-walled carbon nanotubes' (MWCNT) surface, the techniques of copper nanostructure deposition on the MWCNT, and the characterisation analysis of the samples. An analysis on the ineffective demonstration of the desired copper nanoparticles dispersion on the surface of the MWCNT and the loss of samples post catalyst calcination step was discussed to reflect on what could have possibly gone wrong for lessons to be learned in the preparation for the future synthesis. The changes to rectify the issue were identified accordingly. The intention is to record the lessons learned and identifications of areas where repeat mistakes can be avoided, should there be a future work intended for the similar purpose. Whilst the content covered in this part of the Chapter is deemed not publishable in a reputable journal, it is meaningful to report in this research work as an archive record of the overall catalyst synthesis and optimisation steps and the findings along the process. The body of the preliminary investigations is presented in APPENDIX B.

3.2 Rectified work

The lessons learned from the preliminary work were rectified and taken action upon accordingly. The rectified steps and the corresponding outcomes are presented in APPENDIX C. The deemed "successful" synthesis of the copper/multi-walled carbon nanotubes (Cu/MWCNT) catalysts presented in this rectified work based on their characterisation analyses was then brought to proceed with active sites characterisation using CO temperature-programmed desorption (CO-TPD), which will be presented next in Part II of this Chapter.

Part II (Stage 2): CO temperature-programmed desorption of a hexameric copper hydride nanocluster catalyst supported on functionalised MWCNT for active site characterisation in a low-temperature water–gas shift reaction

Part II of this Chapter is a complete reproduction (with some modifications post oral examination) of a published article:

"Baharudin, L., Yip, A.C.K., Golovko, V.B., Polson, M.I.J. & Watson, M.J (2018). CO temperature-programmed desorption of a hexameric copper hydride nanocluster catalyst supported on functionalised MWCNTs for active site characterisation in a low-temperature water–gas shift reaction. *Chemical Engineering Journal*, 0(0), pp."

Highlights

- Crystal structure complex of $[(PPh_3)CuH]_6 \cdot 0.75THF$ was determined.
- Cu_6 nanoclusters precursor changed phase to Cu_2O as active phase for LTWGS.
- Cu_2O is active on its most dominant facets (1 1 0), (1 1 1), (2 0 0) and (2 2 0).

- 1 wt.% Cu_6 on functionalised MWCNT exhibited optimal hypothetical activity.
- Operating temperature range is governed by water dew point and Cu sintering.

Abstract

A family of novel catalysts was generated using chemically synthesised, atomically precise hexameric copper hydride nanoclusters (Cu_6) deposited on carboxyl-pre-functionalised multi-walled carbon nanotubes ($MWCNT_{COOH}$). The $Cu_6/MWCNT_{COOH}$ catalysts were synthesised by wet impregnation of $MWCNT_{COOH}$ with varying copper loading contents (0.5 – 15 wt.%). The study of the interaction between active sites in these materials with CO at low temperatures using CO temperature-programmed desorption in conjunction with the elementary steps in the Langmuir–Hinshelwood mechanism of low-temperature water–gas shift (LTWGS) reaction allowed us to predict the potential catalytic performance of the synthesised catalysts in the LTWGS. The hypothetical activities were correlated with the catalyst surface characterisation by CO chemisorption (Cu dispersion, crystallite size and surface area) and characterisation of the active phase composition by XRD, showing good agreement. Optimal copper loading was identified to be 1 wt.% based on the highest Cu surface area per sample weight and dispersion, and the amount of CO adsorbed per sample weight. The predicted catalytic performance was analysed as a function of support type: $MWCNT_{COOH}$ *cf.* non-functionalised MWCNT and alumina with fixed Cu loading of 1 wt.%. The CO reactivity was analysed on Cu_2O crystallites as the active phase, with a focus on the most dominant facets: (1 1 0), (1 1 1), (2 0 0) and (2 2 0). A comparison was made with a sample consisting of Cu nanoparticles (Cu_{NP}) supported on $MWCNT_{COOH}$, and a reference commercial catalyst, 51%CuO/31%ZnO-Al_2O_3. It is expected that the optimal catalyst, 1%$Cu_6/MWCNT_{COOH}$, is active for LTWGS reaction from temperatures as low as 120 °C (governed by dew point of water) up to temperatures well below industrial operating temperatures (constrained by temperature rise due to the exothermic reaction that leads to Cu_6 sintering).

Keywords: active site characterisation; copper nanoclusters; CO chemisorption; CO temperature-programmed desorption; multi-walled carbon nanotubes; water– gas shift.

Graphical abstract

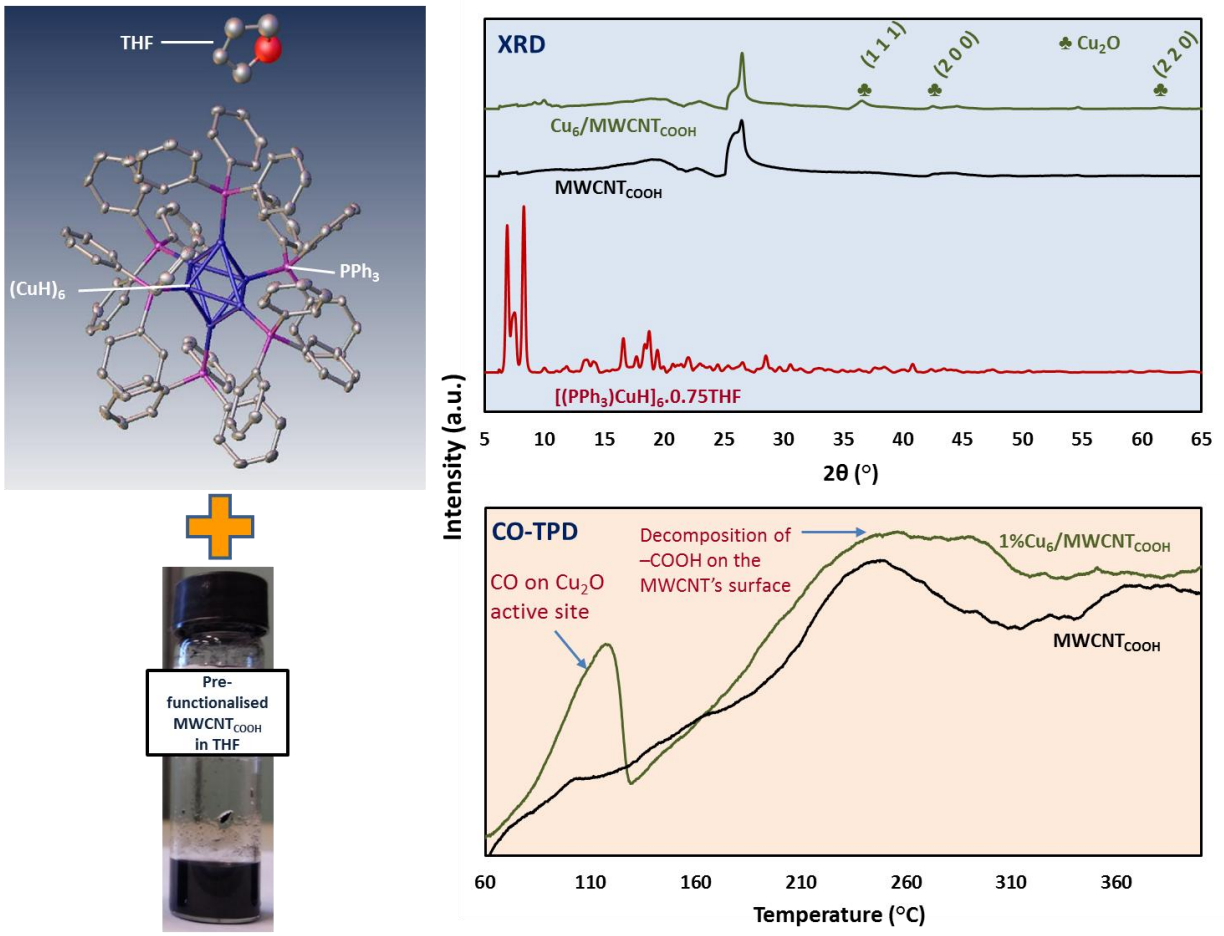

3.3 Introduction

The water–gas shift (WGS) reaction is an industrially important reaction that often follows steam reforming of hydrocarbons in a typical hydrogen production plant [1-2]. The reaction is generally favoured for not only hydrogen enrichment but also the removal of CO for high-purity hydrogen production, in which the remaining ~10 v/v% CO [3-4] content in the synthesis gas of the reformer outlet is further converted to carbon dioxide and additional

hydrogen by a reaction with steam [5-6], reducing the concentration of CO to ~0.5 – 1 v/v% [3]. The hydrogen produced by the reforming reaction and the shift conversion is typically used in ammonia synthesis in the fertiliser industry, in a petroleum refinery for various processes, such as hydrodesulphurisation, and as a fuel in hydrogen-fuelled vehicles and for power generation [1, 5, 7-8].

The water–gas shift reaction is a reversible reaction that can be expressed by eq. (3.1) [1-5, 7, 9]:

$$CO + H_2O \leftrightarrow CO_2 + H_2 \qquad \Delta H^0_{298} = -41.09 \text{ kJ/mol} \qquad (3.1)$$

The reaction is moderately exothermic, and the conversions are limited by chemical equilibrium. For an exothermic reaction, the equilibrium constant is higher at a lower operating temperature, thermodynamically favouring higher equilibrium CO conversion. However, under such low temperature conditions, the reaction is kinetically limited, *e.g.*, the reaction rate is lower [1, 4-5, 7, 10]. The conversions are not affected by the variation of the operating pressure, but the higher concentrations of the reaction products, hydrogen and carbon dioxide, inhibit the rate of the forward reaction [10].

The industrially implemented WGS reaction during early days was operated in a single adiabatic reactor that produced a product mixture with residual CO content between 2 and 4% as equilibrium was approached. The temperature along the reactor length increased as a result of the exothermic reaction, inhibiting further CO conversion. To achieve the highest possible CO conversion and yet maintain a reasonably high rate of reaction for high-purity hydrogen production, lower operating temperatures are required. However, the iron oxide-chromium oxide catalysts commercially used in the reaction were catalytically limited under such conditions and could only be active at high temperatures. Therefore, the scheme has evolved to an array of multi-stage adiabatic reactors arranged in series, with a two-stage adiabatic reactor arrangement known as the high-temperature water–gas shift (HTWGS) followed by the low-temperature water–gas shift (LTWGS) reactors becoming the most common. Such an

arrangement required inter-bed cooling for removal of heat after HTWGS to maintain the inlet temperature of the LTWGS reactor together with the development of copper-based catalysts that are active at low temperatures and capable of achieving sub-1% exit concentration of CO. The catalysts based on iron oxide structurally promoted with chromium oxide remain in use in the HTWGS reaction [1, 5-7, 10-11].

The iron-chromium-based catalyst bed in the HTWGS reactor is operated typically at reaction temperatures of 310 – 500 °C, reducing the outlet CO to concentrations that vary between 1% and 5%, depending on the feed gas compositions and exit temperature [1, 5, 7, 10]. This is followed by operating the copper-based catalyst bed in the LTWGS reactor at operating temperatures of 190 – 250 °C [1, 5], converting the residual CO further down to a sub-1% concentration at the reactor outlet [1, 3, 7, 10].

Commercially available LTWGS catalysts can be found in the form of a mixture of ZnO, CuO and Cr_2O_3/Al_2O_3, in which the compositions and characteristics vary from one vendor to another [5, 7, 12]. Most catalyst development initiatives have been focused on the objective of achieving higher conversions of CO that can approach the equilibrium limit (APPENDIX D) more closely at low temperatures than those obtained on the commercial catalysts [3, 10].

Due to equilibrium-limited CO conversions, research has been focused on the higher-activity catalysts [2-3, 5] that are capable of improving the reaction rates at the thermodynamically favourable low-temperature operation regime of the exothermic LTWGS reaction. Whilst the Cu-ZnO catalysts are active in the temperature range of 190 – 250 °C, their low catalytic activity calls for the use of low gas hourly space velocity (GHSV) of 3,000 – 5,000 hr^{-1} [1, 10]. An increased catalytic activity in the LTWGS reaction could lead to an increase in GHSV, reducing the catalyst volume in the adiabatic bed and thus saving operational and capital costs.

Part II of this Chapter presents a study that aims to demonstrate the characterisation and catalytic activity features of a novel $Cu_6/MWCNT_{COOH}$ catalyst that is potentially suitable for

ultra-low temperature WGS. In general, MWCNT possesses favourable surface textural properties with potential for further chemical modification of the surface for good metal particle dispersion. They possess a large surface area of 100 – 200 m^2/g [13] and have low tortuosity and high meso- and macro- porosity while containing no micropores [13-16]. They also have a high specific pore volume in the range from 0.5 – 2 cm^3/g [14]. These properties maximise the effective diffusion coefficient [14] and minimise the internal mass transfer limitations within the thin filamentous layers [16], hence making them a good catalyst support for the reactant/product diffusion to/from the catalytic active sites in heterogeneous reactions. Furthermore, they have excellent heat transfer capabilities, which could become critical for the removal of heat generated by the exothermic WGS reaction from the catalyst bed [17], as presented in Section 2.3.4 of Chapter 2.

In this work, the copper nanocluster-based catalysts were optimised by varying the Cu loading content. The aim was to predict the optimal Cu loading by comparing materials with Cu contents across a wide range of loadings (0.5, 1, 5, 11, 13 and 15 wt.%). CO chemisorption and X-ray diffraction (XRD) techniques were employed to measure the Cu dispersion, crystallite size and surface area and to characterise the surface chemistry and phase composition of the synthesised catalysts. The surface chemistry and phase composition characteristics of obtained materials were interpreted in light of the proposed active site properties to predict their performance in the LTWGS reaction. The activity predicted based on CO-TPD data was correlated with the analysis based on the established Langmuir–Hinshelwood (L–H) mechanism to provide a means to better screen and predict the activity of the catalyst in the LTWGS reaction.

Furthermore, the effect of supports by comparing functionalised MWCNT ($MWCNT_{COOH}$) with pristine MWCNT and alumina as supports for the predicted optimal (1 wt.%) loading was also investigated with an aim to study the interaction of copper clusters with the novel MWCNT supports and the support commonly used in industry. Finally, a benchmark catalyst made using Cu nanoparticles deposited on functionalised MWCNT at 1 wt.% loading was studied to examine the effect of different pre-synthesised nanostructured Cu precursors (nanoclusters *vs*. nanoparticles). A commercial catalyst, 51%CuO/31%ZnO-Al_2O_3, was used as a reference.

3.4 Experimental

Pre-functionalised multi-walled carbon nanotubes (MWCNT) grafted with carboxyl groups ($MWCNT_{COOH}$) on its wall surface (99.9% purity, OD = 10 – 20 nm, length = 10 – 30 µm, specific surface area (SSA) = >100 m^2/g, Nanostructured and Amorphous Materials Inc., USA), pristine MWCNT (95+% purity, OD = 10 – 20 nm, length = 0.5 – 2.0 µm, SSA = >200 m^2/g, Nanostructured and Amorphous Materials Inc., USA) and alumina (Al_2O_3) (≥99%, SSA = 2.95 m^2/g, Sigma-Aldrich) were used as-purchased as the catalyst supports in this work. A commercial catalyst, 51%CuO/31%ZnO-Al_2O_3 (Johnson Matthey PLC), was used for benchmarking and comparison purposes. The as-received mini-pellet-shaped commercial catalyst was first crushed into powder before use.

3.4.1 Sample preparation

3.4.1.1 Fabrication of Cu_6 cluster-based catalysts

The synthesis of Cu_6 nanoclusters was performed following the procedure described by Albert *et al*. (1989) [18] (APPENDIX D). To crystallise the $[(PPh_3)CuH]_6$ nanoclusters, the procedure described by Cook *et al*. (2016) [19] (APPENDIX D) was employed. Catalyst fabrication was performed using Schlenk-line technique. Weighing of Cu_6 clusters was performed in air as quickly as possible to minimise decomposition of these species, with a known mass of cluster (3.20 g) quickly transferred into a Schlenk tube with 50 mL of tetrahydrofuran ($(CH_2)_4O$ = THF) under Ar immediately after weighing to produce a stock solution with known concentration of cluster. On the basis of a total catalyst weight of 2.0 g, an amount of 1.98 g of pre-functionalised multi-walled carbon nanotubes (MWCNT) grafted with carboxyl groups (–COOH) on its wall surface was vacuum-dried at 200 °C for 5 hours to remove the traces of moisture as the support preparation step. The sample was then dispersed in THF solution under an argon atmosphere. An appropriate volume (10 mL) of the Cu_6 stock solution prepared in THF containing 0.02 g of copper (basis: Cu_6 nanoclusters

empirical formula of $[(PPh_3)CuH]_6 \cdot 0.75THF$) was added to the dispersed MWCNT suspension *via* a syringe. The wet impregnation was carried out by stirring the mixture at 750 rpm and room temperature overnight. After impregnation, the catalyst sample was vacuum-dried, and the flask containing the sample was then placed in a warm water bath (50 °C) for the last 10 min of the vacuum-drying step to remove residual solvent. The catalyst sample is denoted $1\%Cu_6/MWCNT_{COOH}$. The Cu_6 loading content was varied at 0.5, 5, 11, 13 and 15 wt% for a comparative analysis of the effect of loading on the catalytic activity. The same protocol was followed in the synthesis of 1% Cu_6 supported on pristine MWCNT and alumina. The samples are denoted as $1\%Cu_6/MWCNT_p$ and $1\%Cu_6/Al_2O_3$, respectively. The samples were stored in air after their fabrication.

3.4.1.2 Fabrication of Cu nanoparticle-based catalyst

On the basis of a total weight of catalyst of 2.0 g, 1.98 g of $MWCNT_{COOH}$ was dispersed and stirred in methanol (UN 1230, CAS 67-56-1, Burdick & Jackson (B&J Brand ®)). A stock solution of copper chloride was prepared by dissolving 0.54 g of $CuCl_2 \cdot 2H_2O$ (Riedel-De Haën AG, Seelze-Hannover) (containing 0.2 g Cu) in 10 mL of methanol. An amount of 1.0 mL of the stock copper chloride solution (containing 0.02 g Cu) was pipetted into the dispersed $MWCNT_{COOH}$ support for copper loading of 1 wt.%. The wet impregnation was carried out by stirring the mixtures overnight at 750 rpm and room temperature. The methanol dispersing the copper impregnated MWCNT sample was then removed under vacuum. The dry catalyst was then calcined in a nitrogen flow of 100 mL/min at 400 °C in a tubular furnace for 3 hours, at a ramping rate of 2.5 °C/min. The catalyst sample is denoted as $1\%Cu_{NP}/MWCNT_{COOH}$, with the subscript NP referring to the nanoparticles.

3.4.2 Sample characterisation

Phase composition: The powder diffraction patterns of the MWCNT supports, pure micro-crystalline powder of crystallised $[(PPh_3)CuH]_6$, synthesised catalysts (as-prepared) and commercial catalyst (as-received) were recorded on an X-ray diffractometer (SuperNova,

Agilent Technologies) over the 2θ range of 10 – 90°, using Cu-Kα radiation (λ = 1.54056 Å) operated at room temperature. The crystal structure and components of the nanoclusters were validated using the same X-ray diffractometer on a single-crystal form of the Cu_6 nanoclusters at 120 K.

Thermal stability: Both MWCNT support samples were analysed by thermogravimetric analysis (TGA) (SDT Q600, Alphatec Systems Ltd. supported by TA Instruments Universal Analysis 2000 software) under nitrogen flow of 100 mL/min, at a ramping rate of 50 °C/min, from an ambient condition up to 1200 °C to investigate their thermal stability under inert atmosphere. For the crystallised $[(PPh_3)CuH]_6$, the ramping rate used was 10 °C/min up to 400 °C.

Negative surface charge: The zeta potential of the MWCNT samples dispersed in deionised (DI) water was measured using Zetasizer Nano Series (Malvern Instruments Ltd., UK) at room temperature. The results were averaged, with each sample measurement repeated at least 4 times.

Dispersion/sedimentation: An amount of 0.050 g of pre-functionalised $MWCNT_{COOH}$ sample was centrifuged (MULTIFUGE 3 L, Heraeus) in 25 mL of DI water at 10,000 rpm for 20 min, and the parameters were halved for the same amount of pristine MWCNT sample in the same amount of DI water. The assessment was performed at room temperature.

Copper content: An amount of 0.050 g of each of the synthesised catalyst samples was digested in 2 mL *aqua regia* at 80 °C for 2 days (APPENDIX D) to dissolve the copper particles from the MWCNT support, followed by ultrasonication for inductively coupled plasma mass spectrometry (ICP-MS) (7500cx single-quad, Agilent Technologies) analysis. For every sample, a blank solution was prepared for ICP-MS analysis to account for an inherent copper content in the *aqua regia* solution that was not from the tested samples. A duplicate sample was prepared to ensure consistency of the results.

Copper dispersion and crystallite size: The CO chemisorption measurements were performed using BELCAT II Catalyst Analyser (MicrotacBEL) (Figure D1 of APPENDIX D). Prior to measurement, the catalyst samples were first pre-treated in the same unit. Approximately 0.05 g of the as-received commercial catalyst sample was pre-treated by reduction in 5% H_2/95% Ar flowing at 50 sccm at 230 °C for 300 min. Another measurement was also conducted on a commercial catalyst that was reduced at 400 °C for comparison purposes. The as-prepared synthesised sample (0.03 – 0.05 g) was pre-treated under He flowing at 50 sccm

by heating from ambient temperature to 100 °C for 20 min, and the temperature was maintained at 100 °C for 15 min. The same pre-treatment procedure was followed for another measurement of the commercial catalyst without reduction with H_2. In some selected samples, the pre-treatment temperature was varied to study the effect of the pre-treatment temperature over a fixed duration, and the duration of the pre-treatment temperature of 100 °C was varied to study the effect of the pre-treatment duration at a constant temperature. After pre-treatment, CO chemisorption by pulse injection was performed. For all catalyst samples, measurement was performed at 50 °C using CO as adsorption gas (10% CO/90% He flowing at 50 sccm) and stoichiometry factor of 1.0. He was used as the thermal conductivity detector (TCD) carrier gas flowing at 30 sccm in a low sensitivity TCD set at 100 °C. The adsorption gas was set to flow to the loop for 60 s, with the gas being injected to the sample cell in every 5 s. The measurement was repeated 2 times to ensure reproducibility, assessing a sub-set of randomly selected samples.

3.4.3 Active site characterisation study

Measurements were performed using BELCAT II Catalyst Analyser on the same samples used previously for CO chemisorption. The CO adsorption was carried out by flowing 10% CO/90% He mixture at 50 sccm at 50 °C for 1 hour, followed by a post-treatment in He flowing at 50 sccm at 50 °C for another hour. The CO-TPD measurement was then performed starting from 50 °C and heating to a target temperature of 400 °C at a ramping rate of 10 °C/min, in a target temperature holding time of 20 min. TCD was set at 100 °C and high sensitivity. The measurement was repeated 2 times to ensure reproducibility, assessing a sub-set of randomly selected samples. Hydrogen temperature-programmed reduction (H_2-TPR) was performed on the bare pristine and pre-functionalised MWCNTs by flowing 30 sccm of 5% H_2/95% Ar from 50 °C up to 600 °C at a ramping rate of 10 °C/min.

3.5 Results and discussion

3.5.1 Characterisation

3.5.1.1 MWCNT support

Based on the certificate of analysis (COA) supplied by the vendor, the content of the carboxyl groups in the $MWCNT_{COOH}$ sample determined by X-ray photoelectron spectroscopy (XPS) analysis was 0.95 – 1.05%. The XRD patterns of the pristine MWCNT and $MWCNT_{COOH}$ were compared to ascertain the quality and crystallinity of these materials. In the diffraction patterns of the MWCNT samples, focus was given on the peaks at 2θ = ~26.2 and ~42.5°, which correspond to the (0 0 2) and (1 0 0) reflections respectively (International Centre for Diffraction Data (ICDD) 01-075-1621). Peng & Liu (2006) [20] reported that the changes of the ratio of intensity of peak (1 0 0) to peak (0 0 2), I_{100}/I_{002} from the XRD patterns corresponded with the MWCNT's planar order, where a lower ratio of I_{100}/I_{002} indicates an increase in the degree of alignment to the (0 0 2) plane, which is the dominant facet of carbon. It was also found that the lower I_{100}/I_{002} ratio corresponds to an increase in the degree of crystallinity of the carbon ordering analysed using Raman spectroscopy. As seen from Figure 3.1, when compared to the pristine MWCNT sample, the I_{100}/I_{002} ratio was significantly lower in the $MWCNT_{COOH}$ sample. This result supports a higher degree of crystallinity in the pre-functionalised $MWCNT_{COOH}$ sample.

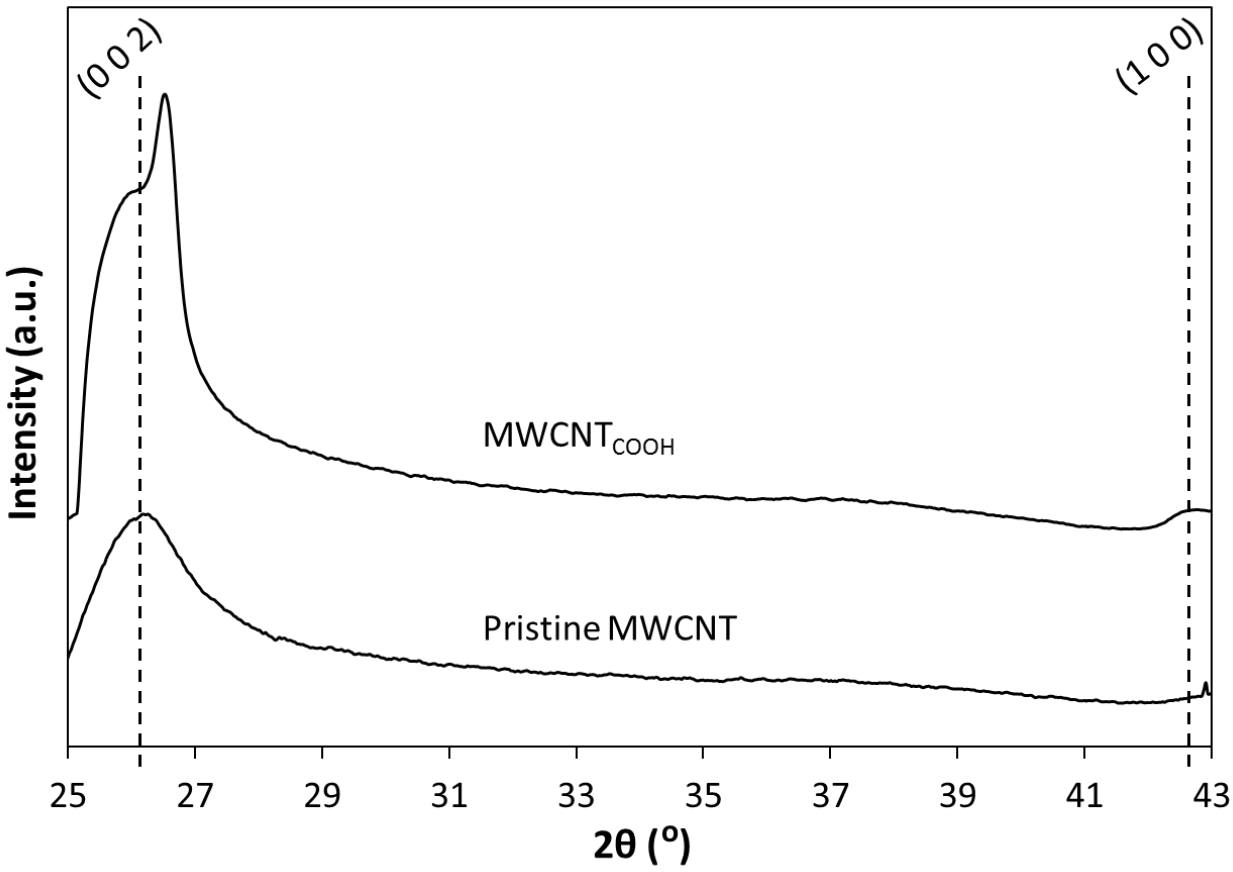

Figure 3.1: XRD patterns of as-purchased pristine and pre-carboxyl-functionalised MWCNTs.

TGA is used to estimate the relative degree of graphitisation of MWCNT by measuring the decrease in mass of sample as a function of annealing temperature. Highly graphitised MWCNT generally decomposes at temperatures higher than that for carbon of lower ordering [21]. Unstable disordered carbon is combusted at temperatures below 500 °C, while the combustion of highly graphitised carbon takes place at temperatures above 600 °C [22-23]. From Figure 3.2, it can be observed that the MWCNTs were, in general, thermally stable under nitrogen with a weight loss of 4.0% or below in the as-received pristine and pre-functionalised samples at 600 °C. At the end of the TGA test at 1200 °C, the pre-functionalised MWCNT$_{COOH}$ showed a weight loss of 11.3%, while the pristine MWCNT showed a weight loss close to two times higher. This indicates the pristine MWCNT contain some disordered carbon components that are unstable at very high temperatures.

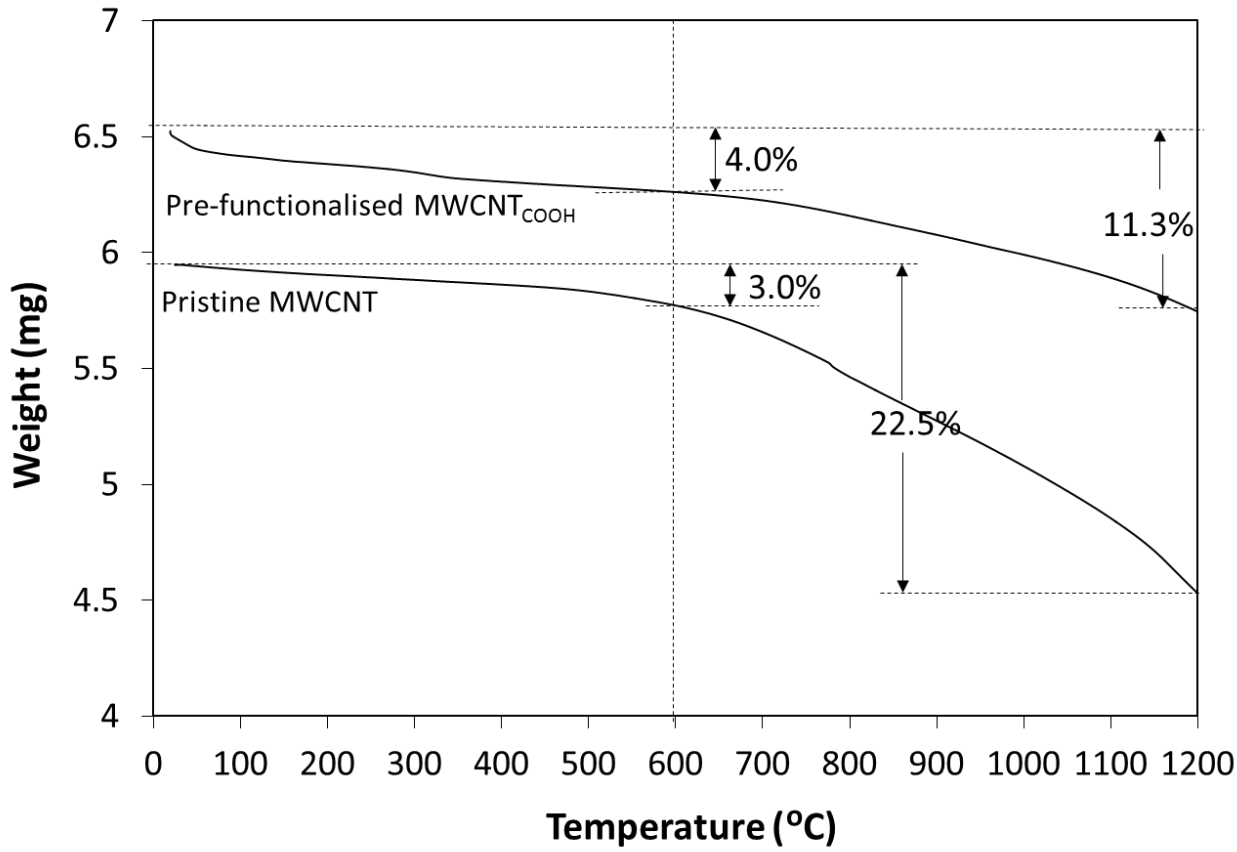

Figure 3.2: TGA of as-purchased pristine and pre-carboxyl-functionalised MWCNTs.

Based on the zeta potential measurements in water at pH 7, the negative surface charge of the pre-functionalised $MWCNT_{COOH}$ was –24.48 ± 1.46 mV, which was close to double the negative charge of the pristine MWCNT; –15.43 ± 2.03 mV. This result is in alignment with the work published by Hamilton *et al*. (2013) [24] and Lee *et al.* (2007) [25]. Hamilton *et al*. (2013) [24] demonstrated that a treatment with HNO_3 resulted in surface carboxylation of the carbon nanomaterials that made their surface charge more negative. This was due to low isoelectric point of the –COOH moiety, which gave rise to dissociation into negative charge – COO^- and hence, helped increase the carbon nanomaterials' hydrophilicity in aqueous phase.

In addition, the zeta potential gives an indication on the ionic stability of the colloidal system in water, in which a more negative surface charge allows an improved stability of the colloidal system against coagulation, which accounts for an improvement of the MWCNTs' dispersibility in water [25]. An attribute to the stabilisation of the functionalised MWCNT

could be the electrostatic repulsions among the hydrophilic head group against van der Waals attractive forces between graphitic surfaces [26].

A brief dispersion/sedimentation test was conducted on the MWCNT samples in DI water. Sedimentation of pristine MWCNT was observed in DI water, even though the centrifugation parameters were halved in comparison to the pre-functionalised MWCNT samples. In contrast, the pre-functionalised $MWCNT_{COOH}$ was observed to disperse well in water, and the suspensions were found to be stable even after more than a week of storage (Figure 3.3). This observation implies a satisfactory increase of the hydrophilicity of the MWCNT's surface in the $MWCNT_{COOH}$ sample.

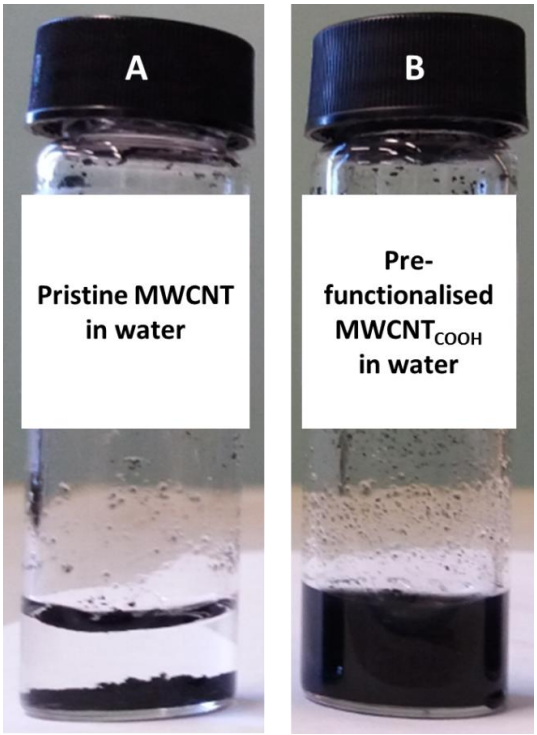

Figure 3.3: Dispersion/sedimentation test.

(A) Sedimentation of pristine MWCNT in water; and (B) stable well-dispersed $MWCNT_{COOH}$ in water after more than a week of storage.

3.5.1.2 Copper nanoclusters

The crystal structure was determined by single-crystal XRD (SCXRD) (Cambridge Crystallographic Data Centre (CCDC) # 1864974). The structure was solved in the monoclinic space group $P2_1$ with a = 14.28467 Å, b = 16.00824 Å, c = 21.39091 Å, α = 90º, β = 92.1229º, γ = 90º, Z = 2 and cell volume, V = 4888.16 Å^3. The structure has the empirical formula of $Cu_6P_6C_{111}H_{102}O_{0.75}$ due to 0.75 of a THF molecule being included in the structure. The complex of hexameric copper hydride ligated by triphenylphosphine, $[(PPh_3)CuH]_6$ (Figure 3.4) can be compared to the hemisolvate structure, $[(PPh_3)CuH]_6 \cdot 0.5THF$ collected at room temperature by Albert *et al*. (1989) [18]. The differences in the unit cells (a = 14.464 Å, b = 16.252 Å, c = 21.487 Å) are likely due to the differences in temperature of the collection and loss of THF during the room temperature collection.

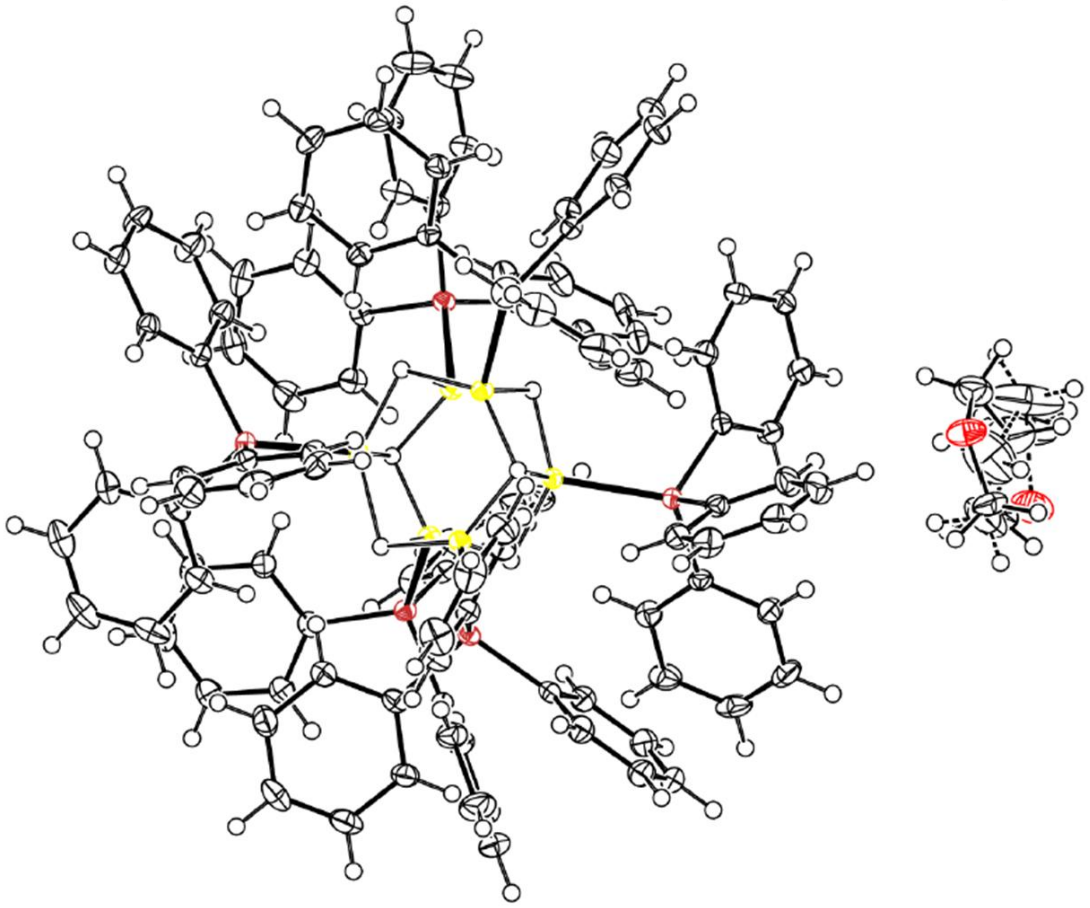

Figure 3.4: Crystal structure complex of $[(PPh_3)CuH]_6$.0.75THF determined by SCXRD.

In the diffraction of the pure microcrystalline powder of Cu_6 nanocluster, the intensities of the experimental powder XRD (PXRD) pattern matched the predicted PXRD pattern generated from the SCXRD result (Figure 3.5), with a slight shift in the peak positions due to the experimental data being collected at two different temperatures (*i.e.* ambient temperature for PXRD and 120 K for SCXRD). The match in the intensities is better between the new structure (CCDC 1864974) than the previously reported one because the previous report [18] omitted the THF from the final refinement cycles. The experimental PXRD did not contain the powder patterns of other crystalline phases associated with copper crystallites; metallic Cu (ICDD 01-085-1326), oxide of Cu(I) (Cu_2O) (ICDD 01-077-0199), and oxide of Cu(II) (CuO) (ICDD 01-080-0076).

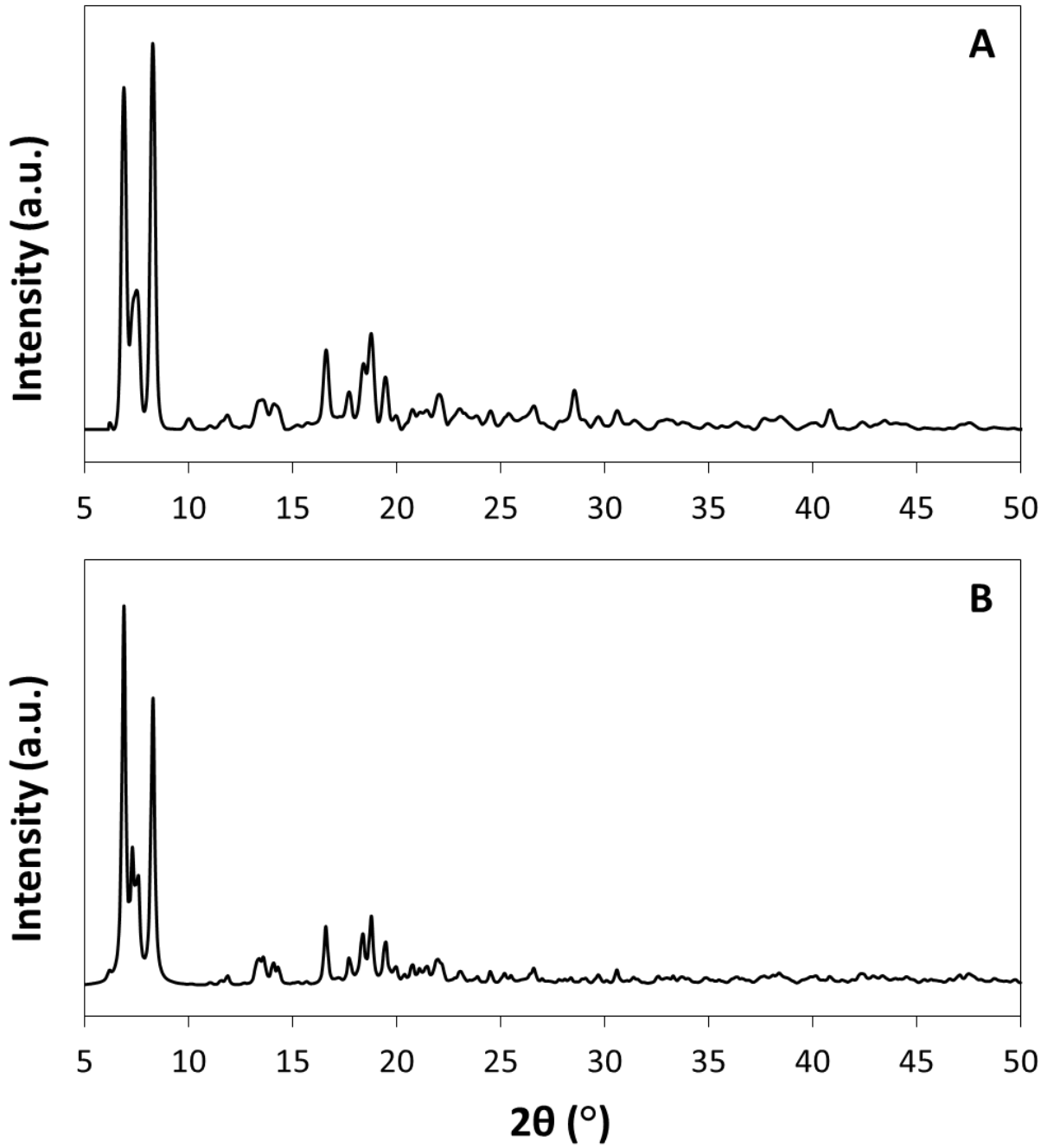

Figure 3.5: PXRD patterns of Cu_6 nanocluster.

(A) Collected experimentally; and (B) generated from SCXRD (CCDC 1864974).

The TGA of the microcrystalline powder of the pure copper nanoclusters (Figure 3.6) revealed that the nanoclusters lost approximately 78.4% of their original weight at 260 °C under nitrogen. The initial mass loss can be attributed to loss of THF solvate molecules (molecular weight (MW) = 72.11 g/mole) and moist content which desorbed first at a

temperature below 100 °C (experimentally measured wt.% due to loss of THF and moist content – 3.5 wt.%; calculated (THF only) based on the empirical formula of $[(PPh_3)CuH]_6.0.75THF$ (MW = 2,015.2 g/mole) – 2.7%). The next stage of sample decomposition can be explained by the loss of the PPh_3 ligand (MW = 262.29 x 6 moles = 1573.74 g/mole) in the temperature range from 150 to 260 °C, leaving behind the copper or copper hydride nanoparticles (experimentally measured wt.% loss due to loss of PPh_3 ligands – 74.9 wt.%; calculated based on the empirical formula of $[(PPh_3)CuH]_6$ – 80.3%). It is impossible to reliably ascertain the fate of hydrides associated with Cu within cluster cores as such small mass loss (0.3% for all 6 of these) is within experimental error. The slight weight gain at the higher temperatures could indicate an onset of nitride or oxide formation, but this was not verified experimentally. The nitride could have been formed due to exposure to nitrogen used in the TGA measurement, while oxide formation could also be possible due to the oxophilic nature of copper when being exposed to air [2, 27-28]. The copper crystal could have interacted with air that traveled into the furnace during the TGA measurement.

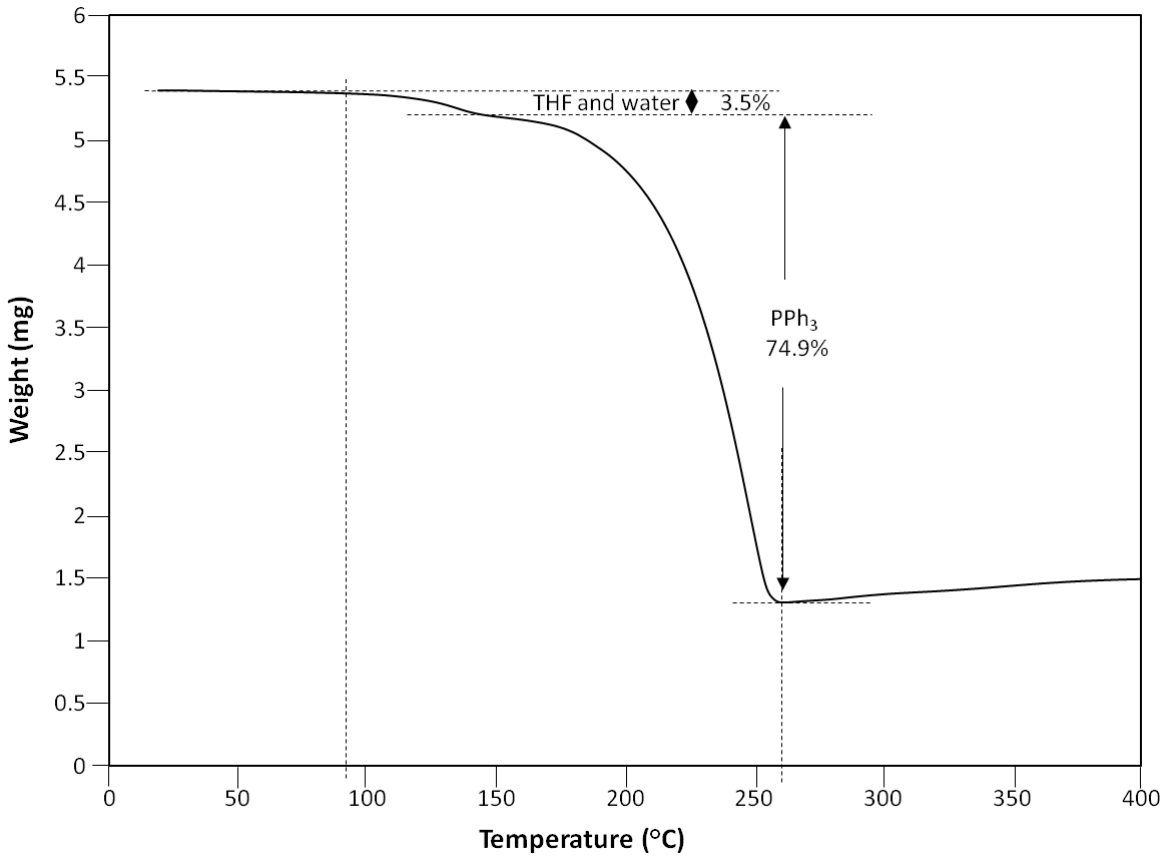

Figure 3.6: TGA of $[(PPh_3)CuH]_6.0.75THF$ nanoclusters.

3.5.1.3 Catalysts

Copper content characterisation: Based on ICP-MS data (Table 3.1), the experimentally measured copper loading in the $Cu_6/MWCNT_{COOH}$ catalyst sample was observed to be close to the calculated loading. The Cu species dispersion, surface area and crystallite size were calculated based on data obtained by using BELCAT II Catalyst Analyser based on the amount of CO chemisorbed on 1.0 g of sample (APPENDIX D). The measurements by pulse CO chemisorption at 50 °C in general revealed an increasing copper crystallite size and reduced copper dispersion in the direction of the increasing copper loading content. The optimal copper loading content was identified to be 1 wt.% based on the highest copper surface area per sample weight and the highest CO-adsorbed amount per sample weight at STP.

Table 3.1: Cu crystallite size and dispersion.

Sample	Synthesis protocol	Sample condition	Calculated Cu species content (wt.%)	Actual Cu content by ICP-MS (wt.%)	Cu species particle diameter (nm)	Cu species dispersion (%)	CO adsorbed amount per sample weight (cm^3/g (STP))	Cu species surface area per sample weight (m^2/g)	Cu species surface area per Cu weight (m^2/g)
$Cu_6/MWCNT_{COOH}$	• Copper (I) chloride + PPh_3 + K-selectride dissolved in THF prepared under Ar environment • Wet impregnation under Ar • No calcination	Heat-pre-treated at 100 °C	0.5	0.64	2.5	41.9	0.95	1.73	269.99
			1	1.01	2.9 *3.0	35.6 *35.4	1.27 *1.25	2.31 *2.28	229.43 *228.02
			5	5.46	61.0	1.7	0.33	0.60	11.03
			11	11.69	66.4	1.6	0.65	1.18	10.13
			13	13.62	79.7	1.3	0.63	1.15	8.44
			15	15.02	111.7	0.9	0.50	0.91	6.02
$Cu_6/MWCNT_p$	• Same as above	Heat-pre-treated at 100 °C	1	N.D.	3.2 *3.4	32.4 *31.1	1.14 *1.10	2.09 *2.01	208.99 *200.60

Cu_6/Al_2O_3	• Same as above	Heat-pre-treated at 100 °C	1	N.D.	6.9	15.2	0.53	0.98	97.72
$Cu_{NP}/MWCNT_{COOH}$	• Copper (II) chloride dissolved in methanol prepared at ambient • Wet impregnation at ambient • Calcination in N_2 at 400 °C	Heat-pre-treated at 100 °C	1	N.D.	3.2	32.8	1.16	2.12	211.56
Commercial catalyst	• Unknown	Heat-pre-treated at 100 °C	51	N.D.	235.6	0.4	0.80	1.46	2.85
		Reduced at 230 °C	51	N.D.	295.8	0.3	0.63	1.16	2.27
		Reduced at 400 °C	51	N.D.	1188.2	0.1	0.16	0.29	0.57

*Experimentally reproduced data of selected samples

N.D. = not determined

It is noted that the crystallite size of Cu species supported on alumina is more than double the size of its counterparts supported on MWCNTs, which could be explained by the huge difference in SSA of the three support materials, where the value is two orders of magnitude higher for MWCNTs than for alumina based on the product information provided by the vendors; 2.95 m^2/g for alumina, >200 m^2/g (pristine MWCNT), and >100 m^2/g ($MWCNT_{COOH}$). The SSA of $MWCNT_{COOH}$ is half that of the pristine due to the carboxyl group occupancy of the sidewall surface of the MWCNT. In addition, the dispersion of the Cu species is halved in alumina. This result indicates that the interaction between the Cu_6 nanoclusters and the alumina support is relatively less effective, resulting in a poorer dispersion.

The measurements were extended to observe the effect on copper sintering as a result of the catalyst pre-treatment temperature increased and the heating duration prolonged. The results are presented in Table 3.2. In general, the copper crystallite size increases and the copper dispersion decreases in the direction of increasing pre-treatment temperature at a fixed duration and with an increasing pre-treatment duration at any given constant temperature.

Table 3.2: Effects of pre-treatment temperature and duration.

Sample	Pre-treatment temperature (°C)	Pre-treatment duration (min)	Cu species particle diameter (nm)	Cu species dispersion (%)	Cu species surface area per sample weight (m^2/g)	Cu species surface area per Cu weight (m^2/g)
0.5%Cu_6/$MWCNT_{COOH}$	100	35	2.5	41.9	1.73	269.99
	400	35	20.4	5.1	0.21	32.96
1%Cu_6/$MWCNT_{COOH}$	100	35	2.9 *3.0	35.6 *35.4	2.31 *2.28	229.43 *228.02
	100	65	2.8	36.7	2.24	221.99
	100	80	23.0	4.5	0.30	29.29
	100	140	43.6	2.4	0.16	15.41
	150	65	28.5 *32.8	3.7 *3.2	0.24 *0.21	23.64 *20.52
	400	35	23.8	4.4	0.29	28.31

	100	35	79.7	1.3	1.15	8.44
	200	35	90.9	1.1	1.01	7.40
13%Cu_6/$MWCNT_{COOH}$						
	300	35	359.4	0.3	0.25	1.87
	400	35	596.0	0.2	0.15	1.13

*Experimentally reproduced data of selected samples

Based on the measurements performed on 1%Cu_6/$MWCNT_{COOH}$, the results in Table 3.2 suggest a significant population of well-dispersed Cu species with high surface area was formed at 100 °C when heating was continued beyond 65 min. When the sample was further heated for another 15 min, the copper nanoparticles sintered rather significantly, as evidenced by an increase in particle size, a reduction in the Cu surface area and diminution of the dispersion by close to 8 times.

The measurements on 1%Cu_6/$MWCNT_{COOH}$ were extended to pre-treatment at 150 °C with an aim to determine the maximum temperature at which the sample could be pre-treated before the effect of sintering started to appear while maintaining the duration of such treatment at 65 min. The 50 °C increase in treatment temperature resulted in 10-fold drop in the copper dispersion at 65 min. Similarly, a pre-treatment at relatively low temperature of 100 °C for 80 min or pre-treatment at relatively high temperature (400 °C) but only a short time (35 min) proved to be detrimental to the copper dispersion in a similar manner. This indicated that thermally, the Cu_6/$MWCNT_{COOH}$ catalysts were highly unstable.

In general, at all the pre-treatment conditions for activation of 1%Cu_6/$MWCNT_{COOH}$ even in the case of up to 400 °C for 35 min, this catalyst exhibited a significantly smaller Cu crystallite size and at least an order of magnitude higher dispersion than that of the commercial catalyst reduced at 230 °C (Table 3.1). Note that the commercial catalyst requires activation by reduction with hydrogen at 230 °C while the Cu_6/$MWCNT_{COOH}$ catalysts are readily active without a specific activation protocol. The data for 13%Cu_6/$MWCNT_{COOH}$ up to 200 °C shows that even in the case of such high metal loading sample, the Cu species crystallite size and dispersion are still better than that of reduced (activated) commercial catalyst.

A comparison of the Cu species surface areas and dispersions between the Cu_6/$MWCNT_{COOH}$ catalysts and the commercial catalyst that were subject to the same heat treatment in He at 100 °C is presented in Table 3.1. The results showed a higher Cu species surface area and dispersion in the former. In addition, even when the Cu_6/$MWCNT_{COOH}$ catalysts were treated at 200 °C (Table 3.2) while the commercial catalyst was treated at 100 °C (Table 3.1), the former still displayed a smaller

copper species crystallite size (*e.g.* Cu species crystallite size = 90.9 nm for 13%Cu_6/$MWCNT_{COOH}$ pre-treated at 200 °C, 235.6 nm for commercial catalyst pre-treated at 100 °C). However, it is generally noted that the Cu_6/$MWCNT_{COOH}$ catalysts exhibited poor thermal stability as evidenced by the significant Cu species sintering behaviour when the pre-treatment temperature of the 13%Cu_6/$MWCNT_{COOH}$ catalyst was increased from 200 °C to 400 °C, in which the Cu species crystallite size increased from 90.9 nm to 596.0 nm.

Cu_6 clusters were used to decorate MWCNTs and alumina supports with well-defined Cu active sites. However, it was expect that prolonged exposure of the as-prepared samples to air would result in oxidation of clusters and formation of oxide nanoparticles even at room temperature [2, 27-28]. Yang *et al*. (2017) [28] synthesised size-selected Cu_n clusters on Al_2O_3 thin films and found that upon exposure of the samples to air, the as-deposited metallic Cu_n clusters underwent oxidation. The formation of Cu_2O phase is presented next in this section. In this work, CO was used as the probe gas to study the chemisorption ability of the supported Cu_2O as the active phase for LTWGS.

Although N_2O has been an established probe gas for Cu site measurement, the dispersion of Cu based on oxygen uptake by Cu(0) sites following the stoichiometry of dissociative N_2O adsorption ($N_2O + 2\ Cu \rightarrow Cu_2O + N_2$) does not take into account the unreduced Cu^+ species [29]. The use of N_2O as the probe gas would not provide a well-represented measurement of the Cu(I) sites. This will have a different connotation since Cu_2O was examined as the active Cu species for the LTWGS reaction in this study. In addition, whilst the catalyst can be reduced from Cu(I) to Cu(0) and then the Cu sites are measured using N_2O, the following concerns are raised as the measurements are affected by variation in:

i) The temperature and duration of Cu(I) reduction to Cu(0) (as evidenced by the findings presented in Table 3.2);
ii) the temperature of Cu(0) oxidation to Cu(I) by dissociative N_2O adsorption (N_2O reduction) [29].

Song *et al.* (2015) [30] studied the stability of nano-Cu_2O against reduction by CO as a function of crystallite size. Hua *et al*. (2013) [31] demonstrated the use of CO as the probe gas to measure the reducibility and chemisorption ability of Cu_2O nanocrystal facets of (1 0

0), (1 1 1) and (1 1 0) towards CO by CO-TPR and CO chemisorption and relate such measurements with the activity of the Cu_2O catalyst in the catalysis of CO oxidation. In their [31] findings, different crystal planes exhibited different levels of activity in chemisorbing CO, which were shown to be consistent with their catalytic performance in CO oxidation. In general, the works by Song *et al.* (2015) [30] and Hua *et al*. (2013) [31] validate the use of CO as the probe gas in the chemisorption on Cu_2O phase and, hence, provides good support for its employment in this study.

Phase composition: The powder diffraction files (PDFs) of four prominent crystalline phases of copper; metallic Cu, CuH (Crystallography Open Database (COD) 96-900-8867), Cu_2O and CuO were used to analyse the as-prepared catalyst diffraction patterns (Figure 3.7). Three peaks assigned to the dominant facets of Cu_2O crystal (1 1 1), (2 0 0) and (2 2 0) were positioned at 2θ = 36.5, 42.4 and 61.6° respectively. Cu_2O (2 0 0) overlapped with carbon plane (1 0 0) at 2θ = ~42.2°. The less dominant Cu_2O (1 1 0) peak could be more profoundly visualised at 29.6° only in higher Cu contents. The formation of Cu_2O in the catalyst samples even though the synthesis protocol did not include a calcination step in air or oxygen flow can be explained by the oxophilic nature of Cu, which is easily oxidised when in prolonged contact with air, even under ambient conditions [2, 27-28].

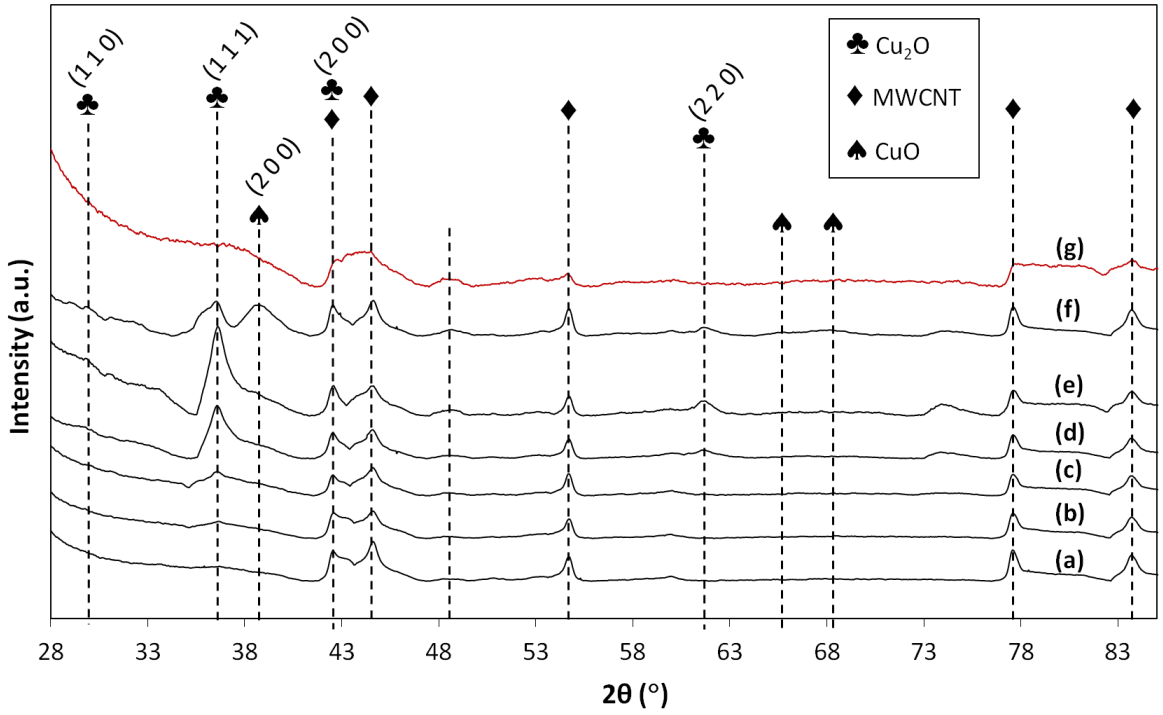

Figure 3.7: XRD patterns of as-prepared Cu_6/$MWCNT_{COOH}$ catalysts of varied copper loading content of: (a) 0.5%, (b) 1%, (c) 5%, (d) 11%, (e) 13%, (f) 15%, and (g) 0%.

The first-order significant Cu_2O peak ($2\theta = 36.5°$), which was the most dominant facet of the Cu_2O crystal phase, showed no distinguishable peak in the case of XRD of the sample containing 0.5% Cu_6. In the 1% Cu_6 sample, the diffraction pattern was almost identical to that of the 0.5% Cu_6 sample, with only a very small Cu_2O (1 1 1) peak appearing at 36.5°. This peak was more pronounced in the 5% Cu_6 catalyst sample, and its intensity increased further as the Cu_6 loading increased to 11% and 13%. However, the sample containing the 15% Cu_6 exhibited a peak of decreased intensity with a relative value between that of 11% and 5% Cu_6. In summary, the intensity of Cu_2O phase plane (1 1 1) increased with an increase in the Cu loading content, following the Cu_6 content in the order of $0.5\%Cu_6 \approx 1\%Cu_6 < 5\%Cu_6 < 15\%Cu_6 < 11\%Cu_6 < 13\%Cu_6$. The remaining dominant Cu_2O facets (2 0 0) and (2 2 0) showed peak intensity trends that were very (but not exactly) similar to Cu_2O (1 1 1).

Based on the results presented in Table 3.1, it is suggested that the surface area of Cu_2O crystallites is the factor that determines its catalytic activity. For instance, in the loading

content order of 5%Cu_6 < 15%Cu_6 < 11%Cu_6, the Cu surface area in a gram of sample is 0.60 < 0.90 < 1.18 m^2, increasing in the same direction as the ratio of intensity of the Cu_2O (1 1 1) peak to intensity of any one of the MWCNT peaks. Although the Cu surface area was larger in the samples containing 0.5 and 1% Cu_6, their negligible intensity Cu_2O (1 1 1) peaks indicated a highly dispersed Cu(I) oxide structure phase, too low copper species loading content on the $MWCNT_{COOH}$ support, and/or a smaller crystallites size than the XRD lower detection limit of 4 nm [2, 11]. These features are in agreement with the findings presented in Table 3.1. An XRD analysis was also performed on the sample of 0.5%Cu_6/$MWCNT_{COOH}$ that had undergone heat pre-treatment at 100 °C. The results revealed an absence of the Cu_2O (1 1 1) peak position at 36.5° (Figure D2 of APPENDIX D), indicating that the crystallite size and dispersion of the Cu_2O phase on $MWCNT_{COOH}$ support were maintained below the XRD detection limit.

The presence of copper oxide in the form of Cu_2O was further validated by H_2-TPR analysis of a representative catalyst sample, 1%Cu_6/$MWCNT_{COOH}$. During the reduction by 5% H_2 flowing in a nitrogen carrier, the sample began to be reduced at approximately 300 °C up to slightly below 500 °C, as shown by the reduction peak (Figure D3 of APPENDIX D). The same reduction behaviour was exhibited by a powdered Cu_2O sample, as demonstrated by Kim *et al*. (2003) [32]. The alignment of these results confirmed the change in the CuH phase to Cu_2O once the Cu_6 nanoclusters had been impregnated on the $MWCNT_{COOH}$ support.

A peak at $2\theta \approx 49°$ attributed to an unknown species present in the bare $MWCNT_{COOH}$ sample was also detected in the 13% and 15% Cu_6/$MWCNT_{COOH}$ samples, which could have originated from an unknown impurity in the $MWCNT_{COOH}$ purchased off-the-shelf.

In a comparison between a representative Cu_6/$MWCNT_{COOH}$ catalyst (as-prepared) and the reference catalyst (as-received), the diffraction pattern of the 13%Cu_6/$MWCNT_{COOH}$ sample was used to represent the Cu_6/$MWCNT_{COOH}$ series due to its obvious appearance and significant intensity of the Cu_2O phase plane (1 1 1) at the peak position of 36.5°, as discussed earlier. Here we were more interested in the crystalline phases associated with Cu, and therefore the attention was focused on the two oxides. As shown in Figure 3.8, no peaks

were detected at 2θ = 36.5 and 42.4° in the commercial catalyst, indicating the absence of the Cu_2O phase in the sample. The peaks that showed the characteristic of the CuO crystalline phase are clearly more profound in the commercial catalyst diffraction pattern at 2θ = 35.5 (–1 1 1), 38.6 (1 1 1), 39.0 (2 0 0), 56.6 (0 2 1), 68.8 (–2 2 1), and 74.9° (004). The peak attributed to the most dominant facet of CuO (–1 1 1) overlaps with ZnO (ICDD 01-075-1533) crystal plane (1 0 1) and Al_2O_3 (ICDD 01-075-0788) crystal plane (1 0 4) at 2θ = 35.5°, which is also observed on CuO (0 0 4) at 74.9°. The CuO phase planes (1 1 1) and (–2 2 1) overlap with alumina (1 1 0) and (3 0 0), respectively. The other remaining detected peaks confirm the presence of the CuO crystalline phase in the commercial catalyst sample.

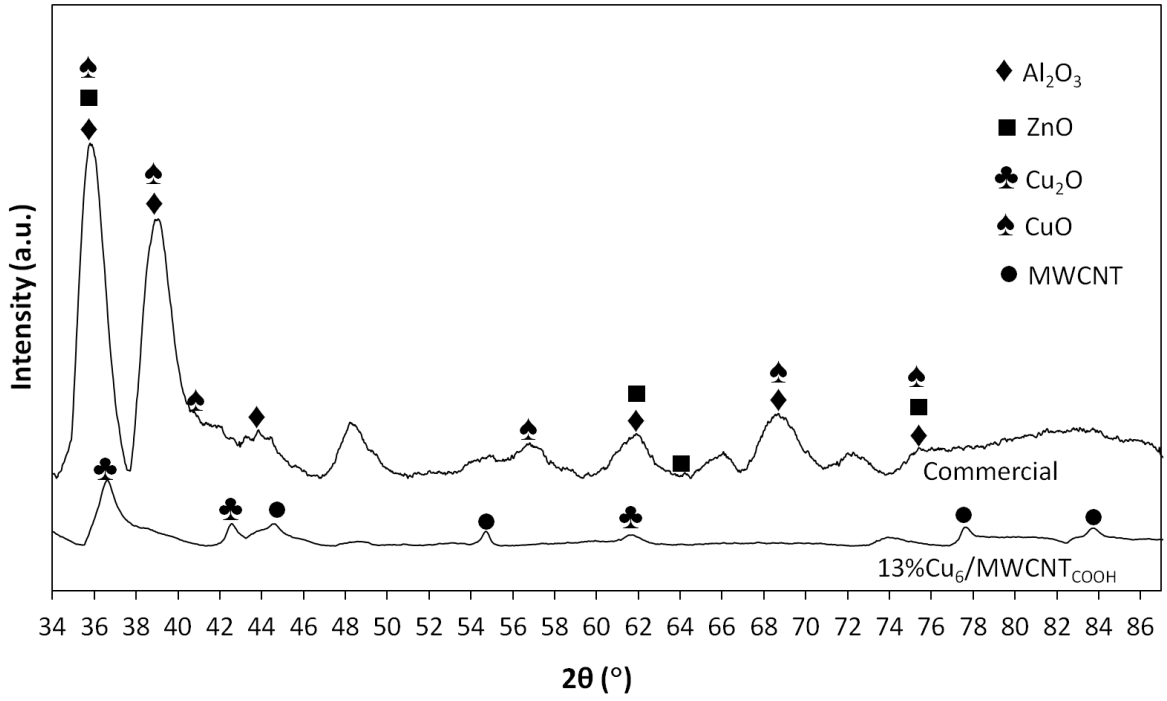

Figure 3.8: XRD patterns of as-prepared $13\%Cu_6/MWCNT_{COOH}$ and as-received commercial catalyst samples.

The presence of the CuO component in the commercial catalyst was further confirmed by H_2-TPR profile of its sample (Figure D4 of APPENDIX D), exhibiting a reduction curve beginning from approximately 200 °C under a mixture of 5% H_2/95% He, which is in alignment with the findings of Kim *et al*. (2003) [32].

The CuO phase was detected in the commercial catalyst sample as a result of its synthesis protocol, which typically involves calcination with oxygen/air to market the catalyst product to industry operators in a stable CuO form. The intensity of the peaks due to the Cu oxide species was more profound in the commercial catalyst due to the higher Cu loading content.

A peak attributed to CuO (2 0 0) was also detected on the 15%Cu_6/$MWCNT_{COOH}$ sample at $2\theta \approx 39.0°$ (Figure 3.7). This peak was significantly more profound in the commercial catalyst (Figure 3.8). Some weak but noticeable signals at $63° < 2\theta < 70°$ in the 13% and 15% Cu_6/$MWCNT_{COOH}$ samples (Figure 3.7) were likely attributed to less dominant facets of CuO phase. These detected peaks could indicate a presence of small amount of Cu(II) oxide phase in the Cu_6/$MWCNT_{COOH}$ samples containing high copper species loading content.

3.5.2 Active site characterisation

Determination of the rate of reaction is possible by an estimation of the surface coverage and activation energy through a representation of the reaction using the microkinetic method, which is based on knowledge of the elementary steps involved in the reaction where the detailed chemistry of the reaction is explored. However, performing the microkinetic simulation by using the kinetics of the elementary steps is computationally intensive, although it can provide the accurate pathway and prediction of the reaction [7]. In this work, the established knowledge on the elementary steps involved in LTWGS was combined with an active site characterisation technique using CO-TPD to hypothesise the activity of the synthesised Cu_6 nanoclusters supported on functionalised MWCNT, as a first step towards qualifying its novelty to contribute to the existing literature.

We consider the associative mechanism, which is an adsorption–desorption model, as the basis of the kinetic model. The working principle of CO-TPD is also based on the adsorption and desorption of the CO species on active sites of the synthesised catalysts. In the associative mechanism, the interaction of the adsorbed CO and H_2O species forms an adsorbed intermediate that decomposes to H_2 and CO_2 [7]:

$CO + H_2O \leftrightarrow \text{Intermediate} \leftrightarrow CO_2 + H_2$ (3.2)

Gokhale *et al*. (2008) [33] proposed a carboxyl-intermediate mechanism based on studies on Cu (1 1 1), the dominant facet of copper crystallites in commercial Cu-ZnO catalysts. The carboxyl intermediate-associative mechanism for the forward LTWGS reaction on Cu (1 1 1), explained as a Langmuir–Hinshelwood (L–H) process given by Gokhale *et al*. (2008) [33], Callaghan *et al*. (2003) [34] and Fishtik & Datta (2002) [35], is used as the basis to hypothesise the activity of the newly developed catalysts:

$CO + * \leftrightarrow CO*$	$K_A = 1.5 \times 10^6$	$E_a = 0$	(3.3)
$H_2O + * \leftrightarrow H_2O*$	$K_A = 1.0 \times 10^6$	$E_a = 0$	(3.4)
$H_2O* + * \leftrightarrow OH* + H*$	$K_S = 1.0 \times 10^{13}$	$E_a = 25.4$	(3.5)
$CO* + OH* \leftrightarrow COOH* + *$	$K_S = 1.0 \times 10^{13}$	$E_a = 0$	(3.6)
$COOH* + * \leftrightarrow CO_2* + H*$	$K_S = 1.0 \times 10^{13}$	$E_a = 1.4$	(3.7)
$COOH* + OH* \leftrightarrow CO_2* + H_2O*$	$K_S = 1.0 \times 10^{13}$	$E_a = 0.9$	(3.8)
$CO_2* \leftrightarrow CO_2 + *$	$K_D = 4.0 \times 10^{12}$	$E_a = 5.3$	(3.9)
$2\ H* \leftrightarrow H_2* + *$	$K_S = 1.0 \times 10^{13}$	$E_a = 15.3$	(3.10)
$H_2* \leftrightarrow H_2 + *$	$K_D = 6.0 \times 10^{12}$	$E_a = 5.5$	(3.11)

K_A, K_S, K_D = rate constants of the adsorption constant ($atm^{-1}.s^{-1}$), surface reaction (s^{-1}) and desorption ($atm^{-1}.s^{-1}$) respectively; E_a = heat of adsorption (kcal/mol).

The nature of the active sites of the Cu species (metallic or oxides) for the LTWGS reaction has remained vague [1]. Although a Cu metal surface has been established to provide the primary active site in the forward and the reverse shift [7, 36], the LTWGS reaction can also be catalysed on both metallic and oxides of Cu [7]. The most recent article discussing the

most active Cu facets for the LTWGS reaction has been published by Zhang *et al.* (2017) [37]. In their work, they found that the activity and activation energy exhibited by Cu_2O nanocrystals when used directly in the LTWGS reaction were nearly identical to those of Cu nanocrystals. It was demonstrated by structural characterisation that the Cu_2O nanocrystals underwent an *in situ* morphology-preserved reduction into Cu nanocrystals, whereby both Cu(0) and Cu(I) species co-existed on the Cu nanocrystals surfaces during the reaction up to 275 °C and were active in catalysing the LTWGS reaction. The typical operating temperature range practised industrially is 190 – 250 °C [1, 10], and hence, the Cu_2O phase can also be active for the LTWGS reaction under industrial operating conditions.

As discussed earlier in this work, once deposited on the MWCNT support, the hexameric copper hydride, $(CuH)_6$ changed its phase to Cu_2O by oxidation with air at ambient. Similar to the findings of Zhang *et al*. (2017) [37], the active facets of the Cu_2O precursor in this work were identified to be (1 1 0), (1 1 1), (2 0 0) and (2 2 0). Therefore, the synthesised catalysts should be readily active for the LTWGS reaction because they undergo an *in situ* morphology-preserved reduction as the reaction commences and progresses. As a result, an activation step by reduction with H_2 is not required. An activation protocol by ligand removal at a temperature above 260 °C through heat treatment under an inert flow may or may not be required for this newly developed catalyst, but this requirement must be experimentally determined prior to the activity test of the catalyst. Nevertheless, pre-treatment at a low temperature of 100 °C is recommended to remove impurities that may be present in the as-prepared sample.

In Figure 3.9, the CO-TPD profile of $1\%Cu_6/MWCNT_{COOH}$ showed a small shoulder, low peak at 120 °C, and a broader, higher peak at approximately 245 °C. The desorption-peak at the lower temperature is identified as the active site on Cu_2O planes for the LTWGS reaction to occur. The appearance of this peak indicates the presence of an active site on the Cu_2O surface that interacts with the CO species and, hence, validates the hypothesis that the catalyst is readily active for the reaction to occur.

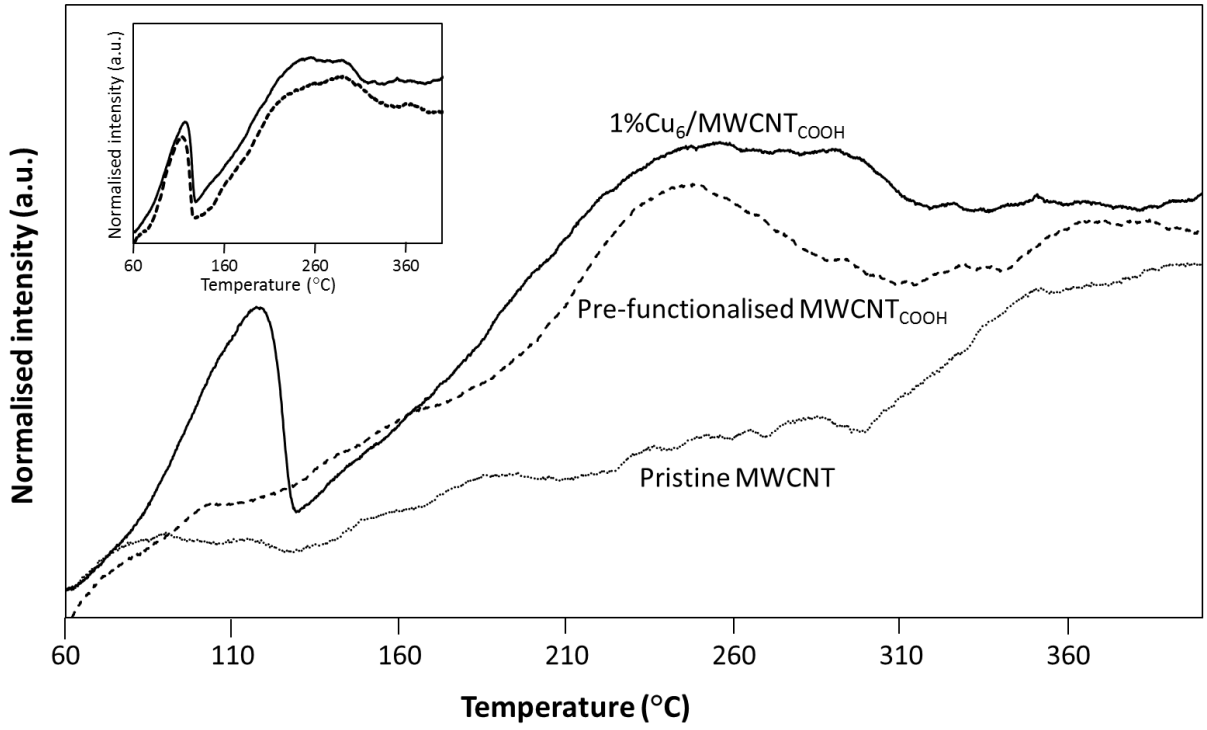

Figure 3.9: CO-TPD profiles of $1\%Cu_6/MWCNT_{COOH}$ and pristine/pre-functionalised MWCNTs (Inset: reproduced CO-TPD profiles of $1\%Cu_6/MWCNT_{COOH}$).

The narrow-shouldered peak at the lower temperature indicates a weak interaction between CO and the active site. The area under the peak profile is proportional to the surface coverage, which is the amount of CO originally adsorbed [38]. Its low peak maximum suggests a low surface coverage of CO (eq. (3.3)), which should be meaningful for the reaction, as the remaining surface of the active site should be reserved for the H_2O molecule to occupy (eq. (3.4)) to allow the remaining elementary steps (eq. (3.5) – (3.11)) to subsequently occur for CO conversion to H_2 and CO_2. According to Mendes *et al.* (2010) [1], one of the L–H models that has good fitting with the experimental results by Ayastuy *et al.* (2005) [39] suggests that both CO and H_2O reactants are adsorbed over similar active sites on the catalyst surface, forming reaction products that are then desorbed.

The peak maximum position along the desorption temperature axis is related to desorption activation energy. As adsorption is a spontaneous process, the heat of adsorption therefore equals the activation energy for desorption [38]. The CO adsorption enthalpy given in eq.

(3.3), E_a = 0 kcal/mol, is nil or extremely low. Therefore, the peak position at the low temperature (120 °C) could well be attributed to elementary step represented by eq. (3.3). This result hypothetically suggests that 1%Cu_6/$MWCNT_{COOH}$ could be catalytically very active at temperatures as low as 120 °C. Based on the operating manuals by various catalyst manufacturers, the bed inlet temperature should be at least 20 °C above the water dew point at a particular operating pressure at all times, to avoid water condensation either in the catalyst pores or onto the bed, which would deactivate the catalyst. Note that 120 °C is the lowest temperature at which the LTWGS reaction can be operated due to water dew point limitation at atmospheric pressure, which is the pressure used in the TPD/R measurements in this work.

The second peak on the CO-TPD profile of 1%Cu_6/$MWCNT_{COOH}$ at the higher peak maximum temperature position of 245 °C is assigned the active site attributed to the surface oxygen (–COOH) grafted on the pre-functionalised MWCNT. This peak was present in the profile of bare pre-functionalised $MWCNT_{COOH}$, but absent in that of bare pristine MWCNT. The broader shoulder and higher peak maximum at higher temperature of the peak indicates a stronger CO interaction and more CO surface coverage on this active site, which is not useful for the LTWGS reaction due to its high activation energy for CO desorption. The CO desorption becomes more difficult because of the need to overcome the higher energy obstacle.

Nevertheless, the peak attributed to the oxygen-moiety groups at 245 °C could hypothetically provide an active site that could have broken the chemical bond between the carboxyl groups grafted on the surface of the functionalised MWCNT and carbon, causing the carboxyl groups to become unstable and hence, decompose, releasing the decomposition product in the CO-TPD. Based on our literature search of thermal decomposition of relevant COOH-containing molecules and materials, the main product of $MWCNT_{COOH}$ decomposition is expected to be CO_2 [40-41].

Performing a hydrogen temperature programmed-reduction (H_2-TPR) on bare $MWCNT_{COOH}$ would help explain this possibility. H_2-TPR up to 600 °C was performed on the bare pristine

and pre-functionalised MWCNTs to determine the temperature at which the oxygen-moiety (carboxyl) groups create an active site for CO adsorption or are possibly reactive in the reaction environment. A close-up of the intensity of the H_2-TPR spectrum of bare $MWCNT_{COOH}$ (Figure 3.10) showed that the as-received sample exhibited a straight line. In contrast, the H_2-TPR profile of the bare $MWCNT_{COOH}$ sample that had undergone CO-TPD up to 400 °C prior to the H_2-TPR measurement exhibited an altered behaviour, where the straight intensity line was followed by a drop in the TCD signal, providing a declination slope from a temperature point of approximately 240 °C. This phenomenon did not occur in the post-CO-TPD pristine MWCNT sample.

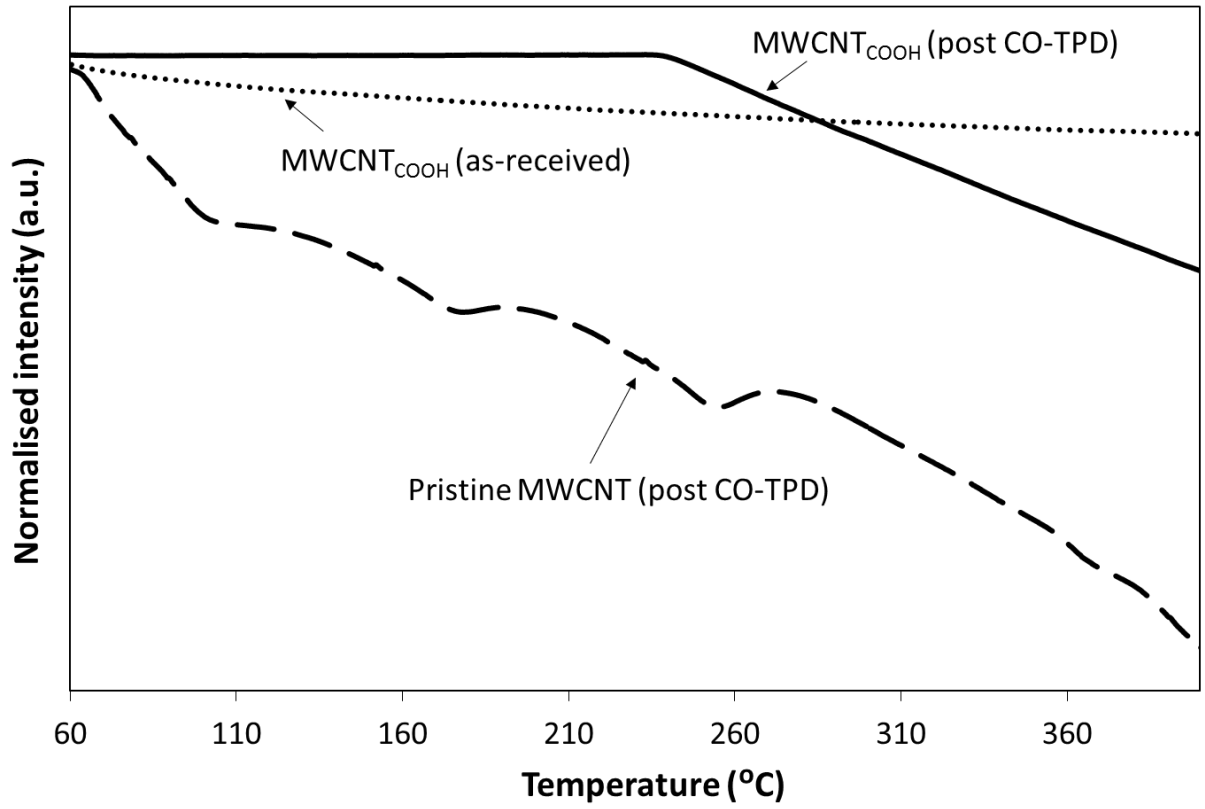

Figure 3.10: H_2-TPR profiles of MWCNTs under various pre-treatment conditions.

It is suggested that the oxygen groups were removed from the vacant sites that had been previously occupied (adsorbed) by CO, at 240 °C and beyond. In the LTWGS reaction environment, the chemical bond binding the carboxyl groups and the carbon would break at 240 °C, resulting in a decomposition of the carboxyl groups. In this H_2-TPR measurement,

the decomposed carboxyl was subsequently swept out of the system by H_2, as indicated by the drop in the TCD signal. H_2 did not react with (reduce) the decomposed oxygen-groups gases, which would have otherwise been signalled as a reduction peak in the H_2-TPR profile.

It is speculated that from 240 °C, the loss of the oxygen groups from the MWCNT's surface deteriorates the dispersion of the Cu_2O phase. This phenomenon is supported by the results shown in Table 3.2, where the dispersion significantly deteriorated when the representative sample, 13%Cu_6/$MWCNT_{COOH}$, was heated at 300 °C (dispersion, d = 0.29%) in comparison to that at 200 °C (d = 1.15%), which was comparable to that at 100 °C (d = 1.31%). However, the possibility that the poor dispersion post-heating at 300 °C could also have been caused by sintering of the Cu species itself. Cu is susceptible to thermal sintering at temperatures beyond 300 °C [7]. Again, this is evident by the results shown in Table 3.2, where the crystallite size of the Cu species became significantly larger after undergoing heat treatment at 300 °C in comparison to those at 200 and 100 °C, which were reasonably comparable to each other.

Therefore, the maximum operating temperature for 1%Cu_6/$MWCNT_{COOH}$ should be capped at below 190 °C, allowing room for the temperature rise associated with the reaction exotherm. This guidance is vital, especially in current industrial practices in existing plants that are designed to typically operate the LTWGS reaction in a range from 190 – 250 °C [1, 10] at a typical operating pressure ranging from 25 – 35 bar [5]. The lower limit of the operating temperatures in which the LTWGS reaction is run under industrial conditions is 190 °C at a typical operating pressure of 30 bar, which is imposed by the water dew point [7, 10].

In the CO-TPD profile of the corresponding 1%Cu_6 catalyst sample supported on pristine MWCNT (Figure 3.11), the peak-maximum position of the first peak, which was attributed to the Cu_2O active site, shifted to 210 °C and became broader and higher, resulting in a larger area under the profile. Without the presence of the carboxyl groups, the active site for the LTWGS reaction exhibited a stronger interaction with more surface coverage of CO species, causing CO desorption to become more difficult due to its higher activation energy and

concentration. This finding indicates a catalytically less active catalyst exhibited by $1\%Cu_6/MWCNT_p$ as elementary steps eq. (3.3) and eq. (3.6) have a higher energy obstacle to overcome.

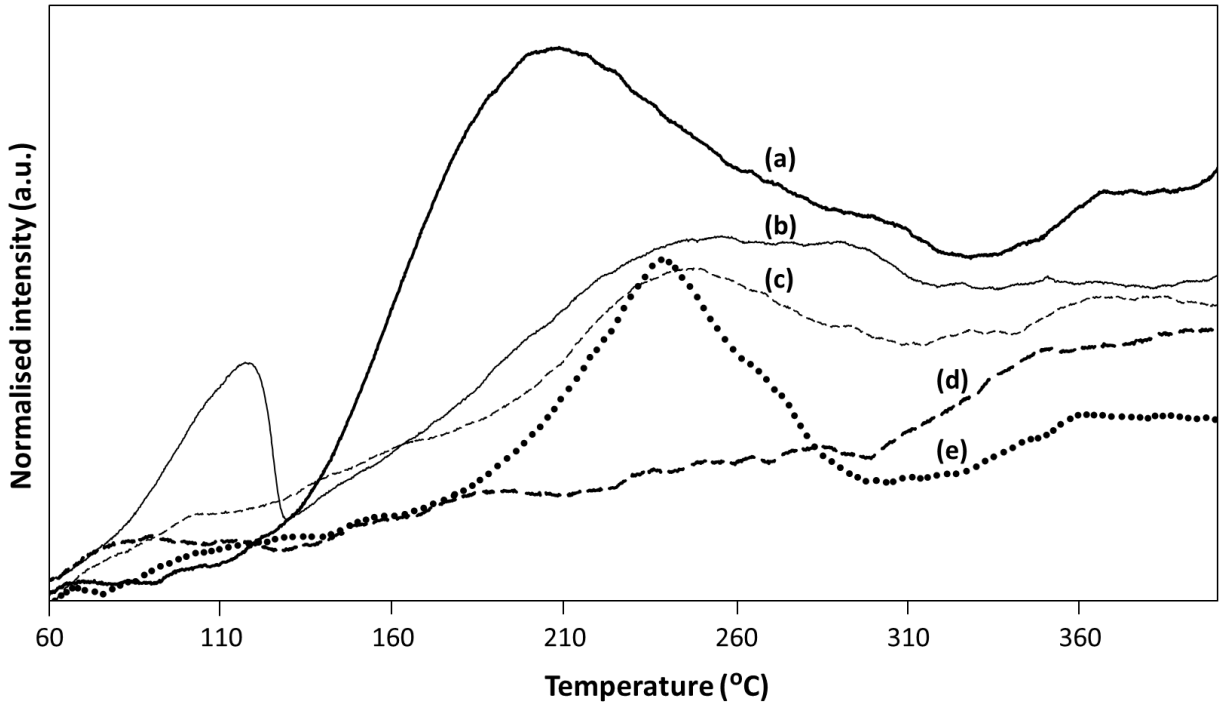

Figure 3.11: CO-TPD profiles of: (a) $1\%Cu_6/MWCNT_p$, (b) $1\%Cu_6/MWCNT_{COOH}$, (c) bare pre-functionalised $MWCNT_{COOH}$, (d) bare pristine MWCNT, and (e) $1\%Cu_{NP}/MWCNT_{COOH}$.

In the case of the corresponding catalyst consisting of Cu nanoparticles supported on $MWCNT_{COOH}$ ($1\%Cu_{NP}/MWCNT_{COOH}$), only one profound peak was observed within the temperature range up to 400 °C. This peak was assigned to the Cu_2O active site. The peak attributed to the carboxyl groups had collapsed, where the oxygen groups should have been removed from the as-prepared sample at the calcination stage that took place at 400 °C [41], which was part of the synthesis protocol. The peak-maximum position was at approximately 240 °C, indicating a catalytically less active catalyst in comparison to its Cu_6 nanocluster counterpart ($1\%Cu_6/MWCNT_{COOH}$). In contrast, the lower peak and narrower shoulder of $1\%Cu_{NP}/MWCNT_{COOH}$ in comparison to that of $1\%Cu_6/MWCNT_p$ indicated a lower CO surface coverage on the active site, which could hypothetically be translated into the possibility of a higher CO conversion performance as the less concentrated surface coverage

by the adsorbed CO species (eq. (3.3)) provided availability for H_2O adsorption (eq. (3.4)) and allowed the subsequent elementary steps to occur [1].

Up to 300 °C, there is no significant peak to represent an active site on the bare pristine MWCNT (Line (d), Figure 3.11), whereby the CO-TPD profile appeared rather flat. Using this as a baseline, in the sample that contained 1%Cu_6 in the pristine MWCNT (Line (a), Figure 3.11), a broad peak was observed at a peak maximum of around 200 °C. This broad and large peak is attributed to the interaction of the CO molecules with the active site provided by the Cu_6. In this particular profile, there was a significant amount of CO molecules originally adsorbed on this Cu_6 active site, and being desorbed at a relatively high temperature, which required a high enthalpy/activation energy for desorption. The peak shows the TCD signal detecting desorption of CO only.

Up to 300 °C, there is a significantly broad peak in the TPD profile of the bare carboxyl-functionalised MWCNT (Line (c), Figure 3.11) at a peak maximum of approximately 250 °C. The peak at high temperature indicates a strong interaction between CO molecules and the site on this material, which indicates a strong CO adsorption effect. In the work by Prado-Burguete *et al.* (1989) [41] studying the effect of oxygen groups on Pt/carbon catalysts, the carboxyl groups decomposed from approximately 250 °C to release CO_2 in an inert environment. Based on this literature evidence, it was convinced that the TCD signal in the peak profile of the bare $MWCNT_{COOH}$ detected the CO molecules from the earlier adsorption in the CO-TPD measurement that emerged with the CO_2 molecules produced from the decomposition of the carboxyl groups. At this stage, we were not able to confirm experimentally the presence of both gases due to the BELCAT II Catalyst Analyser not being equipped with mass spectrometer. However, we do have experimental evidence of CO_2 released from the decomposition of the carboxyl group in the bare $MWCNT_{COOH}$ material from approximately 250 °C in a later work, which will be presented in detail in Chapter 4.

In the broad peak in Line (b) (Figure 3.11) of the carboxyl-functionalised MWCNT containing 1%Cu_6, the peak profile is generally similar to the profile of the bare $MWCNT_{COOH}$ at 250 °C, but the area under the peak profile had increased slightly. Note

again the presence of a smaller desorption peak at a lower temperature of 120 °C, which is attributed to the active site of Cu_6 discussed earlier. The area under the peak profile of the $MWCNT_{COOH}$ containing Cu_6 is larger than without the presence of Cu_6 due to additional CO originally adsorbed on the Cu_6 site. Part of the originally adsorbed CO amount desorbed at the lower temperature of 120 °C (these CO molecules adsorbed weakly on the site). The remaining strongly bonded CO molecules on the Cu_6 site desorbed at the higher temperature, emerged with the CO_2 gas released from the decomposition of the carboxyl groups in the higher desorption-temperature peak profile.

In the sample of Cu_{NP} supported on $MWCNT_{COOH}$, note that the synthesis of this catalyst followed a typical catalyst preparation where it underwent a calcination in nitrogen at 400 °C for 3 hours post catalyst synthesis, unlike its Cu_6 counterpart. Referring to the CO-TPD profile of $Cu_{NP}/MWCNT_{COOH}$ (Line (e), Figure 3.11), we believe that the peak at around 240 °C is attributed to desorption of strongly bonded CO molecules on the Cu_{NP} site and to some extent, a release of CO_2 gas from the remaining small amount of carboxyl groups that was not decomposed during the calcination stage. Part of the carboxyl groups had been decomposed earlier in the as-prepared catalyst, and hence, its area under the peak profile is smaller in comparison to the profiles of $MWCNT_{COOH}$ (Line (c), Figure 3.11) and $Cu_6/MWCNT_{COOH}$ (Line (b), Figure 3.11).

Figure 3.12 shows the different behaviours of the $Cu_6/MWCNT_{COOH}$ catalyst when loaded with various loading contents. At 0.5 wt.% loading (Figure 3.12(A)), the first peak, which is assigned to Cu_2O active site, appeared broader and higher and was shifted to the right. The peak attributed to the carboxyl group had collapsed above 240 °C, but a new, stronger peak appeared at 375 °C, which can be assigned to another active site of Cu_2O but is not useful in the LTWGS reaction as it exceeded the operating temperature limit of 300 °C at which the sintering of Cu occurs. In addition, this peak at higher temperature indicates a stronger CO interaction on this active site, which is hypothetically not useful for the LTWGS reaction due to its higher activation energy, and hence, higher energy obstacle for CO desorption. Therefore, the peak appearance at 375 °C on the CO-TPD profile of the $0.5\%Cu_6/MWCNT_{COOH}$ was deemed not meaningful for the moderately exothermic LTWGS reaction that thermodynamically favours low temperatures for higher conversions. The

existing industrially operated LTWGS takes place between 190 and 250 °C [1, 5], and hence, any catalytic activity on the Cu_2O active site at above 250 °C is deemed low for the intended objective. Hypothetically, the 0.5% Cu_6 catalyst has a lower catalytic activity in comparison to the 1% and 5% (Figure 3.12(A)), which could also be attributed by too low of a Cu_6 loading content in the former, and hence, the peak shifted to the right. The 5% Cu loading content exhibited similar behaviour to that of the 1%, but the position of the peak-maximum of the Cu_2O active site occurred at a temperature that is low for the LTWGS reaction, which is slightly below the dew point of water.

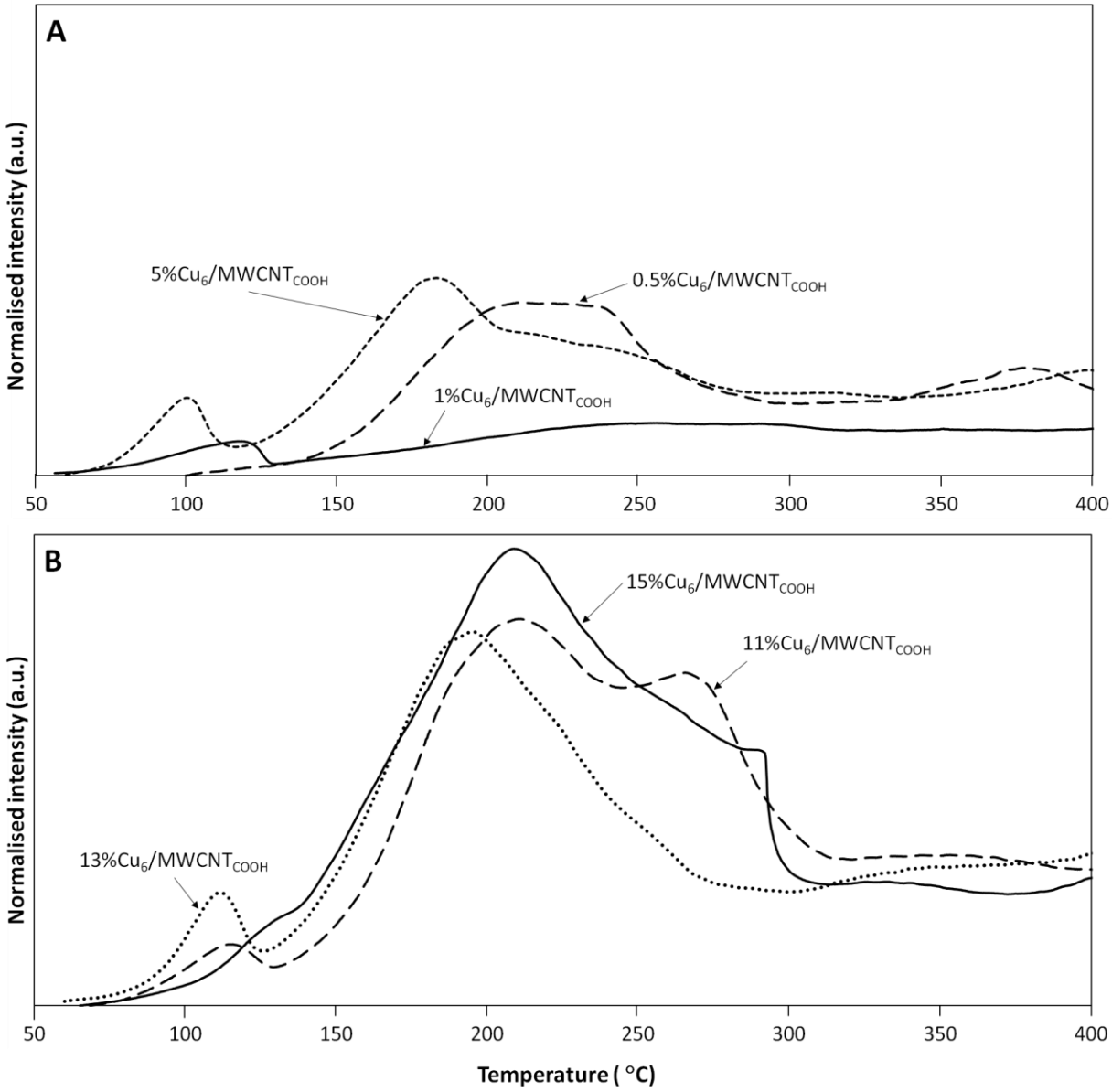

Figure 3.12: CO-TPD profiles of $Cu_6/MWCNT_{COOH}$ catalysts of varied Cu content.

(A) 0.5, 1 and 5%; and (B) 11, 13 and 15%.

The catalysts containing 11% and 13% Cu exhibited a similar profile in their first peak associated with Cu_2O, but their second peak attributed to the carboxyl groups was shifted to 210 and 195 °C, respectively. Hypothetically, this could result in catalyst deactivation at operating temperatures lower than that for the $1\%Cu_6/MWCNT_{COOH}$ catalyst. The third peak in the profile of the $11\%Cu_6/MWCNT_{COOH}$ catalyst at approximately 270 °C could be assigned to decarboxylation or the Cu_2O active sites, but it is not meaningful for LTWGS reaction operating temperatures, which are typically capped at 250 °C to avoid Cu sintering.

The 15%Cu_6/$MWCNT_{COOH}$ catalyst is predicted to lack meaningful catalytic activity for the LTWGS reaction because its Cu_2O peak is almost negligible at the peak-maximum position of 130 °C and overlaps with the broad peak profile belonging to the carboxyl groups.

CuO-ZnO catalysts require activation by exposure to a dilute H_2 flow in the process stream to reduce the Cu(II) directly to Cu(0), following an exothermic reaction (eq. (3.12)) at 230 °C [7, 32, 42]:

$$CuO\ (s) + H_2\ (g) \rightarrow Cu\ (s) + H_2O\ (g) \qquad \Delta H = -80.8\ kJ/mol \qquad (3.12)$$

From the results shown in Table 3.1, the crystallite size of the Cu species was substantially larger in the commercial catalyst sample that was reduced at 400 °C, while the Cu size was comparable between the unreduced catalyst and the catalyst that was reduced at 230 °C. Figure 3.13 shows the CO-TPD profiles of the as-prepared 1%Cu_6/$MWCNT_{COOH}$ and 1%Cu_6/Al_2O_3 catalysts and activated commercial catalyst, reduced at 230 and 400 °C. The two active site peaks observed on the commercial catalyst reduced at 230 °C collapsed in the profile of the one that was reduced at 400 °C, exhibiting an almost negligible active site peak similar to the profile of the inert alumina. It is evident that the Cu particles underwent sintering because of surface migration after heat exposure above 300 °C, which led to catalyst deactivation [5, 7, 34].

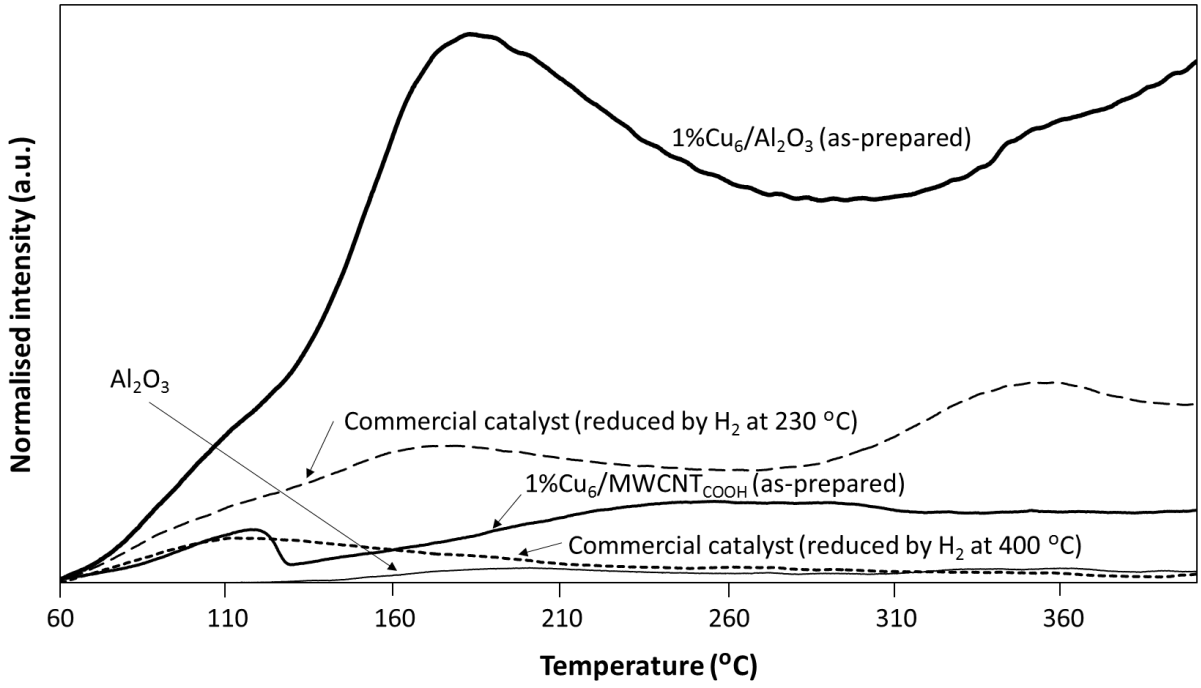

Figure 3.13: CO-TPD profiles of as-prepared 1%Cu_6 supported on $MWCNT_{COOH}$ and alumina and the reduced commercial catalyst.

At lower reaction temperatures than the industrial LTWGS reaction operating temperatures (*i.e.* < 190 °C), the 1%Cu_6/$MWCNT_{COOH}$ catalyst is expected be more active than the commercial catalyst (reduced to Cu(0) at 230 °C) based on the observed predominant peak (between 110 °C and 210 °C) in the CO-TPD profiles attributed to the active sites of the Cu species. However, as discussed earlier, the operating temperature of the 1%Cu_6/$MWCNT_{COOH}$ catalyst has an upper limit and should be capped at below the typical LTWGS operating temperatures to avoid deactivation by Cu sintering. In an actual activity test performed under typical industrial LTWGS operating conditions (reaction temperature = 190 – 250 °C, GHSV = 2,750 – 8,650 h^{-1}), CO conversion over 1%Cu_6/$MWCNT_{COOH}$ was found to be < 1.0%, indicating an effect of deactivation, while the reference catalyst exhibited a conversion of 84.2 – 93.8%. This actual activity test result validates the prediction by CO-TPD that the 1%Cu_6/$MWCNT_{COOH}$ is deactivated when operated under industrial operating conditions. The second peak in the profile of the commercial catalyst is not useful for LTWGS operating conditions. The corresponding Cu_6 catalyst supported on alumina exhibited a Cu_2O active site peak that is much broader and of higher intensity in comparison

to peak observed in the case of an activated commercial catalyst and is therefore speculated to have poor catalytic activity in the LTWGS reaction.

3.6 Conclusions

A prediction of catalytic activity and/or deactivation of catalyst in the LTWGS reaction based on surface chemistry and structural characterisation by XRD and CO chemisorption and active site characterisation by CO-TPD have been demonstrated on a newly developed, potentially novel catalyst consisting of hexameric copper hydride nanoclusters ligated to PPh_3, solvated with THF, supported on functionalised MWCNT, and synthesised by the wet impregnation method without undergoing a calcination post-impregnation.

The hexameric copper hydride nanoclusters changed their phase to a highly dispersed Cu_2O phase with oxidation in air under ambient conditions when the complex had been deposited onto the surface of the functionalised MWCNT. The Cu_2O crystal planes (1 1 0), (1 1 1), (2 0 0) and (2 2 0) were found to be the active facets for CO reactivity based on XRD characterisation. Since Cu_2O phases are readily active for LTWGS to occur, an activation protocol by reduction with H_2 or by ligand removal at a temperature above 260 °C through heat treatment under an inert flow may not be required. However, pre-treatment at a low temperature of 100 °C is recommended to remove impurities that may be present in the as-prepared sample.

The employed CO-TPD technique serves as a first round screening of catalyst activity evaluation, while in parallel provides a means for effective planning in the selection of the operating conditions for the reaction run test because it supplies an indication of the operating conditions in which the catalyst activity may be at its highest potential, and the possible conditions in which deactivation might occur. Hence, an optimal operating condition for a maximum CO conversion allowed by thermodynamics in the equilibrium-limited LTWGS reaction could hypothetically be determined.

It is expected that the optimal catalyst, 1%Cu_6/$MWCNT_{COOH}$, should be active for the LTWGS reaction within a range of lower temperatures compared to the industrial LTWGS reaction operating temperatures. In the case of other catalysts, their feasible operating temperature range will change with the loading of the active Cu species. In general, the lower operating temperature limit is imposed by the water dew point, while the upper limit is constrained by the temperature rise from the reaction exotherm that could lead to Cu sintering. Depending on the Cu_6 content in the catalyst, extra care must be taken when running the exothermic LTWGS reaction over the catalyst to avoid irreversible Cu sintering due to the removal of carboxyl groups, which has been experimentally validated.

Acknowledgements

The authors acknowledge the financial support of the Department of Chemical and Process Engineering (CAPE), University of Canterbury (UC), Christchurch, New Zealand. The authors would like to thank Felicitas Jansen of Rheinisch-Westfälische Technische Hochschule Aachen, Germany for performing the copper nanocluster's TGA and SCXRD experiments; Robert Stainthorpe, Technician of School of Physical and Chemical Sciences, UC for ICP-MS analysis; and Wasim Ullah Khan, CAPE PhD candidate for his help in performing some of the CO-TPD and H_2-TPR analyses.

References of Chapter 3

1. Mendes, D., et al., *Determination of the Low-Temperature Water− Gas Shift Reaction Kinetics Using a Cu-Based Catalyst.* Industrial & Engineering Chemistry Research, 2010. **49**(22): p. 11269-11279.
2. Oliveira, N.M., G.P. Valençaa, and R. Vieirab, *Water Gas Shift Reaction On Copper Catalysts Supported On Alumina And Carbon Nanofibers.* Chemical Engineering, 2015. **43**.

3. Luengnaruemitchai, A., S. Osuwan, and E. Gulari, *Comparative studies of low-temperature water–gas shift reaction over Pt/CeO2, Au/CeO2, and Au/Fe2O3 catalysts.* Catalysis Communications, 2003. **4**(5): p. 215-221.
4. Demirel, E. and N. Azcan. *Thermodynamic modeling of water-gas shift reaction in supercritical water*. in *Proceedings of the World Congress on Engineering and Computer Science*. 2012.
5. Schumacher, N., et al., *Trends in low-temperature water–gas shift reactivity on transition metals.* Journal of Catalysis, 2005. **229**(2): p. 265-275.
6. Li, Y., Q. Fu, and M. Flytzani-Stephanopoulos, *Low-temperature water-gas shift reaction over Cu-and Ni-loaded cerium oxide catalysts.* Applied Catalysis B: Environmental, 2000. **27**(3): p. 179-191.
7. RJ, B.S., M. Loganathan, and M.S. Shantha, *A review of the water gas shift reaction kinetics.* International Journal of Chemical Reactor Engineering, 2010. **8**(1).
8. Baharudin, L. and M.J. Watson, *Hydrogen applications and research activities in its production routes through catalytic hydrocarbon conversion.* Reviews in Chemical Engineering, 2017a. **34**(1): p. 43-72.
9. Smith, R., M. Loganathan, and M.S. Shantha, *A review of the water gas shift reaction kinetics.* International Journal of Chemical Reactor Engineering, 2010. **8**(1).
10. Ratnasamy, C. and J.P. Wagner, *Water gas shift catalysis.* Catalysis Reviews, 2009. **51**(3): p. 325-440.
11. Maniecki, T., P. Mierczyński, and W. Jóźwiak, *Copper-supported catalysts in methanol synthesis and water gas shift reaction.* Kinetics and Catalysis, 2010. **51**(6): p. 843-848.
12. Chinchen, G.C., et al., *Promotion of methanol synthesis and the water-gas shift reactions by adsorbed oxygen on supported copper catalysts.* Journal of the Chemical Society, Faraday Transactions 1: Physical Chemistry in Condensed Phases, 1987. **83**(7): p. 2193-2212.
13. Morales-Torres, S., et al., *Palladium and platinum catalysts supported on carbon nanofiber coated monoliths for low-temperature combustion of BTX*. Applied Catalysis B: Environmental, 2009. **89**(3–4): p. 411-419.
14. Jarrah, N.A., et al., *Immobilization of a layer of carbon nanofibres (CNFs) on Ni foam: A new structured catalyst support.* Journal of Materials Chemistry, 2005. **15**(19): p. 1946-1953.

15. Chinthaginjala, J.K. and L. Lefferts, *Influence of hydrogen on the formation of a thin layer of carbon nanofibers on Ni foam.* Carbon, 2009. **47**(14): p. 3175-3183.
16. Chinthaginjala, J.K., et al., *How Carbon-Nano-Fibers attach to Ni foam.* Carbon, 2008. **46**(13): p. 1638-1647.
17. Baharudin, L., et al., *Potential of metal monoliths with grown carbon nanomaterials as catalyst support in intensified steam reformer: a perspective.* Reviews in Chemical Engineering, 2018a. **ahead of print**.
18. Albert, C.F., et al., *Lewis-base adducts of Group 11 metal (I) compounds. 49. Structural characterization of hexameric and pentameric (triphenylphosphine) copper (I) hydrides.* Inorganic Chemistry, 1989. **28**(7): p. 1300-1306.
19. Cook, A.W., et al., *Synthesis, Characterization, and Reactivity of the Group 11 Hydrido Clusters [Ag6H4 (dppm) 4 (OAc) 2] and [Cu3H (dppm) 3 (OAc) 2]*. Inorganic chemistry, 2016.
20. Peng, Y. and H. Liu, *Effects of oxidation by hydrogen peroxide on the structures of multiwalled carbon nanotubes.* Industrial & engineering chemistry research, 2006. **45**(19): p. 6483-6488.
21. Wepasnick, K.A., et al., *Chemical and structural characterization of carbon nanotube surfaces.* Analytical and Bioanalytical Chemistry, 2010. **396**(3): p. 1003-1014.
22. Datsyuk, V., et al., *Chemical oxidation of multiwalled carbon nanotubes.* Carbon, 2008. **46**(6): p. 833-840.
23. Moraes, R.A., et al., *The effect of different chemical treatments on the structure and stability of aqueous dispersion of iron-and iron oxide-filled multi-walled carbon nanotubes.* Journal of the Brazilian Chemical Society, 2011. **22**(11): p. 2191-2201.
24. Hamilton Jr, R.F., et al., *Purification and sidewall functionalization of multiwalled carbon nanotubes and resulting bioactivity in two macrophage models.* Inhalation toxicology, 2013. **25**(4): p. 199-210.
25. Lee, J., et al., *Measurement of the dispersion stability of pristine and surface-modified multiwalled carbon nanotubes in various nonpolar and polar solvents.* Measurement Science and Technology, 2007. **18**(12): p. 3707.
26. Douroumis, D., et al., *Colloidal stability of carbon nanotubes in an aqueous dispersion of phospholipid.* International journal of nanomedicine, 2007. **2**(4): p. 761.
27. Yang, H.-M. and P.-H. Liao, *Preparation and activity of Cu/ZnO-CNTs nano-catalyst on steam reforming of methanol.* Applied Catalysis A: General, 2007. **317**(2): p. 226-233.

28. Yang, B., et al., *Copper cluster size effect in methanol synthesis from CO2.* The Journal of Physical Chemistry C, 2017. **121**(19): p. 10406-10412.
29. Dandekar, A., R. Baker, and M. Vannice, *Carbon-supported copper catalysts: I. Characterization.* Journal of Catalysis, 1999. **183**(1): p. 131-154.
30. Song, J., et al., *Reduction of nano-Cu2O: crystallite size dependent and the effect of nano-ceria support.* The Journal of Physical Chemistry C, 2015. **119**(31): p. 17667-17672.
31. Hua, Q., et al., *Crystal-Plane-Controlled Surface Chemistry and Catalytic Performance of Surfactant-Free Cu2O Nanocrystals.* ChemSusChem, 2013. **6**(10): p. 1966-1972.
32. Kim, J.Y., et al., *Reduction of CuO and Cu2O with H2: H embedding and kinetic effects in the formation of suboxides.* Journal of the American Chemical Society, 2003. **125**(35): p. 10684-10692.
33. Gokhale, A.A., J.A. Dumesic, and M. Mavrikakis, *On the mechanism of low-temperature water gas shift reaction on copper.* Journal of the American Chemical Society, 2008. **130**(4): p. 1402-1414.
34. Callaghan, C., et al., *An improved microkinetic model for the water gas shift reaction on copper.* Surface Science, 2003. **541**(1-3): p. 21-30.
35. Fishtik, I. and R. Datta, *A UBI–QEP microkinetic model for the water–gas shift reaction on Cu (1 1 1).* Surface Science, 2002. **512**(3): p. 229-254.
36. Galván, C.Á., et al., *Reverse water-gas shift reaction at the Cu/ZnO interface: Influence of the Cu/Zn ratio on structure-activity correlations.* Applied Catalysis B: Environmental, 2016. **195**: p. 104-111.
37. Zhang, Z., et al., *The most active Cu facet for low-temperature water gas shift reaction.* Nature communications, 2017. **8**(1): p. 488.
38. Rakić, V. and L. Damjanović, *Temperature-Programmed Desorption (TPD) Methods*, in *Calorimetry and Thermal Methods in Catalysis*. 2013, Springer. p. 131-174.
39. Ayastuy, J., et al., *Kinetics of the low-temperature WGS reaction over a CuO/ZnO/Al2O3 catalyst.* Industrial & Engineering Chemistry Research, 2005. **44**(1): p. 41-50.
40. Winter, K. and D. Barton, *The thermal decomposition of benzoic acid.* Canadian Journal of Chemistry, 1970. **48**(24): p. 3797-3801.

41. Prado-Burguete, C., et al., *The effect of oxygen surface groups of the support on platinum dispersion in Pt/carbon catalysts.* Journal of Catalysis, 1989. **115**(1): p. 98-106.
42. Rhodes, C. and G.J. Hutchings, *Studies of the role of the copper promoter in the iron oxide/chromia high temperature water gas shift catalyst.* Physical Chemistry Chemical Physics, 2003. **5**(12): p. 2719-2723.

CHAPTER 4

Experimental Work, Results and Discussion: Catalytic Assessment and Feasibility Studies (Stage 3a)

CO oxidation and the inhibition effects of carboxyl-modification and copper-clusters on multi-walled carbon nanotubes

Special note: *In the actual catalytic activity tests performed on the series of catalysts fabricated in this doctoral work in CO oxidation as the model reaction under study, it was found that the bare pristine multi-walled carbon nanotubes (MWCNT) was active for the reaction, while the reaction was inhibited on the carboxyl-functionalised MWCNT and in the presence of the hexameric copper clusters (Cu_6) under low temperature reaction conditions. In this Chapter, the fabricated catalysts are described as simulated interactions of the active pristine MWCNT material with some selected contaminants in a CO oxidation atmosphere of: (i) an acidic wet flue gas environment (by using carboxyl-modified MWCNT); and (ii) a polluted environment formed by trace metal copper particles and other contaminant constituents such as polycyclic aromatic hydrocarbons (PAH), volatile organic compounds (VOC), and phosphorous (by using a copper cluster as a model pollutant and materials made of MWCNT doped with these cluster species).*

This Chapter is a complete reproduction of a submitted article:

"Baharudin, L., Yip, A.C.K., Golovko, V.B., Polson, M.I.J. & Watson, M.J (2019). CO oxidation and the inhibition effects of carboxyl-modification and copper-clusters on multi-walled carbon nanotubes. *Applied Catalysis B: Environmental*, submitted (correction stage post peer-review as at thesis submission point)."

Highlights

- CO conversion of greater than 98% was achieved from approximately 230 °C using pristine multi-walled carbon nanotubes as a catalyst.
- Multi-walled carbon nanotubes modified with carboxyl groups adsorbed significant quantities of CO molecules without further catalytic converting.
- Cu_6 clusters initially formed $CuCO_3$ that decomposed above 400 °C to release CO_2 product.

Abstract

An inhibition of CO oxidation on catalytically active pristine multi-walled carbon nanotubes (MWCNT) in the presence of selected pollutant constituents in flue gas streams was studied. An interaction was simulated between the active MWCNT and the contaminants in an O_2-rich CO oxidation atmosphere of: (i) an acidic wet flue gas environment modelled by using MWCNT grafted with carboxyl (–COOH) groups; and (ii) a polluted environment formed by trace metal copper particles and other contaminant constituents such as polycyclic aromatic hydrocarbons (PAH), volatile organic compounds (VOC), and phosphorous (P), by using a copper cluster as a model pollutant. The model copper pollutant was in the form of a copper cluster species of chemical formulae $[(PPh_3)CuH]_6 \cdot 0.75THF$, and its simulated modification of the active MWCNT was modelled by using MWCNT doped with these cluster species. In the case of pristine, unmodified MWCNT exposed to reaction gas mixture, MWCNT were catalytically active from ~150 °C, achieving close to complete CO oxidation from approximately 230 °C. In an acidic environment where the MWCNT's surface was modified with –COOH groups, the material behaved as an adsorbent of CO molecules without converting them into CO_2 in the presence of O_2. Low concentrations of dispersed Cu particles by themselves (not in the form of copper cluster species) doped on the carboxyl-modified MWCNT prepared by conventional method demonstrated activity in the CO oxidation. The –COOH groups decomposed progressively from approximately 250 °C, releasing CO_2. In the case of copper cluster species pollutant, the model copper cluster was found to have formed

$CuCO_3$ during the CO oxidation reaction at temperatures below 330 °C but decomposed above 400 °C to release CO_2 product.

Keywords: carbon nanotubes; carboxyl groups; catalyst poisoning; CO oxidation; copper cluster; reaction inhibition.

Graphical abstract

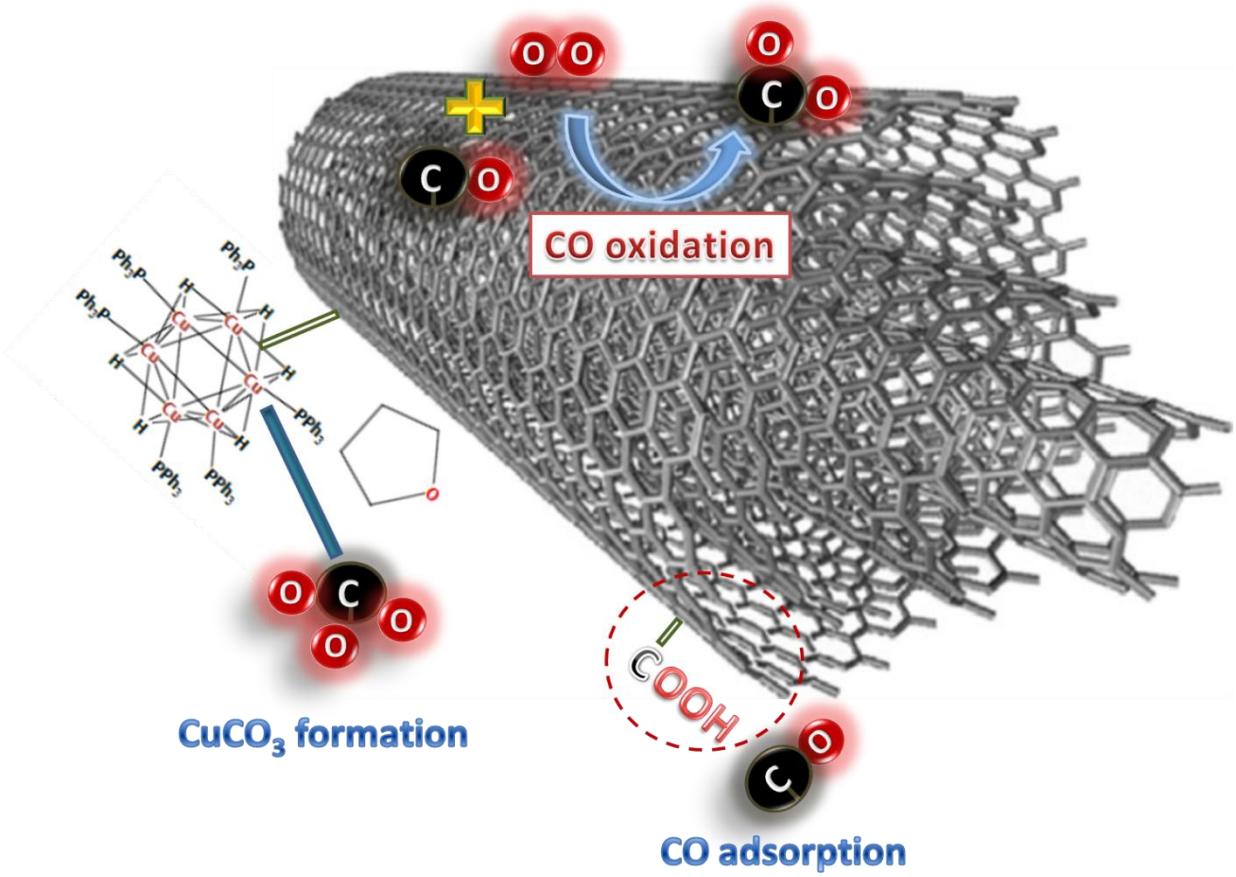

4.1 Introduction

Flue gases are emitted from activities such as gasification and combustion of fossil fuels (*e.g.* natural gas, coal, petroleum, fuel oil and wood) and pyrolysis gas/oil for generation of

electric power and steam, waste-to-energy processes, solid waste incineration, sewage sludge combustion, and other industrial processes [1-9]. Flue gas atmospheres comprise of the combustion products, which are water (H_2O) and carbon dioxide (CO_2), and other major constituents such as oxygen (O_2) and nitrogen (N_2) from air used in the combustion, various unconverted hydrocarbons (C_xH_y), hydrogen (H_2), and trace amounts of carbon monoxide (CO) [1, 7, 10-11].

Carbon monoxide is an air pollutant that is toxic to mammals and vegetation and contributes to global warming. The study of CO oxidation (eq. (4.1)) is of prime importance for meeting the environmental regulations on emission standards in exhaust gas released to the atmosphere [12-15].

CO oxidation [16]: $CO + ½\ O_2 \rightarrow CO_2$ $\Delta H^0_{298} = -283$ kJ/mol (4.1)

The easy removal of CO_2 by absorption in water, and at large scale, in monoethanolamine and/or N,N-dimethylethanolamine [17] has motivated research efforts in catalysis towards attaining total oxidation of CO to CO_2. Pristine carbon nanotubes (CNT) have been demonstrated to be catalytically active for CO oxidation, where complete CO conversion was achieved above 250 °C [18-19].

Depending on their sources, untreated flue gas streams contain varying compositions of (i) residual acid gases such as nitrogen oxides (NO_x), sulphur oxides (SO_x), organic acids (HCOOH, *etc.*), and acidic compounds (*e.g.* HCl and HF) [1, 10-11]; (ii) trace elements pollutants such as Hg, Pb, Cd, Zn, Cu, Cr, K, Zn, Na, Ca, Si, Pb, Al, Mn, Fe, Mo, V, Ba, and Be [2-4, 6-9, 20]; (iii) VOC such as acetone, formaldehyde, tri-chloroethene, and furans [1]; (iv) PAH [20-23]; and (v) to a certain extent, phosphorous P derived from combustion of phosphorus-rich biomass fuels [24-27]. Some possible interactions of the different constituents present in the flue gas with the surface of the catalytic active site can hinder the CO oxidation reaction.

The studies on the inhibition of the CO oxidation on the catalyst's surface that have been reported in the literature are still scarce. There are studies which focus on the effects of halogen species in fluidised bed combustion [28], adsorbed H_2O molecules on RuO_2 (1 1 0) [29] and Pd/Al_2O_3 catalyst [30], concentration of the adsorbed oxygen on polycrystalline Rh [31] and Au/TiO_2 catalyst [32], hydrocarbons on ternary oxide catalyst composed of CuO, Co_3O_4, and CeO_2 [33], and different concentrations and feed sequences of CO and O_2 on carbon-supported Pt catalyst [34].

In this Chapter, an activity test of CO oxidation reaction on pristine multi-walled carbon nanotubes (MWCNT) is presented. The aim is to study an inhibition of the CO oxidation on the catalytically active MWCNT due to modification of the MWCNTs by presence of selected model pollutant constituents of the flue gas. The pollutant constituents can interact with the MWCNT surface in many ways. For instance, in a wet flue gas atmosphere, nitric acid (HNO_3) aerosols can be formed by [35]:

$$3\ NO_2 + H_2O \leftrightarrow 2\ HNO_3 + NO \qquad (4.2)$$

Xia *et al.* (2009) [36] demonstrated that a functionalisation of CNT walls by HNO_3 vapour introduced carboxyl (–COOH) groups on the carbon surface. Therefore, the formation of HNO_3 aerosols in the wet flue gas atmosphere together with the presence of any other organic acid gases can result in modification of the MWCNT surface with –COOH groups.

In a study by Yuan *et al.* (2005) on the metal particles in the flue gas from the municipal solid waste incinerators in Taiwan [6], it was revealed that the distribution of finer particles ($d_p \leq$ 2.5 µm) contained more Pb, Cd, Zn and Cu, while the coarser particles contained more Cr and Hg. In the same study, it was found that the concentrations of Cu in the flue gas streams of the studied municipal solid waste incinerators were between 0.007 and 4.3 mg/Nm^3. In a modern (post-1990) municipal solid waste incinerator, the concentration of Cu in the fly ash was 318 ppm [7]. The typical concentrations of fine Cu particles of d_p < 0.075 mm in the bottom ash of municipal solid waste incinerators were around 3 – 5 wt.% [8]. Other pollutant

constituents in the flue gases such as PAH, P and furans in concentrations significant enough to interact with the Cu metal pollutant may form a cluster that can cover the active sites of MWCNTs. Although it is well-known that Cu-based materials have found applications in catalysing CO oxidation [37], in this Chapter, it is demonstrated that in the presence of some other constituents typical for a copper cluster species, Cu can form $CuCO_3$ species during the reaction at low temperatures.

In the catalytic reaction tests, MWCNTs modified in the following manners were used: (i) MWCNT grafted with –COOH groups ($MWCNT_{COOH}$); (ii) MWCNT doped with a model copper cluster species in the form of hexameric copper hydride $(CuH)_6$ ligated by triphenylphosphine (PPh_3) and solvated with tetrahydrofuran ($(CH_2)_4O$ = THF) molecules ($[(PPh_3)CuH]_6 \cdot 0.75THF$); and (iii) a combination of both. The study of the CO oxidation performance on the copper cluster deposited on inert alumina (Al_2O_3), and on copper particles (not in the form of copper cluster *i.e.* without the presence of the PPh_3 and THF constituents) doped on $MWCNT_{COOH}$ as reference materials, was also included to demonstrate the CO oxidation inhibition effects by MWCNT modified with the –COOH groups and the $[(PPh_3)CuH]_6 \cdot 0.75THF$ clusters.

4.2 Experimental

4.2.1 Materials

Pristine MWCNT (≥ 95% purity on carbon basis) and $MWCNT_{COOH}$ (99.9% purity) were purchased from Nanostructured and Amorphous Materials Inc., USA (NanoAmor). $MWCNT_{COOH}$ contained of 0.95 – 1.05% of –COOH content as determined by X-ray photoelectron spectroscopy (XPS) indicated in Certificate of Analysis (COA).

The synthesis of the $[(PPh_3)CuH]_6 \cdot 0.75THF$ cluster (designated as Cu_6 cluster from this point onwards) and the modification of the pristine MWCNT, $MWCNT_{COOH}$ and Al_2O_3 (≥ 98% purity, Sigma-Aldrich) with the Cu_6 cluster by wet impregnation using the Schlenk-line

technique have been described elsewhere [38-40] (Section 3.4.1.1 of Chapter 3). Corresponding materials are denoted as $Cu_6/MWCNT_p$, $Cu_6/MWCNT_{COOH}$ and Cu_6/Al_2O_3 respectively. Unless otherwise stated, the copper content in each material discussed in this Chapter is *ca.* 1 wt.%.

A copper-based material fabricated in this doctoral work presented previously in Section 3.4.1.2 of Chapter 3 [38] using a copper nanoparticle (Cu_{NP}) precursor of the same copper content deposited on the $MWCNT_{COOH}$ was also used in the present study for comparison purposes, identified as $Cu_{NP}/MWCNT_{COOH}$ with the subscript NP referring to nanoparticle. The Cu_{NP} solution, which was prepared by dissolving $CuCl_2 \cdot 2H_2O$ (Riedel-De Haën AG, Seelze-Hannover) precursor in methanol (UN 1230, CAS 67-56-1, Burdick & Jackson (B&J Brand ®)), was removed under vacuum post wet impregnation on the $MWCNT_{COOH}$ material. The Cu_{NP} doped on the $MWCNT_{COOH}$ was not covered by any surfactants or capping agents. The dry $Cu_{NP}/MWCNT_{COOH}$ material was calcined in a nitrogen flow of 100 mL/min at 400 °C in a tubular furnace for 3 hours.

An industrial catalyst, 51%CuO/31%ZnO-Al_2O_3 (Johnson Matthey PLC) commercialised for low-temperature water–gas shift (LTWGS) reaction was used as a reference for gas chromatography (GC) measurements validation prior to running the reaction over the synthesised materials. The as-received mini-pellet-shaped commercial catalyst was crushed into powder before use.

4.2.2 Characterisation

Characterisations of the structural and phase composition of the materials were carried out by CO chemisorption and X-ray diffraction (XRD), and have been described in Section 3.4.2 of Chapter 3 [38].

Thermogravimetric analysis (TGA) (NETZSCH, STA 449 F3 Jupiter) of the materials (7.0 – 16.0 mg) was performed in synthetic air (N_2:O_2 = 80/20 v/v%) flowing at 50 mL/min that

mixed with nitrogen gas flowing at 20 mL/min with a temperature ramping rate of 10 °C/min up to 500 °C.

Powder diffraction patterns of the materials (as-prepared) were recorded on an X-ray diffractometer (SuperNova, Agilent Technologies) over the 2θ range of 10 – 90°, using Cu-Kα radiation (λ = 1.54056 Å) operated at room temperature. The analysis has been discussed in Section 3.5.1.3 of Chapter 3 [38] but part of it is reproduced in current Chapter for the purpose of making comparison between the as-prepared and the oxidised material samples (post TGA in air as described above). The radiation used on the oxidised samples was Co-Kα radiation (λ = 1.79026 Å) on Rigaku 3kW Smartlab.

Active site characterisations by CO temperature-programmed desorption (CO-TPD) and hydrogen temperature-programmed reaction (H_2-TPR) techniques were performed using BELCAT II Catalyst Analyser (MicrotacBEL). The CO adsorption was carried out by flowing 10:90 v/v% CO:He mixture at 50 sccm total flow at 50 °C for 1 hour, followed by a post-treatment in He flowing at 50 sccm at 50 °C for another hour. The CO-TPD measurement was then performed starting from 50 °C and heating to a target temperature of 400 °C at a ramping rate of 10 °C/min in He flowing at 30 sccm. H_2-TPR was performed by flowing 30 sccm of 5:95 v/v% H_2:Ar from 50 °C up to 600 °C at a ramping rate of 10 °C/min.

4.2.3 Activity tests

The activity test measurements were conducted in a vertical stainless steel tube reactor (internal diameter = 10 mm) charged with ~0.1 g of material supported on a layer of quartz wool at the tube axial-centre, embedded in a temperature-programmable furnace (GSL-1100X, MTI Corporation). The process flow diagram and the pictures of the differential reactor are shown in Figure E1(A) and Figure E1(B) respectively in APPENDIX E. A thermocouple (Intech Instruments) was inserted into the material bed to measure the actual bed temperature (recorded by TracerDAQ software).

The pristine MWCNT and $MWCNT_{COOH}$ materials were used as-purchased, and the Cu_6- and Cu_{NP}-doped materials were used as-prepared. Unless otherwise stated, the activity study was performed in a temperature-step-change experiment in an oxygen-rich atmosphere ($CO:O_2$ = 1:10 v/v%) using a feed gas mixture comprising of 1 vol.% CO (99.2%, BOC Gases Australia Ltd.), 10% O_2/40% N_2 (synthetic air of $N_2:O_2$ = 80:20 v/v% was used as the oxygen source) and the remaining balance of Ar (BOC Ltd., New Zealand) at a low gas hourly space velocity (GHSV) of 3,000 mL/($g_{material}$·h). A lower GHSV than that used in the reference experiments (*i.e.* GHSV = 6,000 mL/($g_{material}$·h), without catalyst charge and on commercial catalyst) was chosen to allow sufficient residence time for an effective interaction between the reactant gases and the studied materials.

The flow rates of the gases were regulated by mass flow controllers (MFCs) (MC-10SCCM-D/5M, ALICAT Scientific). The reaction temperatures, unless otherwise stated, were programmed by increasing the temperature from ambient temperature and approximating the step change using a heating rate of ~2 °C/min, and keeping each step-temperature setting of 190, 270 and 330 °C holding for 4 hours. For the pristine MWCNT and $MWCNT_{COOH}$, the activity tests were performed in a series of temperature programmed experiments with several plateaus at the constant temperatures (170, 190, 270 and 330 °C). Actual temperatures of the catalyst bed measured by the thermocouple immersed inside the bed differed from the temperature settings in most cases and will be reported in the results and discussion section instead of the programmed temperature values. The temperature difference could likely be due to the gas flow (convection) where gas was heating-up from initial room temperature to the temperature measured by the thermocouple as it traveled through the system. The furnace had a separate thermocouple sitting inside the hot zone by which the programming was done. All catalytic tests were conducted at atmospheric pressure.

On-line analysis of gas composition of the reactor outflow was done by a GC (SRI 8610C, SRI Instruments, USA) running on Ar as the carrier gas, equipped with a thermal conductivity detector (TCD) and a flame ionisation detector (FID); chromatograms were analysed using PeakSimple software (Peak444-32bit, SRI Instruments). Prior to the reaction tests, the GC was calibrated with the CO gas used in the feed and CO_2 gas (Instrument Grade,

BOC Gases Australia Ltd.). The activity of the materials was presented as percentage of CO conversion into CO_2 as a function of time on stream or temperature.

In demonstrating the inhibition of CO oxidation in this Chapter, the MWCNT materials modified with the model pollutant constituents were expected to: (i) behave as an inert, where mole of CO_{feed} = mole of $CO_{product}$; or (ii) as an adsorbent by only adsorbing the CO but not catalysing its oxidation, where the difference between the moles of CO_{feed} and $CO_{product}$ is due to the CO adsorption, instead of conversion. Additionally, these materials could also possibly provide an active site for the CO oxidation reaction. Due to the unidentified role of the materials at this stage, we defined "CO adsorption/conversion" as a measure of the materials playing role(s) as a CO adsorbent and/or a catalyst:

$$\text{CO adsorption/conversion (\%)} = \frac{\text{mole of CO}_{\text{feed}} - \text{mole of CO}_{\text{product}}}{\text{mole of CO}_{\text{feed}}} \text{ x } 100\ \% \qquad (4.3)$$

On the other hand, the conversion of CO into CO_2 product using the term "CO conversion (X_{CO})" defined in eq. (4.4) calculated the extent of the materials' ability to catalyse the CO oxidation reaction (only). It will be noted later that eq. (4.4) also takes into account the small extent of the CO_2 produced by the progressive decomposition of the –COOH groups in the case of the materials grafted with these model acidic groups above certain temperatures, which was not be possible to quantify or estimate using our existing facilities.

$$\text{CO conversion, } X_{\text{CO}}\ (\%) = \frac{\text{mole of CO}_{2,\text{product}}}{\text{mole of CO}_{\text{product}} + \text{ mole of CO}_{2,\text{product}}} \text{ x } 100\ \% \qquad (4.4)$$

The amount of CO and CO_2 released in the product stream in eq. (4.3) and eq. (4.4) was calculated from the FID peak area based on the GC's calibration with known CO and CO_2 concentrations in Ar.

4.3 Results and discussion

4.3.1 Characterisation

Materials stability: Figure 4.1 presents the TGA measurements carried out in a flowing air/nitrogen blend to examine the stability of the MWCNT-based materials in an oxidative environment prior to using them for the reaction. The pristine MWCNT (Profile (e)) had a poorer stability than its carboxyl-functionalised counterpart (Profile (a)) where combustion forming gaseous CO_2 (or CO) of the former from approximately 400 °C was substantial, while the latter was thermally stable up to the maximum tested temperature of 500 °C. The significantly poorer thermal stability of Pristine MWCNT (Profile (e)) in oxidative environment could be due to the removal of the carbonaceous materials of lower crystallinity (less stable carbon) during the acidic oxidation treatment at the MWCNT functionalisation stage [41] to introduce the carboxyl groups in the $MWCNT_{COOH}$.

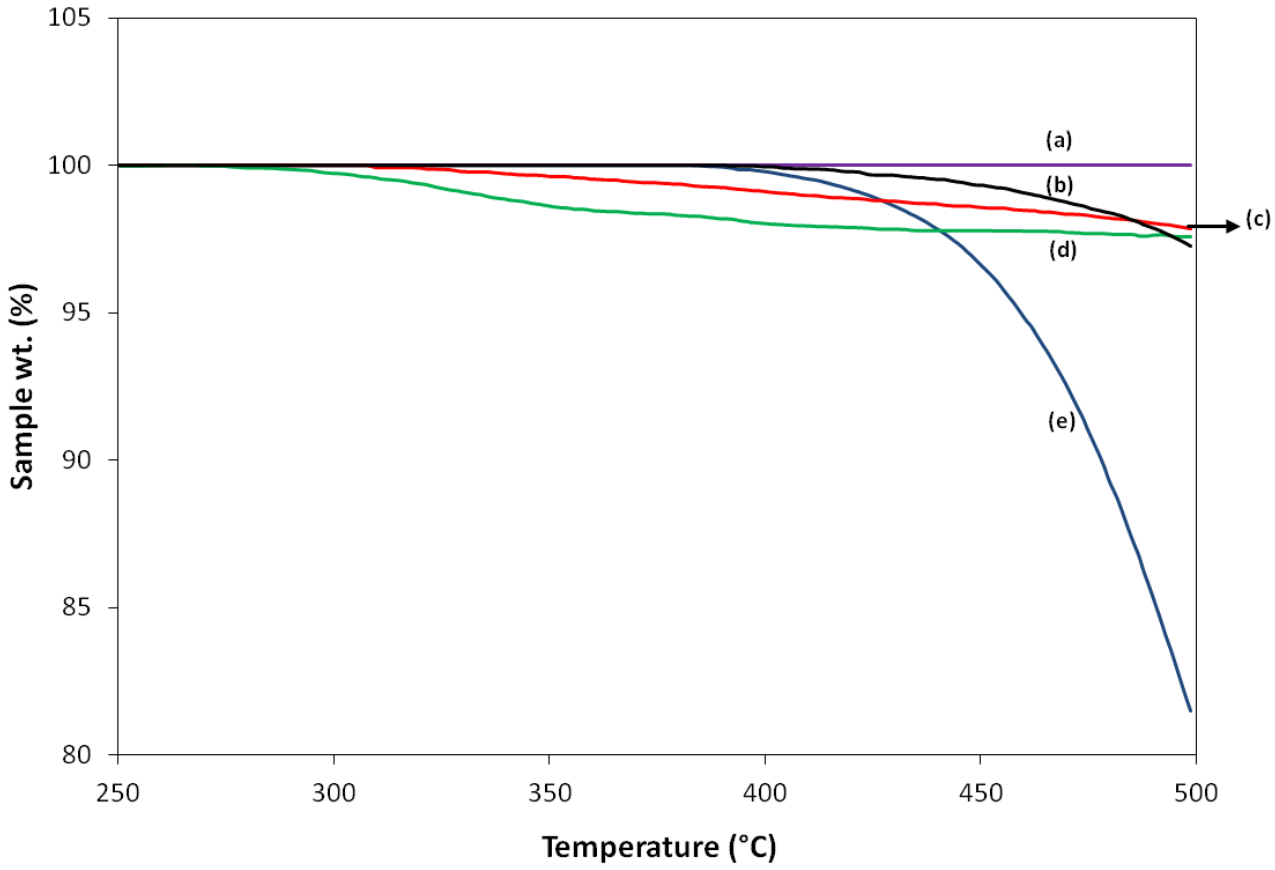

Figure 4.1: TGA (in the flow of air) of (a) $MWCNT_{COOH}$, (b) $Cu_{NP}/MWCNT_{COOH}$, (c) $Cu_6/MWCNT_p$, (d) $Cu_6/MWCNT_{COOH}$, and (e) pristine MWCNT.

The copper-free $MWCNT_{COOH}$ (Profile (a)) did not show a significant weight loss from the decomposition of the carboxyl groups in comparison to the $Cu_6/MWCNT_{COOH}$ (Profile (d)). In the former, the decomposition took place too slowly to be reliably detected by TGA, while the presence of the Cu_6 in the latter facilitated a more rapid decomposition of the carboxyl groups that made its weight loss to be sufficiently reliable to be detected by TGA.

Both the Cu_6-doped materials (Profile (c) $Cu_6/MWCNT_p$ and Profile (d) $Cu_6/MWCNT_{COOH}$) showed noticeable weight loss from below 300 °C, which could partly be due to the PPh_3 ligand removal [38]. In addition, the latter showed a more pronounced loss, which was likely due to the decomposition of the –COOH groups. This was not the case in the Cu_{NP}-based material (Profile (b) $Cu_{NP}/MWCNT_{COOH}$), which showed a beginning of the weight loss from the higher temperature of 400 °C. In this material, the –COOH groups had been removed

upfront in the as-prepared sample, where its preparation included a calcination in a nitrogen flow at 400 °C for 3 hours, post impregnation [38], which was not performed on its Cu_6 analogue doped on $MWCNT_{COOH}$.

Weight loss in all the copper-containing samples (Profile (b) $Cu_{NP}/MWCNT_{COOH}$, Profile (c) $Cu_6/MWCNT_p$, and Profile (d) $Cu_6/MWCNT_{COOH}$) at above 400 °C was a combination of the removal of the –COOH groups (in the case of $MWCNT_{COOH}$-based materials) and possible partial combustion oxidation of the MWCNT materials, facilitated by the presence of the Cu species.

Phase composition: As reported in Section 3.5.1.2 of Chapter 3 [38], the $[(PPh_3)CuH]_6 \cdot 0.75THF$ structure of the cluster was identified by single-crystal XRD (SCXRD) (Cambridge Crystallographic Data Centre (CCDC) # 1864974). Based on powder XRD (PXRD) analysis of the Cu_6-doped materials, the Cu in the cluster species deposited on the $MWCNT_{COOH}$ material (Patterns (a) 1 wt.%, (b) 5 wt. %, and (c) 11 wt.% Cu_6, Figure 4.2(A)) changed to a highly dispersed Cu_2O phase upon exposure to air when stored under ambient conditions [38], which agreed with findings of Yang *et al*. (2017) [42]. To understand the effect of an interaction with oxygen on the phase composition of the materials, the PXRD patterns of the samples that went through the TGA in the air flow were also analysed.

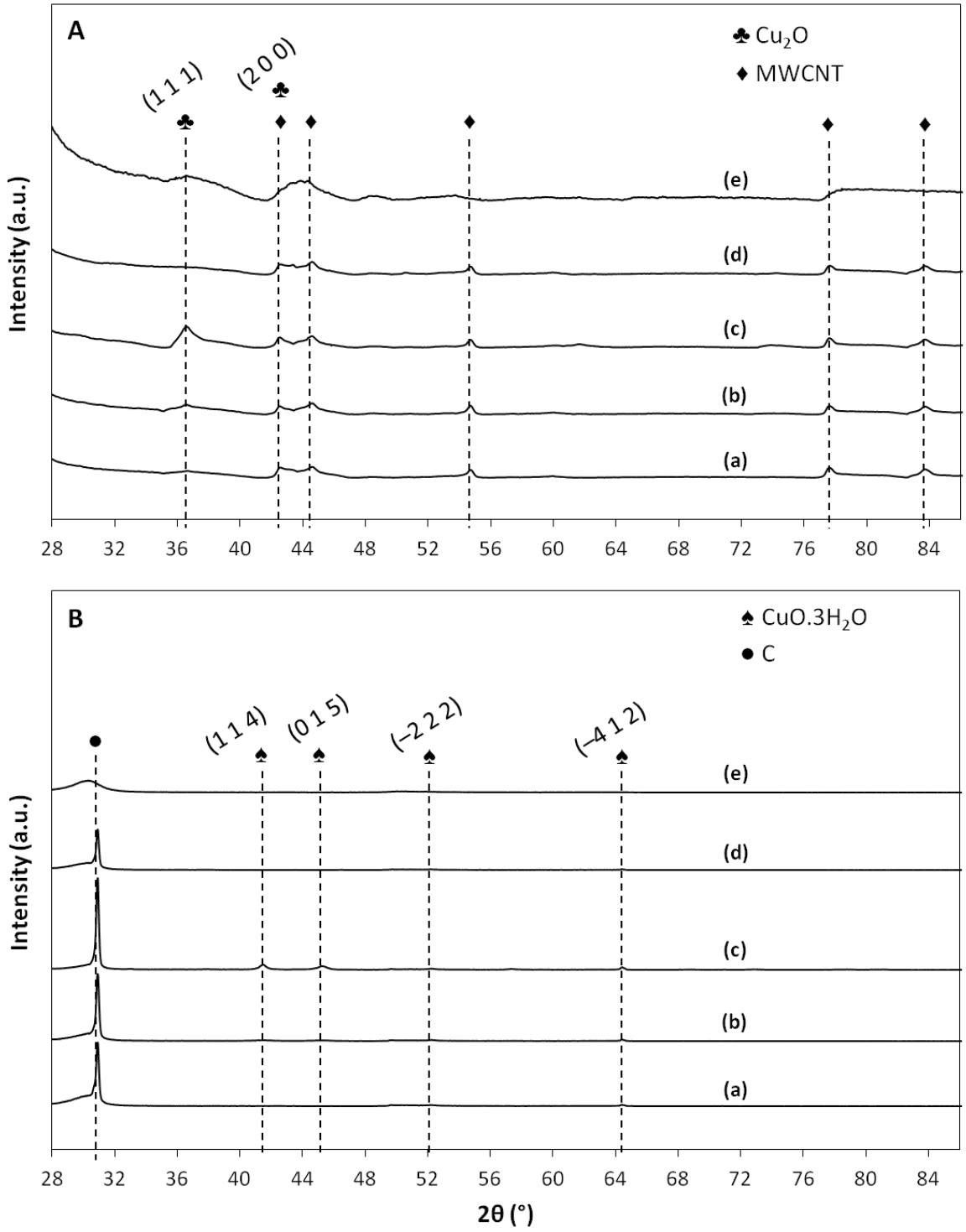

Figure 4.2: PXRD patterns of: (a) 1%Cu_6/$MWCNT_{COOH}$, (b) 5%Cu_6/$MWCNT_{COOH}$, (c) 11%Cu_6/$MWCNT_{COOH}$, (d) 1%Cu_{NP}/$MWCNT_{COOH}$, and (e) 1%Cu_6/$MWCNT_p$.

(A) As-prepared samples; and (B) oxidised samples.

Post oxidation in air (Figure 4.2(B)), the XRD peaks attributed to the Cu_2O phase (International Centre for Diffraction Data (ICDD) 01-077-0199) on the Cu_6-precursored $MWCNT_{COOH}$ materials (Patterns (a), (b) and (c), from Figure 4.2(A) to Figure 4.2(B)) disappeared. The Cu_2O phase changed into copper oxide trihydrate $CuO{\cdot}3H_2O$ phase (Powder Diffraction File (PDF) 36-0545) (Figure 4.2(B)) post heat treatment in the air flow as a result of an interaction with oxygen and decomposition of the carboxyl groups, which will be discussed later in this Chapter.

Note that other than the 11 wt.% Cu_6-precursored sample (Pattern (c), Figure 4.2(B)), which had significant aggregation and enough of Cu species for peaks to show up in XRD, the peaks attributed to the plausible $CuO{\cdot}3H_2O$ phase could not be observed in all other oxidised materials containing 1 and 5 wt.% Cu_6-precursor content (Patterns (a), (b) and (e), Figure 4.2(B)). This was likely due to their high dispersion of Cu species on the MWCNTs and ultra-small cluster metal core size of < 4 nm, which made them undetectable by XRD [38, 43-44] and hence, it is impossible to identify the exact nature of the Cu species based on PXRD.

In all the $MWCNT_{COOH}$-based samples, the carbon crystallinity associated to the crystallinity of the MWCNT disappeared (ICDD 01-075-1621), and a new phase of carbon crystallinity (0 0 4) was introduced at $2\theta = \sim31°$ (PDF 26-1080).

The sharp peak at $2\theta = \sim31°$ attributed to carbon crystallinity (0 0 4) observed for the $MWCNT_{COOH}$-based samples after oxidation (Patterns (a), (b), (c) and (d), Figure 4.2(B)) was not present for the pristine MWCNT-based sample post oxidation (Pattern (e), Figure 4.2(B)), indicating different carbon crystallinities of the pristine MWCNT-based and the $MWCNT_{COOH}$-based samples after oxidation.

In the $1\%Cu_{NP}/MWCNT_{COOH}$ sample (Pattern (d)), the apparent intensity of the peak due to Cu_2O crystal face (2 0 0) at $2\theta = \sim43°$ in its as-prepared form (Figure 4.2(A)) disappeared in its oxidised form (Figure 4.2(B)). This indicated a change in the oxidation state of the Cu species in this material.

4.3.2 Activity tests

The results of CO oxidation reference experiments in absence of catalyst charge and on the commercial catalyst (Figure E2) are presented in APPENDIX E. A complete CO conversion was achieved on the commercial catalyst at approximately 240 °C.

Note that any temperature light-off was not observed during the activity test over 100 mg of material for all the materials tested in this work due to dilute CO concentration (1 vol.%) used in the feed gas.

Note also that all the results of the CO conversion into CO_2 on all the MWCNT-based materials presented in this Chapter calculated using eq. (4.4) were not contributed by the MWCNT combustion oxidation. This was validated by the mass conservation of the samples pre and post reaction experiments. (Note: A test on Cu_6-doped MWCNT material under extreme conditions (O_2-rich, 500 °C) was conducted where the sample mass loss was significant and the CO_2 FID peak areas measured by the GC were exceptionally high, which indicated the combustion of the MWCNT. The results presented in this Chapter were obtained from the experimental conditions under which the MWCNT combustion did not take place to preserve the validity of eq. (4.4).).

4.3.2.1 Activity test of pristine MWCNT

Activity tests of the pristine MWCNT were performed in the O_2-rich environment at GHSV = 3,000 mL/($g_{material}$·h) in a series of constant temperatures (170, 190, 270 and 330 °C). In Figure 4.3, each point is an average of stable CO conversion (X_{CO}) at the respective constant step-temperature maintained for a 4 h hold time on stream, calculated using eq. (4.4). The X_{CO} on the pristine MWCNT performed in this work is in good agreement with results reported by Chuang *et al.* (2010) [19] who used pristine CNT as the catalyst for the CO

oxidation reaction. A CO conversion greater than 98% was achieved from approximately 230 °C in this work, and from 250 °C in the work by Chuang *et al.* (2010) [19], exhibiting almost a similar level of performance as the commercial catalyst. Note that activity test at a temperature between 200 and 250 °C was not conducted by Chuang *et al.* (2010) [19], which could have otherwise matched the temperature at which the pristine CNT started to approach a complete CO conversion at 230 °C as demonstrated in our work.

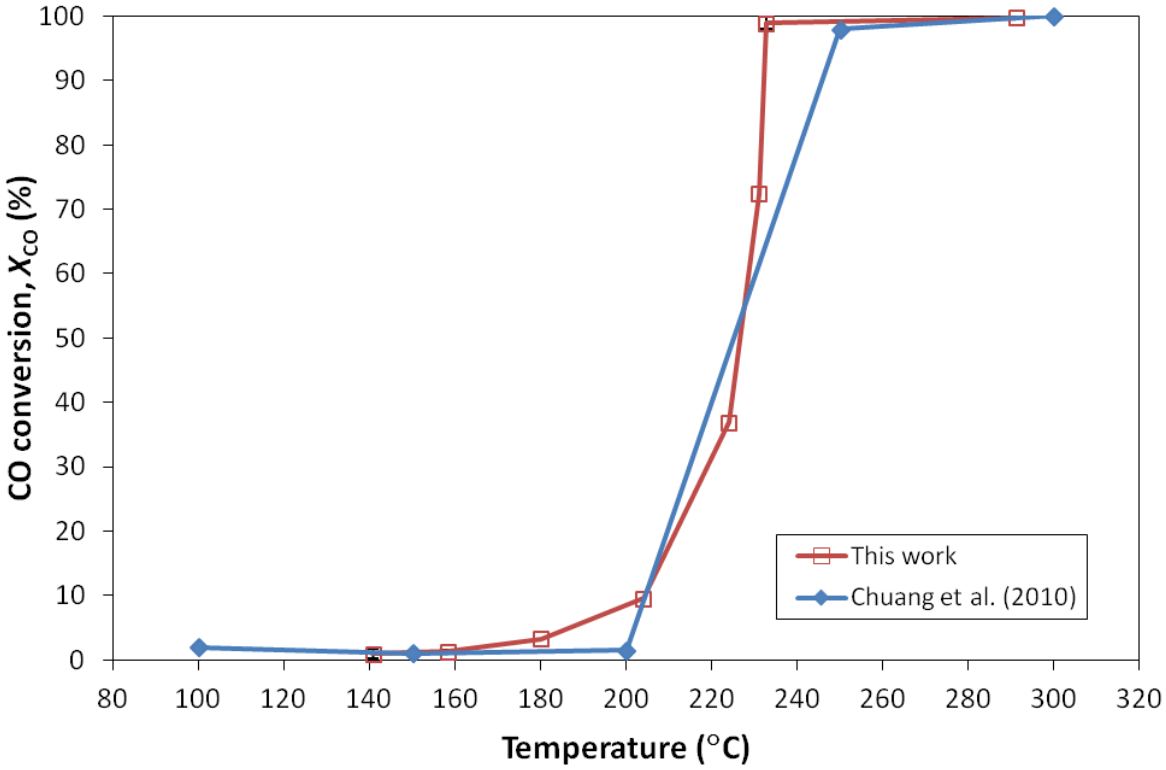

Figure 4.3: CO conversions on pristine CNTs at temperatures of the catalyst bed *cf.* data reported by Chuang *et al.* (2010) [19].

Noteworthy, Chuang *et al.* (2010) [19] used a much higher GHSV of 60,000 mL/($g_{material}$·h) in contrast to our work, which used 20 times lower GHSV. The extremely low GHSV was used in our work to create a much longer residence time for the improved interaction between the reactant gases and the active sites of studied materials when investigating the effects of the CO oxidation inhibition.

High concentrations of oxygen in the feed gas mixture have been proven to inhibit the CO conversion in the selected cases of other catalysts due to O_2-poisoning of the active sites [31-32, 34]. Therefore, although both works were performed in an O_2-rich environment, Chuang *et al.* (2010) [19] gas feed had a $CO:O_2$ ratio of 1:100 while a ratio of 1:10 v/v% was used in our work in order to minimise the effect of potential inhibition of CO conversion by highly concentrated oxygen when studying the inhibition effects due to the modifications by –COOH groups and the Cu_6 clusters.

4.3.2.2 Inhibition of CO oxidation

4.3.2.2.1 Inhibition due to modification by carboxyl groups

In the presence of acidic gases and/or organic acid compounds in the (simulated) flue gas that form carboxyl groups on the MWCNT surface (simulated by using MWCNT grafted with –COOH groups in the CO oxidation reaction) no significant conversion of CO into CO_2 (calculated using eq. (4.4)) was observed in the temperatures below 245 °C (Line 2, Figure 4.4). However, as the temperature increased, slight release of CO_2 can be noticed. Using eq. (4.3), it appeared that although $MWCNT_{COOH}$ was generally not catalytically active within the tested temperature range, adsorption of CO was observed on the material (Line 3). (Note: Each point is an average of steady-state CO conversion (eq. (4.4)) or CO adsorption (eq. (4.3)) at the respective constant step-temperature as measured by the thermocouple inside catalyst bed maintained for a 4 h hold time on stream.).

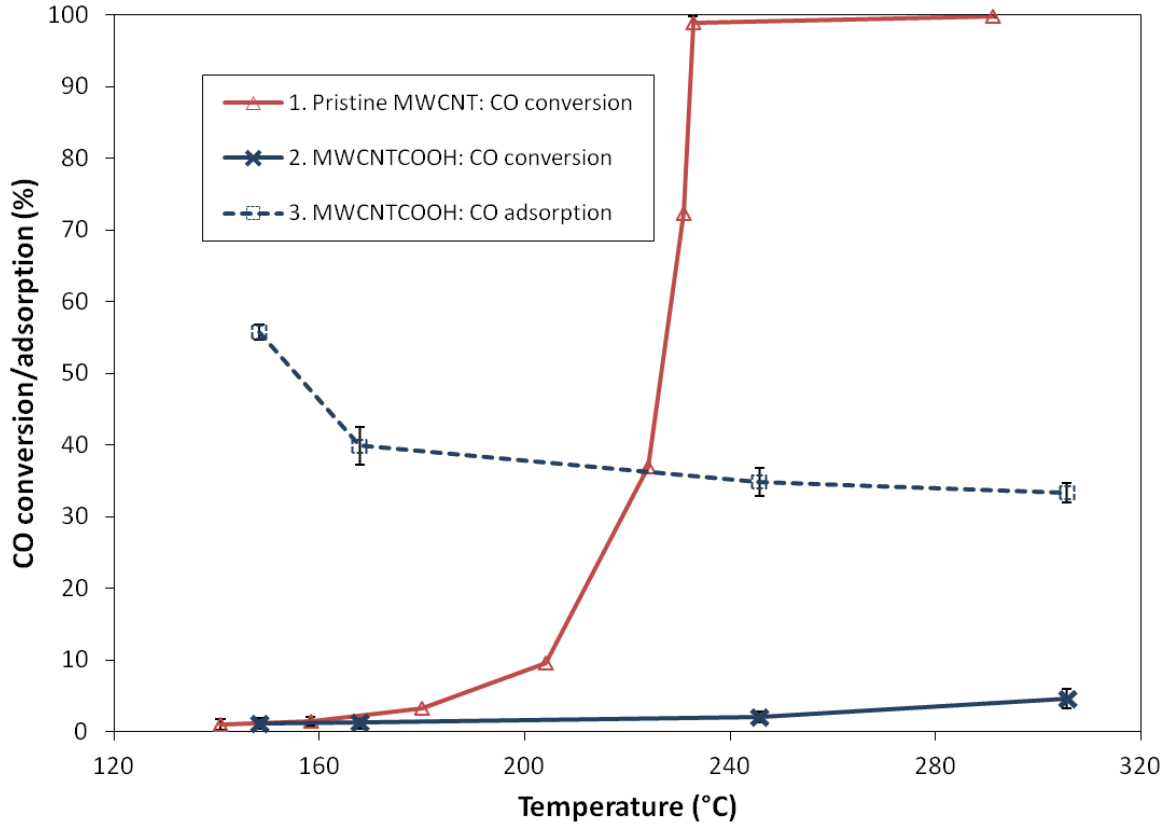

Figure 4.4: CO adsorption/conversion on $MWCNT_{COOH}$ at temperatures of the catalyst bed: O_2-rich, temperature-step change, GHSV = 3,000 mL/($g_{material}$·h).

Below 230 °C, the $MWCNT_{COOH}$ material displays increased CO adsorption compared to all other materials investigated in this study. Above 245 °C, the –COOH functional groups started to be removed (which will be discussed next) from the surface of the $MWCNT_{COOH}$, reducing the $MWCNT_{COOH}$'s capacity to act as an adsorbent due to progressive reduction of the MWCNT surface coverage with the –COOH functional groups.

In the CO oxidation reaction, the molecular oxygen is dissociated into surface-adsorbed (*) oxygen atoms according to eq. (4.5) and eq. (4.6) [45-46]:

$$O_2\ (g) + * \leftrightarrow O_2* \qquad (4.5)$$

$$O_2* + * \rightarrow 2\ O* \qquad (4.6)$$

The reaction between CO molecules and the adsorbed oxygen atoms on the active sites can occur through two possible common mechanisms [45-46]:

Eley–Rideal (E–R):

$$CO\ (g) + O^* \rightarrow CO_2^* \quad (4.7)$$

Langmuir–Hinshelwood (L–H):

$$CO\ (g) \leftrightarrow CO^* \quad (4.8)$$

$$CO^* + O^* \rightarrow CO_2^* + * \quad (4.9)$$

Desorption of the produced CO_2* then takes place to complete the reaction mechanism:

$$CO_2^* \rightarrow CO_2\ (g) + * \quad (4.10)$$

As discussed in Section 3.5.2 of Chapter 3 [38], the –COOH groups started to decompose and release the decomposition product from 245 °C in the CO-TPD profiles of the $MWCNT_{COOH}$-containing materials. Based on our literature search of thermal decomposition of relevant COOH-containing molecules and materials, the main product of $MWCNT_{COOH}$ decomposition is expected to be CO_2 [47-48]. The CO-TPD peak position (indicated by red dashed-line at ~245 °C) of $MWCNT_{COOH}$ (Profile 1A, Figure 4.5(A)) separated the temperature regimes of the $MWCNT_{COOH}$ material's role as a CO adsorbent. This peak was not present in the CO-TPD profile of pristine MWCNT (Profile 2A, Figure 4.5(A)). This finding partially validated the hypothesis made in Section 3.5.2 of Chapter 3 [38] where it was inferred that the –COOH functional groups decomposed at temperatures beyond ~245 °C.

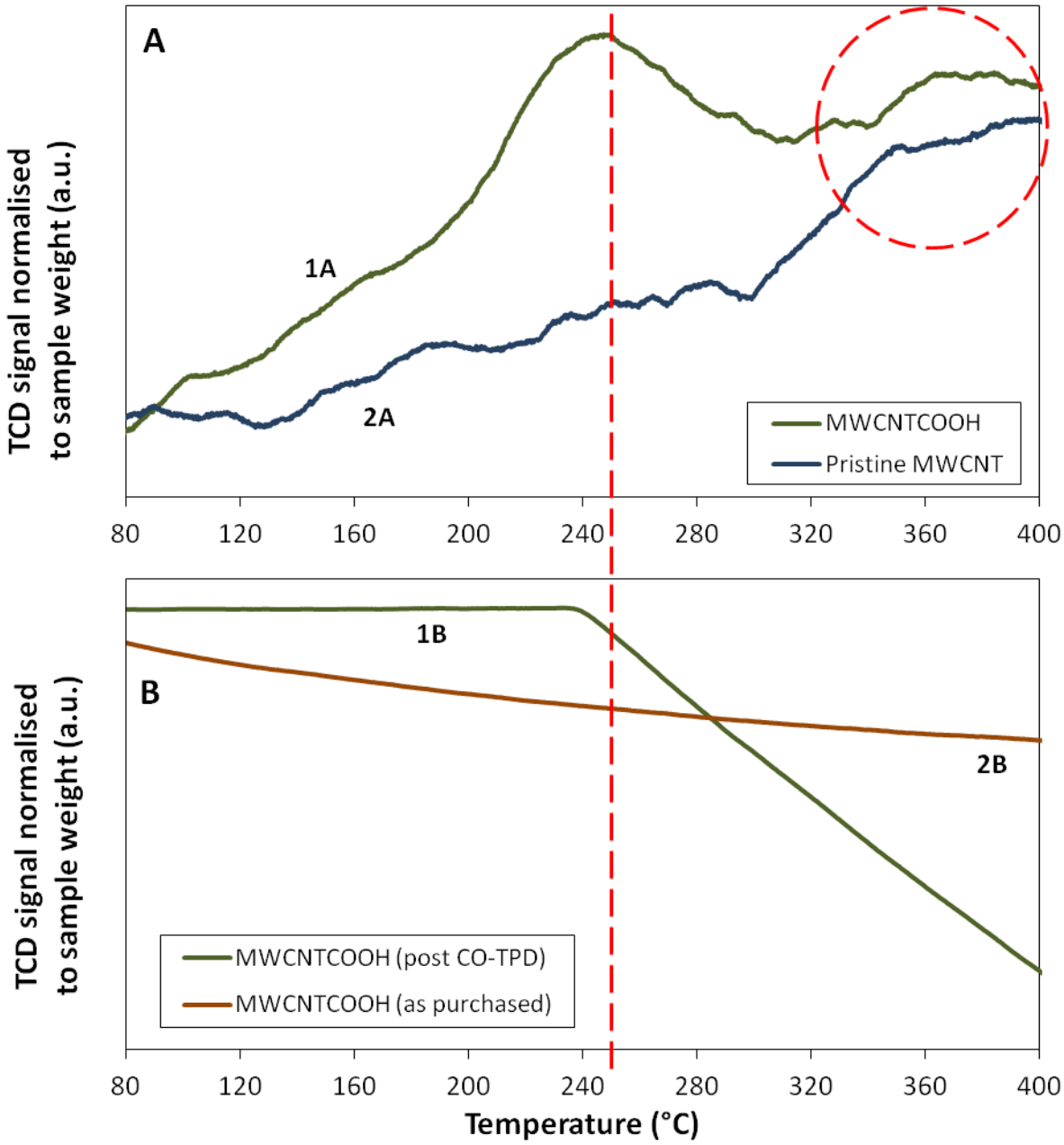

Figure 4.5: CO interactions with MWCNT materials.

(A) CO-TPD profiles; and (B) H_2-TPR profiles. Red dashed-line separates the temperature regimes of the $MWCNT_{COOH}$ material's role as a CO adsorbent.

The H_2-TPR profile of the post-CO-TPD $MWCNT_{COOH}$ (*i.e.* the $MWCNT_{COOH}$ sample that first adsorbed CO molecules at 50 °C and then the CO molecules were desorbed in a temperature-programmed desorption up to 400 °C, before being used in H_2-TPR) (Profile 1B, Figure 4.5(B)) showed a drop in TCD signal from approximately 245 °C. As a comparison,

the H_2-TPR profile of the as-purchased $MWCNT_{COOH}$ (Profile 2B, Figure 4.5(B)) used as reference did not exhibit a notable TCD signal drop. The difference between the two H_2-TPR profiles can be explained by: (1) the decomposition of the –COOH groups in the post-CO-TPD $MWCNT_{COOH}$ sample starting at 245 °C during the CO-TPD process that could have introduced reducible defects, and (2) some reducible groups could have been formed as a consequence of exposure of the defects to CO. The unknown species of the CO-exposed defects were responsible for the uptake of H_2 in the H_2-TPR of the post-CO-TPD $MWCNT_{COOH}$ sample, which was not the case in the as-purchased $MWCNT_{COOH}$. The decomposition of the –COOH groups from approximately 245 °C to release CO_2 was in agreement with the work by Prado-Burguete *et al.* (1989) [48].

To complete the experimental validation, an activity test was performed on the bare $MWCNT_{COOH}$ material (as-purchased) in an oxygen-free environment where CO was maintained at 1 vol.% but no oxygen was introduced in the feed gas mixture, from the beginning of the test at ambient temperature up to a significantly high programmed reaction temperature of 400 °C, which was then kept constant for 2 hours on stream. From Figure 4.6(B), the $MWCNT_{COOH}$ material acted as CO adsorbent (only) at below ~250 °C. From *ca.* 250 °C, decomposition of –COOH groups in the $MWCNT_{COOH}$ material resulted in formation of some detectable quantities of CO_2, which within methodology used here are interpreted as an indication of CO conversion, which was slightly above 20% at 400 °C, calculated using eq. (4.4). In addition, the CO adsorption (calculated using eq. (4.3)) increased from around 40% at 250 °C to slightly below 70% at 400 °C.

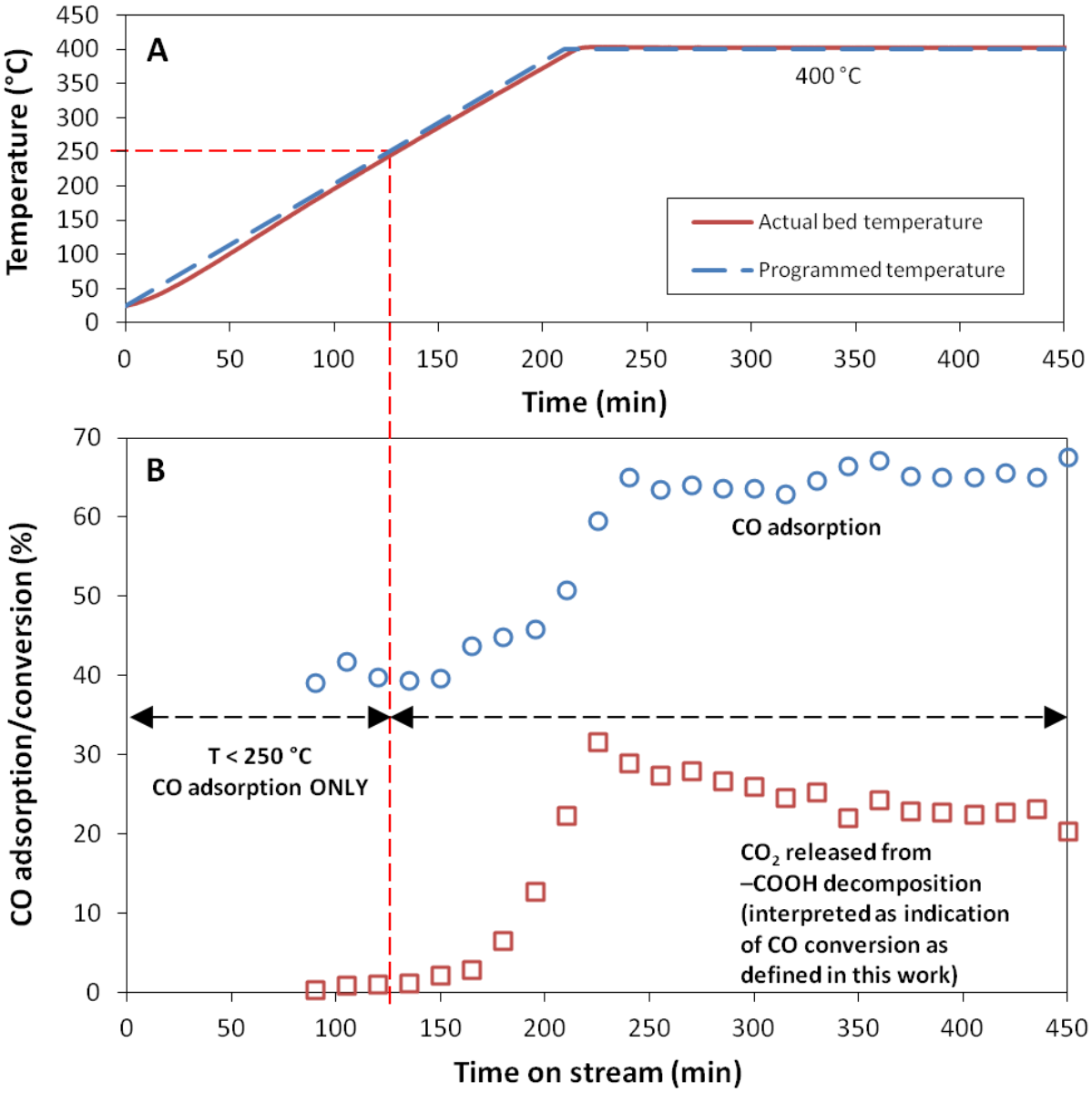

Figure 4.6: Activity test of $MWCNT_{COOH}$: O_2-free, programmed reaction temperature = 400 °C, GHSV = 3,000 mL/($g_{material}$·h).

(A) Reaction temperature; and (B) CO conversion/adsorption. Red dashed-line points to the temperature at which $MWCNT_{COOH}$ started to lose the carboxyl groups, revealing more bare areas on the MWCNT surface.

Based on the findings above, it was hypothesised that $MWCNT_{COOH}$ would act as a catalyst behaving like pristine MWCNT at temperatures high enough that remove significantly the –COOH functional groups, whereby a complete CO conversion could potentially be achieved.

This speculation was supported by the presence of CO-TPD peaks that shared the same desorption-temperature position in both the CO-TPD profiles of pristine MWCNT and $MWCNT_{COOH}$ (Profile 2 and Profile 1 respectively, Figure 4.5(A)), highlighted in a red-dashed circle, which were indicative of the CO desorption from similar sites in both samples at high temperatures, observed at 340 to 380 °C. Therefore, at this temperature and beyond but below 400 °C (beyond which the MWCNT material is combusted in an oxidative environment (Figure 4.1)), by this logic the same conversion of CO should be achieved on the pristine MWCNT and $MWCNT_{COOH}$ materials. However, this did not become possible due to formation of an (unknown) intermediate species as a result of interaction between oxygen and the carboxyl groups that improved the thermal stability of the carboxyl groups (this information was not available from the CO-TPD experiment as oxygen was not present in the measurement), which did not decompose in the same manner it did when oxygen was not present. This will be discussed in the following paragraph.

Reproducing the data in Figure 4.4 by plotting the CO conversion (X_{CO}) into CO_2 (calculated using eq. (4.4)) as a function of time on stream, it was worthy to reiterate that the CO conversion on the pristine MWCNT (Trend-line 1, Figure 4.7(B)) reached values close to 100% at approximately 230 °C, as indicated by the right-side red dashed-line. In addition, it was observed that the CO conversion commenced below the programmed temperature of 190 °C (actual MWCNT bed temperature of slightly above 150 °C), as indicated by the left-side red dashed-line. In the presence of the –COOH groups (Trend-line 2, Figure 4.7(B)), it could clearly be observed that the conversion of CO was halted completely at temperatures below 250 °C, and a little CO_2 evolution was observed thereafter as a result of progressive removal of the –COOH groups. Note that the decomposition of the carboxyl group releasing CO_2 (Trend-line 2, Figure 4.7(B)) was not as significant as what we have seen in Figure 4.6(B) when oxygen was not present. This indicated a formation of an (unknown) intermediate that was thermally more stable than the –COOH groups, as a result of an interaction between the –COOH groups and the oxygen gas. This intermediate remained unknown in this doctoral study due to unavailability of relevant instrument such as diffuse reflectance infrared transform spectroscopy (DRIFTS) in our current facilities to identify the intermediate species. The CO adsorption on the $MWCNT_{COOH}$ (Trend-line 4, Figure 4.7(B)), which was calculated using eq. (4.3) showed a trend of decreasing CO adsorption capacity as the temperature

increased; interestingly, this trend towards decrease in CO adsorption capacity coincides with the progressive removal of the –COOH groups within material upon heating.

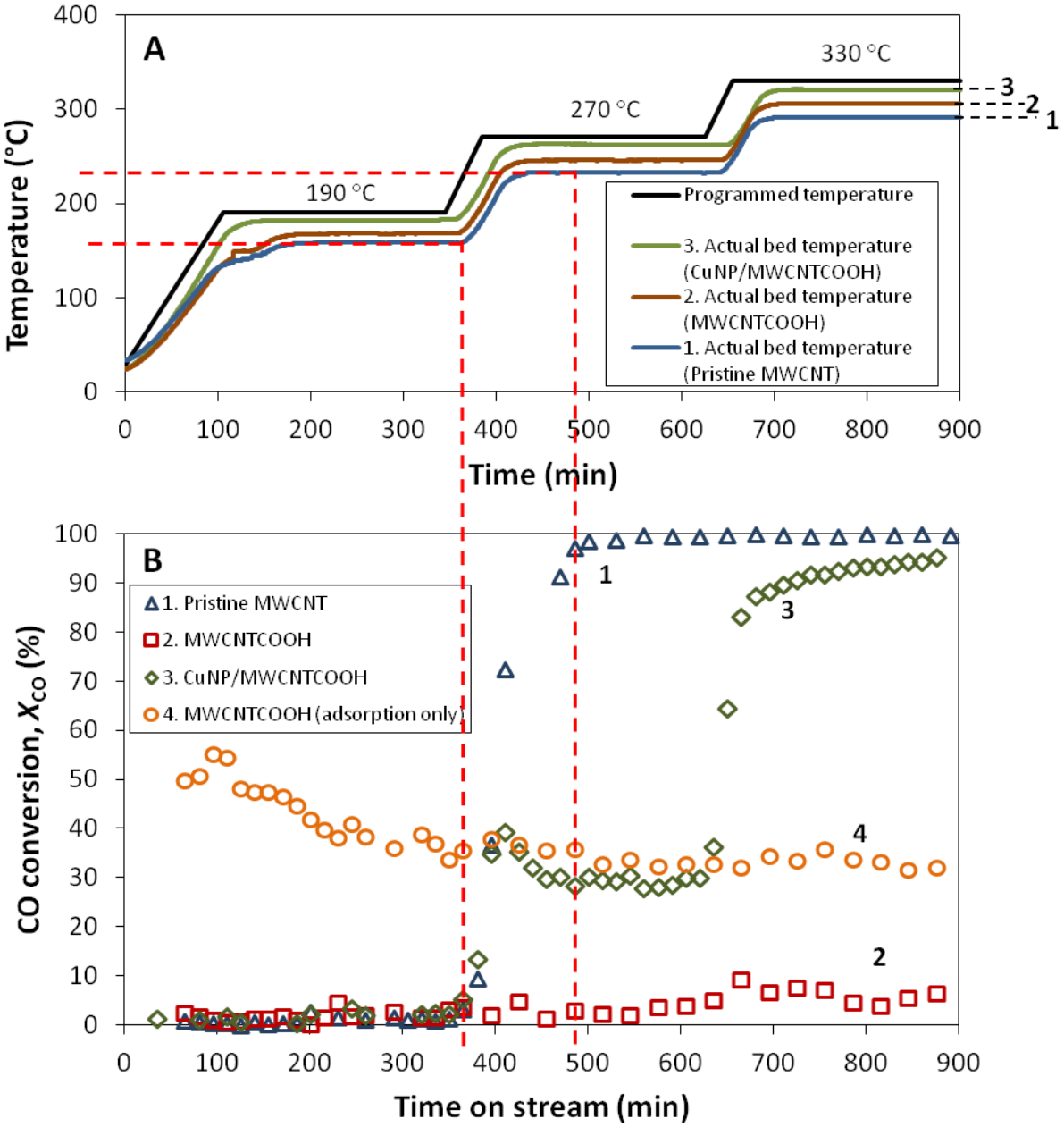

Figure 4.7: CO conversion on pristine MWCNT, $MWCNT_{COOH}$ and $Cu_{NP}/MWCNT_{COOH}$: O_2-rich, temperature-step change, GHSV = 3,000 mL/($g_{material}$·h).

(A) Reaction temperature; and (B) CO conversion into CO_2 product. Left-side red dashed-line points to the temperatures at which pristine MWCNT and $Cu_{NP}/MWCNT_{COOH}$ started to show an effective catalytic activity, right-side red dashed-line points to the temperature at which CO conversion approached a complete conversion on pristine MWCNT.

When copper nanoparticles, $Cu_{NP,}$ were present on the $MWCNT_{COOH}$ surface (Trend-line 3, Figure 4.7(B)), the reappearance of CO conversion at approximately 190 °C could be observed, which reached a steady-state conversion of ~30% in the 4 h on stream at the programmed step-temperature of 270 °C (actual temperature of 265 °C), contributed by the catalytic activity of the Cu_{NP}. However, the conversion level was significantly lower than that on the pristine MWCNT, which showed close to a complete conversion (Trend-line 1, Figure 4.7(B)) at the same reaction set temperature. An approach to a complete conversion on the $Cu_{NP}/MWCNT_{COOH}$ only took place at slightly below 330 °C.

It appeared that the interaction between the copper nanoparticles, Cu_{NP} on the carboxyl-modified MWCNT did not improve the catalytic activity of the MWCNT in CO oxidation reaction. Even though it is well-known that copper has good activity in catalysing reactions that involve CO conversion [37], it may appear that the catalytic activity of Cu_{NP} was inhibited by the carboxyl-modified MWCNT. Earlier discussed results show that carboxyl-modified MWCNT material has surprisingly large CO adsorption capacity at lower temperatures, which was not observed for pristine MWCNT. The mixed adsorbent–catalyst behaviour displayed by the $Cu_{NP}/MWCNT_{COOH}$ still had a lower activity than the pristine MWCNT at the programmed step-temperature of 270 °C, indicating that the inhibitory effect of carboxyl-modified MWCNT environment on Cu_{NP} was strong. As far as we are concerned, there has never been a study reported in the literature investigating the catalytic activity of copper or other metals nanoparticles supported on carbon nanotubes, graphenes or other carbonaceous support materials in CO oxidation that compares the CO conversion performance between carboxyl-modified and unmodified support materials, for us to make a comparison with our finding. In the CO-TPD profiles (Figure 4.8), there is a peak with slightly different profile (Profile 3, Figure 4.8) but similar position to that observed in Cu-free $MWCNT_{COOH}$ material (Profile 2, Figure 4.8) implying similarity of both materials with respect to ability to desorb significant quantities of CO at moderate temperatures (not observed for pristine MWCNT (Profile 1, Figure 4.8)). However, there is no distinctly different feature which could be attributed to the presence of Cu_{NP} species.

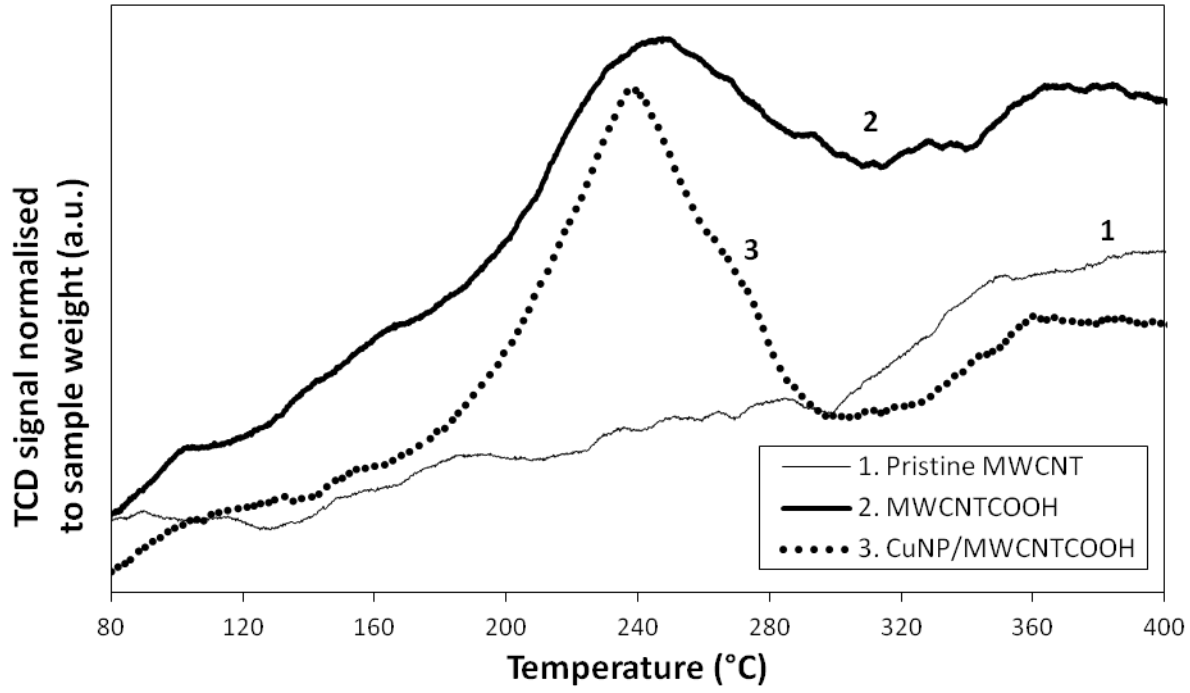

Figure 4.8: CO-TPD profiles of pristine MWCNT, $MWCNT_{COOH}$ and $Cu_{NP}/MWCNT_{COOH}$.

4.3.2.2.2 CO oxidation on Cu_6-doped pristine MWCNT

Cu_6 cluster was used as a model of cluster pollutant, simulating an interaction of Cu metal contaminant with other pollutants consisting of PAH, VOC and P that bind them together. The simulated interaction between the modelled Cu_6 cluster pollutant and the pristine MWCNT represented by the decoration of the reasonably well-dispersed (31.8% dispersion (Table 3.1 of Chapter 3) [38]) Cu_6 cluster on the pristine MWCNT's wall (Trend-line 2, Figure 4.9(B)) appeared to have blocked the originally available MWCNT active site. The reaction on the $Cu_6/MWCNT_p$ commenced from a higher temperature (approximately 240 °C) than that on the pristine MWCNT (indicated by the red dashed-line). However, once the CO conversion reached a maximum of ~12% at the point the step-temperature was achieved, the reaction was then halted when the stable step-temperature was maintained for 4 h time on stream. Upon further heating to the programmed temperature of 330 °C, the CO oxidation continued to progress again to a maximum CO conversion of ~29%. After that, the conversion started to drop steadily during the 4 h time period the temperature was maintained.

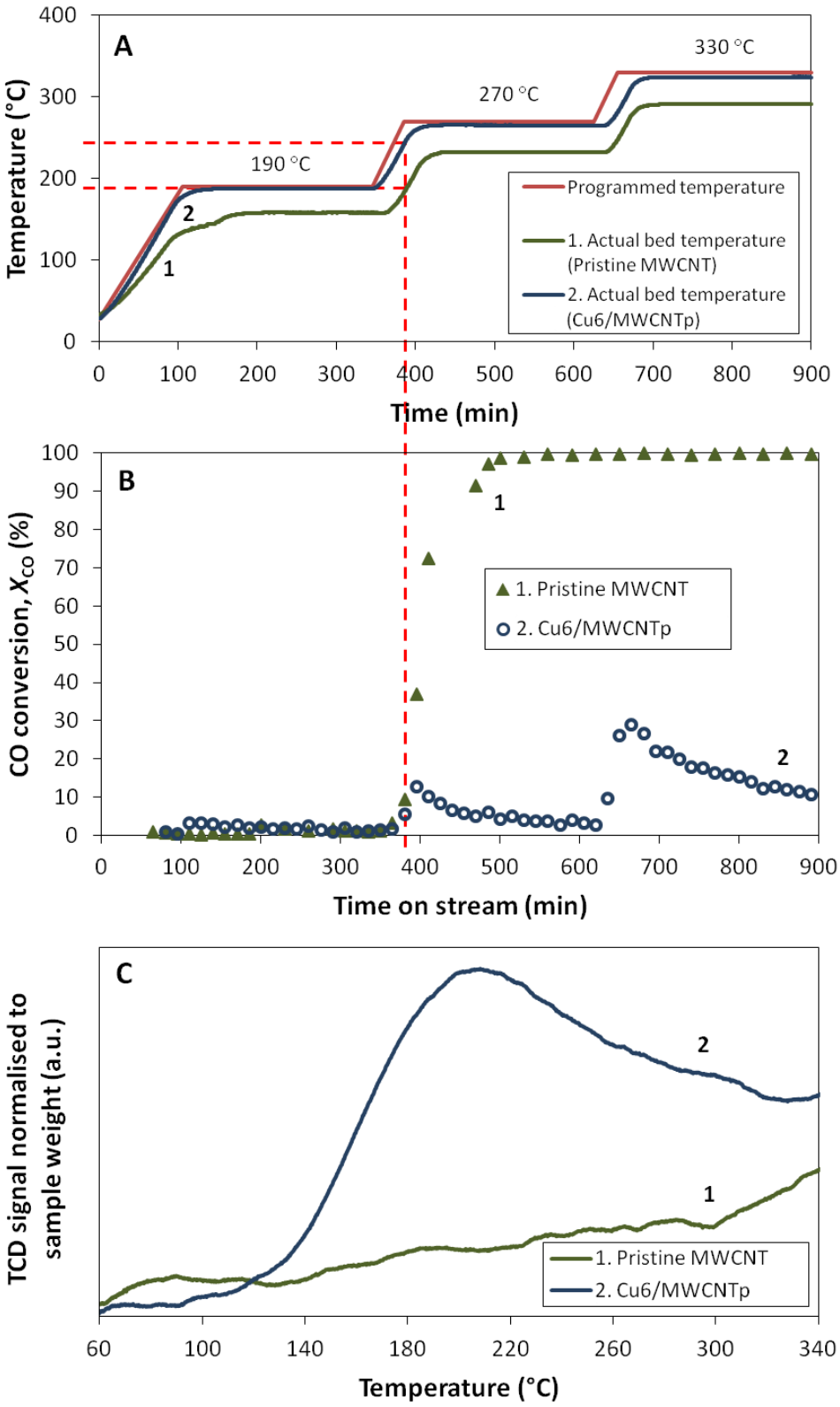

Figure 4.9: CO conversion on $Cu_6/MWCNT_p$: O_2-rich, temperature-step change, GHSV = 3,000 mL/($g_{material}$·h). (A) Reaction temperature; (B) CO conversion into CO_2 product; and (C) CO-TPD profiles. Red dashed-lines point to the temperatures at which pristine MWCNT and $Cu_6/MWCNT_p$ started to show an effective catalytic activity.

As discussed in Section 3.5.2 of Chapter 3 [38], the peak-maximum position in CO-TPD profile represents the strength of the interaction between the CO molecules and the active sites, where peak maximum positioned at lower desorption temperatures indicates weaker interaction, and vice versa. The area under the peak profile indicated surface coverage, which relates to the amount of CO molecules originally adsorbed on the active site [49]. The graph of the CO-TPD profile of the pristine MWCNT (Profile 1, Figure 4.9(C)) appeared relatively flat with a small increase in CO desorption above 300 °C at a higher temperature which indicated a strong chemisorption of the CO molecules on the MWCNT. The relatively low area under that high temperature peak indicated a small amount of CO molecules originally adsorbed on the surface, which should be meaningful for the explanation of high reactivity of pristine MWNTs as the remaining surface active sites would be available for occupancy by the O_2 molecule (eq. (4.5)). The temperature axis in the CO-TPD profiles in Figure 4.9(C) is shown up to 340 °C to understand the adsorption and the desorption of CO on the surface of the materials within the temperature range of our activity tests, which were conducted up to a programmed temperature of 330 °C. There is a significant CO desorption peak with onset at *ca.* 140 °C and maximum at *ca.* 200 °C in CO-TPD of profile of $Cu_6/MWCNT_p$ that is attributed to the presence of Cu_6 cluster-derived species at the surface (Profile 2, Figure 4.9(C)). It is noteworthy that both onset and maximum of CO desorption were observed at lower temperature in this case compared to the cases of $MWCNT_{COOH}$ materials (both Cu_{NP}-loaded and free (Profile 3 and Profile 2, Figure 4.8)), indicating weaker bonding of CO within $Cu_6/MWCNT_p$ material. The shoulder and height of the peak in the CO-TPD profile of the $Cu_6/MWCNT_p$ (Profile 2, Figure 4.9(C)) appeared broad and high, indicating a release of a significant amount of originally weakly-adsorbed CO molecules from the copper species' active sites. The low CO conversion over the $Cu_6/MWCNT_p$ demonstrated in the actual catalytic activity test (Trend-line 2, Figure 4.9(B)) could be due to the fact that the CO molecules were originally weakly-adsorbed on the copper species' active sites and hence, not allowing an effective interaction of O_2 with the active sites. Consequently the surface-reaction of eq. (4.9) involved in the L–H mechanism was inhibited. Nonetheless, this observation does not eliminate completely the E–R mechanism from the possible CO oxidation mechanisms on Cu_6 active sites as the low CO conversion could also be due to the excessively high amount of weakly-adsorbed CO* molecules occupying the active sites and leaving only relatively few available sites for the O_2 gas molecules to occupy (eq. (4.5)).

On the steady drop of the conversion at each time when the temperature was maintained, it is believed that the reaction was inhibited from further progressing as the CO_2 desorption elementary step (eq. (4.10)) was halted due to the blockage of the copper species' active sites. As seen earlier in the PXRD patterns presented in Figure 4.2, Cu_2O phase was present in the as-prepared samples doped with Cu_6 clusters, upon exposure to air. During the CO oxidation reaction, the adsorbed CO_2* product (in the presence of unreacted oxygen) had a chemical interaction with the Cu_2O species' active sites, resulting in the formation of an intermediate material that fit the thermal characteristics of $CuCO_3$ [50-51] (which will be elaborated further later) that deactivated the catalysts by:

$$CO_2^* (g) + ½\ Cu_2O (s) + ¼\ O_2 (g) \rightarrow Cu^*CO_3 (s) \quad (4.11)$$

4.3.2.2.3 CO oxidation on Cu_6-doped $MWCNT_{COOH}$

The Cu_6-doped $MWCNT_{COOH}$ material tested under the same reaction conditions and environment as Cu_6-doped pristine MWCNT (Trend-line 2, Figure 4.10(B) and Figure 4.10(C)), appeared to show behaviour similar to that of Cu_6-doped pristine MWCNT.

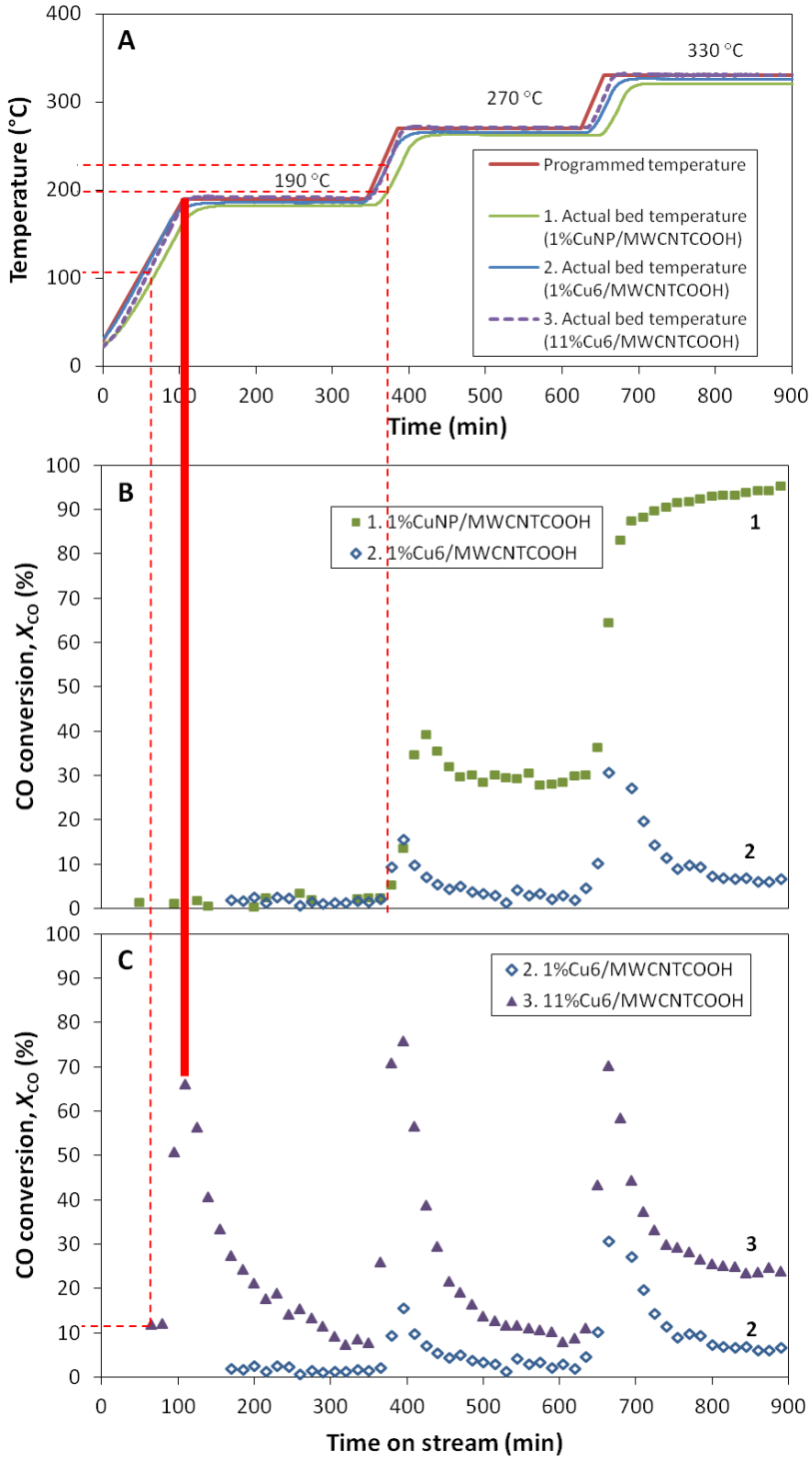

Figure 4.10: CO conversions on copper-containing $MWCNT_{COOH}$: O_2-rich feedstock under temperature-step programme with GHSV = 3,000 mL/($g_{material}$·h). (A) Reaction temperature profiles; (B) Cu_{NP} *vs.* Cu_6; and (C) 11 wt.% Cu_6 *vs.* 1 wt.% Cu_6. Left-side red dashed-line points to the temperature at which $11\%Cu_6/MWCNT_{COOH}$ showed onset of the catalytic activity, left-side red dashed-line points to the temperatures at which $1\%Cu_6/MWCNT_{COOH}$ and $1\%Cu_{NP}/MWCNT_{COOH}$ showed onset of the catalytic activity.

The $MWCNT_{COOH}$ interacting with both the copper particles (Cu_{NP}) and copper cluster (Cu_6) species at low concentrations (1 wt.%) (Trend-line 1 and Trend-line 2 respectively, Figure 4.10(B)) showed onset of the catalytic activity during heating-up stage between 190 and 270 °C. As indicated by the right-side red dashed-line, actual catalyst bed temperature was *ca.* 200 °C for $1\%Cu_{NP}/MWCNT_{COOH}$ and *ca*. 230 °C $1\%Cu_6/MWCNT_{COOH}$. However, the $Cu_{NP}/MWCNT_{COOH}$ appeared to display a different behaviour in comparison to the Cu_6 cluster counterpart, where the former did not exhibit any signs of deactivation. The deactivation in the case of Cu_6 cluster-based materials was speculatively assigned to the $CuCO_3$ formation. In general, the results in Figure 4.10(B) suggested that in the absence of other contaminants such as PAH, VOC, *etc.*, that bind together the Cu pollutant to form ultra-small copper cluster species, the dispersed metal Cu pollutant (represented by Cu_{NP}) in the simulated flue gas by itself can catalyse the CO oxidation somewhat better, which can be attributed to significantly larger particle size in case of Cu_{NP} and a wide range of particle size distribution in this case. Importantly, both Cu_{NP} and Cu_6 containing $MWCNT_{COOH}$ materials significantly outperformed Cu-free material (Trend-line 1 and Trend-line 2, Figure 4.10(B) *cf.* Trend-line 2, Figure 4.7(B)) with latter showing CO conversion below 10% across the range of tested temperatures.

Based on particle size measurement using CO chemisorption, the removal of the –COOH groups from the MWCNT's wall above ~250 °C resulted in copper sintering (Table 3.2 of Chapter 3) [38]. However, it appears that copper sintering alone does not cause notable deactivation of the Cu_6-doped $MWCNT_{COOH}$ material. Indeed, temperature increase did not appear to have an effect on the maximum CO conversion the MWCNT could potentially achieve. For instance, the maximum CO conversion was around 70% at all the step-temperatures (Trend-line 3, Figure 4.10(C)) in the case of Cu_6-doped $MWCNT_{COOH}$ material ($11\%Cu_6/MWCNT_{COOH}$) with more than 10 times higher copper content *cf.* $1\%Cu_6/MWCNT_{COOH}$ and hence more susceptible to sintering.

Interestingly, the $11\%Cu_6/MWCNT_{COOH}$ material appeared to be active from a low temperature of ~110 °C (indicated by the left-side red dashed-line in Figure 4.10(C)), converting slightly above 10% of the CO to CO_2, which was not observed in the 1 wt.% Cu_6-

loaded pristine MWCNT and $MWCNT_{COOH}$. Besides the onset of CO conversion at a lower temperature of ~110 °C, the trend of the CO conversion on the $11\%Cu_6/MWCNT_{COOH}$ was similar to its other Cu_6 counterparts albeit significantly amplified with respect to maximum CO conversions observed: the CO conversion increased to as high as ~70% as the temperature of the reactor was increased each time dropping steadily during temperature plateau stage. Importantly, the first time ~70% conversion of CO using this material was observed at *ca.* 190 °C (highlighted by the solid red line), which is significantly lower than *ca.* 250 °C, confirming that detected CO_2 is not a product of decomposition of –COOH groups alone (Trend-line 2, Figure 4.7(B)) or –COOH interacting with larger Cu particles (Trend-line 1, Figure 4.10(B)) in this case. Further studies are required to pinpoint the exact mechanism behind such spikes in catalyst performance as well as to confirm hypothesis on the mechanism of catalyst deactivation.

It was also observed that the actual bed temperatures of the Cu_6-doped $MWCNT_{COOH}$ materials (Profile 2 and Profile 3, Figure 4.10(A)) were consistent with that of the Cu_6-doped pristine MWCNT seen earlier in Profile 2 of Figure 4.9(A), showing temperature values close to the set programmed temperatures throughout the reaction runs.

Figure 4.11(A) provides comparison of the CO-TPD profiles of Cu-free $MWCNT_{COOH}$ material (Profile 2, Figure 4.11(A)) with $MWCNT_{COOH}$ modified by 1 wt.% Cu_{NP} and 1 wt.% Cu_6 clusters (Profile 3 and Profile 1 respectively, Figure 4.11(A)). All three profiles show similarly pronounced peaks with maxima reached close to ~240 °C, with some notable drop-off of this peak at the higher temperatures in the case of Cu_{NP}-containing material and additional broad feature at the higher temperatures (~290 °C) in the case of Cu_6-containing material. However, the 1 wt. % Cu_6 cluster species on the $MWCNT_{COOH}$ (Profile 1, Figure 4.11(A) and Figure 4.11(B)) introduced an additional small peak at a lower desorption temperature of ~120 °C, which was not observed for any other materials in this study. This peak at the same low desorption temperature also appeared in the CO-TPD profile of $MWCNT_{COOH}$ doped with 11 wt.% Cu_6 cluster species ($11\%Cu_6/MWCNT_{COOH}$) (Profile 4, Figure 4.11(B)).

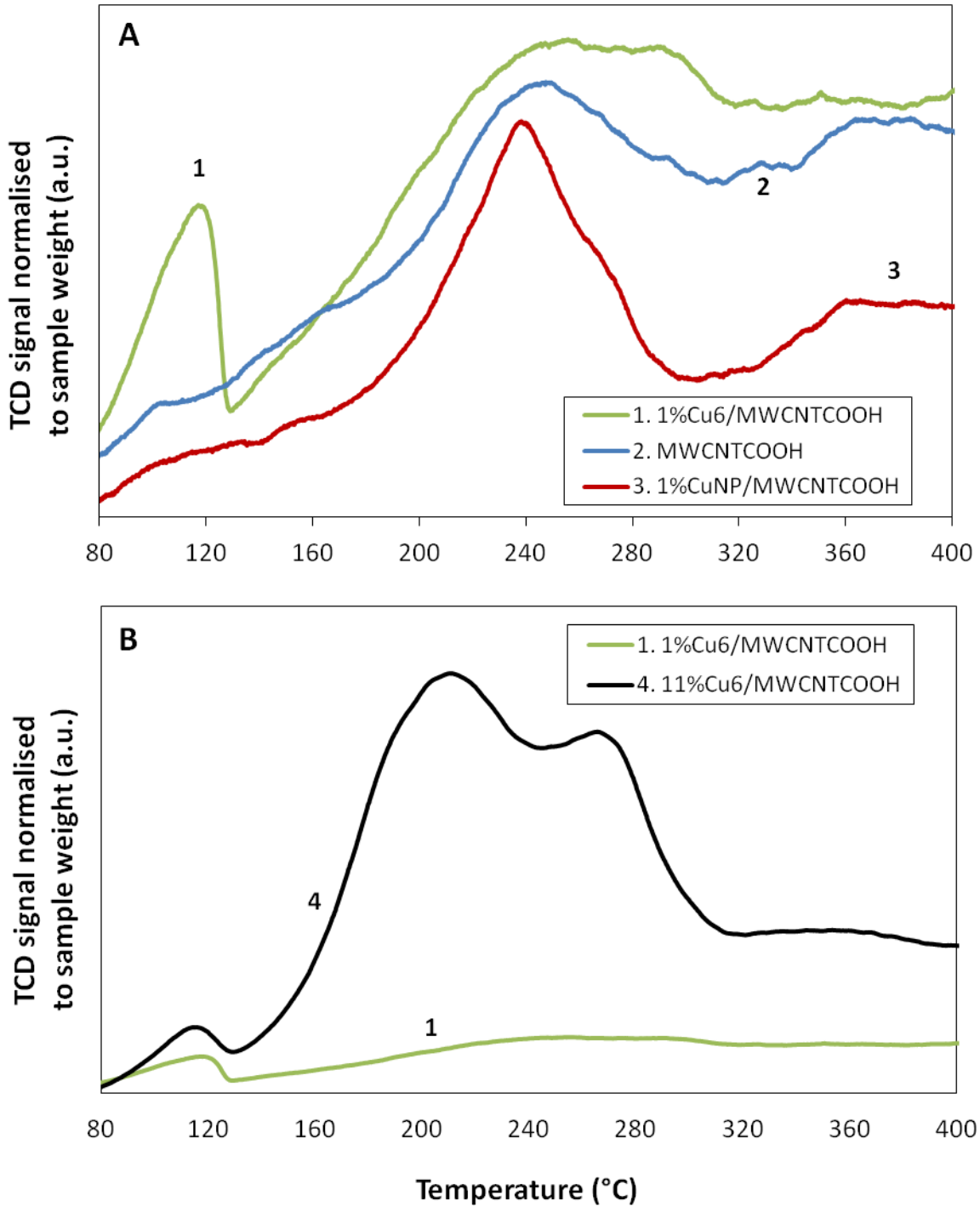

Figure 4.11: CO-TPD profiles of modified MWCNT materials.

(A) MWCNTs grafted with carboxyl groups and doped with 1 wt.% Cu_6 cluster or Cu_{NP}; and (B) $MWCNT_{COOH}$ doped with 1 and 11 wt.% Cu_6 clusters.

To recap, in Section 3.5.2 of Chapter 3 [38], it was mentioned that the peak maximum position along the CO-TPD temperature axis is related to desorption activation energy [49]. The position of the peak maximum at the low temperature of 120 °C indicated that the adsorbed CO* had a (relatively) low desorption activation energy.

This suggested that the Cu_6-doped $MWCNT_{COOH}$ material could catalyse CO oxidation at reaction temperatures of as low as ~120 °C. However, the low Cu_6 cluster content of 1 wt.% appeared to be insufficient to show such performance, which is observed only for material with a higher Cu_6 content ($11\%Cu_6/MWCNT_{COOH}$) as seen earlier in Trend-line 3 of Figure 4.10(C).

In addition, the two CO-TPD peaks at 220 and 270 °C of the $11\%Cu_6/MWCNT_{COOH}$ catalyst (Profile 4, Figure 4.11(B)) indicated significant decomposition of carboxyl groups into CO_2 [48] as discussed in Section 3.5.2 of Chapter 3 [38], catalysed by high Cu_6-precursored species content, which emerged with the originally strongly adsorbed CO molecules on the active sites attributed to the 11% Cu_6.

In a reference catalytic test using Cu_6 cluster deposited on inert alumina (Figure E3, APPENDIX E), the CO conversion performance showed a similar trend as its counterparts doped on the MWCNT materials in the O_2-rich environment, proving the hypothesis that while copper particles pollutant present in the (simulated) flue gas could by itself catalyse the CO oxidation to a certain extent, the reaction was inhibited when other contaminants that formed a copper cluster species were present.

The formation of the $CuCO_3$ on the Cu_6 cluster (eq. (4.11) in all the Cu_6-doped materials was evidenced by experimental observation on the thermal characteristics of the spent Cu_6-doped materials that matched the themogravimetric profile of $CuCO_3$ reported in the literature, which thermally decomposes to release CO_2 by [50-51]:

$$CuCO_3\,(s) \xrightarrow[\Delta]{} CuO\,(s) + CO_2\,(g) \qquad (4.12)$$

Henmi & Hirayama (1985) [51] conducted a thermal decomposition test in air on $CuCO_3{\cdot}Cu(OH)_2.H_2O$ in varying partial pressure of CO_2 (P_{CO2} = 0 – 50 atm) and found that the basic copper carbonate changed to copper oxide (analysed by XRD) at about 295 °C, observing dehydration and decarbonation (analysed by thermogravimetry and differential thermal analysis (TG-DTA)). The release of H_2O and CO_2 increased with the increase in P_{CO2}. Brown *et al.* (1984) [50] performed a similar test on $CuCO_3{\cdot}Cu(OH)_2$ by thermogravimetry and evolved gas analysis (TG-EGA) in helium and found that the material decomposed at 380 °C through simultaneous loss of water and CO_2, leaving behind CuO (analysed by XRD).

In this work, the spent Cu_6-doped materials used in the catalytic activity tests were heated in a flow of argon sweep gas in a ramp-and-hold temperature programme, up to 600 °C. The amount of CO_2 released from the decomposition of the $CuCO_3$ was calculated from the FID peak area based on the GC's calibration of pure CO_2 gas. As seen in Figure 4.12, the release of CO_2 commenced from around 300 °C but the amounts were not significant, until the temperature was increased further to 400 °C, at which CO_2 was released effectively. This trend was in alignment with the thermal decomposition of $CuCO_3$ reported in the literature by Henmi & Hirayama (1985) [51] and Brown *et al.* (1984) [50], which serve as evidence of the formation of $CuCO_3$ that subsequently inhibited the CO oxidation in the case of Cu_6 cluster based materials. The more significant release of CO_2 amount from the spent $11\%Cu_6/MWCNT_{COOH}$ material in comparison to that from the spent $1\%Cu_6/MWCNT_{COOH}$ proved that the CO_2 was formed as a product of the CO oxidation reaction, in which the CO conversion was higher in the former, as seen in Figure 4.10(C) earlier.

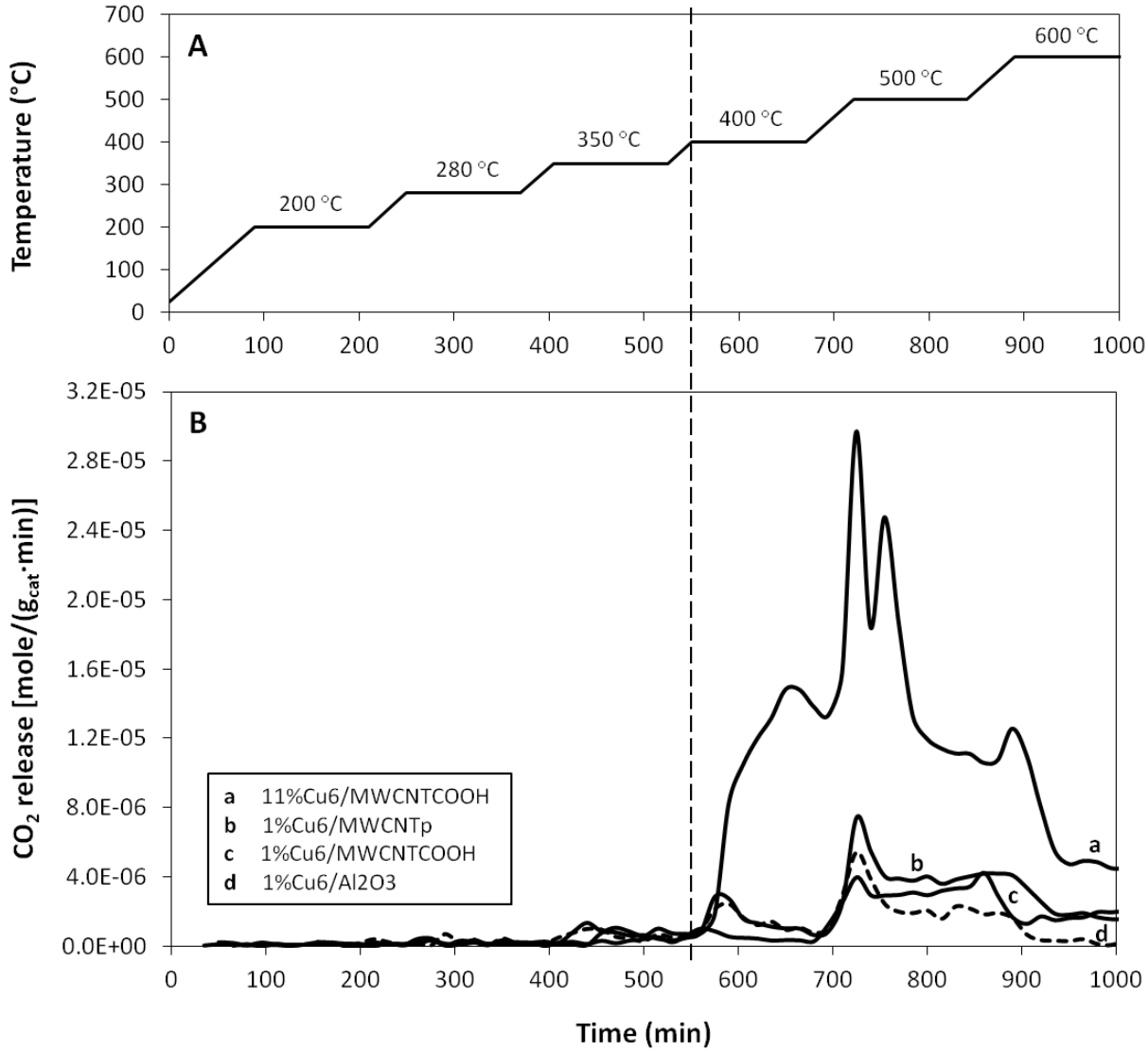

Figure 4.12: CO_2 release from spent Cu_6-based materials in argon sweep gas in ramp-and-hold temperature programme.

The results in Figure 4.12 imply that the reaction inhibition by $CuCO_3$ hinders low-temperature CO oxidation of Cu_6-containing materials, implying need for using a reaction temperature of 400 °C and above. The performance of the catalytic activity tests at and above 400 °C will be presented in Chapter 5.

4.4 Conclusions

In an oxidative atmosphere, pristine MWCNT were demonstrated to be catalytically active for oxidising CO from ~150 °C, approaching a complete conversion from approximately 230 °C. In an acidic environment of wet flue gas, and the presence of carboxyl groups derived from acid constituents on the MWCNT surface modelled by using $MWCNT_{COOH}$ only adsorbed the CO molecules without converting them. The mixed adsorbent–catalyst behaviour on the carboxyl-modified MWCNT's surface doped with dispersed copper particles hindered the full catalytic potential of the active copper particles for CO oxidation reaction.

With the presence of other contaminant constituents such as PAH, VOC, P, *etc*., their interaction with the copper particles pollutant could form a copper cluster species (modelled as $[(PPh_3)CuH]_6 \cdot 0.75THF$) that was demonstrated to then form $CuCO_3$ under the CO oxidation reaction conditions of below 330 °C. The findings in this work highlight the importance of an upstream removal of the studied contaminant constituents in the flue gas prior to the treatment by CO oxidation at low temperatures.

Acknowledgement

The authors acknowledge the financial support of John Sutherland's Fund, Department of Chemical and Process Engineering, University of Canterbury, Christchurch, New Zealand and the supply of the commercial catalyst by Johnson Matthey PLC.

References of Chapter 4

1. Zevenhoven, R. and P. Kilpinen, *Chapter 2 Flue gases and fuel gases*, in *Control of pollutants in flue gases and fuel gases*. 2002, Helsinki University of Technology Espoo: Finland. p. 2.1-2.11.

2. Gromov, S. and V. Ginzburg, *Estimation of heavy metal emissions from coal-fired power plants in Russia.* WIT Transactions on Ecology and the Environment, 1970. **28**.
3. Zhang, H. and X. Zhou, *Speciation variation of trace metals in coal gasification and combustion.* Chemical Speciation & Bioavailability, 2009. **21**(2): p. 93-97.
4. Nalbandian, H., *Trace element emissions from coal.* IEA Clean Coal Centre, 2012. **601**.
5. Martinelli, R., et al., *Flue gas conditioning for the removal of acid gases, air toxics and trace metals*. 1997, Google Patents.
6. Yuan, C.-S., et al., *Partition and size distribution of heavy metals in the flue gas from municipal solid waste incinerators in Taiwan.* Chemosphere, 2005. **59**(1): p. 135-145.
7. Evans, J. and P. Williams, *Heavy metal adsorption onto flyash in waste incineration flue gases.* Process safety and environmental protection, 2000. **78**(1): p. 40-46.
8. Chen, C.-K., et al., *Size distribution of metals in bottom ash of municipal solid waste incinerators.* J Environ Eng Manage, 2008. **18**(2): p. 105-115.
9. Hu, Y., et al., *Characterization on heavy metals transferring into flue gas during sewage sludge combustion.* Energy Procedia, 2014. **61**: p. 2867-2870.
10. Xu, X., et al., *Separation of CO2 from power plant flue gas using a novel CO2" molecular basket" adsorbent.* Fuel Chem. Div. Prepr, 2003. **48**(1): p. 162-163.
11. Elliott, M.A., G.J. Nebel, and F.G. Rounds, *The composition of exhaust gases from diesel, gasoline and propane powered motor coaches.* Journal of the Air Pollution Control Association, 1955. **5**(2): p. 103-108.
12. Szanyi, J. and D.W. Goodman, *CO oxidation on a Cu (100) catalyst.* Catalysis letters, 1993. **21**(1-2): p. 165-174.
13. Prasad, R. and P. Singh, *A review on CO oxidation over copper chromite catalyst.* Catalysis Reviews, 2012. **54**(2): p. 224-279.
14. Liu, W. and M. Flytzanistephanopoulos, *Total oxidation of carbon monoxide and methane over transition metal fluorite oxide composite catalysts: I. Catalyst composition and activity.* Journal of Catalysis, 1995. **153**(2): p. 304-316.
15. Huang, T.-J. and D.-H. Tsai, *CO oxidation behavior of copper and copper oxides.* Catalysis Letters, 2003. **87**(3-4): p. 173-178.
16. Wagman, D.D., et al., *Heats, free energies, and equilibrium constants of some reactions involving O2, H2, H2O, C, CO, CO2, and CH4.* J. Res. Natl. Bur. Stand, 1945. **34**(2): p. 143-201.

17. Conway, W., et al., *CO2 absorption into aqueous amine blended solutions containing monoethanolamine (MEA), N, N-dimethylethanolamine (DMEA), N, N-diethylethanolamine (DEEA) and 2-amino-2-methyl-1-propanol (AMP) for post-combustion capture processes.* Chemical Engineering Science, 2015. **126**: p. 446-454.
18. Lu, C.-Y., et al., *Evaluating the potential of CNT-supported Co catalyst used for gas pollution removal in the incineration flue gas.* Journal of environmental management, 2009. **90**(5): p. 1884-1892.
19. Chuang, K.-H., et al. *Estimating the feasibility of raw carbon nanotubes used as catalyst for CO oxidation*. in *Chemistry and Chemical Engineering (ICCCE), 2010 International Conference on*. 2010: IEEE.
20. Wey, M.-Y., et al., *The relationship between the quantity of heavy metal and PAHs in fly ash.* Journal of the Air & Waste Management Association, 1998. **48**(8): p. 750-756.
21. Abdel-Shafy, H.I. and M.S. Mansour, *A review on polycyclic aromatic hydrocarbons: source, environmental impact, effect on human health and remediation.* Egyptian Journal of Petroleum, 2016. **25**(1): p. 107-123.
22. Zhou, H., et al. *The application of adsorption to remove aromatic hydrocarbons from flue gas*. in *2010 4th International Conference on Bioinformatics and Biomedical Engineering (iCBBE)*. 2010: IEEE.
23. Mastral, A.M. and M.S. Callen, *A review on polycyclic aromatic hydrocarbon (PAH) emissions from energy generation.* Environmental Science & Technology, 2000. **34**(15): p. 3051-3057.
24. Beck, J. and S. Unterberger, *The behaviour of phosphorus in the flue gas during the combustion of high-phosphate fuels.* Fuel, 2006. **85**(10-11): p. 1541-1549.
25. Liaw, S.B. and H. Wu, *High-Phosphorus Fuel Combustion: Effect of Oxyfuel Conditions on PM10 Emission from Homo-and Heterogeneous Phases.* Energy & Fuels, 2016. **31**(3): p. 2317-2323.
26. Bostrom, D., et al., *Ash transformation chemistry during combustion of biomass.* Energy & Fuels, 2011. **26**(1): p. 85-93.
27. Grimm, A., et al., *Bed agglomeration characteristics in fluidized quartz bed combustion of phosphorus-rich biomass fuels.* Energy & Fuels, 2011. **25**(3): p. 937-947.

28. Wang, J. and E. Anthony, *CO oxidation and the inhibition effects of halogen species in fluidised bed combustion.* Combustion Theory and Modelling, 2009. **13**(1): p. 105-119.
29. Paulus, U.A., et al., *Inhibition of CO oxidation on RuO 2 (110) by adsorbed H 2 O molecules.* The Journal of chemical physics, 2004. **121**(22): p. 11301-11308.
30. Caporali, R., et al., *Critical role of water in the direct oxidation of CO and hydrocarbons in diesel exhaust after treatment catalysis.* Applied Catalysis B: Environmental, 2014. **147**: p. 764-769.
31. Kim, Y., S.-K. Shi, and J. White, *Oxygen inhibition of CO oxidation on polycrystalline Rh.* Journal of Catalysis, 1980. **61**(2): p. 374-377.
32. Green, I.X., et al., *Inhibition at perimeter sites of Au/TiO2 oxidation catalyst by reactant oxygen.* Journal of the American Chemical Society, 2012. **134**(30): p. 12717-12723.
33. Binder, A.J., et al., *Low-temperature CO oxidation over a ternary oxide catalyst with high resistance to hydrocarbon inhibition.* Angewandte Chemie International Edition, 2015. **54**(45): p. 13263-13267.
34. Cheah, S.K., et al., *Structural and surface coverage effects on CO oxidation reaction over carbon-supported Pt nanoparticles studied by quadrupole mass spectrometry and diffuse reflectance FTIR spectroscopy.* Physical Chemistry Chemical Physics, 2016. **18**(22): p. 15278-15288.
35. Kuettel, D.A., et al., *Removal of Acidic Gases and Metal Ion Contaminants with PostCapTM Technology.* Energy Procedia, 2013. **37**: p. 1687-1695.
36. Xia, W., et al., *A highly efficient gas-phase route for the oxygen functionalization of carbon nanotubes based on nitric acid vapor.* Carbon, 2009. **47**(3): p. 919-922.
37. Yang, F., et al., *Autocatalytic reduction of a Cu2O/Cu (111) surface by CO: sTM, XPS, and DFT studies.* The Journal of Physical Chemistry C, 2010. **114**(40): p. 17042-17050.
38. Baharudin, L., et al., *CO temperature-programmed desorption of a hexameric copper hydride nanocluster catalyst supported on functionalized MWCNTs for active site characterization in a low-temperature water–gas shift reaction.* Chemical Engineering Journal, 2018b. **In Press, Corrected Proof**.

39. Albert, C.F., et al., *Lewis-base adducts of Group 11 metal (I) compounds. 49. Structural characterization of hexameric and pentameric (triphenylphosphine) copper (I) hydrides.* Inorganic Chemistry, 1989. **28**(7): p. 1300-1306.
40. Cook, A.W., et al., *Synthesis, Characterization, and Reactivity of the Group 11 Hydrido Clusters [Ag6H4 (dppm) 4 (OAc) 2] and [Cu3H (dppm) 3 (OAc) 2]*. Inorganic chemistry, 2016.
41. Baharudin, L., et al., *Potential of metal monoliths with grown carbon nanomaterials as catalyst support in intensified steam reformer: a perspective.* Reviews in Chemical Engineering, 2018a. **ahead of print**.
42. Yang, B., et al., *Copper cluster size effect in methanol synthesis from CO2.* The Journal of Physical Chemistry C, 2017. **121**(19): p. 10406-10412.
43. Oliveira, N.M., G.P. Valençaa, and R. Vieirab, *Water Gas Shift Reaction On Copper Catalysts Supported On Alumina And Carbon Nanofibers.* Chemical Engineering, 2015. **43**.
44. Maniecki, T., P. Mierczyński, and W. Jóźwiak, *Copper-supported catalysts in methanol synthesis and water gas shift reaction.* Kinetics and Catalysis, 2010. **51**(6): p. 843-848.
45. Matsushima, T. and J. White, *On the mechanism and kinetics of the CO-oxidation reaction on polycrystalline palladium: I. The reaction paths.* Journal of Catalysis, 1975. **39**(2): p. 265-276.
46. Domagala, M.E. and C.T. Campbell, *The mechanism of CO oxidation over Cu (110): effect of CO gas energy.* Catalysis Letters, 1991. **9**(1-2): p. 65-70.
47. Winter, K. and D. Barton, *The thermal decomposition of benzoic acid.* Canadian Journal of Chemistry, 1970. **48**(24): p. 3797-3801.
48. Prado-Burguete, C., et al., *The effect of oxygen surface groups of the support on platinum dispersion in Pt/carbon catalysts.* Journal of Catalysis, 1989. **115**(1): p. 98-106.
49. Rakić, V. and L. Damjanović, *Temperature-Programmed Desorption (TPD) Methods*, in *Calorimetry and Thermal Methods in Catalysis*. 2013, Springer. p. 131-174.
50. Brown, I., K. Mackenzie, and G. Gainsford, *Thermal decomposition of the basic copper carbonates malachite and azurite.* Thermochimica acta, 1984. **75**(1-2): p. 23-32.

51. Henmi, H., et al., *Thermal decomposition of basic copper carbonate, CuCO3· Cu (OH) 2· H2O, in carbon dioxide atmosphere (0–50 atm).* Thermochimica acta, 1985. **96**(1): p. 145-153.

CHAPTER 5

Experimental Work, Results and Discussion: Catalytic Assessment and Feasibility Studies (Stage 3b)

Kinetics and constraints of CO oxidation over hexameric copper nanocluster catalyst supported on carboxyl-functionalised MWCNT at high temperatures

This Chapter is a complete reproduction of a manuscript ready for submission:

"Baharudin, L., Severinsen, I., Yip, A.C.K., Golovko, V.B. & Watson, M.J (2019). Kinetics and constraints of CO oxidation over hexameric copper nanocluster catalyst supported on carboxyl-functionalised MWCNT at high temperatures. *Applied Catalysis A: General*, ready for submission."

Highlights

- Below 400 °C, formation of $CuCO_3$ poisoned Cu_6 nanocluster catalysts.
- At 400 °C and above, the deactivated Cu_6 nanocluster catalysts were re-activated as the $CuCO_3$ was thermally decomposed.
- The deactivation hinders low-temperature CO oxidation applications of Cu_6 nanocluster catalysts, thus, working temperature of 400 °C and above is required for these catalysts.

Abstract

Kinetics of CO oxidation over hexameric copper nanocluster catalyst supported on carboxyl-functionalised multi-walled carbon nanotubes ($Cu_6/MWCNT_{COOH}$) was studied in high reaction temperature range of 400 – 475 °C. An excessive amount of O_2 feed hindered the access of the CO molecules to the active sites (maximum CO conversion = ~29% in O_2-rich environment ($CO:O_2$ = 1:10 v/v) *cf*. ~89% in O_2-lean environment ($CO:O_2$ = 1:1.2 v/v) at gas hourly space velocity of 3,000 – 6,000 mL/(g_{cat}·h)). The reaction temperature range was constrained by the catalyst deactivation due to the formation of $CuCO_3$ below the lower limit, and the combustion of the MWCNT support in the oxidative environment at and above the upper limit. The kinetic model was developed based on the assumptions that the reaction was CO-adsorption limited and followed the Langmuir–Hinshelwood mechanism. In the case of CO concentrations below 14 vol.% in the feed gas mixture, the order of reaction was 0.5 with respect to CO and 0.5 with respect to O_2. The activation energy (E_a) for the reaction was determined to be 54.3 kJ/mol in the reaction temperature range studied.

Keywords: CO conversion; CO oxidation; copper nanoclusters; kinetic study; Langmuir–Hinshelwood mechanism; reaction rate expression.

Graphical abstract

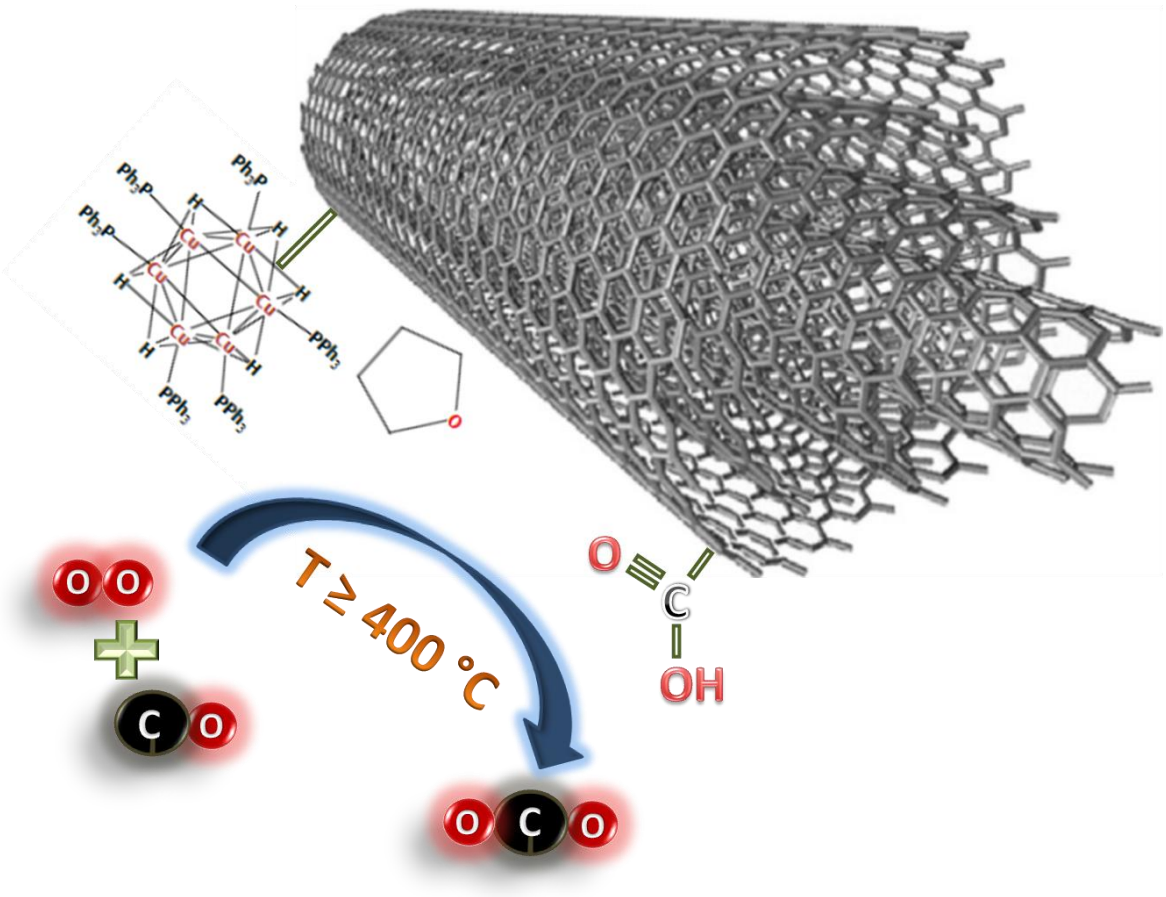

5.1 Introduction

Metal clusters, containing a number of atoms ranging from a few to several thousand, have gained popularity in research in catalysis at both the theoretical and experimental levels due to the prospect of investigating the evolution of bulk matter properties from their atomic properties [1-2]. Additionally, the basic properties of the small metal clusters provide an important insight towards developing an understanding of the fundamental chemical transformations and mechanisms of the reactions of interest on the metal active sites [3-4].

Copper-based materials have found applications in catalysing the reactions that involve carbon monoxide (CO) conversion such as low-temperature water–gas shift (LTWGS) reaction and CO oxidation [5]:

LTWGS [6-11]:	$CO + H_2O \rightarrow CO_2 + H_2$	ΔH^0_{298} = – 41.09 kJ/mol	(5.1)
CO oxidation [12]:	$CO + ½\ O_2 \rightarrow CO_2$	ΔH^0_{298} = –283 kJ/mol	(5.2)

A number of quantum mechanical computational and experimental studies of chemisorption of CO [2, 13-15], O_2 [1, 13] and H_2O [16-17] have been conducted for unsupported copper clusters of various metal core sizes, which discussed the bond strengths between copper clusters and gas molecules as a function of their geometrical structures. The study of the reactivity of the gas molecules on supported Cu clusters is currently lacking. Such a study is necessary so that an understanding on the role played by the interaction between the copper clusters and the supports on the behaviour of the gas molecules on the copper clusters can be established.

In Part II of Chapter 3 [18], we reported the fabrication of novel catalysts by decorating pristine and carboxyl-functionalised multi-walled carbon nanotubes (MWCNTs) and alumina supports with chemically synthesised atomically precise hexameric copper nanocluster (Cu_6) precursors. We hypothesised on the activity of the synthesised catalysts based on active site characterisations interpreted from CO temperature-programmed desorption (CO-TPD) profiles. The interpretation of interaction between the CO molecules and the well-defined active site of the copper species was elucidated using the kinetic information of the elementary steps in the Langmuir–Hinshelwood mechanism for LTWGS reaction. In Part II of Chapter 3 [18], we predicted the kinetics of LTWGS on the synthesised catalysts by identifying the operating temperature range of between 120 and 200 °C in which their catalytic activities were expected to be optimal, and the conditions under which their deactivation would likely occur due to prevalent sintering and dispersion deterioration of the active copper species beyond 250 °C.

The surface mechanism for LTWGS involves the elementary steps whereby water is adsorbed and dissociated on the active site by [6, 10-11, 19]:

$H_2O\ (g) + * \leftrightarrow H_2O*$ (5.3)

$H_2O* + * \rightarrow H* + OH*$ (5.4)

$2\ OH* \leftrightarrow O* + H_2O*$ (5.5)

$OH* + * \rightarrow O* + H*$ (5.6)

$2\ H* \leftrightarrow H_2\ (g) + 2\ *$ (5.7)

Overall: $H_2O\ (g) + * \leftrightarrow O* + H_2\ (g)$ (5.8)

In the CO oxidation reaction, the molecular oxygen is dissociated into surface-adsorbed oxygen atoms by [20-21]:

$O_2\ (g) + * \leftrightarrow O_2*$ (5.9)

$O_2* + * \rightarrow 2\ O*$ (5.10)

In LTWGS reaction, CO molecules scavenge the surface-adsorbed hydroxyl or oxygen produced by water dissociation on the active site in the same manner they react with the surface-adsorbed oxygen atoms that are produced from the dissociation of O_2 gas molecules in CO oxidation [21-22]. The reaction between CO molecules and the adsorbed oxygen atoms on the surface of copper species' active sites can occur through two possible mechanisms [20-21]:

Eley–Rideal (E–R):

$CO\ (g) + O* \rightarrow CO_2*$ (5.11)

Langmuir Hinshelwood (L–H):

$$CO\ (g) \leftrightarrow CO^* \quad (5.12)$$

$$CO^* + O^* \rightarrow CO_2^* + * \quad (5.13)$$

Desorption of the produced CO_2* then takes place to complete the reaction mechanism:

$$CO_2^* \rightarrow CO_2\ (g) + * \quad (5.14)$$

Therefore, the study of oxidation of CO over the copper-based catalysts is imperative in understanding the LTWGS reaction over the same catalysts. Additionally, through the understanding of the reaction mechanism, a representative reaction rate expression can be determined to form a basis for reactor design. In addition, the study of CO oxidation is important towards meeting the environmental regulations especially in automotive exhaust gas treatment and control of gases emitted from heavy industry because CO is a toxic air pollutant [23-26].

In a follow-up to the active site characterisation work that had earlier been presented in Part II of Chapter 3 [18], the more recent work in actual catalytic activity tests (Chapter 4) discovered that the bare pristine MWCNTs by themselves were catalytically active for CO oxidation from approximately 150 °C and approached a complete conversion from 230 °C. The carboxyl group (–COOH) functionalised MWCNT only adsorbed the CO molecules but did not catalyse their conversion. Unlike the catalyst fabricated from a typical copper nanoparticle precursor supported on carboxyl-functionalised MWCNT ($MWCNT_{COOH}$) that was demonstrated to be active from approximately 190 °C (reported in Chapter 4), the Cu_6-precursor complex species was demonstrated to poison the catalytic activity of the MWCNT material when tested below 330 °C. At below 330 °C, it was found that desorption of the CO_2 gas product by the elementary step of eq. (5.14) did not take place. Instead, the Cu_6 complex species (which changed its phase to Cu_2O upon exposure to air (Section 3.5.1.3 of Chapter 3 [18] and Section 4.3.1 of Chapter 4) had an affinity towards formation of $CuCO_3$ [27-28] *via*

a chemical interaction with the adsorbed CO_2* product (in the presence of unreacted oxygen) that deactivated the catalysts by (presented in Section 4.3.2.2.2 of Chapter 4):

$$CO_2^* (g) + ½ Cu_2O (s) + ¼ O_2 (g) \rightarrow Cu^*CO_3 (s) \quad (5.15)$$

The CO oxidation reaction was inhibited from further progressing as the CO_2 desorption elementary step (eq. (5.14)) was halted due to the blockage of the copper species' active sites when the reaction temperature was kept constant. An increase in temperature is required to thermally decompose the $CuCO_3$ to regenerate the catalysts and release CO_2 by [27-28] (presented in Section 4.3.2.2.3 of Chapter 4):

$$CuCO_3 (s) \xrightarrow[\Delta]{} CuO (s) + CO_2 (g) \quad (5.16)$$

The formation of $CuCO_3$ was evidenced in this doctoral work (presented in Section 4.3.2.2.3 of Chapter 4) where the spent Cu_6-precursored catalysts used in the catalytic activity tests at below 330 °C were heated in a flow of argon sweep gas in a ramp-and-hold temperature programme up to 600 °C, in which CO_2 was released effectively from around 400 °C. This was in alignment with the thermal decomposition of $CuCO_3$ reported in the literature by Henmi & Hirayama (1985) [28] and Brown *et al.* (1984) [27]. Therefore, the reaction inhibition would last unless more energy was supplied to the reaction by heating the reactor to a temperature sufficiently high for the reaction shown in eq. (5.16) to happen effectively, which was determined to be a minimum of approximately 400 °C.

The reaction temperature of 400 °C provided an optimal condition for an effective CO conversion without the formation of $CuCO_3$, while maintaining the thermal stability of the MWCNT support (no carbon gasification) in the O_2-rich environment. This will be discussed in more detail later.

In the current work, we perform a kinetic study of CO oxidation at temperatures above 400 °C on Cu_6-based catalysts supported on pristine MWCNT, $MWCNT_{COOH}$, and alumina (Al_2O_3). We aim to experimentally propose a reaction rate expression and determine the activation energy for the CO oxidation over the Cu_6 catalyst supported on $MWCNT_{COOH}$.

5.2 Experimental

5.2.1 Materials

The catalyst supports: pre-functionalised $MWCNT_{COOH}$ (99.9% purity, 0.95 – 1.05% –COOH content, Nanostructured and Amorphous Materials Inc., USA (NanoAmor)), pristine MWCNT (≥ 95% purity, NanoAmor) and Al_2O_3 (≥ 98% purity, Sigma-Aldrich), were used as-purchased in the fabrication of the catalysts.

The synthesis and crystallisation of Cu_6 nanoclusters and their deposition on the pristine and carboxyl-functionalised MWCNTs and alumina supports by wet impregnation using the Schlenk-line technique have been described in Section 3.4.1.1 of Chapter 3 [18, 29-30]. The obtained materials are denoted as $Cu_6/MWCNT_p$, $Cu_6/MWCNT_{COOH}$ and Cu_6/Al_2O_3 respectively. Unless otherwise stated, the Cu_6 content is 1 wt.%.

5.2.2 Characterisation

The Cu_6 content measurement, structural, phase composition, and active site characterisations and analyses of the catalysts and the supports were carried out by inductively coupled plasma mass spectrometry (ICP-MS), CO chemisorption, XRD, and CO temperature-programmed desorption (CO-TPD) techniques. Specific details of experimental procedures for each technique have been reported in Section 3.4.2 and Section 3.4.3 of Chapter 3 [18]. In present work, additional characterisation analyses below were added to complement our discussion.

Materials stability in oxidative environment: Thermogravimetric analysis **(**TGA) (NETZSCH, STA 449 F3 Jupiter) of the materials (7.0 – 16.0 mg) was performed in synthetic air (N_2:O_2 = 80:20 v/v%) flowing at 50 mL/min that mixed with nitrogen gas flowing at 20 mL/min with a temperature ramping rate of 10 °C/min up to 500 °C.

Phase composition: Powder diffraction patterns of the catalysts (as-prepared) were recorded on an X-ray diffractometer (SuperNova, Agilent Technologies) over the 2θ range of 10 – 90°, using Cu-Kα radiation (λ = 1.54056 Å) operated at room temperature. The analysis has been discussed in Section 3.5.1.3 of Chapter 3 [18] and Section 4.3.1 of Chapter 4 but part of it is reproduced in this Chapter for the purpose of making comparison between the as-prepared and the oxidised catalyst samples (post TGA in air described above). The radiation used on the oxidised samples was Co-Kα radiation (λ = 1.79026 Å) on Rigaku 3kW Smartlab.

5.2.3 Kinetic study

The catalytic activity test measurements were conducted in a vertical stainless steel tube reactor (internal diameter = 10 mm) charged with ~0.1 g of catalyst supported on a layer of quartz wool at the tube axial-centre, embedded in a temperature-programmable furnace (GSL-1100X, MTI Corporation). A thermocouple (Intech Instruments) was inserted into the catalyst bed to measure the actual bed temperature (recorded by TracerDAQ software).

The catalysts were used as-prepared without undergoing a specific pre-treatment/activation protocol. The activity tests for the kinetic study were performed in two oxygen concentration atmospheres: (i) oxygen-rich atmosphere (CO:O_2 = 1:10 v/v%) using a feed gas mixture comprising of 1 vol.% CO (99.2%, BOC Gases Australia Ltd.), 10% O_2/40% N_2 (synthetic air of N_2:O_2 = 80:20 v/v% was used as the oxygen source) and balance Ar (BOC Ltd., New Zealand); and (ii) oxygen-lean environment (CO:O_2 = 1:1.2 v/v%) with CO concentration maintained at 1 vol.% in the feed gas mixture, 1.2% O_2/4.8% N_2 and balance Ar, unless otherwise stated.

The flowrates of the gases were regulated by mass flow controllers (MFCs) (MC-10SCCM-D/5M, ALICAT Scientific). Unless otherwise stated, a gas hourly space velocity (GHSV) of 3,000 mL/(g_{cat}·h) was used. The GHSV adjustment to a higher value was done by reducing the amount of catalyst in the bed to a catalyst weight corresponding to the desired GHSV.

The reaction temperature was ramped at a heating rate of ~2 °C/min from ambient temperature to 400 °C (unless otherwise stated), and held constant for 2 – 4 h. All activity tests were conducted at atmospheric pressure.

On-line analysis of gas composition of the reactor outflow was done by a GC (SRI 8610C, SRI Instruments, USA) running on Ar as the carrier gas, equipped with a thermal conductivity detector (TCD) and a flame ionised detector (FID), supported by PeakSimple software (Peak444-32bit, SRI Instruments). Prior to the reaction runs, the GC was calibrated with the CO gas used in the feed and CO_2 gas (Instrument Grade, BOC Gases Australia Ltd.). The activity of the catalysts was presented as CO conversion percentage as a function of time on stream.

The CO conversions were calculated by eq. (5.17):

$$\text{CO conversion, } X_{CO}\ (\%) = \frac{\text{mole of } CO_{2,product}}{\text{mole of } CO_{product} + \text{mole of } CO_{2,product}} \text{ x } 100\ \% \qquad (5.17)$$

Due to the adsorption effect by the $MWCNT_{COOH}$ support material in the $MWCNT_{COOH}$-supported catalysts that adsorbed CO molecules without converting them (discussed in Chapter 4), eq. (5.18) below was not used in the CO conversion calculation as it was not accurate for a real conversion of CO into CO_2 product.

$$\text{CO adsorption/conversion } (\%) = \frac{\text{mole of } CO_{feed} - \text{mole of } CO_{product}}{\text{mole of } CO_{feed}} \text{ x } 100\ \% \qquad (5.18)$$

5.3 Results and discussion

5.3.1 Characterisation

At 400 °C throughout the reaction, all the catalyst samples loaded with 1 wt.% copper maintained their thermal stability in the O_2-rich environment, showing no sample weight loss (activity results will be discussed in Section 5.3.2). However, the activity of the $MWCNT_{COOH}$-supported catalyst loaded with 11 wt.% Cu_6 appeared to catalyse the oxidation (gasification) of the $MWCNT_{COOH}$ support causing remarkable sample weight loss post catalytic test (therefore, experimental result for $11\%Cu_6/MWCNT_{COOH}$ is not shown in this work). This was supported by the TGA results shown in Figure F1 of APPENDIX F, where the 11 wt.% Cu_6 catalyst exhibited thermal degradation from approximately 200 °C, and the 5 wt.% Cu_6 catalyst, from ~250 °C. Thus, the Cu_6 loading content on $MWCNT_{COOH}$ support was limited to a maximum of 1 wt.%, at which loading the material is thermally stable in the O_2-rich environment according to TGA.

As discussed in Section 3.5.1.3 of Chapter 3 [18], based on powder XRD analysis of the as-prepared Cu_6-based catalysts, the Cu complex species supported on the $MWCNT_{COOH}$ (Pattern (a) 11 wt.%, Figure 5.1(A)) changed their phase to Cu_2O phase upon exposure to air when stored in ambient condition. We could see Cu_2O phase in the case of 11 wt%. Cu_6 sample but low Cu_6-loading samples (Patterns (b) 5 wt. % and (c) 1 wt. %, Figure 5.1(A)) would not give any information as the particles were too small to be detected by XRD. However, we may assume that those smaller particles were also close to Cu_2O based on the XRD pattern of the 11 wt.% sample, even though it was NOT evident from the XRD patterns of the lower loaded samples. To understand the effect of an interaction with oxygen on the phase composition of the catalysts, the powder XRD patterns of the samples that went through the TGA in the air flow were also analysed.

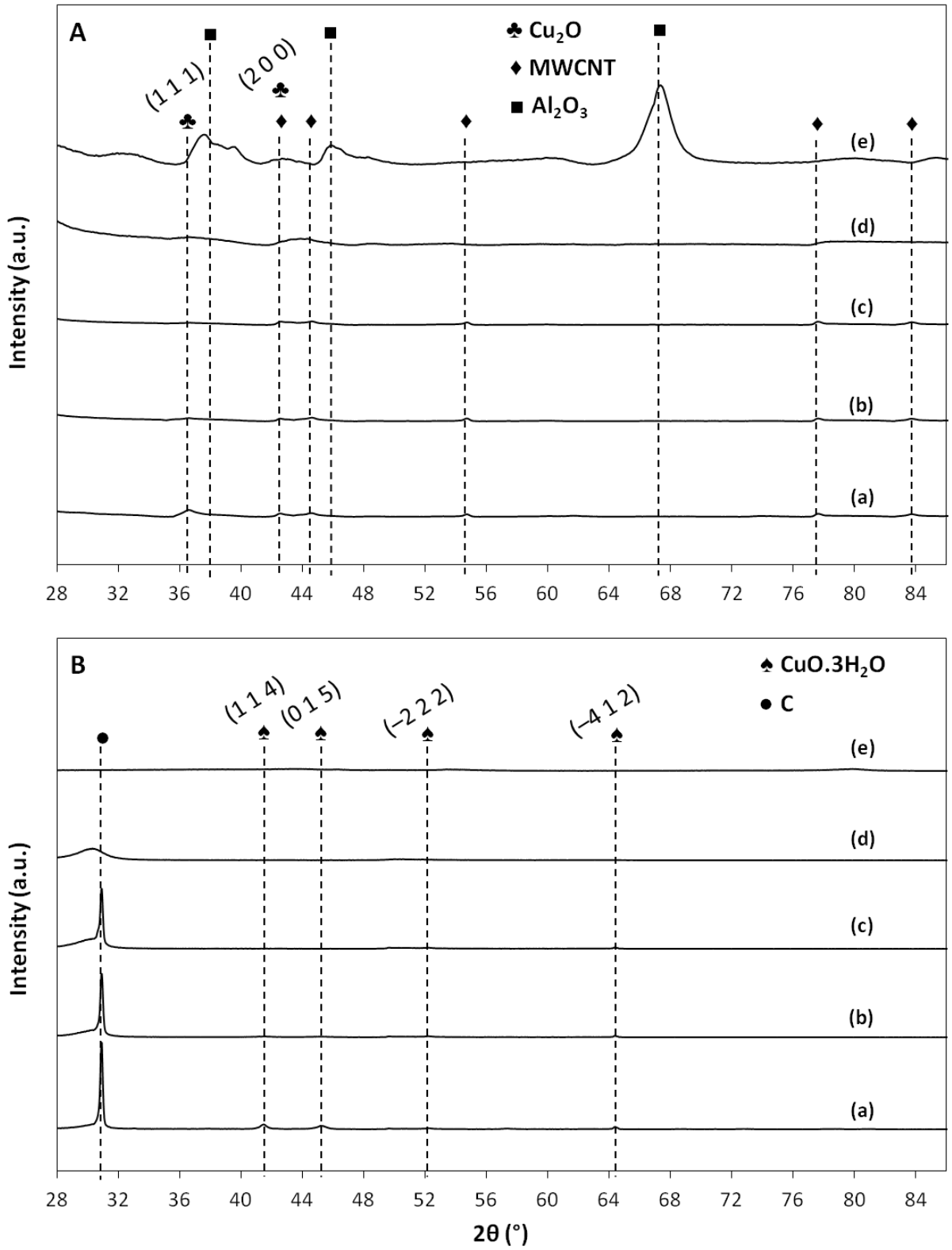

Figure 5.1: XRD patterns of: (a) 11%Cu_6/$MWCNT_{COOH}$, (b) 5%Cu_6/$MWCNT_{COOH}$, (c) 1%Cu_6/$MWCNT_{COOH}$, (d) 1%Cu_6/$MWCNT_p$, and (e) 1%Cu_6/Al_2O_3. (A) As-prepared samples, and (B) oxidised samples.

Post oxidation in air (Figure 5.1(B)), the XRD peaks attributed to the Cu_2O phase (International Centre for Diffraction Data (ICDD) 01-077-0199) on the $MWCNT_{COOH}$-supported Cu_6-precursored catalysts (Pattern (a) from Figure 5.1(A) to Figure 5.1(B)) disappeared. The Cu_2O phase changed into copper oxide trihydrate $CuO{\cdot}3H_2O$ phase (Powder Diffraction File (PDF) 36-0545) (Pattern (a), Figure 5.1(B)) post heat treatment in the air flow as a result of an interaction with oxygen and decomposed carboxyl groups. The carbon crystallinity associated to the crystallinity of the MWCNT disappeared (ICDD 01-075-1621), and a new phase of carbon crystallinity (0 0 4) was introduced at $2\theta = \sim31°$ (PDF 26-1080).

The sharp peak at $2\theta = \sim31°$ attributed to carbon crystallinity (0 0 4) observed for the $MWCNT_{COOH}$-based samples after oxidation (Patterns (a), (b) and (c), Figure 5.1(B)) was not present for the pristine MWCNT-based sample post oxidation (Pattern (d), Figure 5.1(B)), indicating different carbon crystallinities of the pristine MWCNT-based and the $MWCNT_{COOH}$-based samples after oxidation.

The crystal phase of the alumina phase (ICDD 01-075-0788) in the $1\%Cu_6/Al_2O_3$ catalyst (Pattern (e)) observed in the as-prepared sample (Figure 5.1(A)) was not maintained and disappeared in the post air heat treatment (Figure 5.1(B)). No peaks attributed to the Cu species were observed in this catalyst in both states.

Note that in all the as-prepared catalysts containing 1 wt.% Cu_6-precursor (Patterns (c) on $MWCNT_{COOH}$, (d) on pristine MWCNT, and (e) on Al_2O_3, Figure 5.1(A)), no peaks attributed due to the Cu species could be observed due to their high dispersion on the supports and their crystallite size of < 4 nm, which made them undetectable by XRD [7, 18, 31].

5.3.2 Kinetic study

Figure 5.2 shows the CO conversion trends at a reaction temperature of 400 °C on the catalysts in the O_2-rich environment at GHSV = 3,000 $mL/(g_{cat}{\cdot}h)$. The feed gas was

introduced into the reactor from the commencement of experiment at room temperature but the time, t = 0 in Figure 5.2 marked the conversions at the point the temperature first reached 400 °C. As reported in Chapter 4, at reaction temperatures tested below 330 °C, the conversion on the 1 wt.% Cu_6 loaded catalysts showed a continuous steady drop after initial sharp increase when reaching target temperature for the first time. However, at 400 °C, after the initial drop in the CO conversion on the 1 wt.% Cu_6 loaded catalysts, conversion approached a stable plateau towards the end of the 4 h catalytic reaction test time. The 1 wt. % Cu_6 catalyst supported on $MWCNT_{COOH}$ achieved a stable conversion of *ca.* 20% while 1 wt.% Cu_6 supported on pristine MWCNT and alumina achieved a stable conversion of around 30%. The lower conversion on the $MWCNT_{COOH}$-supported Cu_6 catalyst could be due to a different Cu species evolved under these conditions on this specific support in comparison to that on the pristine MWCNT and alumina supports that gave rise to such performance.

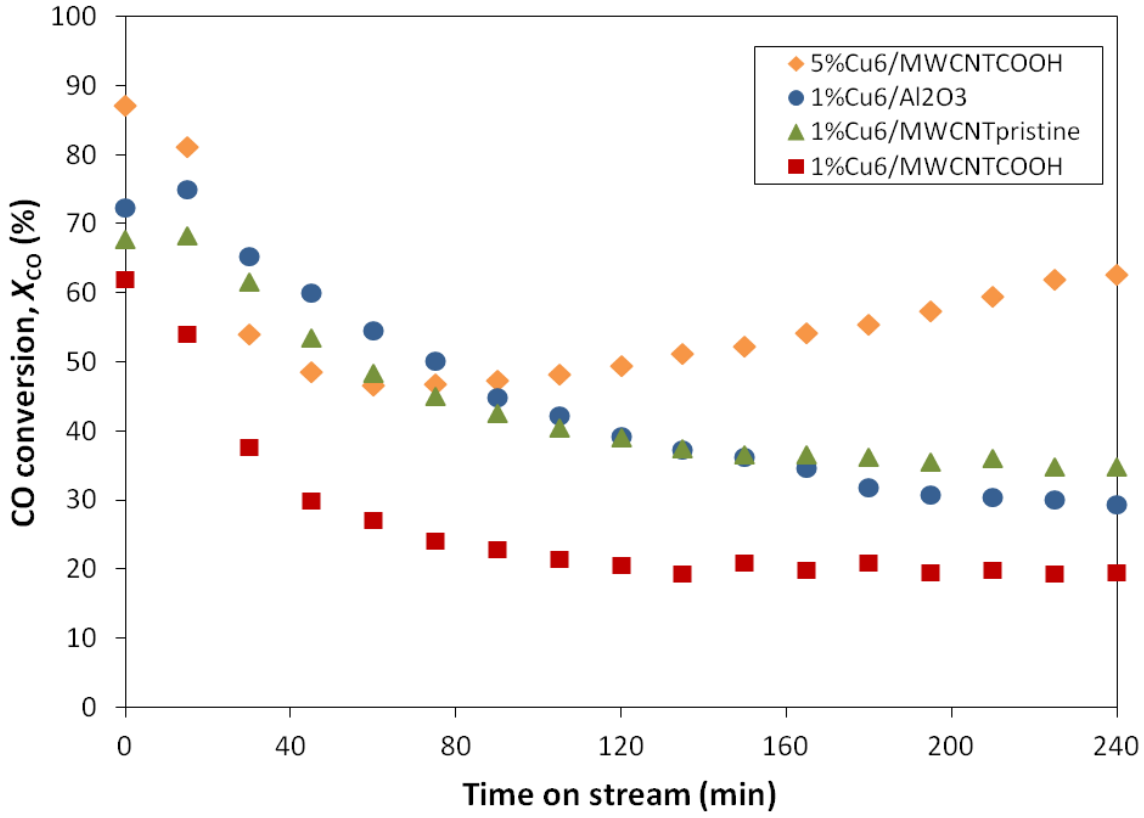

Figure 5.2: CO conversions over Cu_6-based catalysts on different support materials: O_2-rich, 400 °C, GHSV = 3,000 mL/(g_{cat}·h).

Although the amount of Cu_6 content in the $MWCNT_{COOH}$-supported catalyst was limited to 1 wt.% due to its thermal stability issue in an oxidative environment as discussed in Section 5.3.1, the catalytic test was also performed using the 5 wt.% Cu_6 loaded catalyst as a reference test to study the effect of pushing the Cu_6 content higher. In Figure 5.2, it was also observed that the CO conversion trends of the 5 and 1 wt.% $Cu_6/MWCNT_{COOH}$ catalysts were different in that the CO conversion increased steadily after a sharp drop, instead of settling to a stable conversion for the 5 wt.% catalyst. This was explained by the progressive oxidation (gasification) of the carbon support in the 5 wt.% catalyst after prolonged reaction duration, which agreed to capping the Cu_6 content in the $MWCNT_{COOH}$-supported catalysts fabricated in this doctoral work at 1 wt.%, due to the thermal stability issue. The carbon gasification appeared to have commenced after approximately 60 min of the reaction time on stream at 400 °C.

Nonetheless, in t < 60 min before the carbon gasification took place, as expected, the catalyst with 5 wt.% Cu_6 content loaded on $MWCNT_{COOH}$ showed higher CO conversions in comparison to the 1 wt.% Cu_6 content. This can be explained with the aid of the CO-TPD profiles of the catalysts. Figure 5.3(A) provides comparison of the CO-TPD profiles of Cu-free $MWCNT_{COOH}$ (Profile 2, Figure 5.3(A)) with $1\%Cu_6/MWCNT_{COOH}$ (Profile 1, Figure 5.3(A)). Both profiles show similarly pronounced peaks with maxima reached close to ~240 °C. The 1 wt. % Cu_6 cluster species on the $MWCNT_{COOH}$ (Profile 1, Figure 5.3(A) and Figure 5.3(B)) introduced an additional small peak at a lower desorption temperature of ~120 °C. Figure 5.3(B) shows 2 peaks for both 1 and 5 wt.% Cu_6 catalyst loadings. The first low temperature peak attributed to the CO adsorbed on Cu_6 species' site (as discussed in Section 3.5.2 of Chapter 3 [18] and Section 4.3.2.2.3 of Chapter 4) moved from the slightly higher temperature of *ca.* 120 °C in the case of 1 wt.% Cu_6 to even lower temperature of *ca.* 100 °C in the case of 5 wt.% Cu_6, which coincided with a notable increase in this peak area. The second high temperature peak showed similar changes.

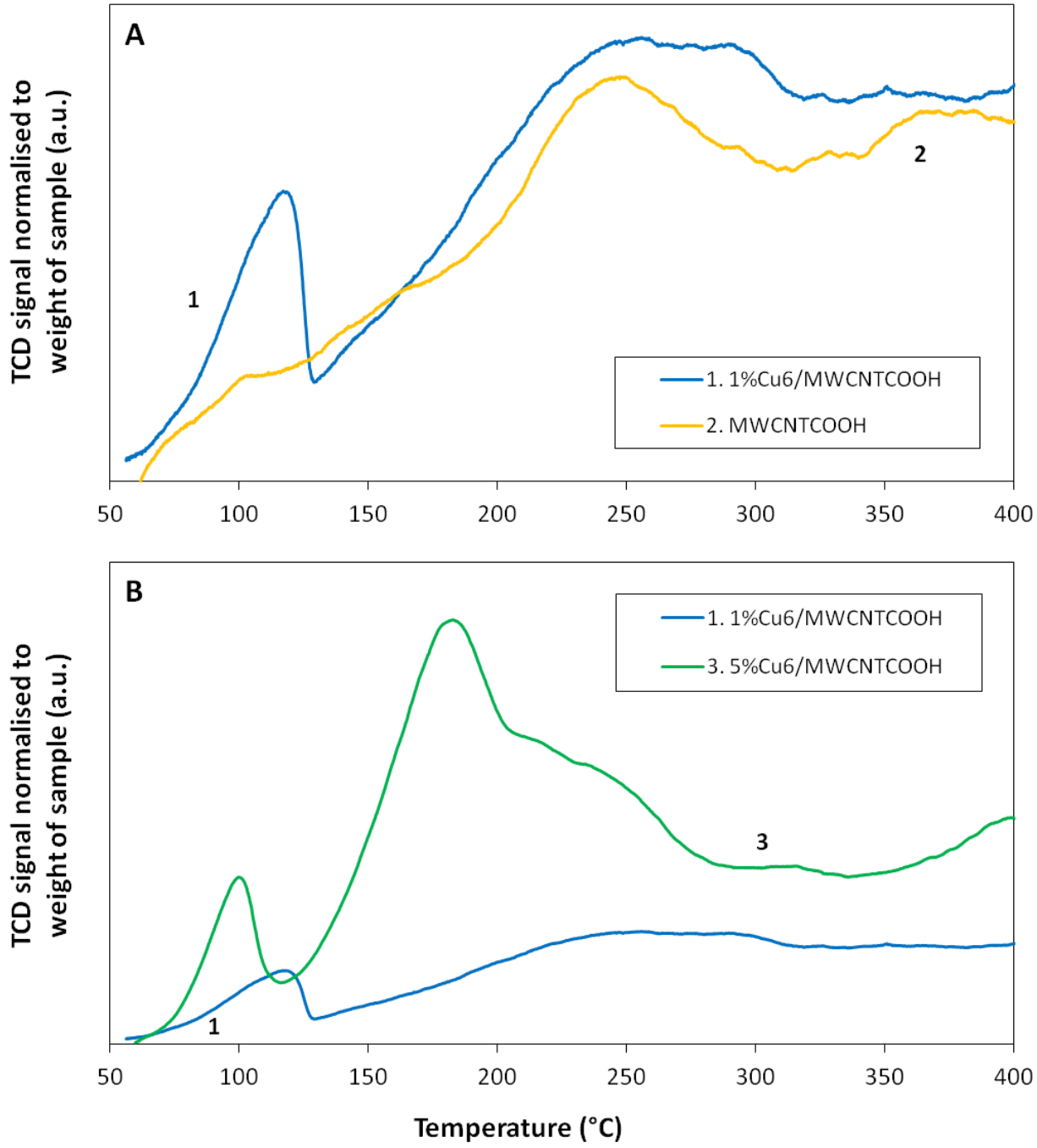

Figure 5.3: Changes of CO-TPD profile of $Cu_6/MWCNT_{COOH}$ catalyst from 1 wt.% to 5 wt.% copper content. (A) $1\%Cu_6/MWCNT_{COOH}$ *vs.* Cu_6-free $MWCNT_{COOH}$; and (B) $1\%Cu_6/MWCNT_{COOH}$ *vs.* $1\%Cu_6/MWCNT_{COOH}$.

As mentioned in Section 3.5.2 of Chapter 3 [18] and Section 4.3.2.2.2 of Chapter 4, the peak maximum position along the CO desorption temperature axis is related to desorption activation energy. The area under the peak profile indicates the amount of CO molecules

originally adsorbed on the material's surface [32]. The shift of the peak-maximum position of both peaks in 1%Cu_6/$MWCNT_{COOH}$ catalyst's CO-TPD profile to a lower temperature in the CO-TPD profile of its 5 wt.% counterpart in Figure 5.3(B) suggested lower CO binding energy in the case of the latter. This could potentially coincide with the higher catalytic activity as a result of a relatively lower energy obstacle to enable facile migration of the weakly adsorbed CO* towards reacting with the adsorbed monoatomic oxygen, O* (eq. (5.13) of L–H mechanism), on the 5%Cu_6/$MWCNT_{COOH}$ catalyst. Also, the larger area under the peak profile of both peaks of 5%Cu_6/$MWCNT_{COOH}$'s CO-TPD profile indicated a higher quantity of CO molecules originally adsorbed on this catalyst's surface.

5.3.2.1 Effect of oxygen concentration

The performance of the pristine MWCNT- and alumina-supported Cu_6-based catalysts in CO oxidation were tested under two different oxygen-containing atmospheres in this work: the O_2-rich (CO:O_2 = 1:10 v/v) and O_2-lean (CO:O_2 = 1:1.2 v/v). Obtained results are shown in Figure 5.4(A) and Figure 5.4(C), respectively. In terms of the CO conversion level, the O_2 concentration seemed to have an impact in the case of 1%Cu_6/$MWCNT_p$ catalyst, where the conversions were generally lower in the O_2-lean environment. On the other hand, the lower O_2 concentration appeared to have (relatively) insignificant impact on the CO conversion level in the case of 1%Cu_6/Al_2O_3 catalyst. We believe that the interactions between the copper species and material of support were substantially different in the cases of the pristine MWCNT *cf.* alumina, which could in part explain the observed results. The copper species in different oxidation states display different levels of catalytic activity [22, 26, 33-34]. The different concentrations of O_2 in the feed gas in the two oxygen atmospheres could have changed differently the oxidation state of the copper species supported on the pristine MWCNT and the alumina. The change in the oxygen state of the copper species with their exact oxidation numbers was not experimentally determined under *operando* conditions in this work.

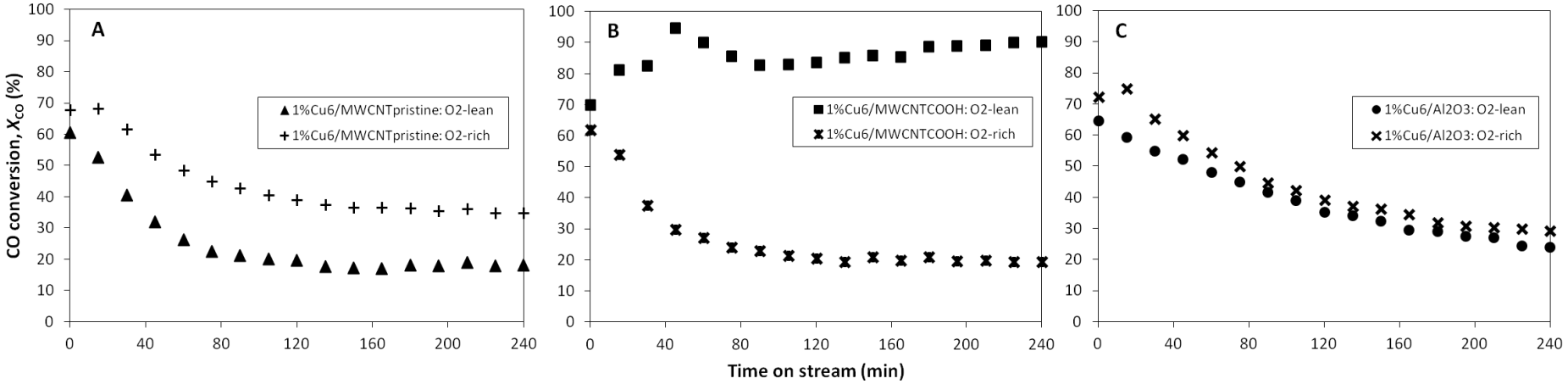

Figure 5.4: CO conversions over Cu_6-based catalysts: O_2-rich *vs.* O_2-lean, 400 °C, GHSV = 3,000 mL/(g_{cat}·h). (A) Pristine MWCNT-supported; (B) $MWCNT_{COOH}$-supported; and (C) Al_2O_3-supported.

The trends of the CO conversion on $MWCNT_{COOH}$-supported Cu_6 catalyst (Figure 5.4(B)) could suggest that the excess of oxygen in the O_2-rich environment resulted in somewhat effective poisoning of the active sites with O_2 and consequently blocked access of CO molecules to the active site. The reaction reached a stable CO conversion of ~20% in the O_2-rich environment, which was 4.5 times lower than performance under the O_2-lean conditions. An alternative explanation to the surface-specific poisoning could be formation of CuO_x nanoparticles with the higher overall oxidation state of Cu under the O_2-rich environment; such species showed lower activity in CO oxidation under the steady state conditions. This hypothesis is in agreement with the observations by Jernigan & Somorjai (1994) [22] and Nagase *et al.* (1999) [34] who demonstrated that the catalytic activity in CO oxidation decreased in the order of Cu > Cu_2O > CuO, but the change in the oxidation state of the copper species in this doctoral work was not determined experimentally under *operando* conditions as mentioned earlier.

To support the hypothesis on the O_2-poisoning effect, Figure 5.5 presents experimental evidence of the blockage of the CO molecules' access to the active site on the $1\%Cu_6/MWCNT_{COOH}$ catalyst (in a series of CO adsorption tests) in the presence of an excess O_2 in the feed gas in the O_2-rich environment. Programmed temperature of 170 °C was selected in these tests to demonstrate the effect of O_2-poisoning on the $Cu_6/MWCNT_{COOH}$ catalyst under the conditions where the pristine MWCNT was active but the $Cu_6/MWCNT_{COOH}$ catalyst was inactive for CO oxidation and the latter acted as CO adsorbent, while the –COOH groups were thermally stable on the surface of the $MWCNT_{COOH}$ (as discussed in Chapter 4). At this temperature, the different levels of CO adsorption on the catalyst under both the O_2-lean and the O_2-rich environments could be observed without interference of the CO conversion.

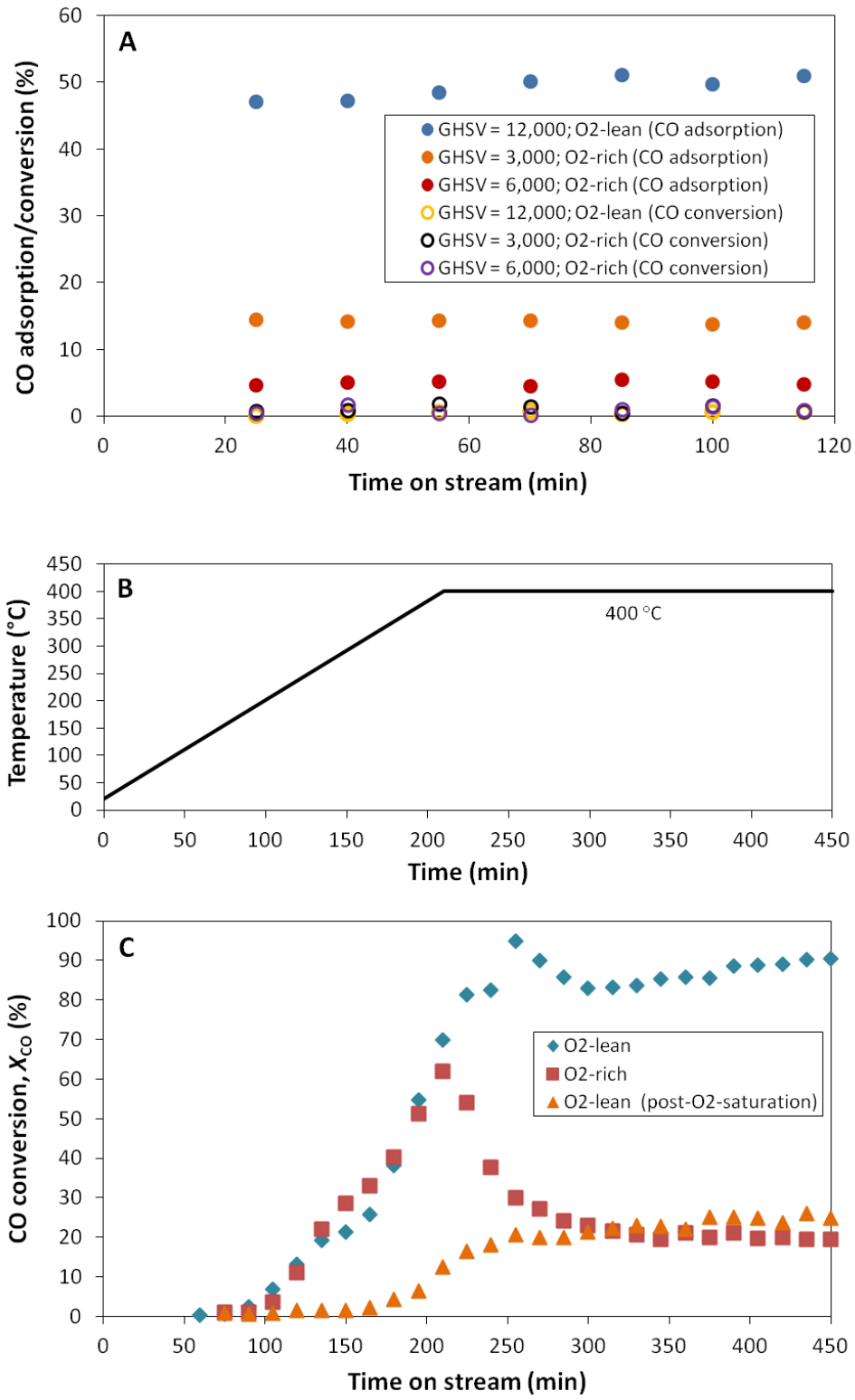

Figure 5.5: Experimental evidences of blockage of CO molecules access to active site by excess O_2 on 1%Cu_6/$MWCNT_{COOH}$ catalyst. (A) CO adsorptions: various O_2-level environments, 170 °C, various GHSVs (mL/(g_{cat}·h)); (B) temperature programme of the reactor corresponding to the conversions shown in (C); and (C) CO conversions: various O_2-level environments, 400 °C, GHSV = 3,000 mL/(g_{cat}.h).

As seen in Figure 5.5(A) (hollow circles), the $Cu_6/MWCNT_{COOH}$ catalyst was inactive for CO oxidation (CO conversion calculated using eq. (5.17)) at the programmed temperature of 170 °C. Eq. (5.18) was used to calculate CO adsorption on the $1\%Cu_6/MWCNT_{COOH}$ catalyst. As can be seen in Figure 5.5(A), even in the case of a significantly shorter residence time (GHSV = 12,000 mL/(g_{cat}·h)), the CO molecules had a significantly better interaction with the $1\%Cu_6/MWCNT_{COOH}$ catalyst in an O_2-lean environment, in comparison to the low GHSV experiments at the same temperature but in O_2-rich environment, as evidenced by the CO adsorption level tested at 170 °C.

As seen earlier in Figure 5.4(B), when the oxygen concentration was decreased from the O_2-rich ($CO:O_2$ = 1:10 v/v) to the O_2-lean ($CO:O_2$ = 1:1.2 v/v) environments at 400 °C and 3,000 mL/(g_{cat}·h) at a maintained CO concentration in the feed gas of 1 vol.%, the CO conversion on the $1\%Cu_6/MWCNT_{COOH}$ catalyst improved. We compared performance of fresh as-made catalysts with the $1\%Cu_6/MWCNT_{COOH}$ catalyst sample that had undergone a pretreatment step called "oxygen saturation" prior to the reaction test (see Figure 5.5(C)). The "oxygen saturation" was performed by first pretreating the catalyst (~0.1 g) in a flow of synthetic air ($N_2:O_2$ = 80/20%) and argon mixture (50:50 v/v%) at 5 sccm total flow with temperature ramped up at ~2 °C/min from room temperature to 330 °C and maintained at 330 °C constant for 2 hours. The CO oxidation in the O_2-lean environment then commenced on the catalyst sample pretreated in this way. We observed that even when tested in the O_2-lean environment, the maximum CO conversion reached on the post-O_2-saturation sample was only slightly above 20%. This was substantially lower than the conversion on the as-made sample under the O_2-lean conditions, which reached as high as 90% conversion of CO. The CO conversion using post-O_2-saturation sample was also not significantly different from the maximum steady-state conversion in the O_2-rich catalytic test on the as-made sample. Hypothesising that catalytic activity of this material is associated with Cu species, exposure to an excessive amount of O_2 in the O_2-saturated sample and/or O_2-rich environment poisons the active site, hindering the CO oxidation.

Based on the CO adsorption trends in the O_2-rich and the O_2-lean environments at various GHSVs presented in Figure 5.5(A), we may well assume that the CO oxidation reaction followed the L–H mechanism, where only a limited amount of the CO molecules could reach

and be adsorbed on the active site due to the O_2-poisoning in the O_2-rich environment. As a result, the CO conversion was limited in the O_2-rich environment as shown in Figure 5.4(B) and Figure 5.5(C). This assumption allows us to hypothesise that the CO conversion was halted by the adsorption of CO on the active site in the L–H mechanism (eq. (5.12)) that hindered the surface-reaction elementary step represented by eq. (5.13).

5.3.2.2 Reaction rate expression on $Cu_6/MWCNT_{COOH}$ catalyst

In the O_2-lean environment at 400 °C (Figure F2 of APPENDIX F), it was observed that the steady-state CO conversion of 90% on the $Cu_6/MWCNT_{COOH}$ catalyst was not affected when the GHSV was increased from 3,000 to 6,000 mL/(g_{cat}·h) but it decreased to approximately 50 % when the GHSV was increased further to 12,000 mL/(g_{cat}·h). Therefore, the rate of reaction as a function of CO concentration in the feed gas was determined by performing a kinetic investigation in the O_2-lean environment at 400 °C and GHSV = 6,000 mL/(g_{cat}·h). The results revealed that the steady-state CO conversion decreased from ~89% to ~35% when the concentration level of CO in the feed gas was increased from 1 to 2 vol.% (Figure 5.6(A)). The CO conversion was maintained at the same level between 2 and 14 vol.% of CO in the feed. Since air was used as the source of oxygen in gas feed, the maximum CO concentration that can be used in this study was limited to 14 vol.% in order to keep the CO:O_2 ratio constant in the O_2-lean environment while maintaining the GHSV at 6,000 mL/(g_{cat}·h).

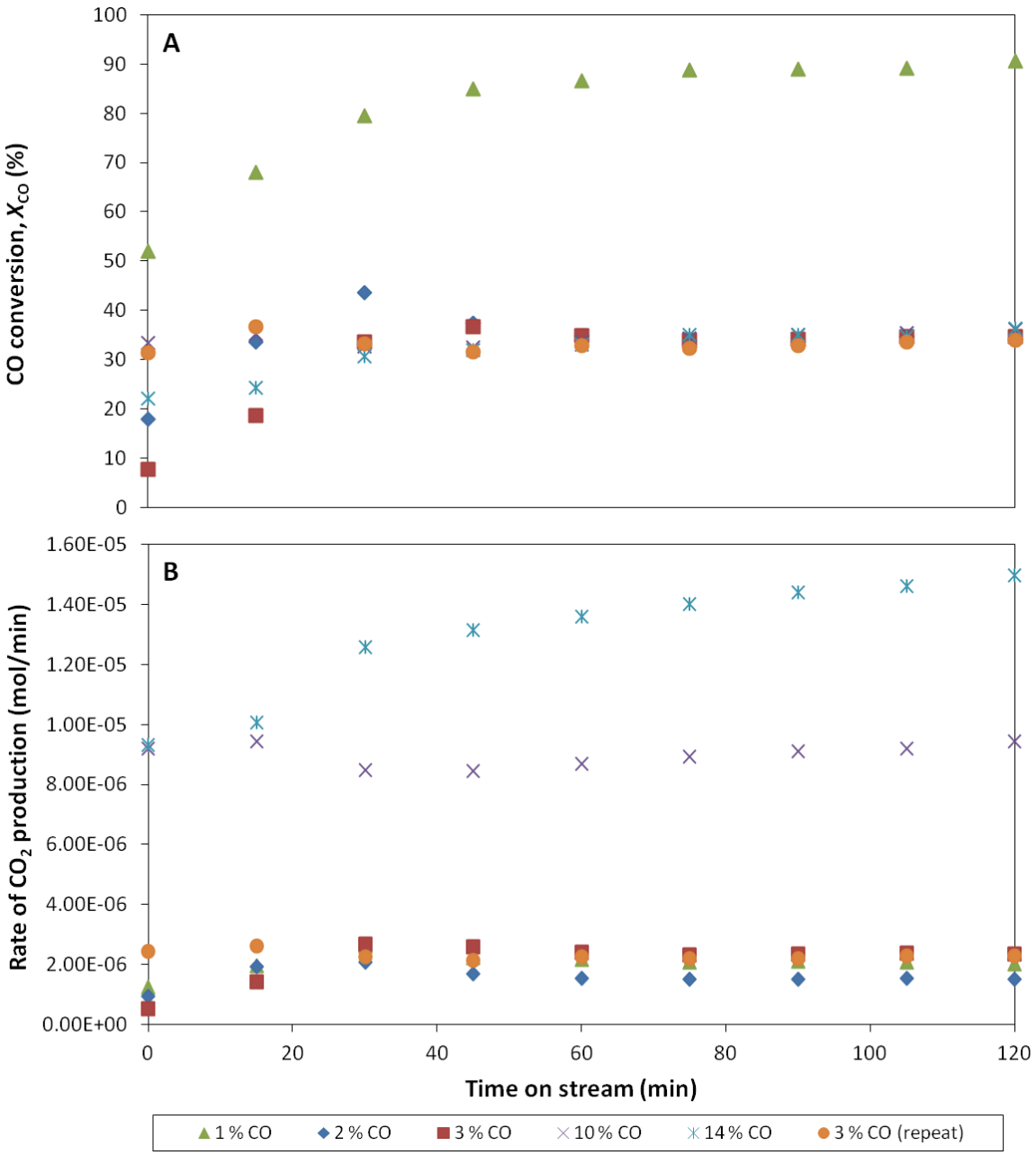

Figure 5.6: CO oxidation kinetics on 1%Cu_6/$MWCNT_{COOH}$ catalyst at various CO concentrations in feed gas: O_2-lean, 400 °C, GHSV = 6,000 mL/(g_{cat}·h). (A) CO conversions; and (B) CO_2 production rates.

The corresponding CO_2 production rates of the CO conversion data in Figure 5.6(A) are presented in Figure 5.6(B). In low CO concentrations in the feed gas of 1 – 3 vol.%, the mole amounts of CO_2 gas production rate appeared to be comparable. As higher CO concentrations were introduced in the feed gas up to 14 vol.%, the mole amounts of CO_2 gas production rate

increased linearly between 3 and 14 vol.% CO. Noteworthy, repeating experiments at 3 vol.% CO show good reproducibility at the steady-state regime later in the catalytic test.

From Figure 5.7, a similar trend of linear increase in the CO_2 production rate was observed when the tests were performed at 440 and 475 °C in the direction of increasing CO concentrations between 3 and 14 vol.%, while other reaction operating parameters were kept constant. The reaction temperature was not increased above 475 °C to allow room for an autogenic catalyst bed temperature rise due to the heat release from the exothermic CO oxidation reaction, which will oxidise (gasify) the MWCNT support at the temperature close to 500 °C. It is interesting to note that at the CO concentration of 3 vol.%, the rate of CO_2 production increased only slightly from 400 to 440 °C, while at the CO concentration of 14 vol.%, the rate of CO_2 production was comparable when the temperature was increased from 440 to 475 °C. The CO conversion (X_{CO}) and CO_2 production as a function of time on stream at 440 and 475 °C can be found in Figure F3, APPENDIX F.

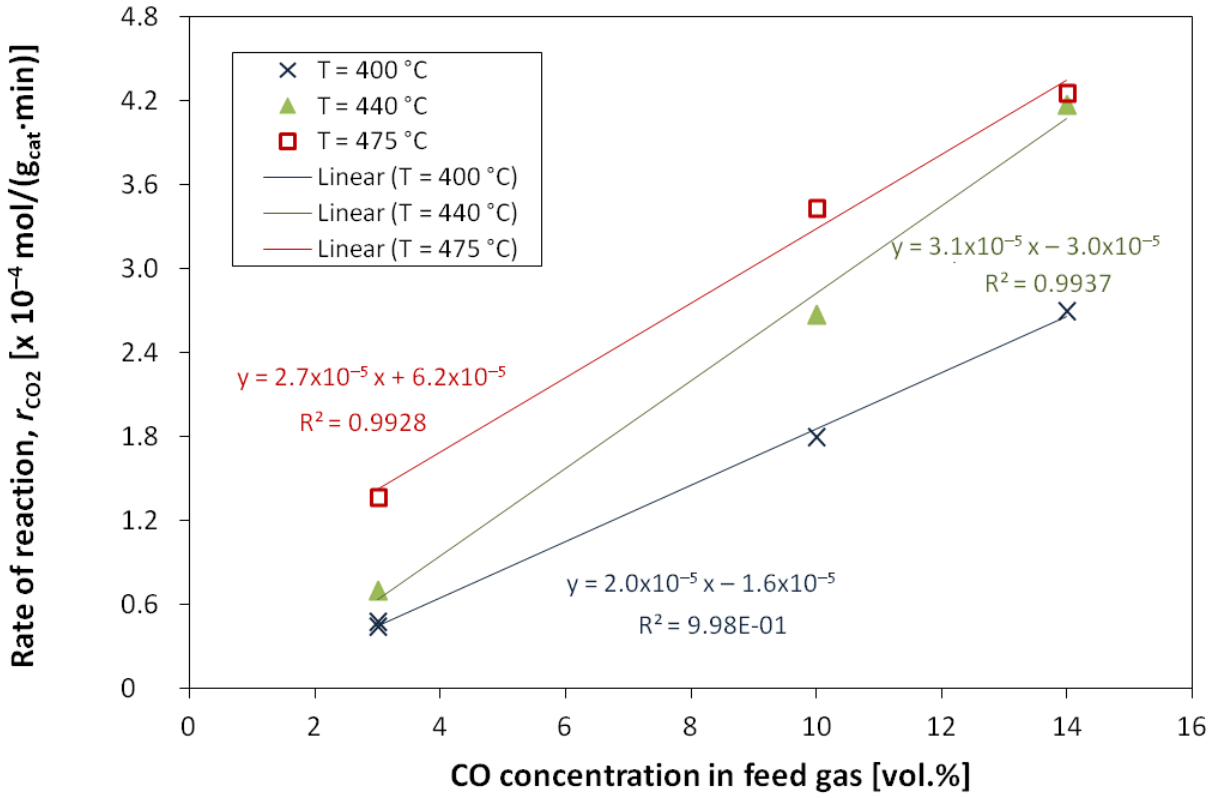

Figure 5.7: Rate of reaction (CO_2 production) as a function of CO concentration in the feed gas and reaction temperature: O_2-lean, GHSV = 6,000 mL/(g_{cat}·h).

For a bimolecular reaction between two adsorbed reactant molecules implied by the L–H mechanism, a general representation of the kinetics of CO oxidation is given by [35] (derivation in APPENDIX F):

$$-r_{CO} = r_{CO_2} = k\frac{K_{CO}K_{O_2}[CO][O_2]}{(1 + K_{CO}[CO] + K_{O_2}[O_2])^2} \quad (5.19)$$

where

[reactant] is concentration of reactant (CO or O_2);

k is reaction rate constant;

$K_{reactant}$ is the equilibrium constant of reactant (CO or O_2) that can be determined by thermodynamic data and is related to the change in the Gibbs free energy.

The order of reaction is half with respect to [CO] and [O_2], with:

$r_{CO2} = f\,(K_{CO}, K_{O2}, [CO], [O_2])$ (determined by experimental measurement)

$K_{reactant} = f\,(T)$ (determined by thermodynamics calculation)

$$\Delta G^{T}_{reactant} = RT \ln K_{reactant} + \Delta G^{0}_{reactant} \qquad (5.20)$$

where

T is reaction temperature (in Kelvin)

R is universal gas constant

$\Delta G^{0}_{reactant}$ is Gibbs free energy change of formation of the reactant component (CO or O_2) at standard temperature and pressure (STP)

$\Delta G^{T}_{reactant}$ is Gibbs free energy change of formation of the reactant component at reaction temperature T and 1 atm, calculated using Gibbs–Helmholtz equation [36-37]:

$$\left[\frac{\partial(G/T)}{\partial T}\right]_P = -\frac{H}{T^2} \qquad (5.21)$$

Solving for eq. (5.21), the $\Delta G^{\mathrm{T}}_{\mathrm{reactant}}$ can be calculated from [36-37]:

$$\frac{\Delta \mathrm{G}^{\mathrm{T}}}{\mathrm{T}} - \frac{\Delta \mathrm{G}^{0}}{298} = \Delta \mathrm{H}^{0} \left(\frac{1}{\mathrm{T}} - \frac{1}{298}\right) \tag{5.22}$$

The reaction rate constant is described by the Arrhenius relationship:

$$k = Ae^{-\frac{E_a}{RT}} \tag{5.23}$$

The following part in RED font is contributed by Isaac Severinsen

The pre-exponential coefficient, A and activation energy, E_a can be determined with non-linear least squares regression against the experimental data (coding in Section F5 of APPENDIX F). The Levenberg-Marquardt algorithm from scipy's optimise package (Part 1.2 of Section F5 in APPENDIX F) was used to determine the parameters. The optimised parameters are A = 10,600 mol/(g_{cat}·min) and E_a = 54.2 kJ/mol.

The fit of these parameters can be seen in a plot of the experimental and modelled rates of reaction as seen in Figure 5.8, where the Arrhenius temperature dependence of the reaction rate constant can clearly be seen. The Shapiro-Wilk test and analysis of a QQ plot showed that the residuals are normally distributed (Part 1.4 and Part 1.5 of Section F5 in APPENDIX F).

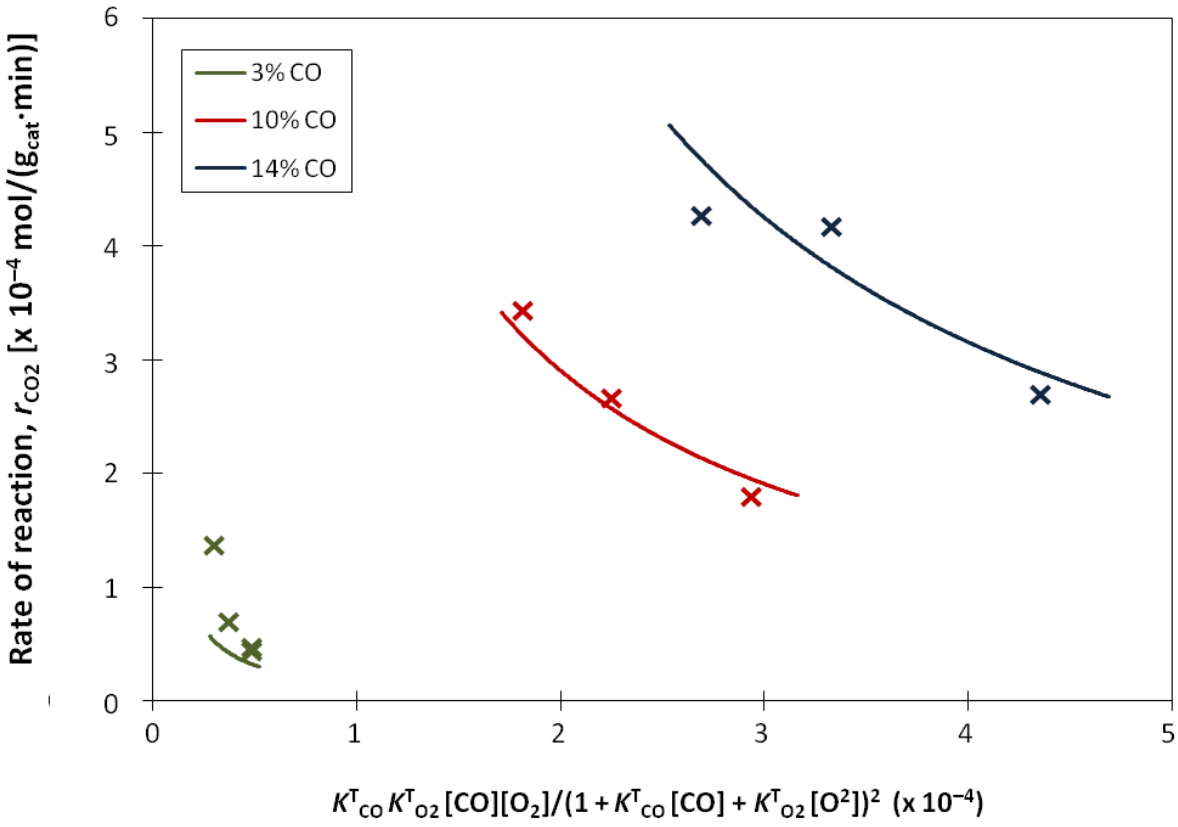

Figure 5.8: Experimental and modelled rates of reaction (CO_2 production): crosses are experimental data, lines are modelled data.

If the relationship between the parameters is assumed to be linearly independent, the 95% confidence interval predicted gave the parameter uncertainties: A = 10,600 ± 29,800 mol/(g_{cat}·min) and E_a = 54.2 ± 16.9 kJ/mol.

This prediction of uncertainty is almost certainly inaccurate as the relationship between the unknown parameters in the Arrhenius relationship (eq. (5.23)) is not independent. By bootstrapping the data and regressing the samples, different parameter estimates can be attained for different subsets of the data. This effectively randomises the weighting on each data point. The result of this is a graphical confidence region as seen in Figure 5.9.

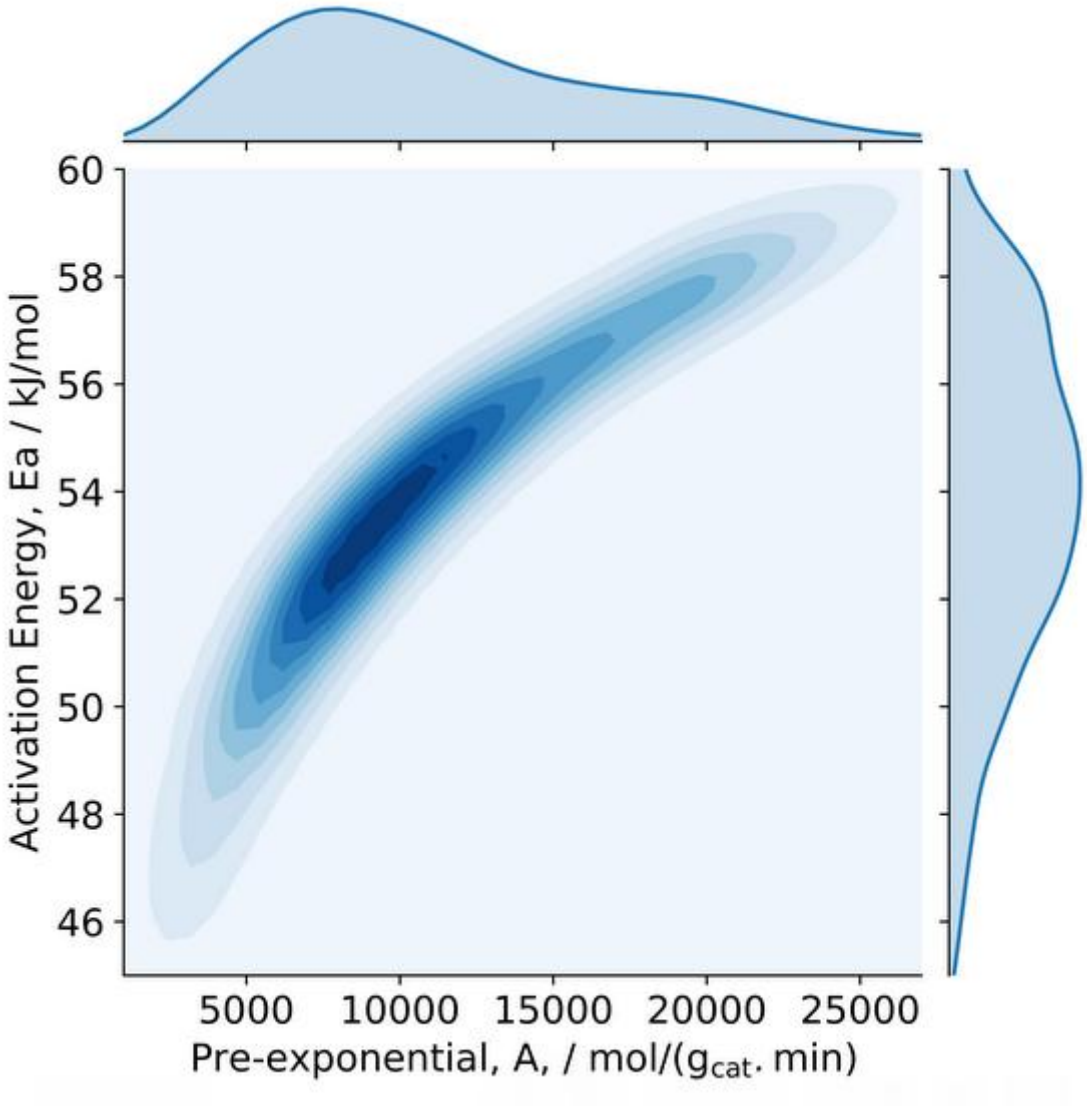

Figure 5.9: Parameter distribution from bootstrapping of experimental data (85.6% of data shown). Note: 10,000 samples were used.

Figure 5.9 shows the range of possible parameter values as predicted by the bootstrapping and the relationship between them. This clearly shows that the activation energy and pre-exponential are intrinsically linked due to the form of the rate constant equation (eq. (5.23)). From this, the reaction rate parameters of CO oxidation on the $Cu_6/MWCNT_{COOH}$ catalyst in the reaction temperature range of 400 – 475 °C are:

E_a = 54.3 (median); Lower bound: 47.3; Upper bound: 64.6 (kJ/mol)

A = 10,700 (median); Lower bound: 3,230; Upper bound: 65,500 [mol/(g_{cat}·min)]

Contribution by Isaac Severinsen ends here

Table 5.1 presents the activation energy for CO oxidation over selected Cu-based catalysts published in the literature. Note that the copper species presented in the first (the most left) column of the table are the initial copper phase (precursor phase) in the as-prepared catalysts prior to their exposure to oxygen in the feed gas in their respective catalytic activity tests. Reference activation energy for the reaction over silica is also presented as a representative material that is active for CO oxidation at the same high reaction temperature range of above 400 °C.

Table 5.1: Activation energy for CO oxidation over different Cu-based catalysts.

Catalyst	**T (°C)**	**E_a (kJ/mol)**	**Ref.**
Cu/MnAgOx	25 – 30	29.9	[38]
Cu/MnOx	20 – 100	57.0	[39]
CuO/CeO_2	20 – 100	51.5	[40]
Cu/MnOx	60 – 110	64.1	[41]
Cu-Pt/Al	125 – 225	5.9	[42]
Cu-Pt/Ce	125 – 225	6.3	[42]
Cu-Pt/CeAl	125 – 225	4.8	[42]
Silica	400 – 560	109.5	[43]
$Cu_6/MWCNT_{COOH}$	400 – 475	54.3	Present work

In general, the $Cu_6/MWCNT_{COOH}$ catalyst demonstrated a low level of catalytic activity in the CO oxidation reaction in comparison to other Cu-based catalysts published in existing literature where the former required comparable activation energy to initiate the reaction but at a much higher temperature needed to decompose Cu carbonate species formed.

5.4 Conclusions

In Chapter 4, it had been demonstrated that the $Cu_6/MWCNT_{COOH}$ had low catalytic activity in CO oxidation at temperatures below 330 °C due to: (i) the carboxyl-functionalised MWCNT only adsorbed the CO molecules without converting them; and (ii) the formation of $CuCO_3$. However, regeneration was possible by decomposing the $CuCO_3$ at temperatures of approximately 400 °C, releasing the CO_2 gas product. Therefore, the minimum working temperature of the $Cu_6/MWCNT_{COOH}$ catalyst in CO oxidation is 400 °C.

While the reaction over the $Cu_6/MWCNT_{COOH}$ catalyst was constrained by the catalyst deactivation by $CuCO_3$ formation in the lower temperature limit, the upper boundary is limited by the combustion of the MWCNT support in the oxidative environment starting from approximately below 500 °C. The maximum feasible reaction operating temperature should be capped at 475 °C to avoid autogenic catalyst bed temperature rise due to exothermic CO oxidation. Excessive amount of O_2 was demonstrated to poison the active sites of $Cu_6/MWCNT_{COOH}$. Within the temperature range of 400 – 475 °C, the activation energy for the CO oxidation reaction over the $Cu_6/MWCNT_{COOH}$ catalyst was 54.3 kJ/mol in CO concentrations of up to 14 vol.% in the feed gas mixture, assuming the reaction followed the L–H mechanism.

The present study was related to our earlier work (Chapter 3 [18]) on hypothetical catalytic activity prediction in LTWGS reaction by active site characterisation analysis using CO-TPD. In the industry, the LTWGS reaction takes place on a copper-based catalyst bed that is typically operated at temperatures of 190 – 250 °C. Our previous prediction by interpretation of the CO-TPD profiles suggested that the catalytic activities of the $Cu_6/MWCNT_{COOH}$ catalyst in the LTWGS reaction were expected to be optimal in the operating temperature range of between 120 and 200 °C. In LTWGS reaction, CO molecules scavenge the surface-adsorbed oxygen produced by water dissociation on the active site in the same manner they react with the surface-adsorbed oxygen atoms O* that are produced from the dissociation of O_2 gas molecules in CO oxidation, to produce adsorbed CO_2* product. At below 330 °C, the Cu_6 complex species, which changed its phase to Cu_2O upon exposure to air, formed $CuCO_3$

via a chemical interaction with the adsorbed CO_2* product, in the presence of unreacted oxygen gas in the CO oxidation environment. The formation of $CuCO_3$ was experimentally demonstrated to inhibit the CO oxidation reaction. However, unlike in the CO oxidation reaction environment, oxygen gas is not present in the LTWGS reaction environment. Therefore, unless oxygen gas is present in a quantity significant enough to react with the Cu_2O species and the adsorbed CO_2* product, the formation of $CuCO_3$ at low temperatures should not occur in the LTWGS reaction environment. The LTWGS reaction should therefore not require an operating temperature of as high as 400 °C for an effective reaction over the Cu_6-based catalysts to avoid the $CuCO_3$ formation as in the case of the CO oxidation.

Literature findings have claimed promising catalytic activity of copper nanoclusters based on single-crystal clusters probed by single reactant-molecule gas. Whilst showing potentials in the catalysis applications, such studies of the reactivity for chemisorption of the single-reactant molecule gas such as CO, O_2, CO_2 or H_2O individually on the (unsupported) copper clusters by measuring copper–gas molecule bond strengths do not necessarily accurately represent the potential catalytic activity of the copper clusters in an actual gas-phase reaction, as demonstrated in this doctoral work. This doctoral study experimentally demonstrated the limitations of the supported copper clusters in a selected gas-phase heterogeneous catalysis application; the CO oxidation reaction.

Acknowledgement

The authors acknowledge the financial support of John Sutherland's Fund, Department of Chemical and Process Engineering, University of Canterbury, Christchurch, New Zealand.

References of Chapter 5

1. Padilla-Campos, L., *Theoretical investigation of the adsorption of oxygen on small copper clusters.* Journal of Molecular Structure: THEOCHEM, 2007. **815**(1-3): p. 63-69.
2. Padilla-Campos, L., *Theoretical study of the adsorption of carbon monoxide on small copper clusters.* Journal of Molecular Structure: THEOCHEM, 2008. **851**(1-3): p. 15-21.
3. Eberhardt, W., *Clusters as new materials.* Surface Science, 2002. **500**(1-3): p. 242-270.
4. Kung, H.H. and M.C. Kung, *Nanotechnology: applications and potentials for heterogeneous catalysis.* Catalysis Today, 2004. **97**(4): p. 219-224.
5. Yang, F., et al., *Autocatalytic reduction of a Cu2O/Cu (111) surface by CO: sTM, XPS, and DFT studies.* The Journal of Physical Chemistry C, 2010. **114**(40): p. 17042-17050.
6. Mendes, D., et al., *Determination of the Low-Temperature Water− Gas Shift Reaction Kinetics Using a Cu-Based Catalyst.* Industrial & Engineering Chemistry Research, 2010. **49**(22): p. 11269-11279.
7. Oliveira, N.M., G.P. Valençaa, and R. Vieirab, *Water Gas Shift Reaction On Copper Catalysts Supported On Alumina And Carbon Nanofibers.* Chemical Engineering, 2015. **43**.
8. Luengnaruemitchai, A., S. Osuwan, and E. Gulari, *Comparative studies of low-temperature water–gas shift reaction over Pt/CeO2, Au/CeO2, and Au/Fe2O3 catalysts.* Catalysis Communications, 2003. **4**(5): p. 215-221.
9. Demirel, E. and N. Azcan. *Thermodynamic modeling of water-gas shift reaction in supercritical water*. in *Proceedings of the World Congress on Engineering and Computer Science 2012*. 2012.
10. Schumacher, N., et al., *Trends in low-temperature water–gas shift reactivity on transition metals.* Journal of Catalysis, 2005. **229**(2): p. 265-275.
11. Smith, R., M. Loganathan, and M.S. Shantha, *A review of the water gas shift reaction kinetics.* International Journal of Chemical Reactor Engineering, 2010. **8**(1).

12. Wagman, D.D., et al., *Heats, free energies, and equilibrium constants of some reactions involving O2, H2, H2O, C, CO, CO2, and CH4.* J. Res. Natl. Bur. Stand, 1945. **34**(2): p. 143-201.
13. Grönbeck, H. and A. Rosén, *CHEMISORPTION OF O 2 AND CO ON COPPER CLUSTERS.* Surface Review and Letters, 1996. **3**(01): p. 687-693.
14. Cox, D., et al., *CO chemisorption on free gas phase metal clusters.* The Journal of chemical physics, 1988. **88**(1): p. 111-119.
15. Nygren, M.A. and P.E. Siegbahn, *Theoretical study of chemisorption of carbon monoxide on copper clusters.* The Journal of Physical Chemistry, 1992. **96**(19): p. 7579-7584.
16. Ribarsky, M., W. Luedtke, and U. Landman, *Molecular-orbital-self-consistent-field cluster model of H 2 O adsorption on copper.* Physical Review B, 1985. **32**(2): p. 1430.
17. Chen, L., et al., *A first principles study of water dissociation on small copper clusters.* Physical Chemistry Chemical Physics, 2010. **12**(33): p. 9845-9851.
18. Baharudin, L., et al., *CO temperature-programmed desorption of a hexameric copper hydride nanocluster catalyst supported on functionalized MWCNTs for active site characterization in a low-temperature water–gas shift reaction.* Chemical Engineering Journal, 2018b. **In Press, Corrected Proof**.
19. Ratnasamy, C. and J.P. Wagner, *Water gas shift catalysis.* Catalysis Reviews, 2009. **51**(3): p. 325-440.
20. Matsushima, T. and J. White, *On the mechanism and kinetics of the CO-oxidation reaction on polycrystalline palladium: I. The reaction paths.* Journal of Catalysis, 1975. **39**(2): p. 265-276.
21. Domagala, M.E. and C.T. Campbell, *The mechanism of CO oxidation over Cu (110): effect of CO gas energy.* Catalysis Letters, 1991. **9**(1-2): p. 65-70.
22. Jernigan, G. and G.A. Somorjai, *Carbon monoxide oxidation over three different oxidation states of copper: metallic copper, copper (I) oxide, and copper (II) oxide-a surface science and kinetic study.* Journal of Catalysis, 1994. **147**(2): p. 567-577.
23. Szanyi, J. and D.W. Goodman, *CO oxidation on a Cu (100) catalyst.* Catalysis letters, 1993. **21**(1-2): p. 165-174.
24. Prasad, R. and P. Singh, *A review on CO oxidation over copper chromite catalyst.* Catalysis Reviews, 2012. **54**(2): p. 224-279.

25. Liu, W. and M. Flytzanistephanopoulos, *Total oxidation of carbon monoxide and methane over transition metal fluorite oxide composite catalysts: I. Catalyst composition and activity.* Journal of Catalysis, 1995. **153**(2): p. 304-316.
26. Huang, T.-J. and D.-H. Tsai, *CO oxidation behavior of copper and copper oxides.* Catalysis Letters, 2003. **87**(3-4): p. 173-178.
27. Brown, I., K. Mackenzie, and G. Gainsford, *Thermal decomposition of the basic copper carbonates malachite and azurite.* Thermochimica acta, 1984. **75**(1-2): p. 23-32.
28. Henmi, H., et al., *Thermal decomposition of basic copper carbonate, CuCO3· Cu (OH) 2· H2O, in carbon dioxide atmosphere (0–50 atm).* Thermochimica acta, 1985. **96**(1): p. 145-153.
29. Albert, C.F., et al., *Lewis-base adducts of Group 11 metal (I) compounds. 49. Structural characterization of hexameric and pentameric (triphenylphosphine) copper (I) hydrides.* Inorganic Chemistry, 1989. **28**(7): p. 1300-1306.
30. Cook, A.W., et al., *Synthesis, Characterization, and Reactivity of the Group 11 Hydrido Clusters [Ag6H4 (dppm) 4 (OAc) 2] and [Cu3H (dppm) 3 (OAc) 2]*. Inorganic chemistry, 2016.
31. Maniecki, T., P. Mierczyński, and W. Jóźwiak, *Copper-supported catalysts in methanol synthesis and water gas shift reaction.* Kinetics and Catalysis, 2010. **51**(6): p. 843-848.
32. Rakić, V. and L. Damjanović, *Temperature-Programmed Desorption (TPD) Methods*, in *Calorimetry and Thermal Methods in Catalysis*. 2013, Springer. p. 131-174.
33. Sadykov, V. and S. Tikhov, *Comment on "Carbon Monoxide Oxidation over Three Different Oxidation States of Copper: Metallic Copper, Copper (I) Oxide, and Copper (II) Oxide—A Surface Science and Kinetic Study" by GG Jernigan and GA Somorjai.* Journal of Catalysis, 1997. **165**(2): p. 279-283.
34. Nagase, K., et al., *Dynamic study of the oxidation state of copper in the course of carbon monoxide oxidation over powdered CuO and Cu2O.* Journal of Catalysis, 1999. **187**(1): p. 123-130.
35. Laidler, K.J. and J.H. Meiser, *Physical chemistry*. 1982, Menlo Park, California: Benjamin/Cummings Pub. Co.
36. Roósz, B., C. Visy, and I. Nagypál, *On the derivation of the Gibbs–Helmholtz equation.* ChemTexts, 2016. **2**(2): p. 1-3.
37. Keszei, E., *Gibbs–Helmholtz equation and entropy.* ChemTexts, 2016. **2**(4): p. 15.

38. Dey, S., et al., *Kinetics of catalytic oxidation of carbon monoxide over CuMnAgOx catalyst.* Materials Discovery, 2017. **8**: p. 18-25.
39. Xia, G., et al., *Efficient stable catalysts for low temperature carbon monoxide oxidation.* Journal of Catalysis, 1999. **185**(1): p. 91-105.
40. Ayastuy, J.L., et al., *Kinetics of carbon monoxide oxidation over CuO supported on nanosized CeO2.* Industrial & Engineering Chemistry Research, 2009. **48**(12): p. 5633-5641.
41. Li, M., et al., *Kinetics of catalytic oxidation of CO over copper-manganese oxide catalyst.* Separation and Purification Technology, 2007. **57**(1): p. 147-151.
42. Loc, L.C., et al., *Kinetics of CO Oxidation over Pt-Modified CuO Nanocatalysts.* Materials Transactions, 2015. **56**(9): p. 1403-1407.
43. McCormick, R.L., M.B. Al-Sahali, and G.O. Alptekin, *Partial oxidation of methane, methanol, formaldehyde, and carbon monoxide over silica: global reaction kinetics.* Applied Catalysis A: General, 2002. **226**(1-2): p. 129-138.

CHAPTER 6

Conclusions

In summary, the underlying basis of the idea to fabricate a catalytic composite made of active metal nanostructures supported on carbon nanomaterials grown on metal monolithic structures was formed.

Based on comparative analysis using information available in the literature, metals were proposed as a substrate of choice for fabricating the monolithic support in a structured steam reforming reactor due to their mechanical strength, good thermal conductivity and equivalent coefficient of thermal expansion (CTE) with the reformer tube material, in contrast to ceramics analogues. However, decent anchoring of the conventional inorganic oxide washcoating material as a textural promoter on the metal monolith is a great challenge due to relatively low surface area and porosity of the metal surface. A poor adhesion is a threat during thermal cycles due to the incompatibility of the CTE of the two materials as it could lead to a cracking of the washcoat layer and subsequent loosening and spalling of the catalytic metals/metal oxides. Growth of a filamentous carbon layer was proposed as a substitute textural promoter in overcoming the adhesion issue. Multi-walled carbon nanotubes (MWCNT) have negligible CTE values. In spite of the CTE difference between the monolith substrate material and MWCNT, the length scale at the adhesion point of the MWCNT on the metal is so small that it is hypothesised that the CTE mismatch does not lead to massive stresses, and hence, the filamentous textural promoter layer is predicted to continue to strongly adhere on the monolith's structure regardless of the thermal cycles.

The carbon nanomaterials offer sufficient surface area for hosting the active metal particles, as well as high porosity and low tortuosity that enhance the internal mass transfer of the reactant molecules at the interface of the graphitic wall and the active metal particles. The active particles can be dispersed well on the surface of the carbon nanomaterials for an effective diffusion of the reactant and product molecules to and from the active site, which subsequently enhances the catalytic activity in many heterogeneous reactions. Clean

MWCNT of high crystallinity with well aligned vertical and parallel walls are expected to not only possess the aforementioned surface textural properties that increase the structure's external surface area but are also predicted to possess a high thermal conductivity. The work in this thesis explored the use of MWCNT as the textural promoter.

The main objective of this thesis is to formulate and introduce a novel MWCNT-supported catalyst that demonstrates a reasonably good level of catalytic activity in a gas-phase heterogeneous reaction model of interest. A family of novel catalysts were fabricated using chemically synthesised, atomically precise hexameric copper hydride nanoclusters (Cu_6) deposited on carboxyl (–COOH)-pre-functionalised MWCNT ($MWCNT_{COOH}$); $Cu_6/MWCNT_{COOH}$ by wet impregnation with varying copper loading contents of 0.5 – 15 wt.% for a kinetic investigation in reactions that involve CO conversion. The synthesised catalysts were benchmarked against a reference commercial catalyst, 51%CuO/31%ZnO-Al_2O_3. The catalytic performance was also analysed as a function of support type: $MWCNT_{COOH}$ *cf.* non-functionalised MWCNTs and alumina with fixed Cu loading of 1 wt.%, which was identified based on the highest Cu surface area per sample weight and the amount of CO adsorbed per sample weight. A comparison was also made with a $MWCNT_{COOH}$-supported sample containing Cu nanoparticles (Cu_{NP}) precursor, which was not covered by any surfactants or capping agents.

The crystal structure of the synthesised Cu_6 nanoclusters was solved by single-crystal X-ray diffraction (SCXRD) at 120 K where an empirical formula of $Cu_6P_6C_{111}H_{102}O_{0.75}$ was determined. The complex, made of hexameric copper hydride $[(CuH)_6]$ ligated by triphenylphosphine (PPh_3) and solvated with 0.75 mole of tetrahydrofuran ($(CH_2)_4O$ = THF) molecule, $[(PPh_3)CuH]_6.0.75THF$ was registered with the Cambridge Crystallographic Data Centre (CCDC) and assigned a number, CCDC 1864974. The simulated powder X-ray diffraction (PXRD) of the crystal structure generated from SCXRD was experimentally validated by an actual PXRD of the ground crystal powder at room temperature. The Cu_6 clusters were used as a precursor to decorate the supports with well-defined Cu active site. Prolonged exposure of the as-prepared samples to air resulted in oxidation of clusters and formation of oxide nanoparticles at room temperature, where facets of Cu_2O crystal (1 1 0),

(1 1 1), (2 0 0) and (2 2 0) were identified to be the active phase of the synthesised catalysts in the phase composition analysis based on their PXRD patterns.

In comparison to the reference commercial catalyst, the structural characterisation of the fabricated materials by CO chemisorption at 50 °C revealed a smaller copper species' crystallite size of below 4 nm and an improved active copper dispersion. The optimal catalyst synthesised in this work, 1%Cu_6/$MWCNT_{COOH}$ (as-prepared, heat pre-treated at 100 °C) showed a copper crystallite size and dispersion of 3.0 nm and 35.5%, in comparison to 235.6 nm and 0.4% for the reference commercial catalyst (as-received, heat pre-treated at 100 °C). The trend of an increasing copper crystallite size and reduced copper dispersion in the direction of the increasing copper loading content was observed. In addition, the copper crystallite size increased, and the copper dispersion decreased in the direction of increasing pre-treatment temperature at a fixed duration, and with an increasing pre-treatment duration at any given constant temperature. The crystallite size of Cu_2O species supported on alumina was more than double the size of its counterparts supported on MWCNTs, which could be explained by the difference in specific surface area (SSA) of the three support materials, where the value was two orders of magnitude higher for MWCNTs than for alumina. The dispersion of the Cu_2O species was halved in alumina indicating relatively less effective interaction between the Cu_6 nanoclusters and the alumina support. Equivalent values of crystallite size and dispersion of active copper species were measured in the 1%Cu_{NP}/$MWCNT_{COOH}$ catalyst in comparison to the 1%Cu_6/$MWCNT_{COOH}$ catalyst but the interaction of CO molecules with the active sites of these two materials analysed by CO temperature-programmed desorption (CO-TPD) technique showed different behaviours.

The active site characterisation based on the CO-TPD profiles of the synthesised materials was elucidated by the Langmuir–Hinshelwood (L–H) mechanism for low-temperature water–gas shift (LTWGS) reaction to predict the potential catalytic performance of the synthesised catalysts in the LTWGS as the reaction model under study. The CO-TPD technique supplied an indication of the operating conditions in which the catalyst activity may be at its highest potential and the possible conditions in which deactivation might occur. Hence, an optimal operating condition for a maximum CO conversion allowed by thermodynamics in the equilibrium-limited LTWGS reaction could hypothetically be determined. In general, the

lower operating temperature limit was imposed by the water dew point, while the upper limit was constrained by the temperature rise from the reaction exotherm that could lead to irreversible Cu sintering. It was expected that the optimal catalyst, $1\%Cu_6/MWCNT_{COOH}$, should be active for the LTWGS reaction within a range of temperatures as low as 120 °C (limited by water dew point), but should be capped at around 190 °C, which is below the typical LTWGS operating temperatures to avoid deactivation by Cu sintering. In the case of other catalysts, their feasible operating temperature range would change with the loading of the active Cu species.

The actual activity of the fabricated materials in a reaction that involves CO conversion was experimentally measured in a kinetic investigation of CO oxidation as the reaction model of interest for the purpose of validating the hypothetical catalytic activity of the materials predicted by CO-TPD. In LTWGS reaction, CO molecules scavenge the surface-adsorbed hydroxyl or oxygen produced by water dissociation on the active site in the same manner they react with the surface-adsorbed oxygen atoms that are produced from the dissociation of O_2 gas molecules in CO oxidation. Therefore, the study of oxidation of CO over the copper-based catalysts is imperative in understanding the LTWGS reaction over the same catalysts.

In the actual experimental measurements, it was discovered that the carboxyl (–COOH) functional groups and the Cu_6 nanocluster complex inhibited the CO oxidation reaction. Whilst the bare pristine MWCNT by itself was catalytically active for CO oxidation from approximately 150 °C and a CO conversion of greater than 98% was achieved from 230 °C, the carboxyl-modified MWCNT on the other hand adsorbed significant quantities of CO molecules without further catalytic converting under the same reaction conditions. The carboxyl groups degraded thermally progressively from approximately 250 °C. The adsorption effect hindered the CO oxidation even in the presence of dispersed copper nanoparticles (Cu_{NP}) that can improve the kinetics of the reaction. This was evidenced by the performance of the catalyst fabricated from a typical Cu_{NP} precursor supported on carboxyl-modified MWCNT, which was demonstrated to be active from approximately 190 °C and approached a full CO conversion at slightly below 330 °C.

On the other hand, the Cu_2O species derived from the Cu_6 precursor was demonstrated to have formed $CuCO_3$ under the reaction conditions *via* a chemical interaction with the CO_2* product adsorbed on the active site (in the presence of unreacted oxygen) and hence, deactivating the catalytic activity of the MWCNT material when tested below 330 °C. The CO oxidation reaction was inhibited from further progressing as the CO_2 desorption elementary step in the reaction mechanism was halted when the reaction temperature was kept constant. The $CuCO_3$ thermally decomposed effectively at 400 °C, releasing the CO_2 product. A minimum working temperature of 400 °C was therefore required to operate the Cu_6-based catalysts.

With the effective reaction temperature of ≥ 400 °C, the kinetics of the CO oxidation reaction over the $Cu_6/MWCNT_{COOH}$ catalyst was studied in a high reaction temperature range of 400 – 475 °C. The reaction temperature range over the $Cu_6/MWCNT_{COOH}$ catalyst was constrained by the $CuCO_3$ formation in the lower limit, and the upper boundary was limited by the combustion (gasification) of the MWCNT support in the oxidative environment, which occurred from approximately below 500 °C. The maximum feasible reaction operating temperature was capped at 475 °C to avoid autogenic catalyst bed temperature rise due to exothermic CO oxidation.

It was demonstrated that an excessive amount of O_2 poisoned the $Cu_6/MWCNT_{COOH}$ catalysts by blocking the access of the CO molecules to the active sites (maximum CO conversion = ~29% in O_2-rich environment ($CO:O_2$ = 1:10 v/v), ~89% in O_2-lean ($CO:O_2$ = 1:1.2 v/v)) at gas hourly space velocity (GHSV) of 3,000 – 6,000 mL/(g_{cat}.h)). The kinetic model of the CO oxidation reaction on the $1\%Cu_6/MWCNT_{COOH}$ catalyst was developed based on the assumptions that the reaction was CO-adsorption limited and followed the Langmuir–Hinshelwood mechanism. In CO concentrations of ≤ 14 vol.% in the feed gas mixture, the order of reaction was 0.5 with respect to CO and 0.5 with respect to O_2. The activation energy for the reaction, E_a = 54.3 kJ/mol in the reaction temperature range studied. In general, the $Cu_6/MWCNT_{COOH}$ catalyst demonstrated a low level of catalytic activity in the CO oxidation reaction in comparison to other Cu-based catalysts published in existing literature where the former required comparable activation energy to initiate the reaction but at a much higher temperature needed to decompose the Cu carbonate species formed.

In the industry, the LTWGS reaction takes place on a copper-based catalyst bed that is typically operated at temperatures of 190 – 250 °C. Our earlier prediction by interpretation of the CO-TPD profiles suggested that the catalytic activities of the $Cu_6/MWCNT_{COOH}$ catalyst in the LTWGS reaction were expected to be optimal in the operating temperature range of between 120 and 200 °C. At below 330 °C, the Cu_6 complex species, which changed its phase to Cu_2O upon exposure to air, formed $CuCO_3$ *via* a chemical interaction with the adsorbed CO_2* product, in the presence of unreacted oxygen gas in the CO oxidation environment. The formation of $CuCO_3$ was experimentally demonstrated to inhibit the CO oxidation reaction. However, unlike in the CO oxidation reaction environment, oxygen gas is not present in the LTWGS reaction environment. Therefore, unless oxygen gas is present in a quantity significant enough to react with the Cu_2O species and the adsorbed CO_2* product, the formation of $CuCO_3$ at low temperatures should not occur in the LTWGS reaction environment. The LTWGS reaction should therefore not require an operating temperature of as high as 400 °C for an effective reaction over the Cu_6-based catalysts to avoid the $CuCO_3$ formation as in the case of the CO oxidation.

Literature findings have claimed promising catalytic activity of copper nanoclusters based on single-crystal clusters probed by single reactant-molecule gas. Whilst showing potentials in the catalysis applications, such studies of the reactivity for chemisorption of the single-reactant molecule gas such as CO, O_2, CO_2 or H_2O individually on the (unsupported) copper clusters by measuring copper–gas molecule bond strengths do not necessarily accurately represent the potential catalytic activity of the copper clusters in an actual gas-phase reaction, as demonstrated in this doctoral work. This doctoral study experimentally demonstrated the limitations of the supported copper clusters in a selected gas-phase heterogeneous catalysis application; the CO oxidation reaction.

Nonetheless, in this thesis, a satisfactory performance of a reactant conversion in a gas-phase heterogeneous reaction over carbon nanomaterials-supported catalysts has successfully been demonstrated. This achievement will lead to the realisation of the idea of fabricating a catalyst made of active metal nanostructure deposited on carbon nanomaterials grown on a metal monolith for a kinetic study in an energy-intensive reaction, which is expected to

exhibit an improvement in the reactant conversion and reduction of the reactor exit temperature.

CHAPTER 7

Future Work Recommendations

Summary

In this work, as demonstrated in the **Catalytic Assessment and Feasibility stage**, a criterion towards qualifying the application of carbon nanomaterials (CNM) as a textural promoter that provides a means of having satisfactory catalytic activity as an alternative to the conventional inert inorganic oxide support, has been fulfilled.

To complete the feasibility study of the novel copper-cluster catalyst supported on functionalised multi-walled carbon nanotubes (MWCNT) developed in this doctoral work, the future work could include running the CO oxidation reaction over the catalyst under the same reaction conditions studied in this doctoral work but in a prolonged duration long enough to observe the effect of catalyst deactivation as a result of thermal sintering of the active copper species. Further analysis on the spent catalyst using CO pulse chemisorption will be able to provide information on the sintering behaviour of the copper species, in understanding its stability and predicting its lifetime. In addition, the reaction duration should also be significantly prolonged to acquire the information on the catalyst lifetime before the MWCNT supports are gasified. By having its stability information, a more detailed CO oxidation kinetic study can be undertaken to develop its reaction rate expression and determine its apparent activation energy that provide more holistic kinetic information on this novel catalyst.

In the big picture, the findings in this doctoral work would lead towards realisation of developing catalytic metal monolithic structures using CNM grown on the surface of the metal monoliths as a textural promoter, with metal nanostructures doped on the CNM.

Towards qualifying the novelty of the proposed catalyst system for its potential application in steam reforming, the proposed future work will include a demonstration of experimental investigations on the catalytic potential of this approach towards extending the surface area of additively manufactured metal alloy monolithic supports. This will be followed by the feasibility study of using this approach to Ni-based catalysts for steam reforming.

The main thrust of this research work as mentioned in Section 1.4 of Chapter 1 has the near-term aims of: (i) synthesising the growth of CNM on a metal monolith structure; (ii) depositing well dispersed active nickel nanostructures on the surface of the CNM; and (iii) demonstrating an employment of this novel composite catalyst system in a kinetic investigation of steam methane reforming (SMR). The plan for the future work to meet the near-term goals above can be developed based on a **Conceptual Framework** as below, broken down into three segmented bodies, each with their own specific objectives:

1) The first part has the objective of demonstrating the synthesis of the growth of MWCNT on structures made of metal substrates by adopting the various techniques presented in Section 2.2 of Chapter 2 [1]. The filamentous layer will be demonstrated to exhibit reasonably strong adhesion and thermodynamic (thermal and chemical) stability.
2) The second part has an objective of synthesising well dispersed catalytically active nickel nanostructures on the surface of MWCNT grown on metal monoliths for utilisation in SMR.
3) The third part will demonstrate the application of the overall active metal nanostructure/carbon nanomaterials/metal monolith composite as a catalyst, by experimental measurements of its catalytic activity in the SMR reaction.

7.1 Carbon nanomaterials growth on structured support

As concluded in Chapter 2 [1], for an application in SMR, the aim for the growth of carbon nanomaterials layer on a geometrically complex metal monolithic structure in the future work would be of the following characteristics; MWCNT of highly crystallised and graphitic sheets with growth mix of straight vertical, parallel alignment, and in random and changing directions that produce a highly interweaving structure. These characteristics offer high

thermal conductivity that improves the conductive heat transfer, as well as high porosity and low tortuosity that enhance the diffusion of the process gas, for an improved overall reaction performance. The carbon nanotubes (CNT) growing in multiple directions produce highly interweaving structures resulting in a stronger carbon aggregate formation, which introduces a greater mechanical strength of the overall composite [2], vital for their sustainability in the harsh physical and chemical conditions of energy intensive heterogeneous reactions. Therefore, finding a balance between having high thermal conductivity (by having vertically aligned and parallel walls) and good mechanical strength (by growing nanotubes in changing directions that produce interweaving structures), is crucial.

An overview of the synthesis techniques to grow the CNM has been covered by Ruiz-Cornejo Juan *et al.* (2019) [3]. An analysis of the properties of the carbon nanomaterials that suit the steam reforming operation, which include their surface textural properties; thermodynamic stability; mechanical properties; thermal conductivity; and surface chemistry properties, has been presented in Section 2.3 of Chapter 2 [1].

Whilst the final target would be to produce the filamentous layer of the structure mentioned above, the challenge in controlling the resulting growth is real due to the peculiar behaviour of the interaction between the carbon precursor (e.g. type of carbon-containing gas, concentration) and the metal particle used to catalyse the carbon filament growth (e.g. type of metal, crystallite size, metal precursor), which varies with the growth conditions [4-7]. Therefore, there are no specific formulas that are fully understood in aiming for a certain structural carbon crystallinity and morphology of interest. In future work, the aim will be to reproduce the desired graphitic carbon structure based on the techniques reported in the literature [4, 8-19], with some modifications to the techniques adopted. Bearing this in mind, the growth of the carbon nanomaterials on the structured substrate will be investigated in terms of their adhesion, morphology and degree of crystallinity.

The heat transfer performance of a material depends on the contact surface area and thermal conductivity of the material used. Based on the comparison between a honeycomb monolith and a foam structure presented in Baharudin & Watson (2017b) [20], the temperature control

for product selectivity is difficult in the honeycomb monolith as radial mixing is not possible due to the segregated flow in its parallel channels. On the other hand, the radial mixing is possible in the open-celled foam structure and hence, reduces the temperature gradients in its radial and axial directions due to the continuous thermally-connected structure of the foam. As a result, the radial heat transfer is further enhanced and the possibility of hot spots is curtailed in the foam structure. In addition, the foam structure possesses open and accessible pores with an interconnecting porosity that provides the surface for the catalytic components' loading. The interaction between the reactants and the catalysts coated on the foam struts is thus enhanced by the high surface area per unit volume of the structure [21-23].

Based on the above justifications, monolithic structures made of metal substrates of an uneven surface and geometries will be used as the structured substrate in the future work of this research. In addition, triply periodic minimal surface structures, also known as gyroids, show promise in many chemical engineering applications and will be explored. Additive manufacturing, commonly known as 3-dimensional printing (3DP), for a rapid fabrication of geometrically complex monolithic structure [24] helps expedite the prototyping of the structure and complement the research theme led by Associate Professor Matthew Watson through his supervision of another doctoral researcher, Michelle Kramer (Kramer). In the future work, the CNM will be grown on the surface of 3DP-fabricated complex metal structures to further increase the specific surface area so that the mass transfer rate in the catalytic reaction can be maximised.

The selection of the geometrically complex metal structures will be based on their possession of high porosity, large specific surface area, good thermal conductivity and coefficient of thermal expansion (CTE) that matches closely with that of a typical reformer tube. In addition, the selected geometrically complex metal structures must also possess mechanical properties of acceptable Weibull modulus and tensile strength to assure their sustainability in the high temperature gradient in the reforming reaction environment, and more importantly, assuring the ability to withstand the stresses associated with start-ups and shut downs (which are alleviated by having a reasonable CTE match when compared to ceramic based structures). The selection will be done based on the outcome of the work by Kramer.

After the growth of the desired MWCNT structure on a metal monolith has successfully been demonstrated, its adhesion quality needs to be tested as well as its thermal and chemical stability under the steam reforming operating conditions. Then, thorough study on the overall composite's physical properties; thermal conductivity, pressure drop and mechanical strength in comparison to the conventional packed bed of pelletised catalysts system need to be undertaken.

7.1.1 Adhesion quality test

There is a need to investigate the adhesion quality of the carbon nanomaterials grown on the geometrically complex structures that are made of different metal substrates to test how strong the filament is anchored to the structures' surface. There has only been a work reported in the literature [25] that specifically demonstrated and discussed a method to measure the adhesion quality and structural stability of the attachment of carbon nanomaterials on a structured substrate. The technique involved investigating the tribological behaviour of CNT grown by plasma enhanced chemical vapour deposition (PECVD) on a stainless steel coated with a layer of metallic cobalt nanoparticles under humid ambient air of 25 – 40% relative humidity at room temperature using reciprocating ball-on-flat sliding. This reported method can be used in a future study on the adhesion of the filamentous carbon layer on the monolithic structure. Additionally, a method of examining the adhesion of the washcoating materials on the monoliths by ultrasonic testing in water or heat-shock testing [26] can also be adopted.

7.1.2 Mechanical strength test

Mechanical strength investigation of the metal monolithic supports with and without the filamentous carbon layer will be conducted. The relevant testing parameters representing mechanical strength of the structure such as Young's modulus and tensile strength will be characterised.

In the industrial application, more often than not, the shutdowns for catalyst replacements are due to the mechanical failure, not the loss of catalytic activity [27]. This makes an overall mechanical test a crucial step in qualifying the utility of monolithic catalysts. Mechanical destructive test for the mechanical strength assessment will also be made part of the future work, adopting the work by Young *et al.* (2017) [28] who performed a crush test on bulk catalyst pellets that were subjected to a thermal cycle.

The bulk catalyst pellets were placed in a tube rig containing layers of bed of randomly packed bulk catalyst pellets, where each layer was separated by a mild steel plate. A 22-kg mild steel mass was placed above the topmost separator plate, simulating the weight of the catalyst bed lying above the bottommost catalyst bed layer. As the tube was subject to repeated temperature cycles of between 20 °C and 900 °C (corresponding to the reformer start-up and shut-down), the changes in its diameter allowed the separator plates to freely move up and down. The collected fragments of fractured catalyst pellets were analysed by the percentage of damaged pellets. This bulk crush test technique can be adopted in the mechanical strength test of the monoliths in the future work, in which each bed of the bulk pellets in each layer separated by the mild steel plates are replaced with the monolith structures.

7.1.3 Thermal and chemical stability test

While CNTs are the stiffest and strongest fibres known [29] with chemical stability of being resistant to acidic [11, 30] and basic media, and physically stable at high temperatures (above 1000 K) [30], carbon support regasification may occur in the presence of hydrogen (at > 700 K) and oxygen (at > 500 K) to yield methane and carbon dioxide respectively [2, 30].

Although the high thermal conductivity of carbon filaments may be advantageous in energy intensive reactions such as SMR, its application has never been demonstrated in such a severe system by any researchers. Although the thermodynamic stability of the CNM in the presence of steam at high temperatures is satisfied by the analysis in Section 2.4.2 of Chapter 2 [1] and

the existing studies in the reactions involving steam reported in the literature [31-35] presented in Section 2.3.2 of Chapter 2 [1], there will still be the need to test this crucial parameter in the future work. Based on the literature alone, it is not possible to analyse at which temperature point the CNM supports of the spent catalysts used in the work above would have started to thermally deteriorate or been gasified as the stability of the CNM in terms of chemical stability and/or thermal degradation was not made part of the above studies.

However, it was demonstrated that in the presence of pure steam, single-walled carbon nanotubes (SWCNT) and MWCNT maintained their stability at temperatures of up to 900 °C, while the amorphous carbon was removed by gasification to yield carbon monoxide and hydrogen [36]. Although it is expected that the CNM would maintain good stability in the presence of steam in the SMR operation with the industrial SMR operation typically taking place between 500 and 950 °C [37-38], a thorough analysis of the conditions of the catalysts in the reactions over reaction time must however be performed to validate this.

The stability of the CNM in the presence of steam at high temperatures for energy intensive reactions such as SMR may have not been satisfied by the existing studies reported in the literature listed above as all of these studies were performed at laboratory scale with the reactions over the same catalysts typically lasting only a few hours, and the catalysts were not operated in a continuous mode. Therefore, the stability tests should be made part of the future work.

7.1.4 Heat transfer effectiveness study

The investigation on heat transfer enhancement of the total composite in comparison to a bed of randomly packed pellets will also be part of the future work scope. The techniques presented by Visconti *et al.* (2016) [39], Ryu *et al.* (2007) [40] and Basile *et al.* (2008) [41] serve as a potential adoption in this heat transfer study. In the work by Visconti *et al.* (2016) [39], a superior overall heat transfer coefficient was obtained in the FeCr-alloy foam packed

with γ-Al_2O_3 pellets, in comparison with a packed bed of the γ-Al_2O_3 pellets of the same volume packed in the foam voids. The same procedure can be employed to compare the heat transfer effectiveness by thermal conduction between a bed of pellets and the geometrically complex metal structure grown with the carbon nanomaterials fabricated in the future work.

A heat transfer effectiveness study in a non-reacting system that highlights and validates the improvement in the thermal conduction with the presence of filamentous carbon layer on the monolithic support will also be conducted. Running carrier gas such as argon or air through the two monolithic supports with and without the presence of filamentous carbon layer, without undergoing any reaction would be able to produce analysis on heat distribution in both systems. Improvement in terms of heat transfer coefficient is expected from the CNT system.

7.1.5 Pressure drop study

A pressure drop comparison study is also another area of future work study within the scope of this project. The experimental setup and technique presented by Richardson *et al.* (2000) [42] in a pressure drop measurement across a bed of ceramic foams pelletised catalyst would be a good reference for an adoption to complete the study in this first part of the overall research work. An experimental setup will be designed to study the pressure drop performances of the two catalyst systems; pelletised and monolithic structured.

7.2 Synthesis of active nickel phase on MWCNT grown on structured metal support for steam reforming kinetic study

The deposition of nickel particles on the CNM grown on the geometrically complex metal structure will need to be undertaken to complete the overall proposed catalytic composite. A demonstration on synthesising the carbon nanomaterials with the Ni nanoparticles as the active phase for SMR reaction on the metal monolith will be a major work on its own. The techniques used in introducing the active phase in the washcoating layer reviewed by Nijhuis

et al. (2001) [26] among others include impregnation, ion exchange, and deposition–precipitation, can be adopted for an application on the CNM grown on the metal monolith structure.

The kinetic study of diffusion-limited, highly endothermic SMR reaction can then be performed over the complete structured catalyst prototype, in order to complete the overall scope in the research theme. A demonstration of improvement in the methane conversion and reduction of the reactor exit temperature will be the main objective in the kinetic study of the SMR reaction.

7.3 Carbon nanomaterials as a removable template to synthesise a catalytic oxide layer on the monolith

Other possible future works worth researching include a demonstration of a catalytic oxide layer synthesis using the CNM as a removable template introduced in Baharudin *et al.* (2018a) [1], to eliminate the risk (if any) of possible CNM gasification in the steam reforming environment. As discussed earlier, the potential of the application of CNM grown on the metal monolith as the structure's surface promoter as an alternative to the conventional oxide washcoat layer that is associated with poor adhesion with the monolith, may or may not survive in some reaction conditions that can be extreme. Any presence of disordered carbon may be thermally unstable above certain temperatures, and consequently results in catalyst deactivation. Therefore, an idea of using the CNM as a removable template to synthesise a catalytic oxide layer on the overall monolithic composite presents a promising option to address (any) scepticisms people may have on using carbon nanomaterials as the catalyst support.

Various techniques have been reported in the literature to synthesise the oxide nanotubes for electronics applications, which can be adopted for the catalysis applications. They are listed below:

- Ajayan *et al.* (1995) [43] demonstrated layering of V_2O_5 nanotubes using carbon nanotubes as a template, by annealing a mixture of oxidised carbon nanotubes (by air oxidation and HNO_3 treatment) and V_2O_5 powder above its melting point in air. The carbon nanotubes template was then oxidised and removed from the system, leaving behind V_2O_5 nanofibers.
- Satishkumar *et al.* (1997) [44] presented a procedure of coating the carbon nanotubes with tetraethylorthosilicate, aluminium isopropoxide, vanadium pentoxide gel, and molybdic acid to produce the nanotubes of SiO_2, Al_2O_3, V_2O_5, and MoO_3, followed by the calcination in air to oxidise the carbon.
- Satishkumar *et al.* (2000) [45] employed the pre-oxidation steps by air and HNO_3 prior to coating the carbon nanotubes template with oxide precursors through a drying and calcination procedure, which was demonstrated to result in nanorod oxides of V_2O_5, WO_3, MoO_3, Sb_2O_5, MoO_2, RuO_2 and IrO_2.
- Munoz-Munoz *et al.* (2015) [46] used a technique called atomic layer deposition utilising carbon nanotubes as a removable template for synthesising Al_2O_3 nanotubes. Through alternating cycles of dosing and purging trimethyl-aluminium and deionized water, the Al_2O_3 coatings were grown in a reactor heated at 100 °C up to 600 °C. A continued heating from 600 °C to 800 °C decomposed the carbon nanotubes.
- Correa-Duarte *et al.* (2004) [47] reported a procedure for the synthesis of SiO_2-coated Au nanoparticles using a template of MWCNT grown on a structured silicon, where polymer-wrapping pretreatment by polystyrene sulphonate and poly(diallyldimethyl) ammonium chloride bilayers was performed prior to deposition. The SiO_2-coated Au nanoparticles have excellent optical properties for an electronic application. The synthesis technique presents an interesting demonstration for an adoption in synthesising an oxide-supported metal catalyst using CNT as the template.

References of Chapter 7

1. Baharudin, L., et al., *Potential of metal monoliths with grown carbon nanomaterials as catalyst support in intensified steam reformer: a perspective.* Reviews in Chemical Engineering, 2018a. **ahead of print**.

2. Chinthaginjala, J.K., K. Seshan, and L. Lefferts, *Preparation and Application of Carbon-Nanofiber Based Microstructured Materials as Catalyst Supports.* Industrial & Engineering Chemistry Research, 2007. **46**(12): p. 3968-3978.
3. Ruiz-Cornejo Juan, C., D. Sebastián, and J. Lázaro Maria, *Synthesis and applications of carbon nanofibers: a review*, in *Reviews in Chemical Engineering*. 2018.
4. Li, P., et al., *Synthesis of carbon nanofiber/graphite-felt composite as a catalyst.* Microporous and Mesoporous Materials, 2006. **95**(1–3): p. 1-7.
5. Rostrup-Nielsen, J.R., *Equilibria of decomposition reactions of carbon monoxide and methane over nickel catalysts.* Journal of Catalysis, 1972. **27**(3): p. 343-356.
6. Li, Y., et al., *Novel Ni catalysts for methane decomposition to hydrogen and carbon nanofibers.* Journal of Catalysis, 2006. **238**(2): p. 412-424.
7. Teo, K.B., et al., *Catalytic synthesis of carbon nanotubes and nanofibers*, in *Encyclopedia of nanoscience and nanotechnology (Vol. 10)*, H.S. Nalwa, Editor. 2003, American Scientific Publishers: USA. p. 1-22.
8. Jarrah, N.A., et al., *Immobilization of a layer of carbon nanofibres (CNFs) on Ni foam: A new structured catalyst support.* Journal of Materials Chemistry, 2005. **15**(19): p. 1946-1953.
9. Pacheco Benito, S. and L. Lefferts, *The production of a homogeneous and well-attached layer of carbon nanofibers on metal foils.* Carbon, 2010. **48**(10): p. 2862-2872.
10. Pacheco Benito, S. and L. Lefferts, *Influence of reaction parameters on the attachment of a carbon nanofiber layer on Ni foils.* Surface and Coatings Technology, 2012. **206**(15): p. 3366-3373.
11. Chinthaginjala, J.K., et al., *How Carbon-Nano-Fibers attach to Ni foam.* Carbon, 2008. **46**(13): p. 1638-1647.
12. Chinthaginjala, J.K. and L. Lefferts, *Influence of hydrogen on the formation of a thin layer of carbon nanofibers on Ni foam.* Carbon, 2009. **47**(14): p. 3175-3183.
13. Chinthaginjala, J.K., et al., *Carbon nanofiber growth on thin rhodium layers.* Carbon, 2012. **50**(3): p. 1434-1437.
14. Tribolet, P. and L. Kiwi-Minsker, *Palladium on carbon nanofibers grown on metallic filters as novel structured catalyst.* Catalysis Today, 2005. **105**(3–4): p. 337-343.
15. Morales-Torres, S., et al., *Palladium and platinum catalysts supported on carbon nanofiber coated monoliths for low-temperature combustion of BTX*. Applied Catalysis B: Environmental, 2009. **89**(3–4): p. 411-419.

16. Chinthaginjala, J.K., J.H. Bitter, and L. Lefferts, *Thin layer of carbon-nano-fibers (CNFs) as catalyst support for fast mass transfer in hydrogenation of nitrite.* Applied Catalysis A: General, 2010. **383**(1–2): p. 24-32.
17. Zhu, J., et al., *Carbon Nanofibers Grown on Anatase Washcoated Cordierite Monolith and Its Supported Palladium Catalyst for Cinnamaldehyde Hydrogenation.* Industrial & Engineering Chemistry Research, 2013. **52**(3): p. 1224-1233.
18. Baird, T., J.R. Fryer, and B. Grant, *Carbon formation on iron and nickel foils by hydrocarbon pyrolysis—reactions at 700°C.* Carbon, 1974. **12**(5): p. 591-602.
19. Parthangal, P.M., R.E. Cavicchi, and M.R. Zachariah, *A generic process of growing aligned carbon nanotube arrays on metals and metal alloys.* Nanotechnology, 2007. **18**(18): p. 185605.
20. Baharudin, L. and M.J. Watson, *Monolithic substrate support catalyst design considerations for steam methane reforming operation.* Reviews in Chemical Engineering, 2017b. **34**(4): p. 481-501.
21. Heck, R.M., S. Gulati, and R.J. Farrauto, *The application of monoliths for gas phase catalytic reactions.* Chemical Engineering Journal, 2001. **82**(1–3): p. 149-156.
22. Tronconi, E., et al., *Monolithic catalysts with 'high conductivity' honeycomb supports for gas/solid exothermic reactions: characterization of the heat-transfer properties.* Chemical Engineering Science, 2004. **59**(22–23): p. 4941-4949.
23. Tronconi, E., G. Groppi, and C.G. Visconti, *Structured catalysts for non-adiabatic applications.* Current Opinion in Chemical Engineering, 2014. **5**: p. 55-67.
24. Guo, N. and M.C. Leu, *Additive manufacturing: technology, applications and research needs.* Frontiers of Mechanical Engineering, 2013. **8**(3): p. 215-243.
25. Abad, M., et al., *Catalytic growth of carbon nanotubes on stainless steel: characterization and frictional properties.* Diamond and Related Materials, 2008. **17**(11): p. 1853-1857.
26. Nijhuis, T.A., et al., *Preparation of monolithic catalysts.* Catalysis Reviews, 2001. **43**(4): p. 345-380.
27. Wu, D. and H. Zhang, *Mechanical stability of monolithic catalysts: scattering of washcoat adhesion and failure mechanism of active material.* Industrial & Engineering Chemistry Research, 2013. **52**(41): p. 14713-14721.
28. Young, A., et al., *Failure of commercial extruded catalysts in simple compression and bulk thermal cycling.* International Journal of Applied Ceramic Technology, 2018. **15**(1): p. 74-88.

29. Harris, P.J.F., *Carbon nanotube science: synthesis, properties and applications*. 2009: Cambridge university press.
30. Rodríguez-reinoso, F., *The role of carbon materials in heterogeneous catalysis.* Carbon, 1998. **36**(3): p. 159-175.
31. Seelam, P., et al., *CNT-based catalysts for H 2 production by ethanol reforming.* international journal of hydrogen energy, 2010. **35**(22): p. 12588-12595.
32. Yang, H.-M. and P.-H. Liao, *Preparation and activity of Cu/ZnO-CNTs nano-catalyst on steam reforming of methanol.* Applied Catalysis A: General, 2007. **317**(2): p. 226-233.
33. López, E., et al., *Multiwalled carbon nanotubes-supported Nickel catalysts for the steam reforming of propane.* Journal of Materials Science, 2012. **47**(6): p. 2985-2994.
34. Mierczynski, P., et al., *Monometallic copper catalysts supported on multi-walled carbon nanotubes for the oxy-steam reforming of methanol.* Reaction Kinetics, Mechanisms and Catalysis, 2016. **117**(2): p. 675-691.
35. Oliveira, N.M., G.P. Valençaa, and R. Vieirab, *Water Gas Shift Reaction On Copper Catalysts Supported On Alumina And Carbon Nanofibers.* Chemical Engineering, 2015. **43**.
36. Tobias, G., et al., *Purification and opening of carbon nanotubes using steam.* The Journal of Physical Chemistry B, 2006. **110**(45): p. 22318-22322.
37. Zamaniyan, A., et al., *Comparative model analysis of the performance of tube fitted bulk monolithic catalyst with conventional pellet shapes for natural gas reforming.* Journal of Industrial and Engineering Chemistry, 2011. **17**(4): p. 767-776.
38. Mohammadzadeh, J.S. and A. Zamaniyan, *Catalyst shape as a design parameter—optimum shape for methane-steam reforming catalyst.* Chemical Engineering Research and Design, 2002. **80**(4): p. 383-391.
39. Visconti, C.G., G. Groppi, and E. Tronconi, *Highly conductive "packed foams": A new concept for the intensification of strongly endo-and exo-thermic catalytic processes in compact tubular reactors.* Catalysis Today, 2016. **273**: p. 178-186.
40. Ryu, J.-H., et al., *Ni catalyst wash-coated on metal monolith with enhanced heat-transfer capability for steam reforming.* Journal of Power Sources, 2007. **171**(2): p. 499-505.
41. Basile, F., et al., *Highly conductive Ni steam reforming catalysts prepared by electrodeposition.* Chemical Communications, 2008(25): p. 2917-2919.

42. Richardson, J.T., Y. Peng, and D. Remue, *Properties of ceramic foam catalyst supports: pressure drop.* Applied Catalysis A: General, 2000. **204**(1): p. 19-32.
43. Ajayan, P., et al., *Carbon nanotubes as removable templates for metal oxide nanocomposites and nanostructures.* Nature, 1995. **375**(6532): p. 564.
44. Satishkumar, B., et al., *Oxide nanotubes prepared using carbon nanotubes as templates.* Journal of materials research, 1997. **12**(03): p. 604-606.
45. Satishkumar, B., et al., *Synthesis of metal oxide nanorods using carbon nanotubes as templates.* Journal of Materials Chemistry, 2000. **10**(9): p. 2115-2119.
46. Muñoz-Muñoz, F., et al., *The control of thickness on aluminum oxide nanotubes by Atomic Layer Deposition using carbon nanotubes as removable templates.* Powder Technology, 2015. **286**: p. 602-609.
47. Correa-Duarte, M.A., et al., *Linear Assemblies of Silica-Coated Gold Nanoparticles Using Carbon Nanotubes as Templates.* Advanced Materials, 2004. **16**(23-24): p. 2179-2184.

APPENDIX A

Introduction to carbon nanomaterial structures and the working principles of their common growth techniques

A1. Introduction to carbon nanomaterial structures

In the definition by Teo *et al.* (2003) [1], carbon nanomaterials are defined as graphitic filaments of diameters between 0.4 and 500 nm and lengths of microns to millimetres. They are generally classified into two subgroups, namely carbon nanofibers (CNF) and carbon nanotubes (CNT). The structural types of carbon filaments are identified as stacked (sometimes referred to as platelet), herringbone (fishbone or cup-stacked), and nanotube [1-3] as shown in Figure A1. They are distinguishable based on the angle of the graphene layers in reference to the filament axis. In the stacked form, the graphite layers are perpendicular to the filament axis. In the herringbone form, the graphene walls are at an angle to the filament axis. In the nanotube form, the graphene walls are parallel to the filament axis [1]. The stacked and herringbone forms are classified under the general nomenclature of CNF, and hence they are clearly differentiated from the CNT. In this Appendix, we are consistent with the definition set by Teo *et al.* (2003) [1] for the classification of filamentous carbon as described above, even though there were also other definitions used in the literature, based on the crystallinity and the diameter of the carbon filaments.

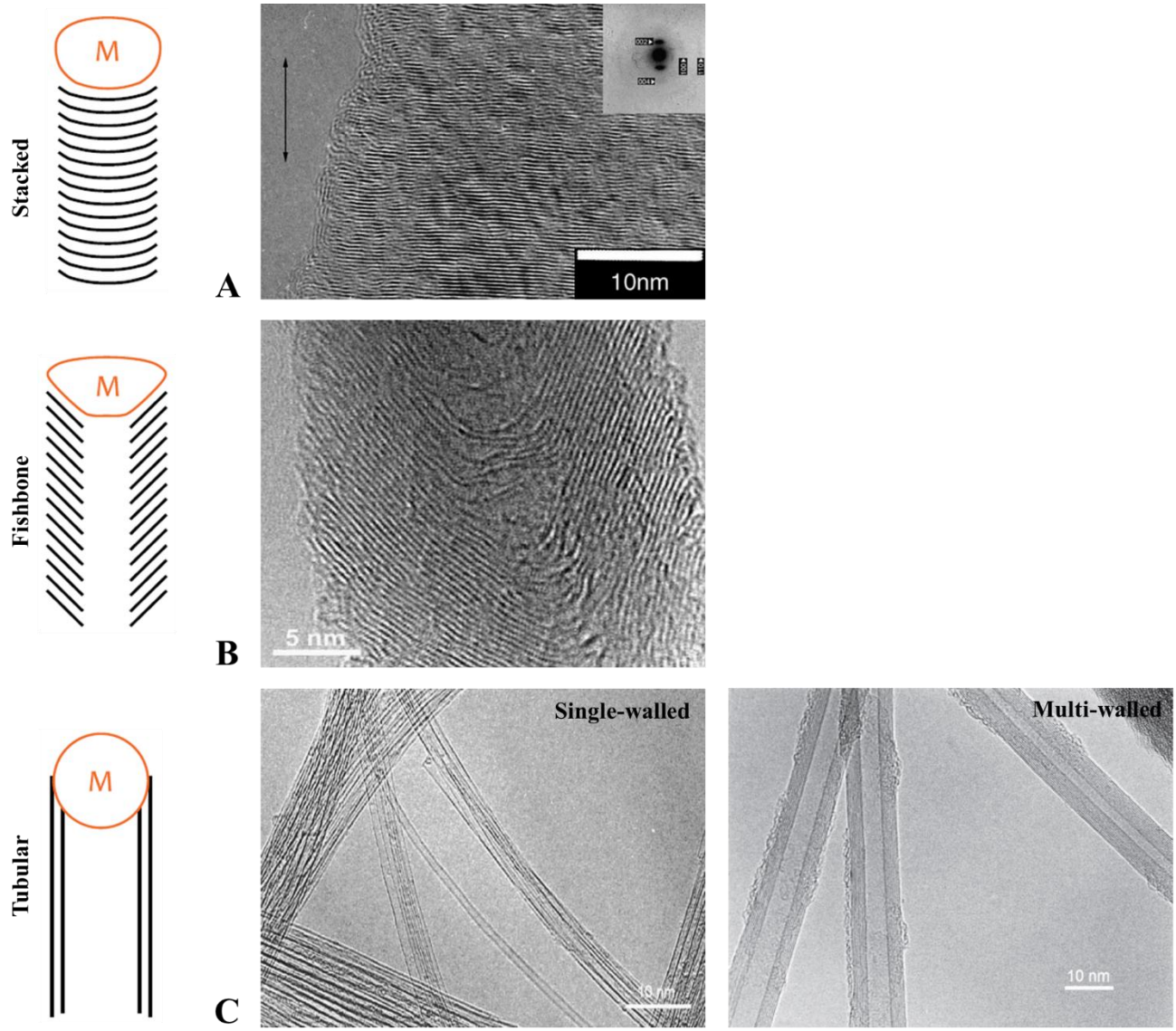

Figure A1: Right: Schematic of carbon nanostructures with different graphene wall (layer) arrangements; M represents catalyst metal particle [2]. Left: Example of transmission electron microscopy (TEM) images.

(A) Stacked carbon nanofibers [4]; (B) example of TEM of herringbone carbon nanofibers [5]; and (C) example of TEM images of single-walled carbon nanotubes [6] and multi-walled carbon nanotubes [6, 7].

The first mention of carbon fibres in a publication was by Wiles & Abrahamson (1978) [8], grown on a graphite electrode by the arc discharge method. The fibres, which were of diameter range of 4 nm to 100 nm and length of up to 15 µm, held small crystalline particles on them, most notably around the intersections of touching fibres. This carbon material is

now known as CNT. In a discovery much later by Sumio Iijima in 1991, the carbon nanotubes consisted of cylindrical graphite sheets with both ends capped by six pentagonal rings. A theoretical illustration of this structure was given by Harris (1999) [7] and Harris (2009) [6], by cutting in half a C_{60} molecule (Figure A2), followed by placing a graphitic cylinder in the two halves.

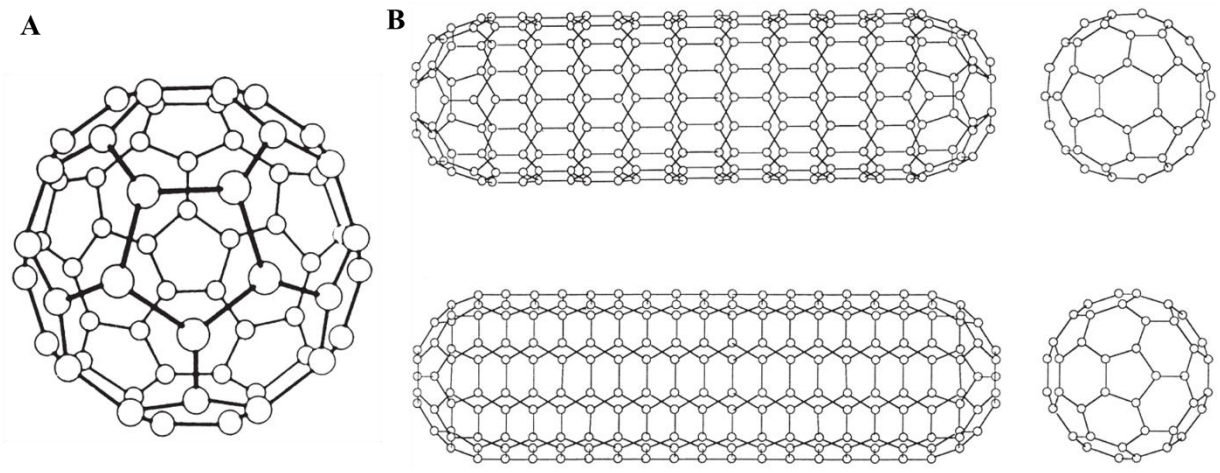

Figure A2: Theoretical illustration of carbon nanotube structure.

(A) C_{60} buckminsterfullerence; and (B) drawings of the nanotubes which can be capped by one half of a C_{60} molecule: zig-zag structure (Top), armchair (Bottom) [6, 7].

Generally, two typical CNTs can be formed depending on the arrangements of the hexagonal cylindrical graphite sheet around the circumference; known as the zig-zag nanotube and armchair nanotube [6, 7]. There is also another class of nanotube structure other than the two arrangements mentioned above, where the hexagons are arranged helically around the tube axis, as illustrated in Figure A3. This nanotube structure is called chiral [6, 7, 9, 10].

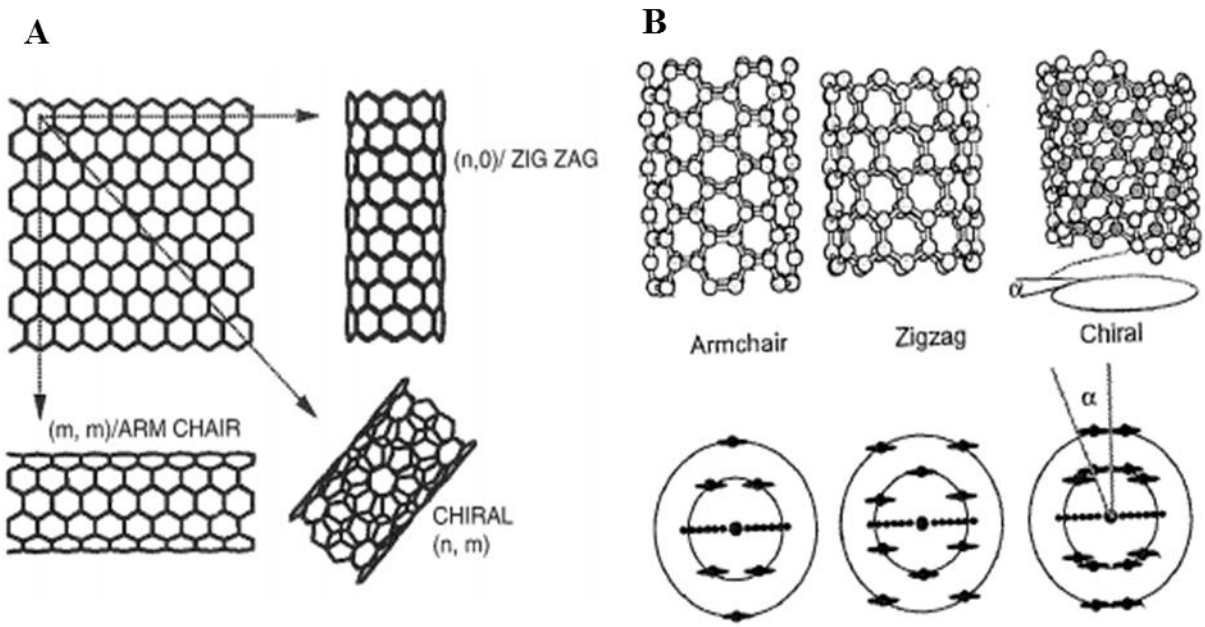

Figure A3: Chirality of carbon nanotubes.

(A) Different chirality of nanotubes can be obtained by rolling the graphite sheet in different directions [9]; and (B) different chirality nanotube structures with simulated TEM-diffraction pattern [10].

The tubes may be either multi-layered or single-layered [6, 7]. Therefore, researchers have further classified the CNT into multi-walled and single-walled. The single-walled carbon nanotubes (SWCNT) is made of one hollow cylinder of a graphite sheet, whereas the multi-walled carbon nanotubes (MWCNT) is made of a group of coaxial SWCNT [9]. In the MWCNT, the several concentric, coaxial graphene cylinders inside its hollow [1, 11] are spaced by ~0.34 to 0.39 nm [1, 12] (Figure A4), and the intershell/layer spacing decreases with increasing carbon nanotube diameter [1].

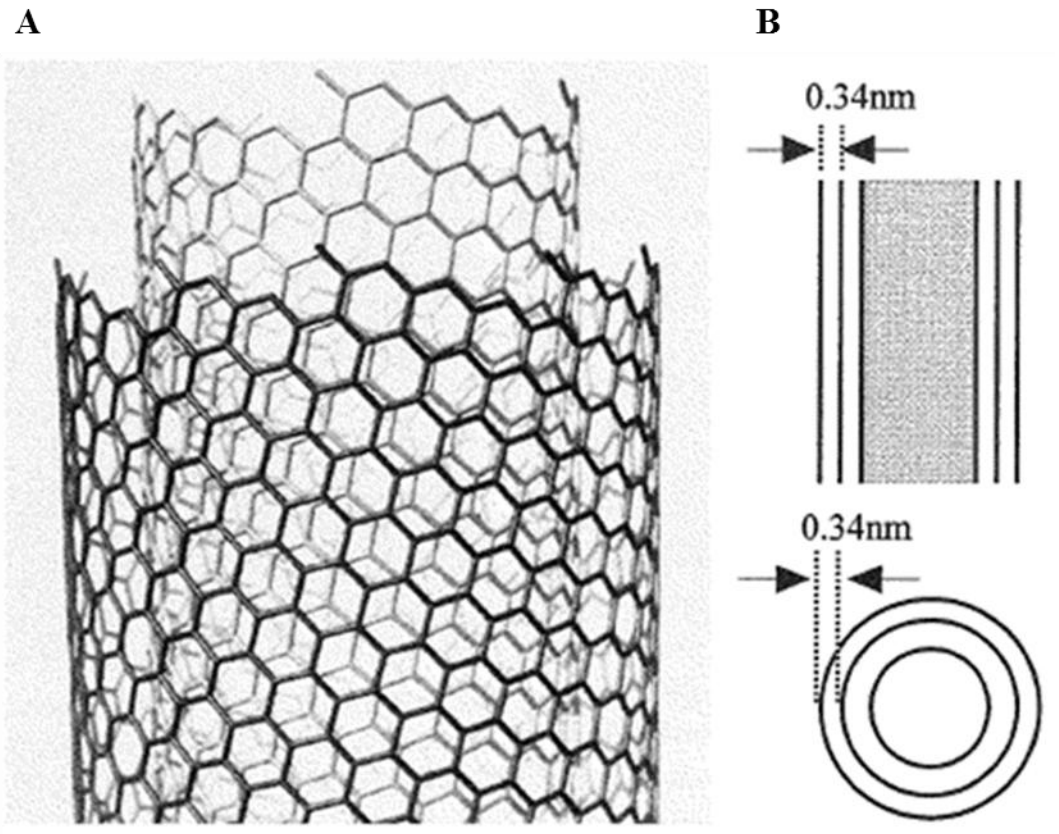

Figure A4: MWCNT structure.

(A) Drawing of two concentric helical tubes [7]; and (B) interlayer spacing between graphene cylinders (top) and its cross-sectional view (bottom) [13].

Ideally, the produced carbon nanotubes should be structurally straight, where all the graphene walls are parallel to the tube axis [1]. However, as can be seen in Figure A1(C) earlier, in comparison between SWCNT and MWCNT, the individual SWCNT in general is of very small diameters of typically 1 nm. Therefore, they are often curved instead of straight, with the tendency to form bundles or 'ropes' [6].

However, both SWCNT and MWCNT are generally found to be less perfect, unlike the idealised illustrations shown in Figure A2. The different variants of CNT are due to their structural relatives of fullerenes, where straight walls of the CNT require six-fold carbon rings [10]. In a non-defected structure, the nanotubes walls are made of hexagonal sheets of carbon atoms (Figure A5).

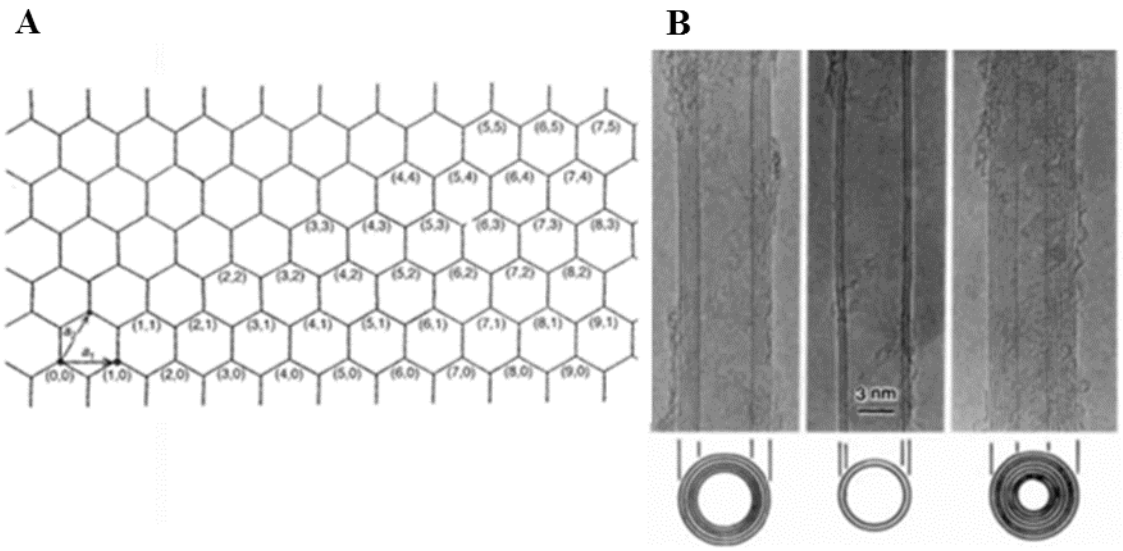

Figure A5: Non-defected structure of carbon nanotubes.

(A) Graphene layer with atoms labelled using (n,m) notation [7]; and (B) example of TEM images of homogeneous carbon nanotubes made of hexagonal carbon network [9].

In general, CNT consists of carbon nanoparticles of hollow and fullerene-related structures, as well as some disordered carbon. Metal (used to synthesise the CNT growth by catalytic chemical vapor deposition (CCVD)) impurities are also present, encapsulated by the cap at the end of the carbon layers [14]. The tube length is in the range of a few tens of nanometres to micrometres, and their outer diameter is between 2.5 nm and 30 nm. Quite frequently, it has been observed that the central hollow portion of a nanotube is crossed by the graphitic walls, and hence capping one or more of the inner tubes, as shown in Figure A6. In this example, a single filament layer that forms a cap across the central tube can be seen [6, 7]. This common structure is referred to as nanotubes containing bamboo compartments. There have been variations in the suggestion on the growth mechanism of CNT with bamboo compartments, as presented by Teo *et al.* (2003) [1] for further reference.

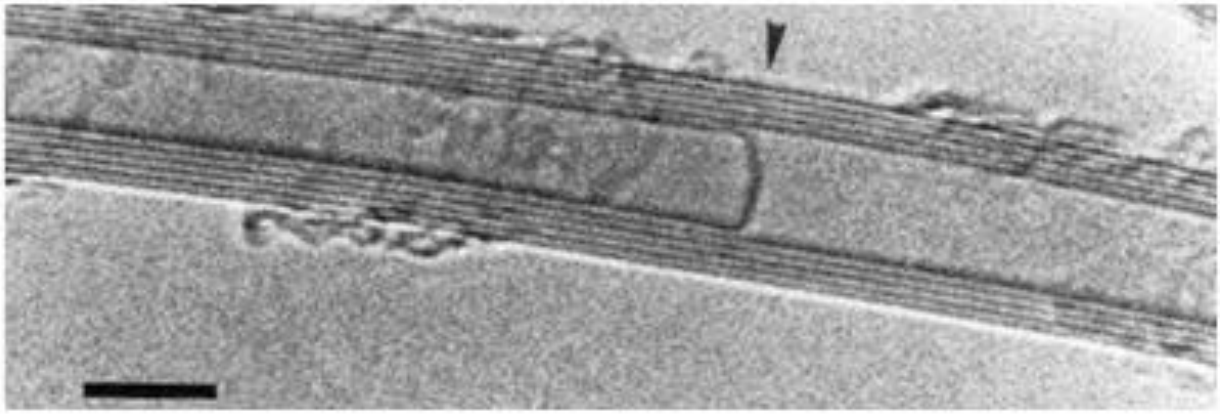

Figure A6: Example of TEM image (scale bar 5 nm) of multiwalled carbon nanotube with ‘internal cap’ (bamboo-structured) [7].

As illustrated earlier in Figure A2, the CNT is virtually capped at both ends with pentagonal carbon rings. However, in reality, the caps are seldom hemispherical in shape, as there can be a variety of other morphologies such as the ones shown in Figure A7 [6, 7].

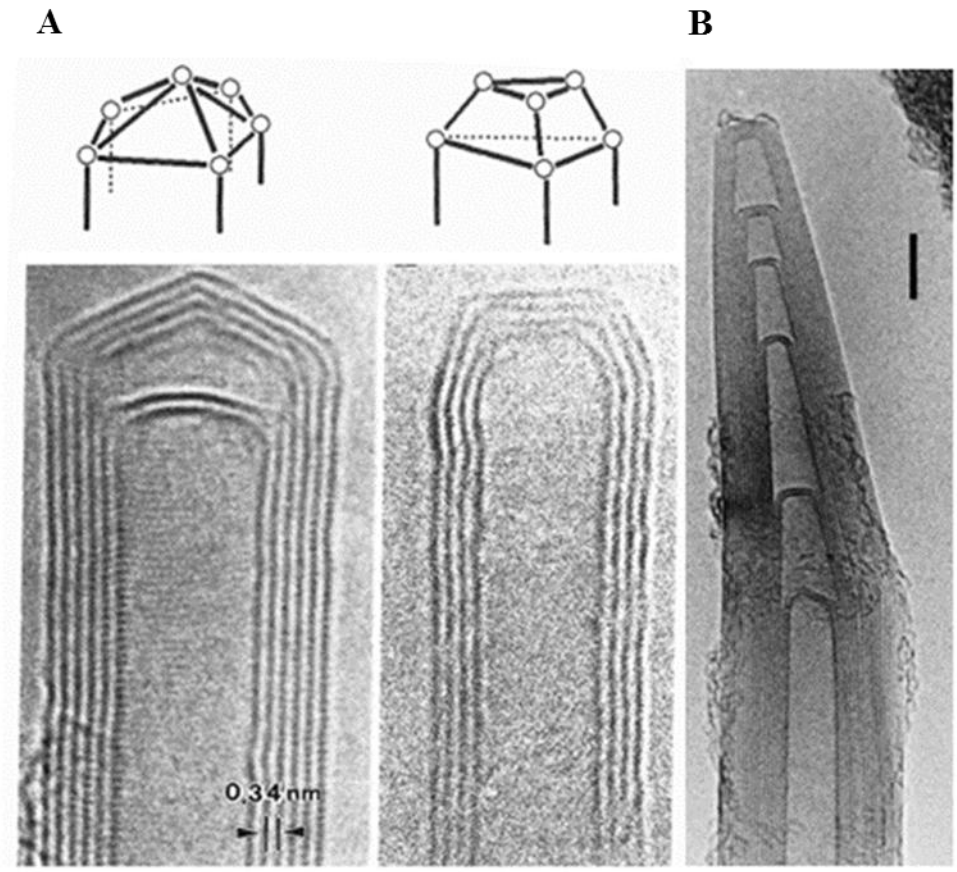

Figure A7: Other morphologies of carbon nanotubes cap.

(A) Example of two images of carbon nanotube variants with non-hemispherical shaped caps [7]; and (B) example of TEM image (scale bar 5 nm) of typical MWCNT cap [6, 7].

In general, the different variants of CNT are caused by small differences in the surface energy of the carbon deposition kinetics, but this has not been fully understood. The carbon structural variants are analogous to sublimating water in nature that shows many beautiful variants that take the form of snow flakes, frost, icicles or ice crystallites. A schematic drawing of the different carbon nanotubes structures containing metal nanoparticles is shown in Figure A8 [10].

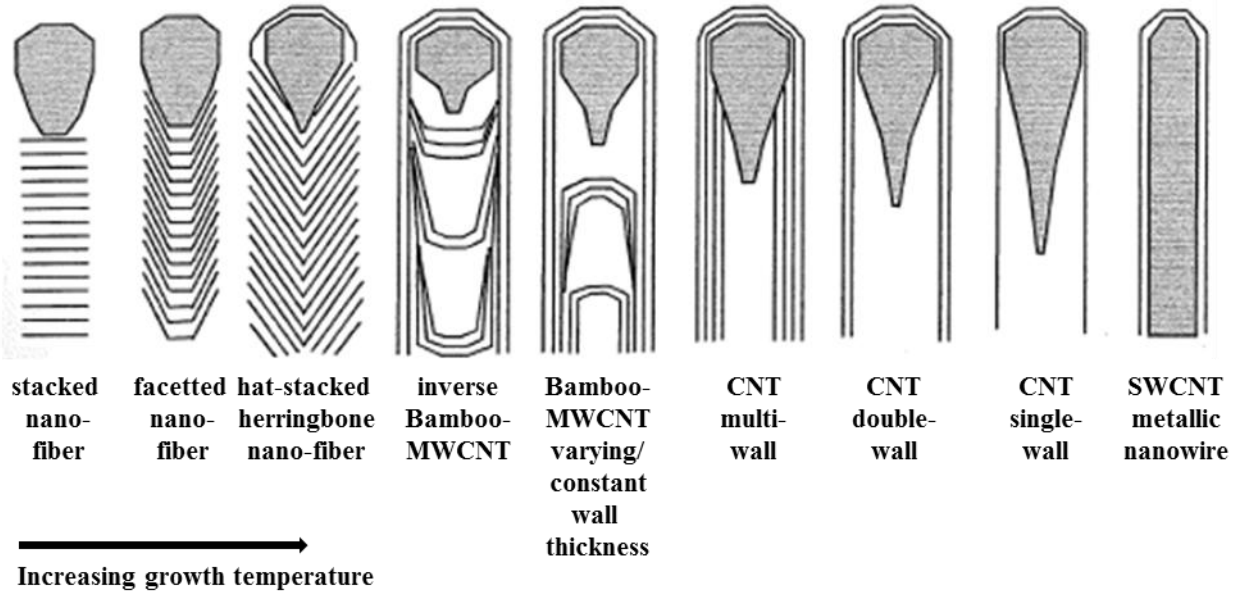

Figure A8: Carbon nanotubes structures and general growth temperature contributing to the variants [10].

Bending or surface curvature in CNT is the result of topological defects such as pentagon-heptagon pairs with less stable chemical bonds [10] incorporated in the nanotube of a hexagonal carbon network [1, 9] (illustrated in Figure A9). A hexagonal carbon network is chemically more stable where each atom is bonded to three neighbouring atoms [10].

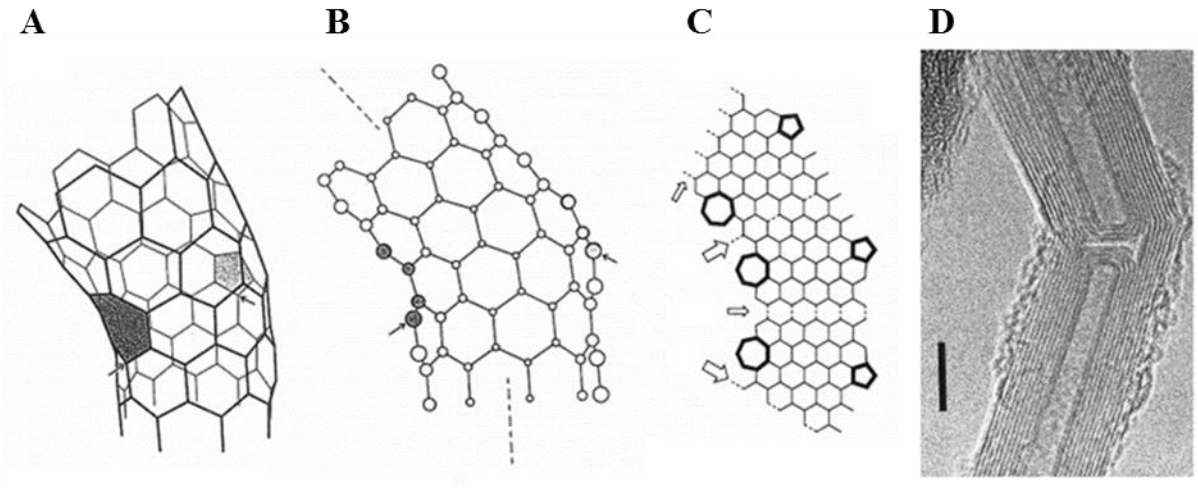

Figure A9: Illustration of an 'elbow connection' between an armchair and a zig-zag nanotubes.

(A) Perspective drawing with pentagonal and heptagonal rings (shaded); (B) structure projected on symmetry plane of elbow; (C) planar representation of the connections; and (D) example of TEM image (scale bar 5 nm) of elbow connection joining two multi-walled carbon nanotubes [7].

Well-crystallised and straight MWCNT is shown in Figure A10(A). This MWCNT consists of walls made of the hexagonal carbon network, indicated by the solid straight lines in the micrographs. In lower temperature processes (~700 – 1400 K), "curly" and "coiled" nanotubes (Figure A10(B) and Figure A10(C)) are commonly produced as a result of the defects [1], which is also the reason for the formation of bundles or 'ropes' of nanotubes [6], as seen earlier in Figure A1(C). In order to anneal out the defects so that straight, well-crystallised nanotubes can be produced, the growth temperature needs to be raised [1] optimally.

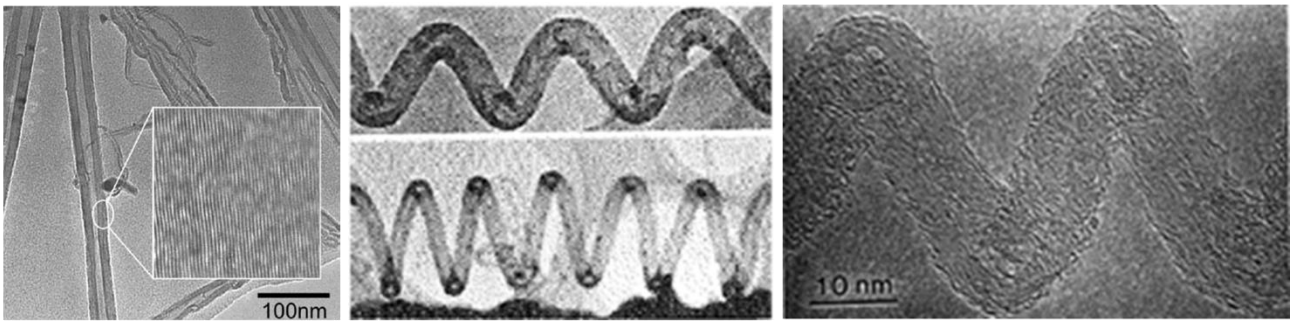

Figure A10: MWCNT variations.

(A) Example of high degree graphitised multi-walled carbon nanotubes image [1, 6]; (B) example of micrographs of carbon nanotubes with bend angles/coils at low resolution (top 50 nm, bottom 300 nm) [9]; and (C) example of micrograph of a coiled nanotube [7].

Carbon filaments with defects in the form of branched structures (such as L, Y, T branching) have also been observed [7, 9, 15], as shown in Figure A11. The branching resulted from the introduction of additives into the catalyst particles (or bi-metal particles), based on the suggestion by Baker (1989) [15]. A number of carbon filament growth mechanism models have been proposed in the literature with the most widely accepted model being the one postulated by Baker (1989) [15], which was discussed in the hydrocarbon decomposition section by Baharudin & Watson (2017) [16]. An important point to note is that none of the proposed models predicted these branched deviations that occurred in carbon filament growth [15]. The discussion of all the possible growth mechanisms in the literature focused only on the formation of whisker-like carbon filaments, which are represented by a single direction, defect-free crystal growth as shown in Figure A11(A) (top left).

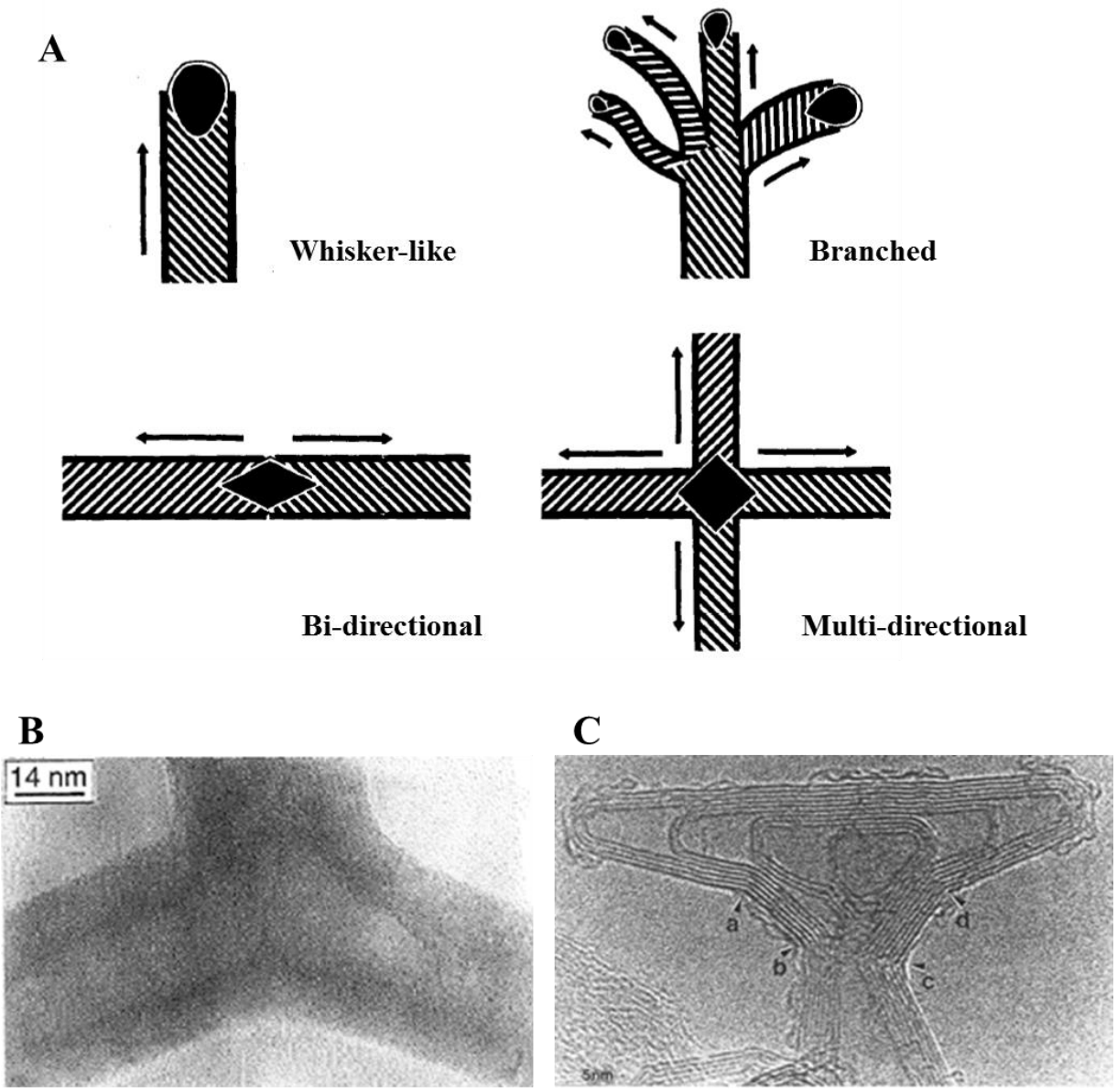

Figure A11: Branched structures of carbon nanomaterials.

(A) Various types of carbon filaments growth [15]; (B) example of TEM image of Y-branched carbon nanotube [9]; and (C) example of TEM image of T-branched carbon nanotube [7].

A2. Working principles of common synthesis techniques of carbon nanomaterials growth

The ability to predict the growth structure of the carbon filaments in order to control their physical and chemical properties has been the subject of interest in the area of carbon nanostructures research [15]. An overview of a wide range of applications of carbon nanofibers and nanotubes was presented by Teo *et al.* (2003) [1], while Chintaginjala *et al.* (2007) [17] reviewed the applications of these novel materials specifically as catalyst supports. Chinthaginjala *et al.* (2007) [17] in their review listed three ways of how carbon nanomaterials are being applied as catalyst supports:

i) Carbon nanomaterials in powdered form loaded with the catalytic active phase;

ii) A high porosity and low tortuosity fixed bed of carbon nanomaterials in pelletised form;

iii) Formation of carbon filament layers on a structured material such as foam, monolith, or felt that helps shorten the diffusion path length.

Here, discussion is focused on the third way of applying carbon nanomaterials as the catalyst support.

There are two different approaches to prepare the thin layers of carbon nanomaterials on the structured supports. In the first approach, small catalytically active metal particles (particularly Ni, Co or Fe) are first deposited on the structured support, and those metal particles then catalyse the growth of the filamentous carbon on the support. In the second approach, structured supports that are made of an intrinsically active material for the formation of the filamentous carbon layers are used [17]. Between the two approaches of growing the carbon filaments on a structured support, Chinthaginjala *et al.* (2007) [17] presented their essential difference in the growth preparation technique, by synthesising the carbon nanomaterials on polycrystalline Ni such as Ni foam, and on supported Ni-particle catalysts. Essentially, the difference between the two systems lies in the pre-treatment steps of the catalysts.

There have also been other non-catalytic methods applied specifically to produce MWCNT. Techniques such as pyrolytic methods and electrochemical synthesis are briefly mentioned in Harris (1999) [7] for further reference. In addition, Loiseau (2006) [12] briefly described another method on a vaporisation induced by a solar beam. This method uses a solar furnace for capturing highly concentrated sunlight for the sublimation of the graphite. By making adjustments to the pressure and the flow of the carbon precursors, it is possible to synthesise long bundles of CNT in the form of bamboo-like MWCNT, mixtures of MW- and SWCNT, or SWCNT only.

In most references [7, 12, 13, 18], the three most commonly used techniques that have been applied in synthesising the carbon nanomaterials are:

i) arc-discharge (sometimes known as arc-evaporation [7]), which is preferred when growing high quality crystalline MWCNT;

ii) laser ablation (sometimes being referred to as laser vaporisation [7, 12]); an important technology favourable for high-yield synthesis of SWCNT [13];

iii) chemical vapour deposition (CVD), which is a catalytic decomposition of a hydrocarbon, a method that offers flexibility to produce the carbon nanomaterials in the range of CNF to CNT, by manipulating the chemical interaction between the carbon precursors and the catalyst metals, with the best possibility for mass production.

In general, arc discharge and laser ablation are categorised as high temperature (> 3000 K) and short-time (μs – ms) filamentous carbon growth processes, whereas the catalytic chemical vapour deposition operates in a medium temperature range (700 – 1400 K) and it is a slower (typically minutes to hours) process. In the 1960s – 1980s, the catalytic chemical vapour deposition was established to focus on the production of a general structure of carbon nanomaterials. In the 1990s, the arc discharge and laser ablation techniques were applied to fundamentally study the properties of specifically carbon nanotubes, as a result of their superior straightness and crystallinity [1], since the two methods encouragingly favour high quality CNT production over CNF.

While the arc discharge has the capability to produce high quality MWCNT as well as acceptable quality SWCNT by careful control of experimental conditions [18], laser ablation does not seem adequate to synthesise MWCNT due to the much shorter length of MWCNT produced as compared to arc discharge [13]. In the synthesis of SWCNT, the arc discharge leads as the cheapest and easiest method if the aim is to obtain SWCNT in significant quantities. However, the SWCNT produced by arc discharge are of a lower purity than those synthesised by laser ablation [18].

The higher growth process temperature in the arc discharge or laser ablation introduces a perfect annealing of defects in the tubular graphene sheets. Therefore, the carbon nanotubes that result from the vaporisation of graphite in these two techniques generally possess fewer structural defects, in comparison to those produced at low temperatures by the catalytic chemical vapour deposition. In the synthesis of the MWCNT, the high temperature methods produce a nanotube structure that is perfectly straight, while the low temperature CVD synthesises kinked tubes [18]. A prolonged annealing at temperatures above 2000 K post low-temperature CVD synthesis can improve the quality of the MWCNT produced. However, their mechanical and electrical properties are not as good as the arc discharge-produced MWCNT.

In many applications, not only are nanotubes of a very high quality required, but the production amount is also sought in multi-ton tube quantities. In order to meet both the quality and the quantity requirements, the two high temperature schemes do not seem to be able to completely substitute the catalytic CVD method that is capable of meeting the mass production requirement. Therefore, a scaling up of the high-temperature techniques is necessary due to the steadily growing industrial need for very high quality carbon nanotubes. This however, remains commercially challenging [18]. Another technological drawback of the high-temperature production methods is that the carbon nanotubes have to be produced separately and not directly on a structured substrate, and then they are purified before being manipulated onto the substrate before it can be used in an application [1]. This can be inconvenient for the purpose of its application as a surface textural promoter of a support structure, in the context of discussion in this thesis.

The CVD method introduces flexibilities of fabrication of the filamentous carbon [1]:

- of stacked layered nanofiber or tube form;
- of high quality single- or multi-walled with controlled diameter and length;
- in horizontal or vertical alignment;
- as an individual nanotube or "en masse"
- synthesised directly onto a substrate or in bulk.

A significant advantage of the CNT grown by catalytic CVD also lies in its low synthesis temperature (relative to the arc discharge and the laser ablation techniques), where manipulations in the control of chemical reaction between 1000 and 1500 °C are possible [13].

A2.1 Electric arc discharge

The basic principle in the electric arc discharge technique is the utilisation of an electrical discharge generated between two graphite electrodes facing each other inside an airtight chamber (Figure A12), operating under an atmosphere of either helium or argon of typically 600 mbar. This consequently increases the temperature that results in a further graphite transformation and eventually leads to the deposition of MWCNT [12]. The whole mechanism involved is a non-catalytic process.

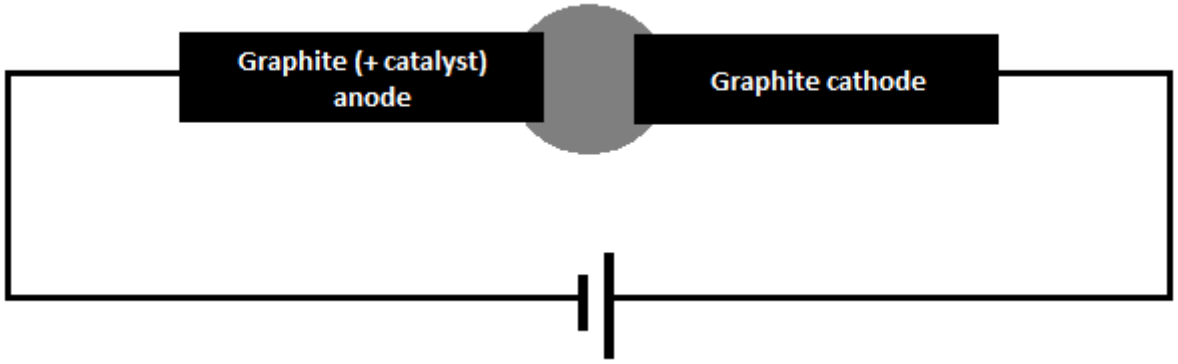

Figure A12: Schematic drawing of the principle of arc discharge [12].

SWCNT production becomes dominant and favourable in an arc discharge technique when small amounts of transition metal catalyst particles of Fe, Co, Ni [12] or rare-earth metals [13] are introduced in the target graphite electrodes. This approach involves an element of co-vaporisation (evaporation) of the graphite (carbon) and the metal (catalyst) during the arc discharge process [12, 13], and hence, it is partially catalytic in nature.

A2.2 Laser ablation

Similar to the arc method, the laser ablation also consists of graphite sublimation in a reduced atmosphere of rare gases. In this technique, the process involves heating a quartz tube in a furnace to about 1200 °C, while maintaining a flow of argon at a sub-atmospheric pressure (Figure A13). Loiseau (2006) described in further detail the two types of methods developed in laser ablation, namely pulsed laser and continuous laser.

In the pulsed-laser configuration, the tube contains a block of compressed graphite (or graphite and catalyst, in the partially catalytic laser ablation process that favours SWCNT production), which becomes a target for a focused laser beam ablation, in an inert atmosphere and at a low pressure. The graphite block is vaporised and converted into smaller aggregates by the intense pulsed laser radiation. These aggregates are then placed in an external furnace heated to 800 °C and beyond, and hence a temperature condition suitable for the growth of

long carbon nanotubes is generated. On the other hand, the continuous-laser configuration applies a 2-kW continuous-wave CO_2 laser to focus on the graphite target, which heats the graphite up to a temperature above 3000 K.

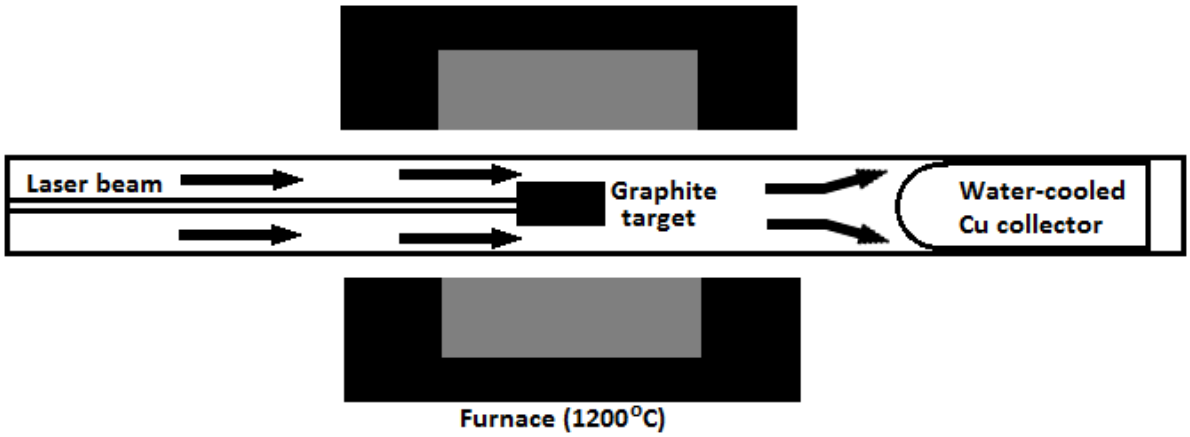

Figure A13: Schematic drawing of the principle of laser ablation [7, 12, 13].

A2.3 Chemical vapour deposition

Essentially, there are three items that need to be present in chemical vapour deposition, namely catalyst nanoparticles, carbon precursor and heat. These three items will have combined effects on the resultant structure of the filamentous carbon layer. The synthesis is generally sensitive to many factors, and researchers have been attempting to establish an understanding of the changes in carbon nanomaterials' structure through adjustments of various parameters.

Prior to synthesising the carbon nanomaterials using the CVD technique, the active catalysts need to be first prepared. Among the techniques employed to prepare the catalysts are colloids, sol-gel, impregnation and physical vapour deposition, to name a few. These catalyst preparation techniques were described by Dupuis (2005) [19] and Moisala *et al.* (2003) [20] in their review articles. There have also been various reactor configurations applied by researchers in the CVD technique such as the horizontal (Figure A14) and vertical furnaces.

Furthermore, there have also been a variety of techniques to catalyse the growth of carbon nanomaterials used such as supported and unsupported (floating) catalyst methods and aerosol synthesis [1, 19, 20].

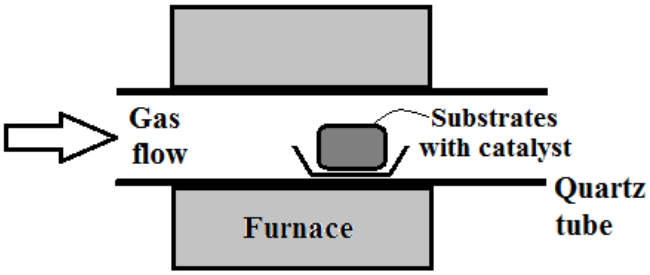

Figure A14: Typical setup to grow carbon nanostructures *via* CVD [1].

In general, every change in any of the contributing factors would result in synthesis of different carbon filament structures, and hence, achieving the structure of our aim can be a challenge. For instance, an increasing size of metal catalyst particles will produce the carbon nanotubes that range from single-walled to multi-walled, and the different particle sizes are dependent on the type of catalyst precursor used. In addition, different types of metal catalyst will favour different structures. Single metal and bi-metal catalysts will introduce different structures and qualities.

The effect of catalyst pre-treatment also contributes to varying the nanostructure of the carbon nanomaterials produced, where too much hydrogen used in the catalyst reduction will tend to produce single-walled carbon nanotubes. In addition, a saturated carbon precursor will tend to produce single-walled while an unsaturated hydrocarbon will favour the production of multi-walled carbon nanotubes. A higher concentration of hydrocarbons will favour decomposition into multi-walled carbon nanotubes instead of single-walled.

Elevated growth temperatures will tend to produce a better crystallinity of the carbon nanotubes but this condition favours the production of single-walled carbon nanotubes. Therefore, an optimisation of the growth temperature is required should one wish to produce

multi-walled carbon nanotubes for their intended application. Simultaneously fine tuning all these parameters in order to synthesise the desired structure with the specific qualities for the desired application remains a challenge, but possible.

References of APPENDIX A

1. Teo, K.B., et al., *Catalytic synthesis of carbon nanotubes and nanofibers*, in *Encyclopedia of nanoscience and nanotechnology (Vol. 10)*, H.S. Nalwa, Editor. 2003, American Scientific Publishers: USA. p. 1-22.
2. Taha, T.J., et al., *Effect of carbon nanofiber surface morphology on convective heat transfer from cylindrical surface: Synthesis, characterization and heat transfer measurement.* International Journal of Thermal Sciences, 2016. **105**: p. 13-21.
3. Feng, L., N. Xie, and J. Zhong, *Carbon nanofibers and their composites: a review of synthesizing, properties and applications.* Materials, 2014. **7**(5): p. 3919-3945.
4. Zheng, R., et al., *Preparation, characterization and growth mechanism of platelet carbon nanofibers.* Carbon, 2006. **44**(4): p. 742-746.
5. Terrones, H., et al., *Graphitic cones in palladium catalysed carbon nanofibres.* Chemical physics letters, 2001. **343**(3): p. 241-250.
6. Harris, P.J.F., *Carbon nanotube science: synthesis, properties and applications*. 2009: Cambridge university press.
7. Harris, P.J.F., *Synthesis: Preparation methods, growth mechanisms and processing techniques*, in *Carbon Nanotubes and Related Structures (New Materials for the Twenty-first Century)*, P.J.F. Harris, Editor. 1999, Cambridge University Press: Cambridge, United Kingdon. p. 16.
8. Wiles, P. and J. Abrahamson, *Carbon fibre layers on arc electrodes—I: their properties and cool-down behaviour.* Carbon, 1978. **16**(5): p. 341-349.
9. Han, J., *Structures and Properties of Carbon Nanotubes*, in *Carbon Nanotubes Science and Applications*, M. Meyyappan, Editor. 2005, CRC Press: United States of America. p. 1.
10. Wunderlich, W.T., M., *Plasma-CVD Growth of Carbon nano-Tubes on Metal Substrates*, in *Trends in Nanotubes Research*, D.A. Martin, Editor. 2006, Nova Science Publishers: New York.

11. Tanaka, K.O., M.; Huang, Y., *Electronic Structures of Single-Walled Carbon Nanotubes*, in *The Science and Technology of Carbon Nanotubes*, K.Y. Tanaka, T.; Fukui, K., Editor. 1999, Elsevier Science Ltd.: The Netherlands.
12. Loiseau, A.B., X.; Charlier, J.; Gadelle, P.; Journet, C.; Laurent, C.; Peigney, A., *Synthesis Methods and Growth Mechanisms*, in *Understanding Carbon Nanotubes: From Basics to Applications*, A.L. Loiseau, P.; Petit, P.; Roche, S.; Salvetat, J.P., Editor. 2006, Springer, Berlin Heidelberg: The Netherlands.
13. Yumura, M., *Synthesis and purification of multi-walled and single-walled carbon nanotubes.* The Science and Technology of Carbon Nanotubes, 1999: p. 1.
14. Hou, P.-X., C. Liu, and H.-M. Cheng, *Purification of carbon nanotubes.* Carbon, 2008. **46**(15): p. 2003-2025.
15. Baker, R.T.K., *Catalytic growth of carbon filaments.* Carbon, 1989. **27**(3): p. 315-323.
16. Baharudin, L. and M.J. Watson, *Hydrogen applications and research activities in its production routes through catalytic hydrocarbon conversion.* Reviews in Chemical Engineering, 2017. **34**(1): p. 43-72.
17. Chinthaginjala, J.K., K. Seshan, and L. Lefferts, *Preparation and Application of Carbon-Nanofiber Based Microstructured Materials as Catalyst Supports.* Industrial & Engineering Chemistry Research, 2007. **46**(12): p. 3968-3978.
18. Moravsky, A.P., E.M. Wexler, and R.O. Loutfy, *Growth of carbon nanotubes by arc discharge and laser ablation.* Carbon nanotubes Science and Applications. CRC Press. Boca Ratón, US, 2005: p. 65-97.
19. Dupuis, A.-C., *The catalyst in the CCVD of carbon nanotubes—a review.* Progress in Materials Science, 2005. **50**(8): p. 929-961.
20. Moisala, A., A.G. Nasibulin, and E.I. Kauppinen, *The role of metal nanoparticles in the catalytic production of single-walled carbon nanotubes—a review.* Journal of Physics: condensed matter, 2003. **15**(42): p. S3011.

APPENDIX B

Development of copper nanostructure/multi-walled carbon nanotubes (Cu/MWCNT) catalyst: PRELIMINARY INVESTIGATIONS

B1. Pre-treatment of carbon nanotubes' surface

This section covers the objectives of the carbon nanotubes' surface functionalisation and purification, and the techniques presented in the literature for an adoption in the preliminary work.

B1.1 The purpose of surface pre-treatment: Literature review

The functionalisation and purification of the carbon nanotubes' surface for a catalysis application has a couple of objectives. Firstly, the steps are vital in the catalyst synthesis procedure to allow well-dispersed metal particles to be deposited on its surface and to improve the stability of the catalyst for its longevity under reaction conditions. Secondly, the functionalisation enhances the interaction of the synthesised catalyst with the reactant.

An experiment by Prado-Burguete *et al.* (1989) [1] demonstrated that the oxygen-containing functional groups grafted on the carbon support surface play a significant role in the metal nanoparticles dispersion, where it was found that the platinum nanoparticle dispersion improved with an increase in the amount of oxygen-moiety groups, while all other parameters such as the carbon's porosity and the catalysts synthesis procedure were kept consistent in all samples.

It must be noted however that the nature of the carbon–oxygen structures has not been fully understood. It has been suggested that the presence of the functional groups on the carbon's surface gives an acid-base character to the support, and the acid-base adsorption properties as well as the amount of oxygen groups generated vary with the pre-treatment conditions employed and the oxidising agents used. Other factors include the carbon's surface area, particle size, ash content and degree of carbonisation [2] or graphitisation.

The pre-treatment using hydrogen peroxide (H_2O_2) by Prado-Burguete *et al.* (1989) [1] demonstrated that the oxygen groups brought down the level of hydrophobicity of the carbon and hence, the carbon's surface became more accessible to the aqueous solution of the metal precursor during catalyst synthesis using wet impregnation technique. Additionally, the oxygen groups improved the interaction between the carbon's surface and the metal nanoparticles and hence, improved the metal nanoparticles dispersion and reduced their sintering propensity.

Typically, the pristine (raw) carbon nanomaterials contain carbonaceous impurities in the form of amorphous carbon encapsulated in the graphitic carbon. Metal impurities may also be present in the nanomaterials synthesised by the catalytic techniques. A further purification treatment by heat under hydrogen environment at 350 °C enhanced the stability of the oxygen-containing groups (the less stable oxygen groups decomposed below this temperature), and consequently resulted in the anchorage of the platinum nanoparticles to be more effective, and hence, enhanced the thermal stability of the nanoparticles supported on the carbon [1].

B1.2 Techniques in purification and functionalisation of carbon nanomaterials sidewall surface: Literature review

Common techniques employed to purify and functionalise the sidewall surface of carbon nanomaterials are presented below.

B1.2.1 Non-covalent method

Li, X.L. *et al.* (2006) [3] presented the functionalisation of the inherently hydrophobic surfaces of pristine multi-walled carbon nanotubes (MWCNT) by a non-destructive (non-covalent) method, where the surface was modified using 1-aminopyrene, which introduced a non-covalent interaction between the pyrenyl groups and the hexagonal carbon rings. This pre-treatment step resulted in amino-modified CNT, which was ready for metal nanoparticles deposition. The amino-modified CNT adsorbed the metal nanoparticles through the mechanisms of electrostatic interactions and/or preferential affinity.

B1.2.2 Covalent method

Various comparative studies on the carbon nanotubes surface functionalisation characterisation based on treatments with various acidic and basic solutions have been presented in the literature [4-8]. The oxidative chemical treatments do not only effectively remove the poorly conducting non-graphitic carbonaceous species, but they also generate the surface polar, hydrophilic groups by the introduction of the oxygen-containing moieties such as hydroxyl and carboxyl for favourable chemical interaction with various polar solvents in terms of homogeneity, surface chemistry, structure, aqueous dispersibility and sedimentation.

These methods are categorised as covalent functionalisation of the pristine carbon nanomaterials, where the oxidative treatment needs to be properly controlled. If treated too excessively they would have an impact on the graphitic structure's integrity where the carbon nanomaterials may be damaged and hence, their thermal stability, mechanical properties and electrical conductivities would considerably be affected by the defects [5, 7].

B1.2.2.1 Non-oxidative acid treatment

Hamilton *et al.* (2013) [9] presented a purification step by a non-oxidative acid treatment using hydrochloric acid (HCl). In principal, the HCl treatment is not able to introduce oxygen-containing groups which are responsible in enhancing the functionalisation of the carbon nanomaterials surface, but able to enhance the exposure of amorphous carbon encapsulated in the graphitic carbon. The hydroxyl group (–OH) grafted on the disordered carbon surface leads to an effective water dispersibility, and at the same time the anionic chloride from the acid electrochemically reacts with the cationic metal to form metal chloride that remains in the liquid phase. Therefore, the hydroxylated amorphous carbon and the metal chloride in the liquid are easily removed from the carbon nanomaterials by centrifugation and decantation, leaving behind the purified graphitic carbon.

B1.2.2.2 Oxidative acid and basic treatment

Nitric acid (HNO_3) is known to react strongly with aromatic carbon surfaces and carbon nanotubes [10]. A further treatment with the carboxyl (–COOH) moiety using HNO_3 results in surface carboxylation of the carbon nanomaterials [9], now functionalised and ready for the deposition of the active metal particles (*e.g.* by wet impregnation or precipitation) for catalysis application. The carboxyl group helps decrease the hydrophobicity of the carbon nanomaterials, and hence, allows an effective synthesis of the catalytic metal particles, in which the precursor is typically dissolved in water. In addition, this functional group also makes the surface charge more negative [9] and therefore, would attract more cationic metal particles to be adsorbed onto the surface for an effective application as a catalyst.

Purification and functionalisation with a mixture of sulphuric acid (H_2SO_4) and HNO_3 have also been demonstrated prior to synthesising the catalytic metal particles [11-12]. Other oxidative reagents used in the chemical oxidation for the carbon nanomaterials surface functionalisation include a mixture of H_2SO_4 and hydrogen peroxide (H_2O_2), as well as a basic oxidative treatment by a mixture of ammonium hydroxide (NH_4OH)/H_2O_2[7].

B1.2.2.3 Air oxidation treatment

According to Datsyuk *et al.* (2008) [7] and Moraes *et al.* (2011) [4], different structural forms of carbon exhibit different level of thermal stability based on thermogravimetric analysis (TGA). The disordered (amorphous) carbon has the tendency to get oxidised under mild conditions of approximately 500 °C due to its high density of defects, whereas temperatures of 600 °C or higher are required for the oxidation of the well graphitised carbon structure due to a higher activation energy requirement. Stancu *et al.* (2011) [13] demonstrated a further purification step to remove the defective carbon by air oxidation at 550 °C, post HCl and HNO_3 treatments. The results revealed a cleaner surface of the MWCNT based on their characterisation analysis.

B1.2.2.4 Hummer's method

In the synthesis of graphene oxide, the graphite is oxidised by the popular Hummers' method to introduce various oxygen-containing groups. Various editions to the original method (known as improved and modified Hummers' methods) have been initiated to reduce the safety risks associated with handling the high concentration of the reagents, and the release of toxic gases in the procedure [10, 14-16]. These method, although have not been adopted in the carbon nanomaterials pre-treatment for the catalyst synthesis, is another option for the surface functionalisation.

B1.2.2.5 Polymer wrapping

The researchers working on the carbon nanotubes in making sensing devices and other electronic applications generally prefer a technique called polymer-wrapping to functionalise the sidewall surface [17-21]. Similar to catalyst synthesis, polymer-wrapping has an initial procedure prior to assembling the metal nanoparticles on the carbon nanotubes in an aqueous

solution. The carbon nanotubes are wrapped using polyelectrolytes that provide the adsorption sites for an electrostatic metal nanoparticle deposition. Depending on the charge required on the surface, the CNT is wrapped with a negatively charged polystyrene sulfonate (PSS), followed by an electrostatic assembly of a cationic poly(diallyldimethyl) ammonium chloride (PDDA), prior to the metal nanoparticle deposition. The polyelectroyte bilayers result in well dispersed CNT in an aqueous medium [17-19]. For an application that requires a highly negative charged surface of the CNT such as in catalysis, a single layer of PSS is already sufficient as this polyelectrolyte possesses a high density of negatively-charged sulfonate functional groups for homogeneous adsorption of the cationic metal nanoparticles, on top of decreasing the hydrophobicity of the CNT's surface.

B1.3 Surface functionalisation by hydrogen peroxide treatment in current preliminary work: Basis of selection

As seen earlier, oxygen-containing groups can be formed by reaction with oxygen and other oxidising gases such as ozone, nitrous oxide, nitric oxide and carbon dioxide. Alternatively, pre-treatment can also be done using oxidising solutions such as nitric acid, hydrogen peroxide, *etc.* To minimise the safety risk of handling high concentration acids, studies have been conducted on the effect of functionalising the MWCNT's surface with hydrogen peroxide only, which is the oxidising agent used in the preliminary study of this research work.

In a H_2O_2 treatment presented by Salmoria *et al.* (2013) [8], 0.3 g of MWCNT was dispersed in H_2O_2 (10%) solution in a flask by ultrasonication for 1 hour, followed by a reflux at 100 °C, and varied durations of 5, 10 and 15 hours. The suspension was then vacuum-dried and washed with an abundant amount of deionised (DI) water and acetone, followed by an 8-hour oven-drying at 100 °C.

In another technique, Peng & Liu (2006) [22] presented the procedure of functionalisation of the MWCNT's surface by H_2O_2 oxidation by stirring 0.5 g of MWCNT in 10 mL of H_2O_2

(30%) at 65 °C, at varied durations of 1 to 6 days. For treatment that took longer than a day, 5 mL of H_2O_2 was added to the mixture on daily basis in order to maintain sufficient concentration of H_2O_2. A 0.45 μm Milli-pore polyvinylidene difluoride membrane was used to filter the treated MWCNT and the filtrate was then washed with DI water, followed by an overnight drying at 110 °C. Finally, the treated MWCNT was vacuum-dried at 150 °C for 6 hours for the removal of any possible H_2O_2 adsorbed and peroxide groups attached on their surface.

They reported the effect of the treatment duration on the final quality of the treated MWCNT, in terms of the functional groups generation on the MWCNT's surface as well as the changes to the degree of graphitisation of the MWCNT's structure as the oxidation was elongated. An X-ray photoelectron spectroscopy (XPS) analysis revealed the formation of several oxygen-containing functional groups; carboxylic (–COOH), carbonyl (–C=O), and hydroxyl (–OH) on the surface of the MWCNT, dominated by the last group. However, a maximum atomic concentration of slightly above 45% of the hydroxyl groups was reached in the fourth day of the H_2O_2 oxidation, followed by the domination of the carbonyl groups in a further extended oxidation.

The effect of H_2O_2 oxidation on the morphologies and structures of the MWCNT were also investigated. It was revealed that the ratio of the (1 0 0) diffraction peak to the (0 0 2) diffraction peak (I_{100}/I_{002}) from X-ray diffraction (XRD) patterns decreased in the first 2 days of the H_2O_2 oxidation, but continued to increase as the oxidation progressed to the sixth day. The I_{100}/I_{002} ratio provided the information on the MWCNT's tubular length in such a way that the intensity of the (1 0 0) peak is the least if most parts of the MWCNT sample are parallel to the (0 0 2) plane. Their guess was that the change of I_{100}/I_{002} was a result of the breaking of the MWCNT, where the breaking of the originally longer tubes into shorter length increased the degree of alignment to the (0 0 2) plane, causing the ratio to decrease in the initial 2 days. Further breaking of the MWCNT's tubular length occurred as the oxidation progressed, resulting in a further increase in the content of nanotube ends ((1 0 0) plane) and thus, further increase in I_{100}/I_{002} was observed. The findings suggested a possibility of breakage of the tubular length in prolonged oxidation.

The findings above were further validated by another analysis using a Raman spectrometer at excitation spectra of 325, 488 and 514.5 nm. The G band and the disorder-induced D and D' bands revealed a decreasing degree of graphitisation in the first day of the oxidation, but the graphitisation degree increased in the prolonged oxidation days. This suggested an existence of disordered carbon in the original sample and a deformation of the graphitic carbon in the beginning of the H_2O_2-oxidation that were then removed as the oxidation progressed, while an elongated oxidation caused a breaking of the tubular length of the graphitised carbon nanotubes, making their length shorter.

TGA revealed a very low thermal stability of the sample that was H_2O_2-oxidised in the first day, where the carbon thermal gasification occurred at a temperature of as low as 128 °C, revealing the existence of some disordered carbon in the original sample, as well as an introduction of carbon deformation in the beginning of the H_2O_2-oxidation. This is in good agreement with the characterisation by XRD and Raman spectroscopy above. As the oxidation progressed into a greater number of days, the thermal stability improved due to the defected carbon removal. At the end of the sixth oxidation day, the carbon gasification in TGA did not take place until the temperature reached 580 °C, which shows that the remaining content of the carbon sample was made of reasonably highly graphitised structures, although the tubular length of the nanotubes had reduced. In order to appreciate these findings, a TEM characterisation analysis was also performed to validate the morphological change. It was concluded by Peng & Liu (2006) [22] that the functionalisation of MWCNT by H_2O_2 oxidation acted to remove the disordered carbon materials that were originally existing in the pristine sample and formed as a result of the graphitic carbon damage due to the treatment (in the beginning). Using the procedure developed in their work, the purification took place in the first 1 to 2 days of H_2O_2 oxidation, but a prolonged treatment to functionalise the graphitic carbon surface would cause breaking of the tubular length of the carbon nanotubes.

Based on the literature review above, we decided to functionalise the MWCNT using H_2O_2 in our preliminary study, as the technique had proven to be capable of generating various

oxygenated functional groups on the MWCNT's surface for the purpose of synthesising our catalysts. In our work however, a milder treatment condition was developed in the procedure with oxidation duration of less than a day, in order to prevent the deformation of the graphitic structure of the MWCNT and the breaking of their tubular length, which theoretically introduces adverse effects on their thermal stability if not properly taken care of during the treatment process.

B2. Preliminary work: Experimental

Multi-walled carbon nanotubes (MWCNT) (Sigma-Aldrich, ≥ 98% carbon basis, produced by catalytic chemical vapor deposition using CoMo catalyst) was used in this part of the study. The MWCNT was functionalised by hydrogen peroxide treatment following the procedures developed in the Chemical and Process Engineering Laboratory, University of Canterbury, described below.

B2.1 Pre-treatment of carbon nanotubes' surface by hydrogen peroxide and air

The pre-treatment of the carbon nanotubes' surface involves two major steps; functionalisation by hydrogen peroxide oxidation followed by purification by air.

B2.1.1 Hydrogen peroxide treatment

A beaker containing an unquantified amount of as-received MWCNT was added with a H_2O_2 solution (35%) (UNILAB) of sufficient volume to immerse all of the MWCNT used. The beaker was placed in a water bath on a hot plate stirrer. The sample was heated and stirred continuously at 80 °C for 4 hours. The H_2O_2-treated MWCNT sample was rinsed with DI water and centrifuged (MULTIFUGE 3 L, Heraeus) at 4000 rpm for 10 minutes, followed by decantation of the DI water. The separated treated MWCNT sample was dried overnight in an

oven (LabServ) at 80 °C. The dried sample was crushed using mortar and pastel to make very fine powder, followed by a further drying in the oven at 80 °C for another couple of hours. The pristine MWCNT sample and the H_2O_2-treated MWCNT are denoted as $MWCNT_p$ and $MWCNT_{hp}$ respectively.

B2.1.2 Air oxidation

The samples of pristine MWCNT and H_2O_2-treated MWCNT were air oxidised at 550 °C in a horizontal tubular furnace (SDT Q600, Alphatec Systems Limited) for 10 minutes, at a temperature ramping rate of 10.6 °C/min from the ambient condition. (Note: Throughout the work performed and reported in this Appendix, the temperature controller of the furnace might have been poorly tuned that there could be a possibility the final temperature was overshot by 20 °C or more. This was not measured at this stage of the work as no independent thermocouple recording the sample temperature inside the furnace was used.). This is a purification step adopted from Stancu *et al.* (2011) [13] to remove the presence of low thermal stability disordered non-graphitic carbon. The air oxidised pristine MWCNT sample and the air oxidised H_2O_2-treated MWCNT are denoted as $MWCNT_{p,air}$ and $MWCNT_{hp,air}$ respectively.

B2.2 Copper nanoparticles deposition onto the H_2O_2-treated MWCNT

There were two types of copper precursor used in this preliminary part of the work; copper (II) chloride dihydrate ($CuCl_2.2H_2O$) (AnalaR, The British Drug Houses Ltd.) dissolved in DI water and copper (II) acetate monohydrate ($Cu(CO_2CH_3)_2.H_2O$) (ACROS Organics) dissolved in ethanol as the solvent. Three different factors in the impregnation technique were employed, in order to compare the outcome of the copper nanoparticles dispersion on the H_2O_2-treated MWCNT ($MWCNT_{hp}$).

The first factor was the variation in copper loading content. Two sets of 20 mL copper chloride solution containing copper amount of 0.06 g (approximately 0.161 g of $CuCl_2.2H_2O$) and 0.01 g each were prepared. Using wet impregnation technique, the solution containing 0.06 g copper was added to an amount of 0.94 g $MWCNT_{hp}$ to make a catalyst sample of 6 wt.% copper loading, and similarly for the 1 wt.% copper loading catalyst sample. The samples were stirred at 410 rpm on a hot plate stirrer kept at 40 °C overnight. The copper impregnated MWCNT samples were then centrifuged at 4000 rpm for 10 minutes, followed by decantation of the solution and drying for 2 hours at 120 °C. The dry catalyst samples were then calcined in air at 475 °C in a muffle furnace for approximately 10 hours, as a heat treatment step to improve the interaction between the metal nanoparticles and the surface of the MWCNT support. The 6% and 1% copper loading catalyst samples are denoted as 6%Cu/$MWCNT_{hp}$ and 1%Cu/$MWCNT_{hp}$ respectively.

The second factor was the metal deposition technique employed. The deposition of the copper nanoparticles on the $MWCNT_{hp}$ was done by incipient wetness impregnation to compare with the catalyst prepared by wet impregnation technique above. A copper chloride solution containing 0.01 g copper was prepared in the DI water of a volume just enough to cover all the $MWCNT_{hp}$ amount (0.99 g) used to prepare the catalyst sample. (Note: Approximately 5 mL of solution is required to cover an amount of 0.99 g of MWCNT.). The copper chloride solution added to the $MWCNT_{hp}$ was stirred manually for 10 minutes in order to allow capillary effect to act on adsorbing the copper nanoparticles into the internal walls of the $MWCNT_{hp}$ and the pores of their surface. The catalyst sample was dried for 2 hours at 120 °C, followed by air calcination at 475 °C for approximately 10 hours. The sample is denoted as 1%Cu/$MWCNT_{hp,incipient}$.

The third factor was the type of copper precursor. A solution containing 0.01 g copper was prepared by dissolving $Cu(CO_2CH_3)_2.H_2O$ in an organic solvent; ethanol. The copper acetate solution was added to 0.99 g of $MWCNT_{hp}$. The mixture was stirred at 410 rpm on a hot plate stirrer kept at 40 °C for an overnight, followed by centrifugation at 4000 rpm for 10 minutes, decantation, 2 hours drying at 120 °C, and calcination in 100 mL/min nitrogen flow in a tubular furnace (GSL1500X, MTI Corporation) (Figure B1) at 350 °C for 8 hours, with temperature ramping rate of 2.7 °C/min. The sample is denoted as 1%Cu/$MWCNT_{hp,CuAc}$.

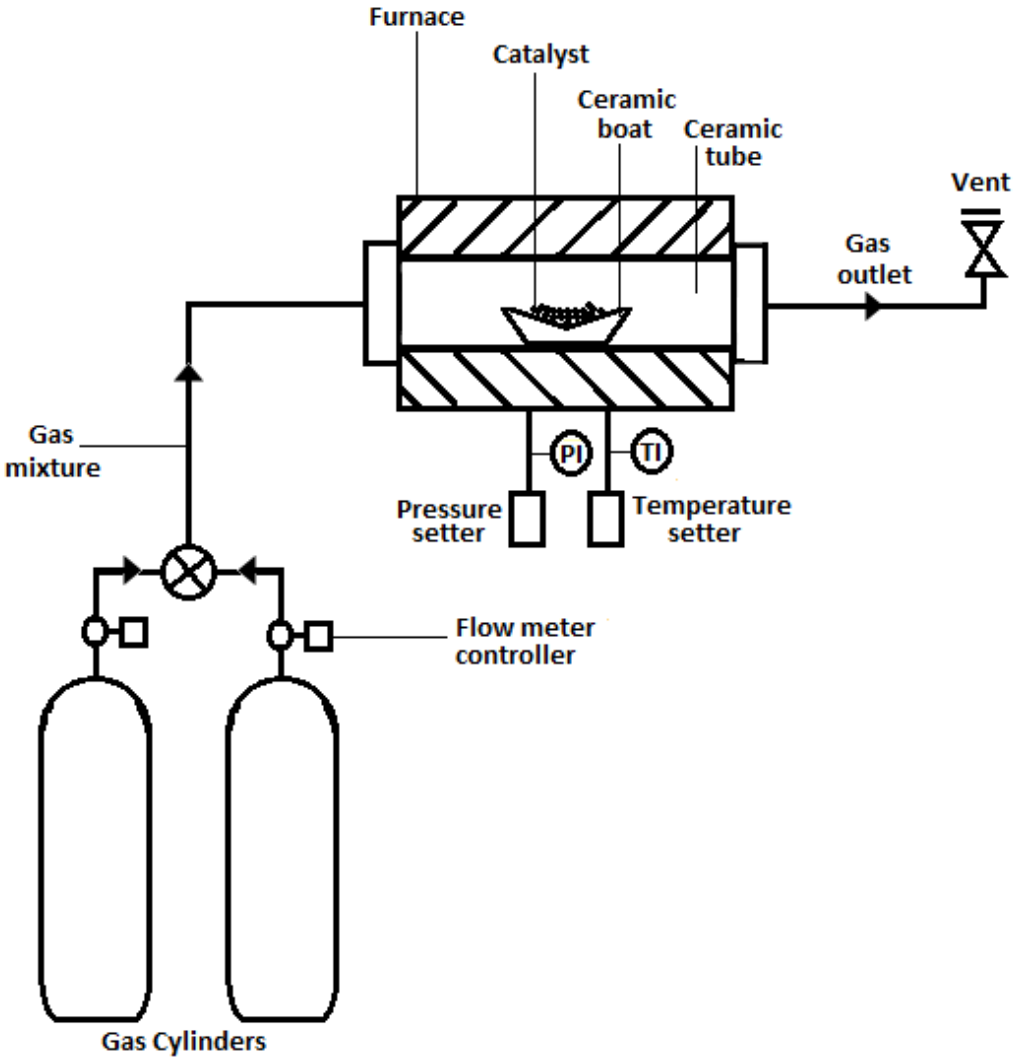

Figure B1: Horizontal tubular furnace setup for calcination.

Table B1 summarises the copper/MWCNT catalyst samples prepared in this preliminary work.

Table B1: Synthesised catalysts in the preliminary study.

Sample	6%Cu/MWCNT$_{hp}$	1%Cu/MWCNT$_{hp}$	1%Cu/MWCNT$_{hp,incipient}$	1%Cu/MWCNT$_{hp,CuAc}$
Technique	Wet impregnation (40 °C overnight)	Wet impregnation (40 °C overnight)	Incipient wetness impregnation (manual stirring for 10 min at room temperature)	Wet impregnation (40 °C overnight)
Catalyst precursor	$CuCl_2$ solution of the desired amount of Cu loading (6%)	$CuCl_2$ solution of the desired amount of Cu loading (1%)	$CuCl_2$ solution of the desired amount of Cu loading (1%)	$Cu(OAc)_2$ solution of the desired amount of Cu loading (1%)
Solvent	DI water	DI water	DI water	Ethanol
Calcination	475 °C in air for 10 hours	475 °C in air for 10 hours	475 °C in air for 10 hours	350 °C in 100 mL/min N_2 flow for 8 hours

B2.3 Characterisation

B2.3.1 Fourier-transform infrared spectroscopy

All the MWCNT samples; $MWCNT_p$, $MWCNT_{hp}$, $MWCNT_{p,air}$ and $MWCNT_{hp,air}$ were brought through Fourier-transform infrared (FTIR) spectrometer (Bruker Optics supported by OPUS Mentor software) equipped with a single reflection attenuated total reflectance (ATR), to identify the oxygen-containing groups present on the surface of the supports, before and after functionalisation by H_2O_2 treatment, air oxidation, and the combination of the two. The average of 16 scans was recorded in each spectrum between 4000 and 400 cm^{-1} at a resolution of 1 cm^{-1}.

B2.3.2 Transmission electron microscopy

All the catalyst samples; $6\%Cu/MWCNT_{hp}$, $1\%Cu/MWCNT_{hp}$, $1\%Cu/MWCNT_{hp,incipient}$ and $1\%Cu/MWCNT_{hp,CuAc}$ were analysed under TEM (Philips CM200 supported by Gatan ORIUS^{TM} CCD Camera Controller and Gatan Digital Micrograph software) to characterise the morphology of the copper nanoparticles dispersion on the $MWCNT_{hp}$ support's surface. Each of the samples was first dispersed and ultrasonicated in high purity ethanol (in extremely low concentration of the suspension) and pipetted onto a film grid (carbon coating on 150 mesh Cu) (ProSciTech), and the face where the sample was pipetted on was further coated with carbon using EMS150T ES (Quorum).

B3. Preliminary work: Results and discussion

B3.1 Functionalisation effectiveness

The FTIR analysis shown in Figure B2 revealed that no significant oxygen-containing groups were present on the surface of the H_2O_2-treated MWCNT prior to air oxidation ($MWCNT_{hp}$), which suggested that the H_2O_2 functionalisation was ineffective in modifying the surface. The air oxidation of the pristine MWCNT ($MWCNT_{p,air}$) seemed to have not managed to graft any oxygen-moiety groups on their surface as well, but appeared to have induced a generation of –C-O groups on the H_2O_2-oxidised MWCNT ($MWCNT_{hp,air}$). In order to validate the presence of the –C-O functional group on the $MWCNT_{hp,air}$ surface sample, the FTIR analysis on this particular sample was repeated. The result showed that the oxygen group did not reappear, indicating its unstable presence on the MWCNT's surface, or insignificant presence in terms of amount.

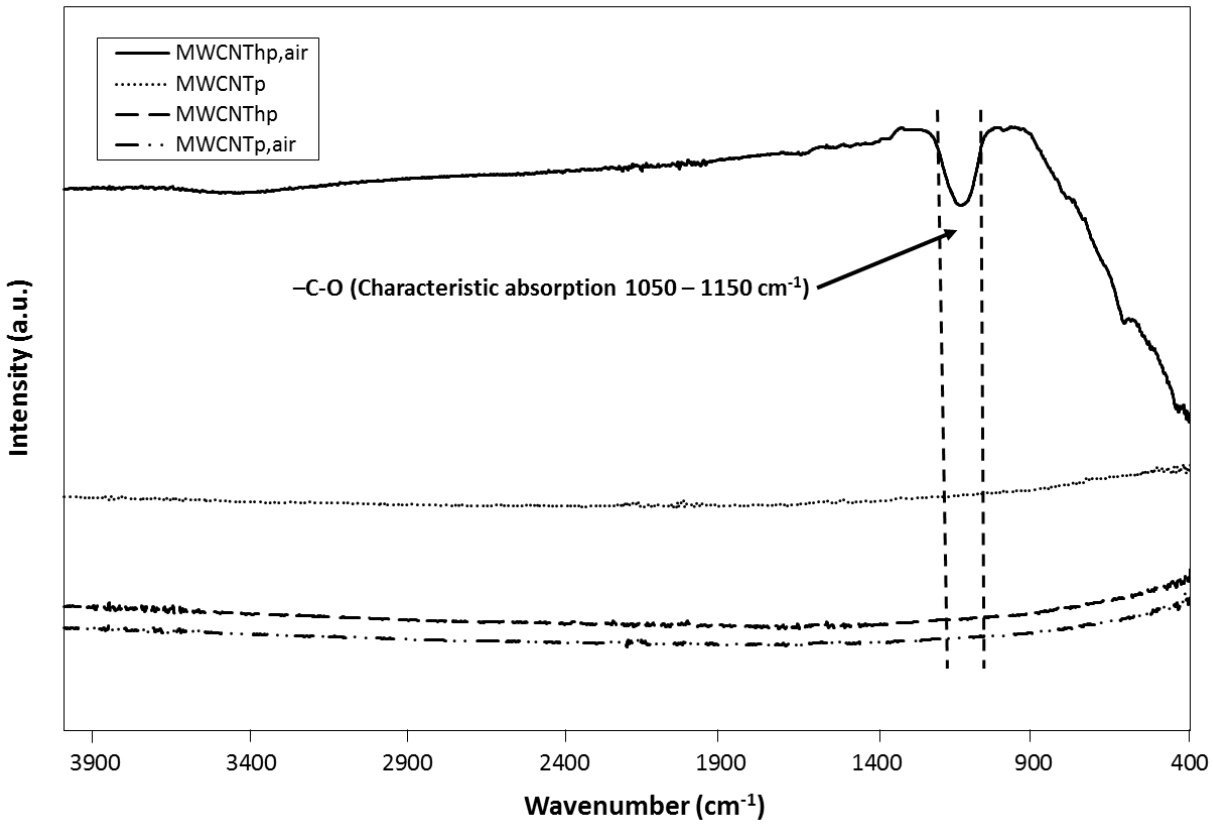

Figure B2: FTIR analysis of the pristine and treated MWCNTs.

It is also worth noting that in this preliminary catalyst synthesis work, the deposition of the copper nanoparticles on the surface of the $MWCNT_{hp}$ was done without prior air oxidation. Air calcination took place after the copper nanoparticles deposition. This means that at the time the catalysts were being synthesised, the MWCNT support used had not been functionalised even slightly. Consequently, the hydrophobicity of the support for improved interaction with the polar solvents used in the copper precursor solutions was not effectively decreased, as shown in Figure B3, which resulted in poor distribution and dispersion of the copper nanoparticles on the support surface, which will be discussed later.

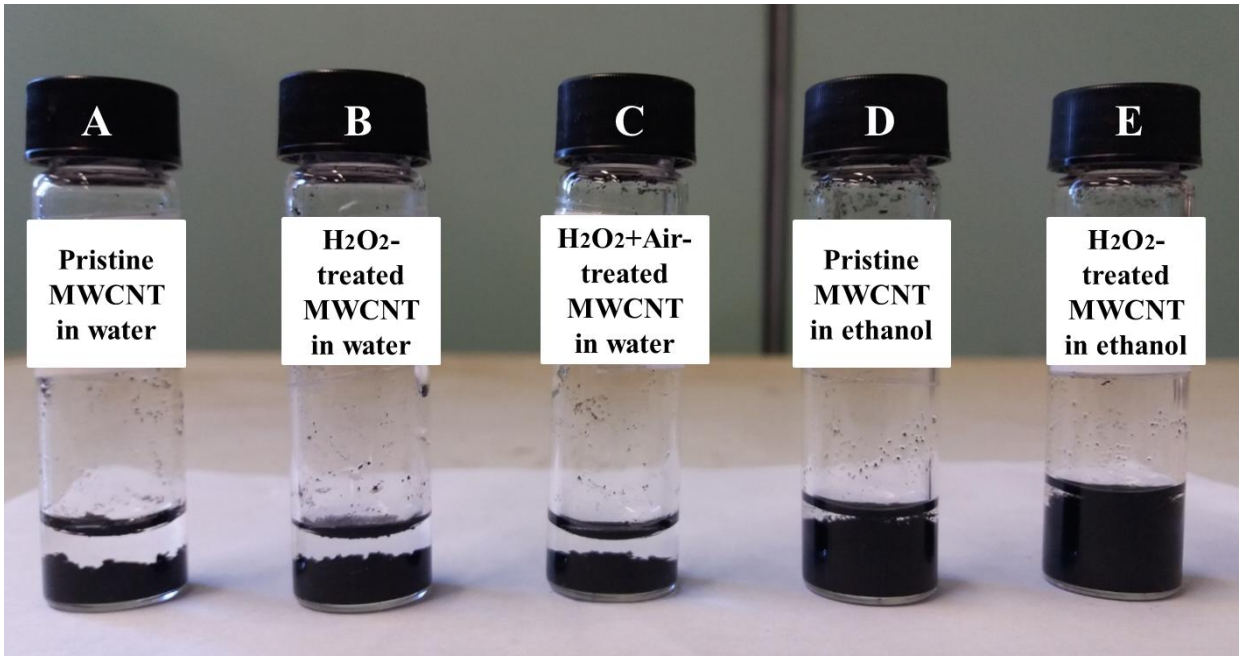

Figure B3: Poor dispersion of: A) $MWCNT_p$ in DI water; B) $MWCNT_{hp}$ in DI water; C) $MWCNT_{hp,air}$ in DI water; D) $MWCNT_p$ in ethanol; and E) $MWCNT_{hp}$ in ethanol.

B3.2 Thermal stability of synthesised catalysts

The preliminary findings revealed that after the long hours of calcination in air at 475 °C in the muffle furnace, the amount of catalyst samples loss was very significant (> 90%), regardless of the synthesis method and the copper loading content used. As mentioned earlier, different structural forms of carbon exhibit different level of thermal stability based on TGA where the disordered carbon has the tendency to get oxidised at approximately 500 °C due to its high density of defects, while higher temperatures than 600 °C are required for the oxidation of the well graphitised carbon structure due to a higher activation energy requirement [4, 7]. This suggests that the amount of impurities in the form of disordered carbon present in the catalyst samples synthesised in this work was significant and therefore their thermal stability was low and hence, carbon oxidation took place during the heat treatment.

The poor thermal stability of the samples could have possibly been caused by several factors. First, the air calcination duration length of approximately 10 hours could have been too

excessive. Second, the presence of CoMo particles encapsulated in the MWCNT originated from their synthesis production might have also catalysed the oxidation of the graphitic carbon at the calcination temperature, in addition to the disordered carbon oxidation. In addition, the presence of the copper nanoparticles deposited on the MWCNT could have also catalysed the oxidation of the amorphous and graphitic carbon. Thirdly, another possibility of the contributing factor to the loss of sample was the introduction of carbon defects due to the damage or deformation of graphitic carbon structure, or the break of the tubular length due to an excessive treatment by hydrogen peroxide; or the pristine (raw) MWCNT used in this work was originally of lower quality with lower degree of carbon graphitisation.

In the synthesis of the catalyst using copper acetate solution, the calcination was conducted at a lower temperature of 350 °C, in a shorter duration and using nitrogen as the purge gas. It was observed that there was no remarkable loss of the amount of sample 1%Cu/$MWCNT_{hp,CuAc}$ after calcination. This suggests that the calcination duration, temperature and purge gas play roles in the calcination step. Therefore, this calcination step will be rectified in the next catalyst synthesis procedure where the duration and temperature will be reduced, and the use of inert gas such as nitrogen as the purge will be implemented.

As discussed by Moraes *et al.* (2011) [4], the oxidation of amorphous carbon can largely be influenced by the presence of iron-based nanoparticles that catalyse the so-called Fenton reaction, producing the oxidant hydroxyl radical (•OH). In our work, the as-received pristine MWCNT used was synthesised by CoMo catalyst and copper nanoparticles were deposited onto the surface of the functionalised MWCNT. It is therefore not a fair comparison to make between our findings and the mechanism proposed by Moraes *et al.* (2011) [4] in order to draw a conclusion. It could however suggest that the metal nanoparticles (CoMo and/or Cu) present in the MWCNT in our preliminary work had catalysed the carbon oxidation, but the mechanism of the catalytic oxidation in our work is not well understood.

Based on the samples of air oxidised MWCNT ($MWCNT_{p,air}$) and H_2O_2-treated MWCNT followed by air oxidation ($MWCNT_{hp,air}$), it was observed that the latter suffered a substantial loss of its original amount (*i.e.* post H_2O_2-treatment, pre air oxidation) even in a very short air

oxidation duration, but the former did not show a similar result. This revealed that the pristine MWCNT received from the supplier was of higher graphitic quality and did not contain significant amount of defected carbon or impurities. On the other hand, the observation suggested that the treatment by H_2O_2 in our work had introduced a deformation of the graphitic carbon structure, or the break of their tubular length. This finding points to the need to use TGA to a greater extent on a small portion of the prepared catalyst before finalising the heat treatment (calcination) step.

A more thorough literature review on the techniques and various other oxidising agents used to functionalise the carbonaceous materials without sacrificing their graphitic structure will be conducted following this finding, in order to rectify the issue. Optimised conditions where the most effective functionalisation without the expense of damaging the graphitic carbon structure, will be employed as part of the future work improvements. This is presented later in APPENDIX C based on a reflection and lessons learned in this preliminary work.

B3.3 Copper nanoparticles dispersion

The resulted copper dispersion on the MWCNT's surface of the synthesised catalyst samples is shown by their respective TEM images in Figure B4. The preliminary work in synthesising the catalyst using copper chloride solution by wet impregnation showed that the presence of copper nanoparticles were in abundance when the copper loading was at 6% (6%Cu/$MWCNT_{hp}$) (Figure B4(A)), whereby the metal particles did not all sit on the surface of the MWCNT. This could have been due to the excessive amount of copper nanoparticles, or their poor interaction with the MWCNT as a result of ineffective MWCNT functionalisation by H_2O_2. In addition, some of the copper nanoparticles appeared to have sintered with each other. In the catalyst sample of 1% copper loading (1%Cu/$MWCNT_{hp}$) (Figure B4(B)), an apparent presence of copper nanoparticles of a more defined structure without significant copper sintering was observed. This suggested that copper loading of *ca.* 1% or less should be used when optimising the copper loading content in the next catalyst synthesis. Too high of a copper loading content would cause the metal particles to sinter. However, the presence of the copper nanoparticles in the system that were not attached well

on the MWCNT support was also found to be excessive, indicating a poor interaction between the copper nanoparticles with the ineffectively functionalised MWCNT.

A

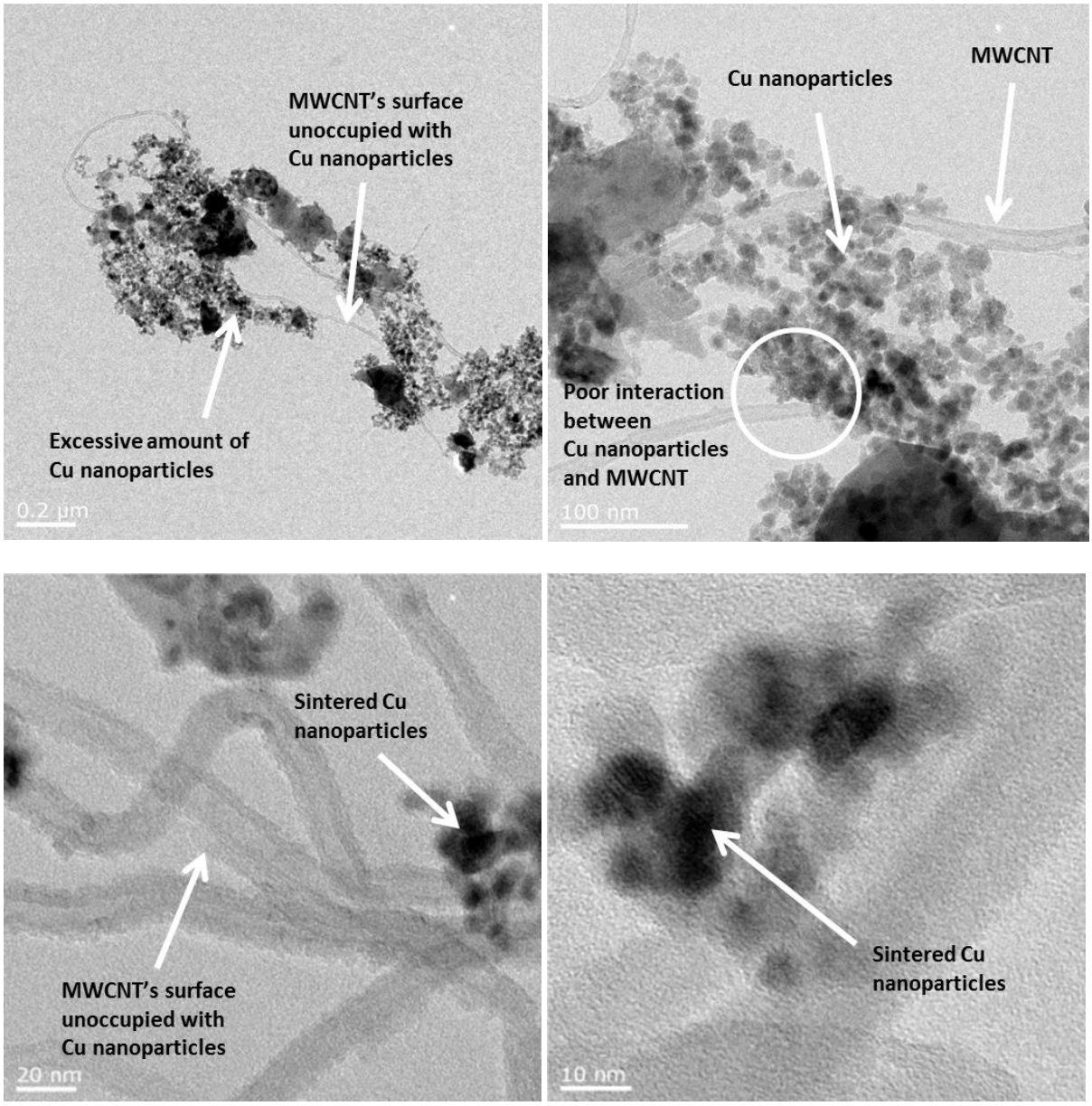

Figure B4(A): TEM images of 6%Cu/MWCNT$_{hp}$.

B

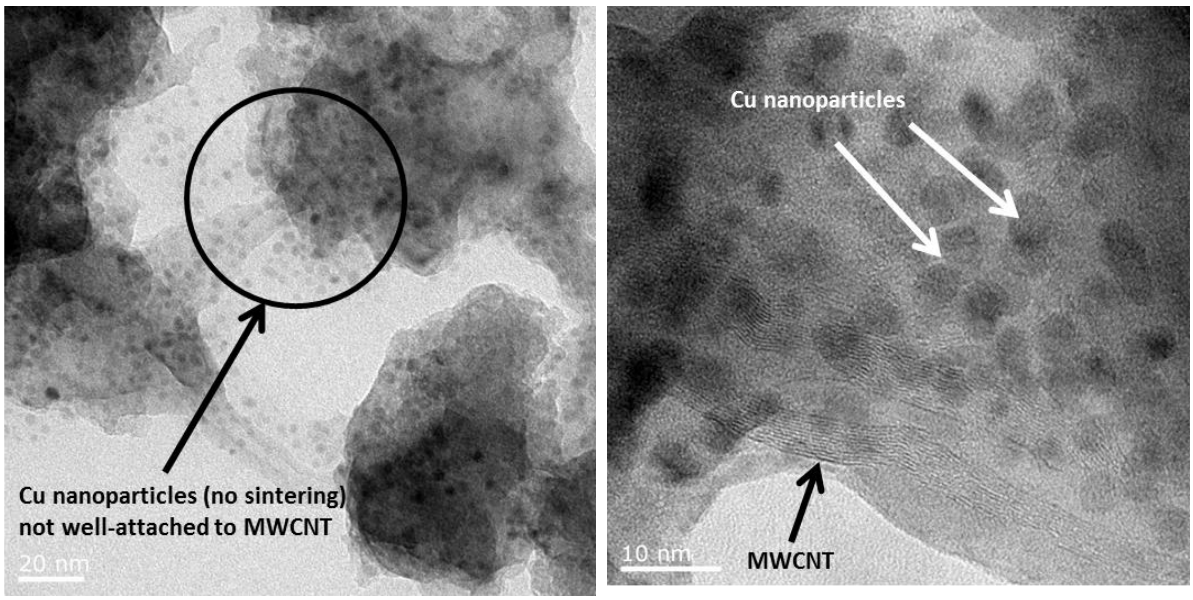

Figure B4(B): TEM images of 1%Cu/MWCNT$_{hp}$.

C

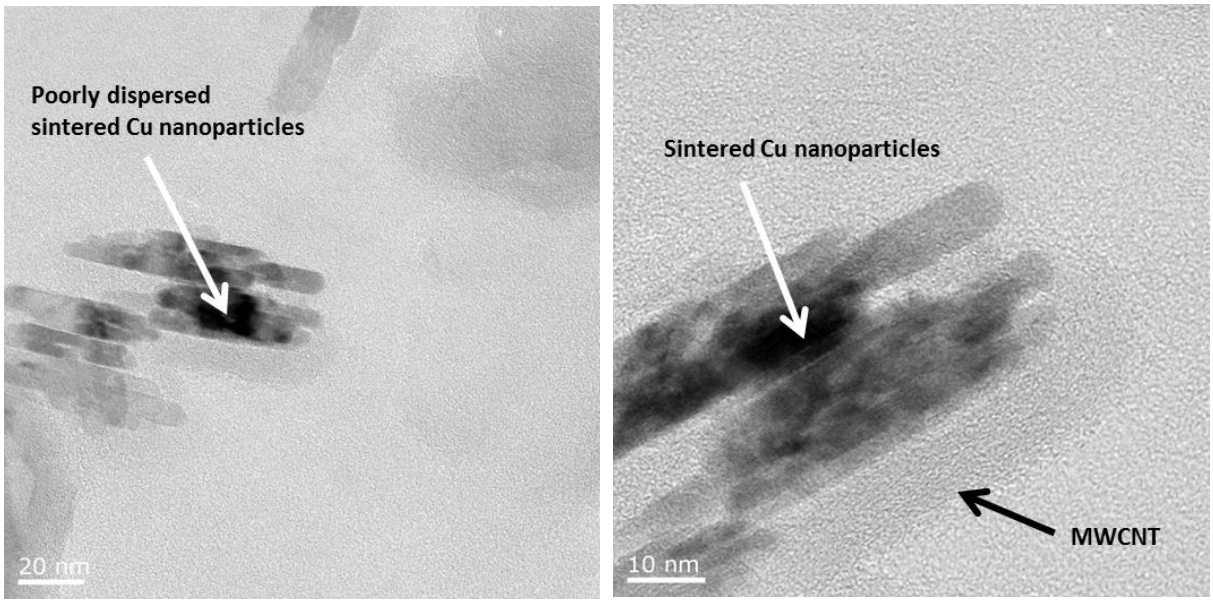

Figure B4(C): TEM images of 1%Cu/MWCNT$_{hp,incipient}$.

D

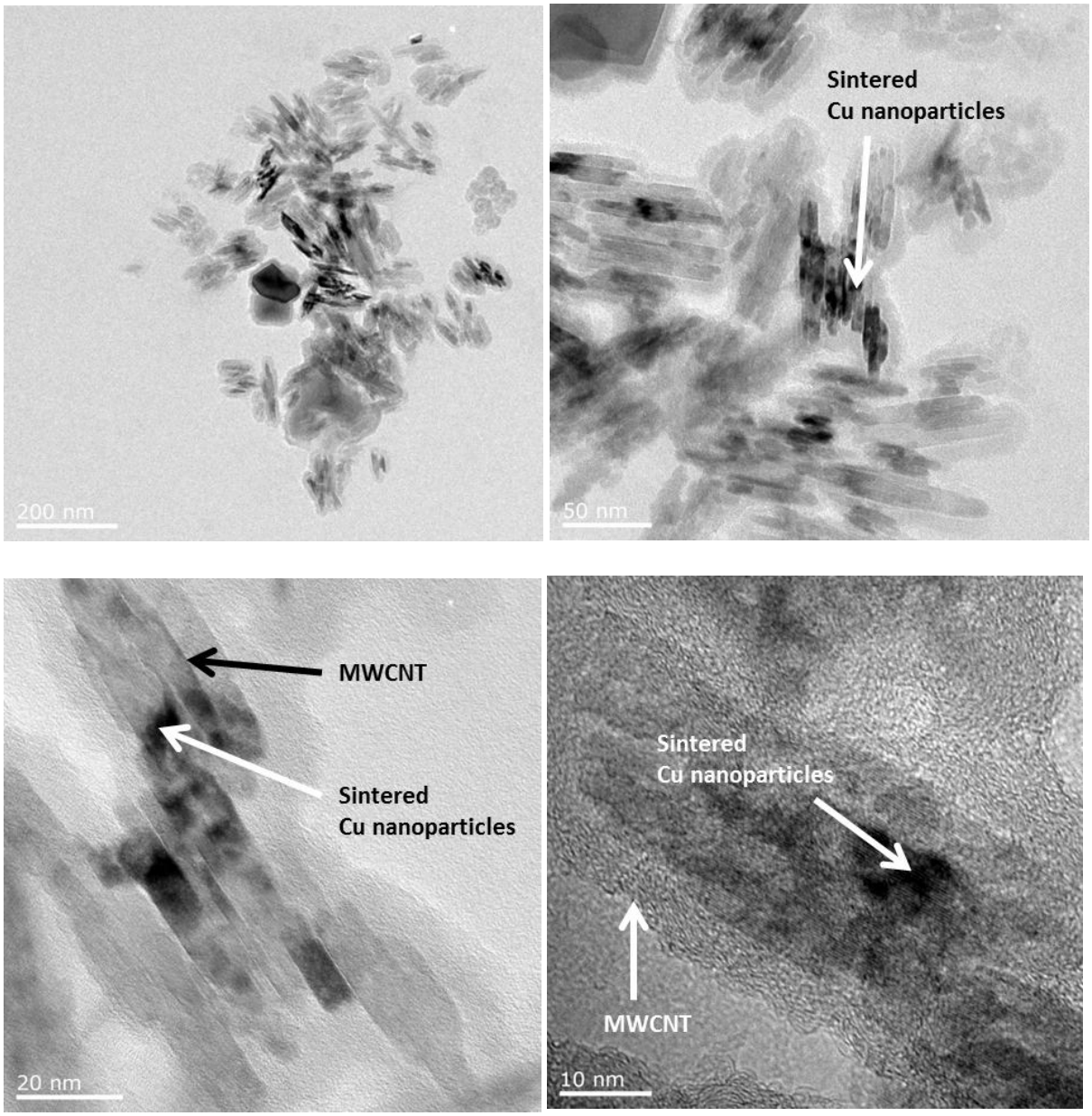

Figure B4(D): TEM images of 1%Cu/MWCNT$_{hp,CuAc}$.

Copper deposition by incipient wetness (1%Cu/MWCNT$_{hp,incipient}$) (Figure B4(C)) did not produce well distributed and dispersed copper nanoparticles. In fact, the copper sintering was apparent. Therefore, this technique has been identified as unsuitable for the deposition of the metal nanoparticles on MWCNT. The observation is similar for the sample prepared by copper acetate solution (1%Cu/MWCNT$_{hp,CuAc}$) (Figure B4(D)), calcined in a slightly milder condition than all the other three samples, and under the flow of an inert nitrogen gas instead

of air. However, the sintered copper nanoparticles were better attached to the surface of the MWCNT, as compared to the samples synthesised using DI water as the solvent in the wet impregnation. This could suggest that while the functionalisation of the MWCNT by H_2O_2 did not introduce a good interaction between the surface of the MWCNT and water, it may have relatively better interaction with an organic solvent such as ethanol in this case. This is also evident by the dispersion test results seen earlier in Figure B3, where the dispersion on the MWCNT was observed to be better in ethanol than in water.

Whilst MWCNT's dispersion in ethanol is better than that in water, the morphology based on TEM images in Figure B4(D) showed that well dispersed and homogeneous copper nanoparticles without sintering was unattainable in the 1%Cu/$MWCNT_{hp,CuAc}$ sample. In comparison with the1%Cu/$MWCNT_{hp}$ sample, the latter did not show sintering of the copper nanoparticles (Figure B4(B)). This could suggest that the acetate precursor is not as good as the chloride precursor in achieving non-sintered, well-dispersed copper nanoparticles.

It was also noted that some TEM images show shorter tube length of the MWCNT, indicating a mixture of short and long tubes in the 1%Cu/$MWCNT_{hp,CuAc}$ sample. The presence of MWCNT of shorter tubes was not observed in other samples calcined in air since they had likely been removed as carbon dioxide *via* carbon oxidation as a result of their poor thermal stability in comparison to the longer tube length MWCNT, which explained the significant sample loss of > 90% in other samples that were calcined in air.

The poor thermal stability of all the samples as evidenced by the significant loss of catalyst sample post air calcination at temperatures of above 475 °C revealed that the presence of disordered carbon in the catalyst samples was significant. Based on the discussion presented by Peng & Liu (2006) [22], the lower thermal stability could mean that the H_2O_2 oxidation had resulted in breaking of the longer carbon tubular length to shorter nanotubes. This suggested that the H_2O_2 oxidation technique developed in this preliminary stage of work had caused damage of the graphitic structure or break of the tubular length of the MWCNT.

B4. Preliminary work: Conclusions and reflections for rectification

Based on the findings by Peng & Liu (2006) [22], the carbonyl (–C=O) group dominated in the H_2O_2-oxidised MWCNT after an extended period, which was at the time when the treatment was already too excessive and caused too much breaking of the tubular length of the carbon nanotubes. In our work, the developed H_2O_2 oxidation procedure could have been too excessive such that the process resulted in too much tubular length breakage as indicated by the appearance of the –C-O (single-bonding carbon) group on the surface (which were induced by the treatment with air, although its presence was not stable or in insignificant amount).

It is concluded that our developed H_2O_2 treatment technique was ineffective in functionalising the surface of the MWCNT as shown by the absence of oxygen-containing functional groups in the FTIR spectra, and hence, the hydrophobicity of the support for improved interaction with the polar solvent used in the copper precursor solutions was not effectively decreased, and consequently good dispersion and distribution of the copper nanoparticles was not achieved. Instead, the tubular length of the carbon nanotubes was broken into shorter nanotubes, and resulted in lower thermal stability of the carbon support, as evidenced by the significant loss of catalyst samples post air calcination.

Copper loading of *ca.* 1% or less should be used when optimising the copper loading content in the next catalyst synthesis by wet impregnation, using copper chloride solution as the precursor. Too high of a copper loading content causes the copper nanoparticles to sinter. Similarly, copper acetate as a precursor results in a more-sintered copper nanoparticles relatively to that of the chloride precursor. Incipient wetness impregnation also produces a similar (sintering) result in comparison to wet impregnation.

Appropriate actions will be taken as rectification steps based on the lessons learned from this preliminary study. Based on the literature reviewed in Section B1.2 on various techniques/agents in functionalising the carbon nanotubes' surfaces performed by other

researchers, a potential workable technique will be adopted as a corrective action, based on the existing facilities available at the Preparative Wet Chemistry Laboratory in the then Rutherford Building (now known as West Building), University of Canterbury. A few analysis techniques to validate the successfulness of the employed functionalisation procedure will be conducted first prior to proceeding with the copper deposition on the treated MWCNT for the synthesis of the catalysts.

In our next work, the rectification steps will include a change in the oxidising agent and technique used to functionalise the MWCNT. The functionalisation effectiveness analysis will include testing the degree of dispersion in water and tetrahydrofuran ($(CH_2)_4O$ = THF) for the purpose of validating the dispersion of the functionalised MWCNT in the solvent that we plan to use in the copper precursor solutions, by adopting a dispersion test demonstrated by Salmoria *et al.* (2013) [8] who confirmed a significant improvement in the polarity of 5 hours H_2O_2-treated MWCNT that had a good degree of dispersion in polar solvents such as isopropyl alcohol, water and THF. The FTIR analysis will be conducted on the treated and untreated supports to identify the presence of oxygen-moiety functional groups, and the TGA analysis will be performed to test their thermal stability. Pre-functionalised MWCNT with –COOH groups purchased from vendor will be used to compare the result of the degree of functionalisation conducted in the rectified work, and to find out if there are any changes that take place on the carbon graphitisation, or breaking of the tubular length.

References of APPENDIX B

1. Prado-Burguete, C., et al., *The effect of oxygen surface groups of the support on platinum dispersion in Pt/carbon catalysts.* Journal of Catalysis, 1989. **115**(1): p. 98-106.
2. Rodríguez-reinoso, F., *The role of carbon materials in heterogeneous catalysis.* Carbon, 1998. **36**(3): p. 159-175.
3. Li, X., et al., *Efficient synthesis of carbon nanotube–nanoparticle hybrids.* Advanced Functional Materials, 2006. **16**(18): p. 2431-2437.

4. Moraes, R.A., et al., *The effect of different chemical treatments on the structure and stability of aqueous dispersion of iron-and iron oxide-filled multi-walled carbon nanotubes.* Journal of the Brazilian Chemical Society, 2011. **22**(11): p. 2191-2201.
5. Špitalský, Z., et al., *Effect of oxidation treatment of multiwalled carbon nanotubes on the mechanical and electrical properties of their epoxy composites.* Composites Part A: Applied Science and Manufacturing, 2009. **40**(6): p. 778-783.
6. Basahel, S.N., et al., *Chemical modification of multi-walled carbon nanotubes using different oxidising agents: optimisation and characterisation.* International Journal of Nanoparticles, 2009. **2**(1-6): p. 200-208.
7. Datsyuk, V., et al., *Chemical oxidation of multiwalled carbon nanotubes.* Carbon, 2008. **46**(6): p. 833-840.
8. Salmoria, G., et al. *Oxidative treatment of carbon nanotubes by hydrogen peroxide and O2 plasma for rapid manufacturing applications*. in *High Value Manufacturing: Advanced Research in Virtual and Rapid Prototyping: Proceedings of the 6th International Conference on Advanced Research in Virtual and Rapid Prototyping, Leiria, Portugal, 1-5 October, 2013*. 2013: CRC Press.
9. Hamilton Jr, R.F., et al., *Purification and sidewall functionalization of multiwalled carbon nanotubes and resulting bioactivity in two macrophage models.* Inhalation toxicology, 2013. **25**(4): p. 199-210.
10. Dreyer, D.R., et al., *The chemistry of graphene oxide.* Chemical Society Reviews, 2010. **39**(1): p. 228-240.
11. López, E., et al., *Multiwalled carbon nanotubes-supported Nickel catalysts for the steam reforming of propane.* Journal of Materials Science, 2012. **47**(6): p. 2985-2994.
12. Yang, H.-M. and P.-H. Liao, *Preparation and activity of Cu/ZnO-CNTs nano-catalyst on steam reforming of methanol.* Applied Catalysis A: General, 2007. **317**(2): p. 226-233.
13. Stancu, M., et al., *Purification of multiwall carbon nanotubes obtained by AC arc discharge method.* Optoelectronics and Advanced Materials, 2011. **5**(8): p. 846-850.
14. Chen, J., et al., *An improved Hummers method for eco-friendly synthesis of graphene oxide*. Carbon, 2013. **64**: p. 225-229.
15. Dimiev, A.M. and J.M. Tour, *Mechanism of graphene oxide formation.* ACS nano, 2014. **8**(3): p. 3060-3068.
16. Marcano, D.C., et al., *Improved synthesis of graphene oxide.* ACS nano, 2010. **4**(8): p. 4806-4814.

17. Correa-Duarte, M.A. and L.M. Liz-Marzán, *Carbon nanotubes as templates for one-dimensional nanoparticle assemblies.* Journal of Materials Chemistry, 2006. **16**(1): p. 22-25.
18. Correa-Duarte, M.A., et al., *Aligning Au nanorods by using carbon nanotubes as templates.* Angewandte Chemie International Edition, 2005. **44**(28): p. 4375-4378.
19. Correa-Duarte, M.A., et al., *Linear Assemblies of Silica-Coated Gold Nanoparticles Using Carbon Nanotubes as Templates.* Advanced Materials, 2004. **16**(23-24): p. 2179-2184.
20. Nam, I., H. Souri, and H. Lee, *Percolation threshold and piezoresistive response of multi-wall carbon nanotube/cement composites.* Smart Structures and Systems, 2016. **18**(2): p. 217-231.
21. Nam, I., et al., *Electromagnetic characteristics of cement matrix materials with carbon nanotubes.* ACI Materials Journal-American Concrete Institute, 2012. **109**(3): p. 363.
22. Peng, Y. and H. Liu, *Effects of oxidation by hydrogen peroxide on the structures of multiwalled carbon nanotubes.* Industrial & engineering chemistry research, 2006. **45**(19): p. 6483-6488.

APPENDIX C

Development of copper nanostructure/multi-walled carbon nanotubes (Cu/MWCNT) catalyst: RECTIFIED WORK

C1. Rectified work: Experimental

In this rectified work, the following multi-walled carbon nanotubes (MWCNT) (Nanostructured and Amorphous Materials Inc., USA) were used; pristine MWCNT (95+% purity, OD = 10 – 20 nm, length = 0.5 – 2.0 μm), pre-functionalised MWCNT: MWCNT-COOH (99.9% purity, OD = 10 – 20 nm, length = 10 – 30 μm). The samples are denoted as $MWCNT_p$ and $MWCNT_{COOH}$ respectively.

C1.1 Functionalisation of surface of MWCNT

The pre-treatment (functionalisation) of the pristine MWCNT ($MWCNT_p$) was performed following the procedure described by López *et al.* (2012) [1]. Basically, 1.0 g of the raw MWCNT was placed in tubular flask containing a magnetic stirrer bar and a 50 mL of 3:1 volume ratio of H_2SO_4 (98%): HNO_3 (62%) as the oxidising agent was added to the flask. A condenser was connected to the top of the tubular flask, with water inlet connected to the condenser's bottom and water outlet to its top and drained. The top of the condenser was connected to an L-shaped tube containing vapour trap. The tubular flask was wrapped in an aluminium foil and placed in an aluminium block, which was preheated to 50 °C, and the oxidising took effect from this temperature until it was raised up to 80 °C and kept for 0.5 hour in continuous stirring and water flowing through the condenser for the reflux of the oxidising agent. The pre-treatment setup is shown in Figure C1. The mixture was then allowed to cool down to room temperature after the oxidising process. The mixture was then diluted by 5 times with deionised (DI) water and vacuum filtered through a filter funnel of porosity 5 (nominal maximum pore size = 1.0 – 1.6 μm). The recovered pre-treated MWCNT

was washed with DI water in abundance and filtered again until the filtrate was neutral. The surface's level of acidity is an important parameter in catalysis [2] as acidity can activate hydrocarbon cracking that forms coke deposit [3].

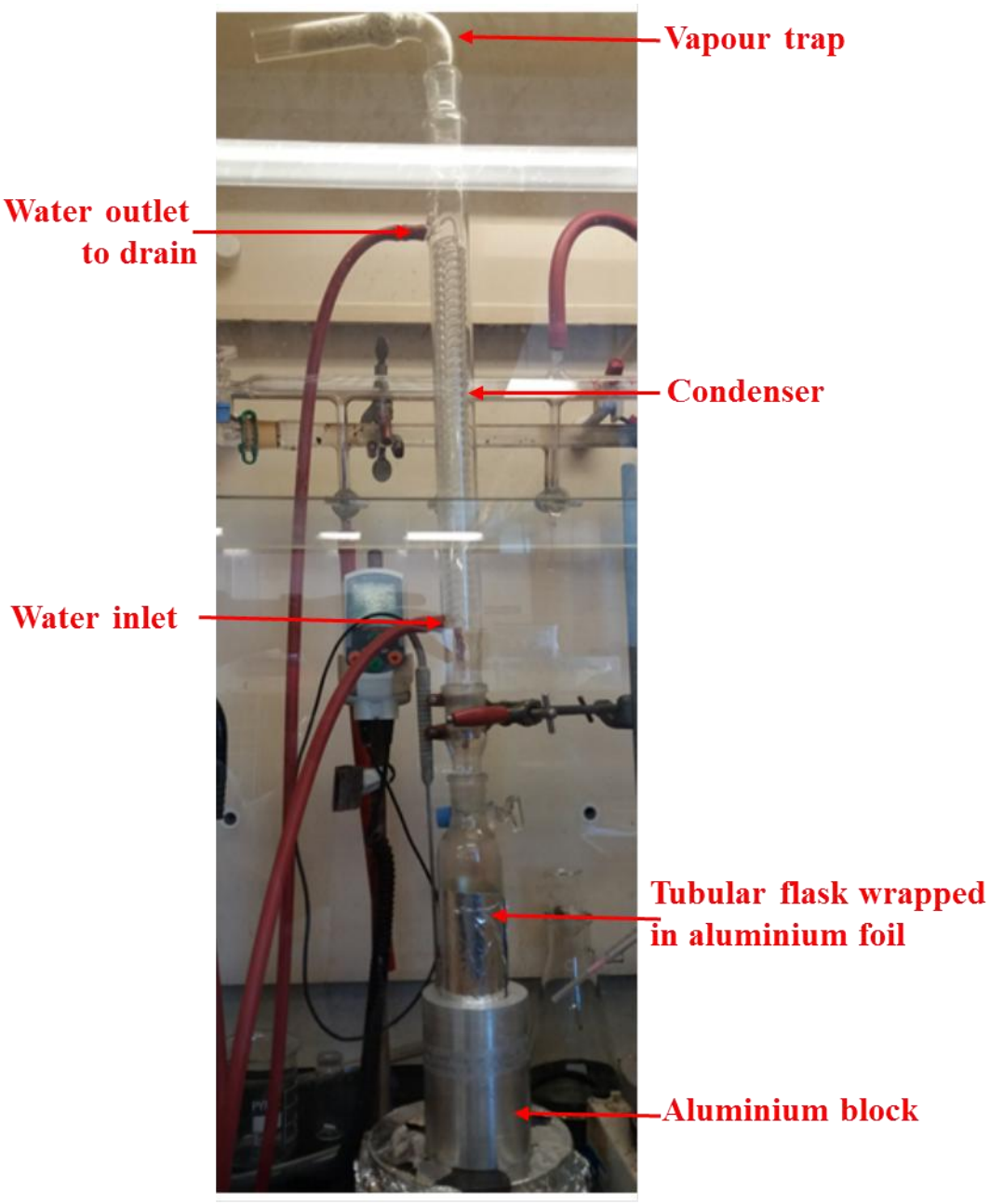

Figure C1: Acid reflux setup for MWCNTs pre-treatment.

The oxidised sample was then dried overnight in an oven at 100 °C followed by crushing the clumped dried samples into fine powders using mortar and pestle. The pre-treatment steps

involved are summarised in Figure C2. This oxidised MWCNT sample is denoted as $MWCNT_{acid}$.

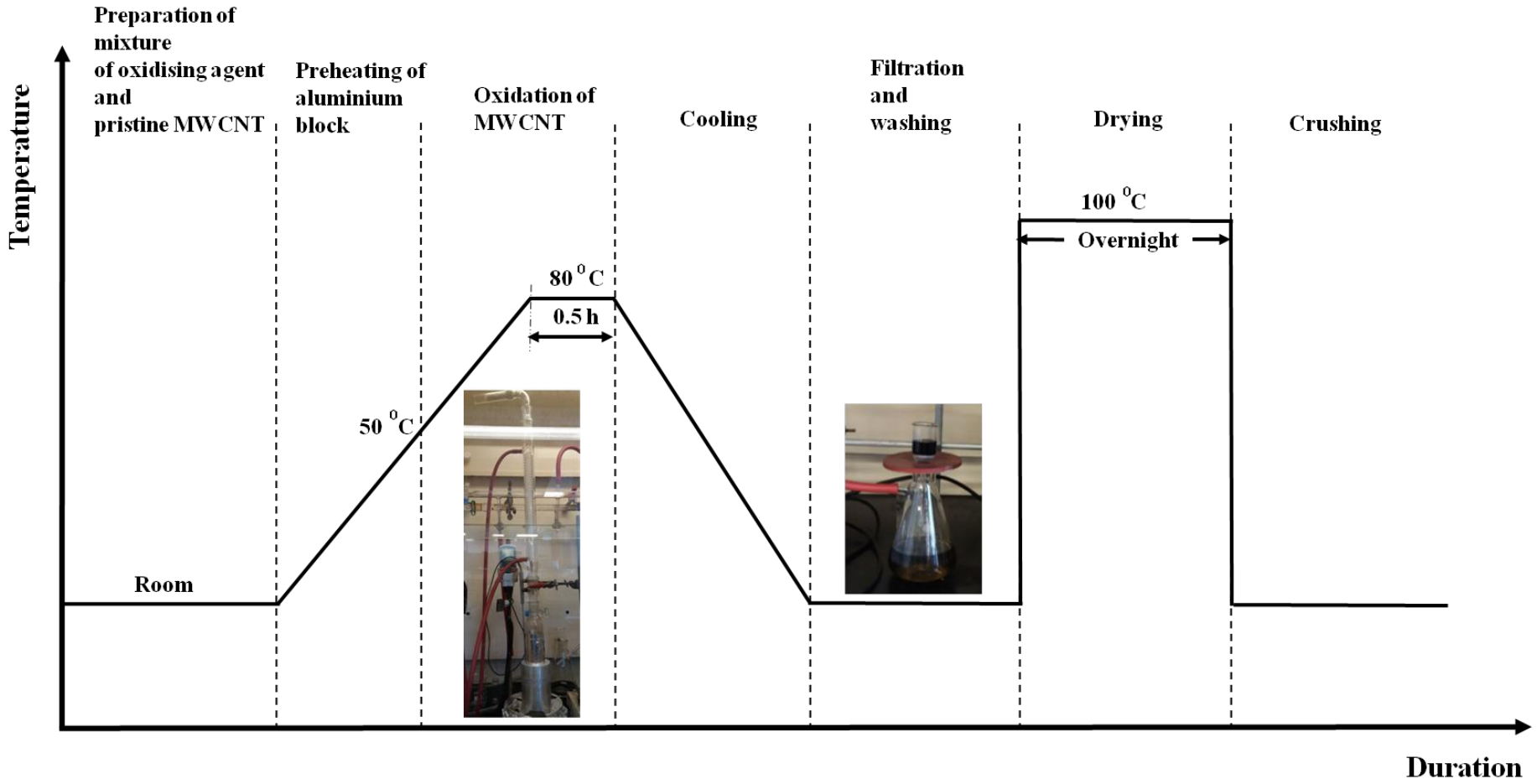

Figure C2: Steps in MWCNT pre-treatment.

C1.2 Catalyst synthesis

In this part of work, in addition to the copper nanoparticles prepared using copper salt dissolved in DI water, nanoclusters of hexameric copper hydride ligated by triphenylphospine (PPh_3), $[(PPh_3)CuH]_6$ nanoclusters, were also synthesised to compare their dispersion on the MWCNT with the former.

C1.2.1 Synthesis of Cu_6 nanoclusters

The synthesis of Cu_6 nanoclusters was performed following the procedure described by Albert *et al.* (1989) [4]. Basically, a colloid of 0.5 g of copper (I) chloride (CuCl) (M&B Laboratory Chemicals, May & Baker Ltd., Dagenham, England) (0.005 mol), 1.3 g of PPh_3 (MERCK-Schuchardt) (0.005 mol), and 10 mL of dry tetrahydrofuran ($(CH_2)_4O$ = THF) was prepared by stirring the mixture under argon at ambient temperature. A colloidal suspension of a white precipitate of $(PPh_3)_3(CuCl)_2$ was formed (Figure C3(A)), and 5 mL of a reducing agent, K-selectride solution (0.005 mol, 1.0 M potassium tri-sec-butylborohydride in THF) (Sigma Aldrich) was added while the mixture (placed in ice bath) was continuously stirred (Figure C3(B)), to dissolve the precipitate and produce a deep red solution (Figure C3(C)). This solution was stored under argon, for later use in wet impregnation for catalyst synthesis.

To crystallise the $[(PPh_3)CuH]_6$ nanoclusters, the solution was filtered through a glass wool supported Celite column (Figure C3(D)) under vacuum until the volume was reduced by around 50%. The procedure described by Cook *et al.* (2016) [5] was employed, where the concentrated filtrate was layered with hexane (of volume of slightly higher than the cluster solution) and stored at room temperature under argon atmosphere for a few days until the Cu_6 nanoclusters crystallised (Figure C3(E)).

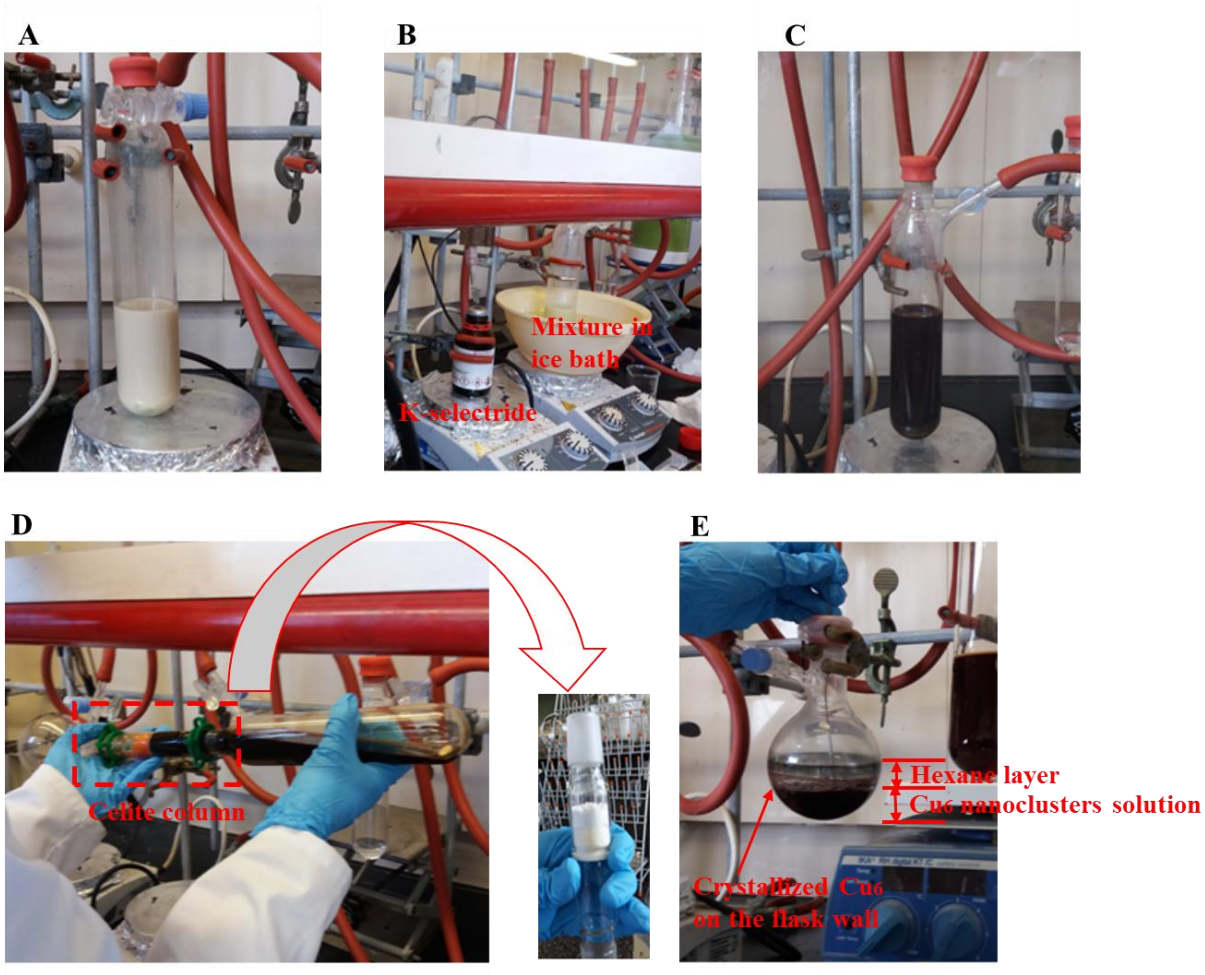

Figure C3: Steps in Cu_6 nanoclusters synthesis.

(A) Formation of $(PPh_3)_3(CuCl)_2$ white precipitate; (B) addition of K-selectride solution; (C) dissolution of the precipitate and production of a deep red solution; (D) solution filtration through Celite column; and (E) storage of nanoclusters solution under argon.

C1.2.2 Copper deposition on MWCNT support

The wet impregnation techniques employed to deposit the two different copper nanostructures on the MWCNT supports were different from each other and they are described hereafter.

C1.2.2.1 Copper nanoparticles deposition

A stock solution of copper chloride was prepared by dissolving 0.54 g of $CuCl_2.2H_2O$ (Riedel-De Haën AG, Seelze-Hannover) (containing 0.2 g Cu) in 10 mL of DI water. Three types of MWCNT support; $MWCNT_p$, $MWCNT_{acid}$, and $MWCNT_{COOH}$ of 0.198 g each were dispersed in DI water (approximately 6 mL). An amount of 0.1 mL of copper chloride solution (containing 0.002 g Cu) was pipetted into each of the dispersed MWCNT supports for copper loading of 1 wt.%. The wet impregnation mixtures were stirred overnight at 750 rpm and room temperature.

The copper impregnated MWCNT samples were then centrifuged at 5000 rpm for 10 minutes, followed by decantation of the solution and an overnight oven-drying at 100 °C. The clumped catalyst samples were crushed by mortar and pestle. The dry catalyst samples were then calcined in a nitrogen flow of 100 mL/min at 400 °C in a tubular furnace for 3 hours, at a ramping rate of 2.5 °C/min, following the calcination procedure described by Abbaslou *et al.* (2009) [6] and López *et al.* (2012). The catalyst samples are denoted as $1\%Cu/MWCNT_p$, $1\%Cu/MWCNT_{acid}$, and $1\%Cu/MWCNT_{COOH}$ respectively.

C1.2.2.2 Cu_6 nanoclusters deposition

Catalyst fabrication was performed using Schlenk-line technique. Weighing of Cu_6 clusters was performed in air as quickly as possible to minimise decomposition of these species, with a known mass of cluster (3.20 g) quickly transferred into a Schlenk tube with 50 mL of THF

under Ar immediately after weighing to produce a stock solution with known concentration of cluster. On the basis of a total catalyst weight of 2.0 g, an amount of 1.98 g of pre-functionalised multi-walled carbon nanotubes (MWCNT) grafted with carboxyl groups (–COOH) on their wall surface was vacuum-dried at 200 °C for 5 hours to remove the traces of moisture as the support preparation step. The sample was then dispersed in THF solution under an argon atmosphere. An appropriate volume (10 mL) of the Cu_6 stock solution prepared in THF containing 0.02 g of copper (basis: Cu_6 nanoclusters empirical formula of $[(PPh_3)CuH]_6.0.75THF$) was added to the dispersed MWCNT suspension *via* a syringe. The wet impregnation was carried out by stirring the mixture at 750 rpm and room temperature overnight. After impregnation, the catalyst sample was vacuum-dried, and the flask containing the sample was then placed in a warm water bath (50 °C) for the last 10 min of the vacuum-drying step to remove residual solvent. The dried sample (now conveniently handled under ambient environment) was then calcined similarly to the step described for copper nanoparticles in Section C1.2.2.1 above. The catalyst sample is denoted $1\%(Cu_6/MWCNT_{COOH})_{calcined}$.

A summary of the copper deposition techniques of the different nanostructures is presented in Figure C4.

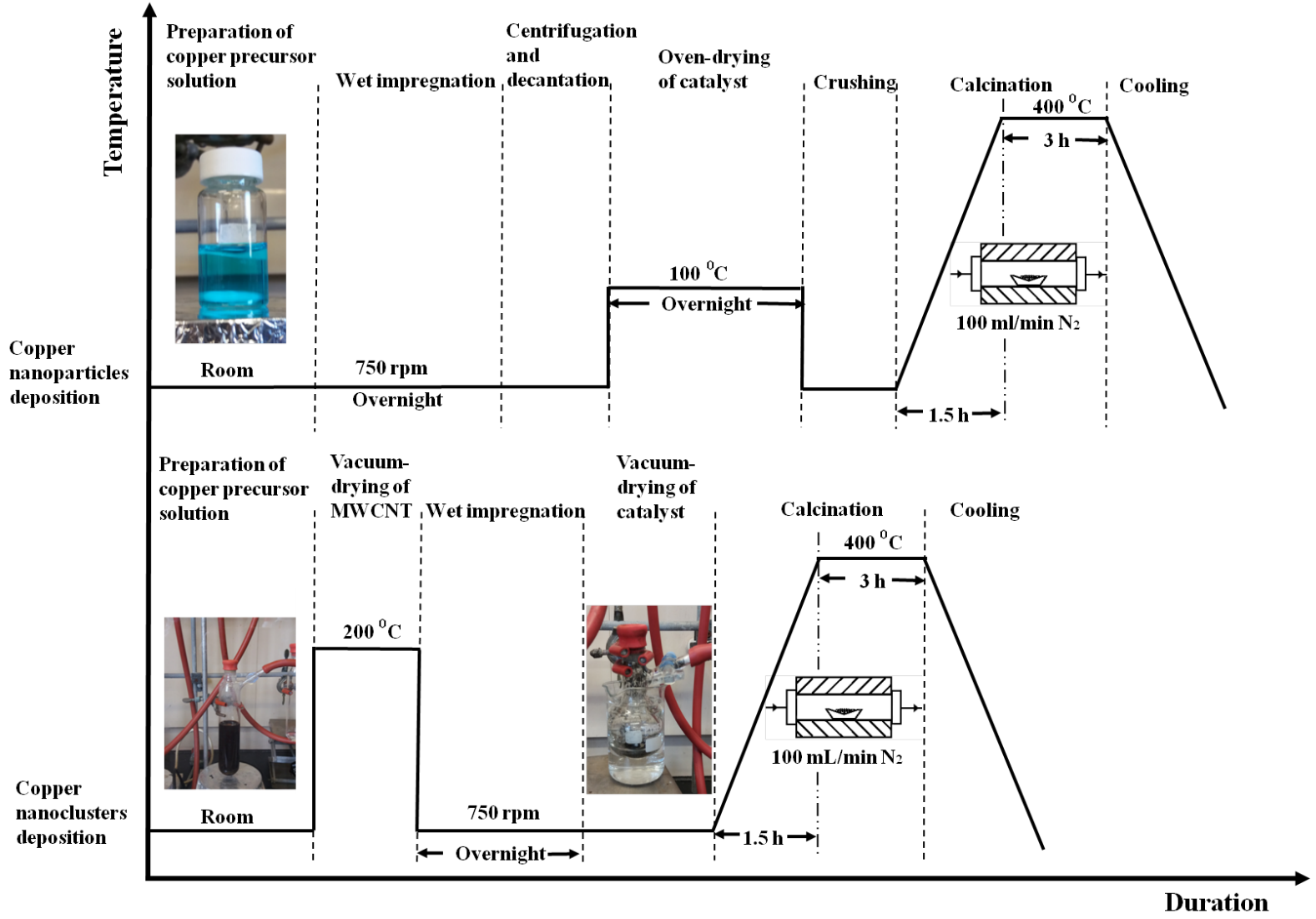

Figure C4: Steps involved in copper nanostructures deposition on MWCNT.

Table C1 summarises the catalyst samples synthesised in this rectified work.

Table C1: Catalyst samples synthesised in rectified work.

Copper nanostructure	**Cu nanoparticles**	**Cu_6 nanoclusters**
Copper precursor	Copper (II) chloride dissolved in DI water	Copper (I) chloride + PPh_3 + K-selectride dissolved in THF
MWCNT preparation	NA	Moisture removed by vacuum for 5 hours at 200°C, dried MWCNT kept under argon environment
Wet impregnation	The MWCNT-copper solution mixture stirred overnight at room temperature	The MWCNT-copper solution mixture stirred overnight at room temperature under argon environment
Drying	Oven-dried at 100 °C overnight	Vacuum-dried at room temperature
Calcination	400 °C for 3 hours under nitrogen flow of 100 mL/min, ramping rate = 2.5 °C/min	400 °C for 3 hours under nitrogen flow of 100 mL/min, ramping rate = 2.5 °C/min
Samples	1%Cu/$MWCNT_p$ 1%Cu/$MWCNT_{acid}$ 1%Cu/$MWCNT_{COOH}$	1%(Cu_6/$MWCNT_{COOH}$)$_{calcined}$

C1.3 Analysis techniques

The analyses include testing of the MWCNT's functionalisation effectiveness, characterisation of the synthesised Cu_6 nanoclusters crystal, and the morphology characterisation of the synthesised Cu/MWCNT catalyst samples.

C1.3.1 MWCNT supports

The tests were conducted on the as-received pristine MWCNT ($MWCNT_p$), pre-treated MWCNT ($MWCNT_{acid}$) and as-received pre-functionalised MWCNT ($MWCNT_{COOH}$).

C1.3.1.1 X-ray diffraction (XRD)

The XRD (SuperNova, Agilent Technologies, 2θ range of 10 – 90°, Cu-Kα radiation (λ = 1.54056 Å) was performed at room temperature.

C1.3.1.2 Dispersion test and suspension stability

Dispersion test was conducted on the MWCNT samples in DI water and THF to observe their dispersion in the solvents used for wet impregnation in the catalyst synthesis step. An amount of 0.050 g of each of the functionalised MWCNT samples; $MWCNT_{acid}$, and $MWCNT_{COOH}$, was centrifuged (MULTIFUGE 3 L, Heraeus) in 25 mL of DI water at 10,000 rpm for 20 min, and the parameters were halved for the same amount of $MWCNT_p$ sample in the same amount of DI water. The assessment was performed at room temperature. In addition, all the samples were ultrasonicated (Elmasonic P, Elma Schmidbauer GmbH) at 53 kHz for 6 min at 40 °C in the THF solvent.

C1.3.1.3 Fourier-transform infrared (FTIR) spectroscopy

There were three different FTIR scanning techniques performed in this rectified work:

1) All the MWCNT samples were analysed through FTIR spectrometer (Bruker Optics supported by OPUS Mentor software) equipped with a single reflection attenuated total reflectance (ATR) to identify the oxygen-containing groups present on the surface of the supports. The ATR surface was cleaned with ethanol before each of the

powdered samples was applied. The average of 16 scans was recorded in each spectrum between 4000 and 400 cm^{-1} at a resolution of 1 cm^{-1}.

2) Each of the MWCNT samples was dispersed and ultrasonicated in dichloromethane (DCM), pipetted onto the surface of potassium bromide (KBr) disc and allowed to dry in ambient, and then brought to FTIR spectrometer for a 16-times scanning within the same spectrum range as the ATR.
3) Each of the MWCNT samples was suspended in DCM solvent and then filled into a KBr sample holder and similarly scanned.

C1.3.1.4 Thermogravimetric analysis (TGA)

All the MWCNT support samples were analysed by thermogravimetric analysis (TGA) (SDT Q600, Alphatec Systems Ltd. supported by TA Instruments Universal Analysis 2000 software) under nitrogen flow of 100 mL/min, at a ramping rate of 50 °C/min, from an ambient condition up to 1200 °C to investigate their thermal stability under inert atmosphere.

C1.3.2 Cu_6 nanoclusters

The characterisation analyses on the copper nanoclusters synthesised in Section C1.2.1 include XRD and TGA.

C1.3.2.1 XRD

The crystal structure and components of the nanoclusters were determined using X-ray diffractometer (SuperNova, Agilent Technologies) on a single-crystal form of the Cu_6 nanoclusters at 120 K.

C1.3.2.2 TGA

The crystallised $[(PPh_3)CuH]_6$ was analysed through TGA under nitrogen flow of 100 mL/min, at a ramping rate of 10 °C/min, from an ambient condition up to 800 °C to investigate its thermal stability.

C1.3.3 Cu/MWCNT catalyst samples

All the catalyst samples;1%Cu/$MWCNT_p$, 1%Cu/$MWCNT_{acid}$, 1%Cu/$MWCNT_{COOH}$, and 1%$(Cu_6/MWCNT_{COOH})_{calcined}$ were analysed under transmission electron microscope (TEM) (Philips CM200 supported by Gatan ORIUS^{TM} CCD Camera Controller and Gatan Digital Micrograph software) to characterise the morphology of the copper nanostructures dispersion on the MWCNT support's surface. Each of the samples was first dispersed and ultrasonicated in high purity ethanol (in extremely low concentration of the suspension) and pipetted onto a film grid (carbon coating on 150 mesh Cu) (ProSciTech), and the face where the sample was pipetted on was further coated with carbon using EMS150T ES (Quorum).

C2. Rectified work: Results and discussion

The outcomes of the characterisation analysis of the MWCNT support samples, synthesised Cu_6 nanoclusters and the synthesised copper/MWCNT catalyst samples prepared in this rectified work will determine if further optimisation is required.

C2.1 MWCNT supports

C2.1.1 XRD

In the diffraction patterns of the MWCNT samples, the peaks at 2θ = ~26.2 and ~42.5°, which correspond to the (0 0 2) and (1 0 0) reflections respectively (International Centre for Diffraction Data (ICDD) 01-075-1621) were given the focus. Peng & Liu (2006) [7] reported that the changes of the ratio of intensity of peak (1 0 0) to peak (0 0 2), I_{100}/I_{002} from the XRD patterns corresponded with the MWCNT's planar order, where a lower ratio of I_{100}/I_{002} indicates an increase in the degree of alignment to the (0 0 2) plane, which is the dominant facet of carbon. It was also found that the lower I_{100}/I_{002} ratio corresponds to an increase in the degree of crystallinity of the carbon ordering analysed using Raman spectroscopy. As seen from Figure C5, when compared to the pristine MWCNT sample, the I_{100}/I_{002} ratio was lower in the $MWCNT_{COOH}$ sample. The ratio was relatively equivalent between the $MWCNT_{COOH}$ sample and the acid-refluxed-functionalised MWCNT, $MWCNT_{acid}$ sample. This result supports a higher degree of crystallinity in the functionalised MWCNT samples. In addition, the peak at 2θ = ~44.4° that corresponds to the (1 0 1) reflection diminished in the functionalised MWCNT samples, suggesting (to a certain extent) an effect of the functionalisation and grafting of the oxygen groups on the surface. The XRD patterns of both functionalised MWCNT samples, $MWCNT_{COOH}$ and $MWCNT_{acid}$ were also almost identical.

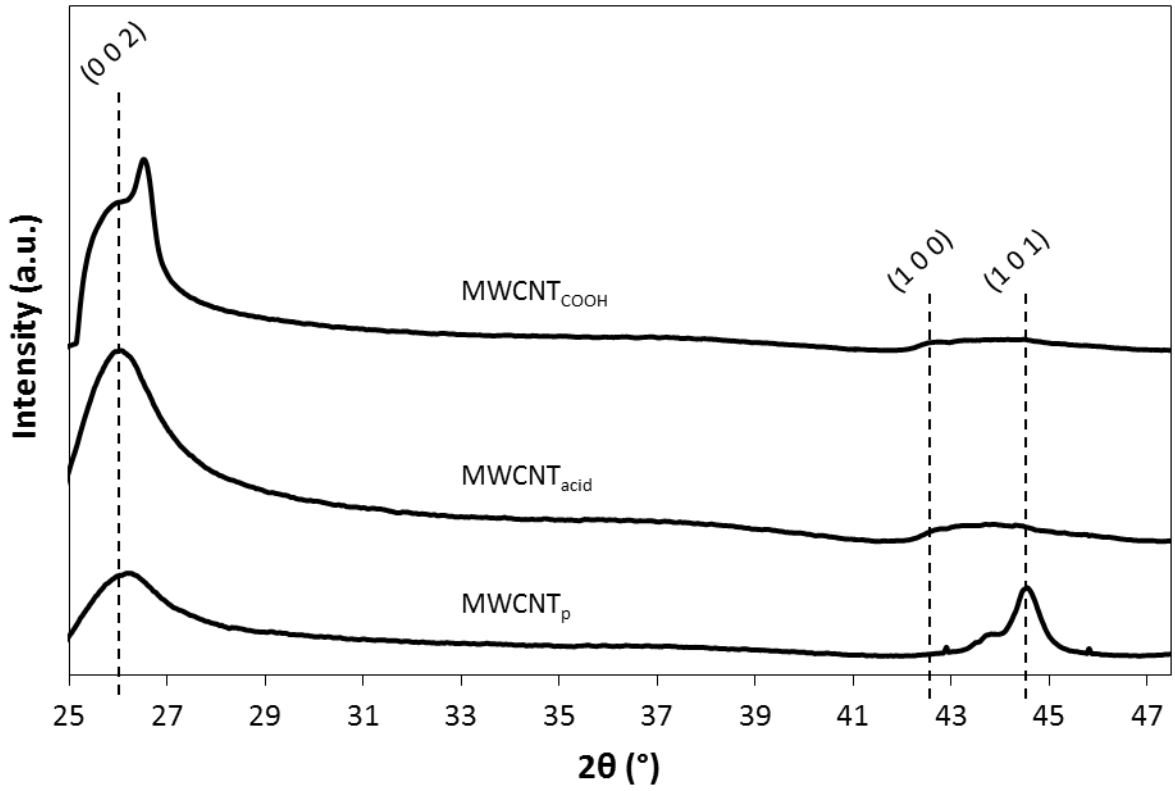

Figure C5: XRD patterns of pristine and functionalised MWCNT samples.

C2.1.2 Modification of the degree of hydrophobicity of MWCNT

The results of the dispersion test are shown in Figure C6. It was observed that the THF interacted well with the MWCNT studied in this work, including the untreated (pristine) sample, MWCNT$_p$. This may suggest that oxidation was not required to decrease the hydrophobicity of MWCNT's surface when using THF as the solvent in the metal precursor solution. However, sedimentation of pristine MWCNT was observed in DI water, even though the centrifugation parameters were halved in comparison to the functionalised MWCNT samples. The functionalised MWCNT; MWCNT$_{acid}$ and MWCNT$_{COOH}$ were observed to disperse satisfactorily in water, and the suspensions were found to be stable even after more than a week. This implied satisfactory decrease of the hydrophobicity of the MWCNT's surface by the acid reflux pre-treatment.

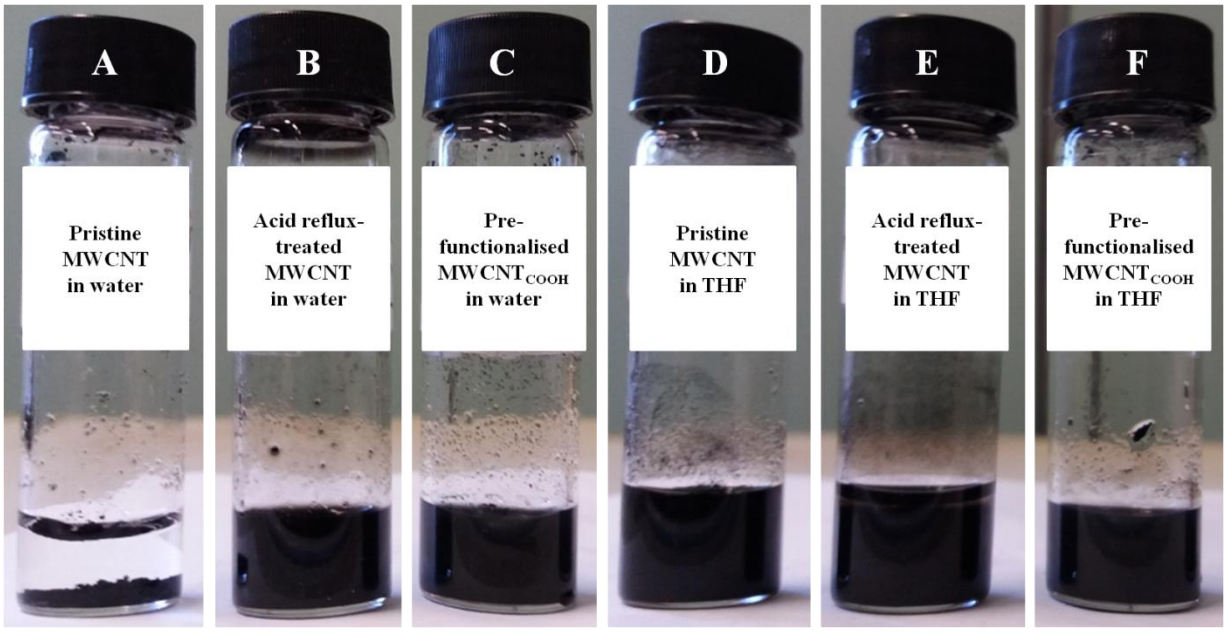

Figure C6: Dispersion of $MWCNT_p$, $MWCNT_{acid}$, and $MWCNT_{COOH}$.

(A – C) In water; and (D – F) in THF.

C2.1.3 Effectiveness of functionalisation of MWCNT

Figure C7 shows the ATR-FTIR spectra of the MWCNT supports studied in this rectified work. Similarly to the other two FTIR scanning techniques described in Section C1.3.1.3, the FTIR technique as a whole did not provide any information on the effectiveness of the functionalisation of the MWCNT's surface. It was found that no oxygen functional groups were identified on the pristine sample and the sample oxidised in this work. Indeed, the analysis on the as-received pre-functionalised MWCNT sample of the proclaimed presence of carboxyl –COOH groups did not reveal the detection of this functional group. Unfortunately, the FTIR analysis of the purchased samples is not made available for our verification. There is a large difference in the FTIR's transmittance intensity between the acid-oxidised MWCNT sample and the other two as-received MWCNT samples, which indicated an effect of acid-functionalisation of the pristine MWCNT performed in this work. However, this difference did not provide useful information for the purpose of drawing a meaningful discussion. Overall, the result implied that FTIR technique was not sensitive enough to detect the type and the amount of the oxygen-moiety groups present on the surface of carbonaceous

materials, even though works in the literature [8-14] showed successful identification of such groups on CNTs by FTIR.

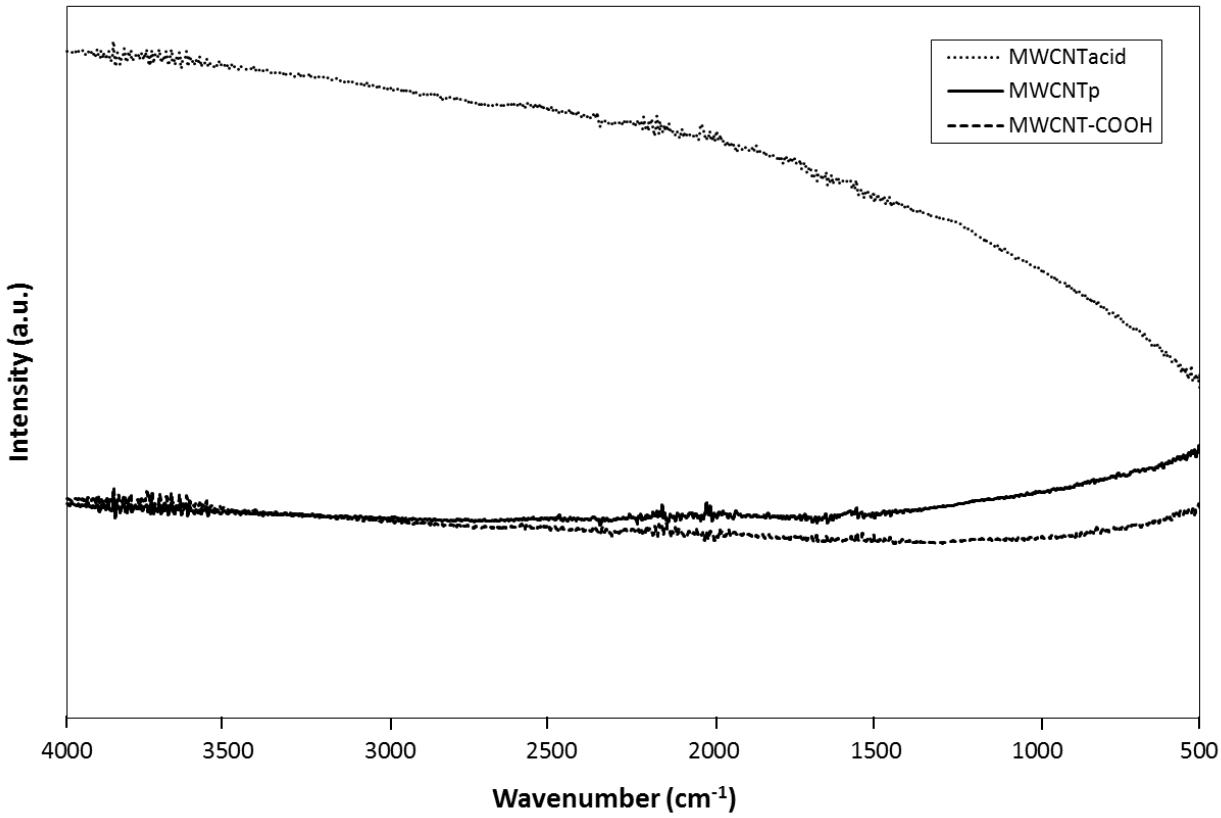

Figure C7: ATR-FTIR spectra of pristine, acid-reflux-oxidised and pre-functionalised MWCNTs. This technique is not sensitive enough to detect oxygen groups on carbonaceous samples.

The FTIR analysis by Sun *et al.* (2003) [12] on their MWCNT–COOH sample showed a peak at 1728 cm^{-1} that was assigned to the carbonyl –C=O stretching vibration of –COOH groups. The analysis by Yudianti *et al.* (2011) [11] on the oxidised MWCNT that was performed by the same oxidising agent procedure as in our work showed the appearance of peak at 1753 cm^{-1}, which was also assigned to the presence of the carbonyl stretching vibration of carboxyl groups, post oxidising. However, the procedure by Yudianti *et al.* (2011) [11] was more extreme where the treatment included a 2 h ultrasonication of the MWCNT at room temperature, followed by a 6 h acid reflux at 100 °C, whereas in our current rectified work; 80 °C for 0.5 hour without prior ultrasonication. At the moment we can only speculate that

carboxyl –COOH groups are present on the acid-reflux-functionalised MWCNT performed in this rectified work, based on the findings in the above literature.

To sum up, the type and the amount of oxygen-containing groups present on the MWCNT samples in this rectified work were not able to be determined by FTIR. Nevertheless, the treatment done in our work had proven to have modified the surface of the MWCNT in terms of its hydrophobicity decrease, which can be seen in Figure C6 above, consistent with the behaviour observed on the as-received pre-functionalised MWCNT containing carboxyl, –COOH groups. Therefore, other techniques to quantify the functionalisation effectiveness of the MWCNT's surface such as zeta potential will be employed in the analysis and presented later at the end of this Appendix.

C2.1.4 Thermal behaviour of MWCNT

The unstable disordered carbon is combusted at temperatures below 500 °C, while the combustion of graphitised carbon takes place at temperatures above 600 °C [15, 16]. From Figure C8, it can be observed that the MWCNTs are in general thermally stable in an inert, non-reacting environment with weight loss of 4.0 wt.% or below in the as-received samples at 600 °C; pristine and pre-functionalised. The sample of $MWCNT_{acid}$, which was oxidised in our work, showed a weight loss of approximately 14.6 wt.% at this temperature, which implies that the pre-treatment may have shortened the length of the MWCNT and introduced some amount of disordered carbon. At the end of the test at 1200 °C (set to represent a slightly higher temperature than in steam methane reforming (SMR) operations), the as-received pre-functionalised MWCNT ($MWCNT_{COOH}$) showed a weight loss of 11.3 wt.%, while the $MWCNT_p$ and $MWCNT_{acid}$ showed a weight loss of 22.5 wt.% and 33.3 wt.% respectively. This serves as an indication that our pre-treated MWCNT may have introduced some carbon components that are unstable at very high temperature.

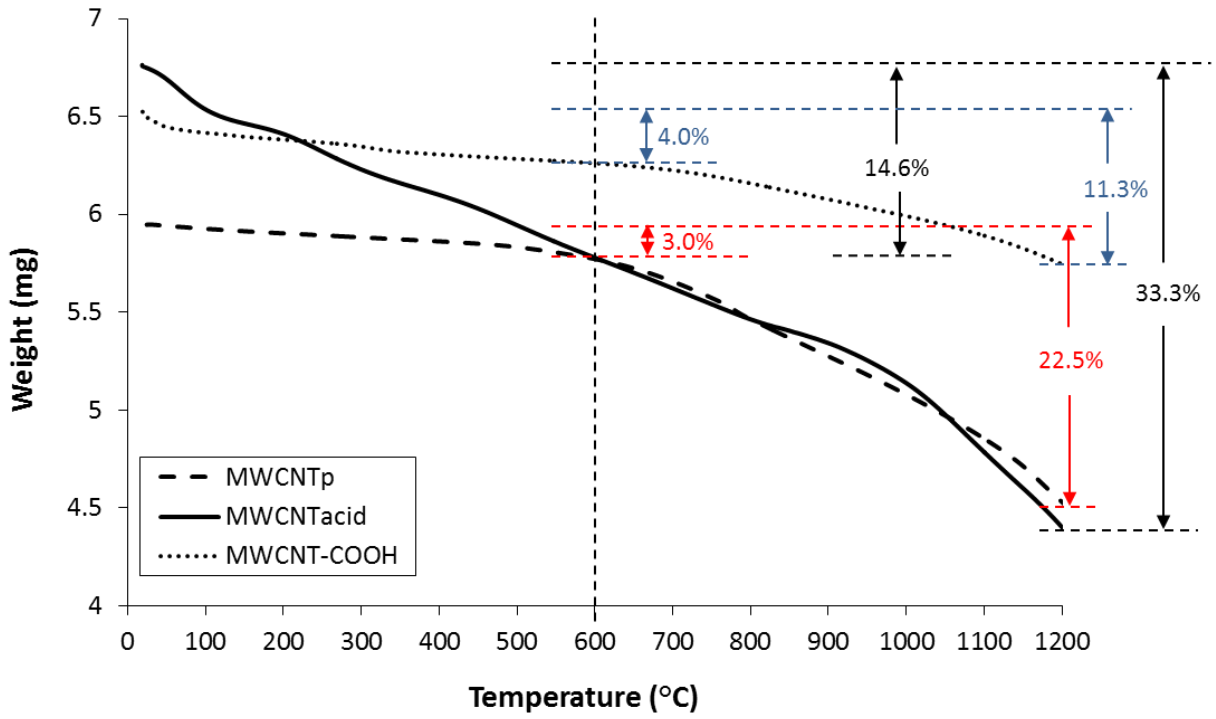

Figure C8: TGA of the MWCNT supports.

In addition, the difference in the thermal stability between the as-received pristine MWCNT and the as-received pre-functionalised MWCNT implied that the manufacturer (Nanostructured and Amorphous Materials Inc., USA) had managed to optimally functionalise and purify the pristine MWCNT by removing further the disordered carbon in their oxidising procedure. Unfortunately, the information on the oxidising agents, functionalisation and purification techniques as well as the treatment conditions was kept in confidence by the vendor. The difference in thermal stability between the $MWCNT_{acid}$ and the as-received pristine MWCNT ($MWCNT_p$) provided the information that although the acid reflux pre-treatment in our rectified work had managed to functionalise the pristine MWCNT's surface, the thermal stability of the MWCNT on the other hand deteriorated possibly due to the breaking of nanotubes tubular length and the damage of some of the graphitic carbon structure to disordered structure.

Therefore, further purification was required to remove the disordered carbon and the broken nanotubes tubular length through combustion, in order to leave behind only the crystallised, well-graphitised, high purity functionalised MWCNT. Therefore, the purification step

adopted from Stancu *et al.* (2011) [17] was then performed by air oxidation in a tubular furnace post the acid-reflux treatment. This step has been described earlier in Section B2.1.2 of APPENDIX B. The analysis of the outcome of the MWCNT treated by acid-reflux followed by air oxidation purification will be presented at the end of this Appendix.

C2.2 Copper nanoclusters structure

C2.2.1 Components in Cu_6 nanoclusters

Based on single-crystal XRD (SCXRD) of the Cu_6 nanocluster, our team has successfully determined and published the crystal structure in Cambridge Crystallographic Data Centre (CCDC) on 31 August 2018. The structure has been assigned a CCDC number of 1864974. The structure was solved in the monoclinic space group $P2_1$ with a = 14.28467 Å, b = 16.00824 Å, c = 21.39091 Å, $\alpha = 90^o$, $\beta = 92.1229^o$, $\gamma = 90^o$, Z = 2 and cell volume, V = 4888.16 $Å^3$. The structure has the empirical formula of $Cu_6P_6C_{111}H_{102}O_{0.75}$ due to 0.75 of a THF molecule being included in the structure. The complex of hexameric copper hydride ligated by triphenylphosphine, $[(PPh_3)CuH]_6$ (Figure C9) can be compared to the hemisolvate structure, $[(PPh_3)CuH]_6$.0.5THF collected at room temperature by Albert *et al.* (1989) [4]. The differences in the unit cells (a = 14.464 Å, b = 16.252 Å, c = 21.487 Å) are likely due to the differences in temperature of the collection and loss of THF during the room temperature collection. A more detailed SCXRD analysis is presented in Part II of Chapter 3. (Note: Credit is given to Felicitas Jansen, an intern from Rheinisch-Westfälische Technische Hochschule Aachen, Germany and Dr. Matthew Polson, Compliance and Instrument Technician, School of Physical and Chemical Sciences, University of Canterbury for the SCXRD analysis.).

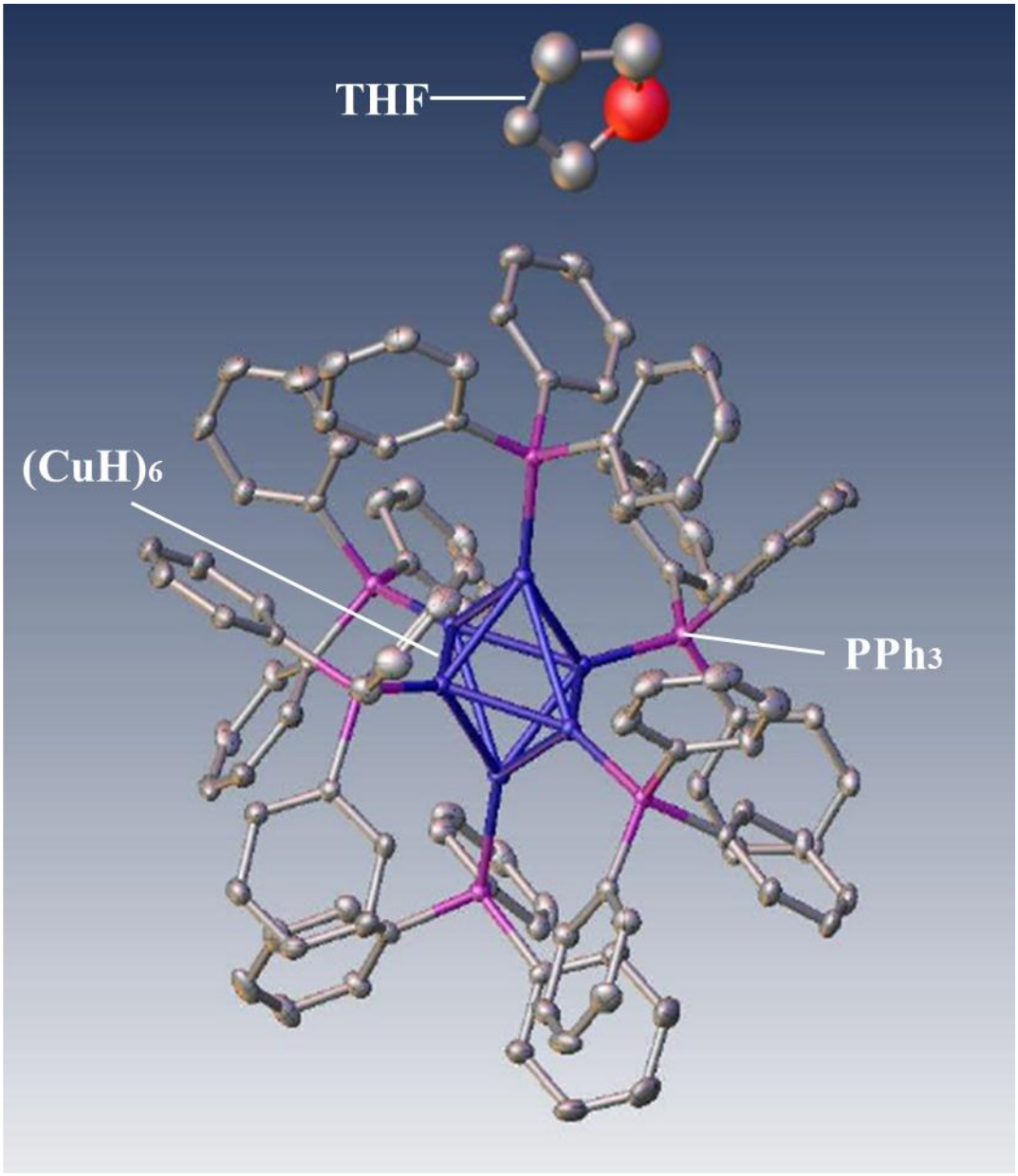

Figure C9: Single crystal structure of Cu_6 nanocluster generated by Olex^2 Crystallography software (Credit to Dr. Matthew Polson for the image).

C2.2.2 Thermal stability of copper nanoclusters

The TGA of the microcrystalline powder of the pure copper nanoclusters (Figure C10) revealed that the nanoclusters lost approximately 78.4% of their original weight at 260 °C under nitrogen. The initial mass loss can be attributed to loss of THF solvate molecules (molecular weight (MW) = 72.11 g/mole) and moist content which desorbed first at a

temperature below 100 °C (experimentally measured wt.% due to loss of THF and moist content – 3.5 wt.%; calculated (THF only) based on the empirical formula of $[(PPh_3)CuH]_6.0.75THF$ (MW = 2,015.2 g/mole) – 2.7%). The next stage of sample decomposition can be explained by the loss of the PPh_3 ligand (MW = 262.29 x 6 moles = 1573.74 g/mole) in the temperature range from 150 to 260 °C, leaving behind the copper or copper hydride nanoparticles (experimentally measured wt.% loss due to loss of PPh_3 ligands – 74.9 wt.%; calculated based on the empirical formula of $[(PPh_3)CuH]_6$ – 80.3%). It is impossible to reliably ascertain the fate of hydrides associated with Cu within cluster cores as such small mass loss (0.3% for all 6 of these) is within experimental error. The slight weight gain at the higher temperatures could indicate an onset of nitride or oxide formation, but this was not verified experimentally. (Note: Credit is given to Felicitas Jansen for her help in performing the TGA of the Cu_6 nanoclusters.).

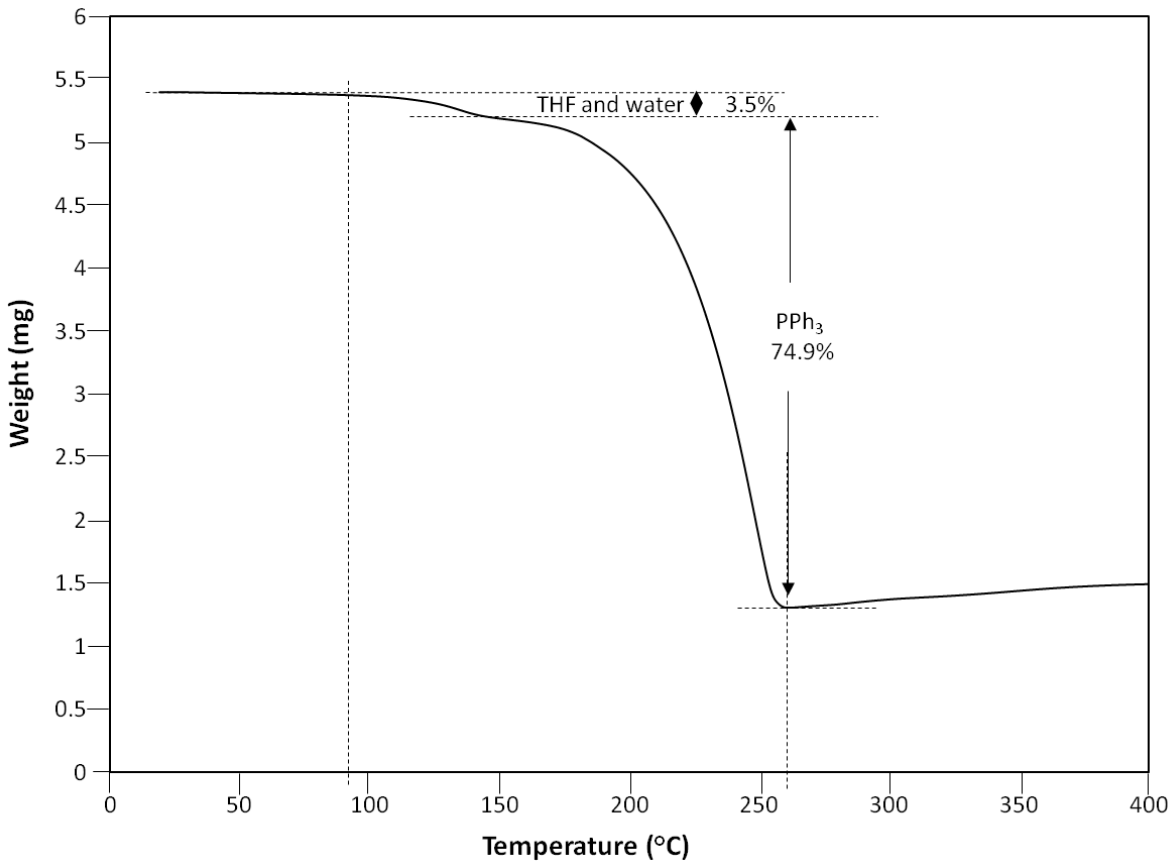

Figure C10: TGA of $[(PPh_3)CuH]_6.0.75THF$ nanoclusters.

C2.3 Cu/MWCNT catalyst samples: Morphology

Since both acid-reflux treated and pre-functionalised MWCNTs; $MWCNT_{acid}$ and $MWCNT_{COOH}$ dispersed equally well in both the THF and DI water for the functionalised and pre-functionalised MWCNTs, it was fair to assume that the copper nanoparticles distribution would show similar degree of dispersion on both the modified surfaces in the synthesised catalysts. Therefore, in this rectified work, only two samples of the catalysts were morphologically analysed by TEM; $1\%Cu/MWCNT_{COOH}$ and $1\%(Cu_6/MWCNT_{COOH})_{calcined}$, in order to see the effect of the different copper nanostructures, *i.e.* nanoparticles and nanoclusters in terms of their dispersion. However, the presence of the copper nanoparticles and the nanoclusters on the MWCNT were not distinguishable as shown in the TEM images in Figure C11 ($1\%Cu/MWCNT_{COOH}$) and Figure C12 ($1\%(Cu_6/MWCNT_{COOH})_{calcined}$), which implied the absence of the nanocluster form of copper in the $1\%(Cu_6/MWCNT_{COOH})_{calcined}$ sample.

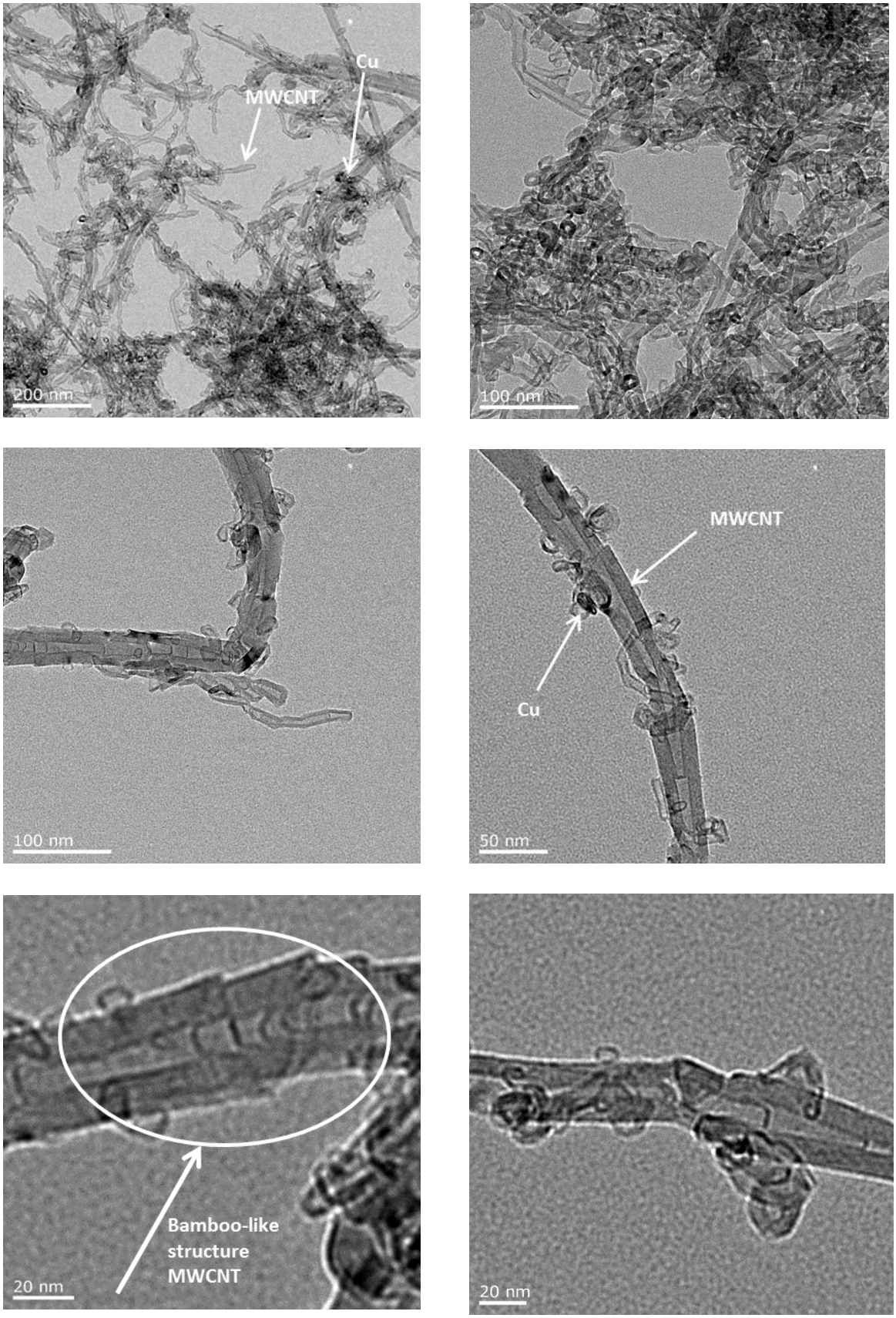

Figure C11: TEM images of 1%Cu/MWCNT$_{COOH}$ sample, arrows indicating suspected Cu sites.

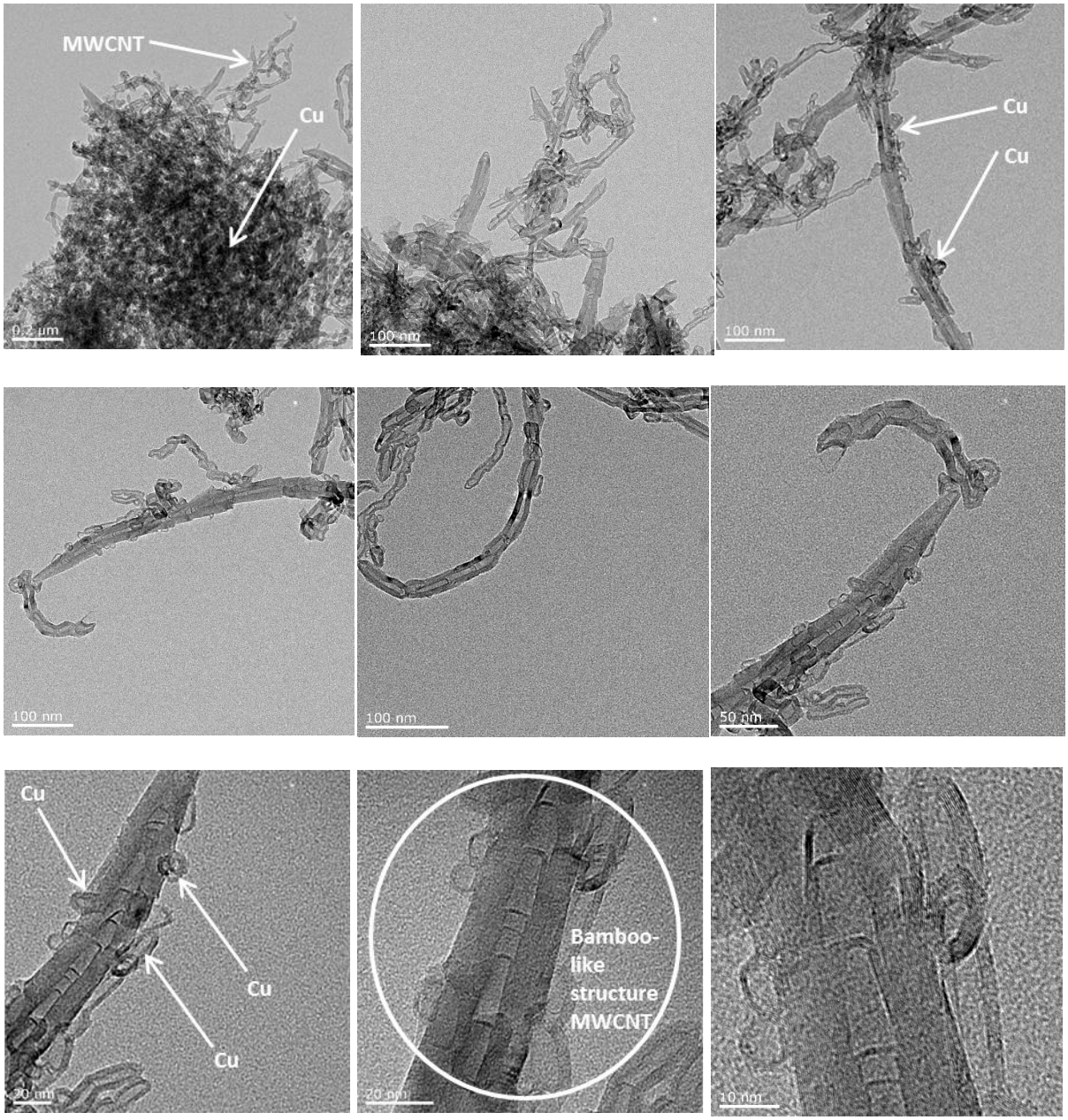

Figure C12: TEM images of 1%(Cu_6/$MWCNT_{COOH}$)$_{calcined}$ sample, arrows indicating suspected Cu sites.

Based on the TGA analysis of the crystallised powder of the copper nanoclusters seen in Figure C10, the ligand that held the hexameric copper atoms together was completely removed at the temperature of 260 °C. In this sample, the copper nanoclusters deteriorated to become copper nanoparticles during the sample calcination at 400 °C, which was overlooked during the overall catalyst synthesis procedure. Therefore, a further rectification step was taken in our next work to analyse the morphology of the copper nanoclusters on the MWCNT

directly after the wet-impregnated catalyst was vacuum-dried, without undergoing the calcination step.

It was also noted that the copper nanoparticles in both samples were not easily recognisable, which could imply that the 1% loading of the copper was insufficient to give a significant presence in the synthesised catalyst samples, or the overnight wet impregnation duration was too short for an effective copper deposition to take place. As seen earlier in Figure B4(B) in the preliminary work (Section B3.3 of APPENDIX B) where 1% copper loading on the MWCNT support seemed to have been present in excess, which contradicted the possibility of insufficient copper loading. However, the possibility of unreliable and unrepresentative TEM images in the preliminary work where the information gathered from the images could be misleading was not completely eliminated. Nonetheless, the presence of the copper nanoparticles in the catalyst samples (preliminary work) was clearly distinguished with the MWCNT, unlike the current samples (rectified work) where their presence was unidentifiable, which could confirm that the loading was indeed insufficient. The heating rate during calcination step was also relatively rapid. This could have led to an overshoot of the desired hold temperature of 400 °C, which might have affected the catalyst samples.

Therefore, further optimisation steps in our next work included the synthesis of the catalyst of a higher copper loading, and in a longer duration of wet impregnation process. In addition, a sample of copper nanoclusters deposition of a higher loading content on MWCNT were also prepared in order to assess the possibility of using the nanoclusters as a precursor that provides a means to disperse well the copper nanoparticles once the ligand was removed after a flow of gas was run over this catalyst at temperatures above 260 °C.

In addition, recalling the procedure employed in the preliminary study presented in APPENDIX B, another parameter that was notably different was the stirring temperature of the overnight impregnation; 40 °C in the preliminary study and room temperature in this current rectified work. As mentioned above, the TEM images of the catalysts synthesised in the preliminary work appeared to be in excess of easily recognisable copper nanoparticles in comparison to the copper nanoparticles on the catalysts synthesised in this current rectified

work, which appeared insufficient to give a significant presence. This may suggest that the wet impregnation requires some level of heating in order to effect the deposition of the metal nanoparticles. However, the condition of the wet impregnation was kept at ambient temperature in order to not influence the observation on changes made to the two parameters (copper loading content and impregnation duration), even though it can be speculated that the wet impregnation needed some heating work for an effective interaction between the copper nanoparticles and the MWCNT support during deposition.

A noteworthy observation on the structure of the MWCNT is the presence of bamboo-type MWCNT (Figure C11 and Figure C12), which indicates a poor graphitisation of the as-received pre-functionalised MWCNT. This could also possibly be the reason for the poor interaction between the copper nanoparticles and the MWCNT support, if the samples were indeed not effectively containing the copper nanoparticles.

A comparison of the TEM images was done with some other work presented in the literature (Figure C13 (transitional metal nanoparticles) and Figure C14 (noble metal nanoparticles)), in order to verify the suspected copper nanoparticles on the images were indeed the metal, or the disoriented carbon materials. It is noted quite obviously from the work in the literature that the noble metal nanoparticles generally provide very good dispersion on the surface of the CNTs, in comparison to the transition metals. Another important point to note is the metal nanoparticles loading contents deposited on the CNTs as presented in the literature were above 10% for all the transition metals.

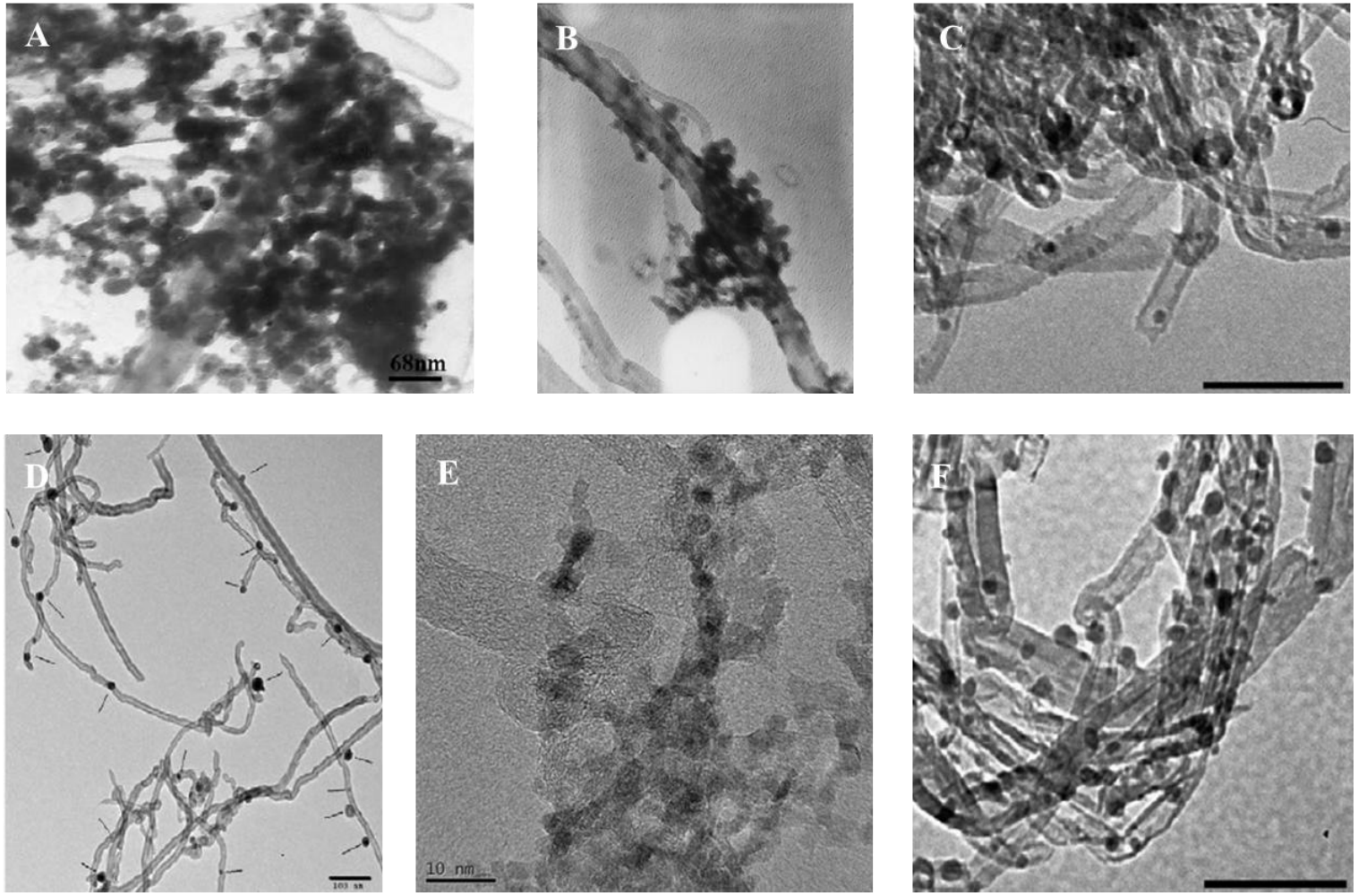

Figure C13: TEM images of transitional metal nanoparticles on CNTs from literature.

(A) 10%Cu-7%Zn/CNT [18]; (B) 18%Cu-4%Zn/CNT [19]; (C) 15%Co/MWCNT [20]; (D) 12%Fe/MWCNT [6]; (E) 20%Ni/MWCNT [1]; and (F) 10%Ni/MWCNT [20].

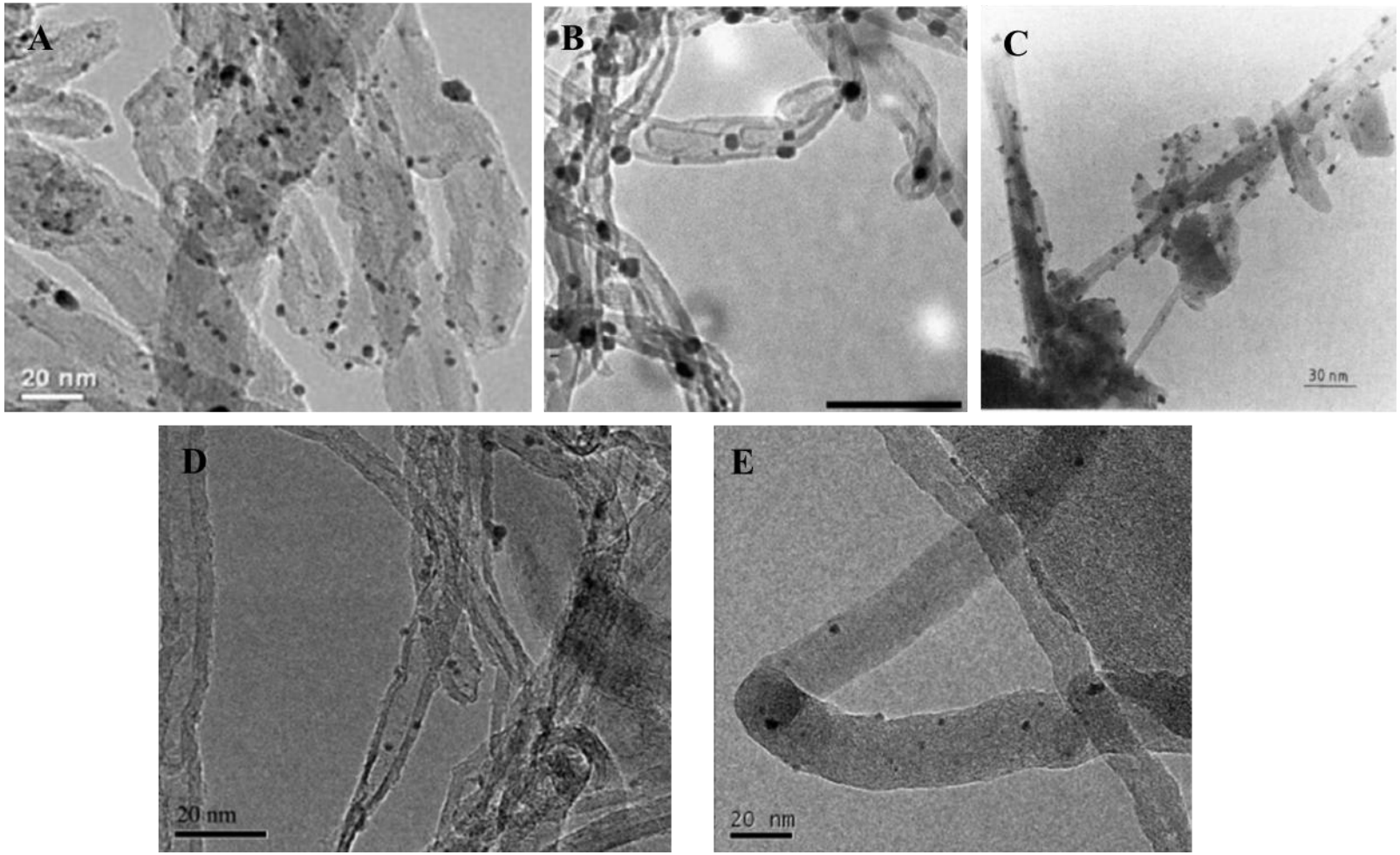

Figure C14: TEM images of noble metal nanoparticles on CNTs from literature.

(A) 1%Pt/MWCNT [21]; (B) 8%Pt/MWCNT [20]; (C) 0.2%Ru/CNT [22]; (D) 3%Pd/MWCNT [23]; and (E) 9%Rh/MWCNT [20].

It is proven from the work presented by Eswaramoorthi *et al.* (2006) [18] (Figure C13(A)) and Yang and Liao (2007) [19] (Figure C13(B)) that copper nanoparticles did not give good dispersion on the CNT, similarly to what was observed in our samples. Indeed, in both of the works demonstrated, bimetal Cu-Zn nanoparticles were used in the catalysts, and the two metals were not able to be distinguished from the TEM images. In addition, the monometallic copper/carbon nanomaterials work conducted relatively recently [24, 25] did not provide TEM images of the synthesised catalysts at all, which could possibly mean that copper may indeed not give a good dispersion on the MWCNT. However, the synthesised catalysts were demonstrated to be active on oxy-steam reforming of methanol [25] and water–gas shift [24] respectively. With the catalytic activity of the Cu/carbon nanomaterials catalysts demonstrated in these works, it is fair to conclude that a homogeneous copper dispersion on the MWCNT may not be attainable, but the catalytic activity of the synthesised catalyst is still worth studying.

C3. Rectified work: Conclusions

In this rectified work, appropriate actions had been taken as rectification steps based on the lessons learned identified from the preliminary study. The acid oxidation had effectively modified the degree of the MWCNT's surface hydrophobicity in polar solvents. The presence of the copper nanoparticles was suspected to be insufficient and not convincingly determined, and hence a meaningful assessment on their degree of dispersion on the MWCNT was not able to be deduced. On the other hand, the copper nanoclusters reverted back to nanoparticles structure due to the decomposition of the ligand during the calcination step, which was mistakenly conducted at a temperature way above the ligand's thermal decomposition temperature. Therefore, the TEM images for both 1%Cu/$MWCNT_{COOH}$ and 1%$(Cu_6/MWCNT_{COOH})_{calcined}$ samples were the same essentially.

C4. Further optimisation work: Experimental, results and discussion

Based on the learning from the rectified work, a small number of samples were synthesised to further optimise our work, with the as-received pre-functionalised $MWCNT_{COOH}$ being used as the support for a quick sample assessment. Table C2 lists the catalyst samples synthesised for the assessment of the wet impregnation effectiveness. The optimisation steps included the synthesis of the copper nanoparticles (Cu_{NP}) catalyst samples of a higher copper loading (denoted as $Cu_{NP,H2O}/MWCNT_{COOH}$ (note: subscript H_2O refers to the solvent used in the copper solution to differentiate this material with an improved material synthesised in Part II of Chapter 3 that used methanol as the solvent) from this point onwards in this Appendix), and in a longer duration of wet impregnation process at room temperature, followed by calcination at 400 °C in nitrogen flow. A sample of copper nanoclusters (Cu_{NC}) deposition of a higher loading content on $MWCNT_{COOH}$ (denoted as $Cu_{NC}/MWCNT_{COOH}$ from this point onwards in this Appendix) was prepared, but this sample was not calcined in order to characterise the copper crystalline morphology and the copper nanoclusters dispersion on the $MWCNT_{COOH}$, using TEM. An analysis by inductively coupled plasma mass spectrometry (ICP-MS) was performed prior to the TEM analysis to verify the presence and measure the content of the copper nanoparticles. Only one sample ($Cu_{NC}/MWCNT_{COOH}$) was analysed by TEM for an assessment.

Table C2: Next optimisation steps in the catalyst synthesis for quick assessment.

	MWCNT	**Copper**		
	$MWCNT_{COOH}$	**Nanoparticles**		**Nanoclusters**
Sample name		$1\%Cu_{NP,H2O}$/ $MWCNT_{COOH}$	$10\%Cu_{NP,H2O}$/ $MWCNT_{COOH}$	Cu_{NC}/ $MWCNT_{COOH}$
Wet impregnation	Loading content	1%	≥ 10%	≥ 10%
	Duration	3 days	1 day	1 day
	Temperature	Room	Room	Room
Calcination	Temperature	400 °C	400 °C	No calcination
ICP-MS	Carried out	Yes	Yes	Yes
TEM	Carried out	No	No	Yes

Three samples of Cu/MWCNT catalyst were prepared following the plan presented in Table C2. The copper nanoparticles catalyst samples ($1\%Cu_{NP,H2O}/MWCNT_{COOH}$ and $10\%Cu_{NP,H2O}/MWCNT_{COOH}$) were prepared following the procedure described in Section C1.2.2.1, while the copper nanoclusters ($Cu_{NC}/MWCNT_{COOH}$) catalyst sample was prepared following the procedure described in Section C1.2.2.2, but without the calcination step. The preparation of $Cu_{NC}/MWCNT_{COOH}$ sample for TEM analysis was done following the procedure described in Section C1.3.3.

The preparation of all the three samples for ICP-MS was done following the procedure below. An amount of 0.05 g of each of the synthesised catalyst samples was digested in 2 mL aqua regia at 80 °C for 2 days to separate the copper particles from the $MWCNT_{COOH}$ support. The suspension was ultrasonicated to homogenize the dissolution of the copper particles in the aqua regia solution, while the $MWCNT_{COOH}$ support was well dispersed in the suspension (well dispersed $MWCNT_{COOH}$ shows good hydrophilicity of the CNTs in aqua regia). The copper and $MWCNT_{COOH}$ suspended solution was centrifuged for 10 minutes at 10,000 rpm and 20 °C to let the $MWCNT_{COOH}$ to settle to the bottom of the centrifuge tube. The copper solution free of the $MWCNT_{COOH}$ suspension was then diluted to the range of 50 – 1000 µg/l (ppb). Using chirana rubber-less syringe, the copper solution was transferred out and filtered through a 0.45 µm hydrophilic/acid-compatible nylon-membrane polypropylene

housing filter, into a new and clean centrifuge tube for ICP-MS (7500cx single-quad, Agilent Technologies) analysis. For every sample, a blank solution was prepared for ICP-MS analysis to account for an inherent copper content in the *aqua regia* solution that was not from the tested samples. A duplicate sample was prepared to ensure consistency of the results. (Note: Credit is given to Robert Stainthorpe, Technician, School of Physical and Chemical Sciences, University of Canterbury for his help in performing the ICP-MS analysis.).

The results of the actual copper loading content in the samples based on ICP-MS are presented in Table C3.

Table C3: Theoretical and actual copper loading on catalyst samples.

Sample	Theoretical loading (%)	Actual loading based on ICP-MS (%)
$1\%Cu_{NP,H2O}/MWCNT_{COOH}$	1	0.08
$10\%Cu_{NP,H2O}/MWCNT_{COOH}$	10	1.20
$Cu_{NC}/MWCNT_{COOH}$	15	15.02

Based on the tabulated results in Table C3, it was found that the actual copper loading on the copper nanoclusters catalyst sample, $Cu_{NC}/MWCNT_{COOH}$ was very close to the theoretical loading content. The copper nanoclusters solution in THF was vacuum-dried post impregnation, evaporating the THF and leaving behind all the copper nanoclusters on the $MWCNT_{COOH}$. However, this did not provide an information if the copper nanoclusters were effectively anchored on the surface of the $MWCNT_{COOH}$. Further analysis was required to examine the interaction between the copper nanoclusters and the $MWCNT_{COOH}$ in order to ensure an effective activity of the catalyst samples when being employed in our reaction model, which is a separate discussion that will be dealt in Part II of Chapter 3.

On the other hand, the wet impregnation was not effective in the case of copper nanoparticles where water was used as the solvent in the copper solution. Longer wet impregnation duration (3 days) in the $1\%Cu_{NP,H2O}/MWCNT_{COOH}$ sample synthesis did not offer a more

effective copper deposition although an additional time was allowed for the copper solution to interact with the $MWCNT_{COOH}$. In both of the copper nanoparticles catalyst samples, the preparation steps included a centrifugation of the suspension followed by a decantation of the remaining solution. It was suspected that due to an insufficient adsorption/contact time or an ineffective interaction of the copper nanoparticles in the solution with the carboxyl-MWCNTs, the actual amount of the copper nanoparticles deposited on the $MWCNT_{COOH}$'s surface was an order of magnitude lower than the calculated theoretical loading. The remaining of the copper particles in the solution was lost in the decantation step, making the reproducibility of the sample difficult to attain.

The TEM images of the $Cu_{NC}/MWCNT_{COOH}$ are presented in Figure C15.

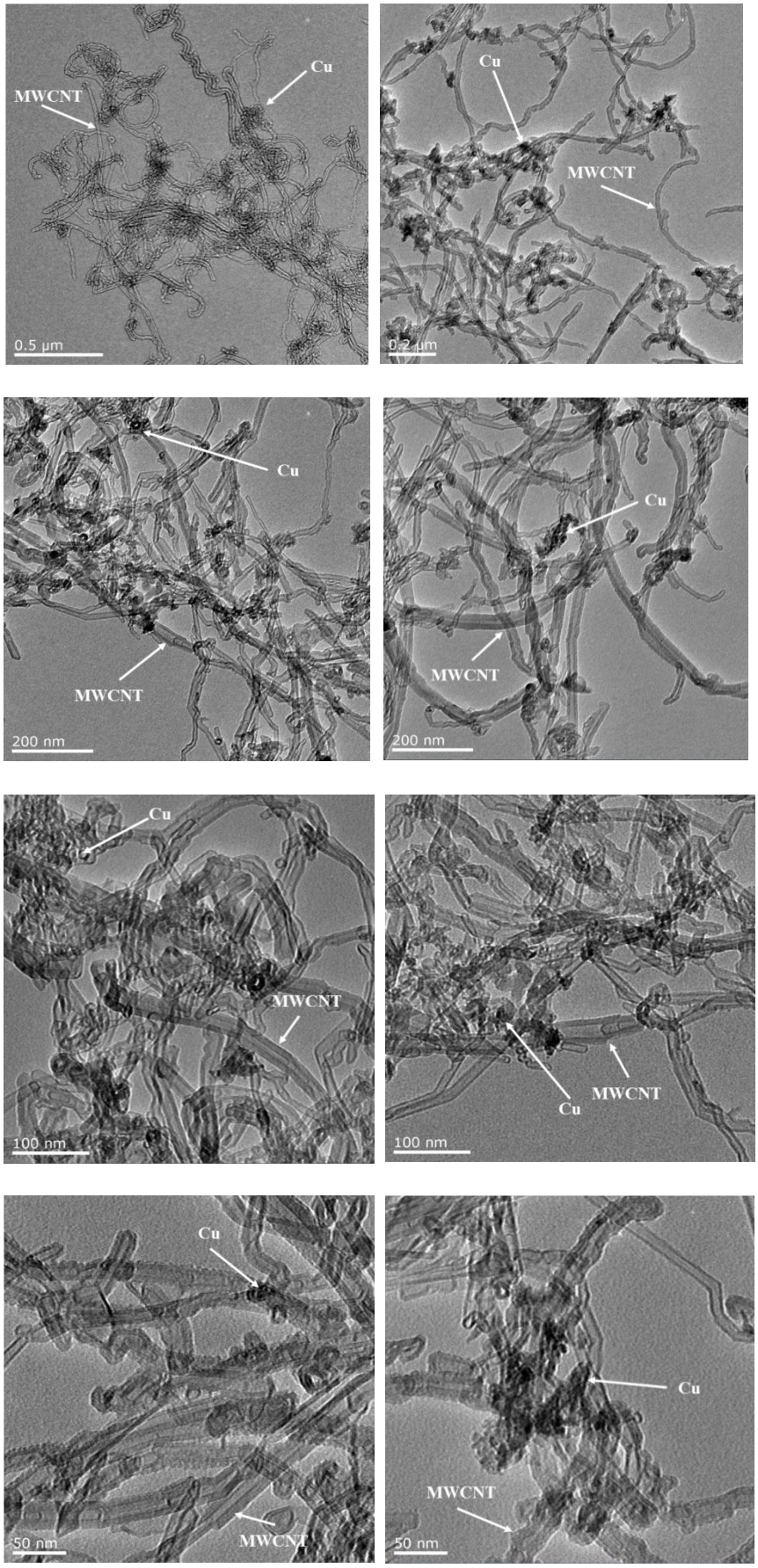

Figure C15: TEM images of Cu_{NC}/$MWCNT_{COOH}$ sample.

Based on the morphology of the $Cu_{NC}/MWCNT_{COOH}$ sample shown in Figure C14, the presence of the copper nanostructures is clearly seen and their morphology is distinguishable from the carbon nanotubes, as compared to the morphology images of the previous samples seen earlier in Figure C11 and Figure C12, containing theoretically 1% copper loading. The morphology of the dispersion of the copper particles in the current sample shown in Figure C15 is in alignment with the literature as seen in Figure C13(A) [18] and Figure C13(B) [19], all containing a copper content of higher than 10%. Based on this finding, it is therefore concluded that TEM may not provide a fair representative analysis to assess the dispersion of copper or other transition metals on the MWCNTs since the information gathered from the dispersion images can be misleading. Therefore, the technique shall not be treated as the final determinant to qualify the Cu/MWCNT as a catalyst for application in the reaction model of interest. The characterisation analysis will be supplemented by ICP-MS to determine the copper content, and CO chemisorption to determine the copper particle size and their dispersion percentage. CO temperature-programmed desorption (CO-TPD) study will be conducted to hypothetically predict the catalytic activity of the synthesised catalysts in the reaction model of interest (low-temperature water–gas shift). This will be presented in Part II of Chapter 3.

C5. Summary of final work plan

C5.1 MWCNT support

In our rectified work, we have seen (Figure C6) that the acid oxidation had effectively modified the degree of the MWCNT's surface hydrophobicity in polar solvents, consistent with the behaviour observed on the as-received pre-functionalised MWCNT ($MWCNT_{COOH}$). However, the pre-treated MWCNT in our rectified work ($MWCNT_{acid}$) may have introduced some carbon components that were unstable at very high temperature.

It can therefore be concluded that the employed oxidation technique has proven to have managed to functionalise the MWCNT's surface, but careful optimisation on parameters such as the oxidation temperature, stirring rate and duration, as well as the concentration of the oxidising acids need to be undertaken. The optimisation of the functionalisation procedure is a separate study that requires investments of substantial time and effort beyond the scope of this work, and hence, will not be demonstrated in this thesis project. The difference in thermal stability between the $MWCNT_{acid}$ and the as-received pristine MWCNT ($MWCNT_p$) (Figure C8) provides the information that although the acid reflux pre-treatment in our rectified work has managed to functionalise the pristine MWCNT's surface, the thermal stability of the MWCNT on the other hand deteriorated possibly due to the breaking of nanotubes tubular length and the damage of some of the graphitic carbon structure to disordered structure.

Therefore, a further purification step adopted from Stancu *et al.* (2011) [17] was introduced post the acid-reflux treatment to remove the disordered carbon and the broken nanotubes tubular length through combustion; in order to leave behind only the crystallised, well-graphitised, high purity functionalised MWCNT. This MWCNT sample is denoted as $MWCNT_{acid,air}$ for the purpose of our following discussion.

As we were only interested in the application of the functionalised MWCNT, it was reasonable to use the as-received pre-functionalised MWCNT as a representation of a pre-treated (by acid reflux) and purified (by air oxidation) MWCNT sample moving forward, for convenience, and to avoid repetitive work that does not introduce new findings and information. A validation based on dispersion and stability in water and THF, TGA (same procedures as described in Section C1.3), and zeta potential (MWCNT samples dispersed in DI water measured using Zetasizer Nano Series (Malvern Instruments Ltd., UK) at room temperature), was done in equating our acid-oxidation-air-purified $MWCNT_{acid,air}$ with the as-received pre-functionalised $MWCNT_{COOH}$. A comparative presentation of the outcome of the characteristics and properties of the two MWCNTs is given below in order to demonstrate a good agreement of $MWCNT_{acid,air} = MWCNT_{COOH}$.

Similarly to $MWCNT_{COOH}$, the functionalised $MWCNT_{acid,air}$ was observed to disperse satisfactorily in water and THF as shown in Figure C16, and the suspensions were found to be stable even after more than a week of storage.

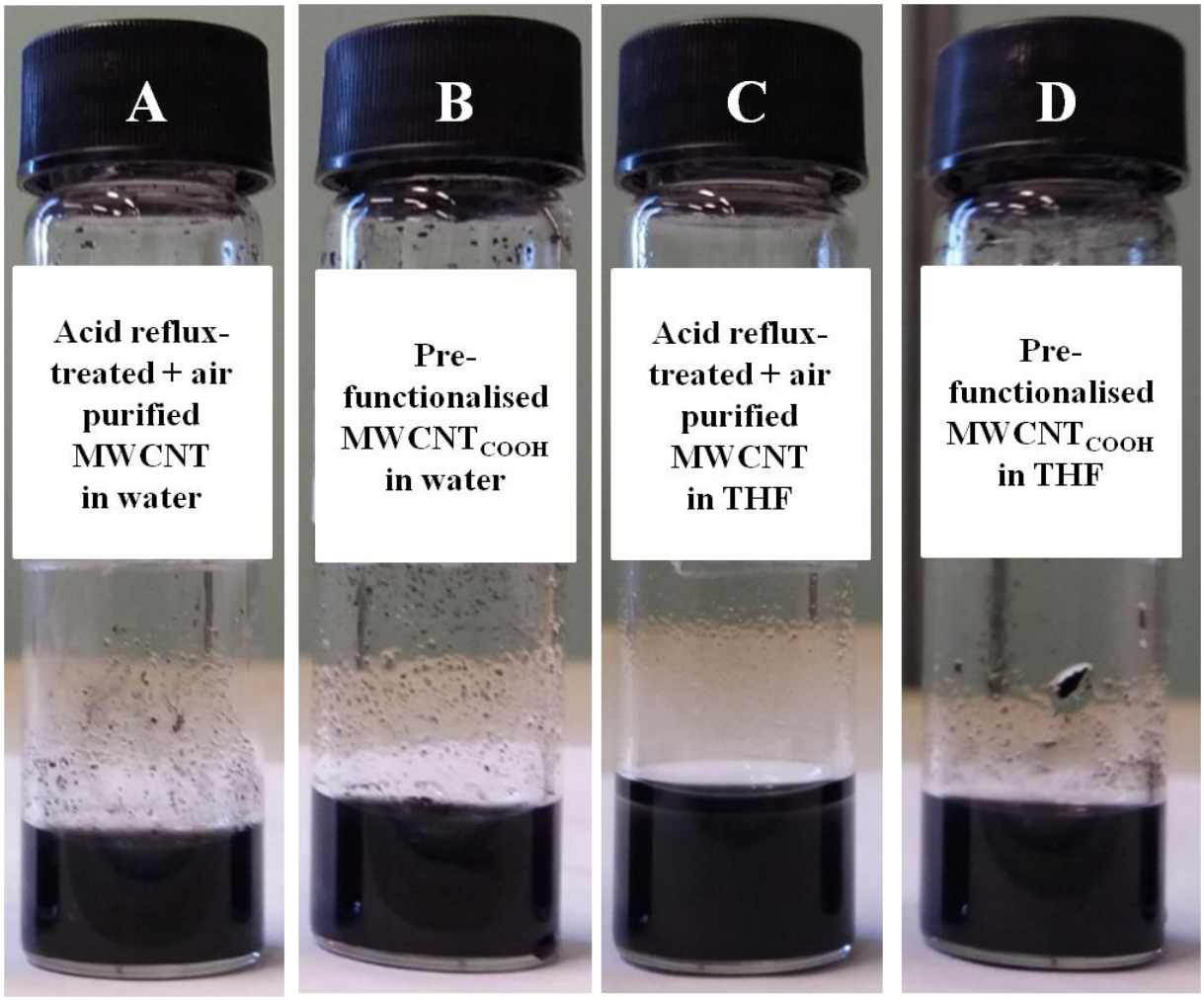

Figure C16: Dispersion of $MWCNT_{acid,air}$ and $MWCNT_{COOH}$.

(A – B) In water; and (C – D) in THF.

From Figure C17, it can be observed that the $MWCNT_{acid,air}$ was in general equally thermally stable as the $MWCNT_{COOH}$ in an inert, non-reacting environment.

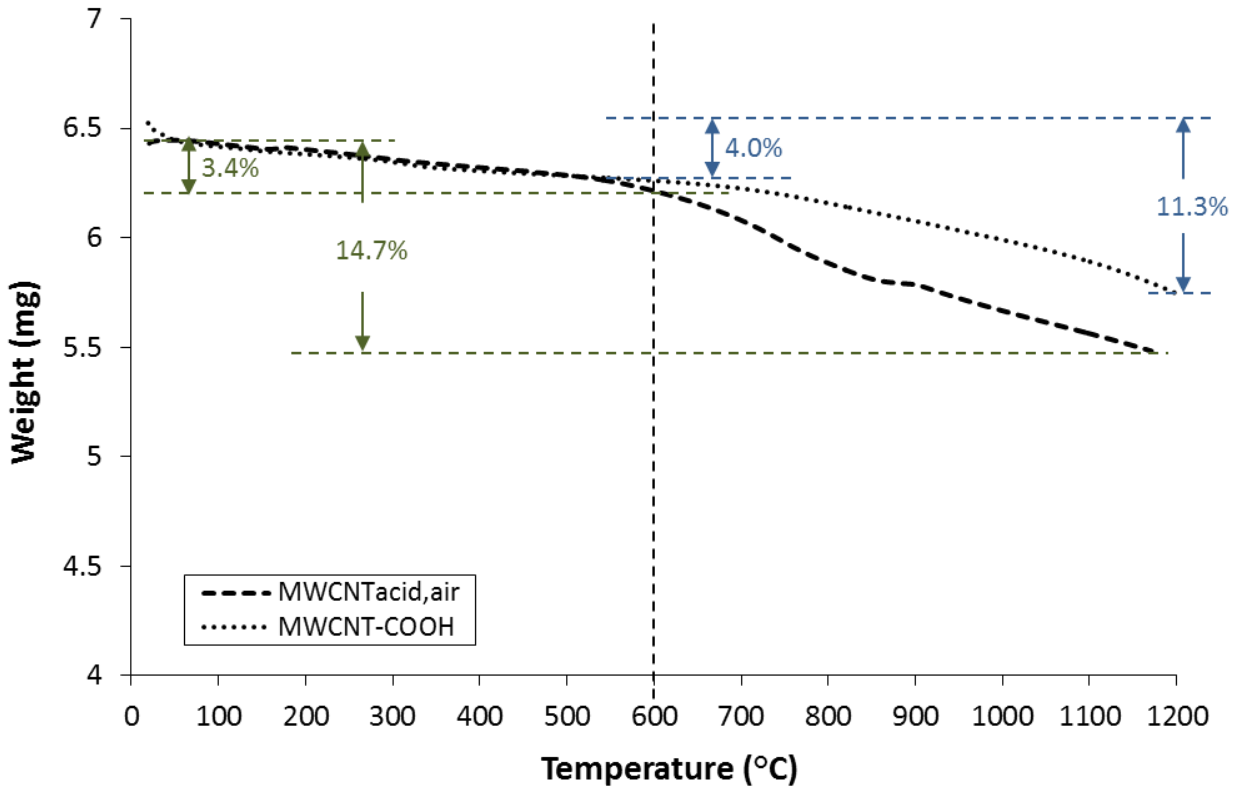

Figure C17: TGA of the acid-refluxed-air-purified functionalised and as-received pre-functionalised MWCNT supports.

Zeta potential of the MWCNT samples dispersed in DI water was measured at room temperature. The results were averaged and presented in Table C4, with each sample's measurement repeated at least 4 times. The negative surface charge increased by close to four times after the pristine MWCNT underwent the acid reflux oxidation. However, the negative surface charge was halved after the acid oxidised sample was purified with air, as the damaged and disoriented, less stable carbon structures that carried with them more negative surface charge were removed by gasification. It can be clearly seen that the MWCNT that underwent acid-refluxed functionalisation followed by air purification had a very close zeta potential value as the pre-functionalised $MWCNT_{COOH}$.

Table C4: Zeta potential of MWCNT samples dispersed in water at room temperature.

Sample	Zeta potential (mV)
$MWCNT_p$	–15.43 ± 2.03
$MWCNT_{acid}$	–51.47 ± 2.15
$MWCNT_{acid,air}$	–24.42 ± 2.69
$MWCNT_{COOH}$	–24.48 ± 1.46

Based on the evidence presented in Figure C16, Figure C17 and Table C4, it was satisfactorily accepted that the $MWCNT_{acid,air}$ has similar characteristics as the $MWCNT_{COOH}$. Therefore, in this thesis, $MWCNT_{COOH}$ will be used as the functionalised MWCNT support in the catalyst synthesis (Part II of Chapter 3) for convenience.

C5.2 Catalysts synthesis

A demonstration of the catalyst application in a reaction model that requires an operating temperature of above 260 °C will result in the Cu_6 nanoclusters structure to revert back to nanoparticles when exposed to high temperatures due to its poor thermal stability. In addition, the tedious handling procedure of the nanoclusters system under argon environment due to their sensitivity in the presence of moisture seems impractical for an intended commercial application. However, the Cu_6 nanoclusters could potentially be a good precursor of copper nanoparticles for an effective dispersion for catalysis application. Therefore, the work in this thesis will demonstrate the potential of the copper nanoclusters as a precursor to achieve well dispersed copper nanoparticles once the ligand is removed.

We will keep the same synthesis steps in the preparation of the copper nanoclusters catalyst samples. The copper nanoclusters catalysts will be optimised further by varying the copper loading content. CO chemisorption and XRD techniques will be used to measure the copper dispersion and particle size; and to characterise the surface chemistry of the synthesised catalysts. CO-TPD will be performed to hypothetically predict their activity performance in

the low-temperature water–gas shift reaction. The optimal copper loading will be used to fix the copper nanoclusters content on raw MWCNT, functionalised MWCNT and alumina in order to study the effect of the copper interaction with the different types of support, and the loading content will be fixed as well on the sample of copper nanoparticles on functionalised MWCNT to examine the effect of different copper nanostructure precursors (nanoclusters *vs.* nanoparticles).

Based on the ICP-MS results seen in Table C3 earlier, the remaining copper particles in the solution were lost in the decantation step that resulted in an actual copper loading to be an order of magnitude lower than the theoretical loading in the catalyst samples. This will result in a difficulty in attaining the reproducibility of the sample when using water as the solvent in the copper solution. Therefore, in our final synthesis work that will be presented in Part II of Chapter 3, an organic solvent; methanol will be used in the copper solution instead of water when synthesising the copper nanoparticles catalyst sample while the synthesis parameters (*i.e.* impregnation temperature, stirring rate and duration) and calcination steps will be kept the same as described in Section C1.2.2.1 for copper solution prepared in water. However, the post wet impregnation step will include vacuum-drying the solution instead of centrifugation and decantation.

This will be followed by an actual reaction run over all the synthesised catalysts above to evaluate their actual performance and hence, validate the hypothetical catalytic activity prediction (Chapter 4), and finally a reaction kinetic study will be performed (Chapter 5).

References of APPENDIX C

1. López, E., et al., *Multiwalled carbon nanotubes-supported Nickel catalysts for the steam reforming of propane.* Journal of Materials Science, 2012. **47**(6): p. 2985-2994.
2. Mohino, F., et al., *High surface area monoliths based on pillared clay materials as carriers for catalytic processes.* Applied Clay Science, 2005. **29**(2): p. 125-136.

3. Baharudin, L. and M.J. Watson, *Hydrogen applications and research activities in its production routes through catalytic hydrocarbon conversion.* Reviews in Chemical Engineering, 2017. **34**(1): p. 43-72.
4. Albert, C.F., et al., *Lewis-base adducts of Group 11 metal (I) compounds. 49. Structural characterization of hexameric and pentameric (triphenylphosphine) copper (I) hydrides.* Inorganic Chemistry, 1989. **28**(7): p. 1300-1306.
5. Cook, A.W., et al., *Synthesis, Characterization, and Reactivity of the Group 11 Hydrido Clusters [Ag6H4 (dppm) 4 (OAc) 2] and [Cu3H (dppm) 3 (OAc) 2]*. Inorganic chemistry, 2016.
6. Abbaslou, R.M.M., et al., *Iron catalysts supported on carbon nanotubes for Fischer–Tropsch synthesis: Effect of catalytic site position.* Applied Catalysis A: General, 2009. **367**(1): p. 47-52.
7. Peng, Y. and H. Liu, *Effects of oxidation by hydrogen peroxide on the structures of multiwalled carbon nanotubes.* Industrial & engineering chemistry research, 2006. **45**(19): p. 6483-6488.
8. Hamilton Jr, R.F., et al., *Purification and sidewall functionalization of multiwalled carbon nanotubes and resulting bioactivity in two macrophage models.* Inhalation toxicology, 2013. **25**(4): p. 199-210.
9. Yu, J.-G., et al., *Preparation and characterization of soluble methyl-β-cyclodextrin functionalized single-walled carbon nanotubes.* Physica E: Low-Dimensional Systems and Nanostructures, 2008. **40**(3): p. 689-692.
10. Basahel, S.N., et al., *Chemical modification of multi-walled carbon nanotubes using different oxidising agents: optimisation and characterisation.* International Journal of Nanoparticles, 2009. **2**(1-6): p. 200-208.
11. Yudianti, R., et al., *Analysis of functional group sited on multi-wall carbon nanotube surface.* Open Materials Science Journal, 2011. **5**: p. 242-247.
12. Sun, W., et al., *Luminescence from multi-walled carbon nanotubes and the Eu (III)/multi-walled carbon nanotube composite.* Carbon, 2003. **41**(8): p. 1685-1687.
13. Lee, S.-Y. and S.-J. Park, *Hydrogen adsorption of acid-treated multi-walled carbon nanotubes at low temperature.* Bulletin of the Korean Chemical Society, 2010. **31**(6): p. 1596-1600.
14. Chen, S., et al., *A new approach to the functionalization of single-walled carbon nanotubes with both alkyl and carboxyl groups.* Chemical Physics Letters, 2005. **402**(4): p. 312-317.

15. Datsyuk, V., et al., *Chemical oxidation of multiwalled carbon nanotubes.* Carbon, 2008. **46**(6): p. 833-840.
16. Moraes, R.A., et al., *The effect of different chemical treatments on the structure and stability of aqueous dispersion of iron-and iron oxide-filled multi-walled carbon nanotubes.* Journal of the Brazilian Chemical Society, 2011. **22**(11): p. 2191-2201.
17. Stancu, M., et al., *Purification of multiwall carbon nanotubes obtained by AC arc discharge method.* Optoelectronics and Advanced Materials, 2011. **5**(8): p. 846-850.
18. Eswaramoorthi, I., V. Sundaramurthy, and A. Dalai, *Partial oxidation of methanol for hydrogen production over carbon nanotubes supported Cu-Zn catalysts.* Applied Catalysis A: General, 2006. **313**(1): p. 22-34.
19. Yang, H.-M. and P.-H. Liao, *Preparation and activity of Cu/ZnO-CNTs nano-catalyst on steam reforming of methanol.* Applied Catalysis A: General, 2007. **317**(2): p. 226-233.
20. Seelam, P., et al., *CNT-based catalysts for H 2 production by ethanol reforming.* international journal of hydrogen energy, 2010. **35**(22): p. 12588-12595.
21. Li, C., et al., *Carbon nanotubes supported Pt catalysts for phenylacetylene hydrogenation: effects of oxygen containing surface groups on Pt dispersion and catalytic performance.* Catalysis today, 2012. **186**(1): p. 69-75.
22. Planeix, J.M., et al., *Application of Carbon Nanotubes as Supports in Heterogeneous Catalysis.* Journal of the American Chemical Society, 1994. **116**(17): p. 7935-7936.
23. Xiang, Y., et al., *Carbon Nanotubes and Activated Carbons Supported Catalysts for Phenol in Situ Hydrogenation: Hydrophobic/Hydrophilic Effect.* Industrial & Engineering Chemistry Research, 2014. **53**(6): p. 2197-2203.
24. Oliveira, N.M., G.P. Valençaa, and R. Vieirab, *Water Gas Shift Reaction On Copper Catalysts Supported On Alumina And Carbon Nanofibers.* Chemical Engineering, 2015. **43**.
25. Mierczynski, P., et al., *Monometallic copper catalysts supported on multi-walled carbon nanotubes for the oxy-steam reforming of methanol.* Reaction Kinetics, Mechanisms and Catalysis, 2016. **117**(2): p. 675-691.

APPENDIX D

Supplementary material for Part II of Chapter 3

D1. Introduction – CO equilibrium conversion of water–gas shift reaction

D1.1 Derivation of equilibrium constant equation

Derivation is made based on Fogler (2006) [1].

Consider gas-phase reaction:

$$\mathrm{A} + \frac{b}{a}\mathrm{B} \leftrightarrow \frac{c}{a}\mathrm{C} + \frac{d}{a}\mathrm{D} \qquad \text{(D1)}$$

The true (dimensionless) equilibrium constant is:

$$K_{eq} = \frac{a_{\mathrm{C}}^{c/a}\, a_{\mathrm{D}}^{d/a}}{a_{\mathrm{A}}\, a_{\mathrm{B}}^{b/a}} \qquad \text{(D2)}$$

where a_{i} is the activity of species i, and $a_{\mathrm{i}} = \frac{f_{\mathrm{i}}}{f_{\mathrm{i}}^{0}}$

where f_{i} = fugacity of species i and

f_{i}^{0} = fugacity of species i at the standard state (1 atm for gas)

The activity of species i:

$$a_{\mathrm{i}} = \frac{f_{\mathrm{i}}}{f_{\mathrm{i}}^{0}} = \gamma_{\mathrm{i}} \mathrm{P_i} \qquad \text{(D3)}$$

where γ_i is activity coefficient of species i

P_i is partial pressure of species i, atm, kPa

Hence, eq. (D2) becomes:

$$K_{eq} = \frac{\gamma_{\mathrm{C}}^{c/a}\, \gamma_{\mathrm{D}}^{d/a}}{\gamma_{\mathrm{A}}\, \gamma_{\mathrm{B}}^{b/a}} \cdot \frac{\mathrm{P_C}^{c/a}\, \mathrm{P_D}^{d/a}}{\mathrm{P_A}\, \mathrm{P_B}^{b/a}} = K_{\gamma} K_{\mathrm{P}} \qquad \text{(D4)}$$

$$\delta = \frac{c}{a} + \frac{d}{a} - \frac{b}{a} - 1$$

where K_γ is activity equilibrium constant = 1.0 $\mathrm{atm}^{-\delta}$ (for ideal gas)

K_P is pressure equilibrium constant, atm^{δ}

Therefore eq. (D4) is simplified to:

$$K_{eq} = K_{\mathrm{P}} = \frac{\mathrm{P_C}^{c/a}\, \mathrm{P_D}^{d/a}}{\mathrm{P_A}\, \mathrm{P_B}^{b/a}} \qquad \text{(D5)}$$

For ideal gas:

$K_P = K_C (RT)^{\delta}$

where K_C is the concentration equilibrium constant

For water–gas shift (WGS) reaction:

$CO + H_2O \leftrightarrow H_2 + CO_2$

$$\delta = \frac{c}{a} + \frac{d}{a} - \frac{b}{a} - 1 = 0$$

Therefore, $K_{eq} = K_P = K_C$

$$K_{eq} = K_P = \frac{P_{CO_2}\, P_{H_2}}{P_{CO}\, P_{H_2O}} = \frac{C_{CO_2}\, C_{H_2}}{C_{CO}\, C_{H_2O}} = K_C \qquad \text{(D6)}$$

where $K_P = K_C$ can also be related by ideal gas law, $P_i = C_i\, R\, T$

From thermodynamics, we know:

$$R\, T \ln K_{eq} = -\Delta G_{Rx} \qquad \text{(D7)}$$

where ΔG_{Rx} is change in Gibbs free energy of reaction

At Standard Temperature and Pressure (STP) (T = 298 K, P = 1 atm):

$$\Delta G^0_{Rx}(298\ K) = G^0_{CO_2}(298\ K) + G^0_{H_2}(298\ K) - G^0_{CO}(298\ K) - G^0_{H_2O}(298\ K) \qquad \text{(D8)}$$

where $G^{0}_{i,298K}$ is Gibbs free energy of formation of species i at STP

Similarly at other reaction temperatures, the change in Gibbs free energy of WGS reaction is related by the Gibbs free energy of formation of the species in the reaction at that particular temperature, T, by:

$$\Delta G_{Rx}(T) = G_{CO_2}(T) + G_{H_2}(T) - G_{CO}(T) - G_{H_2O}(T) \quad \text{(D9)}$$

From thermodynamics, Gibbs free energy is related with enthalpy, H and entropy, S by:

$$G = H - T\,S \quad \text{(D10)}$$

Deriving from eq. (D9) (derivation steps can be found in Roósz *et al.* (2016) [2] and Keszei (2016) [3]), G_i (T) can be calculated using Gibbs–Helmholtz equation:

$$\left[\frac{\partial(G/T)}{\partial T}\right]_P = -\frac{H}{T^2} \quad \text{(D11)}$$

At STP:

$$\left[\frac{\partial(\Delta G^0/T)}{\partial T}\right]_P = -\frac{\Delta H}{T^2} \quad \text{(D12)}$$

where ΔG^0 is change in Gibbs free energy at standard temperature and pressure (STP)

ΔH is enthalpy change (considered independent of temperature)

Integration of eq. (D12) with respect to T (at constant P) becomes:

$$\frac{G(T)}{T} - \frac{G^0(T^0)}{298} = \Delta H^0 \left(\frac{1}{T} - \frac{1}{298}\right) \quad \text{(D13)}$$

With knowledge of standard Gibbs free energy of formation and standard enthalpy change of formation of the individual components (Table D1), eq. (D13) enables the calculation of the Gibbs free energy change for a chemical reaction at any temperature T.

Table D1: Thermodynamics data for components in WGS reaction at STP [4].

Component	ΔG^0 (kJ/mol)	ΔH^0 (kJ/mol)
CO	–137.16	–110.53
H_2O	–228.6	–241.8
CO_2	–394.38	–393.51
H_2	0	0

At the WGS reaction temperatures used in our work, the values of G of each component (eq. (D13)), the ΔG_{Rx} (T) values (eq. (D9)), and K_{eq} (eq. (D7)) can be calculated.

Based on the review by Smith *et al*. (2010) [5], the equilibrium constant for WGS reaction derived from thermodynamics can be simplified to:

$$\ln K_{eq} = \frac{5693.5}{T} + 1.077 \ln T + 5.44 \times 10^{-4} T - 1.125 \times 10^{-7} T^2 - \frac{49170}{T^2} - 13.148 \quad \text{(D14)}$$

Temperature is in unit K.

D1.2 Thermodynamic CO equilibrium conversion

Smith *et al*. (2010) [5] presents a list of kinetic expressions for WGS reaction at high and low temperatures in the form of power law type of kinetic expressions and macro kinetic rate expressions, based on various types of catalysts and noble metals. Since we are calculating the equilibrium conversion using the equilibrium constant data, it does not matter which rate expression we are using as at equilibrium, rate of reaction, $r = 0$ and equilibrium conversion is solely determined by thermodynamics, not catalyst type-dependent. Hence, all the kinetics expressions are reduced to:

$$K_{eq} = K_{\mathrm{P}} = \frac{\mathrm{P_{CO_2}\,P_{H_2}}}{\mathrm{P_{CO}\,P_{H_2O}}} = \frac{\mathrm{C_{CO_2}\,C_{H_2}}}{\mathrm{C_{CO}\,C_{H_2O}}} = K_{\mathrm{C}} \qquad \text{(D15)}$$

Consider Langmuir–Hinshelwood expression:

$$r = \frac{k\,K_{\mathrm{CO}}\,K_{\mathrm{H_2O}}\left[\mathrm{C_{CO}\,C_{H_2O}} - \frac{\mathrm{C_{CO_2}C_{H_2}}}{K_{eq}}\right]}{\left(1 + K_{\mathrm{CO}}\mathrm{C_{CO}} + K_{\mathrm{H_2O}}\mathrm{C_{H_2O}} + K_{\mathrm{CO_2}}\mathrm{C_{CO_2}} + K_{\mathrm{H_2}}\mathrm{C_{H_2}}\right)^2} \qquad \text{(D16)}$$

At equilibrium, $r = 0$, hence:

$$K_{eq} = \frac{\mathrm{C_{CO_2}\,C_{H_2}}}{\mathrm{C_{CO}\,C_{H_2O}}} \qquad \text{(D17)}$$

Therefore, using eq. (D15), K_{eq} is expressed in terms of equilibrium conversion, X_e as:

$$K_{eq} = \frac{\mathrm{C_{CO,0}}X_e\,\mathrm{C_{CO,0}}X_e}{\mathrm{C_{CO,0}}(1-X_e)\mathrm{C_{CO,0}}(1-X_e)}$$

$$= \frac{{X_e}^2}{(1-X_e)^2}$$

$$X_e = \frac{{K_{eq}}^{1/2}}{1 + {K_{eq}}^{1/2}} \quad \text{(D18)}$$

Table D2: Thermodynamic equilibrium conversion for WGS reaction.

T (K)	K_{eq} (eq. (D14))	X_e (eq. (D18))
303	47966.15	0.995455
353	5643.569	0.986863
373	2815.576	0.981503
393	1507.708	0.974893
423	659.9884	0.962533
453	322.3116	0.947238
473	210.2346	0.935482
503	118.0365	0.915715
523	83.34292	0.901276
553	51.83779	0.878046

D2. Experimental

D2.1 Cu_6 nanoclusters synthesis and crystallisation

A colloid of 0.5 g of copper (I) chloride (CuCl) (M&B Laboratory Chemicals, May & Baker Ltd., Dagenham, England) (0.005 mol), 1.3 g of PPh_3 (MERCK-Schuchardt) (0.005 mol), and 10 mL of dry tetrahydrofuran (THF) was prepared by stirring the mixture under argon at ambient temperature. A colloidal suspension of a white precipitate of $(PPh_3)_3(CuCl)_2$ was formed, and 5 mL of a reducing agent, K-selectride solution (0.005 mol, 1.0 M potassium tri-sec-butylborohydride in THF) (Sigma Aldrich) was added while the mixture (placed in ice bath) was continuously stirred, to dissolve the precipitate and produce a deep red solution.

To crystallise the $[(PPh_3)CuH]_6$ nanoclusters, the solution was filtered through a glass wool supported Celite column under vacuum until the volume was reduced by around 50%. The concentrated filtrate was layered with hexane (of volume of slightly higher than the cluster solution) and stored at room temperature under argon atmosphere for a few days until the Cu_6 nanoclusters crystallised.

D2.2 Sample preparation steps for inductively coupled plasma mass spectrometry (ICP-MS) analysis

An amount of 0.05 g of each of the synthesised catalyst samples was digested in 2 mL aqua regia at 80 °C for 2 days to separate the copper particles from the multi-walled carbon nanotubes (MWCNT) support. The suspension was then ultrasonicated to homogenize the dissolution of the copper particles in the aqua regia solution, while the MWCNT support was well dispersed in the suspension (well dispersed MWCNT shows good hydrophilicity of the CNT in aqua regia). The copper and MWCNT suspended solution was centrifuged for 10 minutes at 10,000 rpm and 20 °C to let the MWCNT to settle to the bottom of the centrifuge tube. The copper solution free of the MWCNT suspension was then diluted with 2% HNO_3 to the range of 50 – 1000 µg/L (ppb). Using chirana rubber-less syringe, the copper solution was transferred out and filtered through a 0.45 µm hydrophilic/acid-compatible nylon-membrane polypropylene housing filter, into a new and clean centrifuge tube for ICP-MS analysis.

D2.3 BELCAT II unit

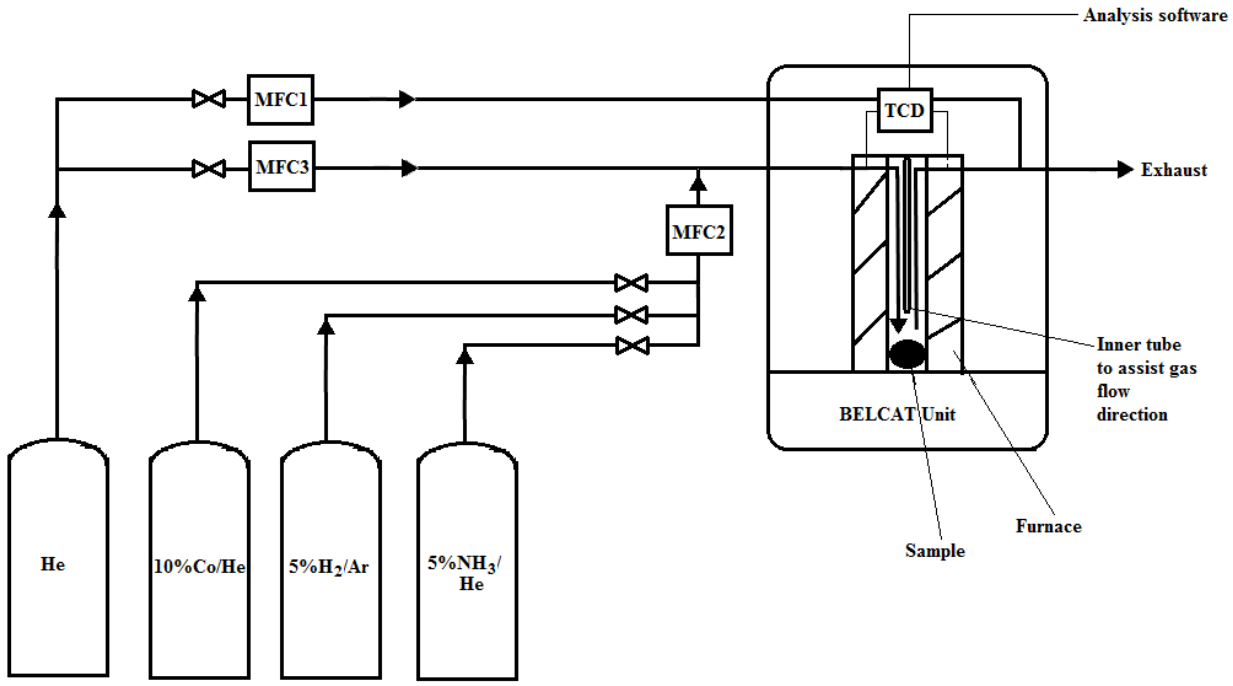

Figure D1: Sketch of BELCAT II catalyst analyser process flow diagram.

D3. Results and discussion

D3.1 Copper content and crystallite size calculations

The Cu species dispersion, surface area and crystallite size were calculated by BELCAT based on the amount of CO chemisorbed on 1 g of sample:

$$V_m(\mathrm{cm}^3/\mathrm{g}) = V_{chem}/m \qquad \text{(D19)}$$

V_{chem} (cm3) = amount of CO adsorbed

m (g) = sample weight

$$\text{Cu dispersion (\%)} = \frac{V_{chem}/22414 \times SF \times MW_{\text{Cu}}}{c} \times 100 \quad \text{(D20)}$$

MW_{Cu} (g/mol) = atomic weight of Cu

SF = stoichiometric factor = 1

$\text{Cu weight in the sample, } c \text{ (g)} = m \times p_{\text{Cu}}/100$, p_{Cu} = weight percentage of Cu in the sample (wt.%)

Surface area of Cu per 1 g of sample:

$$A_{\text{Cu,sample}}(\text{m}^2/\text{g}) = \frac{V_{chem}/22414 \times SF \times 6.02\times10^{23} \times \sigma_{\text{Cu}} \times 10^{-18}}{m} \quad \text{(D21)}$$

σ_{Cu} (nm^2) = cross-sectional area of one Cu atom

Surface area of Cu per 1 g of Cu in the sample:

$$A_{\text{Cu}}(\text{m}^2/\text{g}) = \frac{V_{chem}/22414 \times SF \times 6.02\times10^{23} \times \sigma_{\text{Cu}} \times 10^{-18}}{c} \quad \text{(D22)}$$

$$\text{Cu crystallite size (assuming a spherical particle)(nm)} = 6000/(A_{\text{Cu}} \times \rho) \quad \text{(D23)}$$

ρ (g/cm^3) = density of Cu

D3.2 Effect of sample pre-treatment at 100 °C

An additional X-ray diffraction (XRD) analysis was performed on a representative sample ($0.5\%Cu_6/MWCNT_{COOH}$) that had gone through a pre-treatment at 100 °C in He flow and CO pulse injection used in the Cu crystallite size and dispersion measurement, by comparison with its corresponding as-prepared sample.

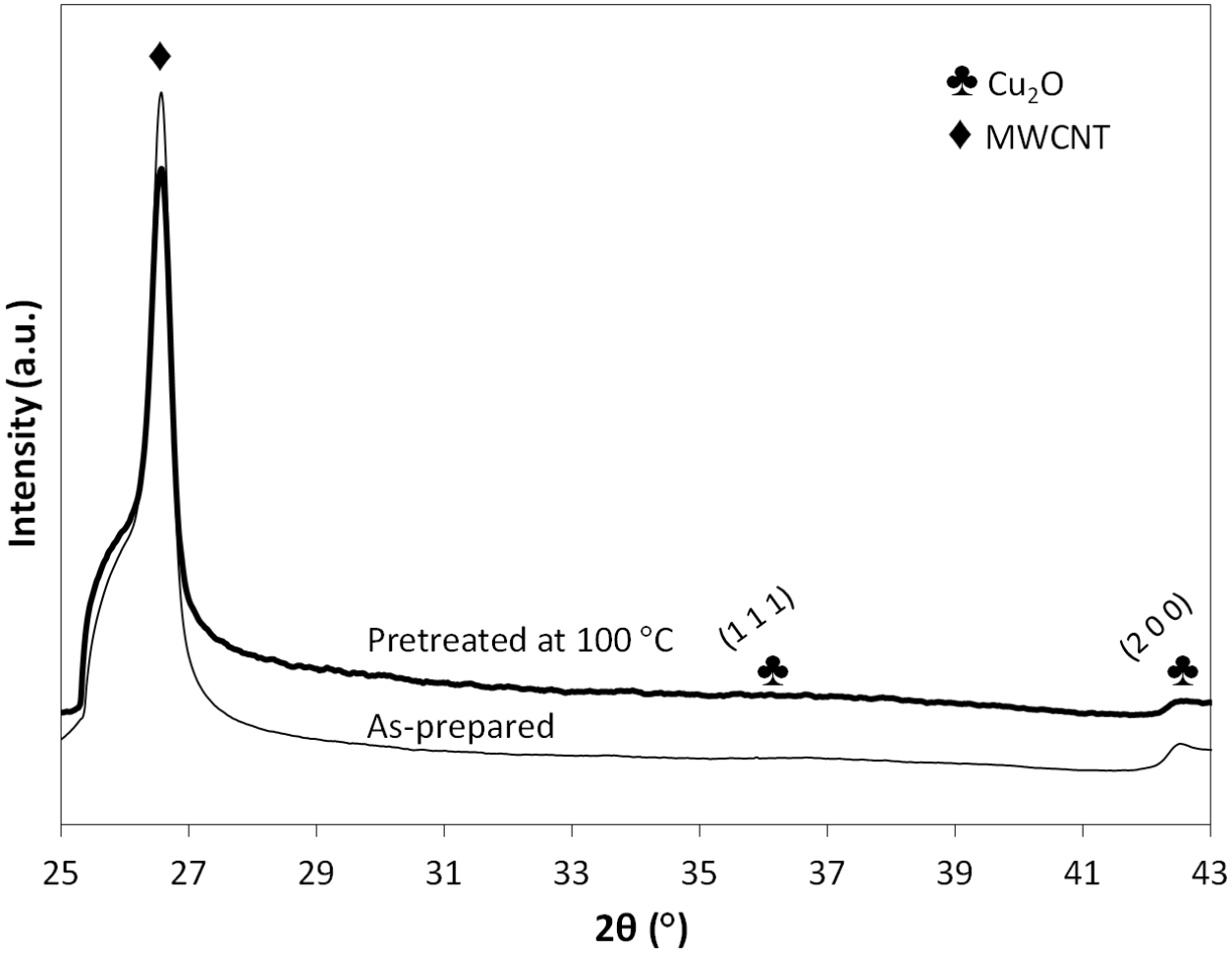

Figure D2: XRD patterns of 0.5%Cu_6/$MWCNT_{COOH}$, as-prepared and pre-treated at 100 °C.

D3.3 Hydrogen temperature-programmed reduction (H_2-TPR) of 1%Cu_6/$MWCNT_{COOH}$ and commercial catalysts

Approximately 0.05 g of fresh 1%Cu_6/$MWCNT_{COOH}$ sample was used as a general representation of Cu_6/$MWCNT_{COOH}$ catalysts to determine the reduction temperature for catalyst activation in the actual activity test. The sample was pre-treated following the same procedure described in the pre-treatment of samples prepared for CO chemisorption (pulse injection) measurement. After the pre-treatment, the H_2-TPR commenced in diluted H_2 flow from 50 °C to 600 °C. The same procedure was followed on the commercial catalyst sample.

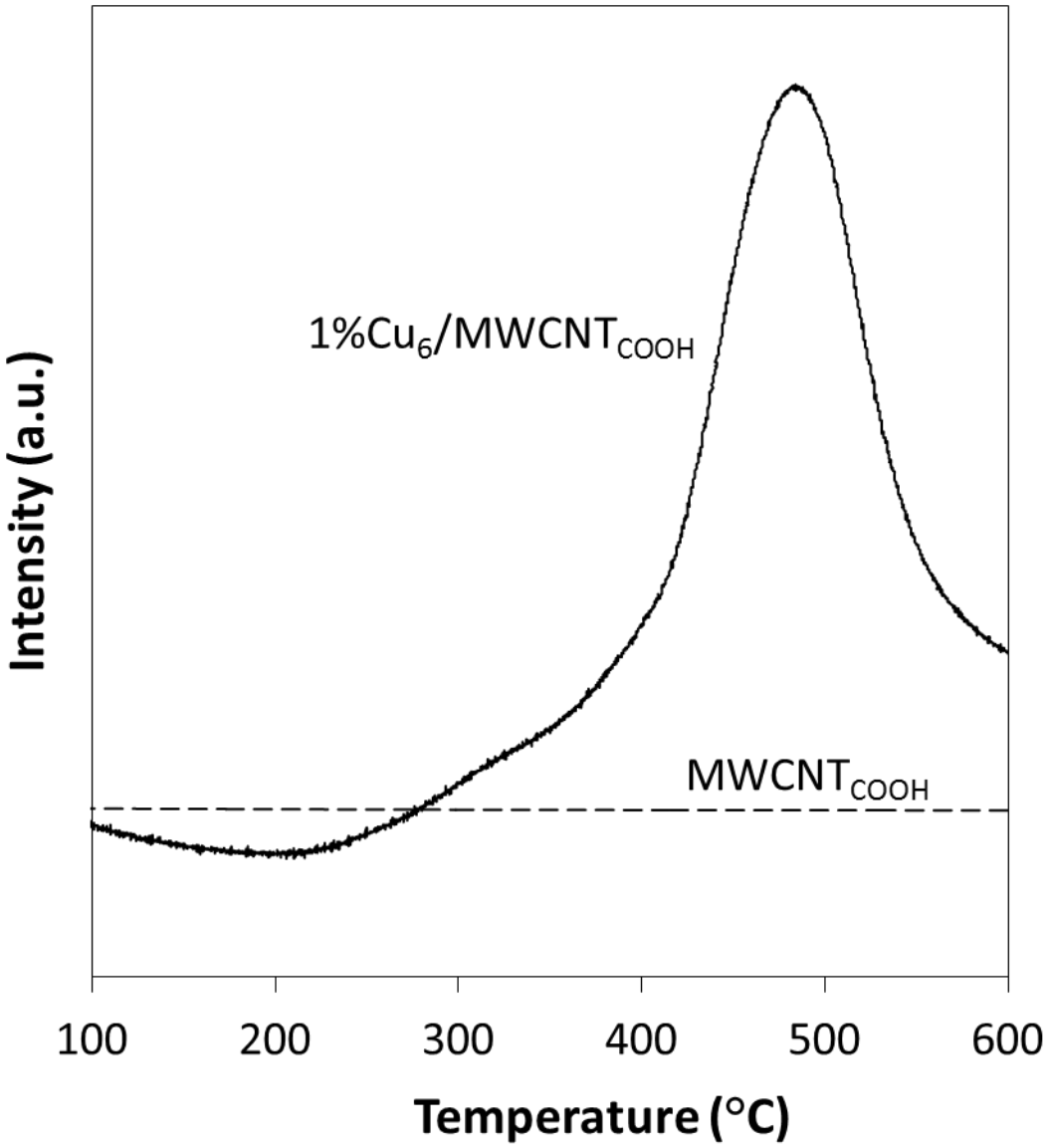

Figure D3: H_2-TPR spectra of 1%Cu_6/$MWCNT_{COOH}$ and bare $MWCNT_{COOH}$.

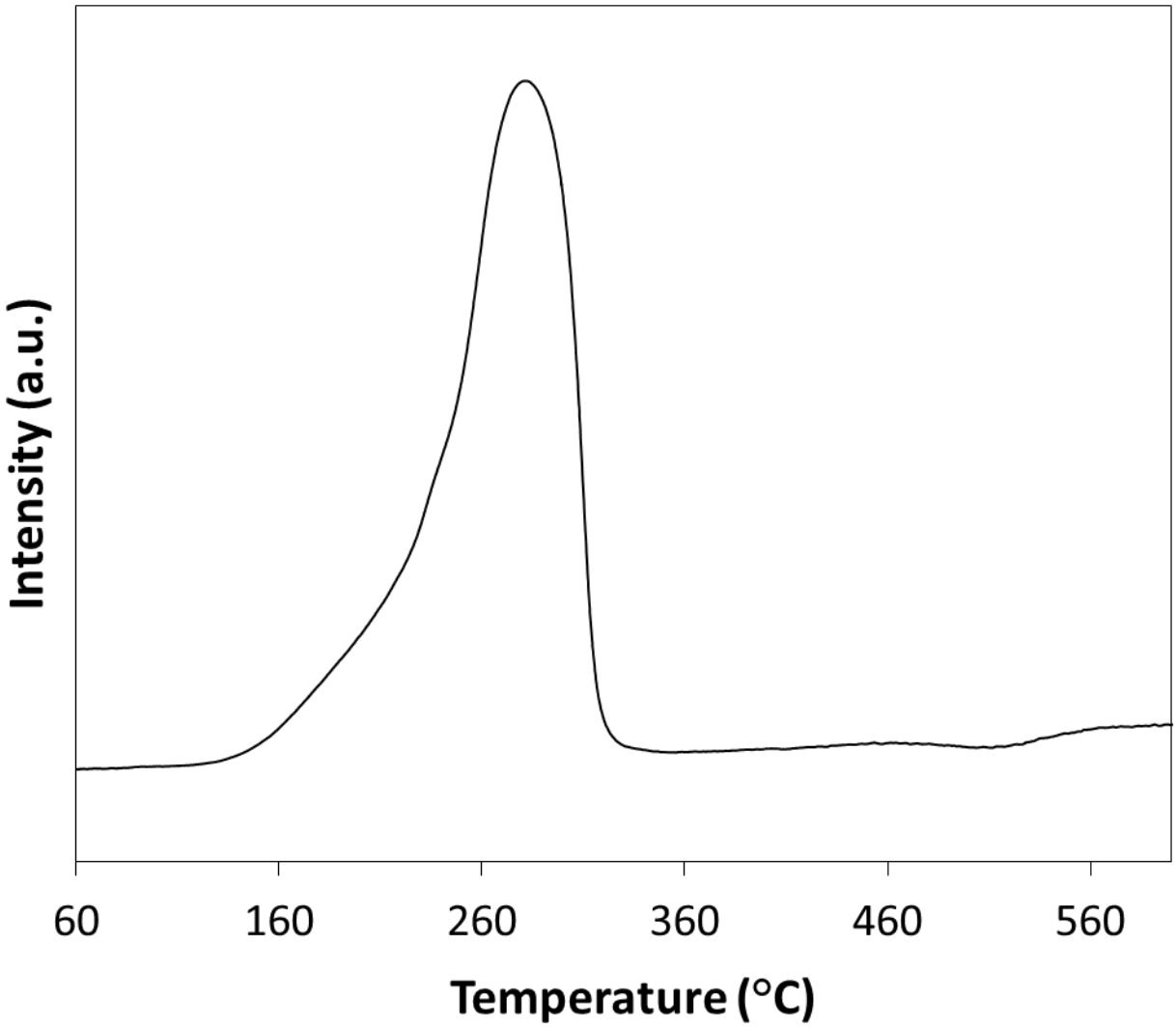

Figure D4: H_2-TPR profile of commercial catalyst.

The appearance of only one reduction peak up to 600 °C in the above H_2-TPR profile indicates that ZnO phase is stable and does not get reduced to metallic Zn. It acts as a structural stabilizer and promoter [6-8]. Instead of playing a definitive role as an active site, which remains controversial, it was agreed that a special synergy exists between copper and zinc oxide [9-10] that helps enhance the catalyst activity and life [6, 11-12]. Alumina is an inert and therefore inactive in LTWGS but plays a role in improving Cu dispersion and minimising pellet shrinkage [7-8].

References of APPENDIX D

1. Fogler, H.S., *Elements of chemical reaction engineering*. 4th ed. 2006, NJ: Prentice Hall.
2. Roósz, B., C. Visy, and I. Nagypál, *On the derivation of the Gibbs–Helmholtz equation.* ChemTexts, 2016. **2**(2): p. 1-3.
3. Keszei, E., *Gibbs–Helmholtz equation and entropy.* ChemTexts, 2016. **2**(4): p. 15.
4. *National Institute of Standards and Technology*. Available from: http://webbook.nist.gov/.
5. Smith, R., M. Loganathan, and M.S. Shantha, *A review of the water gas shift reaction kinetics.* International Journal of Chemical Reactor Engineering, 2010. **8**(1).
6. Spencer, M., *The role of zinc oxide in Cu/ZnO catalysts for methanol synthesis and the water–gas shift reaction.* Topics in Catalysis, 1999. **8**(3-4): p. 259.
7. Li, Y., Q. Fu, and M. Flytzani-Stephanopoulos, *Low-temperature water-gas shift reaction over Cu-and Ni-loaded cerium oxide catalysts.* Applied Catalysis B: Environmental, 2000. **27**(3): p. 179-191.
8. RJ, B.S., M. Loganathan, and M.S. Shantha, *A review of the water gas shift reaction kinetics.* International Journal of Chemical Reactor Engineering, 2010. **8**(1).
9. Chinchen, G.C., et al., *Promotion of methanol synthesis and the water-gas shift reactions by adsorbed oxygen on supported copper catalysts.* Journal of the Chemical Society, Faraday Transactions 1: Physical Chemistry in Condensed Phases, 1987. **83**(7): p. 2193-2212.
10. Mendes, D., et al., *Determination of the Low-Temperature Water− Gas Shift Reaction Kinetics Using a Cu-Based Catalyst.* Industrial & Engineering Chemistry Research, 2010. **49**(22): p. 11269-11279.
11. Uchida, H., et al., *The zinc oxide-copper catalyst for carbon monoxide-shift conversion. I. The dependency of the catalytic activity on the chemical composition of the catalyst.* Bulletin of the Chemical Society of Japan, 1967. **40**(8): p. 1981-1986.
12. Ratnasamy, C. and J.P. Wagner, *Water gas shift catalysis.* Catalysis Reviews, 2009. **51**(3): p. 325-440.

APPENDIX E

Supplementary material for Chapter 4

E1. Flow diagram

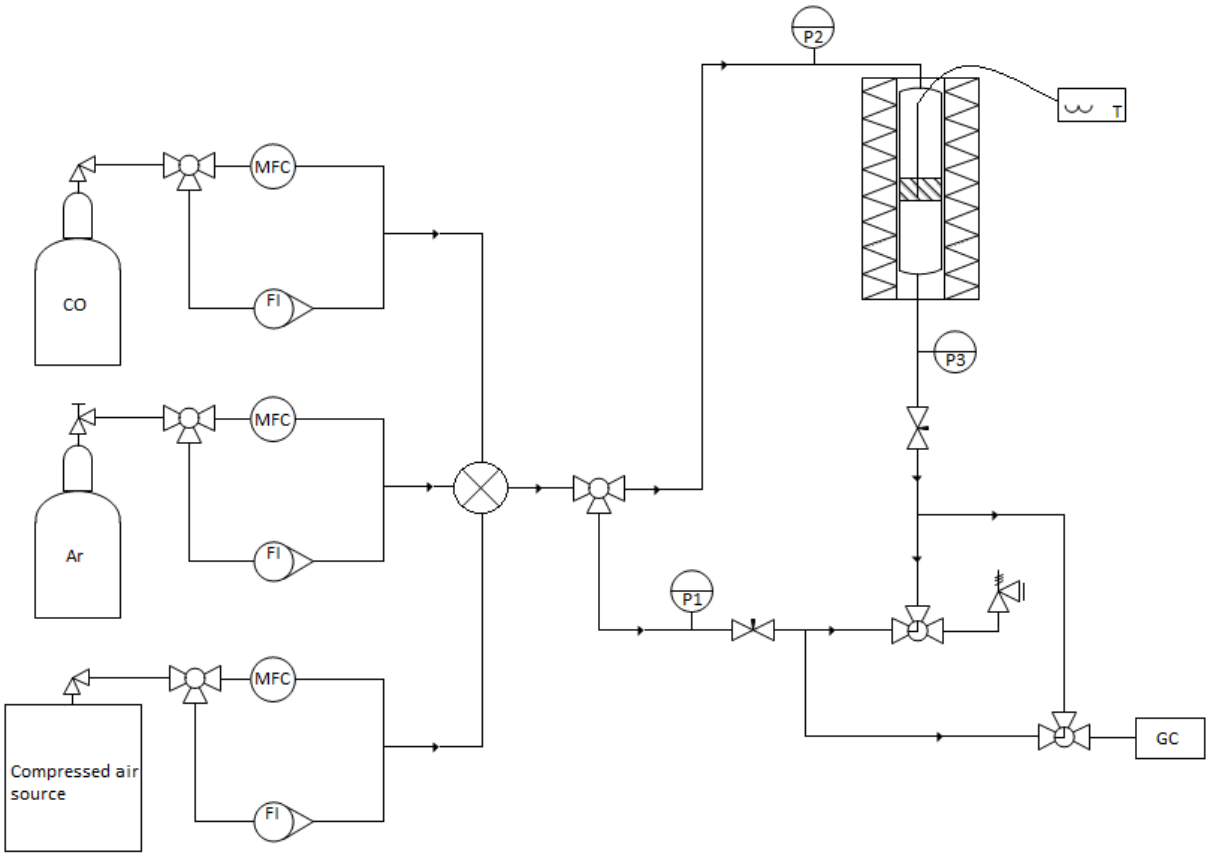

Figure E1(A): Differential reactor setup for CO oxidation. Flow diagram.

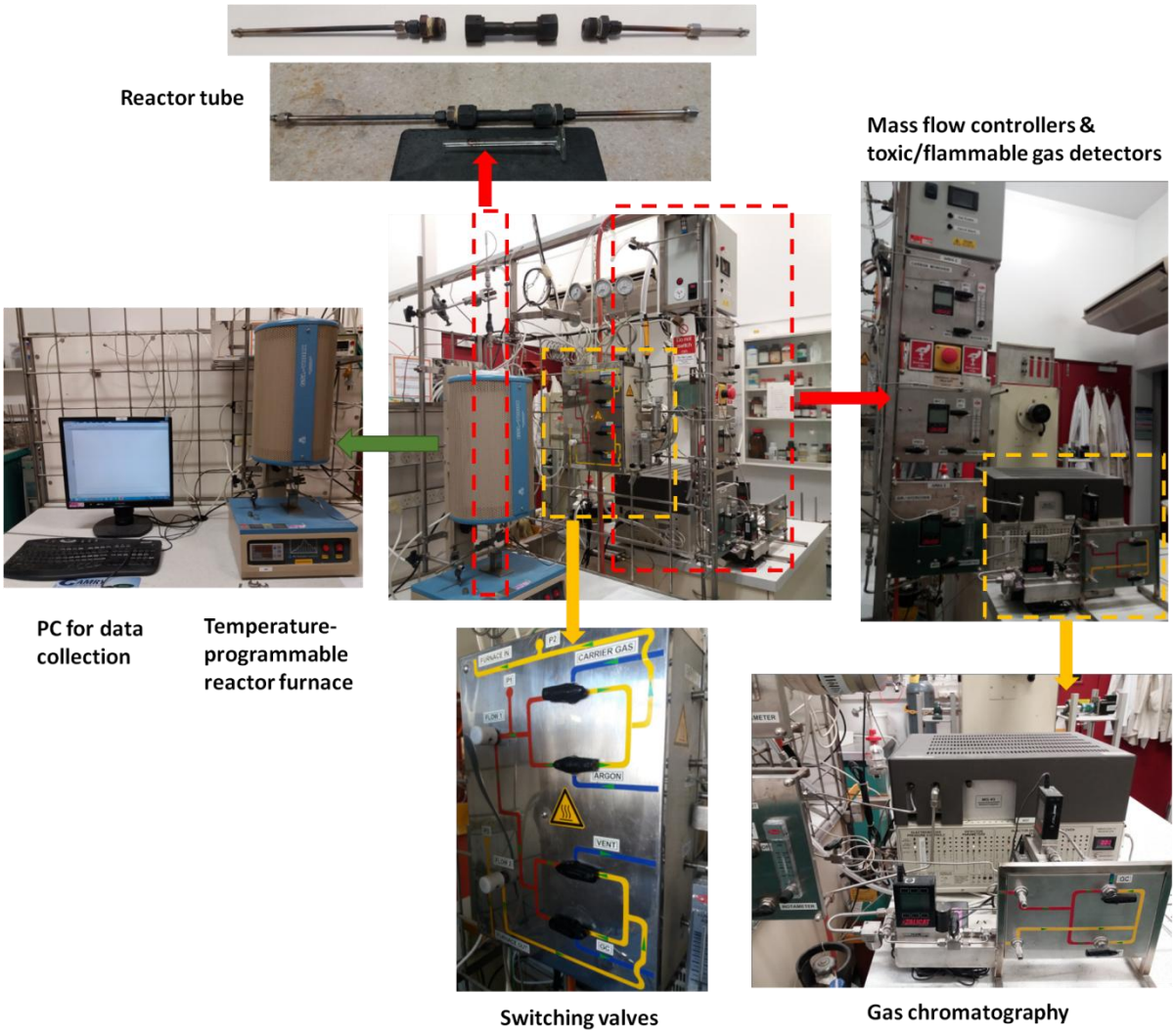

Figure E1(B): Differential reactor setup for CO oxidation. Pictures.

E2. Reference tests in absence of catalyst charge and on commercial catalyst

A reference run in absence of a catalyst charge, was performed in a temperature-step-change run with each temperature setting (between 130 and 330 °C) held constant for 1 h in the oxygen-rich environment at gas hourly space velocity (GHSV) = 6,000 mL/($g_{material}$·h). The actual bed temperature measured by thermocouple was slightly higher than each programmed set-temperature setting by 3.7 ± 1.0 °C in the reference run without the catalyst charge. No CO conversions took place during this reference run, whereby the GC measurement showed unchanged mole of CO_{feed} and $CO_{product}$, and nil CO_2 production throughout the run.

Another reference CO oxidation reaction test was conducted using the commercial catalyst in a temperature-step-change run with each temperature held constant for 45 minutes in the O_2-rich environment at GHSV = 6,000 mL/($g_{material}$·h). The CO conversion performance is presented in Figure E2.

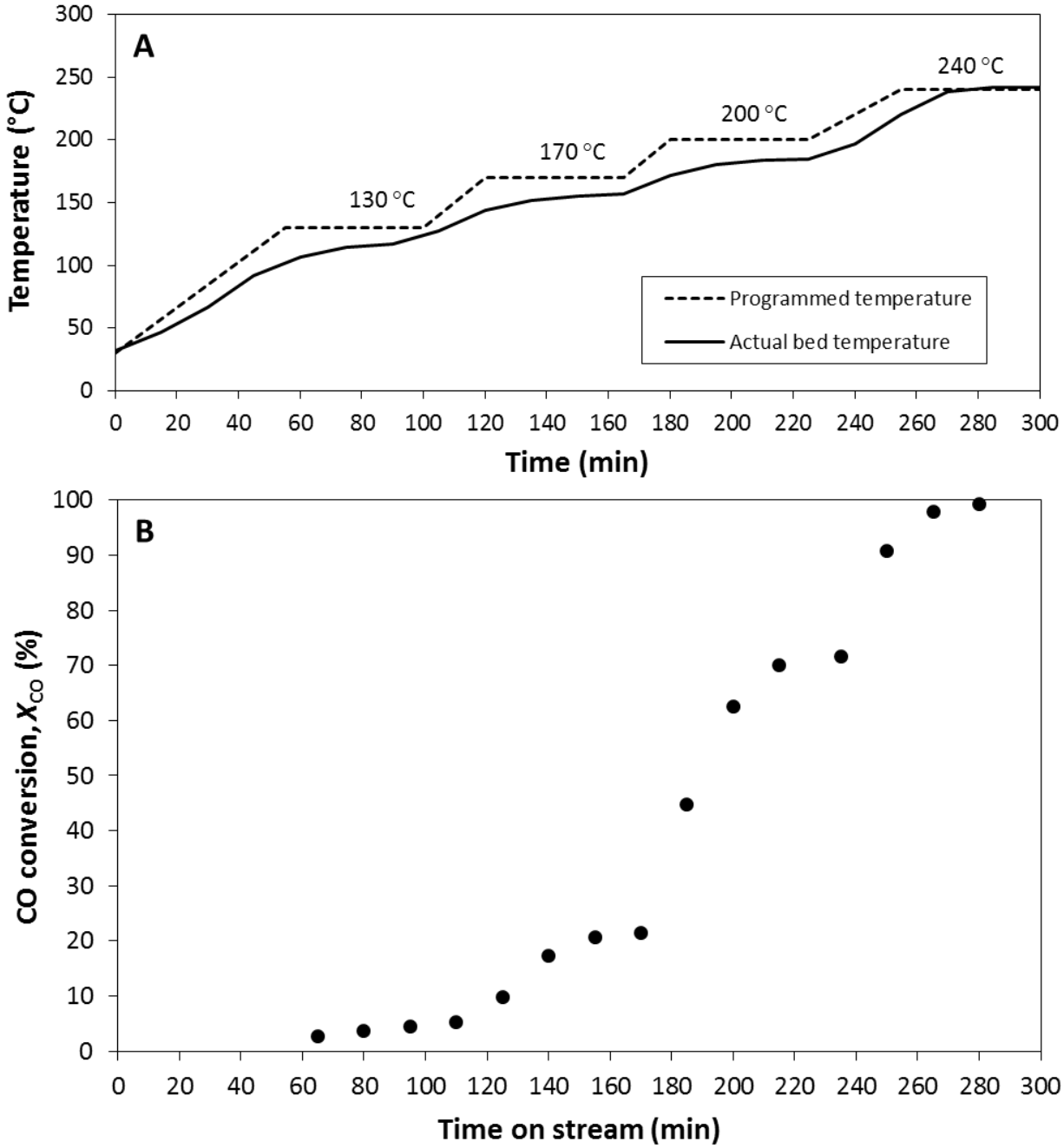

Figure E2: CO conversion on commercial catalyst: O_2-rich, temperature changes, GHSV = 6,000 mL/($g_{material}$·h). (A) Reaction temperature; and (B) CO conversion into CO_2 product.

From Figure E2, it was demonstrated that the CO conversions increased with increasing temperatures and stable conversions were reached at each constant temperature setting in the 45 min hold time on stream. A complete CO conversion was reached at 240 °C.

E3. Reference test on Cu_6 cluster doped on inert alumina surface

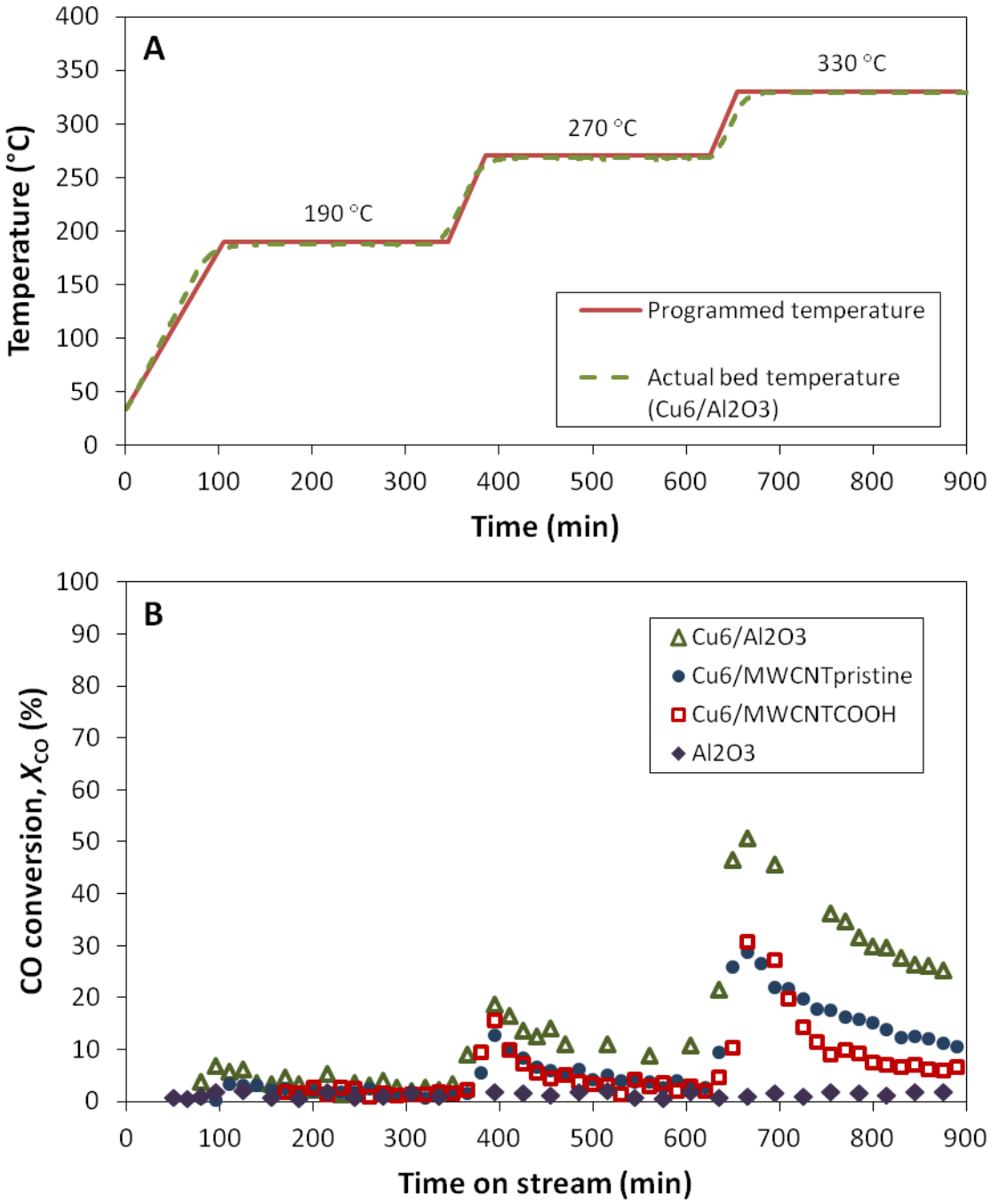

Figure E3: CO conversions over 1 wt.% Cu_6-doped materials: O_2-rich, temperature-step change (190, 270 and 330 °C), GHSV = 3,000 mL/($g_{material}$·h). (A) Reaction temperature; and (B) CO conversion into CO_2 product.

In Figure E3, it was observed that the Cu_6-doped on inert Al_2O_3 surface exhibited similar CO conversion performance and behaviours as its counterparts supported on the MWCNT supports in the O_2-rich environment and GHSV = 3,000 mL/($g_{material}$·h), with the only exception was its highest conversion capability hit 50% at the step-temperature of 330 °C while the latter two hit only ~30%.

APPENDIX F

Supplementary material for Chapter 5

F1. Thermogravimetric analysis (TGA)

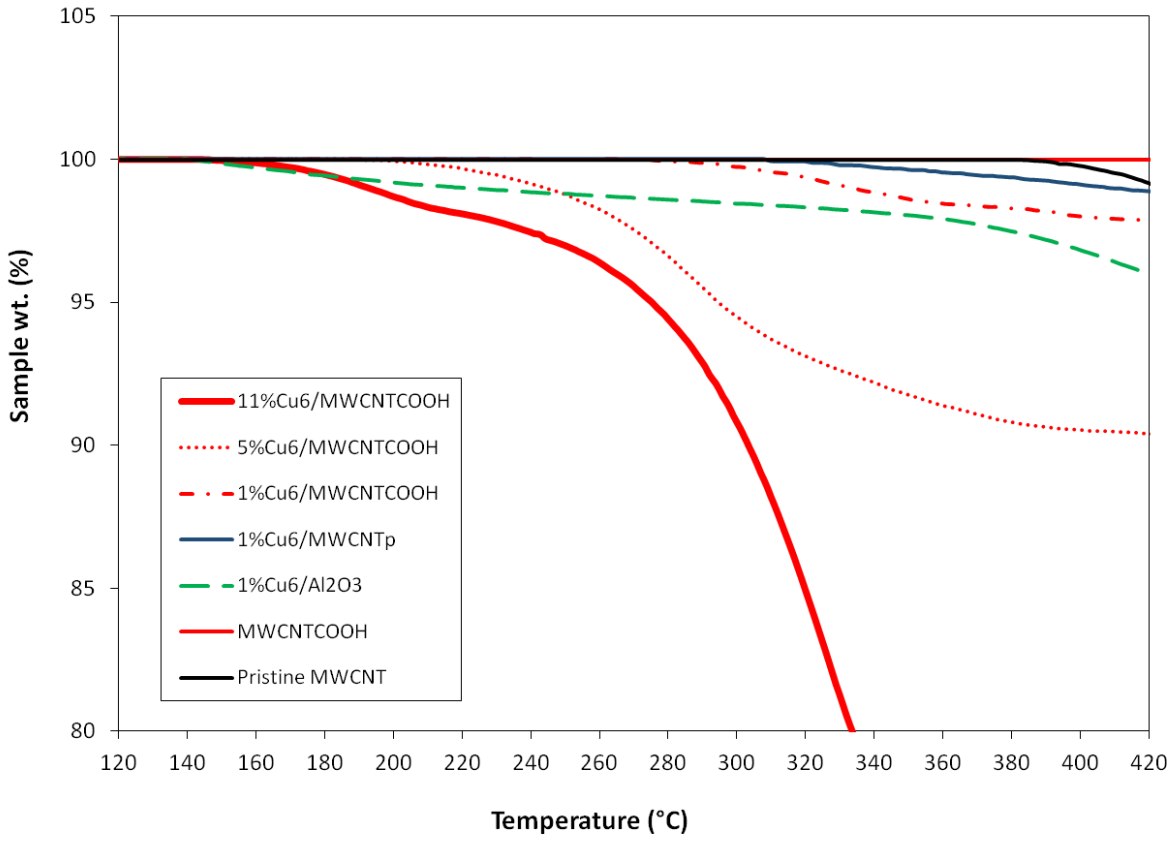

Figure F1: TGA of support materials and catalysts of varying copper loading content in a mixture of synthetic air (N_2:O_2 = 80:20 v/v%) and nitrogen (5:2 v/v).

The TGA run was performed on ~10 mg of sample in a 70 mL/min gas flow containing 14.3 vol.% oxygen and balance nitrogen. However, in our reaction run, the total reactant gas flowrate used on 0.1 g of sample was around 5 mL/min containing 10 vol.% oxygen in the

oxygen-rich environment, with part of the oxygen took part in the CO oxidation. Sample weight before and after the test of all the catalysts containing 1%Cu_6 was weighed and preserved, affirming their stability. On the other hand, the catalyst containing 5% and 11% Cu_6 showed significant loss of sample weight after each reaction run.

F2. Effect of gas hourly space velocity (GHSV)

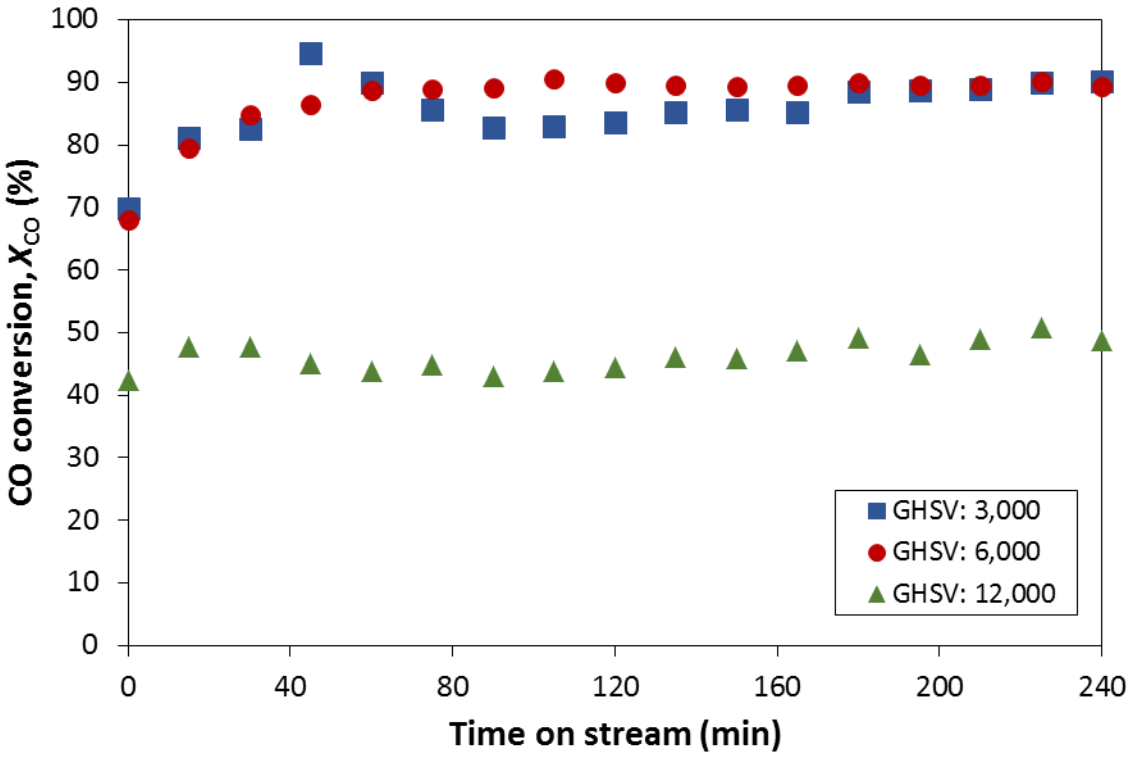

Figure F2: CO conversions over 1%Cu_6/$MWCNT_{COOH}$ catalyst at various GHSVs (mL/(g_{cat}·h)): O_2-lean, 400 °C.

F3. CO oxidation performance at 440 and 475 °C

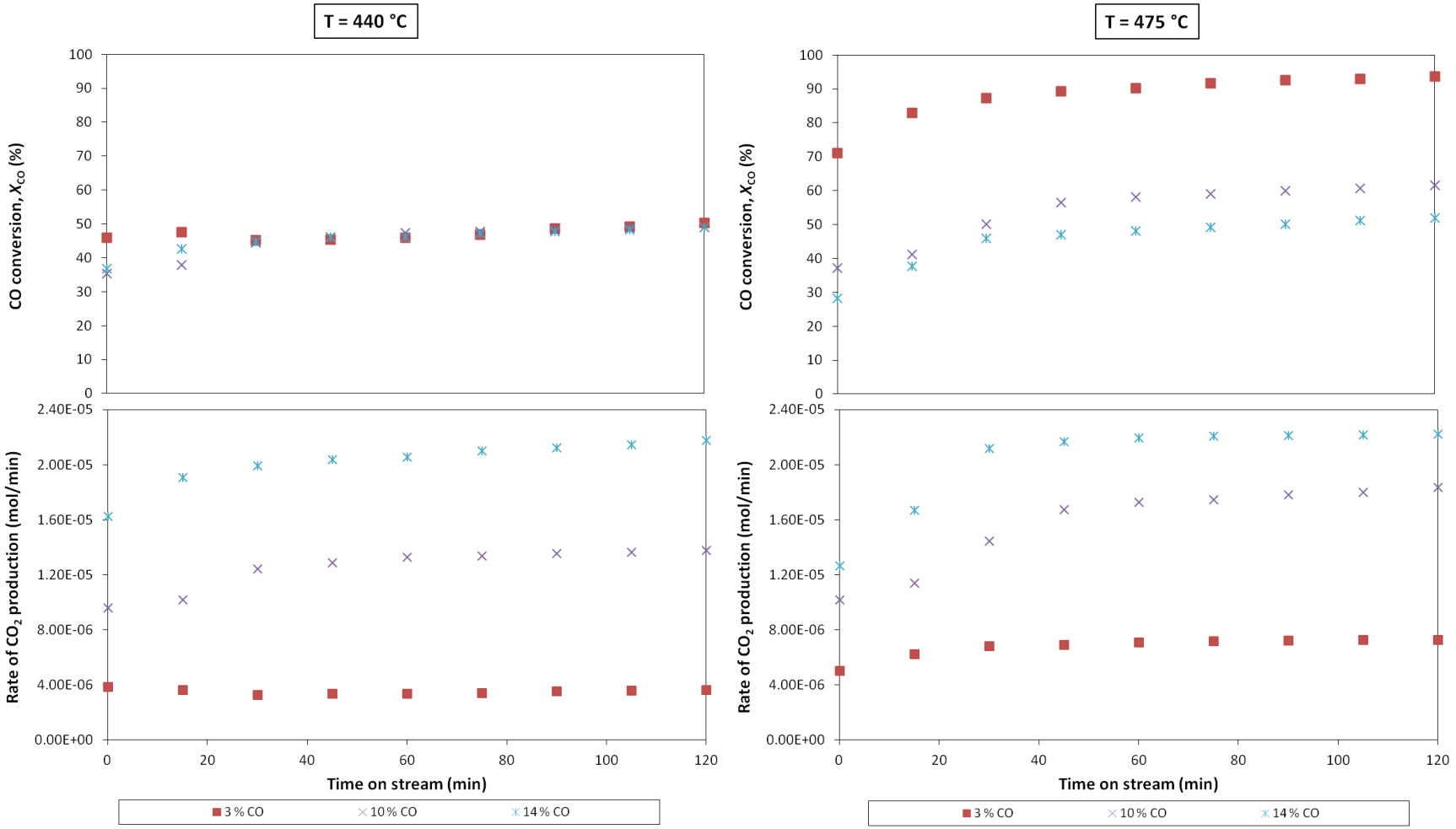

Figure F3: CO conversions and CO_2 production rates at CO oxidation reaction temperatures of 440 and 475 °C, O_2-lean, GHSV = 6,000 mL/(g_{cat}·h).

F4. Theoretical derivation of reaction rate expression

In general, the elementary steps in the L–H mechanism of CO oxidation are described as below [1]:

$$CO + * \xleftrightarrow{K_1 = \frac{k_1}{k_{-1}}} CO* \quad \text{(F1)}$$

$$O_2 + 2* \xleftrightarrow{K_1 = \frac{k_2}{k_{-2}}} 2\,O* \quad \text{(F2)}$$

$$CO* + O* \xleftrightarrow{K_3 = \frac{k_3}{k_{-3}}} CO_2* + * \quad \text{(F3)}$$

$$CO_2* \xleftrightarrow{\frac{1}{K_4} = \frac{k_{-4}}{k_4}} CO_2 + * \quad \text{(F4)}$$

where * = vacant site.

Adsorption of CO:

$$r_1 = k_1\,[CO]\,C_v - k_{-1}\,[CO]*$$

$$r_1 = k_1\,([CO]\,C_v - \frac{[CO]*}{K_1}) \quad \text{(F5)}$$

where C_v is the concentration of the vacant site.

Adsorption of O_2:

$$r_2 = k_2\ ([\mathrm{O_2}]\ C_v - \frac{[\mathrm{O_2}]*}{K_2}) \quad \text{(F6)}$$

Surface reaction:

$$r_3 = k_3\ ([\mathrm{CO}] * [\mathrm{O_2}] * - \frac{[\mathrm{CO_2}]* C_v}{K_3}) \quad \text{(F7)}$$

Desorption of CO_2:

$$r_4 = k_4\ [\mathrm{CO_2}] * - k_{-4}\ [\mathrm{CO_2}]\ C_v$$

$$r_4 = k_4\ ([\mathrm{CO_2}] * - \frac{[\mathrm{CO_2}]\ C_v}{K_4}) \quad \text{(F8)}$$

To derive the reaction rate expression, we assume the reaction is surface-reaction limited. Therefore, k_1, k_2 and k_4 are very large. Eq. (F5), (F6) and (F8) thus respectively become:

$$[\mathrm{CO}] * = K_1\ [\mathrm{CO}]\ C_v \quad \text{(F9)}$$

$$[\mathrm{O_2}] * = K_2\ [\mathrm{O_2}]\ C_v \quad \text{(F10)}$$

$$[\mathrm{CO_2}] * = \frac{[\mathrm{CO_2}]\ C_v}{K_4} \quad \text{(F11)}$$

Hence, eq. (F7) becomes:

$$r_3 = k_3\ C_v^2\ (K_1\ K_2\ [\mathrm{CO}]\ [\mathrm{O_2}] - \frac{[\mathrm{CO_2}]}{K_3\ K_4}) \quad \text{(F12)}$$

Total vacant site:

$$C_T = C_v + [CO]^* + [O_2]^* + [CO_2]^* \quad \text{(F13)}$$

$$C_T = C_v + K_1\,[CO]\,C_v + K_2\,[O_2]\,C_v + \frac{[CO_2]\,C_v}{K_4}$$

$$C_v = \frac{C_T}{1 + K_1\,[CO] + K_2\,[O_2] + \frac{[CO_2]}{K_4}} \quad \text{(F14)}$$

The reaction rate expression represented by eq. (F12) becomes:

$$r_3 = k_3 C_T^2 \frac{K_1\,K_2\,[CO]\,[O_2] - \frac{[CO_2]}{K_3\,K_4}}{(1 + K_1\,[CO] + K_2\,[O_2] + \frac{[CO_2]}{K_4})^2} \quad \text{(F15)}$$

At reaction time, t = 0, $[CO_2] = 0$. Therefore, eq. (F15) is reduced to:

$$r_3 = k_3 C_T^2 \frac{K_1\,K_2\,[CO]\,[O_2]}{(1 + K_1\,[CO] + K_2\,[O_2])^2} \quad \text{(F16)}$$

Defining $k = k_3 C_T^2$ and from thermodynamics, $K_1 = K_{CO}$ and $K_2 = K_{O2}$, eq. (F16) finally becomes:

$$r_3 = k \frac{K_{CO}\,K_{O_2}\,[CO]\,[O_2]}{(1 + K_{CO}[CO] + K_{O_2}[O_2])^2} \quad \text{(F17)}$$

where

$$\Delta G^{\mathrm{T}}_{\mathrm{reactant}} = \mathrm{RT}_{\mathrm{reaction}} \ln K_{\mathrm{reactant}} + \Delta G^{0}_{\mathrm{reactant}} \quad \text{(F18)}$$

$$\Delta G^{\mathrm{T}}_{\mathrm{CO}} = \mathrm{RT}_{\mathrm{CO\ oxidation}} \ln K_{\mathrm{CO}} + \Delta G^{0}_{\mathrm{CO}}$$

$$\Delta G^{\mathrm{T}}_{\mathrm{O_2}} = \mathrm{RT}_{\mathrm{CO\ oxidation}} \ln K_{\mathrm{O_2}} + \Delta G^{0}_{\mathrm{O_2}}$$

$$\frac{\Delta \mathrm{G}^{\mathrm{T}}}{\mathrm{T}} - \frac{\Delta \mathrm{G}^{0}}{298} = \Delta \mathrm{H}^{0} \left(\frac{1}{\mathrm{T}} - \frac{1}{298}\right) \quad \text{(F19)}$$

T (°C)	T (K)	$\Delta G^{0\ \#}_{CO}$ (kJ/mol)	$\Delta H^{0\ \#}_{CO}$ (kJ/mol)	ΔG^{T}_{CO} (kJ/mol)	ln K_{CO}	K_{CO}	$\Delta G^{0\ \#}_{O_2}$ (kJ/mol)	$\Delta H^{0\ \#}_{O_2}$ (kJ/mol)	$\Delta G^{T}_{O_2}$ (kJ/mol)	ln K_{O2}	K_{O2}
400	673	-137.16	-110.53	-170.67	-5.99	2.51×10^{-3}	0.00	0.00	0.00	0.00	1.00
440	713	-137.16	-110.53	-174.25	-6.26	1.92×10^{-3}	0.00	0.00	0.00	0.00	1.00
475	748	-137.16	-110.53	-177.37	-6.47	1.55×10^{-3}	0.00	0.00	0.00	0.00	1.00

Source: [2].

At T = 400 °C

T (K)	K_{CO}	K_{O2}	[CO] (mol/mol)	[O_2] (mol/mol)	$\frac{K_{CO}\, K_{O_2}\, [CO]\, [O_2]}{(1 + K_{CO}[CO] + K_{O_2}[O_2])^2}$	r_{CO2} ‡ [mol/(min·g_{cat})]
673	2.51×10^{-3}	1.00	0.15	0.18	4.86×10^{-5}	4.57×10^{-5}
673	2.51×10^{-3}	1.00	0.5	0.6	2.93×10^{-4}	1.79×10^{-4}
673	2.51×10^{-3}	1.00	0.7	0.84	4.34×10^{-4}	2.69×10^{-4}

‡ Experimentally determined.

At T = 440 °C

T (K)	K_{CO}	K_{O2}	[CO] (mol/mol)	[O_2] (mol/mol)	$\frac{K_{CO}\,K_{O_2}\,[CO]\,[O_2]}{(1+K_{CO}[CO]\,+\,K_{O_2}[O_2])^2}$	r_{CO2} ‡ [mol/(min·g_{cat})]
713	1.92×10^{-3}	1.00	0.15	0.18	3.72×10^{-5}	6.94×10^{-5}
713	1.92×10^{-3}	1.00	0.5	0.6	2.25×10^{-4}	2.66×10^{-4}
713	1.92×10^{-3}	1.00	0.7	0.84	3.33×10^{-4}	4.17×10^{-4}

‡ Experimentally determined.

At T = 475 °C

T (K)	K_{CO}	K_{O2}	[CO] (mol/mol)	[O_2] (mol/mol)	$\frac{K_{CO}\,K_{O_2}\,[CO]\,[O_2]}{(1+K_{CO}[CO]\,+\,K_{O_2}[O_2])^2}$	r_{CO2} ‡ [mol/(min·g_{cat})]
748	1.55×10^{-3}	1.00	0.15	0.18	3.01×10^{-5}	1.37×10^{-4}
748	1.55×10^{-3}	1.00	0.5	0.6	1.82×10^{-4}	3.43×10^{-4}
748	1.55×10^{-3}	1.00	0.7	0.84	2.70×10^{-4}	4.26×10^{-4}

‡ Experimentally determined.

F5. Regression

***Note:** Section F5 is contributed by Isaac Severinsen**

1.0 Non-Linear Regression

This Jupyter notebook describes the non-linear regression of experimental data against a kinetic rate expression.

Anything after In[x]: is code

The reaction being considered is CO oxidation, $$ CO + \frac{1}{2} O_2 \rightarrow CO_2 $$

The Langmuir-Hinshelwood rate equation is:

$$ r_{CO_2} = k \frac{K_{CO}K_{O_2}C_{CO}C_{O_2}}{\left(1 + K_{CO}C_{CO} + K_{O_2}C_{O_2}\right)^2} $$

where,

$$ K_i = e^{\left(\frac{\Delta_f G_{i}^{T} - \Delta_f G_{i}^{◦}}{RT}\right) } $$

$\Delta_f G_{i}^{◦}$ is known and $\Delta_f G_{i}^{T}$ is calculated with,

$$ \Delta_f G_{i}^{T} = T \left(\frac{\Delta_f G_{i}^{◦}}{T^{◦}} + \Delta_f H^{◦} \left(\frac{1}{T} - \frac{1}{T^{◦}} \right) \right) $$

and,

$$ k = A e^{\left(\frac{-Ea}{RT}\right)} $$

In this Arrhenius rate constant expression A and Ea are unknown and will be determined through non-linear regression

In [1]:

```
import numpy as np
import pandas as pd
import scipy.stats as ss
import statsmodels.api as sm
from scipy.optimize import curve_fit
from scipy.stats.distributions import  t
import pprint
import matplotlib.pyplot as plt
import copy

C_CO = np.array([0.15,0.15,0.15,0.15,0.5,0.5,0.5,0.7,0.7,0.7])          #
[mol/mol]
C_O2 = np.array([0.18,0.18,0.18,0.18,0.6,0.6,0.6,0.84,0.84,0.84])      #
[mol/mol]
```

```
T_exp = np.array([673.15,673.15,713.15,748.15,673.15,713.15,748.15,
# [K]
                  673.15,713.15,748.15])
r_exp = np.array([4.40E-5,4.73E-05,6.94E-05,1.37E-04,1.79E-04,2.66E-4,
              3.43E-04,2.69E-04,4.17E-04,4.26E-04])               #
[mol/min.g_cat]

exp_data = pd.DataFrame(data =
np.transpose(np.array([C_CO,C_O2,T_exp,r_exp])),
                        columns = ['C_CO','C_O2','T_exp','r_exp'])

T_O = 298.15       # [K]
dGCO_O = -137.16   # [kJ/mol]
dHCO = -110.53     # [kJ/mol]
R = 8.314/1000     # [kJ/mol]
K_O2 = 1           # [kJ/mol] dG = 0 for element thus K = 1 as e^0 = 1

Params =
{'T_O':T_O,'dGCO_O':dGCO_O,'dHCO':dHCO,'R':R,'K_O2':K_O2,'exp_data':exp_da
ta}
Params_OG = copy.deepcopy(Params)
```

1.1 Define objective function

This function should, given T, A and Ea generate rates of reactions at the experimental conditions studied

In [2]:

```
def gen_r(T, A, Ea,Params):

    dGCO_T = T * (Params['dGCO_O']/Params['T_O'] + Params['dHCO']*(1/T-
1/Params['T_O']))

    K_CO = np.exp((dGCO_T-Params['dGCO_O'])/(Params['R']*T))

    k = A * np.exp(-Ea/((Params['R'])*T))   # Arrhenius Temperature
relationship for k

#     L_H rate equation

    r = (k * K_CO * Params['K_O2'] * Params['exp_data']['C_CO'] *
Params['exp_data']['C_O2'] /
        (1 + K_CO * Params['exp_data']['C_CO'] + Params['K_O2'] *
Params['exp_data']['C_O2'])**2)

    return r

# Little wrapper for scipy

def wrapper(T, A, Ea):
    return gen_r(T,A,Ea,Params)
```

1.2 Curve_fit - use scipy's regression engine

In [3]:

```
initial_guess = [1, 20]

pars, pcov = curve_fit(wrapper, Params['exp_data']['T_exp'],
                               Params['exp_data']['r_exp'],
                        p0 = initial_guess, method = 'lm')

A_opt = pars[0]
Ea_opt = pars[1]
```

1.3 Basic Statistics

Here we assume the relationship between parameters is spherical

In [4]:

```
alpha = 0.05      # 95% confidence interval = 100*(1-alpha)

n = len(r_exp)    # number of data points
p = len(pars)     # number of parameters

dof = max(0, n - p) # number of degrees of freedom

tval = t.ppf(1.0-alpha/2., dof)
variance = np.diag(pcov)

print('A = ',round(A_opt,2) ,'±',round((variance[0]**0.5)*tval,2))
print('Ea = ',round(Ea_opt,2) ,'±',round((variance[1]**0.5)*tval,2))
```

```
A =  10553.51 ± 29849.1
Ea =  54.17 ± 16.96
```

1.4 Test Residuals for normality with Shapiro-Wilk

In [5]:

```
residuals = r_exp - gen_r(T_exp,initial_guess[0],initial_guess[1],Params)

W,p = ss.shapiro(residuals)

if p > 0.05:
    print('p value is: ',round(p,3),' > 0.05, thus according to Shapiro -
Wilk test the residuals are normally distributed')

mu = np.mean(residuals)
sig = np.std(residuals)

x = np.linspace(mu - 3*sig  ,mu + 3*sig , 5000)

y_pdf = ss.norm.pdf(x, mu, sig)

fig = plt.figure(1)
```

```
plt.hist(residuals, density = True)
plt.plot(x,y_pdf)
plt.show()
```

```
p value is:  0.287  > 0.05, thus according to Shapiro - Wilk test the
residuals are normally distributed
```

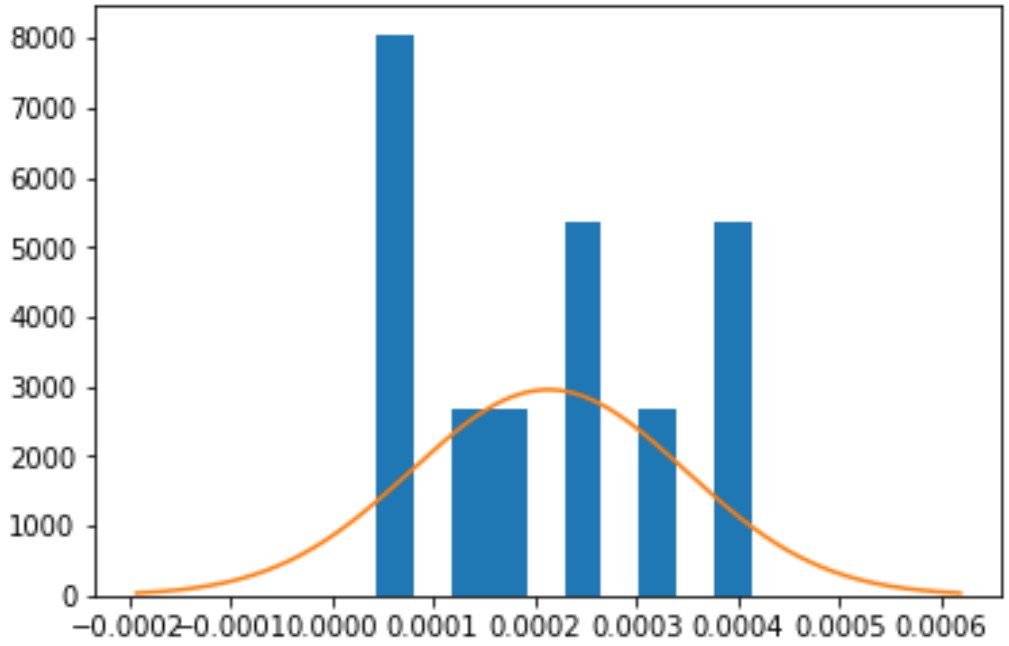

1.5 QQ test

In [6]:

```
fig = sm.qqplot(residuals,line='r')
```

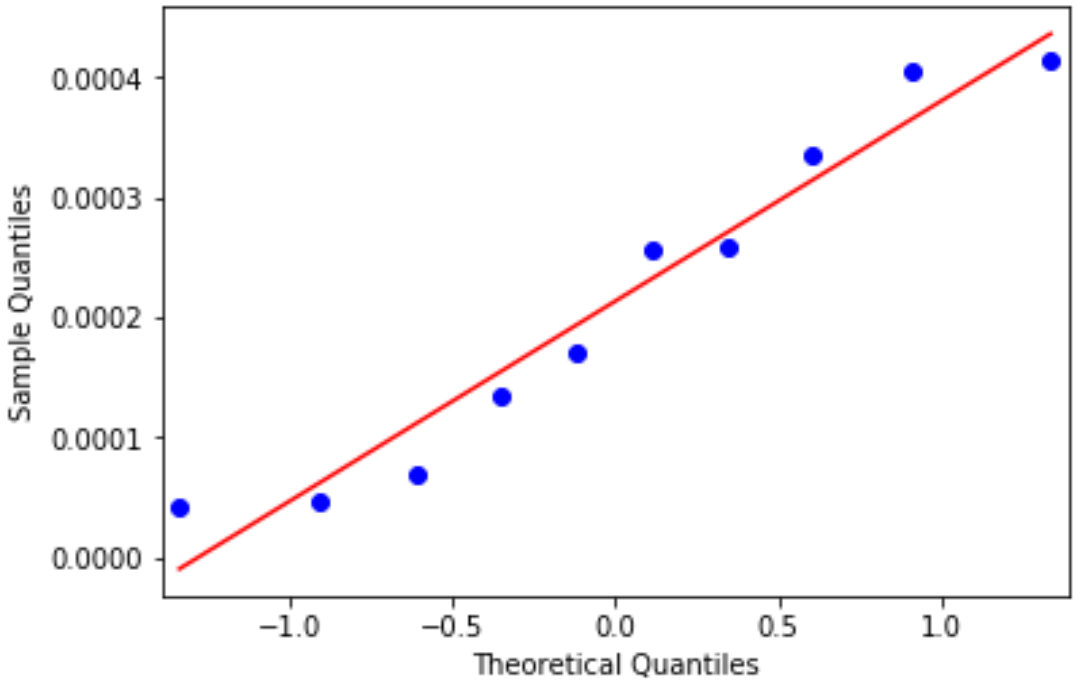

1.6 Pretty plot

In [7]:

```
dGCO_T = Params['exp_data']['T_exp'] * (Params['dGCO_O']/Params['T_O'] +

Params['dHCO']*(1/Params['exp_data']['T_exp']-1/Params['T_O']))

K_CO = np.exp((dGCO_T-
Params['dGCO_O'])/(Params['R']*Params['exp_data']['T_exp']))

X_axis_exp = ( K_CO * Params['K_O2'] * Params['exp_data']['C_CO'] *
Params['exp_data']['C_O2'] /
        (1 + K_CO * Params['exp_data']['C_CO'] + Params['K_O2'] *
Params['exp_data']['C_O2'])**2)

plt.plot(X_axis_exp,Params['exp_data']['r_exp'],'x')

# Model

T =
np.linspace(min(Params['exp_data']['T_exp']),max(Params['exp_data']['T_exp
']),
                int(max(Params['exp_data']['T_exp'])-
min(Params['exp_data']['T_exp'])+1))  # new list of temperature range

dGCO_T = T * (Params['dGCO_O']/Params['T_O'] + Params['dHCO']*(1/T-
1/Params['T_O']))

K_CO = np.exp((dGCO_T-Params['dGCO_O'])/(Params['R']*T))

k = A_opt * np.exp(-Ea_opt/((Params['R'])*T))
```

```
C_CO_list = [0.15,0.5,0.7]
C_O2_list = [0.18,0.6,0.84]

for C_CO_i,C_O2_i in zip(C_CO_list,C_O2_list):
    r_plot = (k * K_CO * Params['K_O2'] * C_CO_i * C_O2_i /
        (1 + K_CO * C_CO_i + Params['K_O2'] * C_O2_i)**2)
    x_axis = (K_CO * Params['K_O2'] * C_CO_i * C_O2_i /
        (1 + K_CO * C_CO_i + Params['K_O2'] * C_O2_i)**2)

    plt.plot(x_axis,r_plot)
```

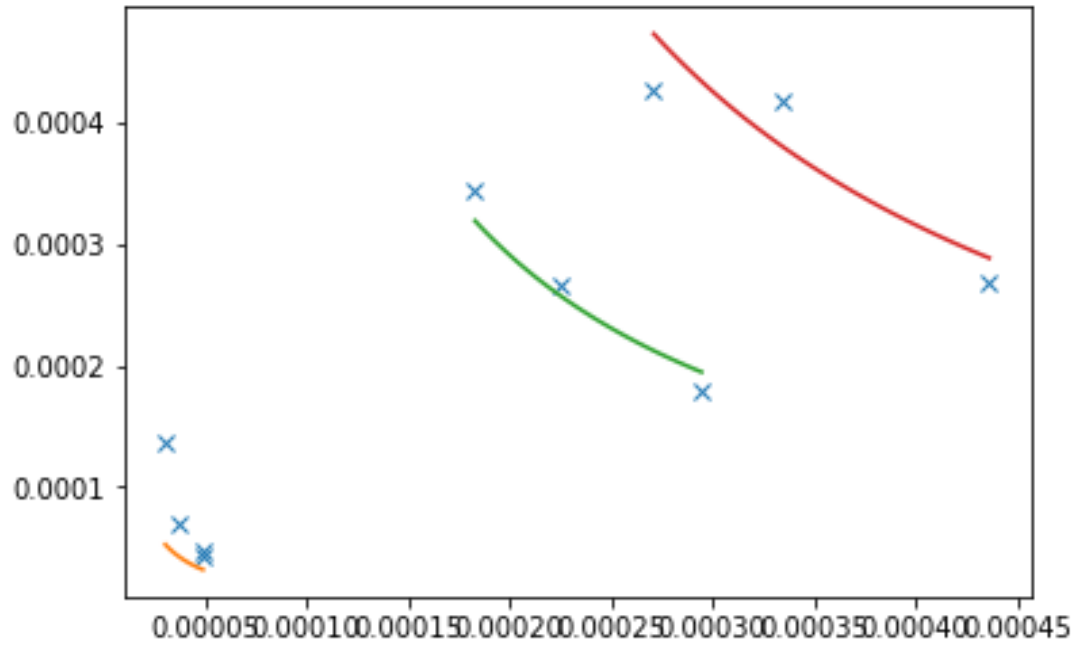

2.0 Bootstrapping

In [8]:

```
import random

exp_data_save = copy.deepcopy(Params['exp_data'])

N = 10000
L = len(exp_data_save['T_exp'])

sample_size = 20
# Regression fails more often if # of unique data points is too low due to
resampling thus sample size > population
# Be careful not to get too large as weighting on points will not be
randomised!

raw_inx = list(np.linspace(0,L-1,L))
raw_inx = [int(j) for j in raw_inx]

A = np.ones(N)
```

```
Ea = np.ones(N)
r_modelled = np.ones((N,sample_size))
r_exp_array = np.ones((N,sample_size))

for i in range(N):
    Params['exp_data'] = exp_data_save.sample(sample_size,replace = True)

    pars, pcov = curve_fit(wrapper, Params['exp_data']['T_exp'],
                                    Params['exp_data']['r_exp'],
                           p0 = [A_opt,Ea_opt], method = 'lm', maxfev =
10000)

    # saving data

    A[i] = pars[0]
    Ea[i] = pars[1]

    r_modelled[i] = gen_r(Params['exp_data']['T_exp'], pars[0],
pars[1],Params)
    r_exp_array[i] = Params['exp_data']['r_exp']

df = pd.DataFrame(Ea,columns = ['Ea'])
df['A'] = A

df = pd.DataFrame(Ea,columns = ['Ea'])
df['A'] = A
# df['r_model'] = r_modelled
# df['r_exp'] = r_exp_array
df2 = df.sort_values('Ea').reset_index().drop(columns = "index")
Ea_min = df2.loc[int(N*0.05)]['Ea']
Ea_max = df2.loc[int(N*0.95)]['Ea']

df3 = df.sort_values('A').reset_index().drop(columns = "index")
A_min = df2.loc[int(N*0.05)]['A']
A_max = df2.loc[int(N*0.95)]['A']

print('Ea = [',round(Ea_min,2),round(Ea_max,2),'] kJ/mol \n',
      'A  = [',round(A_min,2),round(A_max,2),'] mol(g_cat.min)')

# print(round(np.median(Ea),2), '±', round(abs(Ea_min-
Ea_max)/2,2),'kJ/mol')
# print(round(np.median(A),2), '±', round(abs(A_min-
A_max)/2,2),'mol(g_cat.min)')
```

```
Ea = [ 47.25 64.77 ] kJ/mol
 A  = [ 3344.17 67056.9 ] mol(g_cat.min)
```

2.1 Nice 3d histogram

In [9]:

```
df = pd.DataFrame(Ea,columns = ['Ea'])
df['A'] = A
df = df[df['A']<0.3*10**5]
```

```
df = df[df['A']>3000]
df = df[df['Ea']<60]
df = df[df['Ea']>45]
import scipy.io
scipy.io.savemat('E:/WinPython/notebooks/MATLAB/MATLAB', mdict={'arr':
[df['A'],df['Ea']]})
```

Unfortunately 3d histograms are not available in python so matlab was used with the following script:

```
load('MATLAB.mat') arry = arr'; arry(:,1) = log10(arry(:,1));
hist3(arry,'CDataMode','auto','FaceColor','interp','nbins',[30,30])
ylabel('Activation Energy, Ea [kJ/mol]', 'FontSize', 16,
'FontWeight', 'bold', 'FontName', 'Calibri') xlabel('Pre-
exponential, A [log_{10}(mol/(g_{cat}.min))]', 'FontSize', 16,
'FontWeight', 'bold', 'FontName', 'Calibri') zlabel('Observations',
'FontSize', 16, 'FontWeight', 'bold', 'FontName', 'Calibri')

axis([3 5 40 66 1 600 ]) set(get(gca,'ylabel'),'Rotation',-5);
set(get(gca,'xlabel'),'Rotation',62); view([-77 40])

set(get(gca,'XAxis') , 'FontSize', 16)  set(get(gca,'YAxis') ,
'FontSize', 16)  set(get(gca,'ZAxis') , 'FontSize', 16)
```

This should work in octave also

In [10]:

```
# plt.semilogx(A,Ea,'x')
plt.plot(A,Ea,'x')
plt.axis([3000,0.8*10**5,45,70])
plt.xlabel('Pre-exponential, A')
plt.ylabel('Activation Energy, Ea, kJ/mol')
plt.show()
```

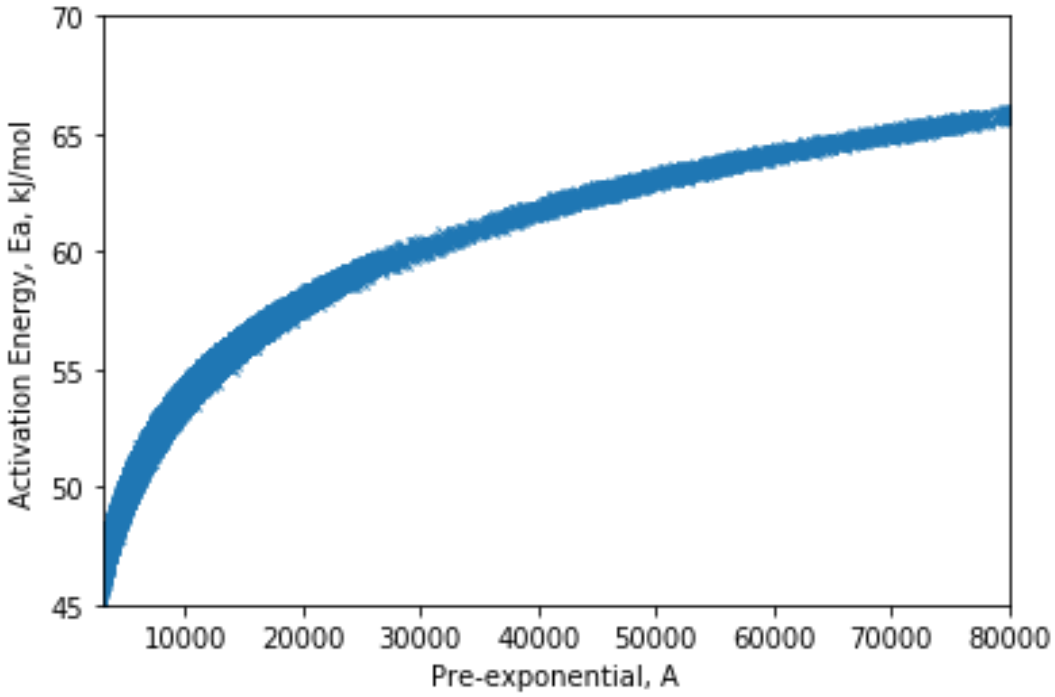

2.2 Calculating percentage of data

In [11]:

```
df = pd.DataFrame(Ea,columns = ['Ea'])
df['A'] = A
df = df[df['A']<0.8*10**5]
df = df[df['A']>3000]
df = df[df['Ea']<70]
df = df[df['Ea']>45]

print(round(len(df['A'])/N * 100,2),'%')
```

```
92.42 %
```

2.3 Top down heat map

In [12]:

```
df = df[df['A']<0.3*10**5]
df = df[df['A']>1000]
df = df[df['Ea']<70]
df = df[df['Ea']>45]
plt.hist2d(df['A'],df['Ea'],bins=50)
# plt.axis([100,10**7,50,70])
plt.show()
print(round(len(df['A'])/N * 100,2),'%')
```

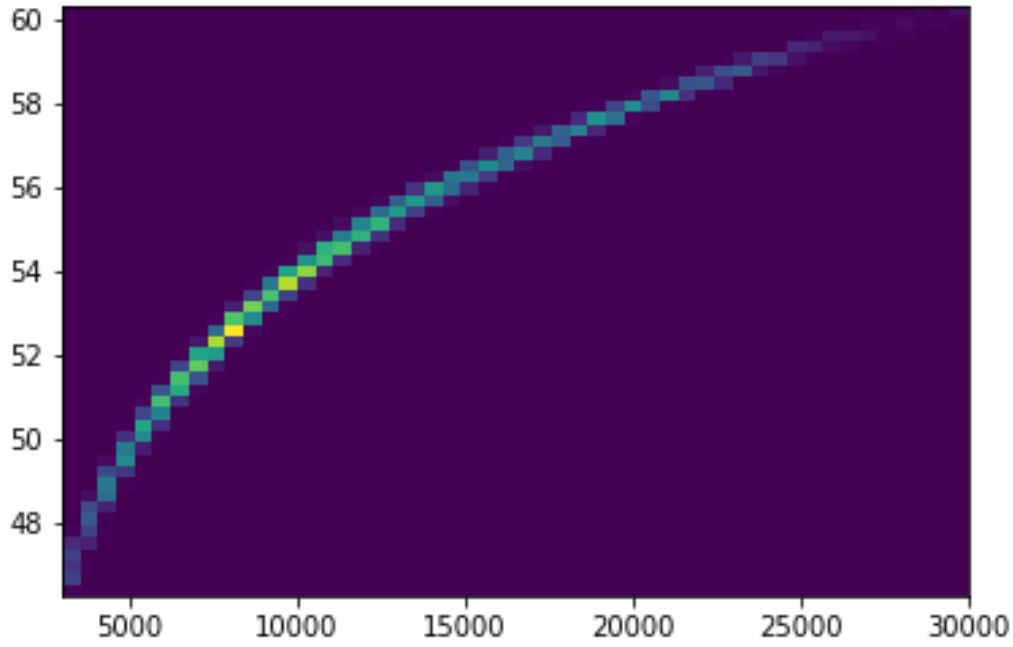


```
84.34 %
```

2.4 r-r plot (experimental vs modelled)

In [13]:

```
plt.plot(r_exp_array,r_modelled,'x')
plt.xlabel('experimental')
plt.ylabel('modelled')
# plt.axis([0,5e-4,0,5e-4])
ax = plt.axes()
x = np.linspace(*ax.get_xlim())
plt.plot(x, x)

plt.plot(Params_OG['exp_data']['r_exp'],Params_OG['exp_data']['r_exp'],'x'
,linewidth=100)
plt.show()
```

```
E:\WinPython\python-3.5.4.amd64\lib\site-
packages\matplotlib\cbook\deprecation.py:107:
MatplotlibDeprecationWarning: Adding an axes using the same arguments as a
previous axes currently reuses the earlier instance.  In a future version,
a new instance will always be created and returned.  Meanwhile, this
warning can be suppressed, and the future behavior ensured, by passing a
unique label to each axes instance.
  warnings.warn(message, mplDeprecation, stacklevel=1)
```

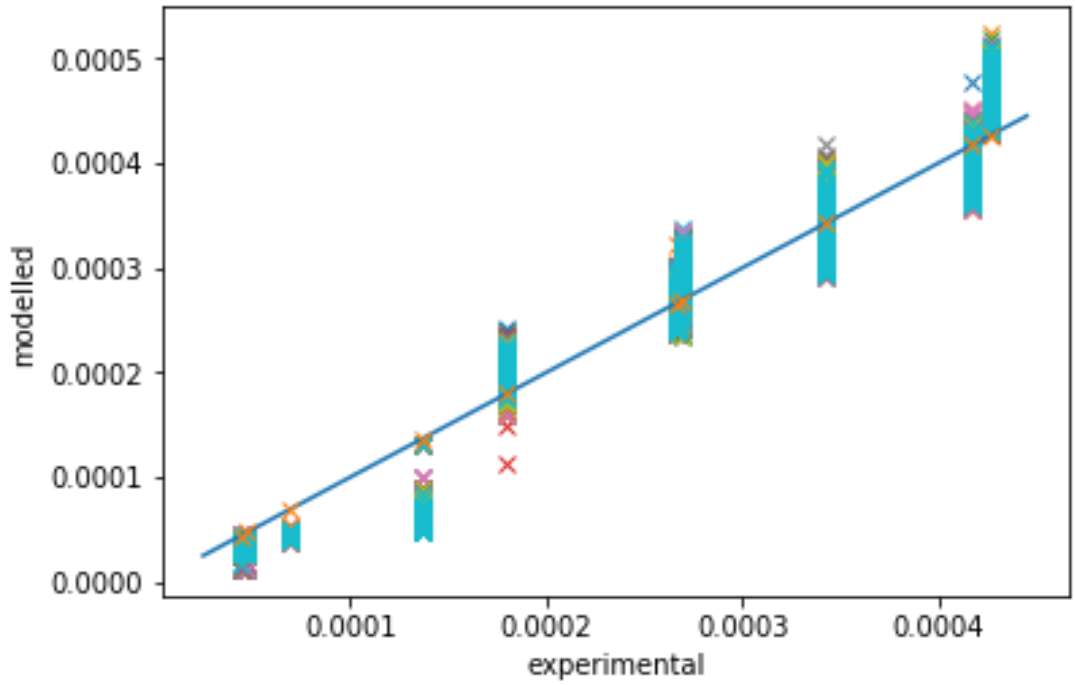

2.5 residual check for bootstrapping

In [14]:

```
res = (r_exp_array - r_modelled).ravel()

W,p = ss.shapiro(res)

if p > 0.05:
    print('p value is: ',round(p,3),' > 0.05, thus according to Shapiro -
Wilk test the residuals are normally distributed')

mu = np.mean(res)
sig = np.std(res)

x = np.linspace(mu - 3*sig  ,mu + 3*sig , 5000)

y_pdf = ss.norm.pdf(x, mu, sig)

plt.hist(res, density = True)
plt.plot(x,y_pdf)
plt.show()

E:\WinPython\python-3.5.4.amd64\lib\site-
packages\scipy\stats\morestats.py:1653: UserWarning: p-value may not be
accurate for N > 5000.
  warnings.warn("p-value may not be accurate for N > 5000.")
```

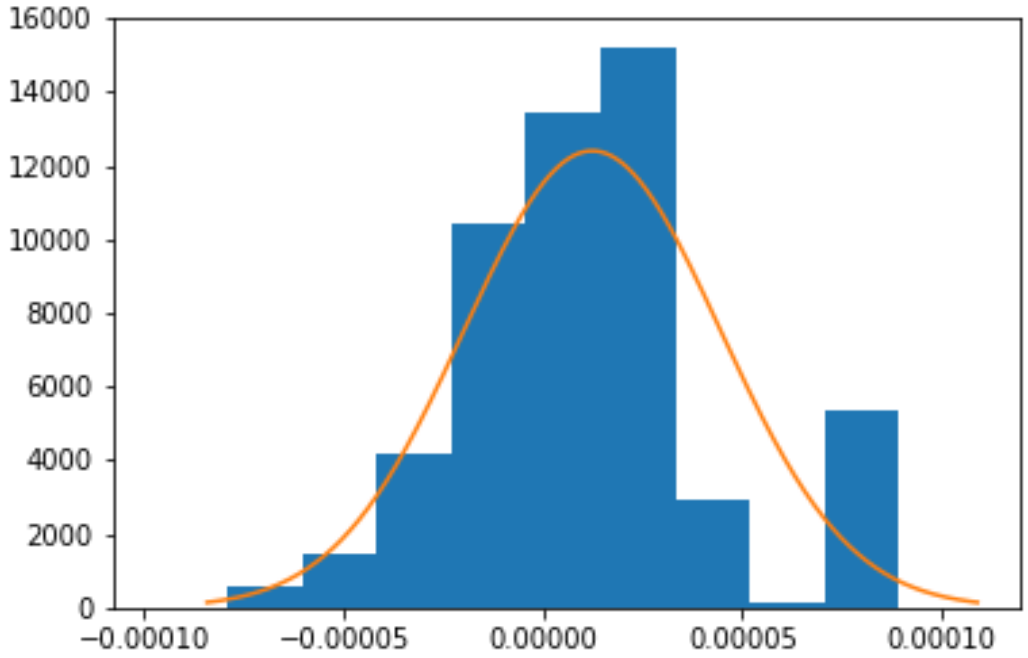

References of APPENDIX F

1. Wang, K. and P. Zhong, *A kinetic study of CO oxidation over the perovskite-like oxide LaSrNiO4.* Journal of the Serbian chemical society, 2010. **75**(2): p. 249-258.
2. *National Institute of Standards and Technology*. Available from: http://webbook.nist.gov/.